MICROWAVE SYNTHESIZED RUTHENIUM ANTIMONY OXIDE-GRAPHENE NANOCOMPOSITE MATERIALS FOR ASYMMETRIC SUPERCAPACITORS

by

PRECIOUS IDINMA EKWERE

BSc. Chemistry (Abia State University), MSc. Chemistry (University of Calabar)

A thesis submitted in fulfilment of the requirements for the degree of

PHILOSOPHIAE DOCTOR

in the

Department of Chemistry

Faculty of Science University of the Western Cape, Cape Town, South Africa

Supervisor: Prof. Emmanuel Iwuoha

Co-supervisor: Dr. Chinwe Ikpo

March 2022

ABSTRACT

With the rapid rise in energy demand and ever-escalating environmental hazards, the need for transition from fossil fuel to renewable energy sources is of paramount importance, requiring better and efficient energy storage devices such as supercapacitors. Supercapacitors are energy storage devices with high power density and long cycle life, but relatively low energy density when compared to batteries. New and advanced electrode materials are required to improve the energy density requirements of next-generation supercapacitors. However, the search for new types of active materials to be used as supercapacitors' electrodes continues to be a tough challenge. Herein, ruthenium antimony oxide (RuSbO) and ruthenium antimony oxide graphene (RuSbO-G) were synthesized via the microwave-assisted method for the first time and tested as a possible electrode material for an asymmetric supercapacitor. Graphene oxide prepared by modified Hummer's method was exfoliated at low temperature and used for the synthesis of RuSbO-G. The successful formation of RuSbO and graphene-incorporated RuSbO were confirmed from X-ray diffraction patterns, which revealed that RuSbO has an orthorhombic crystalline structure with an average crystallite size of 37.30 nm, whereas RuSbO-G crystallite size was calculated to be 36.33 nm. X-ray photoelectron spectroscopy confirmed the presence of the elements Ru, Sb and O in the RuSbO nanomaterial. The high-resolution Ru 3d scan of RuSbO was split into two peaks at 284.5 and 280.1 eV. This indicates the presence Ru_3 d5 (Ru, RuO_2), as confirmed by the FTIR analysis. Asymmetric supercapacitors of RuSbO and RuSbO-G were fabricated with activated carbon in 1 M Li_2SO_4 electrolyte. The result showed that the ternary compound RuSbO had a capacitance of 26.09 F g^{-1} at 0.2 A g^{-1} current density, which resulted in an energy density of 11.74 W h kg^{-1} at a power density of 800 W kg^{-1} at 0.2 A g^{-1} current density. The device maintained 82% capacitance retention, and 100% Columbic efficiency after 4800 cycles. With the incorporation of graphene, the RuSbO-G electrode exhibited rapid electron and ion transport rates and a large electroactive surface area, due to the novel nanocomposite structures and resulting maximized synergistic effect between RuSbO and highly conductive graphene. As a result, the RuSbO-G had a higher capacitance of 129.71 F g^{-1} at 0.2 A g^{-1} current density. The resulting energy density was 58.32

W h kg^{-1} at a power density of 800 W kg^{-1}, the device maintained a higher energy density of 18.2 W h kg$^{-1.}$ at a high-power density of 7200 W kg^{-1}. After over 4900 charge-discharge cycles, the device maintained a better capacitance retention of 96% and 100% Columbic efficiency. This study turns a new research light on RuSbO-based materials as an energy storage material for supercapacitors. Other nanomaterials reported in this work are graphene, ruthenium oxide (RuO), antimony oxide (SbO), ruthenium oxide graphene (RuO-G) and antimony oxide-graphene (SbO-G), as efficient electrodes for asymmetric supercapacitors.

UNIVERSITY *of the*
WESTERN CAPE

ABBREVIATIONS

AC   Activated carbon

ASCs   Asymmetric supercapacitors

CDs   Carbon dots

CNF   Carbon nanofibre

CNTs   carbon nanotubes

CPE   Constant phase element

CQD   Carbon quantum dot

Cs   Specific capacitance

CV   Cyclic voltammetry

CVD   Chemical vapour deposition

ED   Energy density

EDLCS   Electrochemical double-layer capacitors

EDS   Energy dispersive X-ray spectroscopy

EIS   Electrochemical impedance spectroscopy

ERG   Electrochemically reduced graphene

ESR   Equivalent series resistance

FTIR   Fourier transform infra-red spectroscopy

GCD	Galvanostatic charge discharge
GO	Graphene oxide
GQD	Graphene quantum dot
HRSEM	High-resolution scanning electron microscopy
HRTEM	High-resolution transmission electron microscopy
MWNTs	Multiwalled carbon nanotubes
NS	Nanosheets
NP	Nanoparticles
PD	Power density
R_{ct}	Charge transfer resistance
RuSbO-G	Ruthenium antimony oxide-graphene
RGO	Reduced graphene oxide
SC	Supercapacitor
SCs	Supercapacitors
SEM	Scanning electron microscopy
SS-NMR	Solid-state nuclear magnetic resonance spectroscopy
SWCNTs	Single-walled carbon nanotubes
TEM	Transmission electron microscopy

WS   Warburg short component

XRD   X-ray diffraction spectroscopy
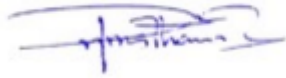
DECLARATION

I hereby declare that "**Microwave synthesized ruthenium antimony oxide-graphene nanocomposite materials for asymmetric supercapacitors",** is my work and it has not been submitted before for any degree or examination in any other university, and all the sources I have used or quoted have been indicated or acknowledged by way of complete references.

Precious Ekwere

Signed: **Date: 01/03/2022**

DEDICATION

This thesis is dedicated to God Almighty, my beloved parent Mr and Mrs Nathaniel Onuigwe, and

my Lovely trio: Etido, Jed and Jamin Ekwere.

ACKNOWLEDGEMENTS

At last!!! What used to be my dream is now my reality and I cannot vividly express the feeling of satisfaction and fulfilment that this major milestone has brought me. First and foremost, all glory be to God who is and always will be my greatest source of strength and inspiration. Consequent upon this, I do wish to appreciate the following individuals for their unflinching support throughout the period of my PhD program.

I will forever be in debts of eternal gratitude to my supervisor, **Prof Emmanuel Iwuoha**, for the opportunity he gave me to be under his mentorship. Being under his supervision was at the topmost range of all my privileges. I never would have been more blessed to have been guided and supervised by one of the finest minds in this field of academic research. He gave me unfettered access to drink from the wealth of his knowledge and pointed me in the right direction. I am deeply grateful for the rare access and opportunity you gave me to research with SensorLab (University of the Western Cape Sensor Laboratories), an opportunity I will never take for granted. From the depths of my heart to the integrity of my spirit, I am grateful. May God in his wisdom reward you.

This acknowledgement will be incomplete if I don't recognize the many contributions of my co-supervisor **Dr Chinwe Ikpo** thank you for being so selfless in pouring out your wealth of experience you were not only a co supervisor but also a sister and friend. I am exceptionally grateful for the technical tools you introduced me to, that made my life easier. Thank you for being so kind and generous with your advice, thank you for all the words of encouragement you gave, I am eternally grateful, may God reward you abundantly. To **Dr Miranda Ndipingwi** you are such an accommodating person and very willing to share knowledge, thank you for all the support, advice and mentorship. I would never have asked for any better than what you freely gave. You can always be assured of my deepest gratitude God bless you.

My sincere appreciation goes to my husband **Etido Ekwere and my boys Jed and Jamin** - thank you for the love, support and all the sacrifices you made within this period, letting me be away for so long to pursue my dreams is a privilege I will never take for granted.

To my **parents my beloved sisters and brothers**, you gave so much of your resources, time, sacrifices and commitment to see me through this program. I have a lot to admire you all for. Truthfully, your sacrifice and love brought me this far.

And finally, to the entire **SensorLab family**; Professor Priscilla Baker, Professor Ajayi Fanelwa, Dr Natasha Ross, Dr Candice Franke, and Dr Tesfaye Waryo thank you for the academic assistance and support rendered throughout my stay in Sensorlab. To my wonderful colleagues and friends; Onyinyechi Uhuo, Kelechi Nwambaekwe, Dr. Sodiq Yusuf, Siyabonga Mduli, Emmanuel Ramoroka, Dr Masikini, Dr Christopher Sunday, Hyelom Hiluf, Kaylin Januarie, Kelvin Tambwe, Shane Willenberg, Dhielnawaaz Abrahams, Dr Anne Djoumessi, Dr Samantha Douman, Miss Vanesa, and Kedibone Moganedi; thank you all for being so wonderful and supportive, I have built relationships and friendships that will last a lifetime.

LIST OF PUBLICATIONS

1. Memela, Muziwenkosi, Usisipho Feleni, Siyabonga Mdluli, Morongwa E. Ramoroka, **Precious Ekwere**, Samantha Douman, and Emmanuel Iwuoha. "Electro-photovoltaics of polymer-stabilized copper–indium selenide quantum dot." *Electroanalysis* 32, no. 12 (2020): 3086-3097.

2. Nwambaekwe, Kelechi C., Vivian John-Denk, Samantha F. Douman, Penny Mathumba, Sodiq T. Yussuf, Onyinyechi V. Uhuo, **Precious I. Ekwere**, and Emmanuel I. Iwuoha. "Crystal engineering and thin-film deposition strategies towards improving the performance of kesterite photovoltaic cell." *Journal of Materials Research and Technology* 32, (2021): 1252-1287.

3. Tumiso E. Mbokela, Assumpta C.Nwanya, Miranda M. Ndipingwi, Sinethemba Kaba, **Precious Ekwere**, Shane T. Werry, Chinwe O. Ikpo, Kwena D. Modibane and Emmanuel I. Iwuoha "Review-Recent advances on high-capacity Li ion-rich Layered manganese oxide cathodes" *Journal of Electrochemical Society*, Volume168. No 7 (2021): 1945-7111

4. **Precious I. Ekwere**, Chinwe O. Ikpo, Emmanuel I. Iwuoha, Platinum group metals based carbonaceous composite materials for supercapacitors **(Manuscript Prepared for Journal of Energy Storage)**

5. **Precious I. Ekwere**, Chinwe O. Ikpo, Emmanuel I. Iwuoha, Graphene incorporated antimony oxide nanomaterial-a new material for asymmetric supercapacitors **(Manuscript Prepared for Journal Energy Conversion and Management)**

6. **Precious I. Ekwere**, Chinwe O. Ikpo, Emmanuel I. Iwuoha, Graphene stabilized ruthenium antimony novel nanomaterial for asymmetric supercapacitor **(Manuscript Prepared for Journal Energy Conversion and Management)**

7. **Precious I. Ekwere**, Chinwe O. Ikpo, Emmanuel I. Iwuoha, Ultra-small ruthenium oxide graphene composite for asymmetric supercapacitors **(Manuscript Prepared for Journal Energy Conversion and Management)**

LIST OF CONFERENCES

1. **Precious I. Ekwere,** Chinwe O. Ikpo, Emmanuel I. Iwuoha, Electrochemistry Graphene stabilized ruthenium antimony oxide. 5th international Symposium on Electrochemistry titled "Electrochemistry at Nanostructured Interfaces". University of the Western Cape, Bellville, South Africa, 11-14th August 2019. **Oral presentation**

2. **Precious I. Ekwere,** Raquel Caballero, Jose M. Merino, Ruthenium antimony oxide novel material for Ultra-Efficient Supercapacitor. Annual Workshop of Young Researchers. Universidad Autonoma de Madrid, Madrid, Spain, 18 November 2019. **Oral presentation**

TABLE OF CONTENT

LIST OF FIGURES

http://etd.uwc.ac.za/

LIST OF TABLES

CHAPTER ONE

Chapter Overview

This chapter discusses, the general energy crises and the role energy storage devices must play for a successful transition from non-renewable to renewable sources of energy. The different energy storage devices were significantly captured, and their energy and power densities were compared. The chapter also introduced the general properties of ruthenium and antimony, highlighting their attractive properties and drawbacks. Lastly, the research motivation, aims, objectives and outline were discussed.

1.1 INTRODUCTION

1.1.1 Background

As the world's population which currently stands at 7.8 billion continues to increase at a projected rate of 1% annually [1,2], the consumption of energy will also increase. The acceleration in world energy consumption driven majorly by an increase in the demand for electricity and gas skyrocketed by 2.8% in 2018 against 1.8%, which was the average trend in previous years [3]. As a result of the current growth trend, the energy sector has undergone a major shift from predominantly conventional fossil fuel to other renewable, clean and eco tolerant energy sources like wind, hydro and solar [4-7]. The world's production of energy stands at a 2.8% growth in 2018 above its historical trend, with a corresponding increase in the growth of renewable energy which has been rising quickly since the year 2000. In 2018, an average 1% increase in renewable energy sources was recorded which is about 26% contribution, a significant increase from the 19.3% in 2015 [8]. This shift can be chiefly attributed to the cost and environmental hazards associated with using fossil fuel and coal as seen in 2017, where energy-related CO_2 emissions grew by 2.1% and 1.9% in 2018. Renewable energy, on the other hand, is clean, cheap and can satisfy our energy demand however, its intermittent nature makes it not so effective. The sun does not shine all the time, and the places where the strongest wind blows is in the less populated areas. However, the densely populated areas are where energy is needed. Therefore, to maximize the use of renewable energy sources, energy storage devices are required to work optimally.

1.1.2 The need for electrochemical energy devices

Energy storage device are needed if the world is to successfully transition from non-renewable to renewable energy sources. Since renewable energy sources are intermittent, storage devices are essential for storing energy generated when supplies are plentiful and transmitting them to the power grid when supplies are low, due to natural occurrences. Furthermore, although the transition to renewable energy sources will be costly at first, it will be cheaper and more environmentally sustainable in the long run if reliable energy storage devices are available. Electrochemical (EC) energy storage systems are currently in use and are being studied for future improvements. If adequately built to be viable and meet environmental requirements, these storage devices can effectively pass as alternative energy/power sources.

1.1.3 Overview of energy storage systems

Electrical energy storage systems may be categorized based on the mechanism by which they store their charges. These types are also classified into chemical energy storage and conversion (e.g. water splitting, fuel cells), mechanical energy storage (e.g. flywheels), thermal and thermochemical energy storage (e.g. solar thermal energy), electrical energy storage (e.g. physical capacitors, double-layer electrical capacitors) and electrochemical energy storage devices (e.g. pseudocapacitors, batteries). Electrochemical energy storage is a system used to store electrical energy in the form of chemical energy. The stored energy may be discharged in the form of electricity, as in the case of rechargeable devices, where electrical energy is converted to chemical energy during charging and chemical energy is converted back to electrical energy

during discharging. The three most significant EC systems available are batteries, supercapacitors, and fuel cells. They are also the most researched and are configured alike. However, the process by which the charge is stored, and the electrode materials used for charge storage are distinct.

Batteries are a very intriguing group of energy storage devices, consisting typically of two electrodes separated by an electrolyte. A battery typically stores its energy generated via electrochemical reactions, in the crystal lattices of electrode materials with good porosity via chemical bonds and convert the chemical energy into direct current electricity via redox reactions, by the intercalations as with lithium-ion batteries. In the battery storage mechanism, the energy is stored in a compound or compounds that make up the positive and negative electrodes, as well as the electrolytes. Li-ion battery is currently used extensively for our everyday electronic devices and has huge potential for powering electric vehicles. They would be no 'today's mobile world' without lithium-ion batteries, as all electronic mobile gadgets, ranging from laptops, mobile phones and cameras to electric cars, depends on lithium-ion batteries for power supply. Today, lithium-ion batteries have doubled their energy density and are ten times more cost-effective, than the first Li-ion battery brought to the market by Sony in 1991.

Fuel cells are energy conversion devices that directly convert chemical energy from fuel, efficiently to electrical energy. They are different from batteries and supercapacitors (energy storage devices) in that they require a continuous supply of fuel and oxygen usually from the air,

which is the oxidizing agent. Thus, they produce electricity continuously if the fuel and oxygen do not go out of supply. A fuel cell typically consists of an anode, a cathode, and an electrolyte. Its working mechanism can be generally described as follows; at the anode, catalytic oxidation of the fuel takes place converting the fuel which is most times hydrogen to a proton and an electron. The electrolyte is designed so that protons can pass through it, therefore, the proton travels through it to the cathode while the electron is forced to travel through a load to the cathode thus supplying electricity to the load as they go through. At the cathode, another catalyzed reaction takes place where the electrons recombine with the proton and another element, usually oxygen, giving up water. Thus, the cell generally consumes fuel, produces electricity and gives water as its by-product.
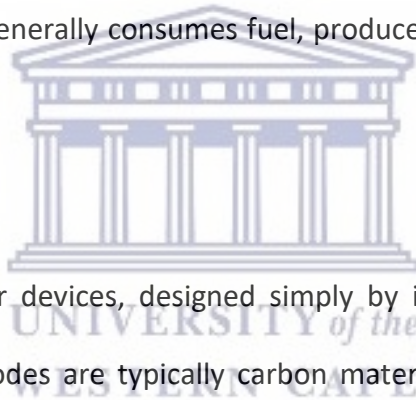
Supercapacitors are high power devices, designed simply by inserting two electrodes in an electrolyte solution. The electrodes are typically carbon materials with massive surface area capable of holding charge merely by physical attraction in the electrochemical double layer, which is formed by the contact the electrode makes with the aqueous electrolyte. Supercapacitors that use this mechanism to store charges are called, electrochemical double-layer capacitors (EDLCs) [9], The whole charge process takes place at the phase boundary between the electrode and electrolyte surface, thus they can be charged and discharged within seconds. Also, because the charging process is physical, they are hardly degraded. As a result, EDLCs have a remarkably high cycle life (>1,000,000,000). This has informed their usage in numerous applications requiring quick charge-discharge. For example, powering hybrid electric vehicles, military equipment's, portable electronic equipment, memory backup systems and

implantable devices [5]. A second mechanism with which supercapacitors stores their charge is by fast faradaic reaction happening at the electrode surface of metal oxide and conducting polymers giving rise to a pseudocapacitance [10]. Ruthenium oxide is one of the most widely used pseudocapacitor electrode material, with very high theoretical capacitance.

The three most important parameters used as tools of comparison between one type of energy storage device to another are; energy density, power density and cycle life [11-13] [9]. The energy density of batteries is higher than that of supercapacitors this means that a given mass of battery will hold more charge than the same mass of a capacitor or even supercapacitors. While the power density of supercapacitors is higher than those of batteries, as a result, supercapacitors release energy faster than batteries. The lifecycle of a supercapacitor is typically longer than those of batteries. Supercapacitors can go through millions of charge-discharge cycles, whereas batteries would only go several thousand. These variations are owing to the mechanism by which they store charges as will be explained in the next chapter.

1.2 Problem statement

Ruthenium oxides are the most widely researched pseudocapacitive electrode material [13-18]. In addition to the low cyclability of ruthenium oxides due to its charge storage mechanism, which involves ion insertion/de-insertion in a fast surface Faradaic process. They are also hampered by nanoparticle agglomeration, intrinsically low electron-proton transport, and weak conductivity between nanoparticles. As a result, the actual experimental specific capacitances are usually

lower than the calculated value. Antimony metals are gradually gaining popularity in sodium/ lithium (Na/Li) ion batteries as efficient anode material [20-21]. Its compounds have been tried for supercapacitor applications severally, however, the major drawback for antimony is its volume expansion resulting in reduced stability, a possible reason why it has not gained so much attractiveness, despite its high calculated capacity of charge storage. Graphene is a one layer thick, two-dimensionally (2D) structured macromolecule with an impressively massive surface area (2600 m^2 g^{-1}) [22-23]. The intrinsic capacitance of single-layer graphene has been reported to be ~21 $\mu F/cm^2$, thus ECs based on graphene material can theoretically attain a capacitance of ~550 F g^{-1} if their entire surface is used. One of the biggest drawbacks of graphene is agglomeration during synthesis, once this happens, the unique property of the 2D form of graphene is lost with its ultrahigh high surface area and replaced by agglomerated graphene sheets, which are no different from the regular graphite with relatively low surface area [24].
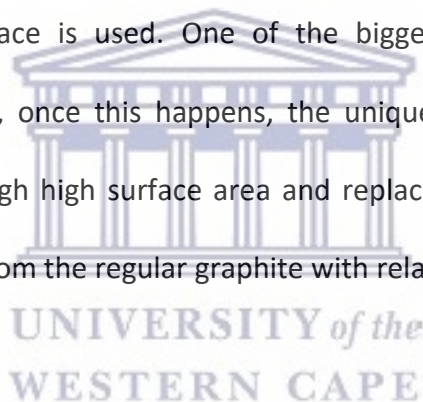
1.3 Hypothesis and motivation for the study

Presently, RuO_2 is known as the best supercapacitor electrode material owing to its reversible redox features, wide potential window, good electrical conductivity (~105 S cm^{-1}), good cycle life and high theoretical capacitance [25-26] (1450 F g^{-1} for RuO_2 and 1360 F g^{-1} for $RuO_2.0.5$ H_2O) based on the reversible Faradaic process. Ruthenium oxides have 3 distinct oxidation states within 1.2 V and undergo fast reversible electron transfers and an electro-sorption of protons on the surface of RuO_2 particles. Antimony compounds have been tried for supercapacitor applications severally. Metal alloys have been found to make an improved capacitive material

because of the availability of more sites for redox activities, therefore the binary composite of ruthenium/antimony metal is proposed to be a suitable pseudocapacitive material. The major drawback for antimony is its volume expansion resulting in reduced stability. They are also hindered by; serious agglomeration of their nanoparticles, intrinsically low electron-proton transport, and weak conductivity between nanoparticles. As a result, the actual experimental specific capacitances are usually lower than the calculated value. To effectively circumvent the above issues, much attention has been focused on developing a hybrid electrode, which will combine a metal oxide with sustainable and cheap high specific surface area carbon material, such as graphene. The use of carbon material such as graphene has been found to provide stability, by acting like a mechanical buffer that will reduce the volume change, while facilitating electron transport during the charge-discharge process, thus maintaining the electrode microstructure and conductivity.
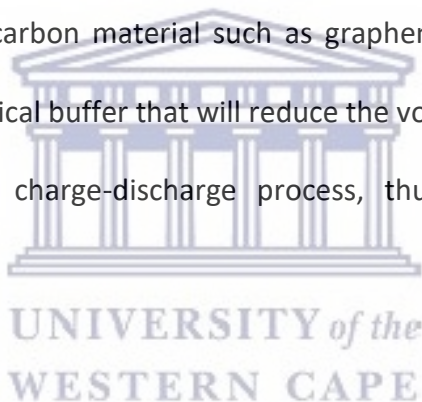
Graphene can be an ideal electrode material, because of its high theoretical surface area and other distinctive properties. However, for graphene to maintain a landmark performance as a supercapacitor electrode material, it must firstly, maintain its large and accessible surface area which will result in sizeable charge capacity accounting for high areal and volumetric capacitance. Therefore, the introduction of RuSbO could act as spacers, enabling graphene to maintain its 2D structure.

1.4 Research aim and objective

This research work was aimed at producing improved electrode materials for high-performance supercapacitors. This was achieved by fabricating graphene// activated carbon (AC), AC//RuO, AC//RuO-G, AC//SbO, AC//SbO-G, AC//RuSbO and AC//RuSbO-G and their electrochemical properties investigated in 1 M Li_2SO_4 electrolytes over a 0 to 1.8 V potential range. The objectives required were:

The synthesis of graphene oxide using the Hummers method.

In-situ reduction of RuO, RuO-G, SbO, SbO-G, RuSbO and RuSbO-G using a microwave-assisted synthesis approach.

Surface, elemental and particle size analysis of the materials by high-resolution transmission electron microscopy (TEM), scanning electron microscopy (SEM) and energy-dispersive X-ray spectroscopy (EDS).

Crystallographic and spectroscopic analysis of the ternary composites by X-ray diffraction (XRD), X-ray photoelectron spectroscopy (XPS), Fourier transform infra-red spectroscopy (FTIR) and solid-state nuclear magnetic resonance spectroscopy (SSNMR).

Electrochemical characterization of graphite, GO, graphene, RuO, RuO-G, SbO, SbO-G, RuSbO and RuSbO-G composite materials and the material dynamics at the electrode surface using cyclic voltammetry (CV), galvanostatic charge/discharge and electrochemical impedance spectroscopy (EIS).
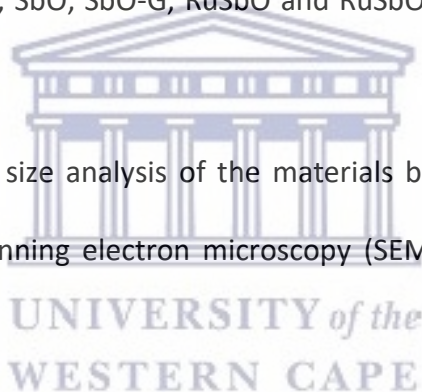
Fabrication of a Swagelok type-cell using graphene, RuO, RuO-G, SbO, SbO-G, RuSbO and RuSbO-G cathode material to determine galvanostatic charge/discharge capacitance profile at different levels.

Chapter 1 covers a brief introduction and background to the research, it also presents the problem statement, hypotheses, and motivation for the research, as well as the research aim and objectives.

Chapter 2 is a comprehensive review on supercapacitors, plus current trends in hybrid electrode material for supercapacitors.

Chapter 3, provides synthesis, characterization and electrochemical properties of graphite graphene oxide and graphene nanomaterial, plus device testing of graphene electrode material.

Chapter 4, provides synthesis, characterization, electrochemical properties, and device testing of RuO and RuO-G electrode material.

Chapter 5, provides synthesis, characterization, electrochemical properties, and device testing of SbO and SbO-G electrode material.

Chapter 6 presents the synthesis, characterization, electrochemical properties and device testing of RuSbO and RuSbO-G electrode material.

Chapter 7 is the conclusion.

1.5 References

[1]   P.D. Wall, Scientists and the CIA, Science 136 (1962) 173–173. https://doi.org/10.1126/science.136.3511.173.

[2]   C. Clark, World Population, Nature 181 (1958) 1235–1236. https://doi.org/10.1038/1811235a0.

[3]   K. Holmberg, P. Kivikytö-Reponen, P. Härkisaari, K. Valtonen, A. Erdemir, Global energy consumption due to friction and wear in the mining industry, Tribol. Int. 115 (2017) 116–139. https://doi.org/10.1016/j.triboint.2017.05.010.

[4]   A. Gigot, M. Fontana, C.F. Pirri, P. Rivolo, Graphene/ruthenium active species aerogel as electrode for supercapacitor applications, Materials 11 (2017) 1–12. https://doi.org/10.3390/ma11010057.

[5]   R. Bolagam, S. Um, L-cysteine-assisted synthesis of ruthenium sulfide/thermally reduced graphene oxide nanocomposites: Promising electrode materials for high-performance energy storage applications, Electrochim. Acta 281 (2018) 571–581. https://doi.org/10.1016/j.electacta.2018.06.004.

[6]   S. Han, F. Hou, X. Yuan, J. Liu, X. Yan, S. Chen, Continuous hierarchical carbon nanotube/reduced graphene oxide hybrid films for supercapacitors, Electrochim. Acta 225 (2017) 566–573. https://doi.org/10.1016/j.electacta.2016.12.159.

[7]   P. Simon, Y. Gogotsi, Materials for electrochemical capacitors, Nat. Mater 7 (2008) 845–854. https://doi.org/10.1038/nmat2297.

[8]   CO$_2$ emissions from fuel combustion | World statistics on CO$_2$ updated | enerdata, (n.d.). https://yearbook.enerdata.net/CO$_2$-fuel-combustion/CO$_2$-emissions-data-from-fuel-combustion.html (accessed April 5, 2020).

[9]   A. Borenstein, O. Hanna, R. Attias, S. Luski, T. Brousse, D. Aurbach, Carbon-based composite materials for supercapacitor electrodes: A review, J. Mater. Chem. A. 5 (2017) 12653–12672. https://doi.org/10.1039/c7ta00863e.

[10]   M.H. Tran, H.K. Jeong, Comparison of ruthenium composites with thermally reduced graphene and activated carbon for supercapacitor applications, J. Mater. Sci. Mater. Electron 28 (2017) 7969–7975. https://doi.org/10.1007/s10854-017-6500-y.

[11]   M. Li, H. He, Nickel-foam-supported ruthenium oxide/graphene sandwich composite constructed via one-step electrodeposition route for high-performance aqueous supercapacitors, Appl. Surf. Sci. 439 (2018) 612–622. https://doi.org/10.1016/j.apsusc.2018.01.064.

[12]   P. Suktha, N. Phattharasupakun, M. Sawangphruk, Transparent supercapacitors of 2 nm ruthenium oxide nanoparticles decorated on a 3D nitrogen-doped graphene aerogel, Sustainable Energy & Fuels 2, no. 8 (2018) 1799–1805. https://doi.org/10.1039/C8SE00177D.

[13]   D. Galizzioli, F. Tantardini, S. Trasatti, Ruthenium dioxide: a new electrode material. I. Behaviour in acid solutions of inert electrolytes, J. Appl. Electrochem. 4 (1974) 57–67. https://doi.org/10.1007/BF00615906.

[14]   M. Ates, C. Fernandez, Ruthenium oxide–carbon-based nanofiller-reinforced conducting polymer nanocomposites and their supercapacitor applications, Polym. Bull. (2018) 1–19. https://doi.org/10.1007/s00289-018-2492-x.

[15]   Y. Guo, W. Zhang, Y. Sun, M. Dai, Ruthenium nanoparticles stabilized by mercaptan and acetylene derivatives with supercapacitor application, MethodsX. 5 (2018) 795–796. https://doi.org/10.1016/j.mex.2018.07.004.

[16]   H. Li, R. Wang, R. Cao, Physical and electrochemical characterization of hydrous ruthenium oxide/ordered mesoporous carbon composites as supercapacitor, Microporous Mesoporous Mater 111 (2008) 32–38. https://doi.org/10.1016/j.micromeso.2007.07.002.

[17]   R.K.V. Prataap, R. Arunachalam, R. Pavul Raj, S. Mohan, L. Peter, Effect of electrodeposition modes on ruthenium oxide electrodes for supercapacitors, Curr. Appl. Phys. 18 (2018) 1143–1148. https://doi.org/10.1016/j.cap.2018.06.015.

[18]   K.Y. Kumar, S. Archana, R. Namitha, B.P. Prasanna, S.C. Sharma, M.S. Raghu, Ruthenium oxide nanostring clusters anchored graphene oxide nanocomposites for high-performance supercapacitors application, Mater. Res. Bull. 107 (2018) 347–354. https://doi.org/10.1016/j.materresbull.2018.08.011.

[19]   T. Cao, Y. Shi, Y. Jiang, N. Cai, Q. Gong, Performance enhancement of liquid antimony anode fuel cell by in-situ electrochemical assisted oxidation process, Energy 125 (2017) 526–532. https://doi.org/10.1016/j.energy.2017.02.106.

[20]   E. Martínez-Periñán, M.P. Down, C. Gibaja, E. Lorenzo, F. Zamora, C.E. Banks, Antimonene: A Novel 2D Nanomaterial for supercapacitor applications, Adv. Energy Mater 8 (2018) 1–8. https://doi.org/10.1002/aenm.201702606.

[21]   S. Chen, R. Ramachandran, V. Mani, R. Saraswathi, Recent Advancements in Electrode Materials for the High- performance Electrochemical Supercapacitors : A Review, Int. J. Electrochem. Sci. 9(8), 4072-4085.

[22]   Y. Wang, Z. Shi, Y. Huang, Y. Ma, C. Wang, M. Chen, Y. Chen, Supercapacitor devices based on graphene materials, The Journal of Physical Chemistry C 113, 30 (2009): 13103-13107. https://doi.org/10.1021/jp902214f

[23]   S. Sengupta, J. Kim, S.D. Kim, Forecasting new features and market adoption of wearable devices using TRIZ and growth curves: Case of fitness tracking products, Int. J. Innov. Technol. Manag. 15 (2018) 1850009. https://doi.org/10.1142/S0219877018500098.

[24]   Y. Yan, T. Wang, X. Li, H. Pang, H. Xue, Noble metal-based materials in high-performance supercapacitors, Inorganic. Chem. Front. 4 (2017) 33–51. https://doi.org/10.1039/c6qi00199h.

[25]   Z.J. Han, S. Pineda, A.T. Murdock, D.H. Seo, K.K. Ostrikov, A. Bendavid, RuO_2-coated vertical graphene hybrid electrodes for high-performance solid-state supercapacitors, J. Mater. Chem. A. 5 (2017) 17293–17301. https://doi.org/10.1039/c7ta03355a.

CHAPTER TWO

Chapter Overview

This chapter focuses on the overview of supercapacitors and their charge-storage mechanism. Emphasis was placed on hybrid electrode materials, and various ways different forms of carbon materials have been combined with ruthenium oxides. Finally, the limitations of these materials are captured, and some of the paths which can be used to improve them for best performance are highlighted.

2.1 INTRODUCTION

The current pattern of development in the energy segment has seen a significant shift from the dominantly regular petroleum product to other sustainable, clean, and eco-friendly energy sources such as wind, hydro and solar. This move is due to natural hazards and costs associated with the use of oil and coal. Renewable energy is clean, modest and can meet our energy demand. However, its accessibility is discontinuous, which makes them unreliable [1]- [2]. To maximize the use of renewable energy sources, storage devices are required to function optimally so that energy can be stored and used on-demand. Existing electrochemical energy storage devices are supercapacitors (also known as ultracapacitors or hybrid capacitors) and batteries [3]. These storage devices can be used as an alternative energy/power source if they are designed appropriately and to meet environmental needs. The conventional Li-ion batteries have a high energy density (ED) but are short in power density (PD) and cycle life relative to the supercapacitor. Supercapacitors, on the other hand, are known for their incredibly high PD and

long cycle life, but they also have a low ED comparatively. This has led to their utilization in various applications requiring speedy charging, such as high-quality electric vehicles, convenient electronic equipment for military hardware, memory reinforcement frames and implantable gadgets [4]. Supercapacitors are either made to have a similar design, i.e. a similar material, these are called symmetrical supercapacitors. Or they are made of materials with different characteristics, called asymmetrical or hybrid supercapacitors. The negative and positive electrodes could be configured with either carbon, Faradic (conducting polymers and metal oxides) or a hybrid material. The make-up of a supercapacitor's electrode material are exceptionally basic, thus to improve the capacitance performance of supercapacitors, fabricating new materials tailored to satisfy high energy storage requirement, is an important angle to focus on [5]. Different approaches have been employed to maximize the performance of electrode materials such as nanostructurisation, increasing the surface area and the use of hybrid materials.
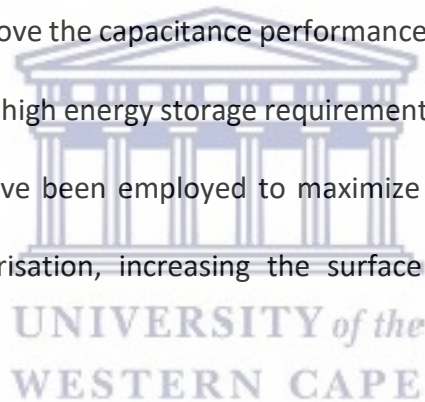
2.1.1 Nanostructurisation;

Materials that are nanostructured, for example nanocrystals, nanorods, nanotubes, nanowires, and quantum dots [6], exhibit improved electronic, magnetic, physical, mechanical, optical, and thermal properties, that make them suitable for several industrial applications [7]. For more than a hundred centuries, researchers have worked on metal nanoparticles, with a major part to evaluate how form, size and shape affect their optical and electrical properties [8]. Innovations

have therefore been developed to see how these properties can be controlled and manipulated for new applications by customizing materials.

2.1.2 Increasing the surface area of electrode material

One of the parameters of supercapacitor electrode material that has been greatly manipulated is the surface area. This is because the capacitance of a capacitor *C* can be mathematically represented as

$$C = \frac{Q}{V}$$
1

where Q is the positive charge stored and V is the applied voltage.

But $\quad C = \varepsilon_0 \, \varepsilon_r \frac{A}{D}$
2

where ε_0 is the free space permittivity (or free space dielectric constant) of the conventional condenser, ε_r is the insulator's permittivity which encloses the electrode. The capacitance of the capacitor C thus is hypothetically linear to the surface area, A of the electrode and inversely to separation D which separates the electrodes. These expressions lead to the belief that the capacitance of a material is largely subject to the measurement of the surface area of the material, and therefore the expansion of the surface area of carbon materials has been seen as the best way to expand the capacitance of EDLCs. However, this view that appeals to 'sound judgment' was negated when, in an experiment, pore sizes larger than two times the size of an electrolyte ion was reduced and, following the reduction, the specific capacitance of the material increased [9]. Today it is crystal clear that there is no linear relationship between a specific
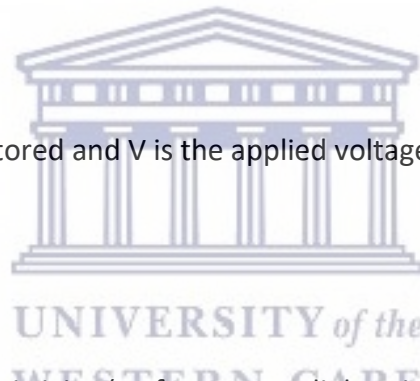
surface area and a specific capacitance, and that the two properties are not directly proportional to each other. Consequently, an increase in one is not necessarily accompanied by an increase in the other. To achieve maximum double-layer capacitance, pores in the material must be near the ionic size in the electrolytes and a significant drop in the capacitance is recorded in situations in which pores are greater or lesser than the size of the ion [10][11]. Although some other research has negated this finding [12], however, it can be reasonably deduced that the most essential parameters are the pores and nanostructures of the material. Effective management of these parameters may increase the capacitance [13].

2.1.3 Use of hybrid electrode materials

Innovative techniques are now used to build the ED of the supercapacitors, with the hybridization of electrode materials at the forefront. Asymmetric capacitor (hybrid capacitor) normally combines a Faradic capacitive electrode (fundamentally, transition metal oxide, conductive polymers) with a carbon electrode [14][15].

In this review, the progress that has been made with combining the different allotropes of carbon and ruthenium-based composites are presented, with features on the disadvantages of a single material and the efforts made to overcome them by the framework of these composites. Such as, additional mechanical strength and the creation of efficient conduction pathways for ion transport, which were evident by the reduction of the charge transfer resistance of the

composites to the solution. Several important carbonaceous ruthenium composites have been highlighted and are the focus of this review, as they are by far the most widely used. The main route of synthesis, characterization and electrochemical performance of these composites are also presented.

2.2 Ruthenium oxide (RuO_2)

Ruthenium metal is paramagnetic and naturally non-reactive, maintaining a high level of stability and resistance to corrosion. The kinetic stability of ruthenium in several distinctive oxidation states (-2 to +8) and the regularly reversible nature of its redox couples make ruthenium, particularly attractive for energy storage. RuO_2 is currently the best supercapacitor electrode material inferable from its; reversible Faradaic reactions, wide potential range, high electrochemical conductivity (~105 S cm^{-1}), good cycle life and high theoritical capacitance in the light of the reversible redox reactions [16]:

$$RuO_x(OH)_y + {}_\delta H^+ + \delta^- \rightleftharpoons RuO_{x-\delta}(OH)_{y+\delta}$$
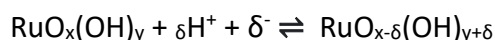
In 1974, the first discovery of ruthenium oxide as a new electrode material for energy storage was made by Trasetti and Buzzanca [17]. They noticed that the rectangular current voltammogram of RuO_2 in 0.5 M of H_2SO_4 electrolyte, looked like the voltammogram of carbon, which can be explained thus, RuO_2 as all other pseudocapacitance has two types of site for charge storage; an inner-less accessible site, and an outer-accessible site [18]. Proton adsorption on the inner site is a diffusion-controlled process, therefore the charging process is strongly dependent on the rate of diffusion of the ions. However, the charging of the outer surface site is purely a

surface process such as double-layer contribution, or reversible surface protonation, hence the rectangular voltammogram. As mentioned earlier, nano materials are currently being explored, because of their outstanding properties. RuO_2 can be used either as a bulk material or broken down as a nanomaterial. However bulk RuO_2 (Figure 2.1) shows diverse physical and electrical properties from its nanoparticles, attributable to their distinctive structures. Ruthenium oxide in its mass structure has a very much characterized 3D rutile-like crystal structure and along these lines carries on like an ordinary metal [19].
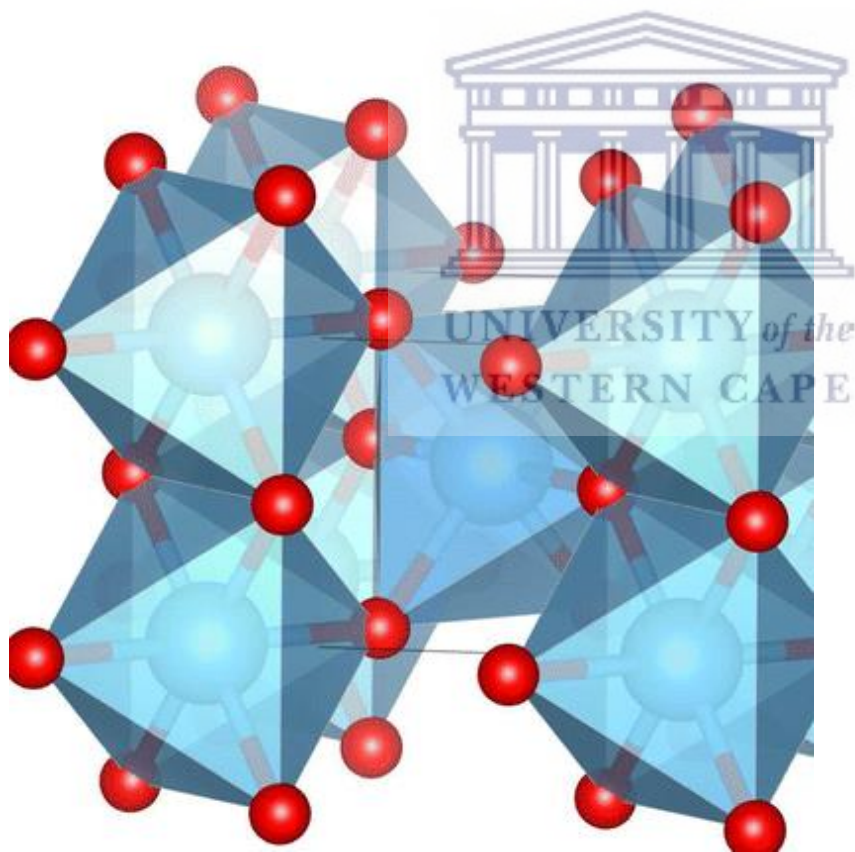
Figure 2.1: Bulk crystal structure of ruthenium oxide. Along the vertical direction is the tetragonal z-axis [29].

Currently, RuO$_2$ nanoparticles have become of interest for energy storage purposes amongst others, because of enhanced electrochemical properties which is a result of their distorted structures [20]. When the ruthenium oxide nanosheet is being exfoliated chemically from its parent bulk, the process involves a structural transition phase from the parent bulk, this change involves compressing leaving extreme strains in the nanosheet, thereby causing a distinction between the nanosheet and its rutile mass parents on their optical and electronic properties. Hence the new structure shows semiconducting properties with a slender band-gap, which is different from the pure metallic attribute of its parent bulk as seen in Figure 2.2.
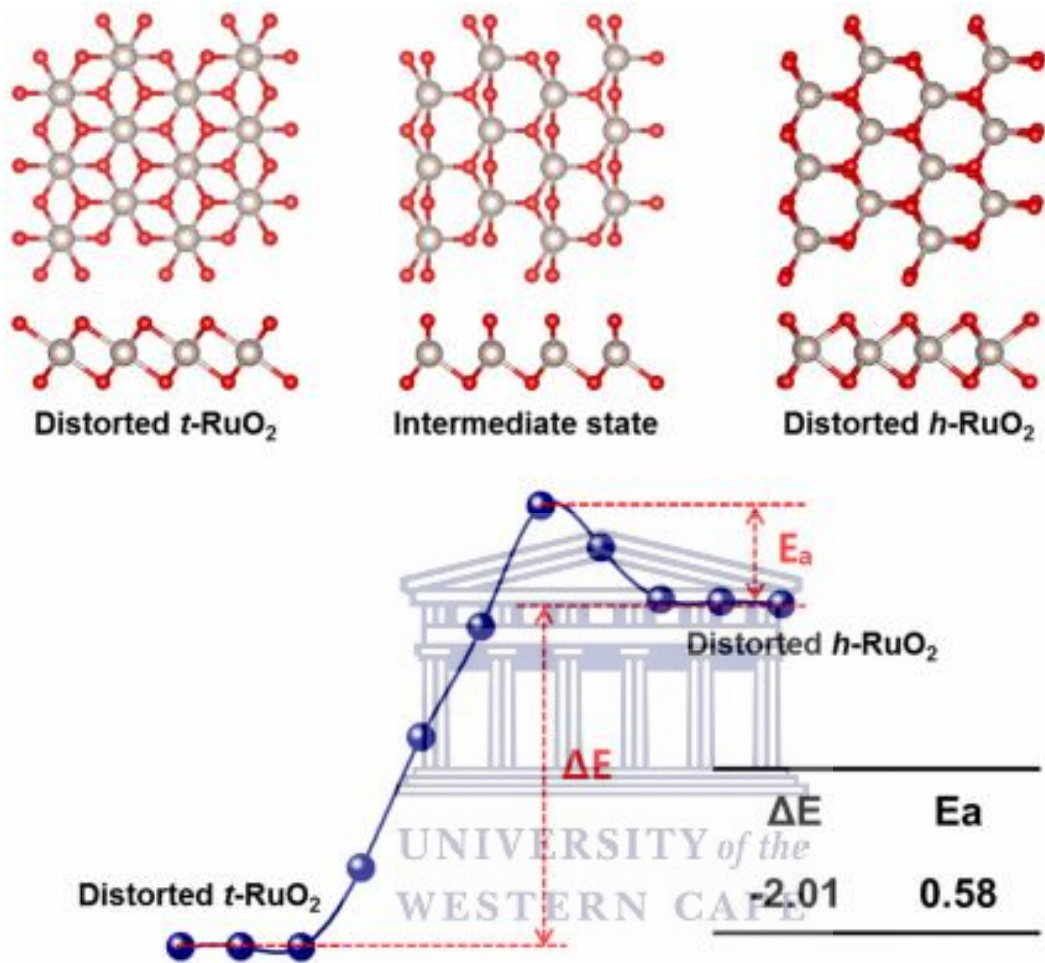
Figure 2.2: Schematic of NEB calculation during the phase transformation of RuO_2 [20].

Apart from reducing ruthenium oxide to its nanoform to improve its properties, ruthenium oxide is also used in its hydrous form for improved conductivity. Hydrous ruthenium oxide shows a higher charging rate and explicit capacitance than monocrystalline anhydrous RuO_2 because of its blended protonic–electronic conductivity [21]. The metallic nanocrystal of RuO_2 is isolated by grain boundaries loaded up with molecules of water, this model structure of $RuO_2.xH_2O$

encourages quick electron transport through the metallic RuO_2 and quick proton transport through the structural water district at the grain boundaries (Figure 2.3) [22]. Excess water at the boundary reduces electron transport while insufficient water reduces proton transport, therefore there must be a balance between the protonic and electronic conduction to achieve maximal performance. When Fue *et al*. [23] measured the rate of proton diffusion for $RuO_2.xH_2O$, he found that samples annealed between 116-175 °C had lower activation energy than those annealed either below 100 °C or above 200 °C, meaning that middle annealing temperature prompts best performances [24]. Thus, in conjunction with the electrodes/electrolytes interface, the hydrous structure, of ruthenium oxide, stores electrical charges in the bulk of oxides which result in high capacitance.
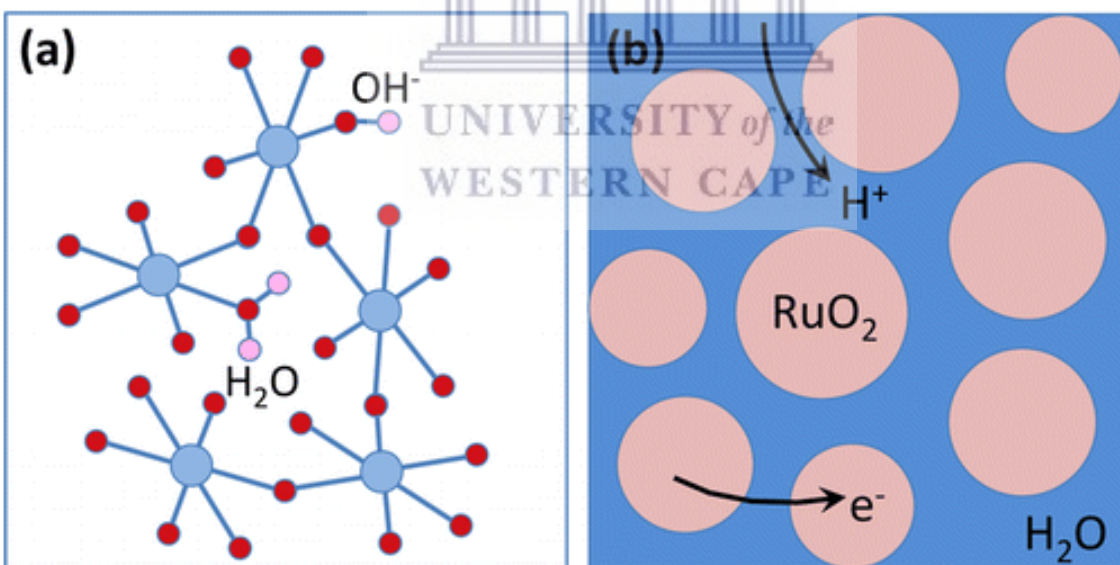
Figure 2.3: The structural model proposed for ruthenium hydroxide. (a) water in bulk vacancies (b) water at grain boundaries. Ruthenium(blue) oxygen (red) and hydrogen (pink)[21].

The control of the structure of $RuO_2.xH_2O$ has a significant effect on the mechanism of the supercapacitors fabricated. Therefore, a variety of methods have been employed to synthesize this material, such as chemical vapour deposition [25], electrodeposition [26], electrospinning, thermal deposition [27], spray pyrolysis [28], sol-gel [29] and hydrothermal method [30]. Because of its high cost one method commonly applied is; developing the electrode in a thin film which is a necessity in other to reduce their cost and also give access to the entire porous structure. In an experiment by Park $et\ al.$ [31] RuO_2 electrode films were prepared by cathodic electrode deposition. The weight of the RuO_2 on the substrate was taken as an indication of the film thickness, the capacitance of RuO_2 was found to increase with increased film thickness, however, the Cs decreased with increase film thickness which can be explained by the decrease in porosity of the outer layer and formation of a more compact inner layer. The maximum capacitance obtained in 0.5 M H_2SO_4 electrolytes was 788 F g^{-1} when the film thickness was 0.0014 g cm^{-2}. Different studies have been carried out using thin films of ruthenium oxide, and it was noted that the strategy used in the deposition of RuO_2 on a substrate also affected the morphology and electrochemical properties of the electrode [32]. In an experiment conducted by Vishnu $et\ al.$ [33] three samples of RuO_2 were set out in three different strategies for electrodeposition. As seen in Figure 2.4, their SEM monograph was distinctive and their Cs values were 790 F g^{-1}, 200 F g^{-1} and 135 F g^{-1} in 0.5 M H_2SO_4 electrolyte for A, B and C samples respectively. Green methods have also been investigated to produce RuO_2 nanoparticles. Nisha $et\ al.$ [34] used a bottom-up strategy to synthesis RuO_2 nanoparticles using biological resources as a reducing agent in a recent study. The reducing agent in this research was root extract from the Anacyclus pyrethrum plant. The formation of RuO_2 nanoparticles was validated by morphological tests, and the XRD result confirmed the material's

crystalline structure. The Cs of RuO_2 nanoparticles coated on a carbon sheet was 209 F g^{-1} at a scan rate of 5 mV s^{-1}.
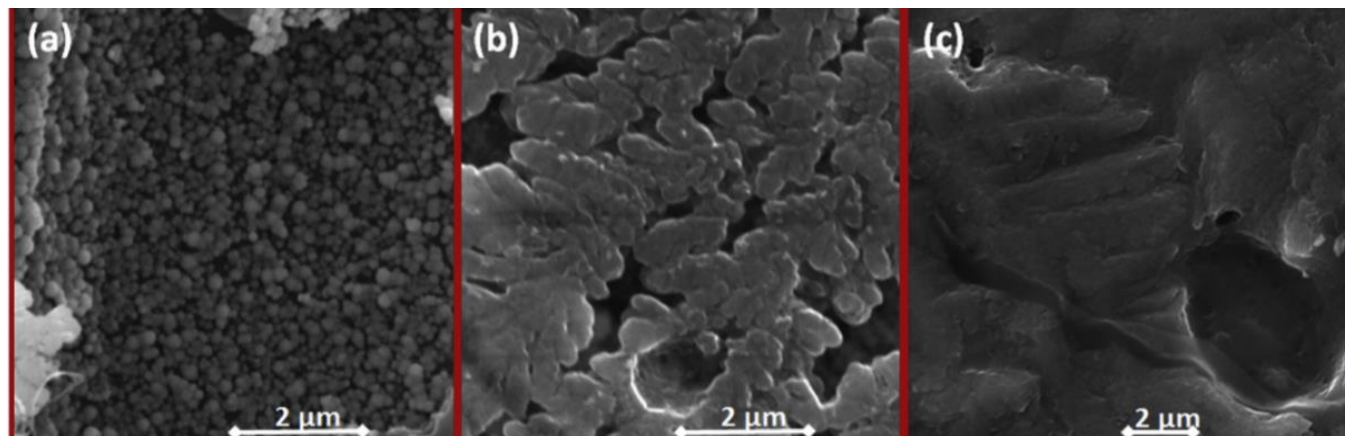
Figure 2.4: RuO_2 Nanofilms produced by 3 different deposition methods in RuO_2 SEM image [33].

In addition to cost, RuO_2 also exhibits poor cycling, for example, hydrous ruthenium oxide electrodes were effectively arranged by electrophoretic deposition by Jang *et al*. [35], and the material was heat-treated to control the water content at 150 °C, 250 °C and 300 °C. The anode conveyed a huge explicit capacitance (734 F g^{-1} and 608 F g^{-1} at an output pace of 1 mV s^{-1} and 50 mV s^{-1} sweep rates respectively) but lacked cyclic stability as just 4% of the underlying capacitance was kept up after 50 cycles. The impact of heat treatment was analyzed based on a cyclic test and the report recommended that heat treatment for hydroxy ruthenium oxide is essential for enhanced capacitance retention. This is because the heat treatment increased the bonding between ruthenium oxides, thus forming a more stable mechanical structure, but the group also recommended that the inclusion of the carbon network in the material could give the

compound cyclic stability. The electrochemical properties of pristine ruthenium-based materials are shown in Table 2-1, notably the materials exhibited high Cs with low cycle life. Aside from the low cyclability of RuO_2, the compound is additionally prevented by; the re-stacking of its particles, and low conductivity between nanoparticles, therefore, the actual test of the Cs are normally lower than the calculated value. The production of hybrid electrodes that combine RuO_2 with a relatively high surface area carbon materials is a matter of great consideration to avoid these drawbacks. The hybrid structure is designed to wrap up the benefits of both the pseudocapacitors and the EDLCs and to address the shortfalls of either material. Furthermore, hybrid EC provides an improved framework for high energy storage as well as high power rate and improved cycle life [36][37].

Table 2-1: Properties of RuO₂/ hydroxide electrodes.

Materials	Electrolyte	Scan rate	Capacitance	No of cycles	Capacitance retained	Ref.
		$(mV\ s^{-1})$	$(F\ g^{-1})$		(%)	
RuO_2	0.5 M H_2SO_4	100	790	1000	82	[33]
$RuO_2 \bullet xH_2O$			734	200	42	[35]
$(Ru+Ir)Ox.$ nH_2O			380			[38]
Hydrous ruthenium oxide	0.1 M NaOH	1	520			[39]
RuO_2	0.5 M H_2SO_4	5	1180	500	82	[33]
RuO_2	H_2SO_4 – PVA gel		0.8 (i)	10,000	84	[40]
RuO_2	Na_2SO_4	5	19 (i)	10,000	92	[41]
RuO_2	1 M H_2SO_4		745	7	88.7	[42]
RuO_2	1 M H_2SO_4		840	1,400	60	
$RuO_2.xH_2O$-S	1 M H_2SO_4	10	338	100,000	100	[43]
$RuO_2 \bullet xH_2O$	0.5 M H_2SO_4		785			[44]
PANI- RuO_2	1 M H_2SO_4	100	664	5,000	89	[45]
RuO_2	1 M H_2SO_4	100	16 (i)		60	[46]
RuO_2	0.5 M H_2SO_4	10,000	185			[47]
$RuO_2 \bullet xH_2O$	0.5 M H_2SO_4	25	569		90	[48]
Ru	H_2SO_4	10	344.3			[49]
$RuO_2 \bullet xH_2O$	0.5 M H_2SO_4	20	650			[50]

RuO$_2$	Nafion	0.5	203 (i)			[51]
RuO$_2$	H$_2$SO$_4$ in Acrylic	20	642			[52]
Ru0$_x$	0.5 M H$_2$SO$_4$		400			[53]
Ru0$_2$. 2.6 H$_2$O	0.5 Mol H$_2$SO$_4$	2	737			[54]
Ru0$_2$	0.5 M H$_2$SO$_4$	2	2192		72	[28]
RuO$_2$.xH$_2$0 - AC	2 M H$_2$O$_4$		650			[55]

(i)   = mF cm^{-2}

2.3 Carbon

Carbon consists of either sp^2 or sp^3 hybridized molecules, which bond together in a variety of ways, the most well-known of its allotropes are; graphite, amorphous carbon and diamond. Others are fullerenes nanotubes, graphene, activated carbon, and so on [56][57]. This material has been used for industrial applications thanks to its high abundance, combined with non-toxicity, lower costs, increased surface area, ease of processing, electrical conductivity, a wide range of operating windows and high chemical stability [58]. As illustrated in Figure 2.5, carbon materials have a rectangular voltammogram which is typical of EDLCs.
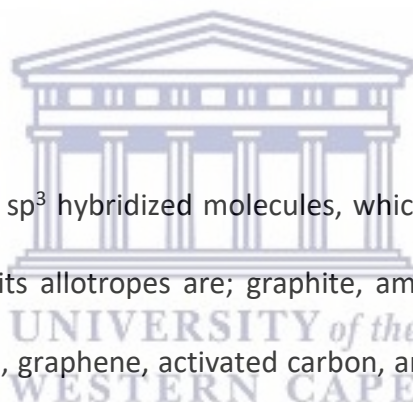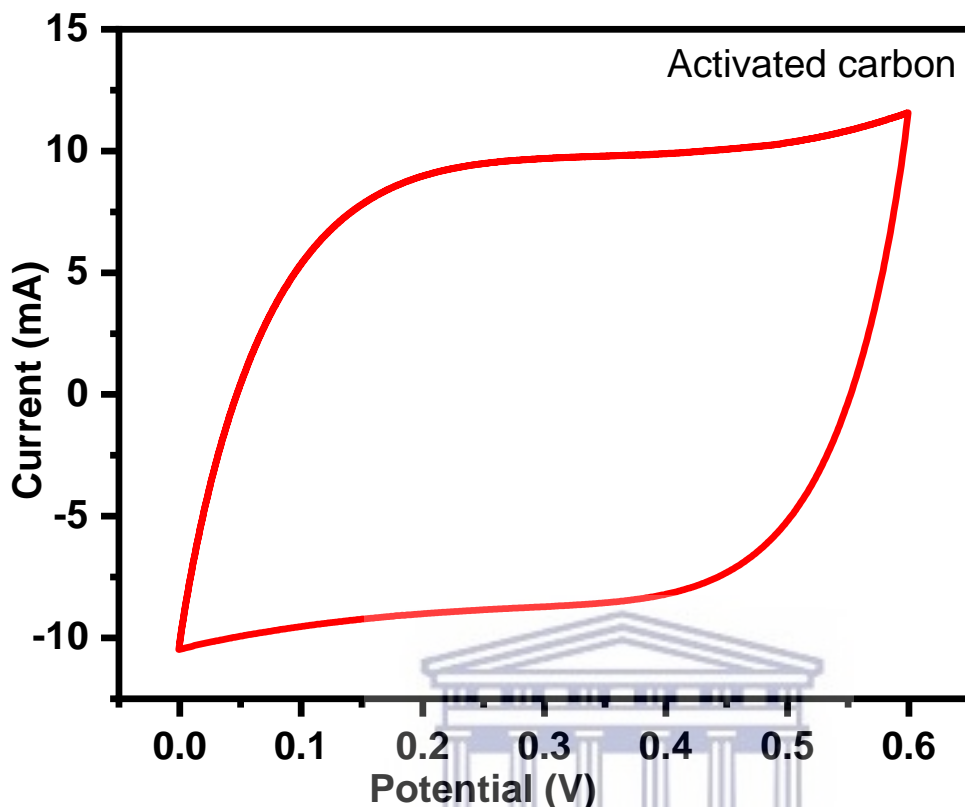
Figure 2.5: CV profile of activated carbon electrode.

Despite their high surface area for charge storage, there is still a serious deficiency in their energy storage capacity. Up to date, the specific surface area and pore-size distribution have been of the highest research interest. However, there is a chance that surface functionalization could be an effective way to improve the specific capacitance of carbon materials and it is being employed by researchers. This is because surface functionalization would introduce heteroatoms, which would make the carbon material more hydrophilic/lipophilic, increase the wettability of the surface and, as a result, increase ion adsorption and diffusion within the pores. Likewise, functionalizing the surface of carbonate materials trigger redox activities, thus increasing overall

capacitance that translates into high ED and PD structures. Composites formed from carbon-based materials and ruthenium oxide nanoparticles have shown pseudo-capacitive behaviour and an improved electrical double-layer capacitance. These are discussed below.

2.3.1 Ruthenium oxide-based graphene

Graphene is one of the most promising carbon materials used for energy storage. The graphene layer structured are stacked in a way that they can be easily separated and can easily slide through each other, this is owing to the week Van der Waals forces holding the structure together (Figure 2.6).
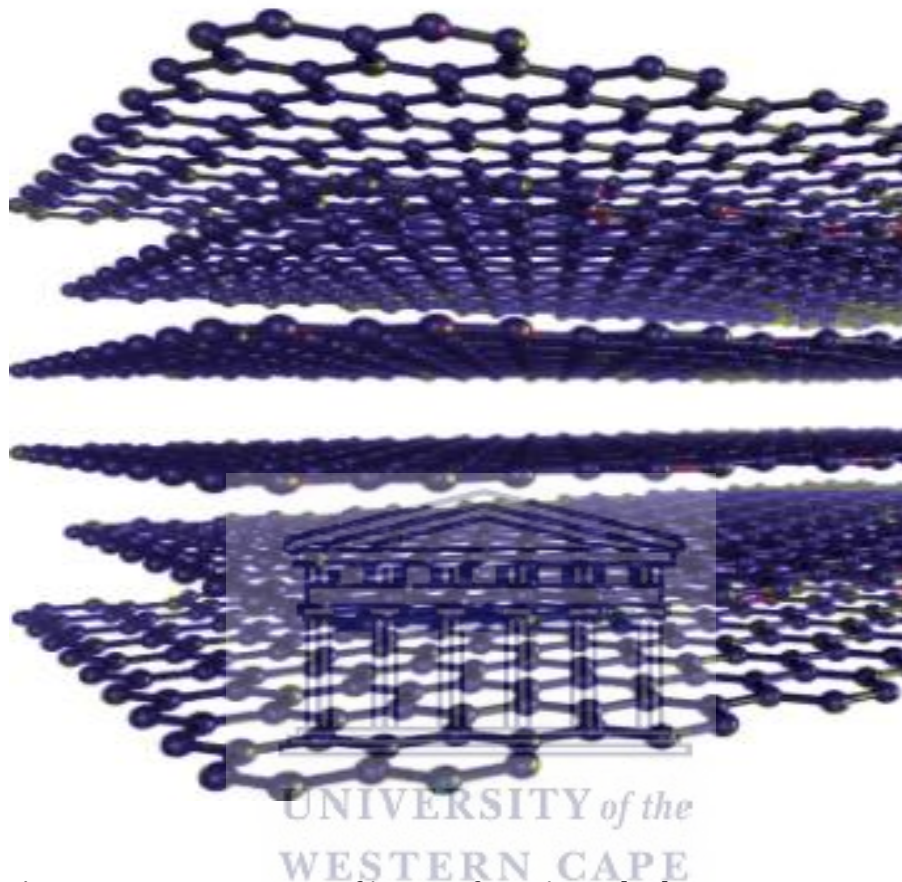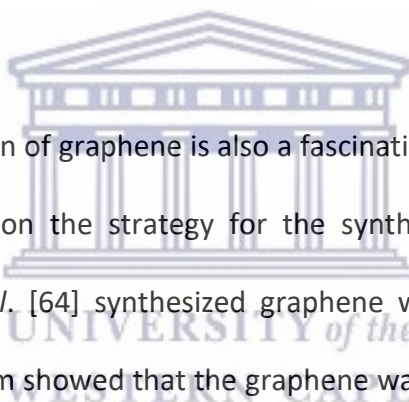
Figure 2.6: Schematic representation of layers of graphene [72].

Graphene is not only thin, but it is also extremely solid with the elasticity of E≈1.01 Tpa, and of extreme quality $^\delta$ ≈130 making it more powerful than the same size of steel and it is biocompatible. In 2004 graphene was extracted and characterized using the basic yet powerful 'scotch tape' technique by Geim and Novoselovis from graphite [59]. Presently, the reduction of graphene via Hummers method using hydrazine is one of the best ways to synthesize the graphene nanosheet (GN) [59]. However, in the event of a lack of force, this process results in agglomeration of the GN, which is caused by the physical attraction between the sheets due to

Van der Waals forces. When this happens, the ultrahigh surface area of the 2D form of graphene is gone, and agglomerated graphene sheets replace it [60]. For graphene to maintain good performance as a supercapacitor electrode material, it must firstly, maintain the large and accessible surface area which will result in sizeable charge capacitance accounting for high areal and volumetric capacitance [61]. Secondly, the reduction process must produce an open network of graphene structures void of agglomeration. These open pores will help facilitate the accessibility of the electrolyte to the electrode surface, optimizing ion diffusion. The graphene must also possess excellent electronic conductivity a necessity for achieving high power [7][62].

The solution to the agglomeration of graphene is also a fascinating research area, The quality of graphene consistently relies upon the strategy for the synthesis and how it is dealt with afterwards [63][62]. Wang *et al*. [64] synthesized graphene with the use of hydrazine in a vapour form. The SEM monogram showed that the graphene was not so agglomerated and had a better network structure, forming a solid carbon continuum like folded sheets that could improve conductivity. The Cs of the fabricated device reached 205 F g^{-1}, leading to an ED of 28.5 W h kg^{-1} at a voltage range of 1.0 V. Up to 90% of the initial capacitance was maintained after 1200 charge-discharge cycles. The supercapacitor with the graphene electrode had an ESR of 3.2 Ω, 10 kW kg^{-1} ED was thusly acquired. Another compelling methodology was by EL. Kady *et al*. [65] where graphene with high open surface area and decreased agglomeration was synthesized by laser reduction technique (Figure 2.7). Graphene was produced in this report using a laser scribing approach and a typical optical Lightscribe DVD drive. The low-power infrared laser instantly converts the stacked GO sheets into a well-exfoliated few-layered laser scribbled

graphene (LSG) film. The laser reduced graphene material showed high electrical conductivity

(1738 S m^{-1}) and high specific surface area (1520 g m^{-1}). These resulted in a high areal capacitance

of 4.04 mF cm^2 in 1.0 M H_2SO_4 at 1 A g^{-1} current load. The LSG electrode device showed a high-

rate capability while keeping up a capacitance of more than 1.84 mF cm^{-2} at high current loads,

the device could work at a very fast charge-discharge pace of 1000 A g^{-1} current load and 96.5%

capacitance retention after 10,000 cycles. The framework supported super high current load

activity, which can imply that it has the potential to deliver ultrahigh-power too.
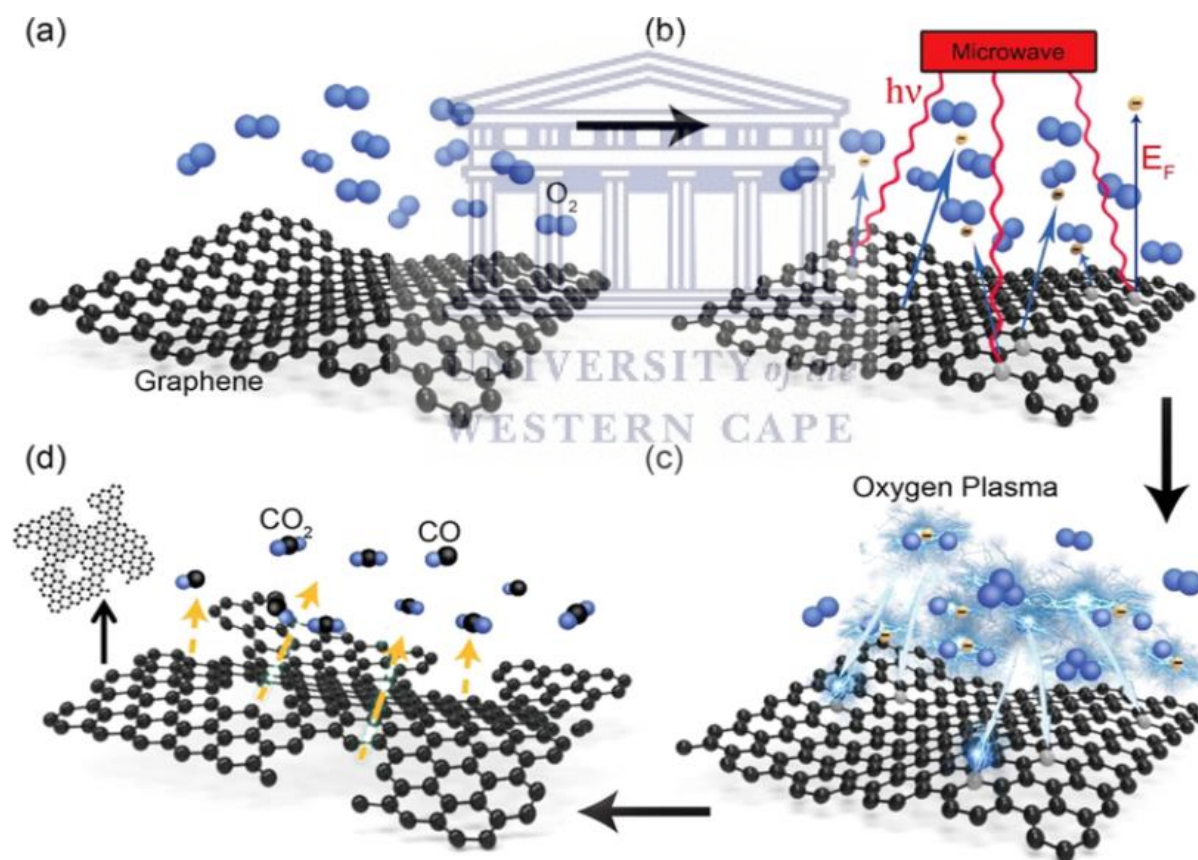
Figure 2.7: Preparation process for holey graphene (HG) [66].
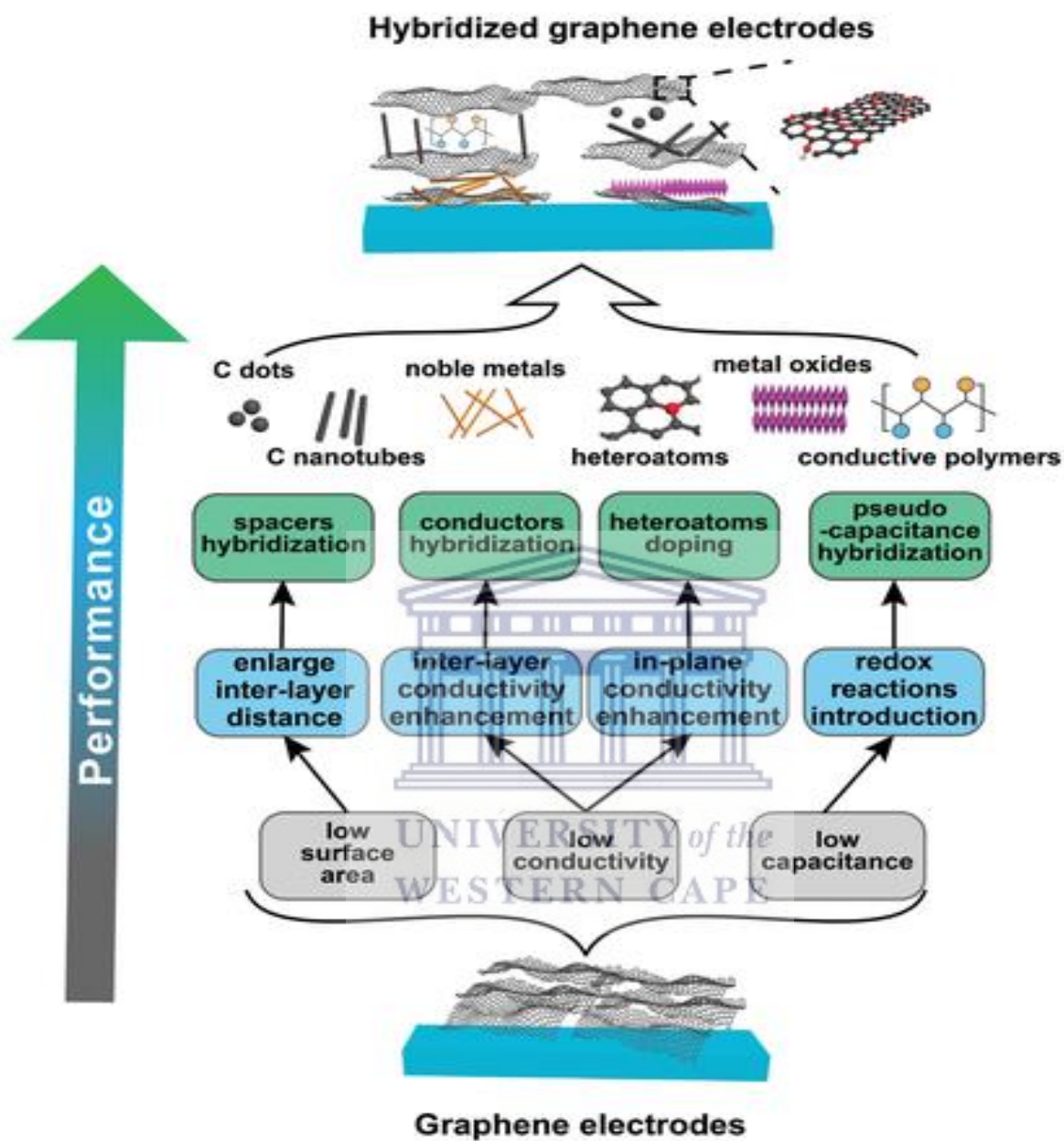
Figure 2.8: Hybridization of graphene electrodes [66].

The addition of a functional group as spacers is another valuable way to limit the restacking of the graphene sheet (Figure 2.8). When Hwang *et al*. [36] performed a similar synthesis of LSG reduction and introduced RuO_2 via redox reaction of its precursor $RuCl_3$ with GO using laser radiation, the morphological characterisation showed that RuO_2 acted like a nanospacer, well dispersed on the LSG prohibiting its restacking and thus maintaining a high surface area 3D configuration. The well-wrapped LSG around the RuO_2 also reduced the strain and stress that comes with volume expansion in RuO_2 which eventually contributed to an improved cycle life. The LSG/RuO_2 electrode capacitor had 1139 F g^{-1} capacitance, which, when contrasted with utilizing graphene alone, as seen prior, is a lot higher. The fabricated device ED was 55.3 W h kg^{-1} at 11.7 kW kg^{-1} PD. A positive increase due to the added RuO_2, shows the capacitance contribution from RuO_2, to the performance of the composite. Wang *et al.* [67] also reported novel hydrous ruthenium oxide nanoparticles in composite with graphene and carbon nanotube (RGM) electrodes. Chemical vapour deposition was used to synthesize the 3D RGM foam at absolute pressure. The SEM image in Figure 2.9 shows the thickly packed high surface area composite. The CNT within the graphene layer played the role of linking the active material to the current collector thereby improving the electronic conduction of the system, while the graphene layer acted both as a current collector and an enhancer of the nickel form substrate which anchored the composite, by insulating it from the electrolyte. The system experienced a wider voltage range which could be owing to the anchored RuO_2 with its unique capability of working both in the negative and positive range amongst other possibilities. The fabricated device had a power density of 128.01 kW kg^{-1} at an ED of 39.28 W h kg^{-1}. The maximum capacitance was 502.78 F g^{-1} within a 1.5 V operational voltage window at a sweep rate of 50 mV

s^{-1}. The supercapacitor device showed good cyclability, with 106 % of capacitance retention for more than 8100 cycles. The RGM showed high quality on a Ragone plot as compared to other RuO_2 composite and their pristine material (Figure 2.10).
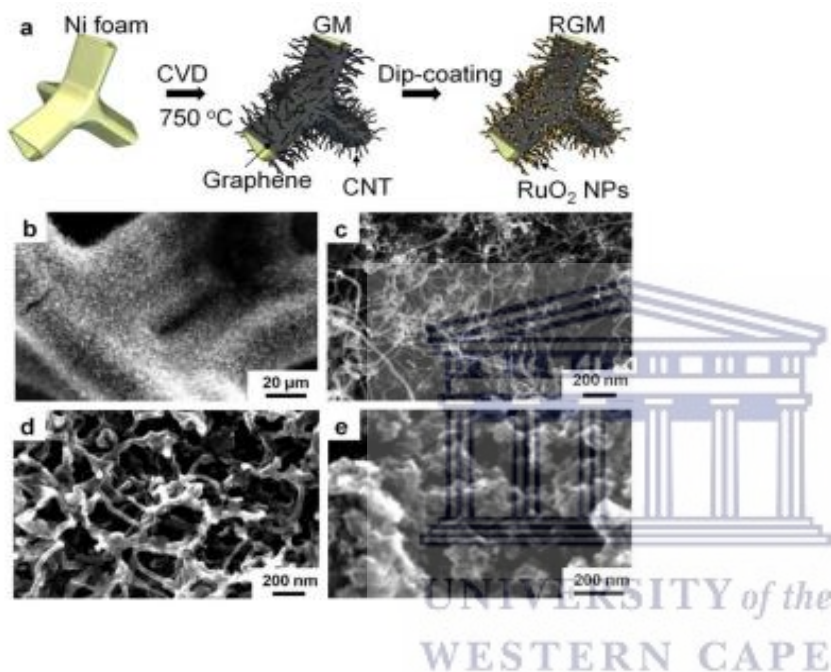
Figure 2.9: Structure of RGM electrode. (a) Illustration of the process of preparation of the nanostructure foam. SEM images of (b and c) GM foam (d) lightly loaded RGM and (e) heavily loaded RGM [79].
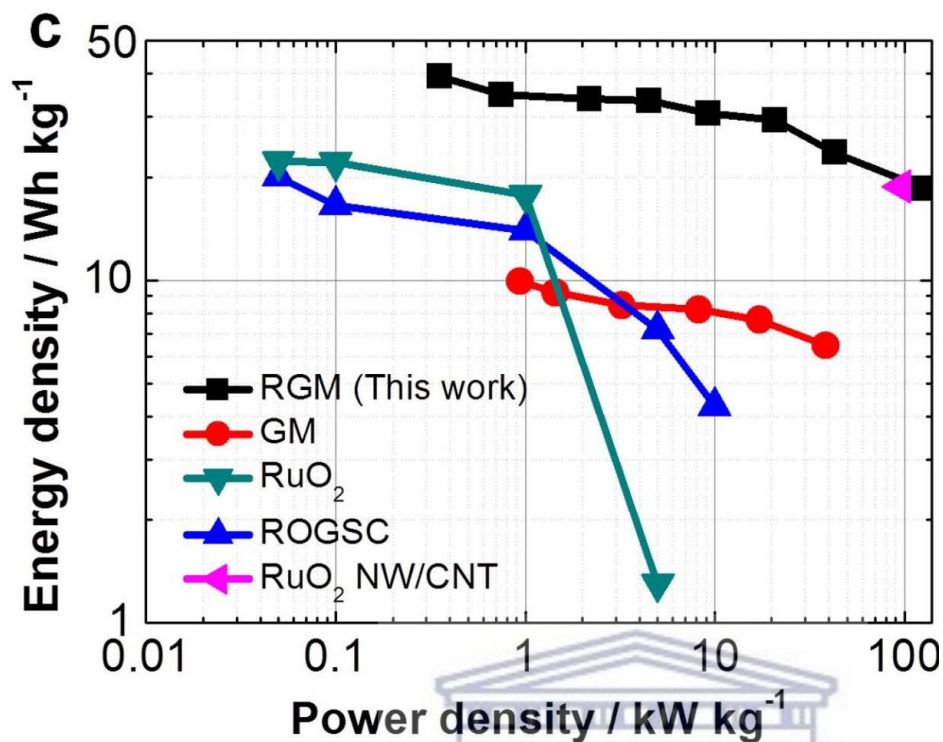
Figure 2.10: Ragone plot showing the relationship of ED to PD of cells packed with RGM, GM-graphene and CNT hybrid foams, RuO_2 nanoparticles, hydrous RuO_2/graphene sheets composite, RuO_2 nanowire/single-walled carbon nanotube [67].

Ruthenium oxide nanostring and graphene were prepared by the hydrothermal method by Kumar *et al*. [68]. The morphological characterization showed that RuO_2 Nanostrings were uniformly anchored on the graphene acting both as spacers, for the graphene sheets and providing good conduction pathways for ions. The composite showed low charge transfer and solution resistance and a good capacitance of 859 F g^{-1} with high capacitance retention. Another savvy and cost-effective technique for manufacturing graphene with RuO_2 was introduced by Han *et al*. [69] that synthesized a composite of RuO_2 and doped it with vertically aligned graphene

(VG), via sputtering. The structure was mechanically rigid, thus, forestalling RGM agglomeration. SEM pictures of the composite showed that VG uniformly covered RuO_2 without deforming the porosity. The fabricated device displayed great capacitance and stability. The areal capacitance expanded from 6.5 - 15.3 mF cm^{-2} for RuO_2/VG electrode with 3 nm to 50 nm mass of active material. The percentage contribution of RuO_2 to the overall capacitance of the composite was estimated to be 445%. The stability of the electrode was found to be dependent on the mass of the active material loaded and was from 71.7% - 64 % for 3 nm - 50 nm after 10,000 cycles. The lowest ESR was 1.4 Ω cm^{-2} for 5 nm mass loading, confirming great conductivity. Lee *et al*. [68] fabricated an interdigital in planer micro-supercapacitor using hydrous ruthenium oxide and reduced graphene oxide for enhanced performance by a photolithography free laser-printing process. The electrochemical characterization showed an improved equivalent series resistance, charge transfer resistance and relaxation time constant. Which led to a faster operating system, because of the inclusion of hydrous ruthenium oxide. The mechanical quality of graphene is one reason it has gotten research interest. Graphene is among the most alluring materials used to support RuO_2 for supercapacitor application and has consistently been added in nanoparticles synthesis, to upgrade their matrix so they can achieve great stability. $RuO_2.H_2O$/graphene was synthesized by Li *et al*. [34] by in-situ vapour-phase hydrothermal method for fibre supercapacitors, a technique that transformed the $RuCl_3$ precursor to $RuO_2.H_2O$/graphene on the surface of carbon fibre. The mechanical strength of the composite was enhanced by the addition of graphene as demonstrated by a sample in which graphene was not incorporated. The electrode material exhibited a large areal capacitance of 210.14 F Cm^{-3} at a current load of 39.80 mA cm^2. When fabricated into an asymmetric supercapacitor, the device had impressive cycling

stability, retaining 98.4 % of the initial capacitance after 50,000 cycles. Surktha *et al*. [70] synthesized a composite of RuO_2 with pre-nitrogen-doped reduced graphene oxide aerogel (NGA), the electrode material had a 79.6 F g^{-1} capacitance and a 64 u W cm^2 PD with 16.3 ug mass of active material. The electrode maintained 100% stability for about 200 cycles. The capacitance of NGA alone was also calculated and was lower than that of the composite which shows the contribution from the RuO_2. The need to improve the performance of RuO_2 as storage material is on the increase, Cho's group, synthesized a flexible RuO_2/graphene thin film for bendable supercapacitor using an electrodeposition method. The framework showed a good capacitance of 1561 F g^{-1} at a sweep rate of 5 mV s^{-1} thusly, a high 13 W h kg^{-1} ED at 21 kW kg^{-1} PD was accomplished, with 98% capacitance maintenance [71]. Also, the $RuO_2 \cdot xH_2O$@graphene electrode was synthesized using a vapour-phase hydrothermal method by Li *et al.* [72]. The morphological results show that graphene formed a useful link with the $RuO_2 \cdot xH_2O$, which helped in increasing the electronic conductivity and mechanical strength of the electrode. The electrode achieved a capacitance of 210.14 F cm^{-3} at 3.99 mA cm^{-2} current density retaining 98.40% of the initial capacitance after 50,000 cycles. In recent research by Xie *et al.* [73], a thermal decomposition method was used to synthesize electrochemically exfoliated graphene and ruthenium oxide thin-film electrodes. The technique involved thermal annealing of the RuO2/ECG on a Ti substrate. At a 5% weight contribution of the ECG to the composite, a 3-D framework was achieved capable of optimal charge transfer and diffusion of ions. The electrode delivered a Cs of 407 Fg^{-1} at 5 mV s^{-1}, the system also delivered a high energy density of 10.2 Wh kg^{-1} at a power density of 9.2 kW kg^{-1}. The electrode retained 97% of its initial capacitance after 2000 cycles. The above-cited literature has shown that the inclusion of ruthenium in graphene

can improve the conductivity of graphene for energy storage. Table 2-2 shows an investigation of different RuO_2-graphene composites that have been synthesized and their performance as electrode materials for supercapacitors. From the table, a clear increase in the material stability can be observed compared to the pristine ruthenium oxide material in Table 2-1.

Table 2-2: Properties of RuO_2/graphene electrodes.

Materials	Electrolyte	Scan rate	Capacitance	No. of cycles	Capacitance retained	PD	Ref.
		$(mV\ s^{-1})$	$(F\ g^{-1})$		(%)	$(kW\ kg^{-1})$	
RuO_2-G	2 M Li_2SO_4		502.78	8100	106	128.01	[67]
RuO_2-G	1 M H_2O_4	100	1139	4000	93	81.4	[36]
RuO_2-G	0.5 H_2O_4	5	1561			21	[71]
RuO_2-G	1 M H_2O_4	5	859		99	1028(iii)	[68]
RuO_2-G	1 M H_2SO_4	5	542	1000	94		[74]
RuO_2-G	1 M H_2SO_4	10	116(i)	3000	90.2	0.86 (iv)	[75]
RuO_2-G	2 M H_2O_4			1000	80	49.8	[76]
RuO_2-G			15.3 (i)	10,000	71.7		[69]
RuO_2-G	30 wt % KOH	5	205	1200	90	10	[64]
RuO_2-G	1 M H_2O_4	200	1099		98.4		[77]
RuO_2-G - CNT	1 M H_2O_4	200	966		98		[77]
RuO_2-G	1 M Na_2SO_4	20	332.6	5000	85.7	453.9	[78]
RuO_2-G	1 M H_2O_4	10	265		85		[79]
RuO_2-G	1 M H_2O_4	10	570	1000	97.9	10	[80]
RuO_2-G	2 M H_2O_4	200	357	1000	80	10	[76]
RuO_2-G	PVA/H_3PO_4 gel	2	199 (ii)	5000	88.9	2954.1 (v)	[81]
RuO_2-G	1 M H_2O_4	10	565	5000	80	32.9 (vi)	[82]
RuO_2-G	1 M H_2O_4	50	440				[29]

2.3.2 Ruthenium oxide-based carbon nanotubes

Carbon nanotubes (CNT) are carbon tubes with a single-dimensional, rounded structure and in the form of 'rolled-up graphene sheets. To date, CNT-based supercapacitors do not meet industry specifications for supercapacitor applications. A typical issue is its stability, caused by its poor adherence to a substrate which causes the CNTs to disengage from the substrate when wetted with an electrolyte and thus cause a material breakdown. Furthermore, because the CNT is insufficiently linked to the supporting metal, it requires more adhesive agents, thus increasing the material's internal resistance [83]. Researchers have used various techniques to improve the synthesis of this material. Using a vacuum chemical vapour deposition approach, Lu *et al.* [84] synthesized CNT stacked vertically. The carbon nanotube surface was altered via plasma etching. The morphological analysis revealed that the CNT structures were unbundled mesoporous vertically oriented. This resulted in great electrolyte accessibility and excellent capacitive performance. The plasma itching assisted in the removal of amorphous carbon from the CNT film surface, the introduction of flaws and oxygenated functionalization, and the opening of the CNT end tips. The electrode had a capacitance of 440 F g^{-1} at 5 mV s^{-1} sweep rate in imidazole electrolytes leading to a high cell voltage of 4 V and therefore a high ED of 148 W h kg^{-1} at 315 kW g^{-1} PD. Geo *et al.* [85] effectively arranged multi-walled CNTs with a stable permeable structure through a splash drying strategy, to quicken the pace of dissemination of particles. The MWCNT electrode was 7.2 mg cm^{-2} thick and delivered an area capacitance of 105 mF cm^{-3} at 30 A g^{-1}. To further improve CNT performance Masarapu's group optimized temperature and

studied its effect on the capacitance of CNTs [86]. The supercapacitor was collected with SWNTs film electrode and was tested electrochemically over a temperature range of 25 to 100 °C using an organic electrolyte, the capacitance generally increased with an increase in temperature. Physisorption of gas evolved by the electrolyte at high temperature brought about surface modification which provided more site for the Faradaic process and hence an increase in the pseudocapacitance with increasing temperature. This effect of the physisorption was not reversible as the capacitance of the SWNTs at 25 °C after cooling from 100 °C was higher when compared to the capacitance of the SWNTs at 25 °C that was not previously heated. The composite showed excellent stability even at 50 and 100 A g^{-1} current load and maintained 83% efficiency after about 22,400 cycles over all temperature ranges.
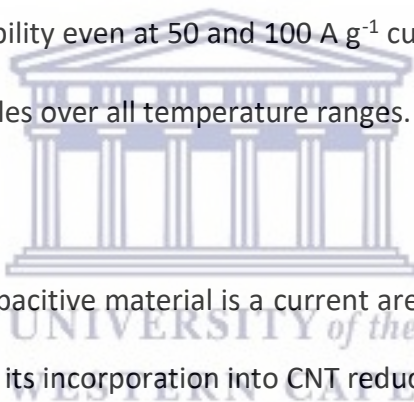
Synthesizing CNT with pseudocapacitive material is a current area of research interest, because of the high conductivity of RuO_2, its incorporation into CNT reduces its internal resistance. Liu *et al*. [87]. Synthesized a composite of RuO_2-CNT by spontaneously reducing Ru (V1 and V11) from two ruthenium sources. The composites capacitance was stable for over 20,000 cycles, with an increased cycling rate, generally showing low resistance and durability, with an increase in cycling. The composite capacitance was about ~231 F g^{-1}, pristine RuO_2 was also synthesized and had a Cs of ~ 803 F $g^{-1.}$ Even though the contribution of the RuO_2 to the composite wasn't reported it had impacted the overall capacitance of the composite while the CNTs provided the stability that would be impossible for pristine RuO_2 to achieve. Kim *et al*. [88] synthesized RuO_2/CNT, the electrode material delivered a 1170 F g^{-1} capacitance at 10 mV s^{-1} even at a high scan rate of 400 mV s^{-1} a Cs of 965 F g^{-1} was still maintained. The CNTs electrode prepared on a

Pt-coated Si wafer current collector by electrochemical deposition provided stability to the nanocomposite when compared to the pristine RuO_2 which originally dissolved in the acidic electrolyte. Wang's group [89] fabricated a ripple-like RuO_2-CNT composite films electrode, synthesized using electrodeposition technique. The composite yielded a specific capacitance of 272 mF cm^{-2} at a scan rate of 5 mV s^{-1}. The fabricated 3-D supercapacitor had a PD of 19.04 mW cm^2 at 50 mA cm^2 current load and an ED of 11.05 mJ cm^2. A strong cyclability was achieved by the composite, which was attributed to the nanotubes network because it hindered the film's breakdown like reinforcement bars in concrete. Recently, Chen *et al*. [90] developed supercapacitors with CNTs/ RuO_2 nanowire. The electrode was fabricated on cloth materials and flexible substrates using SWNT ink and regular ink jet printers. The specific capacitance of 138 F g $^{-1}$ was obtained, and as a result, a PD of 96 kW kg $^{-1}$, at 18,8 W h kg $^{-1}$ ED was obtained. The system maintained good stability without a noticeable reduction in capacitance after 1000 cycles.
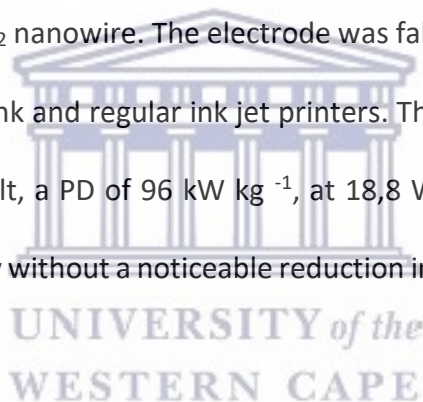
2.3.3   Ruthenium oxide-based activated carbon

Activated carbon is made from materials with high carbon content like coal, nutshells, and wood; that will not fuse during the process of thermal decomposition. The carbon-based substance is converted into activated carbon through physical change and thermal decay in a furnace with a regulated environment and temperature. Typically, the production of activated carbon is in two parts: carbonizing the raw materials and then activating them at low temperatures. The final product is a fine complex structure of carbon atoms, with a very large surface area per volume, and good porosity [55]. Presently, activated carbon is the major electrode material used

industrially for supercapacitors, however, it has not yet achieved the desired energy level for emerging technologies. This is because, even though activated carbon has a high surface area (1000 to 2000 m^2 g^{-1}) the difficulty encountered in controlling their pore size, pore volume and pore structure distribution possess a low porosity and low electrolyte accessibility challenge. The type of precursor used and the method by which activated carbon is synthesized has been found to significantly influence its surface properties. Research has employed various precursors to improve their properties as efficient supercapacitor electrode materials. Rice husk has been used as precursors and capacitance of 172.3 F g^{-1} [91], 34 7 F g^{-1} [92], 12 F g^{-1} [93] and 147 F g^{-1} have been obtained [94]. Other precursors like; carton box (Cs 307 F g^{-1}) [95], willow catkins (Cs 340 F g^{-1}) [96], cow dung (Cs 124 F g^{-1}) [97], waste tea (Cs 203 F g^{-1}) [98], demineralized (waste) cumin plant (Cs 155 F g^{-1}) [99] are few examples of the many precursors used to improve the surface of the material. Recently Wang *et al*. [100] synthesized activated carbon from rotten tomatoes in a self-catalytic activation reaction. The synthesized activated carbon had a capacitance of 220 F g^{-1} at 0.5 A g^{-1} current density and maintained 100% capacitance retention after 5000 cycles. Activated carbon was also recently extracted from wheat husks using KOH and prepared on a Ni foam substrate. The electrode demonstrated a capacitance of 271.5 F g^{-1} at 0.5 A g^{-1} and maintained 82% of its capacitance after 5000 cycles [101]. Activated carbon have shown great stability as electrode material for supercapacitors, hence its application in the industry. When combined with RuO_2 the AC excellent stability makes up for the poor stability of RuO_2, while the RuO_2 improves the surface wettability of the AC thus optimizing its performance. Itoi *et al*. [102] created hydrous RuO_2 nanoparticles in activated carbon pores. Two activated carbon samples were used: the first included solely micropores (mAC), whereas the

second had both mesopores and micropores (mmAC) According to the BET study, the surface area of the was 1980 $m^2 g^{-1}$ and 3160 $m^2 g^{-1}$ for mAC and mmAC respectively. RuO_2 was injected into the samples in varied ratios, and the two samples behaved differently to the ruthenium loading. While mAC/RuO_2 (AC:Ru = 4:1) produced the maximum capacitance of 166.1 F g^{-1} at 2.0 A g^{-1}, $mmAC/RuO_2$ (AC:Ru = 7.3) produced the highest capacitance of 160.4 F g^{-1} at 2.0 A g^{-1}. After 2000 cycles, all the hybrid samples had capacitance retention of 65 to 75%, but the pure activated carbon samples had capacitance retention of up to 97%.

2.3.4   Ruthenium oxide-based carbon aerogel

Carbon aerogels are a special class of high-surface-area, amorphous and porous carbon [102]. They consist of interconnected carbon nanoparticle clusters ranging in diameter from 3 nm to 20 nm. Their preparation method is majorly by pyrolysis of resorcinol-formaldehyde (RF) aerogels [103]. The distribution of the carbon network's porosity and pore size of carbon aerogels depends on the ratios of the precursors used, therefore optimizing the ratio of the precursors is an excellent way of customizing the material and defining its porosity. The massive specific surface area, electrical conductivity, environmental compatibility and chemical inertness of carbon aerogel has made them very promising materials for supercapacitors [104]. By controlling the resorcinol to catalyst ratio, Yangs *et al.* prepared carbon aerogel of different pore sizes and investigated the effect of pore size on their electrochemical performances [105]. Mesoporous carbon aerogel was prepared with different pore sizes and their electrochemical properties were investigated, carbon aerogel with large pore sizes was electrochemically favoured at low sweep

rates and low charge-discharge rates, while those with small pore sizes were favoured at high

sweep rates and high charge-discharge rates (Figure 2.11). Also, the electronic resistance of the

carbon aerogel increases with increasing pore sizes, while the inverse was the case for ionic

resistance [106]. Therefore, it is safe to say that when using carbon aerogel electrode material,

the end-use should first be considered before adopting a particular pore size.
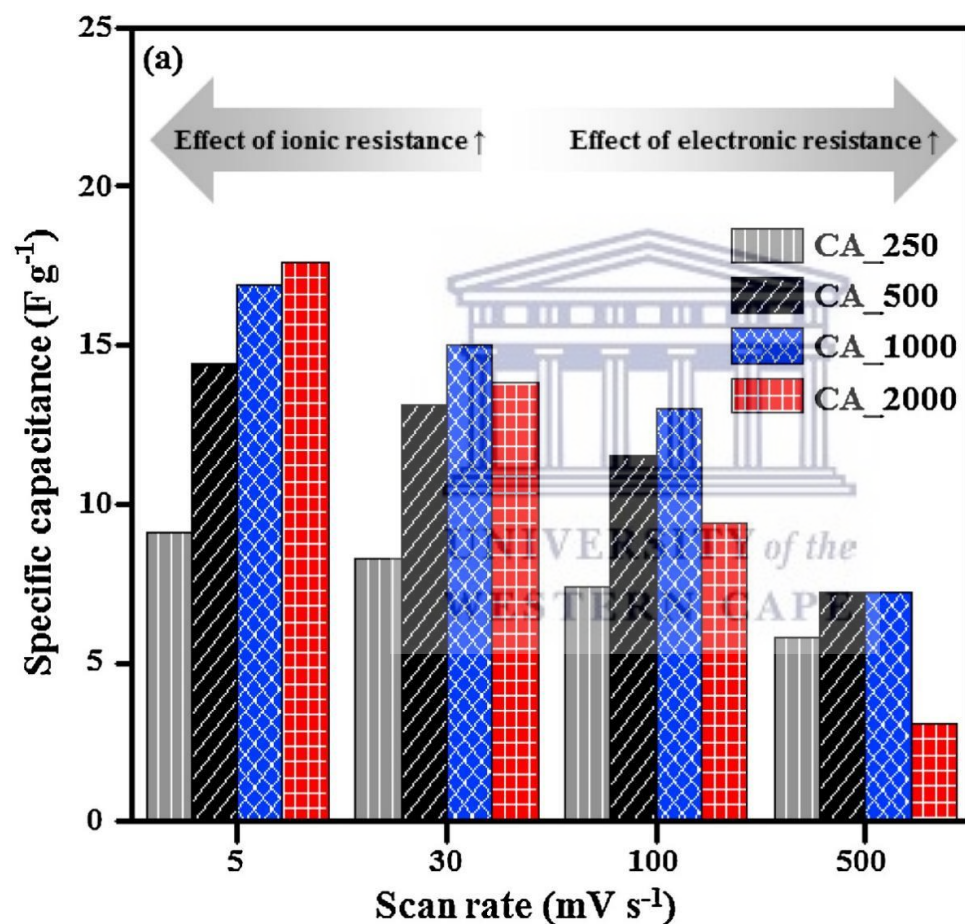
Figure 2.11: Cs of aerogels of different pore sizes concerning [106].

Various investigation on how to improve the performance of carbon aerogel has been carried

out, the method of preparation, type of catalyst, the temperature of pyrolysis and method of

activation affects the pore sizes and pore size distribution of carbon aerogel. Halama *et al.* [105] in an experiment confirmed that the method of preparation when other parameters are fixed affects the physical morphology of the carbon aerogel. The particle size, pore dimension and the roughness of the surface characterized by agglomeration were different for one sample prepared by a sol-gel polycondensation from another prepared by inverse emulsion polymerization hence, the electrochemical properties were also different. Today, several other methods have been used to synthesize carbon aerogel, in a recent study, Zhao *et al.* [104] synthesized carbon aerogel from discarded dates by first treating it hydrothermally, then freeze-drying and activating it with KOH. The carbon aerogel had micro/macropores and had a specific surface area of 1348.87 $m^2 g^{-1}$. At a current density of 0.5 A g^{-1}, the material had a specific capacitance of 769 F g^{-1} in 6 M KOH. The supercapacitor device produced an energy density of 8.75 Wh kg^{-1} and a power density of 252 W kg^{-1}.
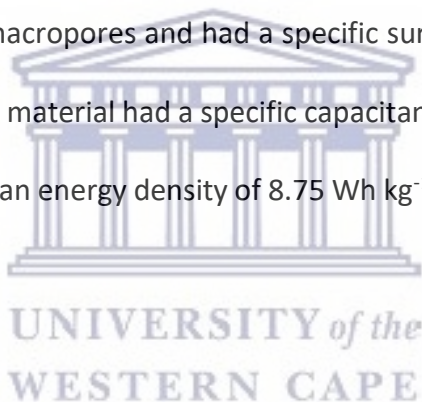
Increased surface area, surface modification and composite preparation include promising ways to increase the capacitance of carbon aerogel materials. Liu *et al*. [107] achieved an increased surface area of 3431 m^2 g^{-1} by activating the aerogel with CO_2. Correspondingly, the supercapacitor device showed a maximum Cs of 152 F g^{-1} and an ED of 27.5 W h kg^{-1} at 0.3 A g^{-1} current load in 1 M organic electrolyte Et_4NBF_4-AN. Liu *et al*. [108] also modified carbon aerogel with CO_2 and KOH, the carbon aerogel had a vast surface area (2119 $m^2 g^{-1}$) resulting in an equally impressive maximum capacitance (250 F g^{-1}) at 0.5 A g^{-1} current load in 6 M KOH electrolytes. A sponge-like carbonaceous aerogel was synthesized by Wu *et al*. [109] using crude biomass and

watermelon as the carbon precursor. 333 F g^{-1} capacitance was reached at 1 A g^{-1} current load in 6 M KOH electrolyte. The charge-discharge test showed that 96 % of the initial capacitance was maintained after 1000 cycles. Although CO_2 activation has been shown to increase the capacitance of carbon aerogel, the addition of a RuO nanoparticle enhances the material's capacitance. In an experiment by Singh *et al*. [110], the capacitance of carbon aerogel prepared by the polycondensation of resorcinol with formaldehyde was activated with CO_2. The CO_2 activation increased the capacitance of the carbon aerogel to 153 F g^{-1} from 95 F g^{-1}. When the carbon aerogel was further impregnated with ruthenium oxide nanoparticles a Cs of 308 F g^{-1} was obtained at 1 A g^{-1} current load in 1 M electrolyte H_2SO_4. In another experiment by Crane *et al*. [111] transition metal chalcogenide (TMD) (MoS_2 and MoS_2) and carbon aerogel compounds were synthesized via liquid-phase exfoliation. Due to the support of the carbon aerogel matrix, the composite had a 620 m^2 g^{-1} surface area. The transition metal chalcogenide did not affect the aerogel structure, however, its impact on the composites' Cs was not negligible. On fabricating the system with the carbon aerogel electrode material alone, the system yielded 80 F g^{-1} maximum capacitance at the lowest applied current. However, the system exhibited a volumetric capacitance of 59.8 F cm^{-3} when the TMD/aerogel was used as the electrode material, which is up to 127% greater than the pristine aerogels' volumetric capacitance. Also, after more than 2000 charge-discharge cycles, the TMD/aerogels composite electrode showed no degradation.

2.3.5 Ruthenium oxide-based carbon dots

Carbon dots (CD) are carbon materials with 0 dimensions. The attractive properties of most carbon allotropes are also present in this new class of fluorescent carbon nanomaterials [112][113]. Two main forms; "top-down" and "bottom-up" approaches can be used to synthesize CDs this can be achieved via various synthetic approaches with proper optimization pre and post treatment, to obtain good surface properties [114]. The 'top-down' synthesis breaks down carbon with large structures such as graphite, carbon nanotubes and carbon nanodiamonds into CDs using electrochemical techniques, laser ablation, soaking, arc discharge, proper molecular precursor thermal oxidation, soot vapour deposition, microwave synthesis, nanodiamond proton-beam irradiation, etc. [115]-[116]. These various methods of synthesis result in the formation of different morphology of crystals and the varied properties of carbon dots are determined. A few attempts have been made to pack CD as a supercapacitor electrode material, one of such is by Chen *et al*. who synthesized CD by KOH activation of fullerenes C60 which yielded a novel 15 wt%. CD layered structure which was freeze-dried and annealed at 800 °C and 600 °C to give it stability [117]. The CD electrodes showed an aerial capacitance of 0.66 F cm^{-2} and volumetric capacitance of 157.4 F cm^{-3} in 6 M KOH electrolytes at 0.5 A g^{-1} current load following annealing. A strong carbon matrix generally has high stability and can be used to support electrode material. CQD has been used to support polypyrrole a pseudocapacitive electrode material with low cyclability. Jian *et al*. [118] produced a polypyrrole nanowire electrode material system that is generally characterized by low cycle life but stabilized the material by the introduction of carbon quantum dots. The as-fabricated system at 0.5 A g^{-1} current load reached a capacitance of 306 F g^{-1} and retained 85.2% of the capacitance after 5000

cycles. Similarly, via in situ polymerization, Zhang *et al*. [119] synthesized ternary nanocomposite of polypyrrole-GO-CD electrode material. The material retained 92.9% of its Cs after 5000 cycles, a maximum capacitance of 576 F g^{-1} was obtained at a current load of 0.5 A g^{-1}. With this material, Liu *et al*. [120] manufactured a micro-supercapacitor by assembling GQDs made of graphite oxide to interdigital finger electrodes using an electrophoretic deposition technique that achieved a Cs of 534.7 μ F cm^{-2}, a good power response and stable cycling. Although the composite ruthenium oxide-carbon dot appears to have excellent usability in supercapacitors, its literature is limited. However, the composite materials CQD/RuO_2 synthesized by Zhu *et al*. [121] had an incentive Cs of 460 F g^{-1} with a remarkably high current load of 10 A g^{-1}. The system demonstrated good cyclability, retaining 96.9% of the capacitance at a high current load of 5 A g^{-1} over 5000 cycles. The composite maintained good capacitive behaviour even at a high scan rate [122].
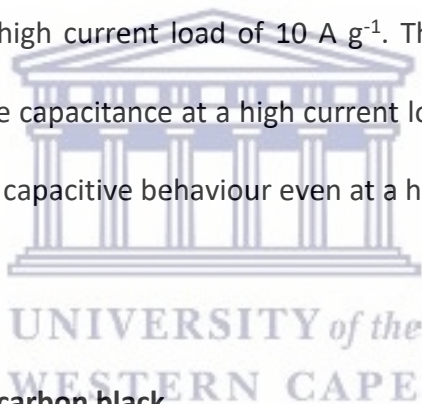
2.3.6 Ruthenium oxide-based carbon black

Carbon Black (CB) has the form of colloidal particles, consisting of spherically arranged particle aggregates. These aggregates can lead, if not controlled during the production process, to larger agglomerates. Depending on its production parameters, the surface area of carbon black spans from around 10 m^2 g^{-1} to an excess of 1500 m^2 g^{-1}[123]. Carbon black is currently being used as a material for electrodes for EDLCs [124]. It is used primarily as a conductive activated carbon additive and have been combined with reduced graphene oxide electrodes for supercapacitors [125]. As with any other form of carbon, the surface of carbon black is very large. For that reason, carbon blacks have been proposed and used not just as an additive in EDLCs but also as the sole

active material, substituting activated carbons and providing a large-scale commercial alternative electrode material [126][127]. However, carbon black still faces some drawbacks like low surface area due to severe agglomeration and poor mechanical stability [124]. Due to their small particle sizes, an increase in polymer binder levels is most times needed to fabricate the electrode, however, this leads to an increase in the ESR. Kozyrev *et al*. [128] produced a supercapacitor device using thin films of large surface area carbon black by using the inkjet method to coat the current collector with carbon black to improve the packing and reduce the amount of binder used. The device achieved a capacitance of 115 F g^{-1}, showing that its capacitance performance can be compared with other carbon materials [129].

Functionalizing carbon black with PGM has also been researched to improve the use of the material. He *et al*. [130] synthesized hydrous ruthenium oxide with activated carbon black, by chemical impregnation for an improved composite material. The capacitance of the composite increased with the addition of RuO_2 while the capacitance of RuO_2 oxide decreased from 1255.8 to 533.7 F g^{-1}. Min *et al*. [131] used a wet incipient approach to create a 3D porous structure of RuO_2/carbon nanoparticle. The SEM image revealed a porous structure with little agglomeration. As a result, the composite achieved 70% high ruthenium utilization for a RuO_2 mass loading of 60%, which could be attributable to the porous structure's enhanced ion route. Overall, the addition of RuO_2 to the carbon black increased the composite's performance, resulting in a capacitance of 647 F g^{-1}. However, more research on how to effectively anchor the RuO_2 nanoparticles on the carbon black material is required for enhanced stability.

2.3.7 Antimony compounds for supercapacitors

Because of their great reversibility, antimony-based electrode materials have been an intriguing research area in the Li-ion and Na-ion industries [132][133]. In supercapacitors, two-dimensional antimonene has shown promising potential as a supercapacitor material, with capacitance as high as 1578 F g^{-1} at a high current density of 14 A g^{-1} [134]. Presently, antimony sulphides/phosphates have been utilized as an electrode material. It has also been used as a dopant and addition on different occasions [135]; nevertheless, the use of its oxides is still rare. Copper Antimony sulphide (Cu_3SbS_4) was successfully synthesized by Mariapan *et al*. [136] through a one-pot hydrothermal technique as electrode material for supercapacitor. $CuSbS_2$, a member of the chalcogenide family with more than one earth-abundant and low toxicity material arranged in a layered structure, is one compound of antimony that have gained relevant recognition in the fields of optoelectronics, sensing and photovoltaics catalysis because the composite has shown remarkably high electron transport properties, mechanical stability, cost efficiency, incredibly large surface area and tunable bandgap. $CuSbS_2$ orthorhombic crystal system is made of SbS_2 chains formed by linking Sb square like a pyramid and tetrahedral linked CuS_4 along the b-axis, the two chains are then interconnected to yield sheets perpendicular to the c-axis. When $CuSbS_2$ was applied as electrode material for a supercapacitor, it delivered an energy density of 11.373 Wh Kg^{-1} with a specific capacitance of 60 F g^{-1} at 5 mV s^{-1} and a power density of 175 W Kg^{-1}. It also displayed good capacitance retention after 2500 cycles. Ramasamy *et al*. [137] substituted the sulphur in $CuSbS_2$ with selenium $CuSbSe_xS_{2-x}$ and investigated the electrochemical properties. The system showed good stability with a capacitance of 48 F g^{-1}, which consequently results in an energy density of 1.31 Wh Kg^{-1} and a power density of 60.88 W

Kg^{-1}. The good cyclic stability together with its attractive solar conversion ability. Lin *et al*. [138] synthesized a micro spindle hierarchical structure of antimony phosphate, following a facile solvothermal route. The electrochemical micro spindle antimony phosphate (SbPO$_4$-Ms) was compared with nanoparticles of antimony phosphate (SbPO$_4$-Np). The reversible redox transition between Sb^{3+} and Sb metal states provides pseudocapacitance and makes this material suitable for energy storage. More so, the Sb-O-P bond of PO$_4^{3-}$ provides stability to the Sb^{3+} by creating an Sb-O-P bond inductive effect. The SbPO$_4$-Ms showed a higher electrochemical capacitance than the nanoparticle antimony phosphate. Its capacitance was 234.23 F g^{-1} at 0.5 A g^{-1} and 43.88 F g^{-1} at 10 A g^{-1} while that of the latter was 3.44 and 142.10 F g^{-1} at 0.5 and 10 A g^{-1} current density respectively. The SbPO$_4$-Ms was also more stable with 90% capacitance retention as compared to SbPO$_4$ Np which only exhibited 59% capacitance retention. This improved electrochemical property exhibited by SbPO$_4$-Ms can be attributed to its 3D hierarchical structure, buffering the effect of volume expansion associated with the use of antimony metal. Shanmugavani *et al*. [139] fabricated a CoSb$_2$O$_4$//N$_3$(Fe(CN)$_6$)^2(H$_2$O)) asymmetric capacitor. The energy storage of the cathode electrode material was via a redox reaction. The material delivered a capacitance of 598 F g^{-1} at 2 mV s^{-1} in 1 M KOH. However, the capacitance of the asymmetric device was 30 F g^{-1} at 1 mA cm^{-2} with a cycling stability of 100% after over 100 cycles. Raknual *et al*. [140] synthesized zinc antimony oxide (ZAO, ZnSb$_2$O$_4$) via Sb^{3+} doping in ZnO utilizing the dropped casting and screening process from a wet chemical solution. The ZAO electrode's specific capacitance was measured at a scan rate of 10 mV s^{-1} to be 434 mAh g^{-1}. Korkmaz *et al*. [141] reported thin films of graphene oxide/antimony sulfide (on Si substrate) generated at various deposition temperatures using a chemical bath deposition method and their supercapacitor properties.

Their specific capacitance values at 5 mV s^{-1} were 562 F g^{-1} between the -0.2 V to 0.8 V range. Ali *et al*. [135] synthesized antimony doped cobalt oxide material by altering the antimony content value in the range of 2–6% using a hydrothermal technique. The capacitance from the cyclic voltammogram showed that among the SbCo-0, SbCo-2, SbCo-4, and SbCo-6 materials, SbCo-4 had a higher specific capacitance value of 894.15 F g^{-1} than the others, at a rate of 5 mV s^{-1}. The Galvanostatic charge-discharge profiles for SbCo-4 material produced revealed even better capacitance retention, with 75.7% at a high current density of 10 A g^{-1}. The addition of carbon to stabilize Sb has also been investigated. Anchored antimony species on reduced graphene oxide composite was symmetrically fabricated as an electrode for supercapacitor and their electrochemical properties were tested by Ciszewski *et al.* [142]. The system yielded 289 F g^{-1} specific capacitance which was a combined effort from the double layer charging and pseudocapacitance from the redox reactions fastened by the presence of the antimony species. However, the system did not show any outstanding stability. The literature of antimony carbon-based compounds for supercapacitors is discussed in detail in chapter five.

2.4 CONCLUSIONS AND PERSPECTIVES

The latest progress made in the preparation method and application of Ru-based carbon nanocomposites for supercapacitors has been summarized. Metal compounds of the platinum group with their incredible properties and relatively high energy densities have been explored for energy storage purposes over the years, however, disadvantages such as high price, low utilization rate, low specific surface areas, relatively poor electrical conductivity and low cyclic stability are major challenges that have restricted their use. Conversely, high-surface, good porosity, affordable and eco-friendly carbon materials have low energy densities, mainly due to severe agglomeration, which has prevented their use in emerging applications. To overcome these challenges, new composite materials are currently being researched and developed to improve the disadvantages of a single material through a complementary relationship with another material. The nanocomposites show increased electrochemical performance in supercapacitors by combining the unique properties of the individual components, due to the synergistic effect of both carbon and the RuO_2 materials.

This review introduces the various RuO_2-carbon composite materials which are being studied for supercapacitor applications. Specifically, we discussed RuO_2 binary and ternary oxide composites of graphene, carbon nanotube, carbon aerogel, activated carbon, and carbon black. Their method of synthesis and electrochemical properties were also discussed. The study points out that; 1) Efficient utilization of RuO_2 is recommended for cost efficiency because the capacitance of the material does not linearly increase with the quantity of the RuO_2 compound used. Also, the

particle size of the RuO_2 is important to its capacitance contribution and shares an inverse relationship with the capacitance. With these, optimizing the amount of the RuO_2 in the composite is one way to achieve high efficiency. 2) The method by which the composite is synthesized plays a vital role in its performance, the handling and treatment of materials, before, during and after synthesis determines to a large extent the morphological property of the material, and hence its electrochemical properties. 3) Some allotropes of carbon are more accommodating to the RuO_2 nanomaterial than others, due to their pore sizes, surface area and defects. Therefore, it is important to consider precursor materials. 4) The RuO_2 nanomaterials have been seen to act as spacers for carbon materials to reduce agglomeration and increase the conductivity by an improving conduction pathway for electrolyte ions, thus reducing the composites internal resistance. 5) Antimony has shown very useful properties for energy storage purposes; however, it has never been combined with ruthenium. Its major drawback is its volume expansion during the insertion of ions. The alloying of it with another metal and the introduction of carbon to its matrix might be a way to reduce this challenge.

In general, these composites were found not only to offer their unique advantages but also to address the flaws of a single material and thus to achieve improved performance.

2.5 REFERENCE

[1]   S.E. Hosseini, An outlook on the global development of renewable and sustainable energy at the time of COVID-19, Energy Res. Soc. Sci. 68 (2020) 101633. https://doi.org/10.1016/j.erss.2020.101633.

[2]   I. Gunnarsdottir, B. Davidsdottir, E. Worrell, S. Sigurgeirsdottir, Sustainable energy development: History of the concept and emerging themes, Renew. Sustain. Energy Rev. 141 (2021) 110770. https://doi.org/10.1016/j.rser.2021.110770.

[3]   D.M. Kammen, D.A. Sunter, City-integrated renewable energy for urban sustainability, Science 352 (6288) (2016) 922–928. https://doi.org/10.1126/science.aad9302.

[4]   J.P. Holdren, Energy and sustainability, Science 315 (2007) 781-813. https://doi.org/10.1126/science.1139792.

[5]   H. Parsimehr, A. Ehsani, Corn-based electrochemical energy storage devices, Chem. Rec. 20 (2020) 1163–1180. https://doi.org/10.1002/tcr.202000058.

[6]   Poonam, K. Sharma, A. Arora, S.K. Tripathi, Review of supercapacitors: Materials and devices, J. Energy Storage. 21 (2019) 801–825. https://doi.org/10.1016/j.est.2019.01.010.

[7]   C.N. Chervin, A.M. Lubers, J.W. Long, D.R. Rolison, Effect of temperature and atmosphere on the conductivity and electrochemical capacitance of single-unit-thick ruthenium dioxide, J. Electroanal. Chem. 644 (2010) 155–163. https://doi.org/10.1016/j.jelechem.2010.01.002.

[8]   S.A. Mazari, E. Ali, R. Abro, F.S.A. Khan, I. Ahmed, M. Ahmed, S. Nizamuddin, T.H. Siddiqui, N. Hossain, N.M. Mubarak, A. Shah, Nanomaterials: Applications, waste-handling, environmental toxicities, and future challenges - A review, J. Environ. Chem. Eng. 9 (2021) 105028. https://doi.org/10.1016/j.jece.2021.105028.

[9]   A.R. Thiruppathi, B. Sidhureddy, E. Boateng, D. V. Soldatov, A. Chen, Synthesis and electrochemical study of three-dimensional graphene-based nanomaterials for energy applications, Nanomaterials 10 (2020) 1–25. https://doi.org/10.3390/nano10071295.

[10]   Q. Wang, Y. Zhou, X. Zhao, K. Chen, G. Bingni, T. Yang, H. Zhang, W. Yang, J. Chen, Tailoring carbon nanomaterials via a molecular scissor, Nano Today. 36 (2021) 101033. https://doi.org/10.1016/j.nantod.2020.101033.

[11]   F.C. Wu, R.L. Tseng, C.C. Hu, C.C. Wang, Effects of pore structure and electrolyte on the capacitive characteristics of steam- and KOH-activated carbons for supercapacitors, J. Power Sources. 144 (2005) 302–309. https://doi.org/10.1016/j.jpowsour.2004.12.020.

[12]   C. Largeot, C. Portet, J. Chmiola, P.L. Taberna, Y. Gogotsi, P. Simon, Relation between the ion size and pore size for an electric double-layer capacitor, J. Am. Chem. Soc. 130 (2008) 2730–2731. https://doi.org/10.1021/ja7106178.

[13]   F. Barzegar, D.Y. Momodu, O.O. Fashedemi, A. Bello, J.K. Dangbegnon, N. Manyala, Investigation of different aqueous electrolytes on the electrochemical performance of activated carbon-based supercapacitors, RSC Adv. 5 (2015) 107482–107487. https://doi.org/10.1039/c5ra21962k.

[14]   T.E. Kibona, G.N. Shao, H.T. Kim, C.K. King'ondu, Specific capacitance–pore texture

relationship of biogas slurry mesoporous carbon/MnO₂ composite electrodes for supercapacitors, Nano-Structures and Nano-Objects 17 (2019) 21–33. https://doi.org/10.1016/j.nanoso.2018.10.002.

[15]   R. Heimböckel, F. Hoffmann, M. Fröba, Insights into the influence of the pore size and surface area of activated carbons on the energy storage of electric double layer capacitors with a new potentially universally applicable capacitor model, Phys. Chem. Chem. Phys. 21 (2019) 3122–3133. https://doi.org/10.1039/c8cp06443a.

[16]   D. Kim, K. Lee, M. Kim, Y. Kim, H. Lee, Carbon-based asymmetric capacitor for high-performance energy storage devices, Electrochim. Acta. 300 (2019) 461–469. https://doi.org/10.1016/j.electacta.2019.01.141.

[17]   S.A. Hesse, P.A. Beaucage, D.M. Smilgies, U. Wiesner, Structurally asymmetric porous carbon materials with ordered top surface layers from nonequilibrium block copolymer self-assembly, Macromolecules. 54 (2021) 2979–2991. https://doi.org/10.1021/acs.macromol.0c02720.

[18]   J.-D. Xie, J. Patra, A. Taimiyah, I. Muhammad, Y. Ashraf Gandomi, T.-Y. Wu, S.-W. Lee, J.-K. Chang, Graphene induced crystallinity and hydrous state variations of ruthenium oxide electrodes for superior energy storage performance, Electrochim. Acta, 360 (2020) 136995. https://doi.org/10.1016/j.electacta.2020.136995.

[19]   D. Galizzioli, F. Tantardini, S. Trasatti, Ruthenium dioxide: a new electrode material. I. Behaviour in acid solutions of inert electrolytes, J. Appl. Electrochem. 4 (1974) 57–67. https://doi.org/10.1007/BF00615906.

[20] S Ardizzone,G Fregonara, S, Trasatti " Inner " and " outer " active surface electrodes of RuO$_2$, Electrochimica Acta, 35 (1) (1990) 263-267.

[21] W.D. Ryden, A.W. Lawson, C.C. Sartain, Temperature dependence of the resistivity of RuO$_2$ and IrO$_2$, Phys. Lett. A. 26 (1968) 209–210. https://doi.org/10.1016/0375-9601(68)90126-6.

[22] D.S. Ko, W.J. Lee, S. Sul, C. Jung, D.J. Yun, H.G. Kim, W.J. Son, J.G. Chung, D.W. Jung, S.Y. Kim, J. Kim, W. Lee, C. Kwak, J.K. Shin, J.H. Kim, J.W. Roh, Understanding the structural, electrical, and optical properties of monolayer h-phase RuO$_2$ nanosheets: A combined experimental and computational study, NPG Asia Mater. 10 (2018) 266–276. https://doi.org/10.1038/s41427-018-0020-y.

[23] W. Sugimoto, H. Iwata, K. Yokoshima, Y. Murakami, Y. Takasu, Proton and electron conductivity in hydrous ruthenium oxides evaluated by electrochemical impedance spectroscopy: The origin of large capacitance, J. Phys. Chem. B. 109 (2005) 7330–7338. https://doi.org/10.1021/jp044252o.

[24] V. Ozoliņš, F. Zhou, M. Asta, Ruthenia-based electrochemical supercapacitors: Insights from first-principles calculations, Acc. Chem. Res. 46 (2013) 1084–1093. https://doi.org/10.1021/ar3002987.

[25] W. Sugimoto, K. Yokoshima, Y. Murakami, Y. Takasu, Charge storage mechanism of nanostructured anhydrous and hydrous ruthenium-based oxides, 52 (2006) 1742–1748. https://doi.org/10.1016/j.electacta.2006.02.054.

[26] R. Fu, Z. Ma, J.P. Zheng, Proton NMR and dynamic studies of hydrous ruthenium oxide, The

Journal of Physical Chemisrty B 106 (14) (2002) 3592–3596. https://doi.org/10.1021/jp013860q.

[27] S. Han, F. Hou, X. Yuan, J. Liu, X. Yan, S. Chen, Continuous hierarchical carbon nanotube/reduced graphene oxide hybrid films for supercapacitors, Electrochim. Acta, 225 (2017) 566–573. https://doi.org/10.1016/j.electacta.2016.12.159.

[28] K.H. Kim, K.S. Kim, G.P. Kim, S.H. Baeck, Electrodeposition of mesoporous ruthenium oxide using an aqueous mixture of CTAB and SDS as a templating agent, Curr. Appl. Phys. 12 (2012) 36–39. https://doi.org/10.1016/j.cap.2011.04.029.

[29] J. De Xie, J. Patra, A.T.I. Muhammad, Y.A. Gandomi, T.Y. Wu, S.W. Lee, J.K. Chang, Graphene induced crystallinity and hydrous state variations of ruthenium oxide electrodes for superior energy storage performance, Electrochim. Acta, 360 (2020) 136995. https://doi.org/10.1016/j.electacta.2020.136995.

[30] B.Y. Fugare, B.J. Lokhande, Study on structural, morphological, electrochemical and corrosion properties of mesoporous RuO_2 thin films prepared by ultrasonic spray pyrolysis for supercapacitor electrode application, Mater. Sci. Semicond. Process, 71 (2017) 121–127. https://doi.org/10.1016/j.mssp.2017.07.016.

[31] M.H. Tran, H.K. Jeong, Comparison of ruthenium composites with thermally reduced graphene and activated carbon for supercapacitor applications, J. Mater. Sci. Mater. Electron, 28 (2017) 7969–7975. https://doi.org/10.1007/s10854-017-6500-y.

[32] V. Vijayabala, N. Senthilkumar, K. Nehru, R. Karvembu, Hydrothermal synthesis and characterization of ruthenium oxide nanosheets using polymer additive for supercapacitor

applications, J. Mater. Sci. Mater. Electron, 29 (2018) 323–330. https://doi.org/10.1007/s10854-017-7919-x.

[33]   B.O. Park, C.D. Lokhande, H.S. Park, K.D. Jung, O.S. Joo, Performance of supercapacitor with electrodeposited ruthenium oxide film electrodes - Effect of film thickness, J. Power Sources, 134 (2004) 148–152. https://doi.org/10.1016/j.jpowsour.2004.02.027.

[34]   E. Petrucci, M. Orsini, F. Porcelli, S. De Santis, G. Sotgiu, Effect of spin coating parameters on the electrochemical properties of ruthenium oxide thin films, Electrochem. 2 (2021) 83–94. https://doi.org/10.3390/electrochem2010008.

[35]   R.K.V. Prataap, R. Arunachalam, R. Pavul Raj, S. Mohan, L. Peter, Effect of electrodeposition modes on ruthenium oxide electrodes for supercapacitors, Curr. Appl. Phys. 18 (2018) 1143–1148. https://doi.org/10.1016/j.cap.2018.06.015.

[36]   N. B., V. Y., S. Abdul Razack, Enhanced formation of ruthenium oxide nanoparticles through green synthesis for highly efficient supercapacitor applications, Adv. Powder Technol. 31 (2020) 1001–1006. https://doi.org/10.1016/j.apt.2019.12.026.

[37]   J.H. Jang, A. Kato, K. Machida, K. Naoi, Supercapacitor performance of hydrous ruthenium oxide electrodes prepared by electrophoretic deposition, J. Electrochem. Soc. 153 (2006) A321. https://doi.org/10.1149/1.2138672.

[38]   J.Y. Hwang, M.F. El-Kady, Y. Wang, L. Wang, Y. Shao, K. Marsh, J.M. Ko, R.B. Kaner, Direct preparation and processing of graphene/RuO_2 nanocomposite electrodes for high-performance capacitive energy storage, Nano Energy, 18 (2015) 57–70. https://doi.org/10.1016/j.nanoen.2015.09.009.

[39] J. Zhang, Y. Duan, Z. Jiang, T. Chen, K. Wang, K. Wang, W. Zhang, J. Hu, Investigation of the supercapacitance of ruthenium-based/ hemp stem activated carbon, J. Phys. Chem. Solids 153 (2021) 110019. https://doi.org/10.1016/j.jpcs.2021.110019.

[40] C.C. Hu, K.H. Chang, Cyclic voltammetric deposition of hydrous ruthenium oxide for electrochemical supercapacitors: Effects of the chloride precursor transformation, J. Power Sources, 112 (2002) 401–409. https://doi.org/10.1016/S0378-7753(02)00397-X.

[41] R. Arunachalam, R.M. Gnanamuthu, M. Al Ahmad, S. Mohan, R. Pavul Raj, J. Maharaja, N. Al Taradeh, A. Al-Hinai, Development of nano-spherical RuO_2 active material on AISI 317 steel substrate via pulse electrodeposition for supercapacitors, Surf. Coatings Technol. 276 (2015) 336–340. https://doi.org/10.1016/j.surfcoat.2015.06.054.

[42] C. (John) Zhang, T.M. Higgins, S.H. Park, S.E. O'Brien, D. Long, J.N. Coleman, V. Nicolosi, Highly flexible and transparent solid-state supercapacitors based on RuO2/PEDOT:PSS conductive ultrathin films, Nano Energy, 28 (2016) 495–505. https://doi.org/10.1016/j.nanoen.2016.08.052.

[43] W. Zheng, Q. Cheng, D. Wang, C. V. Thompson, High-performance solid-state on-chip supercapacitors based on Si nanowires coated with ruthenium oxide via atomic layer deposition, J. Power Sources, 341 (2017) 1–10. https://doi.org/10.1016/j.jpowsour.2016.11.093.

[44] X. Wu, W. Xiong, Y. Chen, D. Lan, X. Pu, Y. Zeng, H. Gao, J. Chen, H. Tong, Z. Zhu, High-rate supercapacitor utilizing hydrous ruthenium dioxide nanotubes, J. Power Sources, 294 (2015) 88–93. https://doi.org/10.1016/j.jpowsour.2015.06.064.

[45] J. Wang, Y. Xu, L. Li, J. Lin, Hydrous ruthenium oxide prepared by steam-assisted thermolysis: Capacitance and stability, Solid State Ionics, 268 (2014) 312–315. https://doi.org/10.1016/j.ssi.2014.03.007.

[46] Y.Z. Zheng, H.Y. Ding, M.L. Zhang, Hydrous-ruthenium-oxide thin film electrodes prepared by cathodic electrodeposition for supercapacitors, Thin Solid Films, 516 (2008) 7381–7385. https://doi.org/10.1016/j.tsf.2008.02.022.

[47] P.R. Deshmukh, S. V. Patil, R.N. Bulakhe, S.D. Sartale, C.D. Lokhande, Inexpensive synthesis route of porous polyaniline-ruthenium oxide composite for supercapacitor application, Chem. Eng. J. 257 (2014) 82–89. https://doi.org/10.1016/j.cej.2014.06.038.

[48] K. Brousse, S. Nguyen, A. Gillet, S. Pinaud, R. Tan, A. Meffre, K. Soulantica, B. Chaudret, P.L. Taberna, M. Respaud, P. Simon, Laser-scribed Ru organometallic complex for the preparation of RuO_2 micro-supercapacitor electrodes on flexible substrate, Electrochim. Acta. 281 (2018) 816–821. https://doi.org/10.1016/j.electacta.2018.05.198.

[49] K.M. Lin, K.H. Chang, C.C. Hu, Y.Y. Li, Mesoporous RuO_2 for the next generation supercapacitors with an ultrahigh power density, Electrochim. Acta, 54 (2009) 4574–4581. https://doi.org/10.1016/j.electacta.2009.03.058.

[50] M. Riccioni, R. Marmo, L'enteroscopia con video capsula vs procedure alternative nella Malattia di Crohn: Una meta-analisi sul guadagno diagnostico, G. Ital. Di Endosc. Dig. 33 (2010) 277–280. https://doi.org/10.1016/j.jpowsour.2014.06.035.

[51] Y. Guo, W. Zhang, Y. Sun, M. Dai, Ruthenium nanoparticles stabilized by mercaptan and acetylene derivatives with supercapacitor application, MethodsX. 5 (2018) 795–796.

https://doi.org/10.1016/j.mex.2018.07.004.

[52]   I.-H. Kim, K.-B. Kim, Ruthenium Oxide Thin Film Electrodes Prepared by Electrostatic Spray

Deposition and Their Charge Storage Mechanism, J. Electrochem. Soc. 151 (2004) E7.

https://doi.org/10.1149/1.1631823.

[53]   M. Gnerlich, H. Ben-Yoav, J.N. Culver, D.R. Ketchum, R. Ghodssi, Selective deposition of

nanostructured ruthenium oxide using Tobacco mosaic virus for micro-supercapacitors in

solid   Nafion   electrolyte,   J.   Power   Sources,   293   (2015)   649–656.

https://doi.org/10.1016/j.jpowsour.2015.05.053.

[54]   J.M. Ko, J.H. Nam, J.H. Won, K.M. Kim, Supercapacitive properties of electrodeposited

polyaniline electrode in acrylic gel polymer electrolytes, Synth. Met. 189 (2014) 152–156.

https://doi.org/10.1016/j.synthmet.2014.01.011.

[55]   S. Makino, Y. Yamauchi, W. Sugimoto, Synthesis of electro-deposited ordered mesoporous

RuOxusing lyotropic liquid crystal and application toward micro-supercapacitors, J. Power

Sources, 227 (2013) 153–160. https://doi.org/10.1016/j.jpowsour.2012.11.032.

[56]   A. Devadas, S. Baranton, T.W. Napporn, C. Coutanceau, Tailoring of RuO2nanoparticles by

microwave assisted "instant method" for energy storage applications, J. Power Sources,

196 (2011) 4044–4053. https://doi.org/10.1016/j.jpowsour.2010.11.149.

[57]   F. Pico, E. Morales, J.A. Fernandez, T.A. Centeno, J. Ibañez, R.M. Rojas, J.M. Amarilla, J.M.

Rojo, Ruthenium oxide/carbon composites with microporous or mesoporous carbon as

support   and   prepared   by   two   procedures.   A   comparative   study   as   supercapacitor

electrodes,   Electrochim.   Acta,   54   (2009)   2239–2245.

https://doi.org/10.1016/j.electacta.2008.10.028.

[58]   K. Kaiser, L.M. Scriven, F. Schulz, P. Gawel, L. Gross, H.L. Anderson, An sp-hybridized molecular carbon allotrope, cyclo [18] carbon, Science, 365 (6459) (2019) 1299–1301. https://doi.org/10.1126/science.aay1914.

[59]   B. Ram, H. Mizuseki, C568: A new two-dimensional sp2-sp3 hybridized allotrope of carbon, Carbon N. Y. 158 (2020) 827–835. https://doi.org/10.1016/j.carbon.2019.11.062.

[60]   A.G. Pandolfo, A.F. Hollenkamp, Carbon properties and their role in supercapacitors, J. Power Sources, 157 (2006) 11–27. https://doi.org/10.1016/j.jpowsour.2006.02.065.

[61]   A.K. Geim, K.S. Novoselov, The rise of graphene, in: Nanosci. Technol. A Collect. Rev. from Nat. Journals, World Scientific Publishing Co., 2009: pp. 11–19. https://doi.org/10.1142/9789814287005_0002.

[62]   M.H.A. Kudus, M.R. Zakaria, H.M. Akil, F. Ullah, F. Javed, Oxidation of graphene via a simplified Hummers' method for graphene-diamine colloid production, J. King Saud Univ. - Sci. 32 (2020) 910–913. https://doi.org/10.1016/j.jksus.2019.05.002.

[63]   E.E. Mathew, M. Balachandran, Crumpled and porous graphene for supercapacitor applications: a short review, Carbon Lett. (2021). https://doi.org/10.1007/s42823-021-00229-2.

[64]   W. Wu, M. Liu, Y. Gu, B. Guo, H.X. Ma, P. Wang, X. Wang, R. Zhang, Fast chemical exfoliation of graphite to few-layer graphene with high quality and large size via a two-step microwave-assisted process, Chem. Eng. J. 381 (2020) 122592. https://doi.org/10.1016/j.cej.2019.122592.

[65] Y. Bai, Y. Yin, Y. Xuan, X. Han, Scalable and fast fabrication of holey multilayer graphene via microwave and its application in supercapacitors, Nanotechnology, 32 (2021) 045602. https://doi.org/10.1088/1361-6528/abbfd4.

[66] Y. Wang, Z. Shi, Y. Huang, Y. Ma, C. Wang, M. Chen, Y. Chen, Supercapacitor devices based on graphene materials, The Journal of Phy. Chem. C 113. 30 (2009) 13103–13107.

[67] M.F. El-Kady, V. Strong, S. Dubin, R.B. Kaner, Laser scribing of high-performance and flexible graphene-based electrochemical capacitors, Science, 335.6074 (2012) 1326–1330. https://doi.org/10.1126/science.1216744.

[68] Y. Bai, Y. Yin, Y. Xuan, X. Han, Scalable and fast fabrication of holey multilayer graphene via microwave and its application in supercapacitors, Nanotechnology, 32 (2021) 045602. https://doi.org/10.1088/1361-6528/abbfd4.

[69] W. Wang, S. Guo, I. Lee, K. Ahmed, J. Zhong, Z. Favors, F. Zaera, M. Ozkan, C.S. Ozkan, Hydrous ruthenium oxide nanoparticles anchored to graphene and carbon nanotube hybrid foam for supercapacitors, Sci. Rep. 4 (2014) 9–14. https://doi.org/10.1038/srep04452.

[70] K.Y. Kumar, S. Archana, R. Namitha, B.P. Prasanna, S.C. Sharma, M.S. Raghu, Ruthenium oxide nanostring clusters anchored Graphene oxide nanocomposites for high-performance supercapacitors application, Mater. Res. Bull. 107 (2018) 347–354. https://doi.org/10.1016/j.materresbull.2018.08.011.

[71] Z.J. Han, S. Pineda, A.T. Murdock, D.H. Seo, K.K. Ostrikov, A. Bendavid, RuO_2-coated vertical graphene hybrid electrodes for high-performance solid-state supercapacitors, J. Mater.

Chem. A. 5 (2017) 17293–17301. https://doi.org/10.1039/c7ta03355a.

[72] P. Suktha, N. Phattharasupakun, M. Sawangphruk, Transparent supercapacitors of 2 nm ruthenium oxide nanoparticles decorated on a 3D nitrogen-doped graphene aerogel, Sustain. Energy Fuels, 2 (2018) 1799–1805. https://doi.org/10.1039/C8SE00177D.

[73] S. Cho, J. Kim, Y. Jo, A.T.A. Ahmed, H.S. Chavan, H. Woo, A.I. Inamdar, J.L. Gunjakar, S.M. Pawar, Y. Park, H. Kim, H. Im, Bendable RuO_2/graphene thin film for fully flexible supercapacitor electrodes with superior stability, J. Alloys Compd. 725 (2017) 108–114. https://doi.org/10.1016/j.jallcom.2017.07.135.

[74] X. Li, D. Liu, X. Yin, C. Zhang, P. Cheng, H. Guo, W. Song, J. Wang, Hydrated ruthenium dioxides @ graphene based fiber supercapacitor for wearable electronics, J. Power Sources, 440 (2019) 227143. https://doi.org/10.1016/j.jpowsour.2019.227143.

[75] Y.L. Wu, X. Li, Y.S. Wei, Z. Fu, W. Wei, X.T. Wu, Q.L. Zhu, Q. Xu, Ordered macroporous superstructure of nitrogen-doped nanoporous carbon implanted with ultrafine ru nanoclusters for efficient ph-universal hydrogen evolution reaction, Adv. Mater. 33 (2021) 2006965. https://doi.org/10.1002/adma.202006965.

[76] X. Leng, J. Zou, X. Xiong, H. He, Hydrothermal synthesis and pseudo capacitance behavior of a highly homogeneous dispersed graphene sheets/ruthenium oxide nanocomposite, RSC Adv. 4 (2014) 61596–61603. https://doi.org/10.1039/c4ra10321a.

[77] J. Li, M. Zhu, Z. An, Z. Wang, M. Toda, T. Ono, Constructing in-chip micro-supercapacitors of 3D graphene nanowall/ruthenium oxides electrode through silicon-based microfabrication technique, J. Power Sources, 401 (2018) 204–212.

https://doi.org/10.1016/j.jpowsour.2018.08.099.

[78]   J. Zhang, J. Jiang, H. Li, X.S. Zhao, A high-performance asymmetric supercapacitor

fabricated with graphene-based electrodes, Energy Environ. Sci. 4 (2011) 4009–4015.

https://doi.org/10.1039/c1ee01354h.

[79]   P. Wang, H. Liu, Y. Xu, Y. Chen, J. Yang, Q. Tan, Supported ultrafine ruthenium oxides with

specific capacitance up to 1099 F g-1for a supercapacitor, Electrochim. Acta 194 (2016)

211–218. https://doi.org/10.1016/j.electacta.2016.02.089.

[80]   L.Q. Fan, G.J. Liu, J.H. Wu, L. Liu, J.M. Lin, Y.L. Wei, Asymmetric supercapacitor based on

graphene oxide/polypyrrole composite and activated carbon electrodes, Electrochim.

Acta, 137 (2014) 26–33. https://doi.org/10.1016/j.electacta.2014.05.137.

[81]   A.K. Mishra, S. Ramaprabhu, Functionalized graphene-based nanocomposites for

supercapacitor application, The Journal of Phy. Chem C, 115.29 (2011) 14006–14013.

https://doi.org/10.1021/jp201673e.

[82]   B.Z. Wu, D. Wang, W. Ren, J. Zhao, G. Zhou, Anchoring hydrous RuO_2 on graphene sheets

for high-performance electrochemical capacitors, Adv. Functional Mat. 20.20 (2010)

3595–3602. https://doi.org/10.1002/adfm.201001054.

[83]   S. Zhai, C. Wang, H.E. Karahan, Y. Wang, X. Chen, X. Sui, Q. Huang, X. Liao, X. Wang, Y. Chen,

Nano-RuO_2 -Decorated holey graphene composite fibers for micro-supercapacitors with

ultrahigh   energy   density,   Small,   1800582   (2018)   28–34.

https://doi.org/10.1002/smll.201800582.

[84]   H. Ma, D. Kong, Y. Xu, X. Xie, Y. Tao, Z. Xiao, W. Lv, Disassembly – Reassembly Approach to

RuO$_2$ / Graphene composites for ultrahigh volumetric capacitance supercapacitor, (2017) 1–7. https://doi.org/10.1002/smll.201701026.

[85]   J. Ma, S. Tang, J.A. Syed, D. Su, X. Meng, High-performance asymmetric supercapacitors based on reduced graphene oxide/polyaniline composite electrodes with sandwich-like structure, J. Mater. Sci. Technol. 34 (2018) 1103–1109. https://doi.org/10.1016/j.jmst.2017.12.006.

[86]   W. Lu, L. Qu, K. Henry, L. Dai, High performance electrochemical capacitors from aligned carbon nanotube electrodes and ionic liquid electrolytes, J. Power Sources, 189 (2009) 1270–1277. https://doi.org/10.1016/j.jpowsour.2009.01.009.

[87]   S. Gao, K. Wang, Z. Du, Y. Wang, A. Yuan, W. Lu, L. Chen, High power density electric double-layer capacitor based on a porous multi-walled carbon nanotube microsphere as a local electrolyte micro-reservoir, Carbon N. Y. 92 (2015) 254–261. https://doi.org/10.1016/j.carbon.2015.04.034.

[88]   B.W. Charan Masarapu, Hai Feng Zeng, Kai Hsuan Hung, Temperature Effect on the Capacitance of Carbon Nanotube, ACS Nano. 3 (2010) 2199–2206.

[89]   X. Liu, T.A. Huber, M.C. Kopac, P.G. Pickup, Ru oxide/carbon nanotube composites for supercapacitors prepared by spontaneous reduction of Ru(VI) and Ru(VII), Electrochim. Acta. 54 (2009) 7141–7147. https://doi.org/10.1016/j.electacta.2009.07.044.

[90]   I.-H. Kim, K.-B. Kim, Electrochemical characterization of hydrous ruthenium oxide thin-film electrodes for electrochemical capacitor applications, J. Electrochem. Soc. 153 (2006) A383. https://doi.org/10.1149/1.2147406.

[91] X. Wang, Y. Yin, C. Hao, Z. You, A high-performance three-dimensional micro supercapacitor based on ripple-like ruthenium oxide-carbon nanotube composite films, Carbon N. Y. 82 (2015) 436–445. https://doi.org/10.1016/j.carbon.2014.10.087.

[92] P. Chen, H. Chen, J. Qiu, C. Zhou, Inkjet printing of single-walled carbon nanotube/RuO_2 nanowire supercapacitors on cloth fabrics and flexible substrates, Nano Res. 3 (2010) 594–603. https://doi.org/10.1007/s12274-010-0020-x.

[93] K. Le Van, T.T. Luong Thi, Activated carbon derived from rice husk by NaOH activation and its application in supercapacitor, Prog. Nat. Sci. Mater. Int. 24 (2014) 191–198. https://doi.org/10.1016/j.pnsc.2014.05.012.

[94] Y. Gao, L. Li, Y. Jin, Y. Wang, C. Yuan, Y. Wei, G. Chen, J. Ge, H. Lu, Porous carbon made from rice husk as electrode material for electrochemical double layer capacitor, Appl. Energy, 153 (2015) 41–47. https://doi.org/10.1016/j.apenergy.2014.12.070.

[95] W. Zhang, N. Lin, D. Liu, J. Xu, J. Sha, J. Yin, X. Tan, H. Yang, H. Lu, H. Lin, Direct carbonization of rice husk to prepare porous carbon for supercapacitor applications, Energy, 128 (2017) 618–625. https://doi.org/10.1016/j.energy.2017.04.065.

[96] E.Y.L. Teo, L. Muniandy, E.P. Ng, F. Adam, A.R. Mohamed, R. Jose, K.F. Chong, High surface area activated carbon from rice husk as a high performance supercapacitor electrode, Electrochim. Acta, 192 (2016) 110–119. https://doi.org/10.1016/j.electacta.2016.01.140.

[97] D. Wang, G. Fang, T. Xue, J. Ma, G. Geng, A melt route for the synthesis of activated carbon derived from carton box for high performance symmetric supercapacitor applications, J. Power Sources, 307 (2016) 401–409. https://doi.org/10.1016/j.jpowsour.2016.01.009.

[98] K. Wang, N. Zhao, S. Lei, R. Yan, X. Tian, J. Wang, Y. Song, D. Xu, Q. Guo, L. Liu, Promising biomass-based activated carbons derived from willow catkins for high performance supercapacitors, Electrochim. Acta, 166 (2015) 1–11. https://doi.org/10.1016/j.electacta.2015.03.048.

[99] D. Bhattacharjya, J.S. Yu, Activated carbon made from cow dung as electrode material for electrochemical double layer capacitor, J. Power Sources, 262 (2014) 224–231. https://doi.org/10.1016/j.jpowsour.2014.03.143.

[100] I.I.G. Inal, S.M. Holmes, A. Banford, Z. Aktas, The performance of supercapacitor electrodes developed from chemically activated carbon produced from waste tea, Appl. Surf. Sci. 357 (2015) 696–703. https://doi.org/10.1016/j.apsusc.2015.09.067.

[101] I.I. Gurten Inal, S.M. Holmes, E. Yagmur, N. Ermumcu, A. Banford, Z. Aktas, The supercapacitor performance of hierarchical porous activated carbon electrodes synthesised from demineralised (waste) cumin plant by microwave pretreatment, J. Ind. Eng. Chem. 61 (2018) 124–132. https://doi.org/10.1016/j.jiec.2017.12.009.

[102] A. Wang, K. Sun, R. Xu, Y. Sun, J. Jiang, Cleanly synthesizing rotten potato-based activated carbon for supercapacitor by self-catalytic activation, J. Clean. Prod. 283 (2021) 125385. https://doi.org/10.1016/j.jclepro.2020.125385.

[103] M.M. Baig, I.H. Gul, Conversion of wheat husk to high surface area activated carbon for energy storage in high-performance supercapacitors, Biomass and Bioenergy, 144 (2021) 105909. https://doi.org/10.1016/j.biombioe.2020.105909.

[104] H. Itoi, M. Ito, Y. Kasai, Y. Tanabe, R. Suzuki, H. Hasegawa, M. Miyaji, H. Iwata, Y. Ohzawa,

A. Beniya, S. Higashi, Study of the pore size effect on the charge storage of hydrous RuO_2 nanoparticles supported within the pores of activated carbon, Solid State Sci. 111 (2021) 106472. https://doi.org/10.1016/j.solidstatesciences.2020.106472.

[105] M. Kéri, B. Nagy, K. László, I. Bányai, Structural changes in resorcinol formaldehyde aerogel seen by NMR, Microporous Mesoporous Mater, 317 (2021) 110988. https://doi.org/10.1016/j.micromeso.2021.110988.

[106] Y. Zhu, H. Hu, W. Li, X. Zhang, Resorcinol-formaldehyde based porous carbon as an electrode material for supercapacitors, Carbon N. Y. 45 (2007) 160–165. https://doi.org/10.1016/j.carbon.2006.07.010.

[107] A. Halama, B. Szubzda, G. Pasciak, Carbon aerogels as electrode material for electrical double layer supercapacitors - Synthesis and properties, Electrochim. Acta 55 (2010) 7501–7505. https://doi.org/10.1016/j.electacta.2010.03.040.

[108] I. Yang, S.G. Kim, S.H. Kwon, M.S. Kim, J.C. Jung, Relationships between pore size and charge transfer resistance of carbon aerogels for organic electric double-layer capacitor electrodes, Electrochim. Acta, 223 (2017) 21–30. https://doi.org/10.1016/j.electacta.2016.11.177.

[109] N. Liu, J. Shen, D. Liu, Activated high specific surface area carbon aerogels for EDLCs, Microporous Mesoporous Mater, 167 (2013) 176–181. https://doi.org/10.1016/j.micromeso.2012.09.009.

[110] D. Liu, J. Shen, N. Liu, H. Yang, A. Du, Preparation of activated carbon aerogels with hierarchically porous structures for electrical double layer capacitors, Electrochim. Acta,

89 (2013) 571–576. https://doi.org/10.1016/j.electacta.2012.11.033.

[111] X.L. Wu, T. Wen, H.L. Guo, S. Yang, X. Wang, A.W. Xu, Biomass-derived sponge-like carbonaceous hydrogels and aerogels for supercapacitors, ACS Nano, 7 (2013) 3589–3597. https://doi.org/10.1021/nn400566d.

[112] A. Singh, D.K. Kohli, S. Bhartiya, R. Singh, M.K. Singh, P.K. Gupta, Ruthenium doped carbon aerogel with CO_2 surface activation for enhanced electrochemical capacitance, Curr. Appl. Phys. 17 (2017) 885–889. https://doi.org/10.1016/j.cap.2017.03.003.

[113] M.J. Crane, M.B. Lim, X. Zhou, P.J. Pauzauskie, Rapid synthesis of transition metal dichalcogenide–carbon aerogel composites for supercapacitor electrodes, Microsystems Nanoeng. 3 (2017) 1–9. https://doi.org/10.1038/micronano.2017.32.

[114] Z. Zeng, S. Chen, T.T.Y. Tan, F.-X. Xiao, Graphene quantum dots (GQDs) and its derivatives for multifarious photocatalysis and photoelectrocatalysis, Catal. Today. 315 (2018) 171–183. https://doi.org/10.1016/j.cattod.2018.01.005.

[115] F.A. Permatasari, M.A. Irham, S.Z. Bisri, F. Iskandar, Carbon-based quantum dots for supercapacitors: Recent advances and future challenges, Nanomaterials, 11 (2021) 1–34. https://doi.org/10.3390/nano11010091.

[116] I.Y. Goryacheva, A. V. Sapelkin, G.B. Sukhorukov, Carbon nanodots: Mechanisms of photoluminescence and principles of application, TrAC - Trends Anal. Chem. 90 (2017) 27–37. https://doi.org/10.1016/j.trac.2017.02.012.

[117] Y.P. Sun, B. Zhou, Y. Lin, W. Wang, K.A.S. Fernando, P. Pathak, M.J. Meziani, B.A. Harruff, X. Wang, H. Wang, P.G. Luo, H. Yang, M.E. Kose, B. Chen, L.M. Veca, S.Y. Xie, Quantum-

sized carbon dots for bright and colorful photoluminescence, J. Am. Chem. Soc. 128 (2006) 7756–7757. https://doi.org/10.1021/ja062677d.

[118]   S.L. Hu, K.Y. Niu, J. Sun, J. Yang, N.Q. Zhao, X.W. Du, One-step synthesis of fluorescent carbon nanoparticles by laser irradiation, J. Mater. Chem. 19 (2009) 484–488. https://doi.org/10.1039/b812943f.

[119]   S.J. Yu, M.W. Kang, H.C. Chang, K.M. Chen, Y.C. Yu, Bright fluorescent nanodiamonds: No photobleaching and low cytotoxicity, J. Am. Chem. Soc. 127 (2005) 17604–17605. https://doi.org/10.1021/ja0567081.

[120]   L. Cao, X. Wang, M.J. Meziani, F. Lu, H. Wang, P.G. Luo, Y. Lin, B.A. Harruff, L.M. Veca, D. Murray, S.Y. Xie, Y.P. Sun, Carbon dots for multiphoton bioimaging, J. Am. Chem. Soc. 129 (2007) 11318–11319. https://doi.org/10.1021/ja073527l.

[121]   H. Wang, J. Cao, Y. Zhou, Z. Wang, Y. Zhao, Y. Liu, H. Huang, M. Shao, Y. Liu, Z. Kang, Carbon dot-modified mesoporous carbon as a supercapacitor with enhanced light-assisted capacitance, Nanoscale, 12 (2020) 17925–17930. https://doi.org/10.1039/d0nr05532h.

[122]   G. Chen, S. Wu, L. Hui, Y. Zhao, J. Ye, Z. Tan, W. Zeng, Z. Tao, L. Yang, Y. Zhu, Assembling carbon quantum dots to a layered carbon for high-density supercapacitor electrodes, Sci. Rep. 6 (2016) 1–9. https://doi.org/10.1038/srep19028.

[123]   X. Jian, J. gang Li, H. min Yang, L. le Cao, E. hui Zhang, Z. hai Liang, Carbon quantum dots reinforced polypyrrole nanowire via electrostatic self-assembly strategy for high-performance supercapacitors, Carbon N. Y. 114 (2017) 533–543. https://doi.org/10.1016/j.carbon.2016.12.033.

[124] X. Zhang, J. Wang, J. Liu, J. Wu, H. Chen, H. Bi, Design and preparation of a ternary composite of graphene oxide/carbon dots/polypyrrole for supercapacitor application: Importance and unique role of carbon dots, Carbon N. Y. 115 (2017) 134–146. https://doi.org/10.1016/j.carbon.2017.01.005.

[125] W.W. Liu, Y.Q. Feng, X. Bin Yan, J.T. Chen, Q.J. Xue, Superior micro-supercapacitors based on graphene quantum dots, Adv. Funct. Mater. 23 (2013) 4111–4122. https://doi.org/10.1002/adfm.201203771.

[126] Y. Zhu, X. Ji, C. Pan, Q. Sun, W. Song, L. Fang, Q. Chen, C.E. Banks, A carbon quantum dot decorated RuO_2 network: Outstanding supercapacitances under ultrafast charge and discharge, Energy Environ. Sci. 6 (2013) 3665–3675. https://doi.org/10.1039/c3ee41776j.

[127] Y. Zhu, X. Ji, C. Pan, Q. Sun, W. Song, L. Fang, Q. Chen, C.E. Banks, A carbon quantum dot decorated RuO_2 network: outstanding supercapacitances under ultrafast charge and discharge, Energy Environ. Sci. 6 (2013) 3665. https://doi.org/10.1039/c3ee41776j.

[128] J. Janzen, G. Kraus, Specific Surface Area Measurements on Carbon Black, Rubber Chem. Technol. 44 (1971) 1287–1296. https://doi.org/10.5254/1.3544809.

[129] C. Fan, Y. Dong, Y. Liu, L. Zhang, D. Wang, X. Lin, Y. Lv, S. Zhang, H. Song, D. Jia, Mesopore-dominated hollow carbon nanoparticles prepared by simple air oxidation of carbon black for high mass loading supercapacitors, Carbon N. Y. 160 (2020) 328–334. https://doi.org/10.1016/J.CARBON.2020.01.034.

[130] K. Yang, K. Cho, S. Kim, Effect of carbon black addition on thermal stability and capacitive performances of supercapacitors, Sci. Rep. 8 (2018) 1–7. https://doi.org/10.1038/s41598-

018-30507-5.

[131] N. Jayababu, D. Kim, ZnO nanorods@conductive carbon black nanocomposite based flexible integrated system for energy conversion and storage through triboelectric nanogenerator and supercapacitor, Nano Energy, 82 (2021) 105726. https://doi.org/10.1016/J.NANOEN.2020.105726.

[132] M. Ates, Y. Yuruk, Facile preparation of reduced graphene oxide, polypyrrole, carbon black, and polyvinyl alcohol nanocomposite by electrospinning: a low-cost and sustainable approach for supercapacitor application, Ionics, 2021 276. 27 (2021) 2659–2672. https://doi.org/10.1007/S11581-021-04007-Y.

[133] P. Kossyrev, Carbon black supercapacitors employing thin electrodes, J. Power Sources, 201 (2012) 347–352. https://doi.org/10.1016/j.jpowsour.2011.10.106.

[134] A. Krause, P. Kossyrev, M. Oljaca, S. Passerini, M. Winter, A. Balducci, Electrochemical double layer capacitor and lithium-ion capacitor based on carbon black, J. Power Sources 196 (2011) 8836–8842. https://doi.org/10.1016/j.jpowsour.2011.06.019.

[135] X.J. He, Y.J. Geng, S. Oke, K. Higashi, M. Yamamoto, H. Takikawa, Electrochemical performance of $RuOx$/activated carbon black composite for supercapacitors, Synth. Met. 159 (2009) 7–12. https://doi.org/10.1016/j.synthmet.2008.07.008.

[136] M. Min, K. Machida, J.H. Jang, K. Naoi, Hydrous RuO_2/Carbon black nanocomposites with 3d porous structure by novel incipient wetness method for supercapacitors, J. Electrochem. Soc. 153 (2006) A334. https://doi.org/10.1149/1.2140677.

[137] D.S. Kim, J. Bae, S.H. Kwon, J. Hur, S.G. Lee, I.T. Kim, Synergistic effect of antimony-

triselenide on addition of conductive hybrid matrix for high-performance lithium-ion batteries, J. Alloys Compd. 828 (2020) 154410. https://doi.org/10.1016/j.jallcom.2020.154410.

[138] D.Y.W. Yu, P. V. Prikhodchenko, C.W. Mason, S.K. Batabyal, J. Gun, S. Sladkevich, A.G. Medvedev, O. Lev, High-capacity antimony sulphide nanoparticle-decorated graphene composite as anode for sodium-ion batteries, Nat. Commun. 4 (2013) 1–7. https://doi.org/10.1038/ncomms3922.

[139] E. Martínez-Periñán, M.P. Down, C. Gibaja, E. Lorenzo, F. Zamora, C.E. Banks, Antimonene: A Novel 2D Nanomaterial for Supercapacitor Applications, Adv. Energy Mater, 8 (2018) 1–8. https://doi.org/10.1002/aenm.201702606.

[140] F. Ali, N.R. Khalid, M.B. Tahir, G. Nabi, K. Shahzad, A.M. Ali, M.R. Kabli, Capacitive properties of novel Sb-doped Co_3O_4 electrode material synthesized by hydrothermal method, Ceram. Int. 47 (2021) 32210–32217. https://doi.org/10.1016/j.ceramint.2021.08.114.

[141] V.K. Mariappan, K. Krishnamoorthy, P. Pazhamalai, S. Sahoo, S.J. Kim, Layered famatinite nanoplates as an advanced pseudocapacitive electrode material for supercapacitor applications, Electrochim. Acta, 275 (2018) 110–118. https://doi.org/10.1016/j.electacta.2018.04.126.

[142] K. Ramasamy, R.K. Gupta, S. Palchoudhury, S. Ivanov, A. Gupta, Layer-structured copper antimony chalcogenides: Stable electrode materials for supercapacitors, Chem. Mater. 27 (2015) 379–386. https://doi.org/10.1021/cm5041166.

[143] Z. Lin, L. Xu, Y. Ling, X. Zhou, L. Ma, Solvothermal synthesis of antimony phosphate hierarchical microspindles and their capacitive property, Mater. Lett. 227 (2018) 264–267. https://doi.org/10.1016/j.matlet.2018.05.104.

[144] A. Shanmugavani, M. Lalitha, R.K. Narayanan Kutty, L. Vasylechko, Y.S. Lee, S. Lakshmipathi, R. Kalai Selvan, The first-principles study of $CoSb_2O_4$ and its electrochemical properties for supercapacitors, Electrochim. Acta, 283 (2018) 949–958. https://doi.org/10.1016/j.electacta.2018.06.193.

[145] D. Raknual, S. Charoenphon, P. Reunchan, A. Tubtimtae, Structural and electrochemical properties of undoped and In^{3+}-doped multi-phase zinc- antimony oxide for a high-performance pseudocapacitor, Electrochim. Acta, 389 (2021) 138773. https://doi.org/10.1016/j.electacta.2021.138773.

[146] S. Korkmaz, F. Meydaneri Tezel, A. Kariper, A. Serin, Effects of deposition temperatures on the supercapacitor cathode performances of GO:SnSbS/Si thin films, J. Energy Storage, 33 (2021) 102116. https://doi.org/10.1016/j.est.2020.102116.

[147] M. Ciszewski, A. Mianowski, G. Nawrat, P. Szatkowski, Reduced Graphene Oxide Supported Antimony Species for High-Performance Supercapacitor Electrodes, ISRN Electrochem. 2014 (2014) 1–7. https://doi.org/10.1155/2014/826832.

CHAPTER THREE

SYNTHESIS AND CHARACTERIZATION OF GRAPHENE FOR SUPERCAPACITOR APPLICATION

ABSTRACT

A chemical synthetic approach was used to make multi-layer graphene nanosheets, which requires first, oxidizing graphite to graphene oxide (GO) and then chemically reducing GO to graphene. The conversion of GO to graphene is confirmed by Fourier transform infra-red spectroscopy (FTIR). The ordered graphite crystal structure of graphene nanosheets was validated by high-resolution TEM (HRTEM) and selected area electron diffraction (SAED) studies. When compared to GO and graphite, the electrochemical characterization revealed enhanced capacitive performance. Finally, a graphene/activated carbon electrode was made, and the device delivered a maximum energy density of 14.80 W h kg^{-1}, at a power density of 360 W kg^{-1}, at 0.1 A g^{-1} current load.

KEYWORDS

EDLC, energy density, graphene, power density, supercapacitors.

3.1 INTRODUCTION

Nanomaterial design involves different steps such as; synthesis of a precursor, characterization and optimization. Among the naturally occurring precursors, carbon is the most prevalent element and can be found in all organic materials [1]. It occurs in many forms like graphite and diamond. Graphite, an allotrope of carbon exist as individual layers of graphene stacked together [2]. The graphene layer structured are stacked in a way that they can be easily separated and can easily slide through each other, this is owing to the week Van der Waals forces holding the structure together. Graphene is one layer thick, two-dimension (2D) structured macro-molecule with an impressively massive surface area (2600 m^2 g^{-1})[3][4]. It is not only the thinnest material tested, but it is also very strong with a tensile strength of E≈1.01 Tpa, ultimate strength of $^\delta$ ≈130 which makes it 200 times stronger than an equivalent amount of steel. Graphene is biodegradable, and biocompatible. The intrinsic capacitance of single-layer graphene has been reported to be ~21µF/cm^2, thus ECs based on graphene material can theoretically attain a capacitance of ~550F g^{-1} if their entire surface is put to use [5].

One of the most successful approaches to preparing graphene nano sheets (GN) involves hydrazine reduction of in-solution graphene oxide (GO) prepared by the Hummers method. In this method, GO is first synthesized chemically from graphite flakes [6], it is then reduced to graphene. Graphene oxide in its structure contains different functional groups attached to the basal planes and the sideways of the structure such as hydroxyl, carbonyl, epoxide, lactone, or ether groups [7]. Therefore, the reduction process must involve the removal of the above oxygen

functional groups. Since the GO can be directly converted to crystalline graphene, the conjugated

graphene network (sp^2 carbon) must be reestablished during the reduction process, which is

associated with the ring-opening of the epoxides [8]. A successful reduction of GO yields

graphene; an sp^2 C-C bonded material with a high surface area. The high surface area makes

graphene a suitable material for energy storage devices like batteries and supercapacitors. Other

methods have been used to synthesize graphene in recent times. Villalobos *et al.* [9] synthesized

films of porous nanocrystals of graphene using a bottom-up approach. Here, carbon precipitate

was dissolved in Ni matrix through controlled pyrolysis of polymers and sugar processors Zhang

et al. [10] recently presented a sulfur-assisted method for producing a large amount of graphene

where the conversion of benzene rings of tetraphenyltin resulted in the formation of a three-

dimensional few-layered graphene microsphere with high electron mobility. Graphene has been

optimized to obtain higher performance for supercapacitor applications. In an experiment by Bai

et al. [11], holey graphene was synthesized via microwave irradiation of graphene powder. The

basic concept includes the development of nanosized holes in the defect area of graphene

because of interactions between carbon atoms, oxygen in the air, electrons, and microwaves.

The holey graphene yielded higher specific capacitance than the pristine graphene sheet and

increased capacitance retention of up to 96.25% at a high current density of 8 A g^{-1} after 10000

cycles.

 The optimization of new materials for energy storage is to solve the challenges faced by

manufacturing industries. Graphene is used as an electrode material for supercapacitors /EDLC

[12][13]. The EDLC has a high capacity of producing high power compared to batteries with a

mechanism of charge transfer through the structure of the material using electrolytes and a separator between the electrodes [14][15]. EDLCs have low weight, high cycle life, high power, low maintenance and work at a different thermal range from as low as −40 °C to as high as 70 °C without affecting its efficiency and no fear for an explosion [14]. These devices can be used in systems where short cycle load is needed more frequently, such as in electric motor vehicles, mechanical systems with motors, washing machines, electric trains among others [16]. The performance of those materials greatly depends on electrical properties, surface area, pore-volume, stability, interaction with the electrolyte among others [16]. The EDLC stores its charge with a non-Faradaic or electrostatic process where there is no charge transfer between electrolyte and electrode materials [17]. When the device is biased, the charge just accumulates at the surface of the electrode which causes charge attraction due to the potential difference resulting in diffusion of the electrolyte ions to go through the separator pores to another electrode, enhancing high power density [14]. Scientists have shown great interest in exploring graphene as an ideal electrode material because of its high theoretical surface area and other distinctive properties as earlier mentioned. However, for graphene to maintain a landmark performance as a supercapacitor electrode material, it must firstly, maintain the large and accessible surface area which will result in sizeable charge capacity accounting for high areal and volumetric capacitance. Secondly, the reduction process must produce an open network of graphene structures void of agglomeration. These open pores will help facilitate the accessibility of the electrolyte to the electrode surface, optimizing ion diffusion. The graphene must possess excellent electronic conductivity a necessity for achieving high power. The current research study focuses on the synthesis and characterization of graphene from graphite flakes and its application

for energy storage as supercapacitor electrode materials. The study presents the conversion of

graphite flakes into GO using Hummer's method, and the reduction of GO to graphene.

3.2 EXPERIMENTAL

3.2.1 Materials

Microcrystalline graphite (2-15 µm, 99.99%) was purchased from Alfar Aesar (Kandel, Germany)

Nickel foam (1.6 mm thick, 0.25 µm pore diameter) was purchased from MTI Corporation,

(Richmond, Califonia, USA). Hydrogen peroxide solution (30 wt. % in water, American chemical

society (ACS) reagent), concentrated hydrochloric acid (reagent grade and assay 36.5-38.0%),

sodium borohydride (98.0%), potassium permanganate (≥ 99.0%, ACS reagent), concentrated

sulphuric acid (99.999%), polytetrafluoroethylene (mean particle size 20 µm), activated charcoal

(Norit ® pallets), anhydrous N-methyl-2-pyrrolidone (99.5%) and carbon black (4 µm mesoporous

carbon matrix, ≥ 99.95% metal bases), ethylene glycol (EG) (99.8%), ethanol (absolute, ≥ 99.8%)

were purchased from Sigma-Aldrich (St Louis, Missouri, USA) and were all used without further

purification.
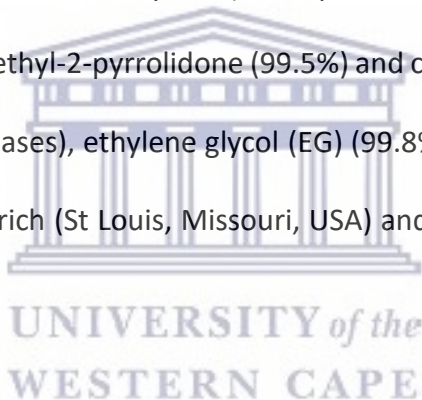
Figure 3.1: Graphical representation of GO synthesis

3.2.2 Synthesis of graphene oxide

Figure 3.1 is the schematic representation of GO synthesis. GO was synthesized using a modified

Hummers method; In a flask containing 2 g of graphite, 50 mL of concentrated H_2SO_4 was added

at room temperature and allowed to cool to 0 ℃ in an ice bath for 25 min. Seven grams of $KMnO_4$

was added slowly, and a dark green colour solution was observed. The flask was removed from

the ice bath and allowed to cool to 35℃ temperatures for 45 min. The mixture was continuously

stirred for 2 h, followed by cooling in an ice bath, and the addition of 120 mL of distilled water,

which revealed a light pink colouration. Enough H_2O_2 was used to stop the reaction, by dropwise

addition. The resultant mixture was intensively washed with HCl and water, by centrifuging the

mixture and decanting the supernatant away. The residual GO was dried at 65 ℃ overnight in a

vacuum oven.

3.2.3 Synthesis of graphene from GO

200 mg of graphene oxide was dispersed in 100 ml of water and sonicated for 1 h. 800mg of

$NaBH_4$ were added to the dispersion and the mixture was stirred for 30 min and heated under

reflux at 125 ℃ for 3 h. During the reduction, the yellow-brown solution gradually yielded a black

solid. The black solid was isolated by centrifugation, washed with water, and finally dried.

3.2.4 Material characterization

The elemental and morphological composition of the nanoparticles were obtained using a Carl

ZEISS ULTRA scanning electron microscope GmbH. Fitted with an energy dispersion

spectrometer. (Jena, Germany). All analysis was performed on a nickel-copper grid. The samples

for TEM characterization were drop-coated into the Cu TEM grids and scanned in high-resolution

transmission electron microscopy (HR-TEM) with an FEI Technai G20 F20X-Twin MAT 200 Kv Field

Emission Transmission Electron Microscope (Eindhoven, Netherlands) equipped with both EDS

and selected area electron diffraction (SAED). The X-ray powder diffraction (XRD) pattern was

obtained for all the nanoparticles with a D8 advance multipurpose X-ray diffractometer

(BRUCKER-AXS, Berlin, Germany) using copper kα1 radiation (λ ~ 0.154 nm) operating at 40 kV

and 40 mA. XRD patterns were collected from 15 to 70 (2q) with a step size of 0.034° in 2q. The

functional group present in the sample was determined using a Perkin Elimer Spectrum 100 series

Attenuated Total Reflectance (ATR) Fourier transform infra-red spectrometer with 4 cm^{-1} resolutions (Perkin-Elmer, Boston, MA, USA). The particle size distribution was determined by a small-angle X-ray scattering (SAXS) measurement, performed on an Anton Paar GmbH SAXSpace P/N 100100 (Graz, Austria). It was equipped with a 1 D mythen 2 position-sensitive detectors, a beamstop alignment, and a Copper Kα (0,154 nm) instrument radiation was used. The nanoparticles Raman spectra were obtained using an Xplora Olympus BX41 Raman Spectrometer (Horiba, Tokyo, Japan) using a 532 nm laser as the excitation source. Optical absorption spectra were acquired from ethanolic dispersions of the nanocrystals at room temperature using a Varian Cary 300 UV-Vis-NIR spectrophotometer (Agilent, Santa Clara, CA, USA). At room temperature, infrared spectroscopic investigations between 4000 and 400 cm^{-1} were carried out. The powdered nanocrystals were deposited on a diamond disc, and infrared spectra were acquired using an Attenuated Total Reflectance/Perkin-Elmer Spectrum 100 Series Fourier Transform Infrared (FTIR) Spectrometer (Perkin-Elmer, Boston, MA, USA). All electrochemical studies were performed on a VMP-300 potentiostat from the Bio-Logic SAS instrument (France).

3.2.5 Electrode preparation and electrochemical measurements

To prepare the working electrode, the active material; graphene (70%), a conducting agent; carbon black (20%) and a binder; polytetrafluoroethylene (10%) was mixed in a mortar, and crushed to fine powder, then 3 drops of anhydrous N-methyl-2-pyrrolidone was added and mixed to form a uniform slurry. Nickel foam was cut into rectangular shapes of 0.5 x 1cm^2 and coined shapes of 20 mm in diameter. The foams were cleaned to remove all surface oxide layers in 1 M

HCL solution, absolute ethanol, and deionized water respectively, with ultra-sonication for 15 min in each solvent, and dried at 90 °C for 12 h. The homogenous paste was coated on 0.5 cm^2 diameter of the nickel foam and dried at 80 °C for 12 h. In a three-electrode cell setup, Ag/AgCl and Pt wire were used as the reference and counter electrode respectively. While for the full cell, the paste was coated into the coin-shaped nickel foam and assembled in a Swagelok with activated carbon as the positive electrode. The cyclic voltammograms were recorded between 1.0 to 6.0 V potential windows at different scan rates, the electrochemical impedance measurements were obtained at a frequency range of 0.1 MHz to 100 MHz with 10 points per decade, and the galvanostatic charge-discharge profiles were measured at different current densities. All electrochemical characterisation of material was done in the three-electrode cell using 1 M Li$_2$SO$_4$ electrolyte. The same electrolyte was used for the device testing at 1.8 V.
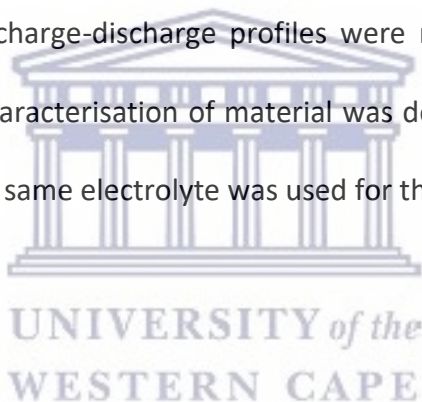
3.3 RESULT AND DISCUSSION

3.3.1 Morphology of graphene nanomaterial

The SEM measurements demonstrate that graphite has a broad and thick particle size distribution (Figure 3.2). The study demonstrates the presence of multiple stacks in the graphite structure, demonstrating that graphite is layered. As a result of the oxidative treatment, graphene layers are significantly disordered (Figure 3.2b) and partial separation of graphene layers occurs. The images of graphene oxide show that there are fewer stacks, indicating that the structure on graphite has been exfoliated. The resulting graphene nanosheets structure is multi-layered. This suggests a smoother accumulation, indicating that it has been reduced by the structure's exfoliation process [18].
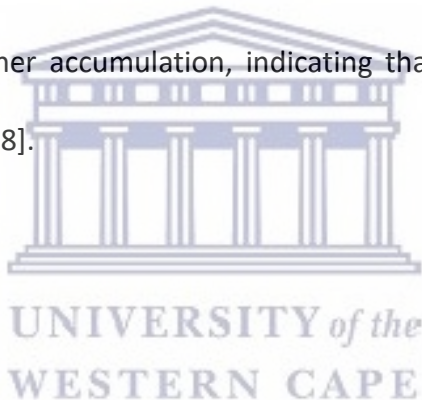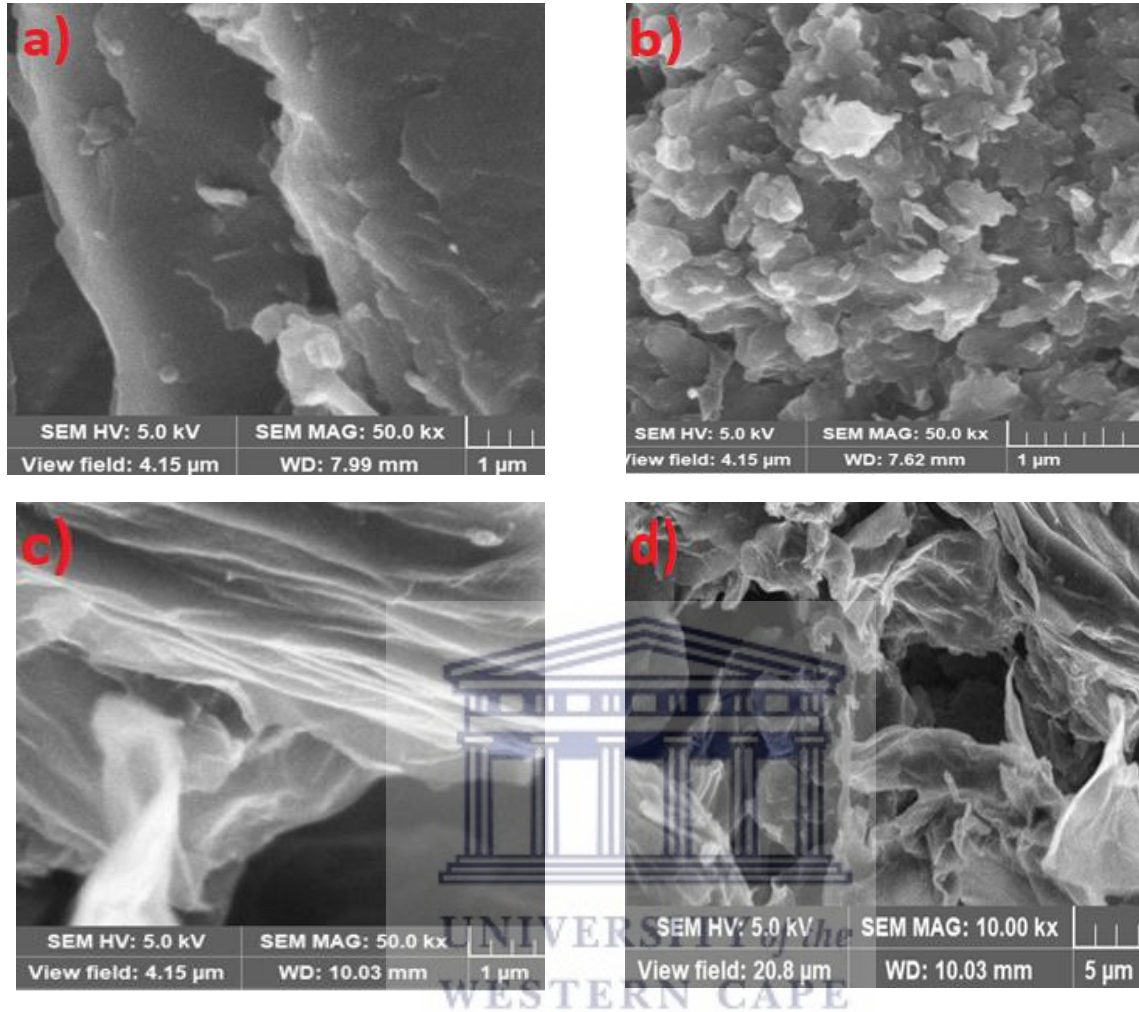
Figure 3.2: SEM images of a) graphite; b) GO, c and d) graphene at different magnifications

 TEM was used to examine the shape and structure of the graphite, GO and graphene. Figure 3.3a depicts a broad view of graphite nanosheets, emphasizing its flake-like morphologies. Figure 3.3b shows a TEM image of a GO nanosheet at high magnification, revealing a fully amorphous and disordered structure.

Figure 3.3c is a high magnification TEM image of a graphene nanosheet. Organized graphite lattices can be seen. However, disordered portions are also seen, showing that the graphene nanosheets were partially restored to an ordered crystal structure. The image shows few-layered graphene until towards the grain edge, where the grains reduced to a single layer and gradually culminate into defects at a node where more grains meet. The most transparent and featureless regions in Figure 3.3d, shown by an arrow, are most likely monolayer graphene nanosheets. Scrolled graphene nanosheets were also seen (as shown Figure 3.3d inset). Corrugation and scrolling are inherent in graphene nanosheets [19]. This is due to the thermodynamic stability of the 2D membrane being caused by microscopic crumpling caused by bending or buckling.

The chaotic nature of the GO nanoplatelets was confirmed further by selected area electron diffraction (SAED), (Figure 3.4b). The SAED pattern of GO displays only diffraction rings and unresolved diffraction dots, suggesting unequivocally that the GO flakes are amorphous. This finding agrees with the XRD analysis. Figure 3.4c depicts the SAED pattern of graphene. The well-defined diffraction spots demonstrate the graphene nanosheets' crystalline structure. As a result, HRTEM, and SAED studies indicated that the GO was successfully reduced to generate crystalline 2D graphene nanosheets.
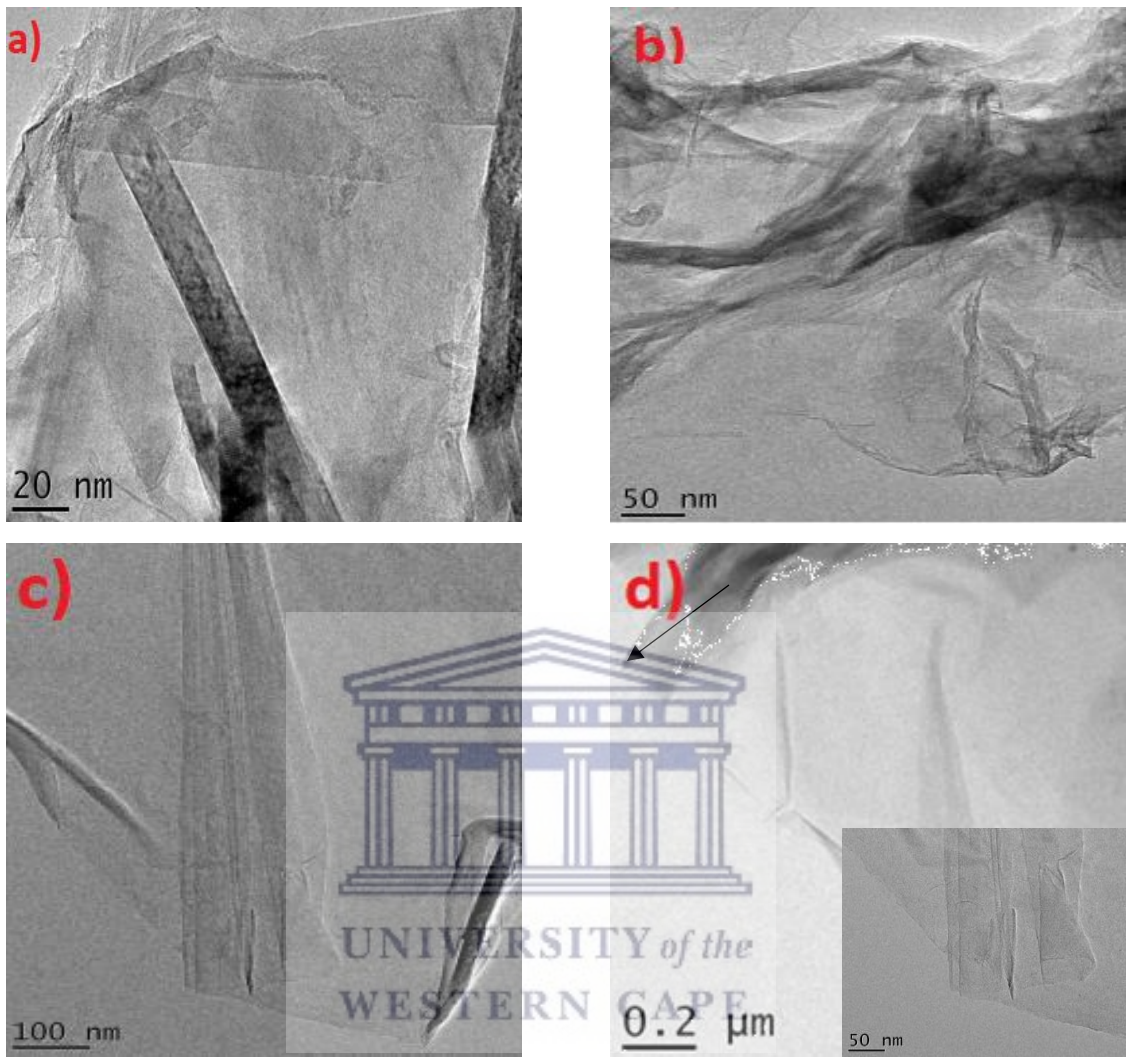
Figure 3.3: TEM images of a) graphite; b) GO, c and d) graphene at different magnifications.
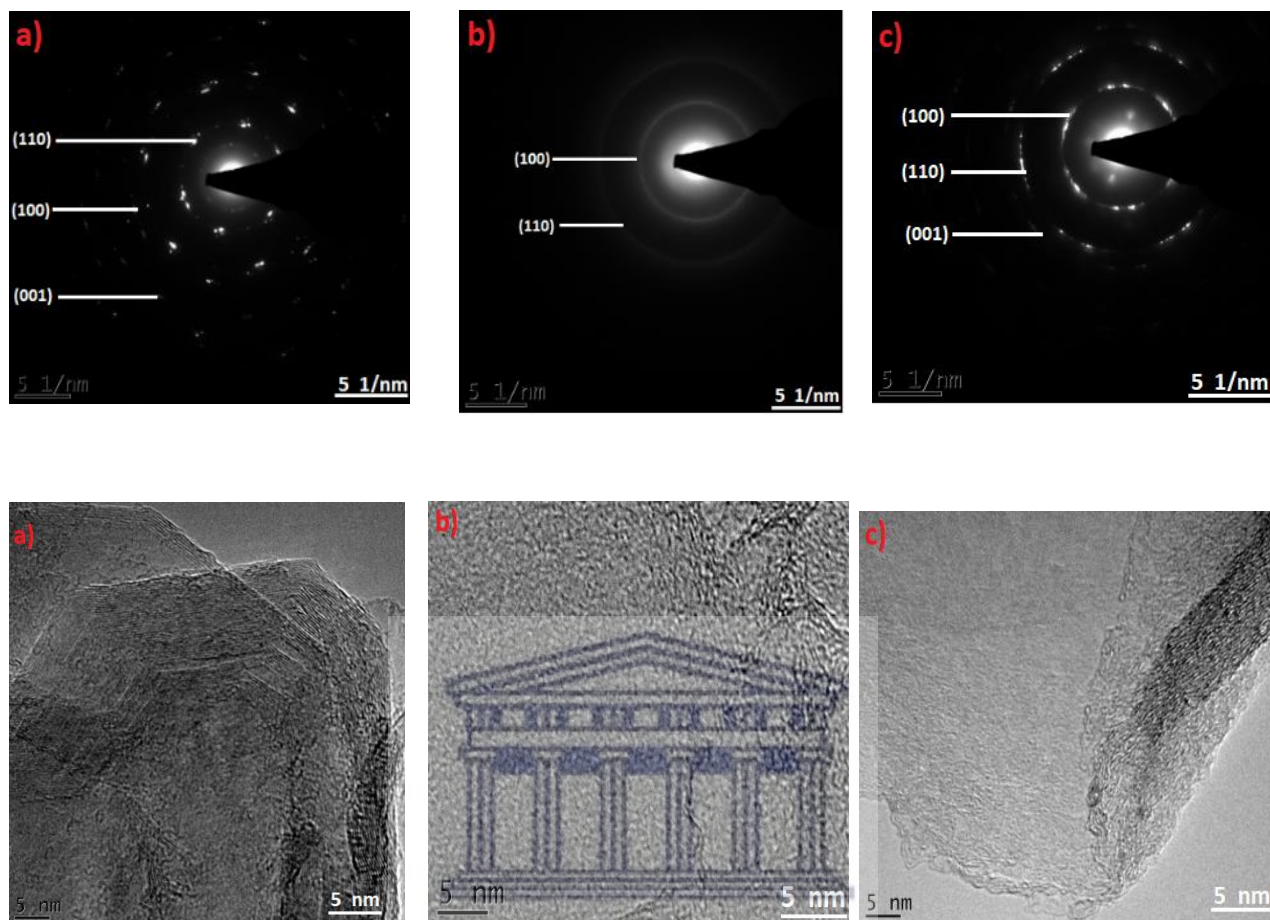
Figure 3.4: HRTEM showing the SAED pattern (first row) and the FFT (second row) of a) graphite, b) GO and c) graphene.

3.3.2 Spectroscopic studies

3.3.2.1   Energy-dispersive X-ray spectroscopy (EDS)

EDS has been used to show the elemental composition of graphite, GO and graphene nanomaterials. EDS focusing on various spectrum areas and corresponding peaks are shown in Figure 3.5 to 3,7. The EDS analysis confirms the presence of carbon in all three samples. While graphite is made up of pure carbon, GO has carbon oxygen and sulphur. This is due to the sulfuric

acid and KMnO₄ that was used to oxidize graphite. Graphene had a high percentage of carbon

with a small percent of oxygen that was not completely reduced. Details of the quantity of each

element measured in the weight per cent are shown in the in-set.
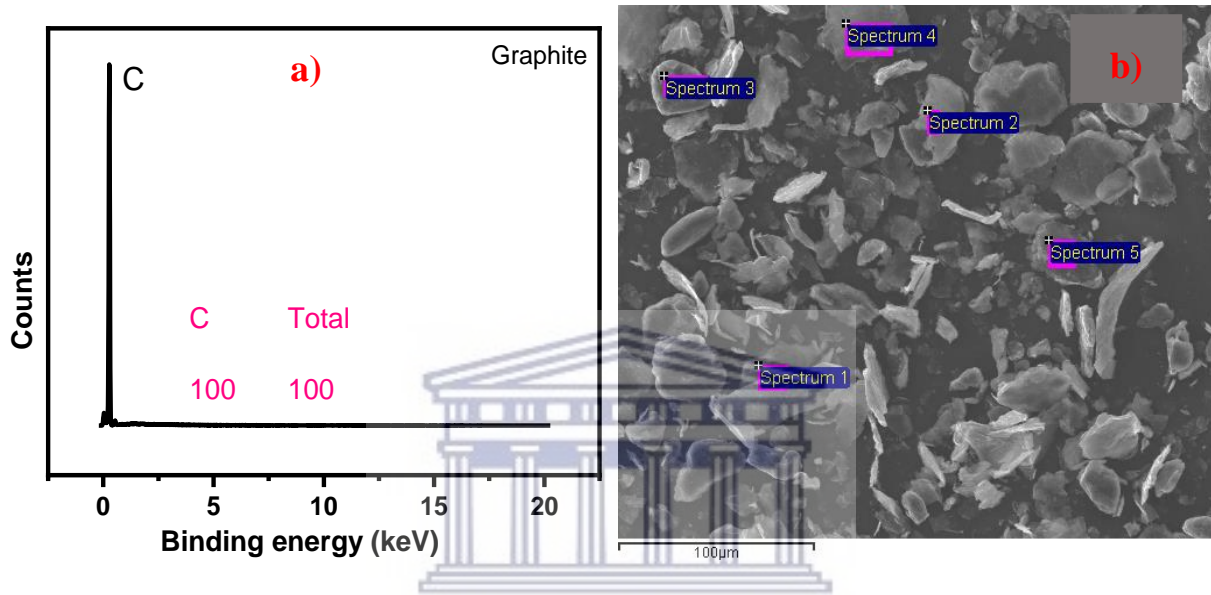
Figure 3.5: EDS spectrum a) and SEM image b) of graphite. Inset in (a) is the percentage

elemental composition. The labels in the SEM image (b) represent sampling points for the EDS.
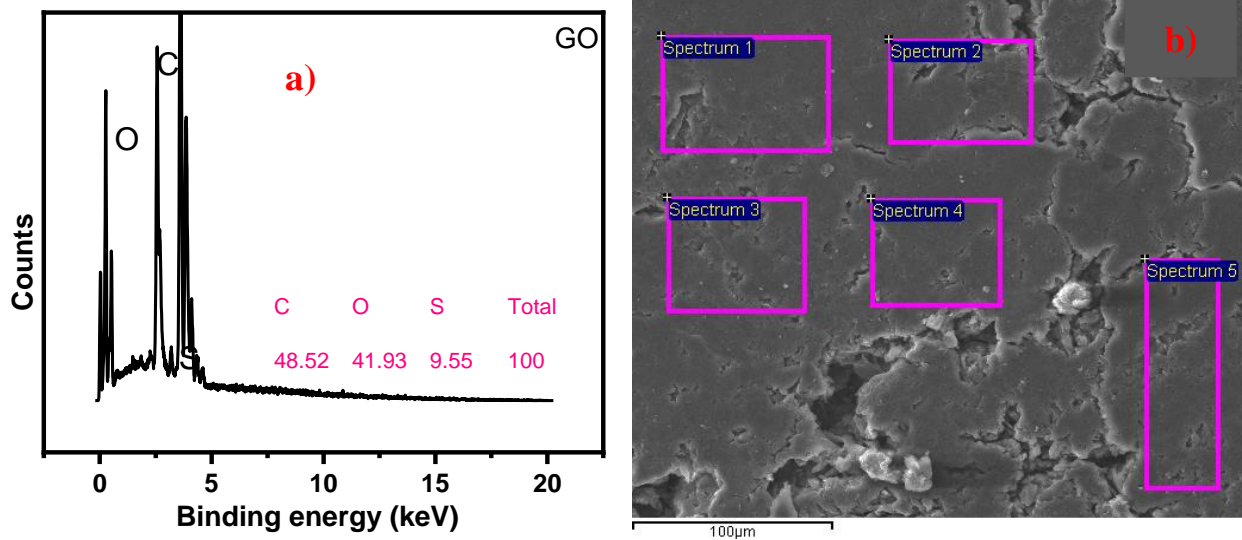
Figure 3.6: EDS spectrum a) and SEM image b) of GO. Inset in (a) is the percentage elemental composition. The labels in the SEM image (b) represent sampling points for the EDS.
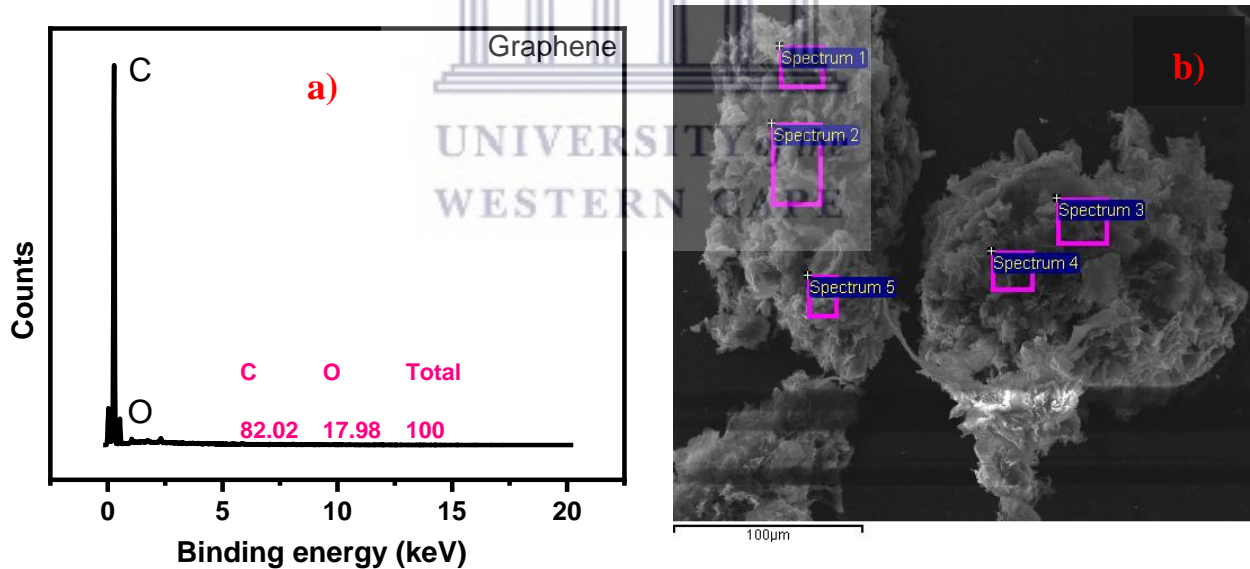
Figure 3.7: EDS spectrum a) and SEM image b) of graphene. Inset in (a) is the percentage elemental composition. The labels in the SEM image (b) represent sampling points for the EDS.

3.3.2.2   X-ray powder diffraction (XRD)

The crystal structure of graphite, GO and graphene was investigated using XRD analysis. The XRD spectrum of all 3 materials are shown in Figure 3.8 and are all indexed to a Hexagonal structure space group (P63/mmc (1964), JCPD card No 2_41-1487), with lattice parameter a = 2.47040 Å and c = 6.72440 Å.

Figure 3.9 depicts the XRD patterns of graphite and GO; the strong (002) diffraction line (d-space 0.34 nm at 26.23°) visible in graphite has nearly totally gone in GO, indicating that the graphite powder has been oxidized. Simultaneously, oxidation enhanced the strength of the diffraction peak at 11.8° (corresponding to a d-spacing of 0.80 nm). GO nanosheets were reduced to graphene nanosheets and recovered to an ordered crystal structure after chemical reduction with $NaBH_4$. The recovery of the (002) diffraction line and the disappearance of the diffraction peak at 11.8° in the XRD pattern of graphene demonstrate this. The starting material was natural flake graphite with a particle size of 2-15 µm. The inter-graphene layers can be intercalated by various molecular species or ions, during exfoliation, changing the interlayer spacing along the c-axis. The interlayer spacing increased from 3.4 nm in graphite to 6.25–7.5 nm in GO [20][21]. Also, the introduction of sulfuric acid and $KMnO_4$ to oxidize the natural graphite powders in a water-based solution introduced hydroxyl, carbonyl, epoxy, and peroxy groups, bonded to the edges of the graphite basal planes, leading to carbon hydrolysis which converts sp^2 bonds to sp^3 bonds. Therefore, H_2O, NO_3, or SO_4^{-2} ions could enter the graphene layer, causing an increase in interlayer space [22].
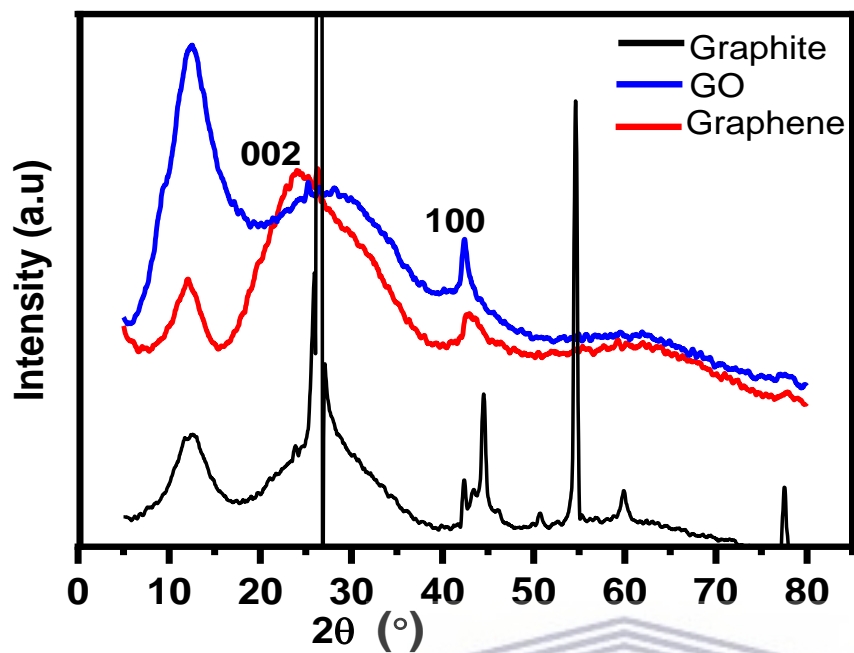
Figure 3.8: XRD spectra of graphite, GO, and graphene showing the typical graphene hump

around 20º
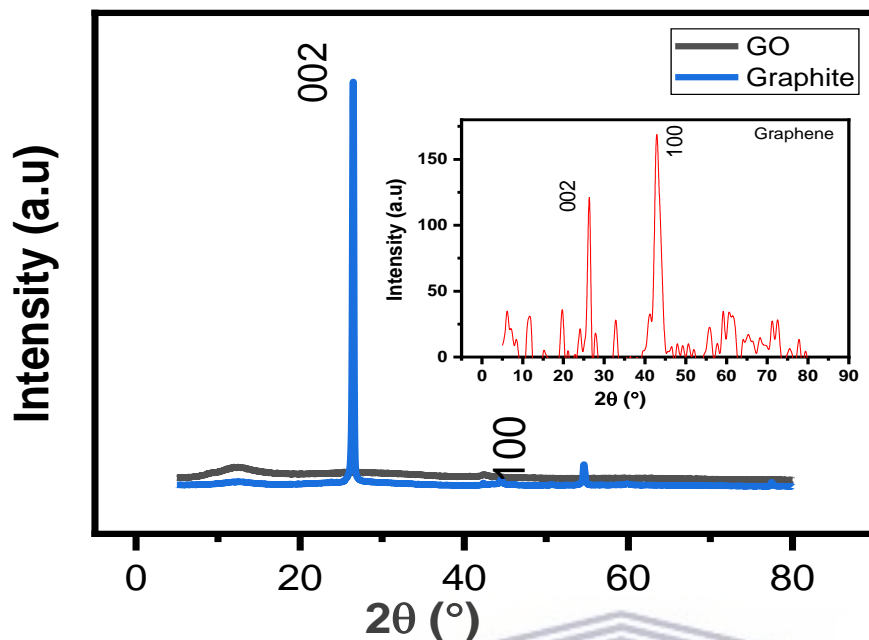
Figure 3.9: XRD spectrum of GO and graphene showing the reduced 002 graphitic phase. The

inset is the smoothed graphene spectrum.
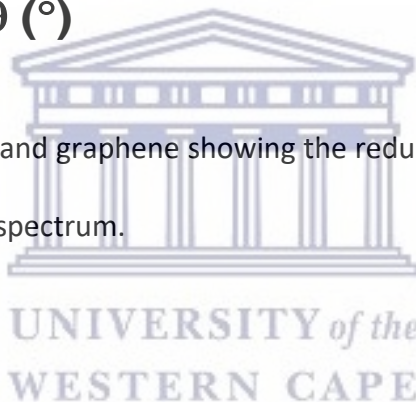
3.3.2.3 Solid-state nuclear magnetic resonance spectroscopy (NMR)

The NMR of graphite, GO, graphene and the corresponding deconvoluted peaks of GO are

represented in Figure 3.10. Three prominent peaks can be found in the spectrum of GO (Figure

3.10b): 58 ppm (FWHM, 16 ppm), 69 ppm (FWHM 6 ppm), and 127 ppm (FWHM 23 ppm). The

presence of (C-O-C) and (C-OH) is shown by the first two peaks, while graphitic Sp^2 carbon is

indicated by the third peak. Peaks around 163 and 190 ppm are less intense and can be attributed

to the COOH and C-O groups, respectively. The pattern is quite like the findings of Johra and Das

et al. [23][24]. The peaks at 58, 69, and 163 ppm vanished after reduction, while the peak at 127

ppm was displaced to 117 ppm, which is the same as the pure graphite sample. Graphite and

http://etd.uwc.ac.za/

graphene have similar broad peaks, but their FWHMs are different. Graphite has an FWHM of 28 ppm, while graphene has an FWHM of 32 ppm. This is because the chemical environment of the Sp^2 carbons is different. The chemical distribution, which corresponds to change in the carbon atom environment, explains the widened peak in comparison to that of GO [24].
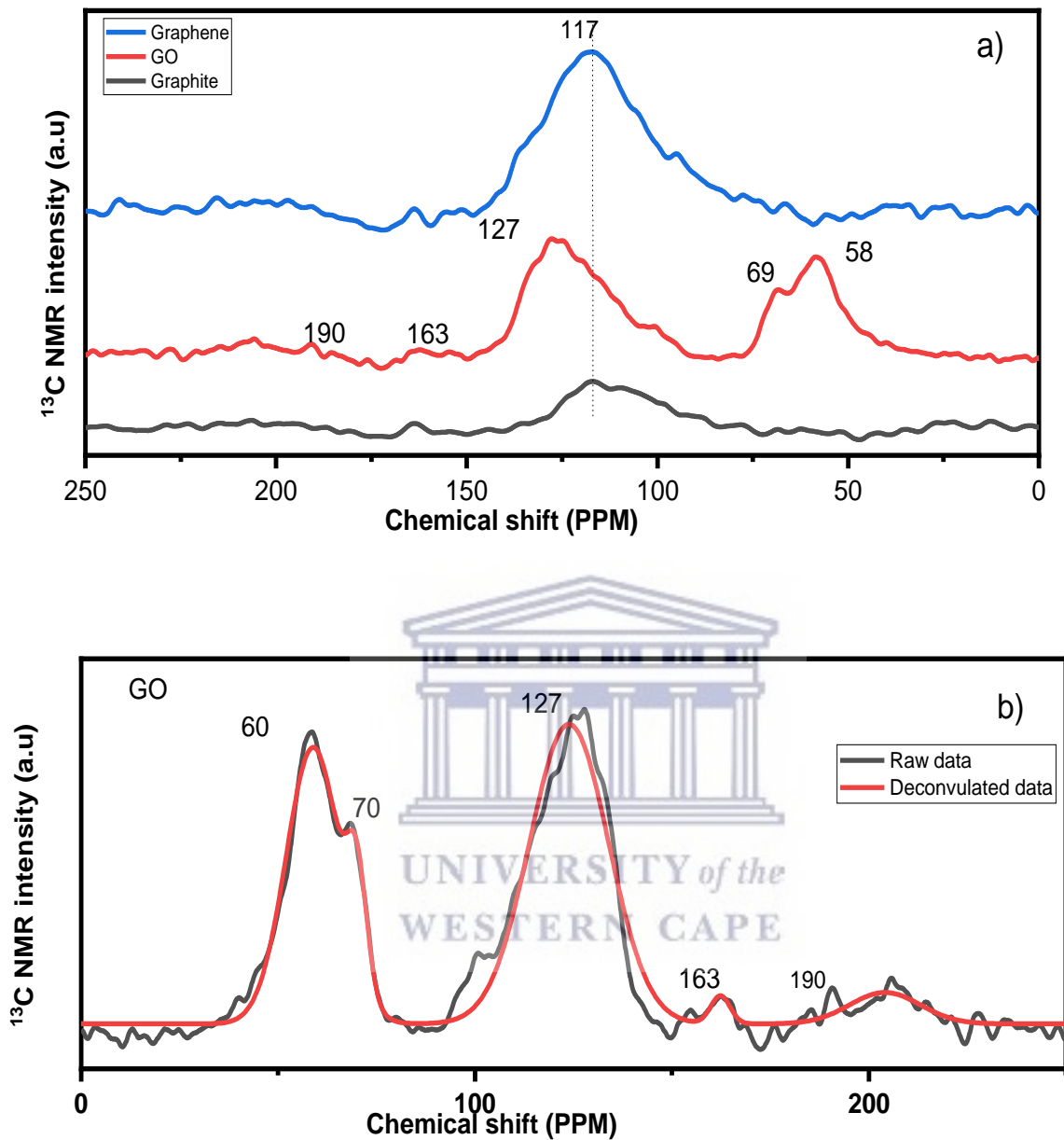
Figure 3.10: NMR spectra of a) graphite, GO and graphene, b) deconvoluted GO

3.3.2.4   Fourier transform infra-red spectroscopy (FTIR)

FTIR was used to identify the presence of bending or stretching vibrations in the synthesized

materials. The FTIR absorption spectra of graphite, graphene oxide and graphene were recorded

in the range of 4000-400 cm^{-1} as shown in Figure 3.11. The graphite spectrum had existing C–OH and C-O vibrations at 3396 cm^{-1} and 1054 cm^{-1}, respectively, which might be attributed to the porosity and hygroscopic nature of graphite. The distinctive band in the GO spectrum at 3396, 1746, 1609, 1184, 1054, and 599 cm^{-1} were caused by C–OH stretching, C=C stretching, C–H bending, C–O stretching, and OH out-of-plane bend, respectively [25][26]. The broadband at 3396 cm^{-1} confirms the characteristic OH stretch. This emergence of these bands which were not present in the graphite sample shows that the oxidation stages induced significant oxygen-containing functional groups in the GO sample. After reducing GO to graphene, the vibrational band corresponding to the carboxyl and hydroxyl groups disappeared, and there was a significant reduction in vibrational band intensity across the spectrum, showing that the GO was successfully reduced and exfoliated [27]. Table 3-1 is a representation of the functional groups and vibrational bonds present in the graphite, GO and graphene samples.
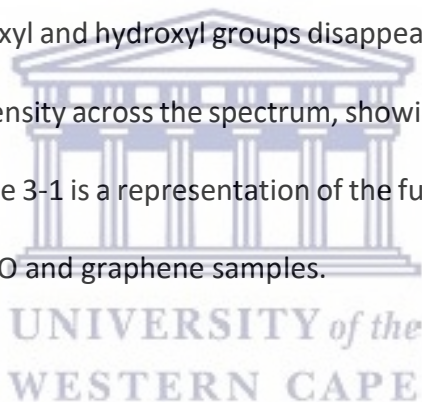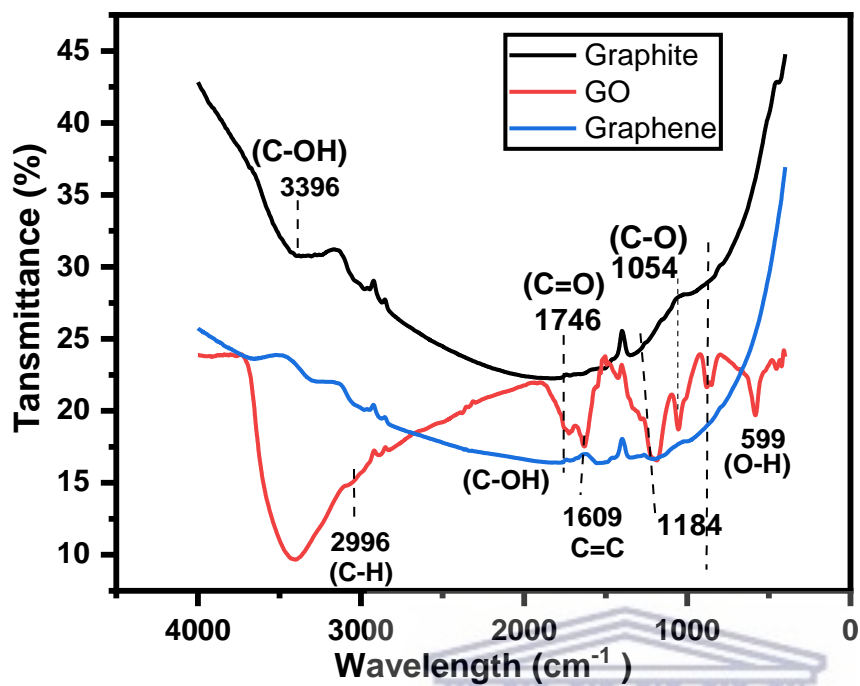
Figure 3.11: FTIR spectra of graphite, GO, and graphene
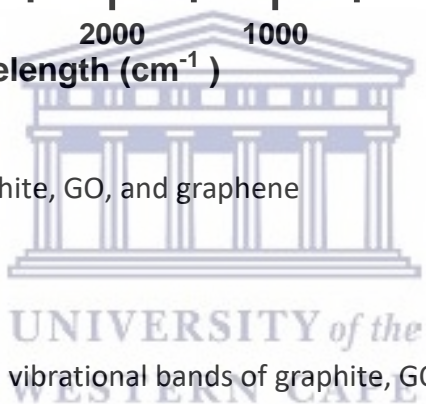
Table 3-1: Functional groups and vibrational bands of graphite, GO and graphene

Functional group	Material/ wavenumber (cm^1)		
	Graphite	GO	Graphene
CO-H	3396	3396	3292
C=H	2996	2996	2996
C=O	1746	1746	
C=C		1609	
C-OH		1184	

C-O	1054	1054	
O-H		599	

3.3.2.5　　　Raman spectroscopy

Raman spectroscopy was used to assess the quality of the graphene sheets produced. The technique has established itself as the most basic and non-destructive method for analyzing carbon structures. Figure 3.12 is the Raman spectra of graphene displaying the D and G bands that characterize carbon compounds. The G-band is produced by in-plane sp^2 C-C stretching and can be found in all carbon structures, whereas the D-band is produced by flaws and edges in the carbon grid [28][29]. The intensity ratio of the D and G bands (ID/IG) is an indirect measure of the material's disorder. The D and G bands can be found at 1342.2 and 1585.1 cm^{-1} respectively. The D band is more intense than the G band and the ID/IG =1.37. Exfoliation-reduction of graphene oxide produces graphene, which is made up of partially healed carbon basal planes due to the removal of functional groups. The graphene has a strong G band at 1585 cm^{-1} and a strong and clear D band at 1342 cm^{-1} that does not broaden or overlap with the G band. This means that the samples have fewer defects. At the 2D region (2400 to 3250 cm^{-1}), two distinguishable peak profiles can be seen at 2665 and 2910 cm^{-1} and they are assigned to G' and D+G mode. The G' band is an overtone of the D band and can also be detected in graphite, therefore it is not activated by defect [30]. It can however be attributable to a vibrational mode characterized by the breathing of six carbons forming a hexagon in graphene's hexagonal lattice. The breathing vibration frequency is usually half of the recorded value of D[31][32]. The D+G bands are defect

activated and present in samples with defective graphene sheets. This defects /disorder is evident in the SEM and TEM images, and it is typical of all chemically exfoliated graphene.
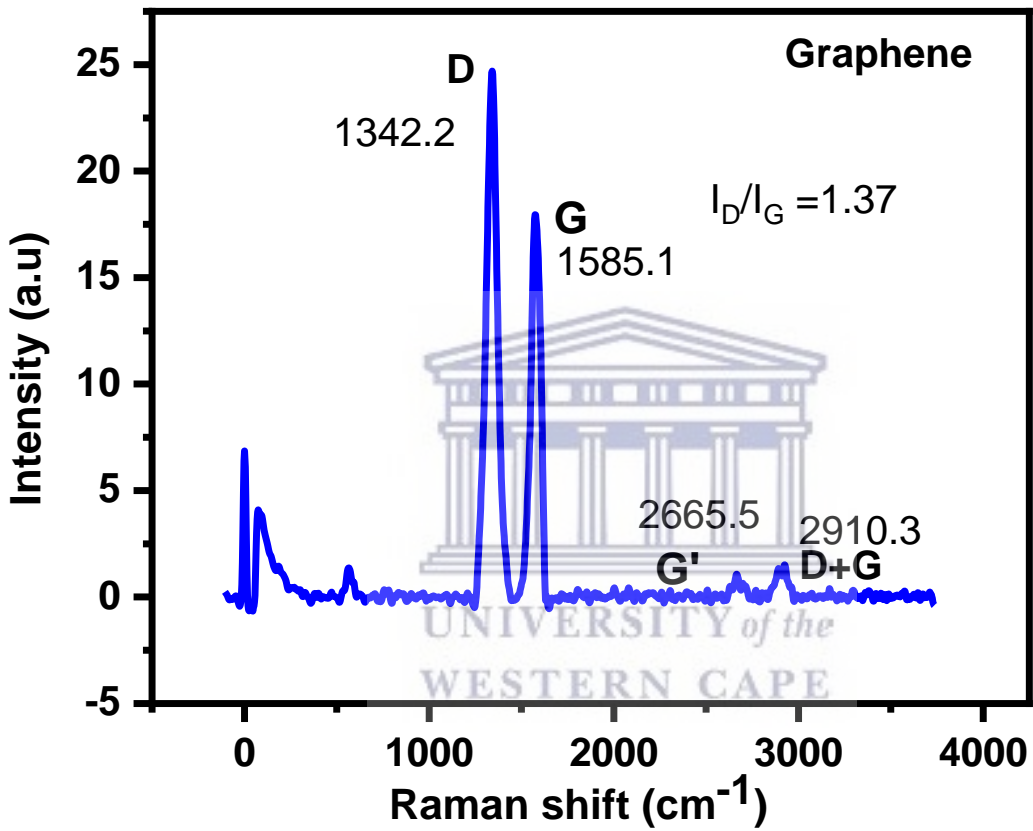
Figure 3.12: Raman spectrum of graphene

3.3.3 Electrochemical studies

3.3.3.1   Cyclic voltammetry (CV)

CV was used to analyze all three materials in 1 M Li_2SO_4 electrolyte. The capacitive currents were measured between 0.0 and 0.6 V vs an Ag/AgCl electrode at scan rates ranging from 10 to 100 mV s^{-1} (Figure 3.13 to 3.15). Regardless of their diverse physical and chemical properties, all three materials possess a common voltammetric feature which is, a constant increase in cathodic currents as potential increases with no pseudocapacitive/redox peak. This shows a pure capacitive behavior and will result in a higher power [33]. The cyclic voltammograms obtained show a significant increase in capacitive currents as the scan rate increases. This implies that the charge storage mechanism is capacitive, and the process is electrochemically reversible [34]. Voltammograms for graphite show no significant deviations from rectangular shape, in contrast, to GO and graphene, which shows deviances from ideal EDLC behavior. The quasi-rectangular shape obtained for the three materials shows a contribution of EDLC and pseudocapacitance charge storage mechanism. As the voltage scan rate increased, the deviation of the voltammogram from the ideal rectangular structure also increased. This can be due to the electrochemical polarization of the electrode with the graphene material showing a higher degree of polarization. The various functional groups attached to the basal planes of the GO, and the oxygen groups at the edges of the graphene nanosheet as seen in the FTIR are responsible for the pseudocapacitance contribution and the electrochemical polarization of the electrode [35].

The specific capacitance of the three materials was calculated from the equation below:

$$C_{sp} = \frac{1}{2mv \triangle V} \int\limits_{-v}^{+v} Idv \qquad \text{3-1}$$

where m is the active mass of the electrode (g), v is the scan rate (V s^{-1}), $\triangle$V is the potential window in (V) and $\int_{-v}^{+v} Idv$ is the charge obtained from the integrated area of the voltammogram. Amongst the three materials, graphene showed a better electrochemical performance with a specific capacitance 16.23 F g^{-1} at 10 mV s^{-1} and up to 3.89 F g^{-1} at 100 mV s^{-1} (Table 3-2). The values vary from 11.67 F g^{-1} at 10 mV s^{-1} to 4.00 F g^{-1} at 100 mV s^{-1} for graphite, while GO delivered a specific capacitance of 7.44 F g^{-1} at 10 mV s^{-1} and 2.02 F g^{-1} at 100 mV s^{-1}. The specific capacitance values are plotted against potential sweep rates as shown in Figure 3.16. When the voltage scan rate was raised, the specific capacitance values for all three-material decreased gradually. The drop in capacitance value as the scan rate increases is a frequent phenomenon caused by insufficient time for electrolyte ion diffusion, and charge storage is limited to the outer surface area only [36]. In our analysis, we found a similar type of trend in specific capacitance values. The CV curves of graphite, GO and graphene are shown in Figure 3.17 at a scan rate of 40 mV s^{-1}. The area under the CV curve of the graphene was found to be bigger than the area of the graphite and GO. Because the average value of the area under the CV curves is directly connected to the capacitance value, this result showed that graphene has improved capacitive behaviour. The high capacitance of the graphene is mostly owing to the composite's large specific surface area and the high conductivity of graphene [37].
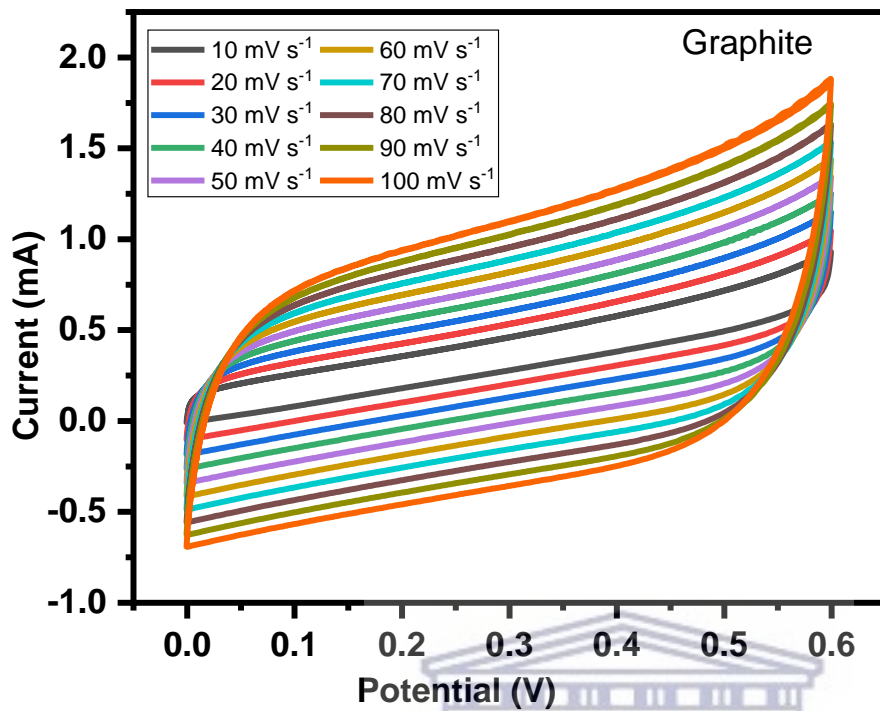
Figure 3.13: CV of graphite
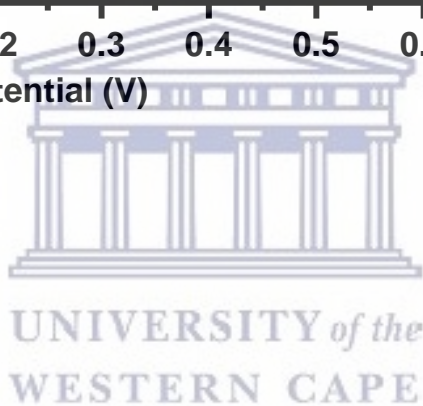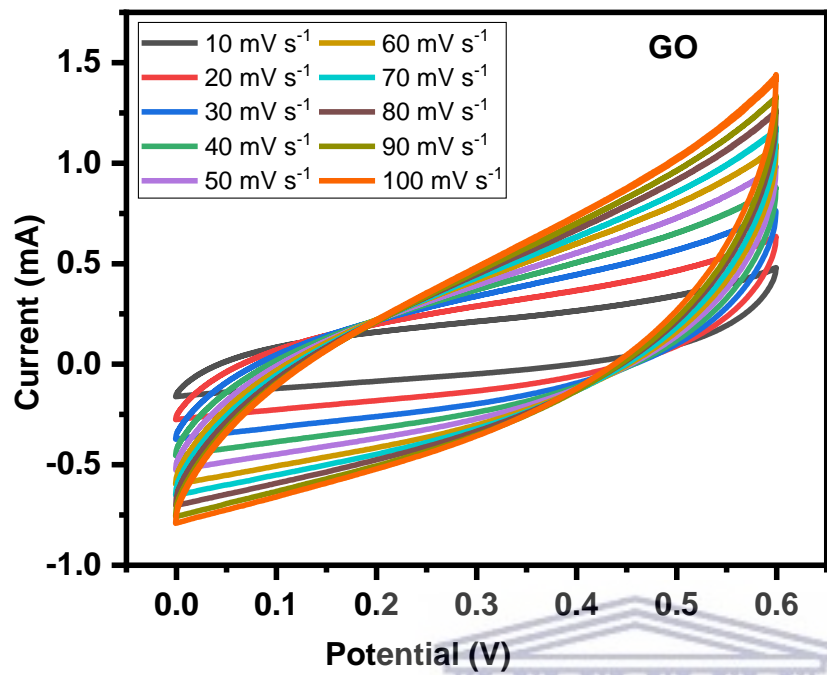
Figure 3.14: CV of graphene oxide
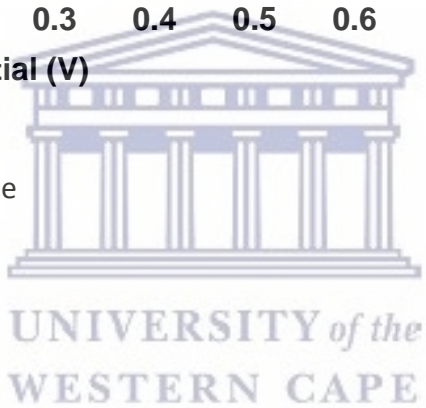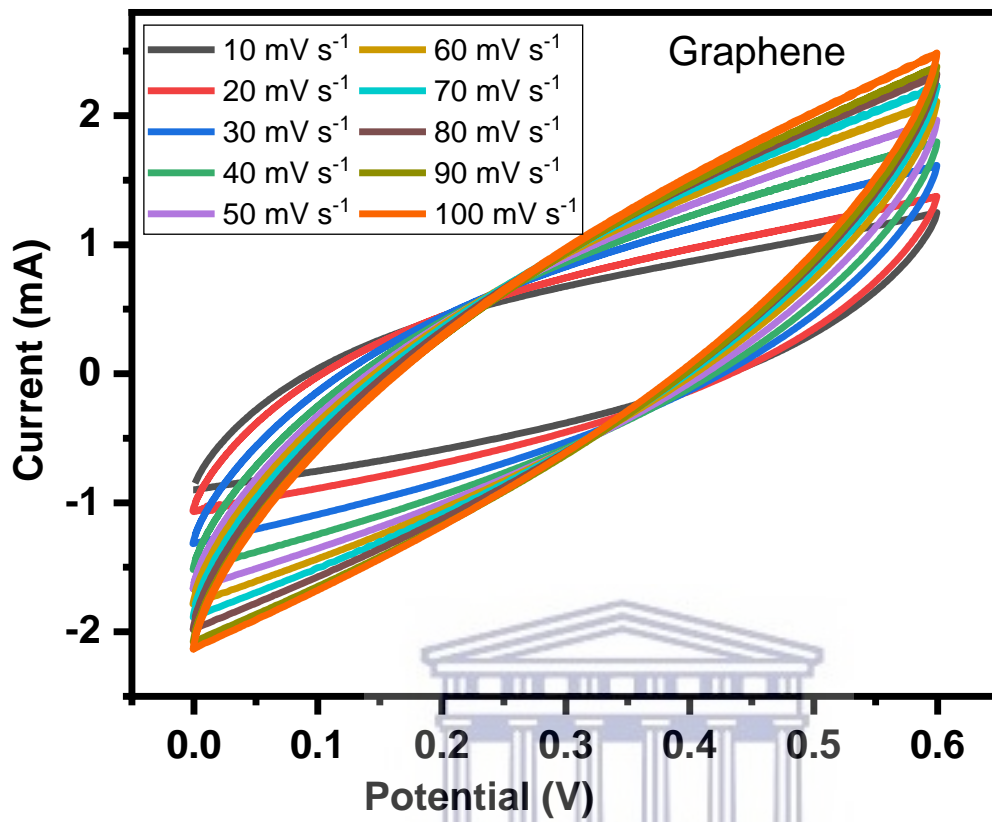
Figure 3.15: CV of graphene
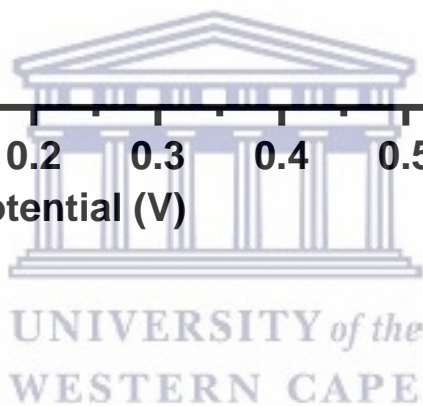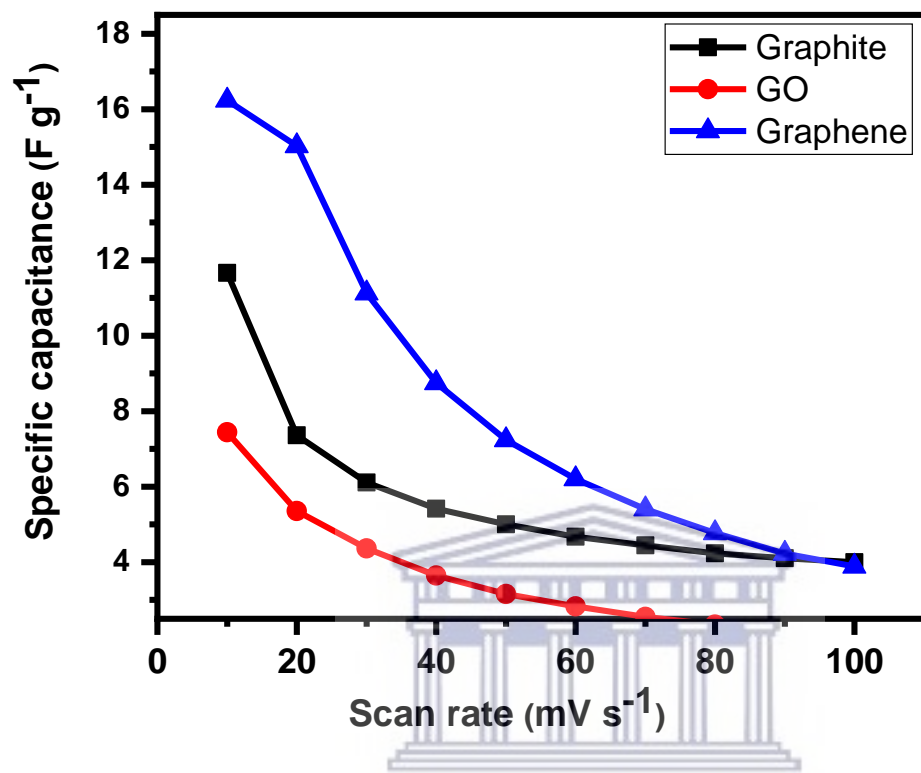
Figure 3.16: Plot showing the relationship between Cs and scan rate for graphite, GO and graphene.
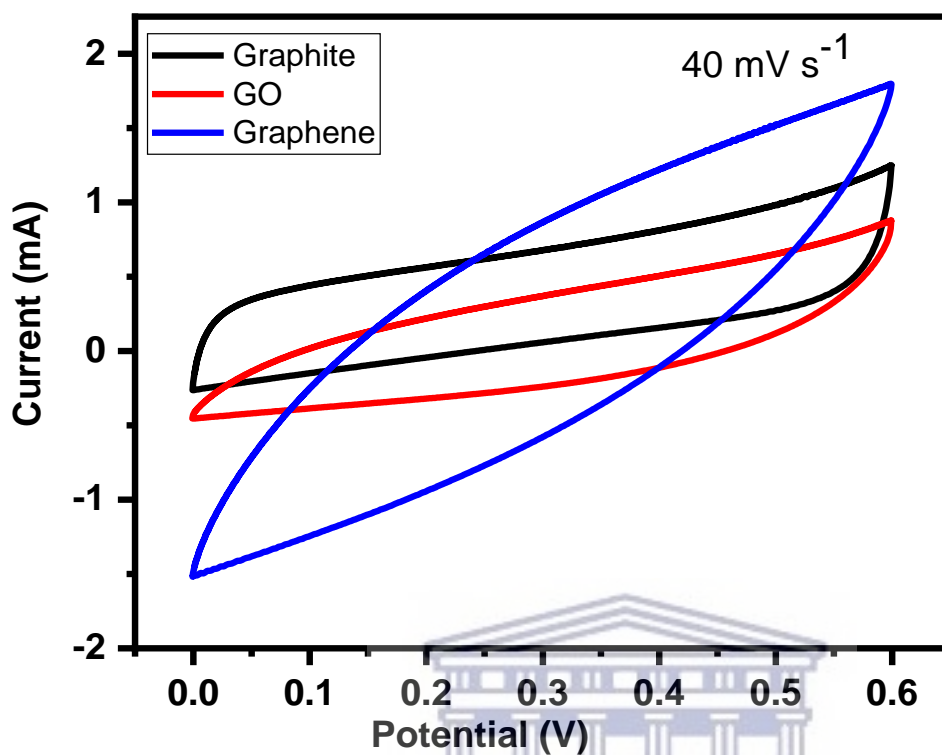
Figure 3.17: CV of graphite, GO and graphene at 40 mV s^{-1}.

Table 3-2: The capacitance of graphite, GO and graphene.

	Capacitance (F g^{-1})		
Scan rates (mV s^{-1})	Graphite	GO	Graphene
10	11.67	7.44	16.23
20	7.36	5.36	15.03
30	6.11	4.37	11.13
40	5.42	3.65	8.75
50	5	3.15	7.24
60	4.68	2.83	6.2
70	4.44	2.55	5.4

80	4.24	2.34	4.77
90	4.1	2.15	4.23
100	4	2.02	3.89

3.3.3.2   Galvanostatic charge discharge (GCD)

The performance of graphite, graphene oxide, and graphene electrodes was investigated at current densities of 0.1, 0.2, 0.3, 0.4, 0.6, 0.8, 1 and 2 A g^{-1} (Figure 3.18). The graphene electrode's GCD curves show a higher specific capacitance when compared to graphene oxide and graphite. The presence of typical triangular curves confirms the electric double layer capacitive charge storage mechanism occurring at the electrode-electrolyte interface [38]. The GCD curves are nearly symmetrical, with only a minor voltage drop due to the equivalent series resistance (ESR). The timing for the charge and discharge process is similar, indicating a high Coulombic efficiency and electrochemical reversibility [37]. These observations are consistent with the oxidation and reduction profiles reported in the CV curves. The specific capacitance (C) was determined using equation 3-2;

$$C_s = \frac{I \times t}{m \times V - IR_{drop}} \qquad\qquad\qquad 3\text{-}2$$

where I is the constant current, m is the active material mass, and t is the discharge time corresponding to the voltage change V [22]. The graphene electrode has the highest specific capacitance at the same current density when compared to GO and graphite electrodes. The highest capacitance (C) of graphene electrode, for example, reached up to 63.33 F g^{-1} at 1 A g^{-1}, while GO was 17.4 F g^{-1} and graphite was 19.3 F g^{-1} at the same current density. This is due to

graphene's porous microstructure, which facilitates electrolyte infiltration and contributes to the development of electric double-layer capacitance. The specific capacitance decreases as the current increases. The drop in specific capacitance values was noticeable in the discharge time of GCD curves (Figure 3.19). This drop-in specific capacitance at increased current density could be attributed to the limited flow of electrolyte ions into the active material's inner side [39]. Figure 3.20 shows a comparison of the rate capabilities of graphite, graphene oxide, and graphene electrodes at various current densities. At a current density of 0.4 A g^{-1}, graphene has a specific capacitance 24 F g^{-1}, which is substantially higher than that of graphene oxide (2.4 F g^{-1}) and graphite (16.95 F g^{-1}). Notably, as the current density increased to 2 A g^{-1}, the graphene maintained a capacitance of 2.0 F g^{-1}.
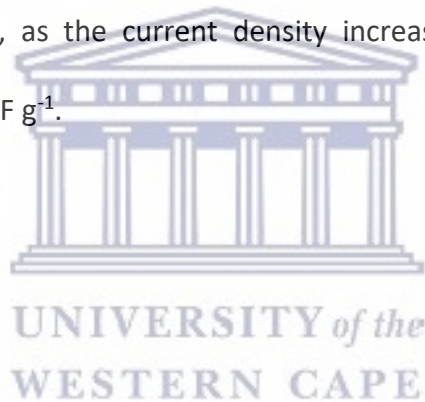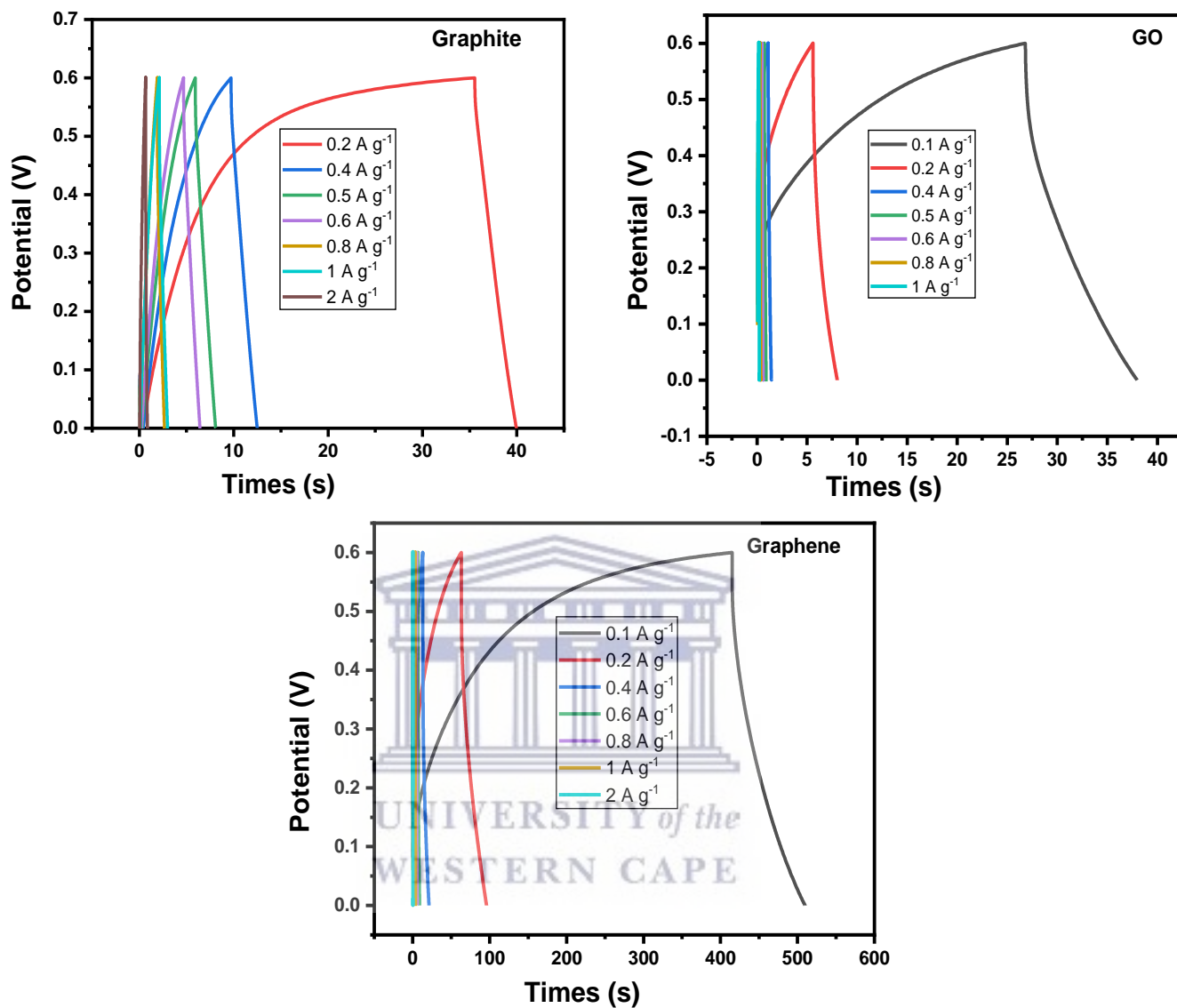
Figure 3.18: GCD of graphite, GO and graphene at different current densities.
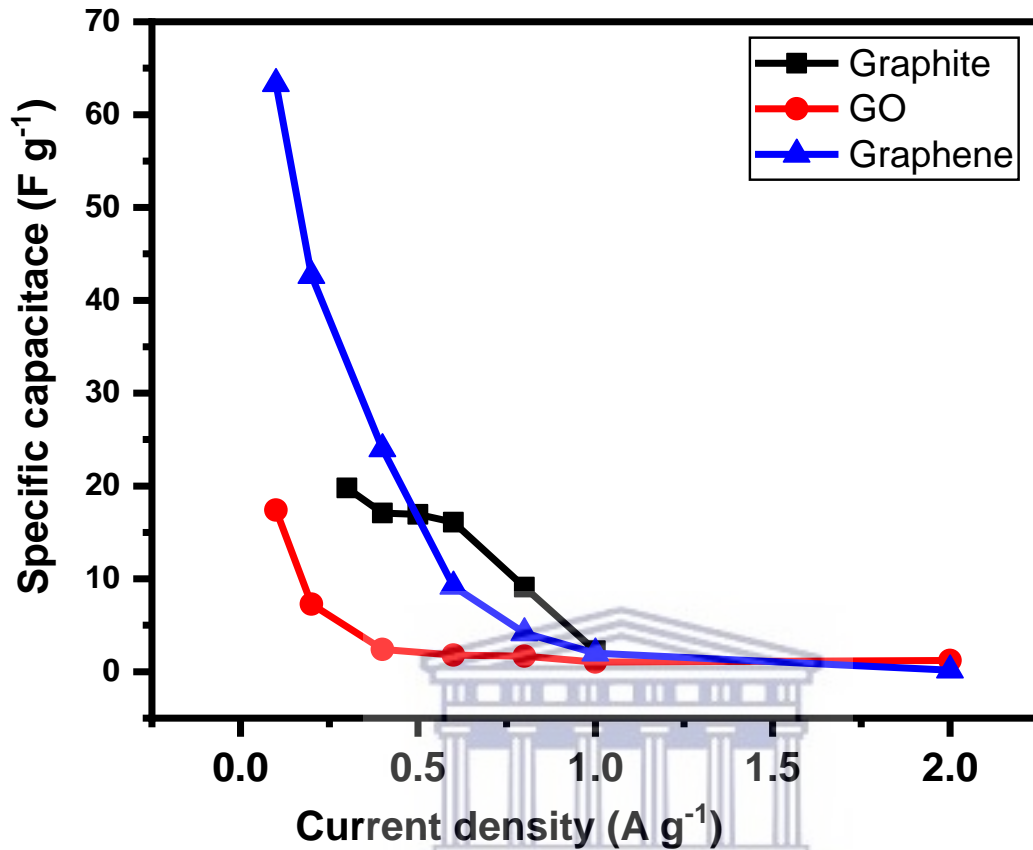
Figure 3.19: Plot showing the relationship between Cs and current density for graphite, GO and
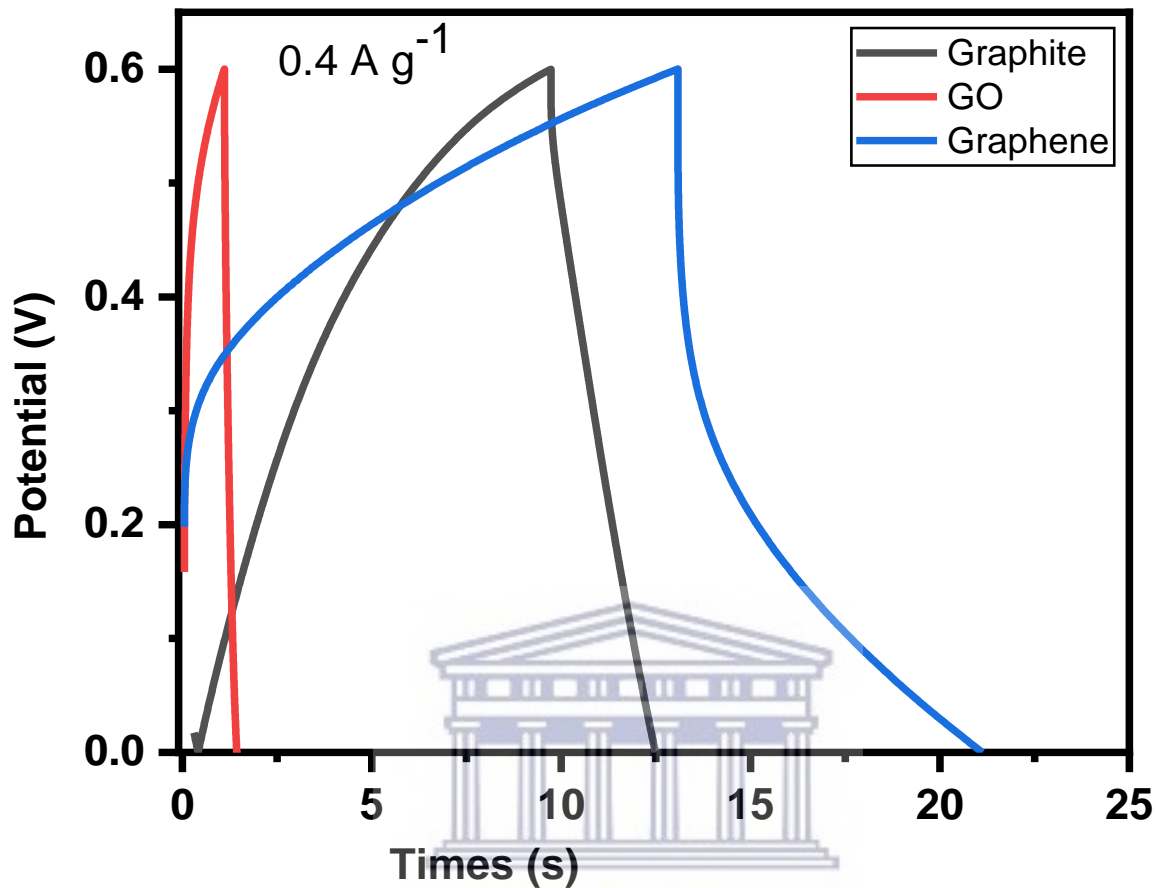
graphene.

Figure 3.20: GCD of graphite, GO and graphene at 0.4 A g^{-1}

3.3.3.3   Electrochemical impedance spectroscopy (EIS)

As illustrated in Figure 3.21, Nyquist plots were used to analyze the electrochemical impedance spectroscopy (EIS) data and were displayed with an equivalent circuit as seen in the inset. Three electrodes all displayed typical AC impedance characteristics of supercapacitors [40]. In the high-frequency region, the intersection of the curve at the real component reveals the bulk resistance of the electrochemical system. This includes ionic resistance from the electrolytes, intrinsic grain to grain resistance of the electrode, and contact resistance at the interphase between the active

material and the substrate [41]. The radius of the semicircle in the high-frequency region displays the charge-transfer process, at the interface of the electrode and the electrolyte. As we approach lower frequencies the semicircle breaks into a 45º nearly vertical line which is related to the Warburg (W_2) diffusion of ions within the electrode inter-phase [33]. The EIS graphs demonstrated that graphite (5.1 Ω) and graphene (5.5 Ω) had identical Rs, which were both bigger than the Rs for GO (1.3 Ω). GO has a larger semicircle radius than graphene and graphite, which both have very small semicircles reflecting the materials' near-perfect capacitive nature. Graphite, GO, and graphene have fitting R_{ct} values of 4.7 Ω, 115.3 Ω, and 5.4 Ω, respectively. The high R_{ct} of GO must be attributed to the oxidation of the oxygenated and hydroxyl groups linked to its basal plane. Extra water molecules that hinder electron routes can be absorbed by this group [42]. The slope of the 45° section of the curves in the intermediate frequency area was used to illustrate the Warburg resistance, which indicates ion diffusion/transport in the electrolyte and its relationship to frequencies. A well-defined and short Warburg area part in the graphite sample demonstrates that the ions in the electrolyte have a short and equal diffusion path length. Furthermore, the Warburg resistance value (Table 3-3) is low. Due to the low charge transfer resistance and lower diffusion effect, relatively reversible reactions can occur at the interface, which explains the near rectangular voltammogram which is retained even at high scan rates. Also, as observed in the curve, the graphite and graphene electrodes exhibit better capacitive behaviour with their almost vertical line, like an ideal capacitor [43]. The fact that graphite and graphene have similar EIS responses must be due to their identical structure, which indicates that GO was transformed into graphene.

The Bode plot from the EIS data is shown as the phase angle and total impedance plot in Figure 3.22 and Figure 3.23. The phase angle for graphene is less than 45°, indicating greater resistance to transition to capacitive behaviour. Graphite and GO have greater capacitive phase angles because their values are nearer to 90°, which is the optimal phase angle for an EDLC. It is clear from the phase angle that the materials store charges utilizing both the EDL and the pseudocapacitive mechanisms. The magnitude of total impedance was lowest in graphene and largest in GO. The mechanism of charge storage and structure of graphite, GO, and graphene can be summarized based on the EIS results as follows: graphite, GO and graphene's charge storage mechanism is both EDL and pseudocapacitive. However, because graphene has a more porous sheet, ion diffusion is more likely. The, variation in pore sizes caused by functionalization of the graphitic sheet, agglomeration, and defect in the edges of the graphene sheet as seen in TEM can lead to resistance in its capacitive behaviour. The capacitive characteristics of graphene can be increased by optimizing the material by altering the pore diameters and introducing metal oxide to keep its separate sheets from agglomerating.
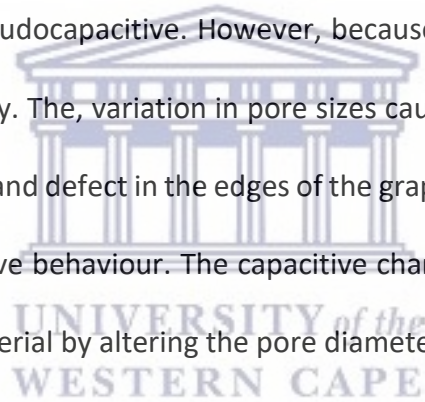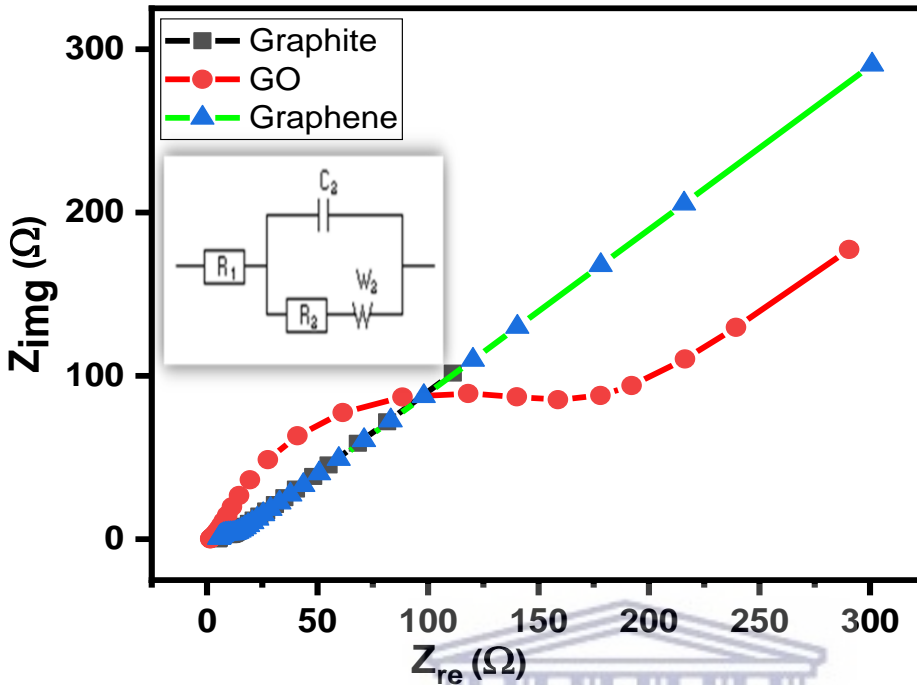
Figure 3.21: Nyquist plot of graphite, GO and graphene, the inset is the equivalent circuit.
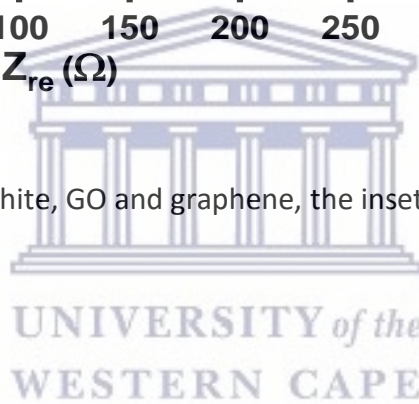
Table 3-3: EIS curve fitting data of graphite, GO and graphene electrode material

Sample		R_s (Ω)	CPE (µF)	R_{ct} (Ω)	W^2 (Ω s- ½)	Phase angle (º)
Graphite		5.1	16.8	4.7	80.6	65.8
GO		1.3	393	115.3	230.3	63.18
Graphene		5.49	0.393	5.4	138.1	43.4
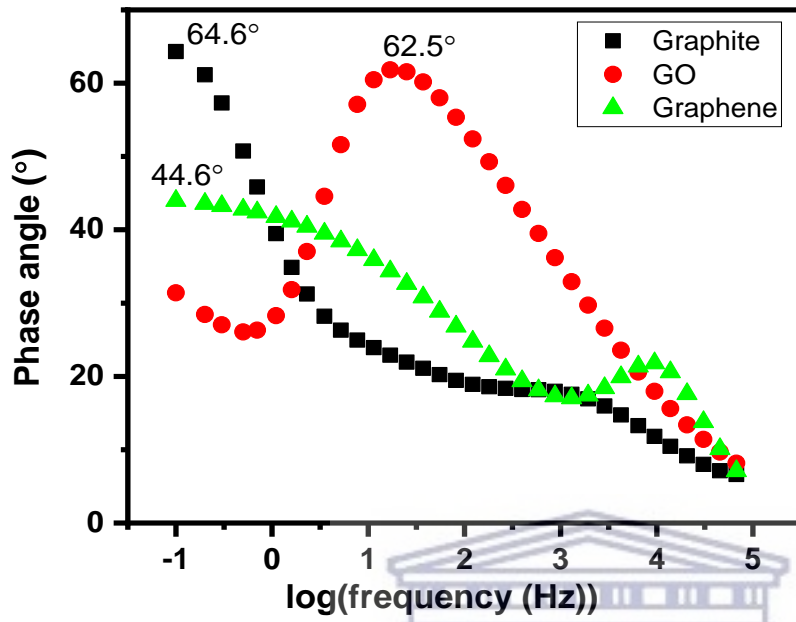
Figure 3.22: Bode plot of graphite, GO and graphene
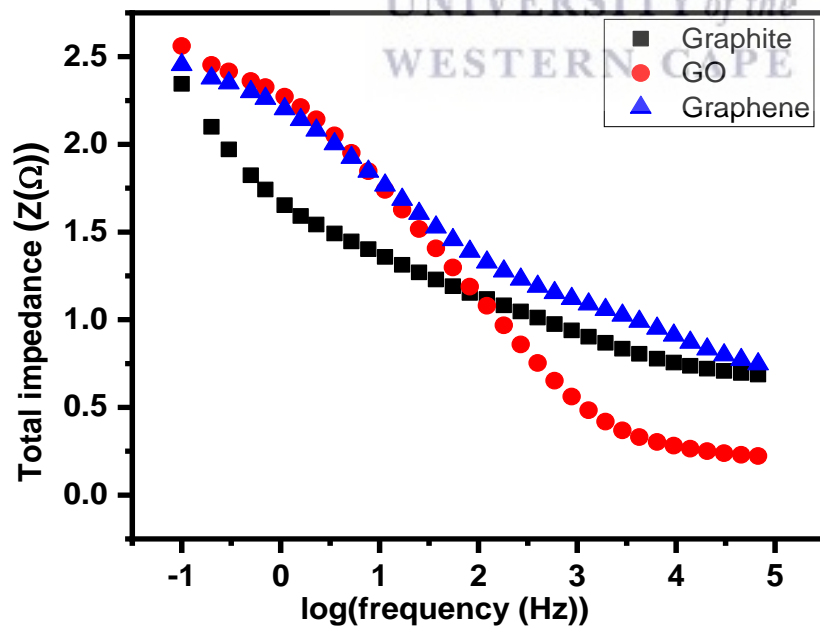
Figure 3.23: Total impedance plot of graphite, GO and graphene

3.3.4 Device fabrication

An asymmetric supercapacitor was fabricated to investigate the supercapacitive performance of Activated carbon (AC) // graphene electrode in a 1 M Li_2SO_4 aqueous electrolyte. Graphene was coated on a Ni foam substrate and assembled in a Swagelok; a filter paper was used as the separator. The supercapacitive performance of the graphene-based asymmetric device was studied using GCD and EIS techniques.
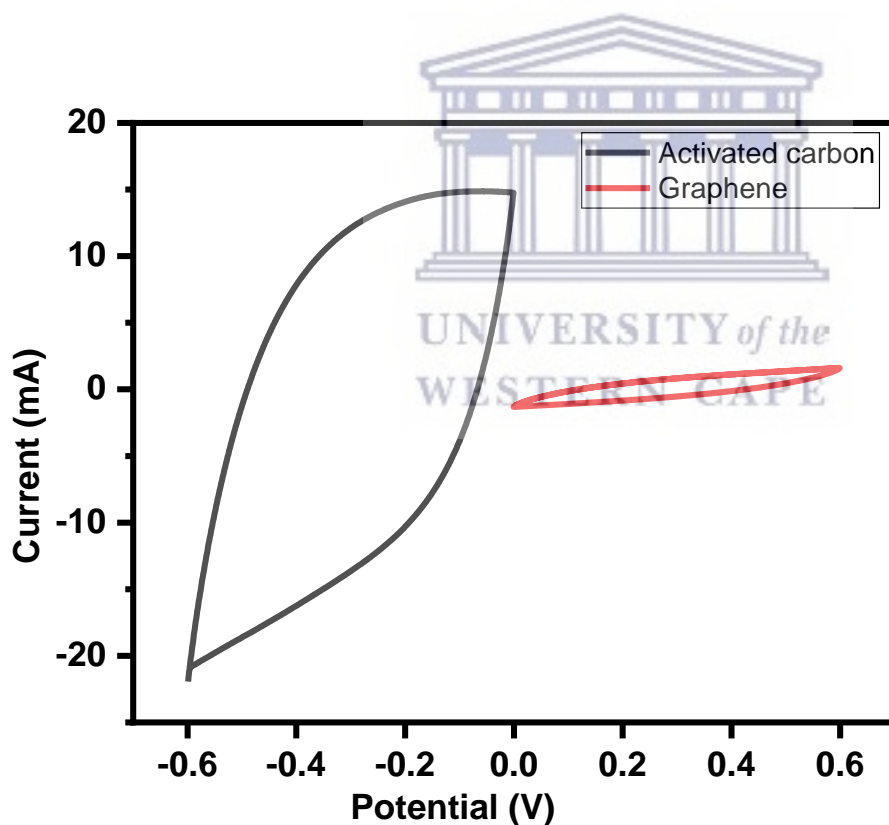
Figure 3.24: CV plot of graphene and activated carbon in a 3-electrode cell at 30 mV s^{-1} showing the suitability of AC as the negative electrode.

3.3.4.1 Galvanostatic charge discharge

The GCD plot as shown in Figure 3.25 was carried out at different current densities (0.2 A g^{-1},0.5 A g^{-1},0.8 A g^{-1} and 1 A g^{-1}). The capacitance at each current density was calculated and the result is as shown in Table 3-4. Figure 3.26 shows the relationship between the capacitance and the current density, the capacitance reduced with an increase in the current density. Energy density and power density are the two vital parameters to characterize the performance of an energy storage device. The specific energy and power were calculated according to the following equations:

$$E_{sp} \left(Wh/Kg \right) = \frac{CV^2}{2m} \times \frac{1}{3.6} \qquad \text{3-3}$$

$$P_{max} \left(W/Kg \right) = \frac{E}{\triangle t} \times 3600 \qquad \text{3-4}$$

where C (F g^{-1}) is the specific capacitance determined from equation 3-2, V is the maximum working potential, m (kg) is the mass of the active material in the electrode, and $\triangle$t is the capacitors discharge time. Figure 3.27 is a Ragone plot showing the relationship between energy density and power density of the asymmetric device at different current densies. An optimal supercapacitor device would have a high energy density at a high-power density. Notably, the asymmetric Cs cell delivered a maximum energy density of 14.80 W h kg^{-1} at a power density of 360 W kg^{-1} at 0.1 A g^{-1} current load. This obtained energy density and power density could be improved by optimizing the pore sizes of this material and introducing metal oxides that will act

as spacers to keep the graphene sheets from agglomerating. Thereby leading to the enhanced surface area.
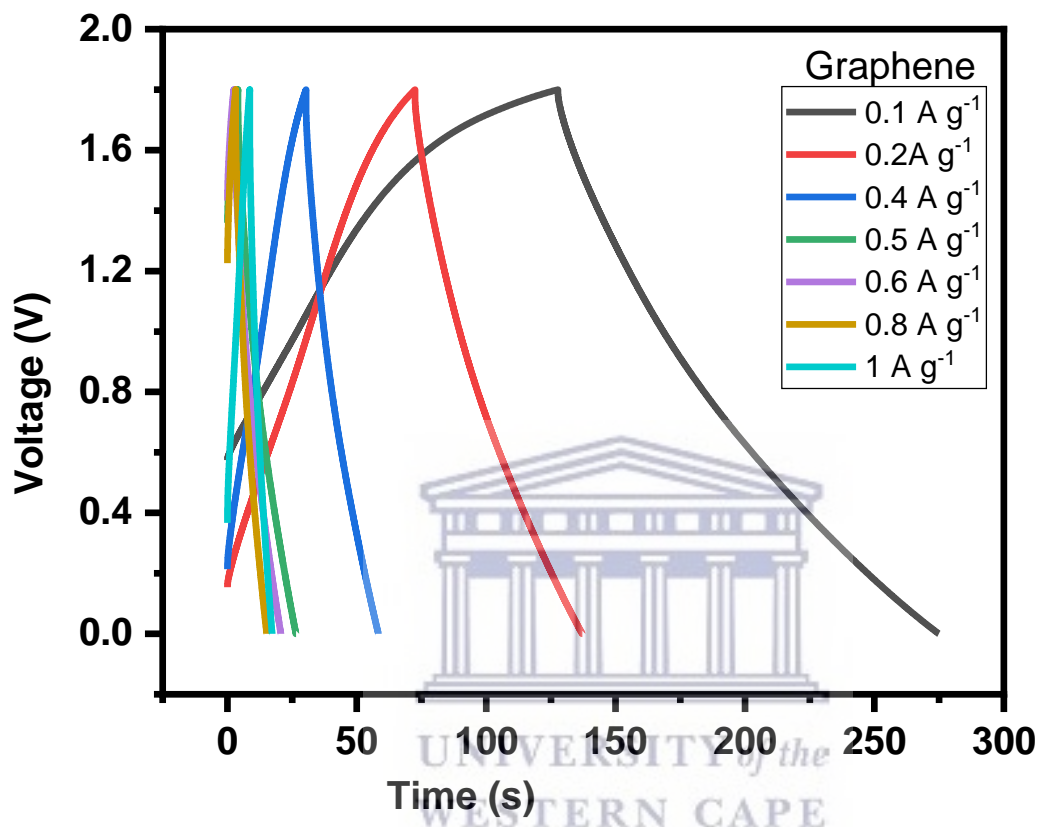
Figure 3.25: GCD Plot of AC//graphene electrode in 1 M Li_2SO_4

Table 3-4: Capacitance, ED and PD of AC//graphene device from the GCD data.

Current density	Capacitance	PD	ED
(A g^{-1})	(F g^{-1})	(W kg^{-1})	(W h kg^{-1})
0.1	32.89	360.00	14.80

0.2	29.33	720.00	13.20
0.4	25.42	1440.00	11.44
0.5	24.82	1800.00	11.17
0.6	24.15	2160.00	10.87
0.8	21.16	2880.00	9.52
1	19.33	3600.00	8.70
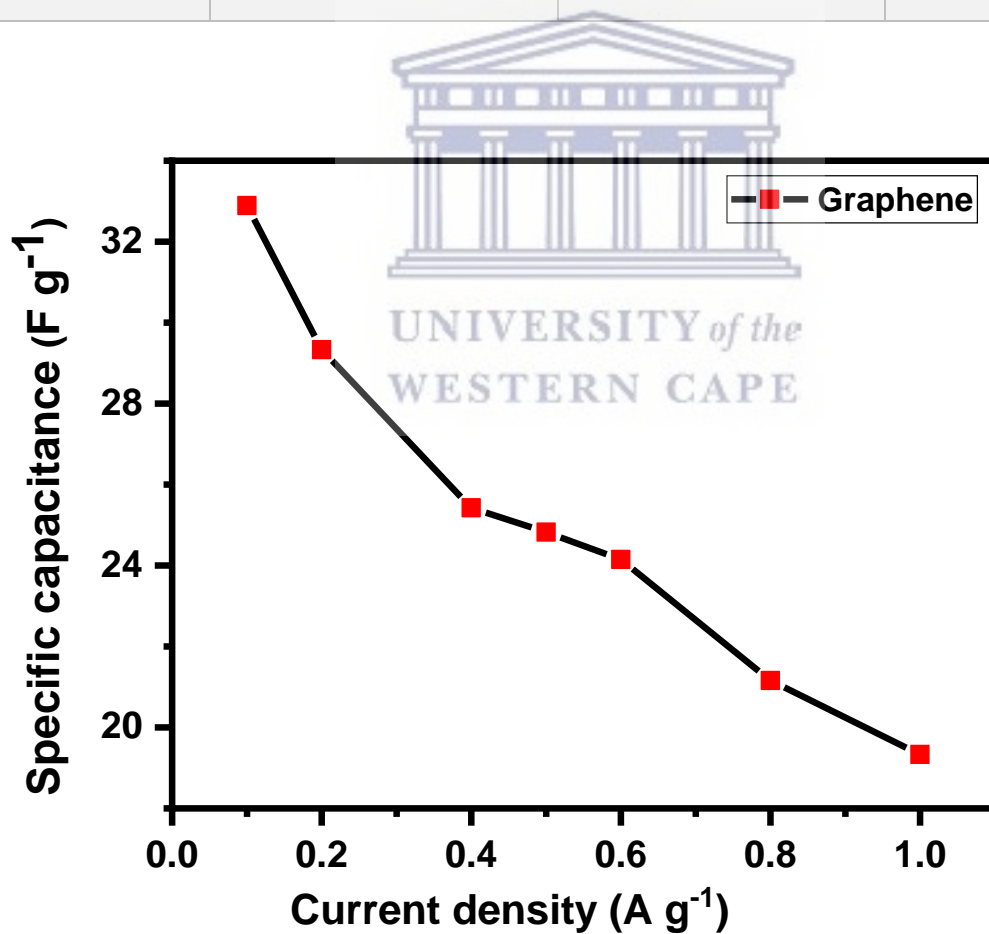
Figure 3.26: A plot of Cs vs current densities for AC//graphene device
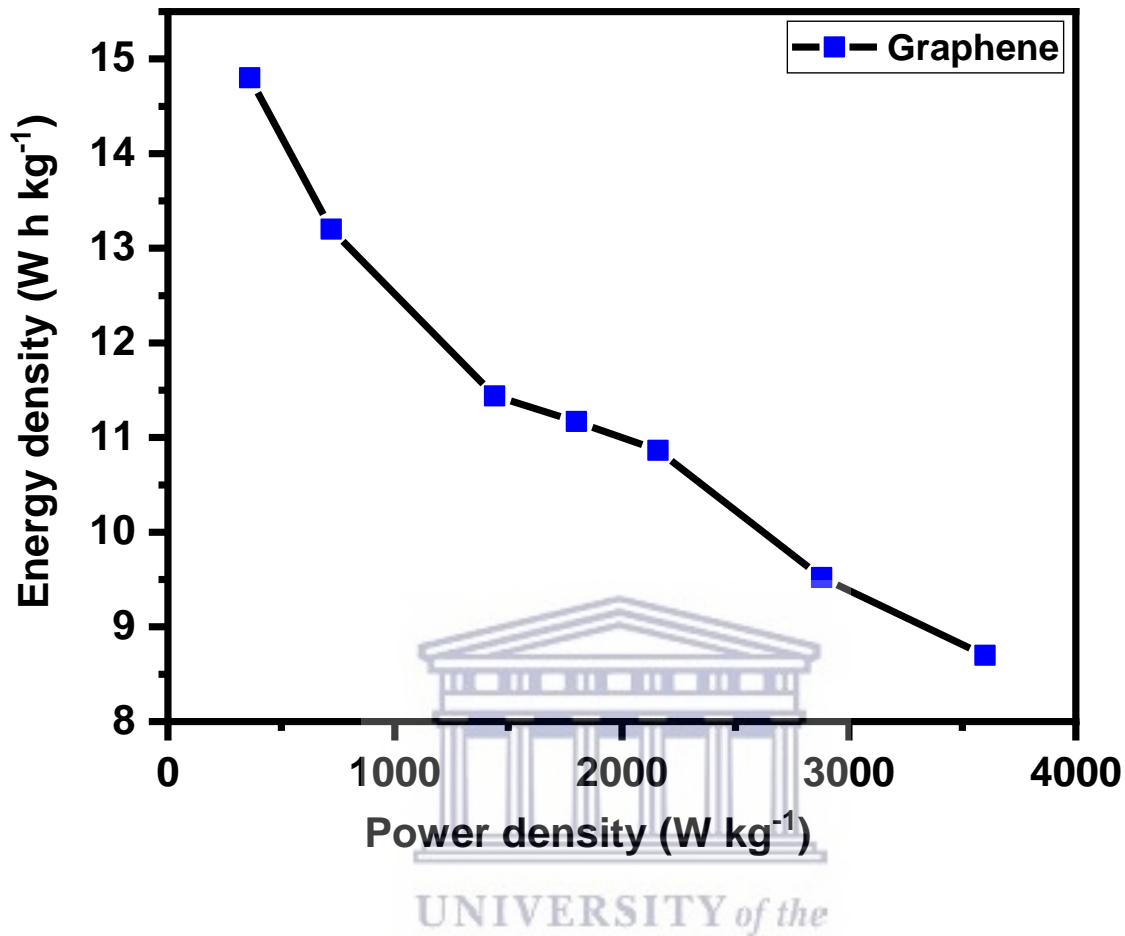
Figure 3.27: Ragone plot for AC//graphene electrode showing the relationship between ED and PD of the device.

3.3.4.2   Electrochemical impedance spectroscopy

Figure 3.28 is the Nyquist plot of the graphene asymmetric device. The in-set is the fitted equivalent circuit data. From the impedance spectrum, the asymmetric device shows an ESR of 1.19 Ω, which is expected to impact the power density [44]. In the mid-high frequency region of the spectrum, the charge transfer resistance was calculated to be 1.34 Ω, the low R_{ct} would result in rapid diffusion and would imply good capacitive behaviour. As the semi-circle breaks into an

inclined line, a Warburg constant of 7.08 Ω, is achieved due to the diffusion of the electrolyte ion into the graphene material. The Bode plot from the EIS data is shown as the phase angle and total impedance plot in Figure 3.29. The phase angle of the graphene device is at 62°, indicating a capacitive behaviour which is from the contribution of both EDLC and pseudocapacitance. The magnitude of total impedance had a low value of 0.02 Ω. Both plots confirm a capacitive electrode.
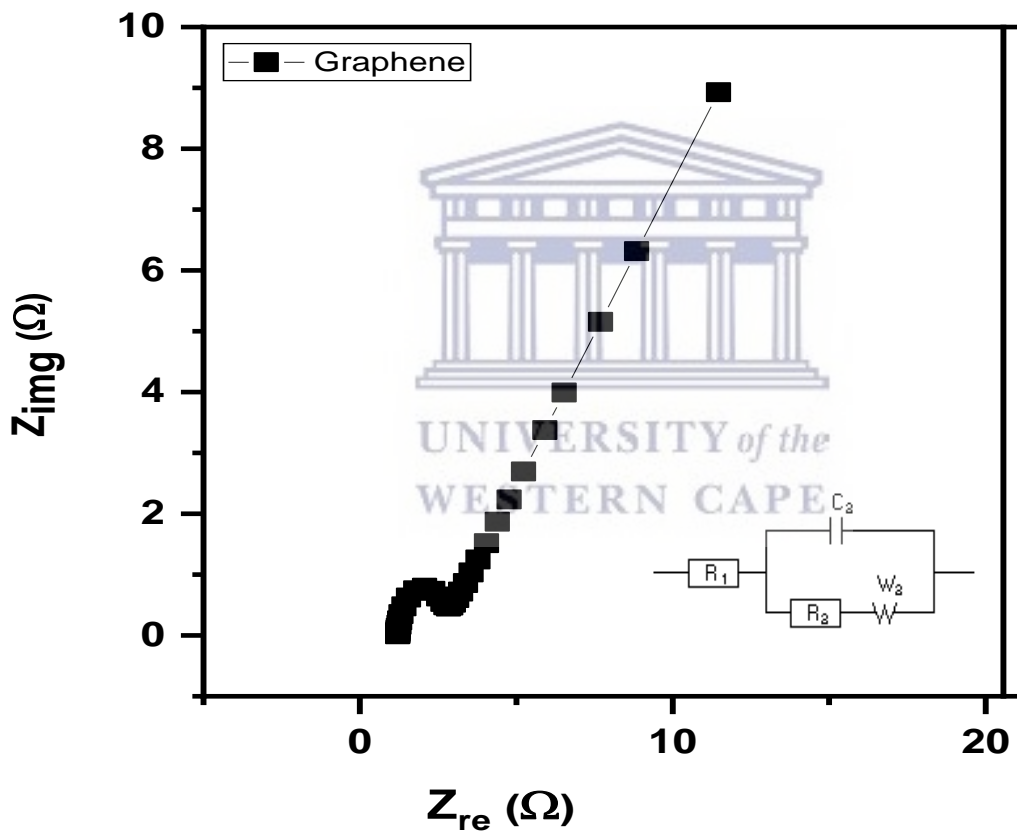
Figure 3.28: Nyquist plot of AC//graphene electrode, the inset is the equivalent circuit.
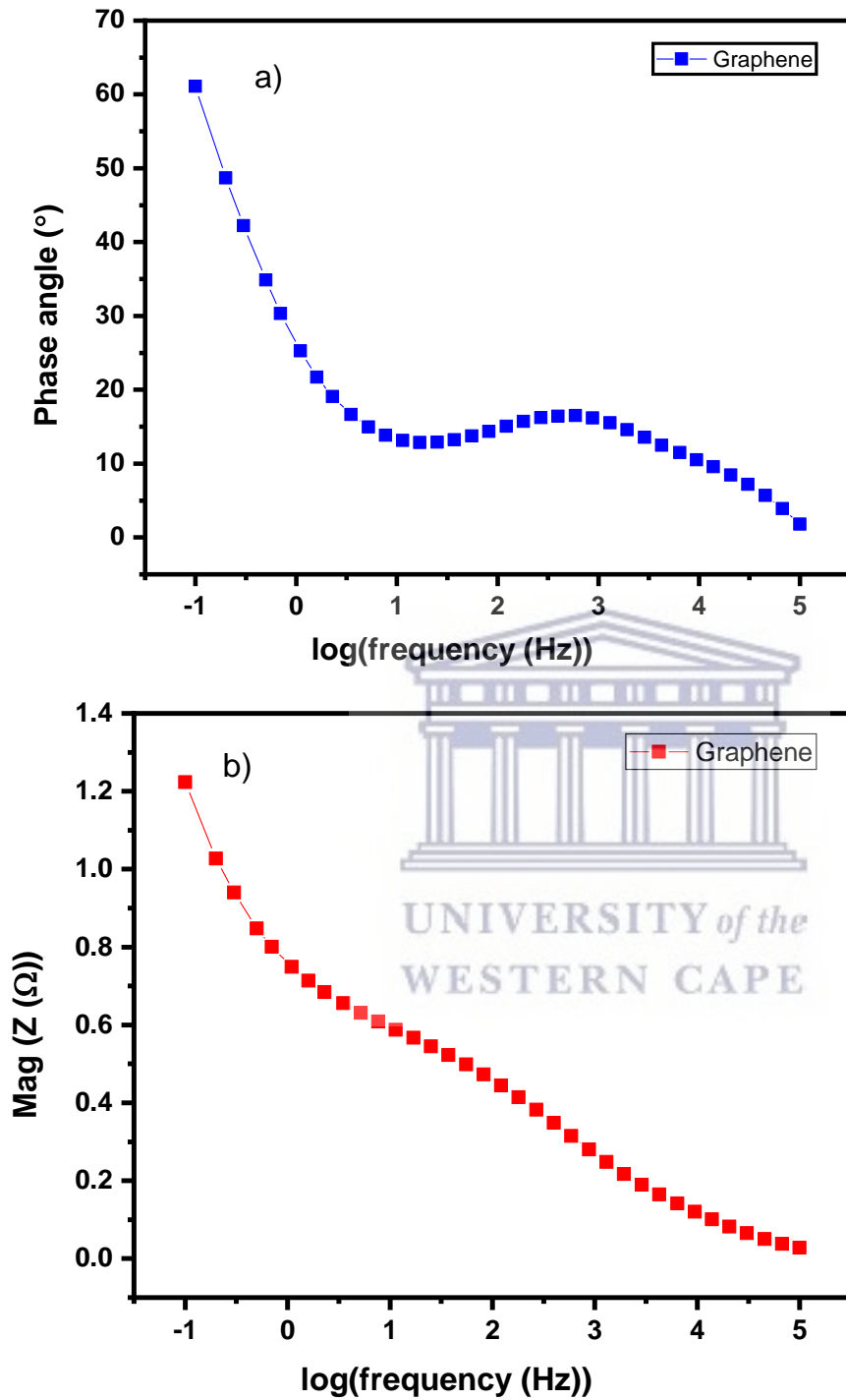
Figure 3.29: Bode plot of AC//graphene electrode represented as a) phase angle plot and b) total impedance plot.

3.3.4.3   Cycle life

Long cycle life is an important criterion for supercapacitors. The cyclic stability was performed using the galvanostatic charge-discharge techniques at a current density of 0.5 A g^{-1} and a voltage range of 0-1.8V. Figure 3.30 shows that the system remained stable for more than 2500 charging and discharging cycles and maintained 100 % of its initial capacitance. Figure 3.30 also shows a plot of Coloumbic efficiency vs cycle number. The Columbic efficiency is the rate of the discharge time to the charge time. The material retained a 100% Columbic efficiency during the life cycle. As seen in the in-set, the shape of the GCD curve in the first cycle and the 2500 cycle shows no significant change in their linearity, indicating good stability.
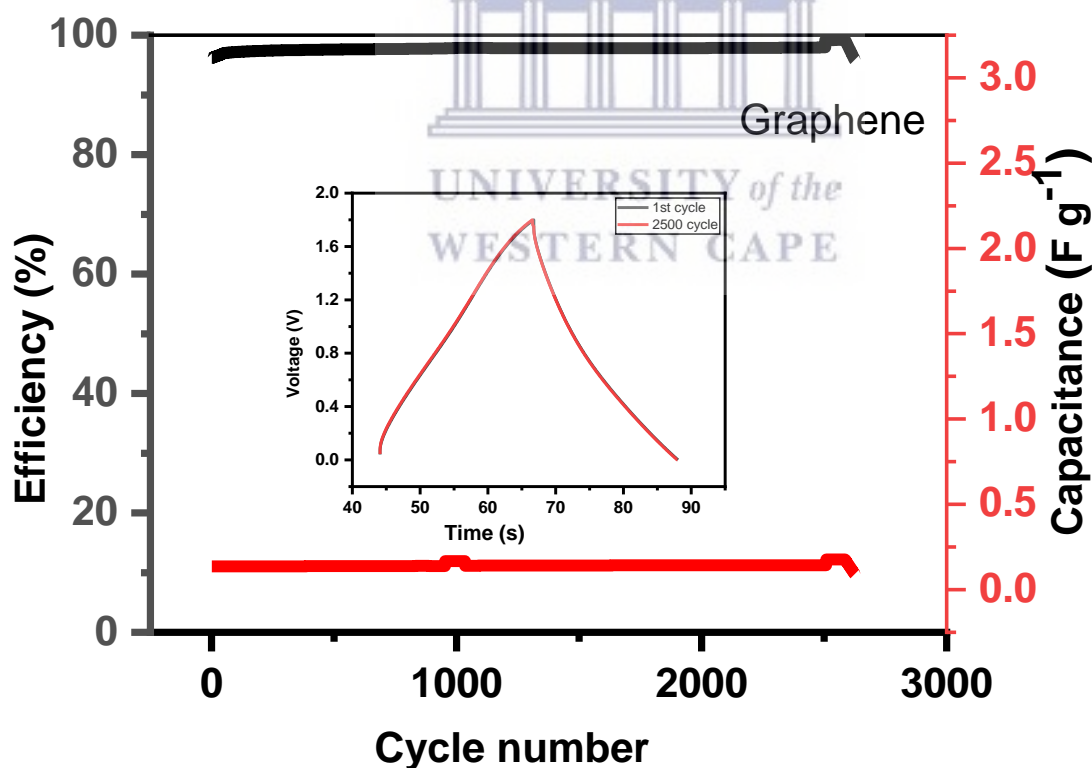
Figure 3.30: Cycling stability of AC//graphene supercapacitor. The in-set is the GCD plot at 1_{st} and 2500_{th} cycles

3.4 CONCLUSION

The electrochemistry of graphene has been explored and compared with that of GO and graphite in this research. The morphological, structural, and electrochemical analyses demonstrate that graphene structures have better electrochemical characteristics than GO and graphite structures. According to the GCD profile, the specific capacitance of the graphene electrode has the highest specific capacitance in a three-electrode cell configuration. At 1 A g^{-1} the graphene electrode had a specific capacitance of 63.33 F g^{-1} while that of GO was 17.4 F g^{-1} and graphite was 19.3 F g^{-1}. An asymmetric device was fabricated with the graphene electrode. The asymmetric cell delivered a maximum energy density of 14.80 W h kg^{-1} at a power density of 360 W kg^{-1} at 0.1 A g^{-1} current load.
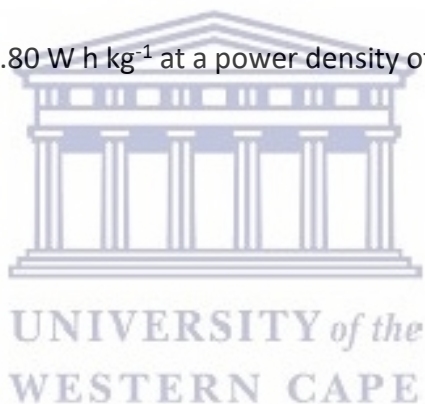
3.5 REFERENCE

[1]   K. Kaiser, L.M. Scriven, F. Schulz, P. Gawel, L. Gross, H.L. Anderson, An sp-hybridized molecular carbon allotrope, cyclo[18]carbon, Science (80-.). 365 (2019) 1299–1301. https://doi.org/10.1126/science.aay1914.

[2]   W. Wu, M. Liu, Y. Gu, B. Guo, H.X. Ma, P. Wang, X. Wang, R. Zhang, Fast chemical exfoliation of graphite to few-layer graphene with high quality and large size via a two-step microwave-assisted process, Chem. Eng. J. 381 (2020) 122592. https://doi.org/10.1016/j.cej.2019.122592.

[3]   S. Chen, R. Ramachandran, V. Mani, R. Saraswathi, Recent Advancements in Electrode Materials for the High- performance Electrochemical Supercapacitors : A Review, 9 (2014) 4072–4085.

[4]   Y. Wang, Z. Shi, Y. Huang, Y. Ma, C. Wang, M. Chen, Y. Chen, Supercapacitor Devices Based on Graphene Materials, (2009) 13103–13107.

[5]   P. Iamprasertkun, R.A.W. Dryfe, The Capacitance of Graphene: FromModel Systems to Large-Scale Devices, in: Nanocarbon Electrochem., wiley, 2019: pp. 33–84. https://doi.org/10.1002/9781119468288.ch2.

[6]   M.H.A. Kudus, M.R. Zakaria, H.M. Akil, F. Ullah, F. Javed, Oxidation of graphene via a simplified Hummers' method for graphene-diamine colloid production, J. King Saud Univ. - Sci. 32 (2020) 910–913. https://doi.org/10.1016/j.jksus.2019.05.002.

[7]   W. Gao, L.B. Alemany, L. Ci, P.M. Ajayan, New insights into the structure and reduction of graphite oxide, Nat. Chem. 1 (2009) 403–408. https://doi.org/10.1038/nchem.281.

[8]   S. Stankovich, D.A. Dikin, R.D. Piner, K.A. Kohlhaas, A. Kleinhammes, Y. Jia, Y. Wu, S.B.T. Nguyen, R.S. Ruoff, Synthesis of graphene-based nanosheets via chemical reduction of exfoliated graphite oxide, Carbon N. Y. 45 (2007) 1558–1565. https://doi.org/10.1016/j.carbon.2007.02.034.

[9]   L.F. Villalobos, C. Van Goethem, K.-J. Hsu, S. Li, M. Moradi, K. Zhao, M. Dakhchoune, S. Huang, Y. Shen, E. Oveisi, V. Boureau, K.V. Agrawal, Bottom-up synthesis of graphene films hosting atom-thick molecular-sieving apertures, Proc. Natl. Acad. Sci. 118 (2021) e2022201118. https://doi.org/10.1073/pnas.2022201118.

[10]   Q. Zhang, X. Cheng, C. Wang, A.M. Rao, B. Lu, Sulfur-assisted large-scale synthesis of graphene microspheres for superior potassium-ion batteries, Energy Environ. Sci. 14 (2021) 965–974. https://doi.org/10.1039/d0ee03203d.

[11]   Y. Bai, Y. Yin, Y. Xuan, X. Han, Scalable and fast fabrication of holey multilayer graphene via microwave and its application in supercapacitors, Nanotechnology. 32 (2021) 045602. https://doi.org/10.1088/1361-6528/abbfd4.

[12]   L. Lai, H. Yang, L. Wang, B.K. Teh, J. Zhong, H. Chou, L. Chen, W. Chen, Z. Shen, R.S. Ruoff, J. Lin, Preparation of Supercapacitor Electrodes through Selection of Graphene Surface Functionalities, ACS Nano. 6 (2012) 5941–5951. https://doi.org/10.1021/NN3008096.

[13]   H. Gómez, M.K. Ram, F. Alvi, P. Villalba, E. Stefanakos, A. Kumar, Graphene-conducting polymer nanocomposite as novel electrode for supercapacitors, J. Power Sources. 196 (2011) 4102–4108. https://doi.org/10.1016/j.jpowsour.2010.11.002.

[14]   Z.S. Iro, C. Subramani, S.S. Dash, A brief review on electrode materials for supercapacitor,

Int. J. Electrochem. Sci. 11 (2016) 10628–10643. https://doi.org/10.20964/2016.12.50.

[15] M.A. Pope, S. Korkut, C. Punckt, I.A. Aksay, Supercapacitor Electrodes Produced through

      Evaporative Consolidation of Graphene Oxide-Water-Ionic Liquid Gels, J. Electrochem. Soc.

      160 (2013) A1653–A1660. https://doi.org/10.1149/2.017310jes.

[16] Y. Chang, S. Xia, G. Han, H. Zhou, D. Fu, H. Song, Y. Xiao, Y. Zhang, Flexible supercapacitor

      electrode with high performance prepared from graphene oxide films assembled in the

      presence of p-phenylenediamine and urea, J. Mater. Sci. Mater. Electron. 30 (2019) 7216–

      7225. https://doi.org/10.1007/s10854-019-01000-0.

[17] M.V. Kiamahalleh, S.H.S. Zein, G. Najafpour, S.A. Sata, S. Buniran, Multiwalled carbon

      nanotubes based nanocomposites for supercapacitors: A review of electrode materials,

      Nano. 7 (2012). https://doi.org/10.1142/S1793292012300022.

[18] J.W. Han, J. Kim, Green synthesis of graphene and its cytotoxic effects in human breast

      cancer cells, (2013). https://doi.org/10.2147/IJN.S42047.

[19] J.C. Meyer, A.K. Geim, M.I. Katsnelson, K.S. Novoselov, T.J. Booth, S. Roth, The structure of

      suspended   graphene   sheets,   Nature.   446   (2007)   60–63.

      https://doi.org/10.1038/nature05545.

[20] J. Zhu, G. Zeng, F. Nie, X. Xu, S. Chen, Q. Han, X. Wang, Decorating graphene oxide with

      CuO nanoparticles in a water-isopropanol system, Nanoscale. 2 (2010) 988–994.

      https://doi.org/10.1039/b9nr00414a.

[21] L.M. Viculis, J.J. Mack, O.M. Mayer, H.T. Hahn, R.B. Kaner, Intercalation and exfoliation

      routes   to   graphite   nanoplatelets,   J.   Mater.   Chem.   15   (2005)   974–978.

https://doi.org/10.1039/b413029d.

[22]   C. Hontoria-Lucas, A.J. López-Peinado, J. de D. López-González, M.L. Rojas-Cervantes, R.M. Martín-Aranda, Study of oxygen-containing groups in a series of graphite oxides: Physical and chemical characterization, Carbon N. Y. 33 (1995) 1585–1592. https://doi.org/10.1016/0008-6223(95)00120-3.

[23]   Conway B.E, Electrochemical Supercapacitors: Scientific Fundamentals and Technological ... - B. E. Conway - Google Books, springer science+Business Media, New York, new york, 1999. (accessed November 16, 2018).

[24]   Q.Y. Li, Z.S. Li, L. Lin, X.Y. Wang, Y.F. Wang, C.H. Zhang, H.Q. Wang, Facile synthesis of activated carbon/carbon nanotubes compound for supercapacitor application, Chem. Eng. J. 156 (2010) 500–504. https://doi.org/10.1016/j.cej.2009.10.025.

[25]   IR Spectrum Table, (n.d.). https://www.sigmaaldrich.com/ZA/en/technical-documents/technical-article/analytical-chemistry/photometry-and-reflectometry/ir-spectrum-table (accessed August 4, 2021).

[26]   M. Bera, Chandravati, P. Gupta, P.K. Maji, Facile one-pot synthesis of graphene oxide by sonication assisted mechanochemical approach and its surface chemistry, J. Nanosci. Nanotechnol. 18 (2018) 902–912. https://doi.org/10.1166/jnn.2018.14306.

[27]   I.O. Faniyi, O. Fasakin, B. Olofinjana, A.S. Adekunle, T. V. Oluwasusi, M.A. Eleruja, E.O.B. Ajayi, The comparative analyses of reduced graphene oxide (RGO) prepared via green, mild and chemical approaches, SN Appl. Sci. 2019 110. 1 (2019) 1–7. https://doi.org/10.1007/S42452-019-1188-7.

[28]   P.H.S. Borges, A.C. Catto, E. Longo, E. Nossol, Electrochemical synthesis of reduced graphene oxide/ruthenium oxide hexacyanoferrate nanocomposite film and its application for ranitidine detection, J. Electroanal. Chem. 878 (2020) 114558. https://doi.org/10.1016/J.JELECHEM.2020.114558.

[29]   J. Bin Wu, M.L. Lin, X. Cong, H.N. Liu, P.H. Tan, Raman spectroscopy of graphene-based materials and its applications in related devices, Chem. Soc. Rev. 47 (2018) 1822–1873. https://doi.org/10.1039/c6cs00915h.

[30]   A. Kaniyoor, S. Ramaprabhu, A Raman spectroscopic investigation of graphite oxide derived graphene, AIP Adv. 2 (2012) 032183. https://doi.org/10.1063/1.4756995.

[31]   A. Jorio, R. Saito, Raman spectroscopy for carbon nanotube, J. Appl. Phys. 129 (2021) 21102. https://doi.org/10.1063/5.0030809.

[32]   V. Scardaci, G. Compagnini, Raman Spectroscopy Investigation of Graphene Oxide Reduction by Laser Scribing, C. 7 (2021) 48. https://doi.org/10.3390/c7020048.

[33]   Y. Gong, D. Li, Q. Fu, C. Pan, Influence of graphene microstructures on electrochemical performance for supercapacitors, Prog. Nat. Sci. Mater. Int. 25 (2015) 379–385. https://doi.org/10.1016/j.pnsc.2015.10.004.

[34]   Poonam, K. Sharma, A. Arora, S.K. Tripathi, Review of supercapacitors: Materials and devices, J. Energy Storage. 21 (2019) 801–825. https://doi.org/10.1016/j.est.2019.01.010.

[35]   B.J. Choudhury, K. Roy, V.S. Moholkar, Improvement of Supercapacitor Performance through Enhanced Interfacial Interactions Induced by Sonication, Ind. Eng. Chem. Res. 60 (2021) 7611–7623. https://doi.org/10.1021/acs.iecr.1c00279.

[36]   J. Yan, T. Wei, W. Qiao, B. Shao, Q. Zhao, L. Zhang, Z. Fan, Rapid microwave-assisted synthesis of graphene nanosheet/Co_3O_4 composite for supercapacitors, Electrochim. Acta. 55 (2010) 6973–6978. https://doi.org/10.1016/j.electacta.2010.06.081.

[37]   T. Pettong, P. Iamprasertkun, A. Krittayavathananon, P. Sukha, P. Sirisinudomkit, A. Seubsai, M. Chareonpanich, P. Kongkachuichay, J. Limtrakul, M. Sawangphruk, High-Performance Asymmetric Supercapacitors of $MnCo_2O_4$ Nanofibers and N-Doped Reduced Graphene Oxide Aerogel, ACS Appl. Mater. Interfaces. 8 (2016) 34045–34053. https://doi.org/10.1021/acsami.6b09440.

[38]   C. Wang, J. Zhao, S. Luo, X. Yu, Improved Pseudocapacitive Performance of Graphene Architectures Modulating by Nitrogen/Phosphorus Dual-Doping and Steam-Activation, Macromol. Res. 29 (2021) 582–588. https://doi.org/10.1007/s13233-021-9075-7.

[39]   M. Dvoyashkin, D. Leistenschneider, J.D. Evans, M. Sander, L. Borchardt, Revealing the Impact of Hierarchical Pore Organization in Supercapacitor Electrodes by Coupling Ionic Dynamics at Micro- and Macroscales, Adv. Energy Mater. 11 (2021) 2100700. https://doi.org/10.1002/aenm.202100700.

[40]   D. Qu, Studies of the activated mesocarbon microbeads used in double-layer supercapacitors, J. Power Sources. 109 (2002) 403–411.

[41]   D. Mandal, P. Routh, A.K. Mahato, A.K. Nandi, Electrochemically modified graphite paper as an advanced electrode substrate for supercapacitor application, J. Mater. Chem. A. 7 (2019) 17547–17560. https://doi.org/10.1039/c9ta04496e.

[42]   A.K. Singh, D. Sarkar, K. Karmakar, K. Mandal, G.G. Khan, High-Performance Supercapacitor

Electrode Based on Cobalt Oxide-Manganese Dioxide-Nickel Oxide Ternary 1D Hybrid Nanotubes, ACS Appl. Mater. Interfaces. 8 (2016) 20786–20792. https://doi.org/10.1021/acsami.6b05933.

[43] N. Bundaleska, J. Henriques, M. Abrashev, A.M. Botelho do Rego, A.M. Ferraria, A. Almeida, F.M. Dias, E. Valcheva, B. Arnaudov, K.K. Upadhyay, M.F. Montemor, E. Tatarova, Large-scale synthesis of free-standing N-doped graphene using microwave plasma, Sci. Rep. 8 (2018) 1–11. https://doi.org/10.1038/s41598-018-30870-3.

[44] A. Noori, M.F. El-kady, M.S. Rahmanifar, R.B. Kaner, M.F. Mousavi, Chem Soc Rev metrics for batteries , supercapacitors and beyond, Chem. Soc. Rev. (2019). https://doi.org/10.1039/c8cs00581h.

CHAPTER FOUR

ULTRA-SMALL RUTHENIUM OXIDE GRAPHENE COMPOSITE FOR ASYMMETRIC SUPERCAPACITORS

Highlights

- Microwave synthesis of ruthenium oxide (RuO) and ruthenium oxide-graphene nanoparticles.

- RuO-G showed better electrochemical behaviors in Li_2SO_4 electrolytes than RuO due to the addition of graphene.

- RuO-G asymmetric supercapacitor device demonstrated better stability and efficiency than the RuO device in 1.8 V voltage window.
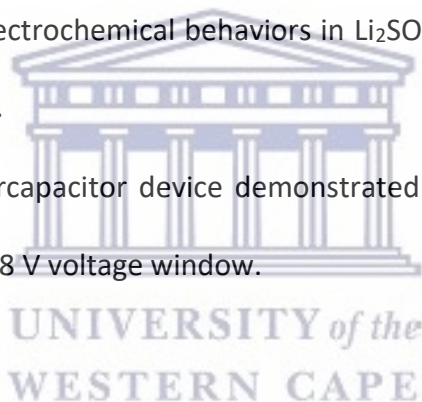
ABSTRACT

A modern technological society necessitates the large-scale consumption and storage of energy. In this regard, present scientific research is centered on the development of high-performance supercapacitors. Ruthenium oxide (RuO) and ruthenium oxide graphene (RuO-G) has received interest for supercapacitor applications, due to their good characteristics. In this study, RuO-G was produced using a microwave-assisted technique; SEM revealed ruthenium oxide particles randomly scattered on the graphene, and EDS validated the material's elemental composition. When compared to pristine RuO and graphene, the composite was shown to have superior electrochemical characteristics than both pristine materials. Ruthenium oxide and graphinized ruthenium oxide were used as the positive electrode to assemble an asymmetric supercapacitor (ASC). The ASC has much better capacitance performance than ruthenium oxide alone. According to the GCD, the specific capacitance of RuO-G was 7.96 F g^{-1}, whereas that of RuO was 3.01 F g^{-1} at 0.1 A g^{-1}. The energy density and power density were calculated to be 3.98 W h kg^{-1} and 360 W kg^{-1} respectively, for RuO-G while that of RuO was 1.41 W h kg^{-1} and 360 W kg^{-1}, indicating a good synergistic impact of graphene and RuO in the composite. These findings highlight the importance and enormous potential of graphene-based composites in the growth of advanced energy storage systems.

KEYWORDS

Asymmetric supercapacitors, graphene, pseudocapacitance, ruthenium oxide, ultra-small particle size.

4.1 INTRODUCTION

A supercapacitor is a high-power storage system for electrochemical energy storage. Its advantages include high power density, reliability, long life cycle and low maintenance costs [1]. It also, however, has a low energy density that has severely impacted its practical application. Theoretically, by raising the real capacitance and maximizing the voltage applied, energy density can be increased [2]. The voltage window range is typically affected by; the type of electrolyte used. Although organic electrolytes and ionic electrolytes have higher potential windows than aqueous electrolytes resulting in higher capacitance, there is still a major concern about the environmental risks posed by these electrolytes and their synthesis complications. Research into the use of aqueous electrolytes is thus growing [3]. Owing to the degradation of H_2O, aqueous electrolytes typically have a lower voltage window. However, in laboratories, they are cheaper and simpler to handle. Secondly, generally, aqueous electrolytes have higher conductivity, thereby reducing ESR, leading to a higher power. The smaller aqueous electrolyte ion sizes often promote the redox reactions between the electrode and the electrolytes leading to higher pseudocapacitance [4]. Asymmetric supercapacitors (ASCs) are efficient systems used to improve supercapacitor energy density. They are usually made with electrodes of different characteristics; composition and masses [5][6][7]. The key to making ASCs is to use electrode materials that work in multiple potential windows in the same electrolyte. As a result, the cell voltage can be extended, enhancing the super capacitor's energy density [8] [9]. Zhang *et al*. [10] fabricated an ASC using a graphene oxide sheet that was either modified with ruthenium oxide (RGO-RuO) or polyaniline (RGO-PANI) as the positive electrode and activated carbon as the

negative electrode. In comparison, a symmetrical supercapacitor was fabricated using either RGO-RuO or EGO-PANI as both positive and negative electrodes. The report showed that the ASC showed better electrochemical performance. This is majorly due to the expanded potential window in an aqueous electrolyte which leads to an improved energy density of 26.3 W h kg $^{-1}$. This was roughly twice as high as the symmetrical RGO–RuO$_2$ supercapacitors (12.4 W h kg $^{-1}$) as well as RGO–PANi (13.9 W h kg $^{-1}$) electrodes. In addition, a power density of 49.8 kW kg $^{-1}$ was obtained at an energy density of 6.8 W h kg $^{-1}$. Xuan *et al*. [11] reported an asymmetric capacitor with Fe$_3$O$_4$/activated carbon electrodes with a capacitance of 37.9 F g^{-1} in 6 M KOH aqueous electrolyte. Asbani *et al*. [12] reported an asymmetric micro-supercapacitor (A-MSC) made of sputtered vanadium nitride (VN) and electrodeposited hydrous ruthenium oxide (hRuO$_2$). Using complementary electrochemical potential windows in 1 M KOH electrolyte, the A-MSC produced a cell voltage of up to 1.15 V, which corresponds to a high specific capacitance value for the device (100 mF cm^{-2}). At a power density of 3 mW cm^{-2}, the energy density of this asymmetric VN / hRuO$_2$ micro-supercapacitor was 20 Wh cm^{-2}. Kumar *et al*. [13] fabricated an activated carbon/RuS$_2$ ASC in an aqueous electrolyte with an optimal cell voltage of 2 V. The device obtained a volumetric energy density of 1.57 mWh cm^{-3} and a volumetric power density of 23.71 mW cm^{-3}.

RuO oxide has been the focus of research in recent times with great potential for achieving higher energy and power densities than carbon-based EDLCs and polymer-based pseudocapacitors. This is due to their high capacitance, reversible charge-discharge characteristics, and good electrical conductivity. The production and dispersion of amorphous hydrous RuO$_2$ particles are critical for

improving the pseudocapacitive capacitance of the RuO_2 electrode [29,30]. However, RuO_2 particles frequently form large agglomerates, which can significantly degrade their electrochemical performance due to the incomplete reaction of RuO_2 during the electrochemical redox process, which begins at the surface of RuO_2 particles and becomes slower as the reaction progresses, particularly for agglomerated large particles. The use of graphene with metal oxide nanoparticles minimizes nanoparticle aggregation, allowing for greater exploitation of metal oxide properties. This aids in getting a high capacitance value. In recent work, rGO/RuO_2 aerogels were synthesized; according to CV voltammograms, the greatest specific capacitance of rGO/RuO_2 aerogels was calculated to be 328.6 F g^{-1} at a potential scan rate of 5 mV s^{-1}. The assembled rGO/RuO_2 aerogel-based device had an energy density value of 31.1 W h kg^{-1} at a power density of 8.365 kW kg^{-1}.
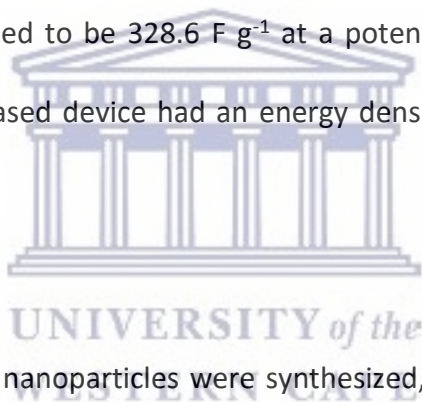
In this study, ultra-small RuO-G nanoparticles were synthesized, using the microwave method and their electrochemical performances in 1 M Li_2SO_4 electrolyte were investigated. An ASC was fabricated by using graphene-based RuO as positive electrodes and activated carbon as negative electrodes. RuO//AC was also fabricated for comparison purposes. Each nanocomposite's capacitance behaviour was evaluated using cyclic voltammetry, galvanostatic charge-discharge and impedance spectroscopy techniques. The ASC has an energy density of 5.29 W h kg^{-1} because of the expanded potential window (1.8 V).

4.2 EXPERIMENTAL

4.2.1 Materials

Microcrystalline graphite (2-15 µm, 99.99%) was purchased from Alfar Aesar (Kandel, Germany)

Nickel foam (1.6 mm thick, 0.25 µm pore diameter) was purchased from MTI Corporation,

(Richmond, Califonia, USA). Hydrogen peroxide solution (30 wt. % in water, American chemical

society (ACS) reagent), concentrated hydrochloric acid (reagent grade and assay 36.5-38.0%),

sodium borohydride (98.0%), potassium permanganate (≥ 99.0%, ACS reagent), concentrated

sulphuric acid (99.9%), Ruthenium (111) chloride hydrate (99.98% trace metal bases),

polytetrafluoroethylene (mean particle size 20 µm), activated charcoal (Norit ® pallets),

anhydrous N-methyl-2-pyrrolidone (99.5%) and carbon black (4 µm mesoporous carbon matrix,

≥ 99.95% metal bases), ethylene glycol (EG) (99.8%), ethanol (absolute, ≥ 99.8%) were purchased

from Sigma-Aldrich (St Louis, Missouri, USA) and were all used without further purification.
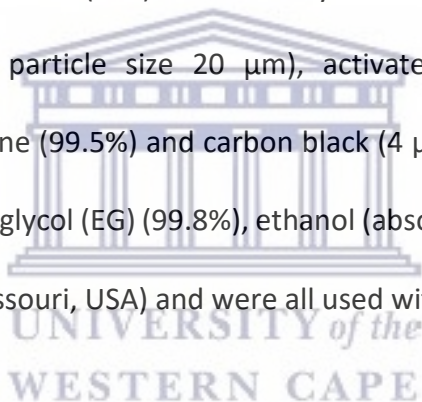
4.2.2 MW-assisted synthesis of the nanomaterials.

The MW-assisted synthesis of RuO was carried out using an Anton Parr multi-wave Pro

microwave system. It is equipped with an IR temperature sensor that controls the temperature

during the process. $RuCl_3.xH_2O$ (1 mmol) was added to 30 mL of ethylene glycol with continuous

stirring for 0.5 h. $NaBH_4$ (1.5 g) was slowly added to the above-mixed solution, sonicated for 10

min, and allowed to cool. The resultant mixture was MW-irradiated at 190 ℃ for 10 min. The

resulting products were separated by centrifuging, washed with deionized water, and dried at 60

℃ under vacuum for 12 h.

In another reaction vessel, one hundred milligrams of synthesized GO is dissolved in 30 mL of ethylene glycol and sonicated for 2 h to form a homogenous dispersion. $RuCl_3.xH_2O$ (1 mmol) was added to the dispersed solution and sonicated for 0.5 h. $NaBH_4$ (2 g) was slowly added to the above mixture, which was sonicated for 10 min and transferred to a microwave vessel. The resultant mixture was MW-irradiated at 190 °C for 10 min. The resulting products were separated by centrifuging, washed with deionized water and dried at 60 °C under vacuum for 12 h.

4.2.3 Material characterization

The elemental and morphological composition of the nanoparticles were obtained using a Carl ZEISS ULTRA scanning electron microscope GmbH. Fitted with an energy dispersion spectrometer. (Jena, Germany). All analysis was performed on a nickel-copper grid. The samples for TEM characterization were drop-coated into the Cu TEM grids and scanned in high-resolution transmission electron microscopy (HR-TEM) with an FEI Technai G20 F20X-Twin MAT 200 Kv Field Emission Transmission Electron Microscope (Eindhoven, Netherlands) equipped with both EDS and selected area electron diffraction (SAED). The X-ray powder diffraction (XRD) pattern was obtained for all the nanoparticles with a D8 advance multipurpose X-ray diffractometer (BRUCKER-AXS, Berlin, Germany) using copper kα1 radiation (λ ~ 0.154 nm) operating at 40 kV and 40 mA. XRD patterns were collected from 15 to 70 (2q) with a step size of 0.034° in 2q. The functional group present in the sample was determined using a Perkin Elimer Spectrum 100 series Attenuated total reflectance (ATR) Fourier transform Infra-red spectrometer with 4 cm^{-1}

resolutions (Perkin-Elmer, Boston, MA, USA). The particle size distribution was determined by a small-angle X-ray scattering (SAXS) measurement, performed on an Anton Paar GmbH SAXSpace P/N 100100 (Graz, Austria). It was equipped with a 1 D mythen 2 position-sensitive detector, a beamstop alignment, and a Copper Kα (0,154 nm) instrument radiation was used. The nanoparticles Raman spectra were obtained using an Xplora Olympus BX41 Raman Spectrometer (Horiba, Tokyo, Japan) using a 532 nm laser as the excitation source. Optical absorption spectra were acquired from ethanolic dispersions of the nanocrystals at room temperature using a Varian Cary 300 UV-Vis-NIR spectrophotometer (Agilent, Santa Clara, CA, USA). The photoluminescence properties were obtained from NanoLog HORIBA using the software FluorEssence V3.9. (Johannesburg, South Africa). At room temperature, infrared spectroscopic investigations between 4000 and 400 cm^{-1} were carried out. The powdered nanocrystals were deposited on a diamond disc, and infrared spectra were acquired using an Attenuated Total reflectance/Perkin-Elmer Spectrum 100 series Fourier transform Infrared (FTIR) spectrometer (Perkin-Elmer, Boston, MA, USA). All electrochemical studies were performed on a VMP-300 potentiostat from the Bio-Logic SAS instrument (France).

4.2.4 Electrode preparation and electrochemical measurements

To prepare the working electrode, the active material; RuO and RuO-G (70%), a conducting agent; carbon black (20%) and a binder; polytetrafluoroethylene (10%) were mixed in a mortar, and crushed to fine powder, then 3 drops of anhydrous N-methyl-2-pyrrolidone were added and mixed to form a uniform slurry. Nickel foam was cut into rectangular shapes of 0.5 x 1cm^2 and

coined shapes of 20 mm in diameter. The foams were cleaned to remove all surface oxide layers in 1 M HCL solution, absolute ethanol and deionized water respectively, with ultra-sonication for 15 min in each solvent, and dried at 90 ℃ for 12 h. The homogenous paste was coated on 0.5 cm^2 diameter of the nickel foam and dried at 80 ℃ for 12 h. In a three-electrode cell setup, Ag/AgCl and Pt wire were used as the reference and counter electrode respectively. For the full cell, the paste was coated into the coin-shaped nickel foam and assembled in a Swagelok with activated carbon as the negative electrode. The cyclic voltammograms were recorded between 0 to 0.6 V potential window at different scan rates, the electrochemical impedance measurements were obtained at a frequency range of 0.1 MHz to 100 MHz with 10 points per decade, and the galvanostatic charge-discharge profiles were measured at different current densities. All electrochemical characterisation of material was done in the three-electrode cell using 1 M Li$_2$SO$_4$, electrolyte, the device testing was done at 1.8 V in 1 M Li$_2$SO$_4$.
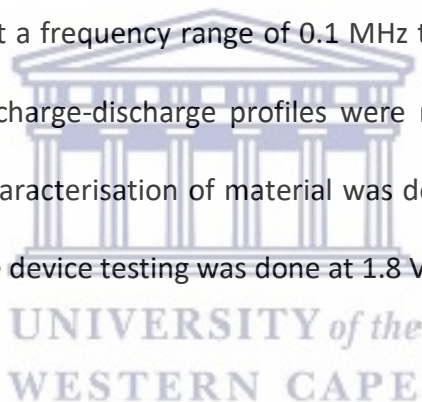
4.3 RESULT AND DISCUSSION

4.3.1 Morphological studies

4.3.1.1 Scanning electron microscopy (SEM)

SEM was used to investigate the surface morphology and shape of the RuO and RuO-G nanoparticles. Figure 4.1
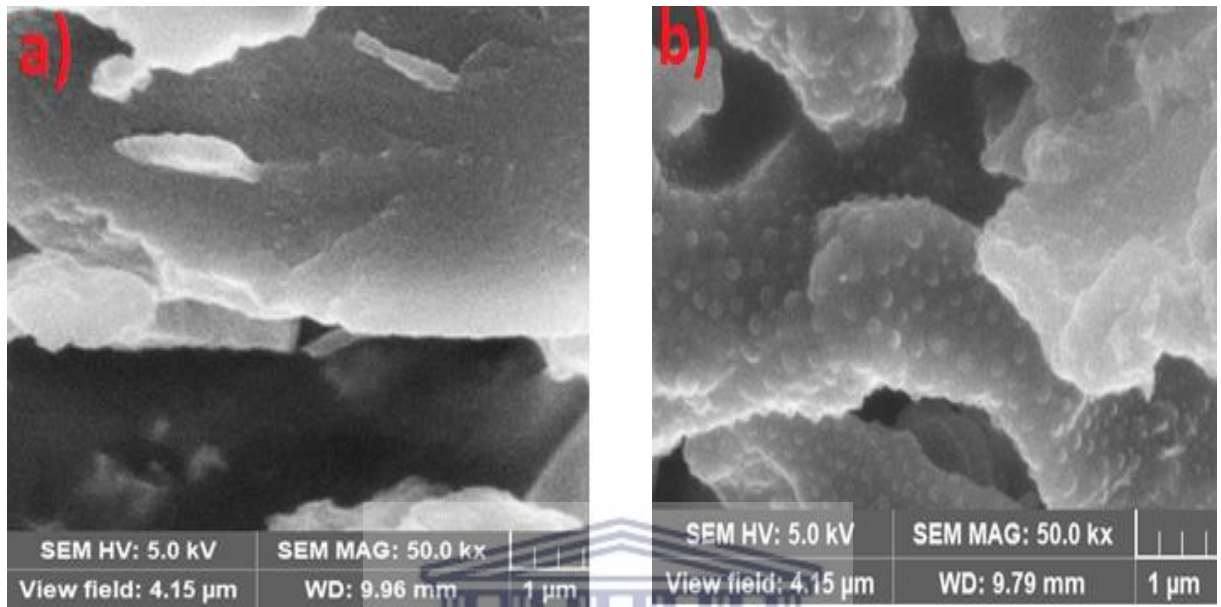
a shows severely agglomerated spherical particles that are in the form of sheets. Figure 4.1b

)
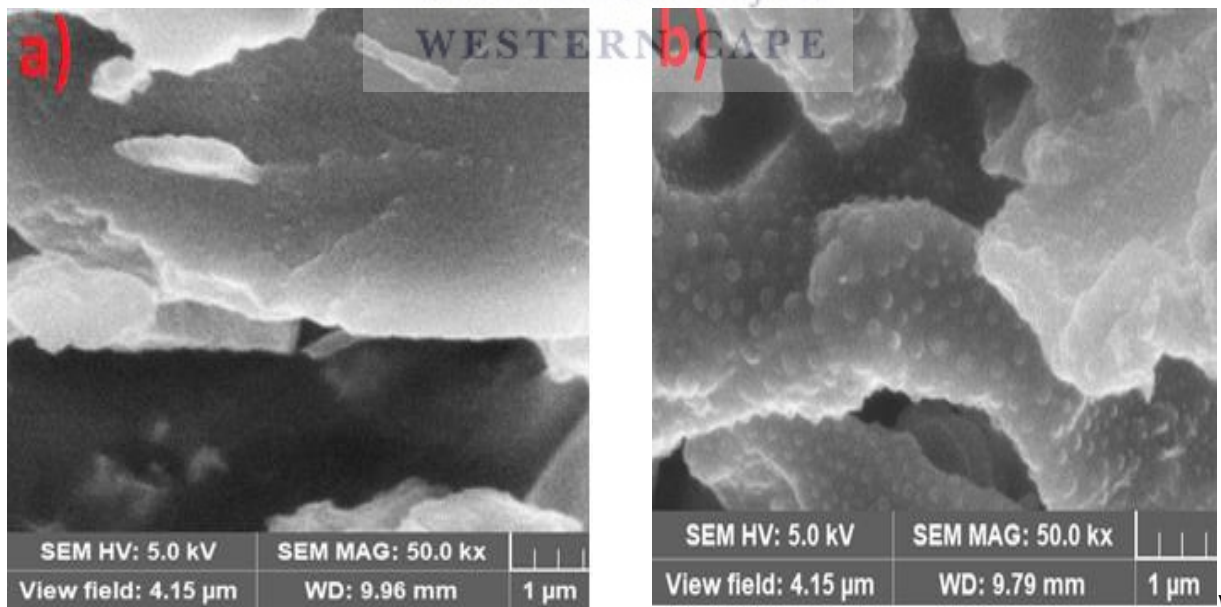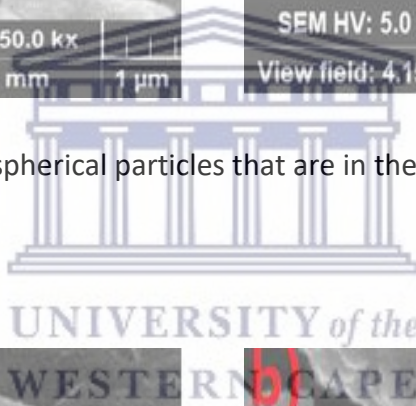
is the image of RuO-G which shows a visible graphene sheet with RuO nanoparticles scattered

147

randomly on the surface of the sheet and in between the sheet. Thus ruthenium oxide

nanoparticles must have acted as spacers and reduced the agglomeration of the graphene. This

will lead to an improved surface area and hence high charge storage and high capacitance [14].
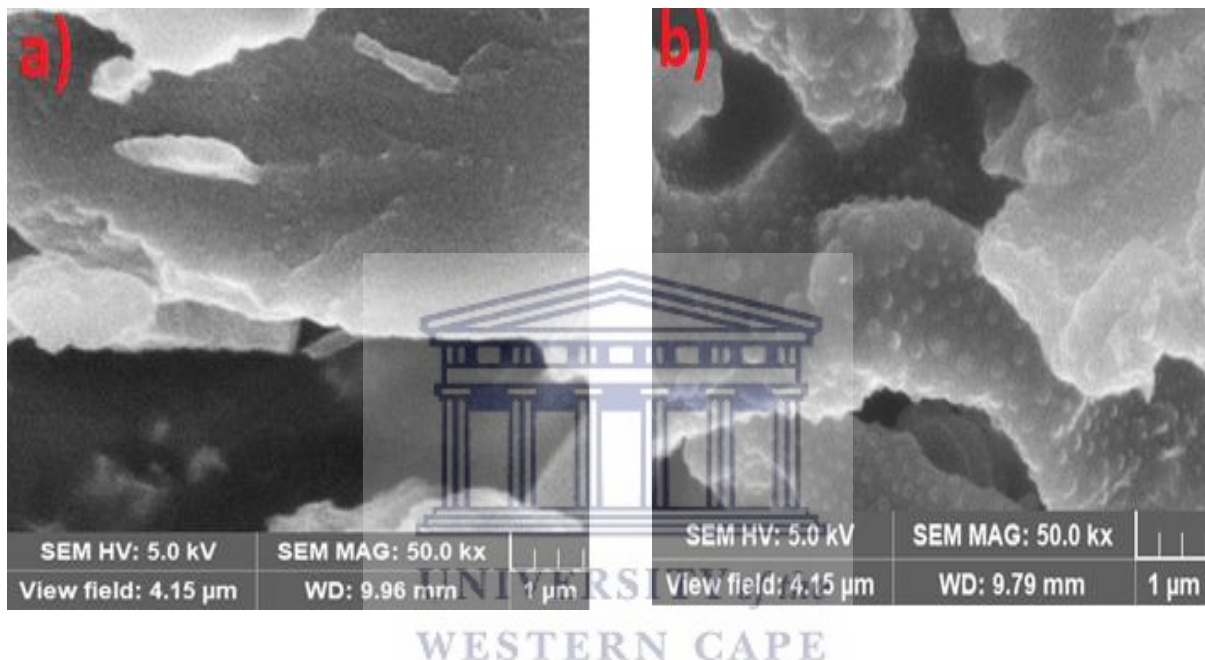
Figure 4.1: SEM image of: a) ruthenium oxide b) ruthenium oxide/graphene

4.3.1.2   Transmission emission microscopy (TEM)

The representation of the TEM in Figure 4.2 demonstrates severely agglomerated nanoparticles

with a particle size between 5-10 nm, for the pristine RuO while the material displays a high

degree of agglomeration, its small grain size suggests it's a porous material [15]. For the

graphinized material, the spherical nanoparticles can be seen randomly distributed on the

surface of the material. This confirms that the RuO nanoparticles were graphinized. Porosity

148

would increase the ion transfer mechanism and therefore increase the efficiency of energy storage [16].

HRTEM has been used to research the crystal structure of the RuO material. The lattice fringes 0.20 nm, and 0.14 nm along the (101) and (210) planes are in line with the Joint Committee on Powder Diffraction Standards (JCPD card No 2 37 08 54) and (JCPD card No 2_40-1290). Its orientation can be seen along different planes showing polycrystallinity. The selected area electron diffraction (SAED) pattern (Figure 4.2d) reveals concentric circles, due to the polycrystallinity of the material, showing that the material is crystalline in the (210), and (101) direction. The crystallinity of the material will mean faster ion transport inside the grains of the materials and higher conductivity [24]. The HRTEM of RuO-G (Figure 4.3) showed a more amorphous structure, due to the addition of the graphene material. The lattice fringes are more disordered and the FFT in the inset shows that the material is more amorphous than RuO. The selected area electron diffraction (SAED) pattern (Figure 4.3b) reveals sporty concentric circles, showing that the material is crystalline in the (210), and (101) directions. The increase in disorder of the RuO-G must be due to the addition of amorphous GO in the synthesis, and the attachment of graphene to the RuO particles. Therefore, the HRTEM confirm a structural change because of the addition of graphene.
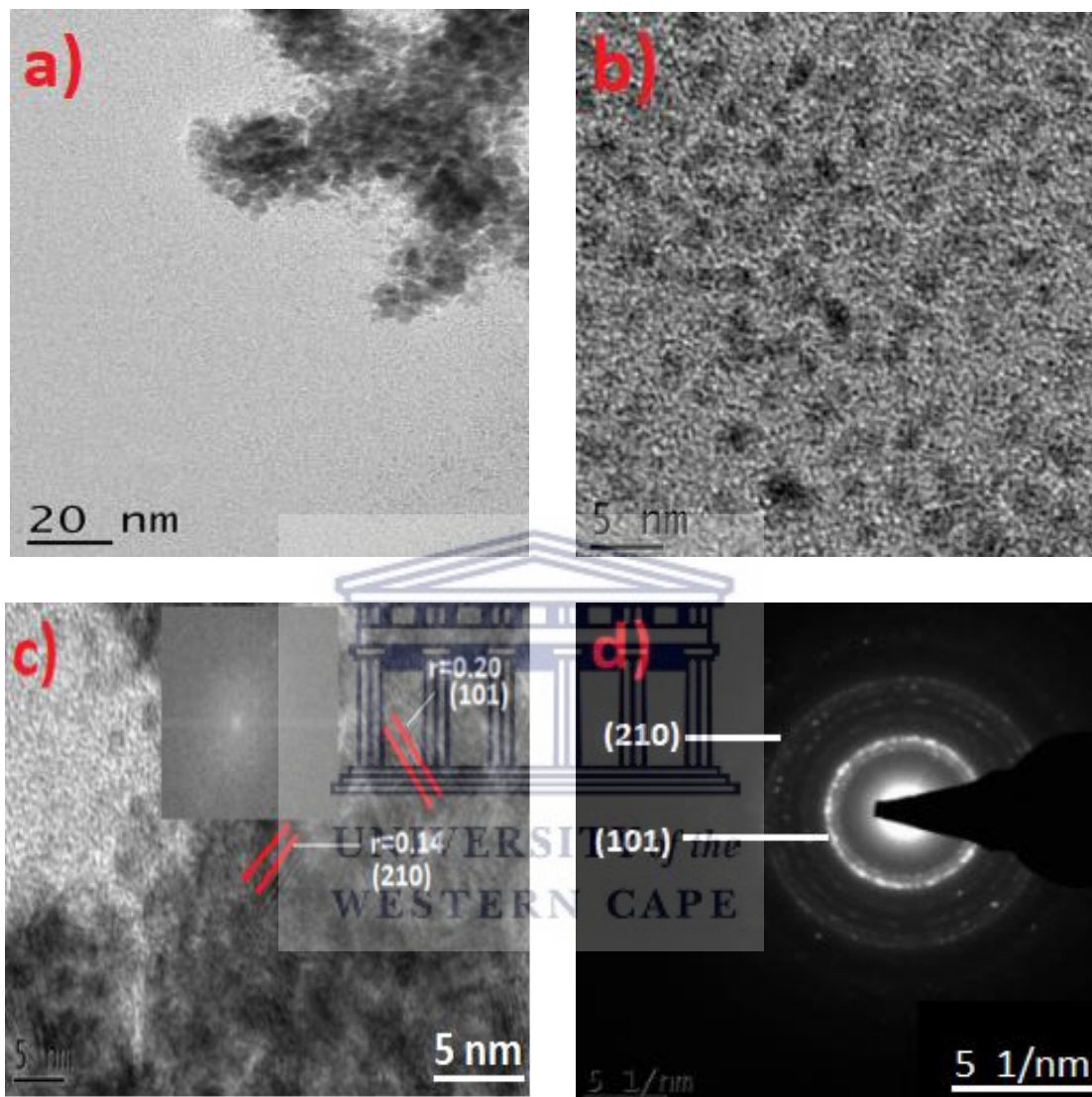
Figure 4.2: RuO a,b) TEM images at different magnifications; c) HRTEM showing the lattice fringes the inset is the FFT image; d) SAED pattern
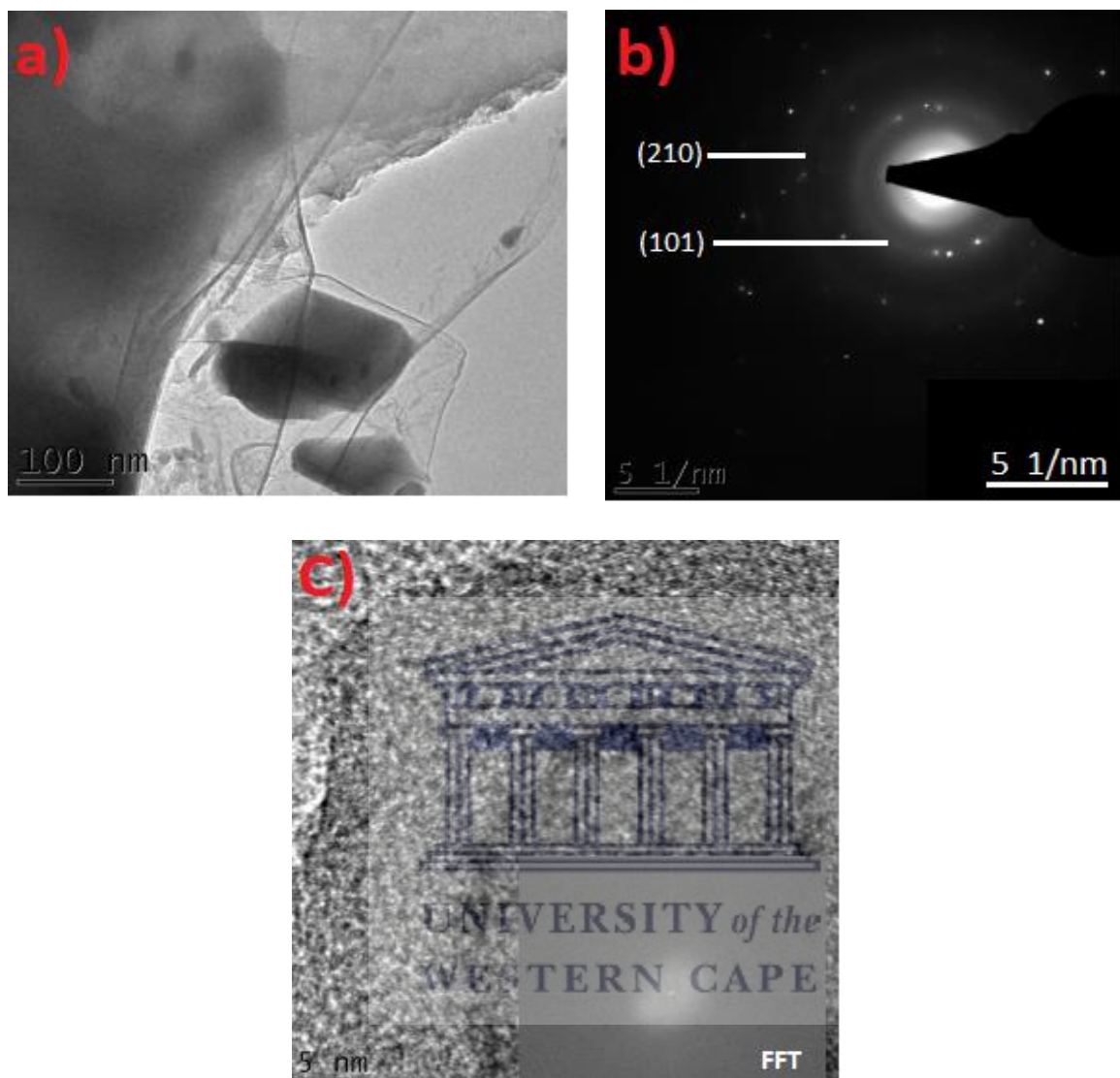
Figure 4.3: RuO-G: a) TEM image; b) SAED pattern; c) HRTEM showing the lattice fringes the inset is the FFT.

4.3.1.3 Atomic force microscopy (AFM)

AFM was used to characterize the topography of RuO and RuO-G nanoparticles. The results were analyzed using Gwyddion software and reported in terms of topographic and diffraction images, with a 2D, Line and a 3D chart type. The surface roughness and height distribution were the

parameters extracted from the analysis. The AFM showed sheet-like images of the samples, RuO the RuO-G surface has a similar topography except that the sheets were more spaced in RuO-G (Figure 4.4 and Figure 4.5). The average surface roughness (Ra) and the root mean square roughness (Rq) were used to study the changes in electrode modifications (Table 4-1). The surface area of the pristine RuO electrode ($6.18\ nm^2$) increased drastically after modification with the graphene ($3.96\ \mu m^2$) due to the prominent surface features of the graphene. The trends in calculated values for Ra, Rq, and surface area are consistent with the observed topography trends. This provides a quantitative measure of the effect of the modification [17].

Table 4-1: AFM parameters for RuO and RuO-G

Parameters	RuO (μm)	RuO-G (mm)
Ra	1579.6	5.147
Rms/Rq	1830.3	9.299
Surface area	2237	3.229
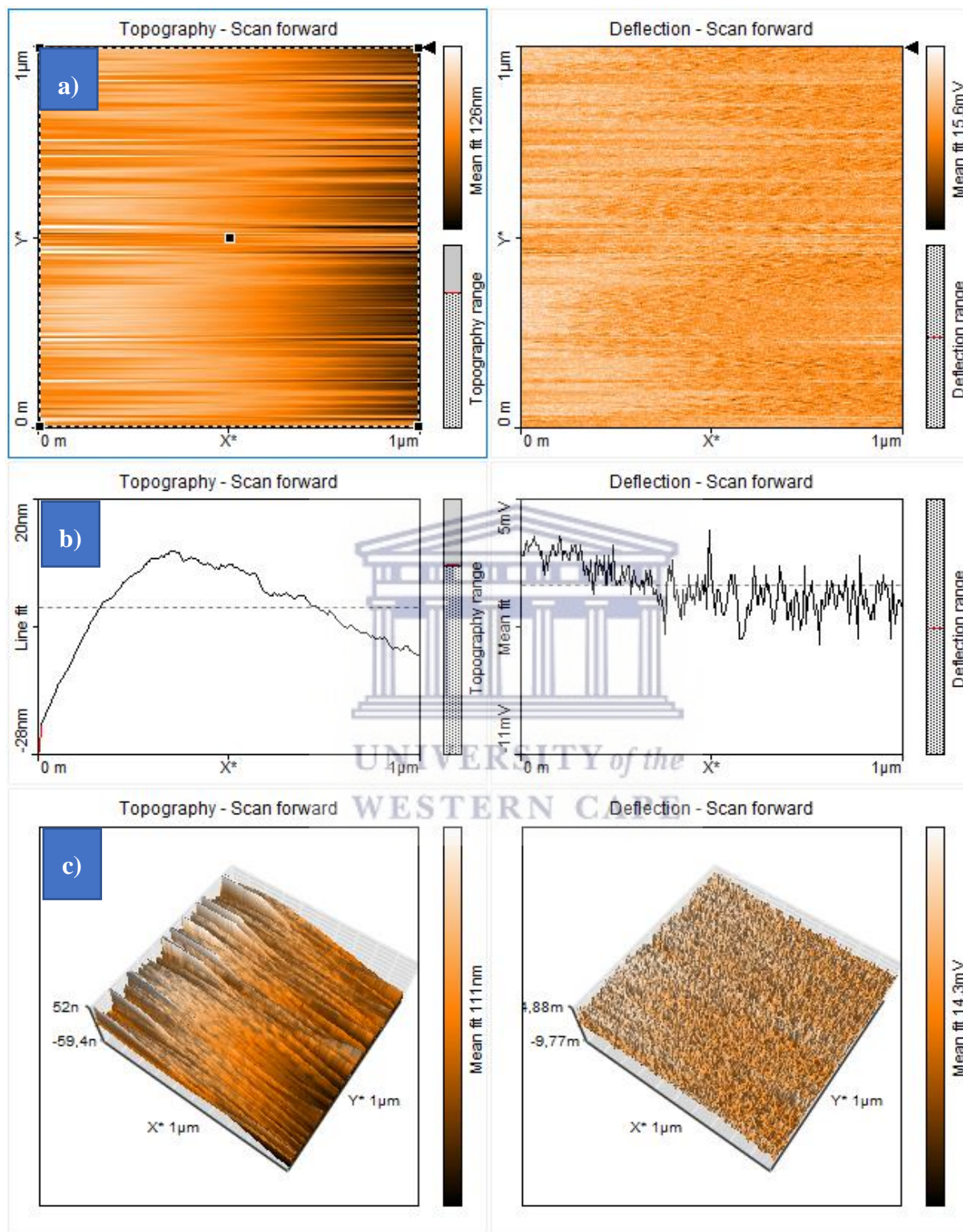
Figure 4.4: AFM a) 2D, b) line and c) 3-D topography and deflection images of RuO
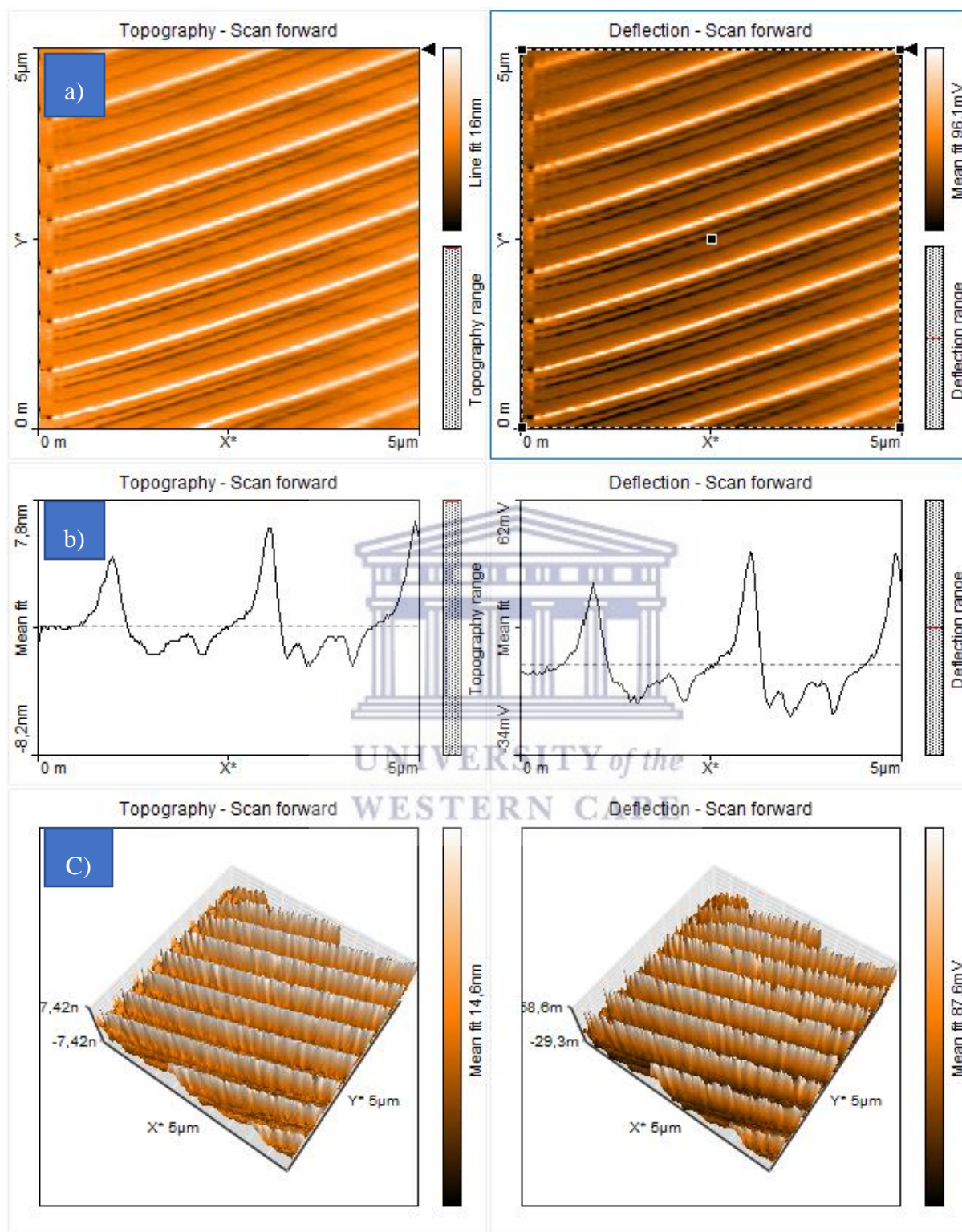
Figure 4.5: AFM a) 2D, b) line and c) 3-D topography and deflection images of RuO-G

4.3.2 Spectroscopical studies

4.3.2.1 Energy-dispersive X-ray spectroscopy (EDS)

EDS has been used to validate the formation of RuO and RuO-G nanomaterials. EDS focusing on various spectrum areas and corresponding peaks are shown in Figure 4.6 and Figure 4.7. The EDS analysis confirms that Ru and O are in RuO, while Ru, O and C are in RuO-G. The little amount of carbon in the pure ruthenium oxide sample is from the carbon glue and carbon substrate used in the analysis. The percentage of carbon spikes up in the RuO-G sample, confirming incorporation of carbon in the sample. Details of the quantity of each element measured in the atomic per cent are shown in the in-set. The data confirms that a significant amount of graphene was in the composite. This will bring about improved stability to the composite.
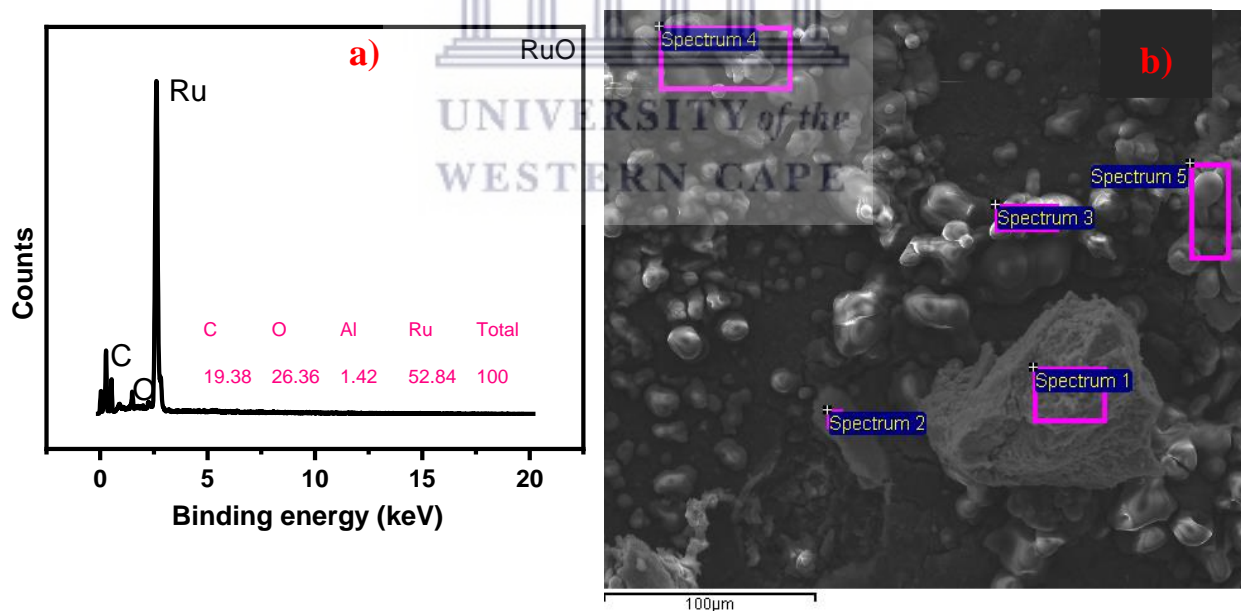
Figure 4.6: EDS spectrum a) and SEM image b) of RuO. Inset in (a) is the percentage elemental composition. The labels in the SEM image (b) represent sampling points for the EDS.
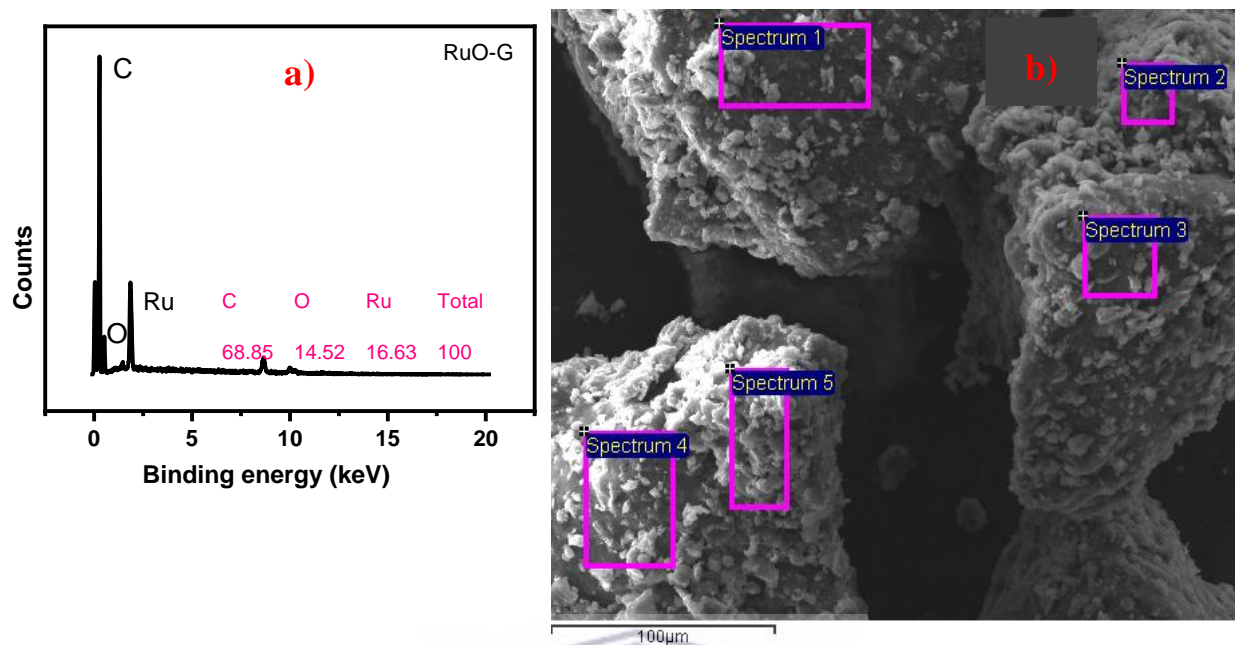
Figure 4.7: EDS spectrum a) and SEM image b) RuO-G. Inset in (a) is the percentage elemental composition. The labels in the SEM image (b) represent sampling points for the EDS.
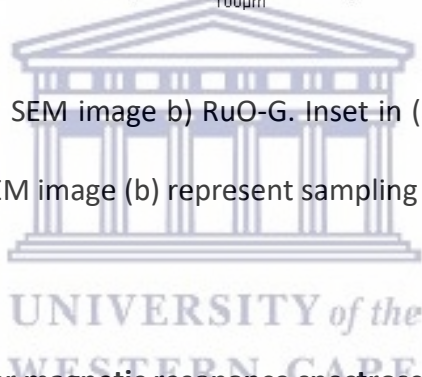
4.3.2.2   Solid-state nuclear magnetic resonance spectroscopy (NMR)

Figure 4.8 shows the NMR spectra of RuO-G and graphene. The carbon environment of pure graphene was compared to that of graphene samples with ruthenium oxide incorporation. The prominent peak at 117 ppm, which belongs to graphitic sp^2 carbon as seen in graphene, shifted to 126 ppm, while a shoulder peak can be seen at 117 ppm which when deconvoluted (the inset) reveals a broad peak with FWHM- 34 ppm, indicating that the chemical environment of carbon must have been influenced by the interaction of RuO nanoparticles with graphene [18].
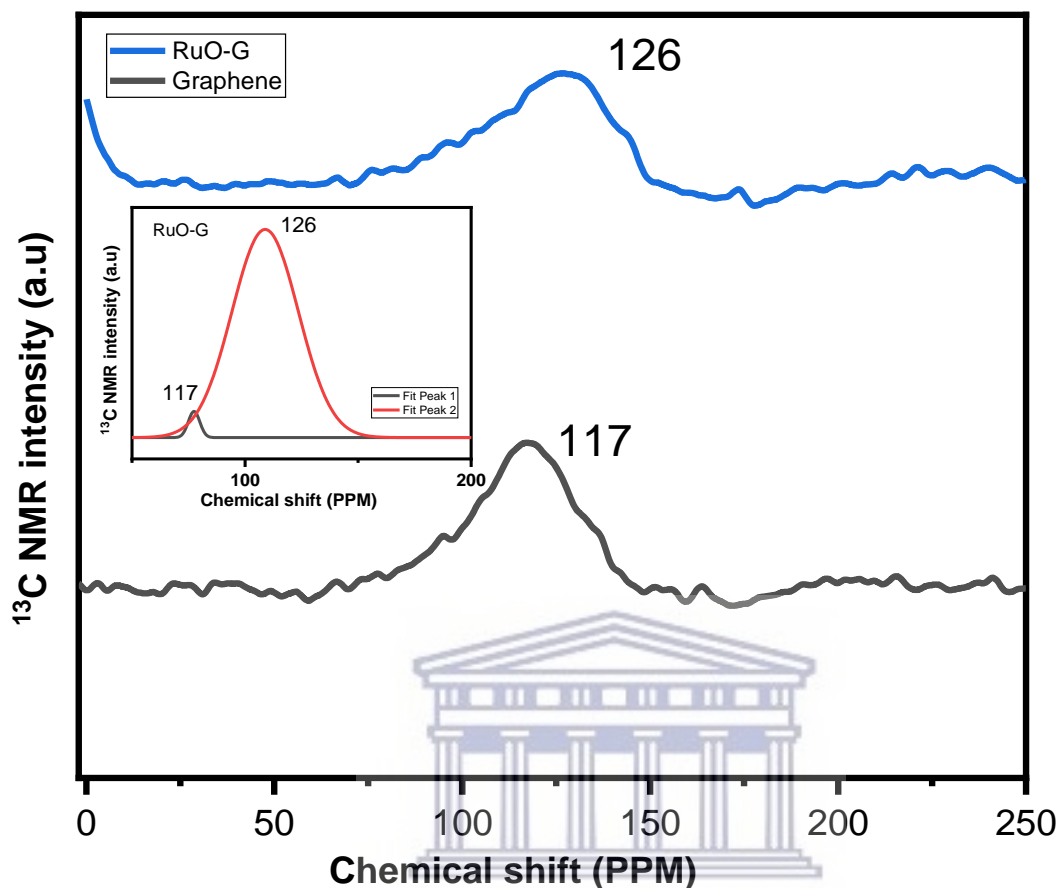
Figure 4.8: NMR results spectra of graphene and RuO-G the inset is the deconvoluted 126 ppm

peak of RuO-G

4.3.2.3 X-ray powder diffraction (XRD)

Figure 4.9 shows the XRD pattern of the material. All the diffraction peaks are indexed to

tetragonal RuO_2; JCPD card No 2_4-1290), with lattice parameter a = 4.4994 Å and c = 3.10710 Å.

A diffraction peak at 2θ = 24.7°, 42.9° and 63.7° which belongs to the (002), (210) and (301) phases

of RuO_2 were observed for both RuO and RuO-G samples. However, the intensity of all peaks

decreased, and most of the peaks broadened slightly with the addition of graphene as seen in

Figure 4.10 and Figure 4.11. The broadness of the peaks suggests either very small crystalline sizes or the presence of semi-crystalline particles [19]. The peak at 24.7° in the RuO-G sample became broadened and looked like the pristine graphene bump at 24.7°. The most intensive peak, at 44.0°, broadened out and almost disappeared in the RuO-G sample. And all peaks shifted to lower angles in the RuO-G samples this is suspected to be due to the incorporation of graphene in the ruthenium oxide lattice. The broad diffraction peaks in RuO-G show that during the oxidation-reduction treatment, exfoliation and restacking occurred, leading to poorer crystallinity, and numerous mono-layer graphene may exist in the RuO-G samples [20]. There were no strong peaks in the RuO-G XRD pattern, indicating that the composites are formed of extremely disordered graphene sheets and nanometer-sized amorphous RuO, which is consistent with the nanometer-sized RuO lattice fringes in the HRTEM results. The (002) peak of RuO-G agrees with the FFT patterns in Figure 4.3 and because, the predominant phase in the RuO-G composite may be graphitic due to the low RuO level, as evidenced by the EDS results. As a result, abundant mono-layer graphenes in RuO-G exhibit an amorphous spectrum, which is consistent with Figure 4.3c. As it can be seen from Figure 4.9, RuO-G (002) crystal plane values of $2\theta = 24.7$ and $d_{002} = 1.74$ Å have slightly changed compared with those of RuO, which are equal to $2\theta = 26.8$ θ and $d_{002} = 0.36$ Å. Since a few functional groups and curved surface structures have been retained after reduction, the interplanar spacing of RuO-G (1.74 Å) is a larger than that of pristine ruthenium oxide (0.36 Å). The most intense peak in RuO-G composite ($2\theta = 42.9°$) is slightly shifted to a lower angle as compared to pristine RuO nanoparticle ($2\theta = 44.09°$) indicating the enlargement in RuO interlayers due to defects/embedding of the graphene nanoparticles. A clear shift in the interlayer spacing between RuO and RuO-G indicates that the addition of graphene

can effectively expand the interlayer spacing of the composite, which will facilitate the diffusion

and transport of electrolyte ions during the charge/discharge process [21]. The XRD data also

suggests that the possible crystal structure of the RuO is tetrahedral. This was achieved through

estimated refinement and simulation with VESTA software as shown in Figure 4.12 for RuO, with

Ru bonded to Oxygen. Figure 4.14 is showing Ru, O and C bonds. Crystal size was also estimated

using the Debye-Scherer formula for the most intense peaks in the XRD patterns. The size was an

average of ~1 nm and ~ 10 nm for RuO and RuO-G respectively.
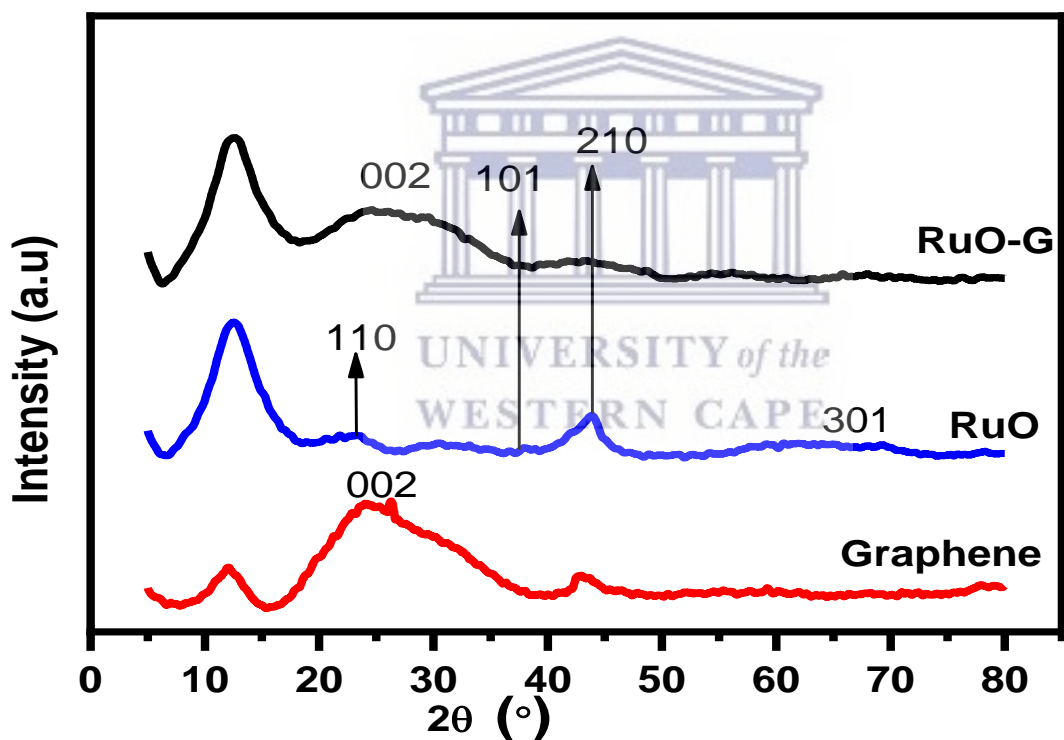
Figure 4.9: XRD analysis of RuO and RuO-G.
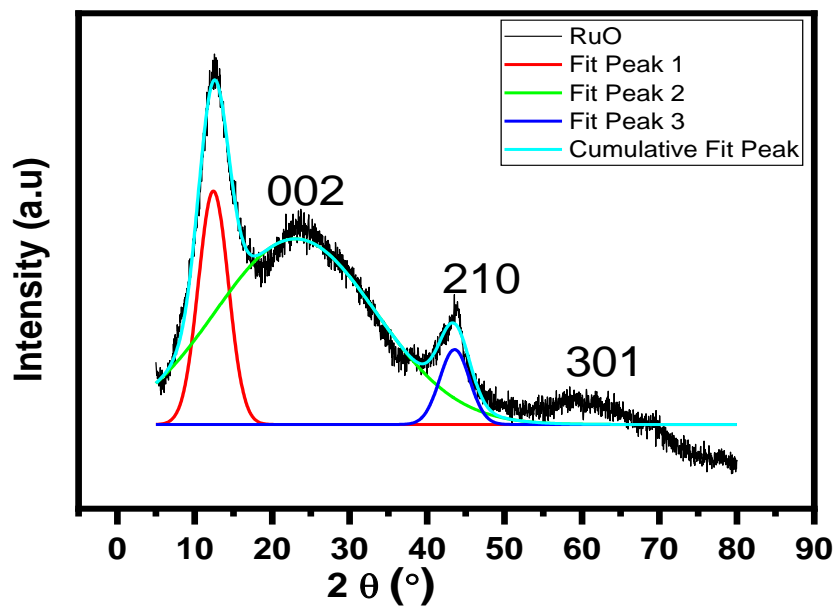
Figure 4.10: XRD analysis of RuO with deconvoluted peaks.
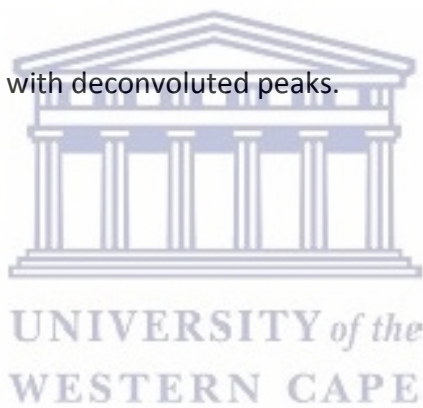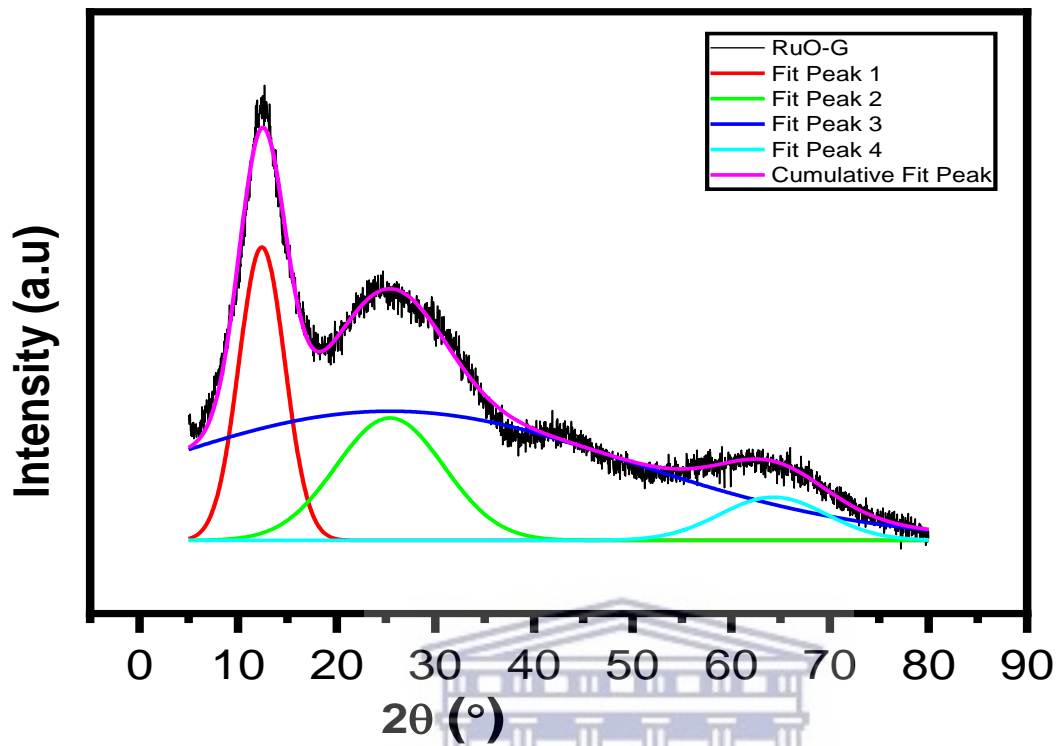
Figure 4.11: XRD analysis of RuO-G with deconvoluted peaks.
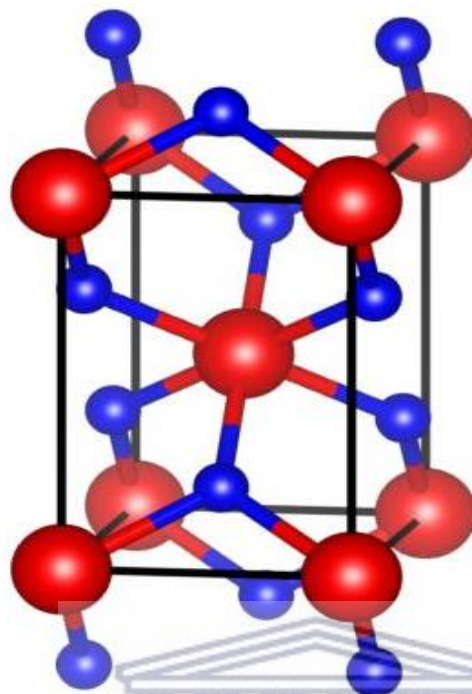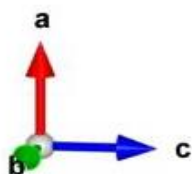
Blue - O

Red - Ru

Figure 4.12: Crystal structure models of RuO simulated from VESTA using the XRD data showing a body centered (BC) tetragonal unit cell of RuO with Ru atom located at the BC position.
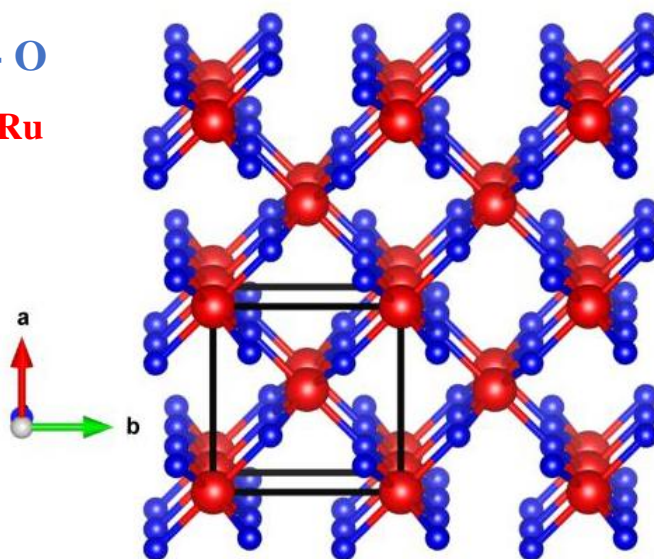
Blue - O

Red - Ru

Figure 4.13: Closely packed tetragonal structure of RuO, repeated unit cells along the a' b and c coordinate.

Blue - O

Red - Ru

Carbon- C
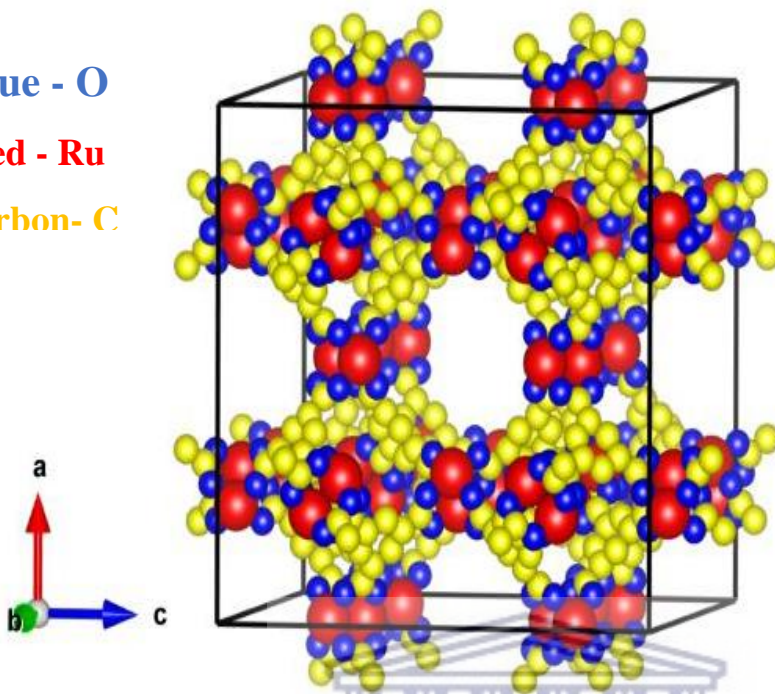
Figure 4.14: Crystal structure models of RuO-G simulated from VESTA from XRD data a

tetragonal unit cell of RuO-G .

Blue - O

Red - Ru

Carbon- C
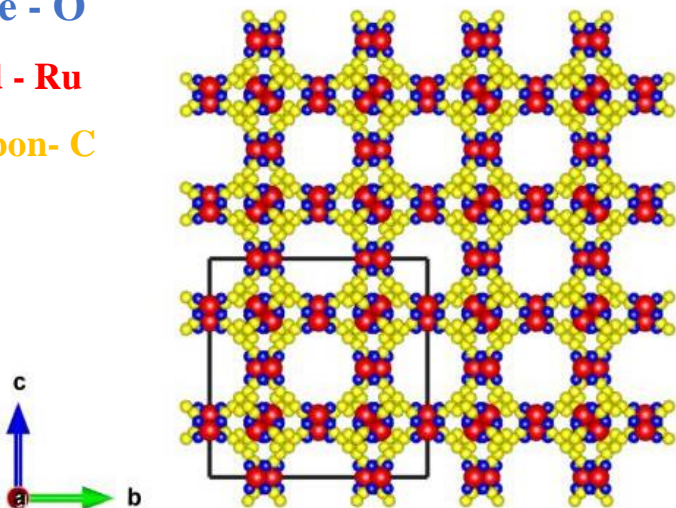
Figure 4.15: Repeated unit cells of RuO-G crystals along the a' b and c coordinate closely packed.

4.3.2.4   Fourier transform infra-red spectroscopy (FTIR)

The FTIR absorption spectra of RuO and RuO-G in the 4000-400 cm^{-1} region is shown in Figure 4.16. The analysis was carried out to determine the presence of bending or stretching vibrations in the synthesized RuO and RuO-G. The distinctive OH stretch is confirmed by the broadband at 3386 cm^{-1} in the RuO spectrum. The vibration of molecular water's hydroxyl groups and the stretching vibration of the peroxo group induce the absorption band around 2928, 1647, and 1067 cm^{-1}. The vibrational band at 981 cm^{-1} is characterized by the presence of Ru-O, also the tiny band at 459 cm^{-1} is induced by the asymmetric stretch of RuO. In the RuO-G spectrum, The distinctive OH stretch is confirmed by the band at 3790 cm^{-1} and broadband at 3421 cm^{-1} . The bending and stretching of C-H, C=C=C, C-O, C-C group induce the absorption band around 3000 - 1000 cm^{-1}. The vibrational band at 941 cm^{-1} is characterized by the presence of Ru-O, also the tiny band at 786 and 638 cm^{-1} is induced by the asymmetric stretch of RuO [22][23]. Table 4-2 shows the functional groups present in RuO and RuO-G nanomaterial. From the FTIR spectra, the change in the structure of RuO-G which included the emergence of many new vibrational nodes indicates the incorporation of graphene into the lattice of RuO.
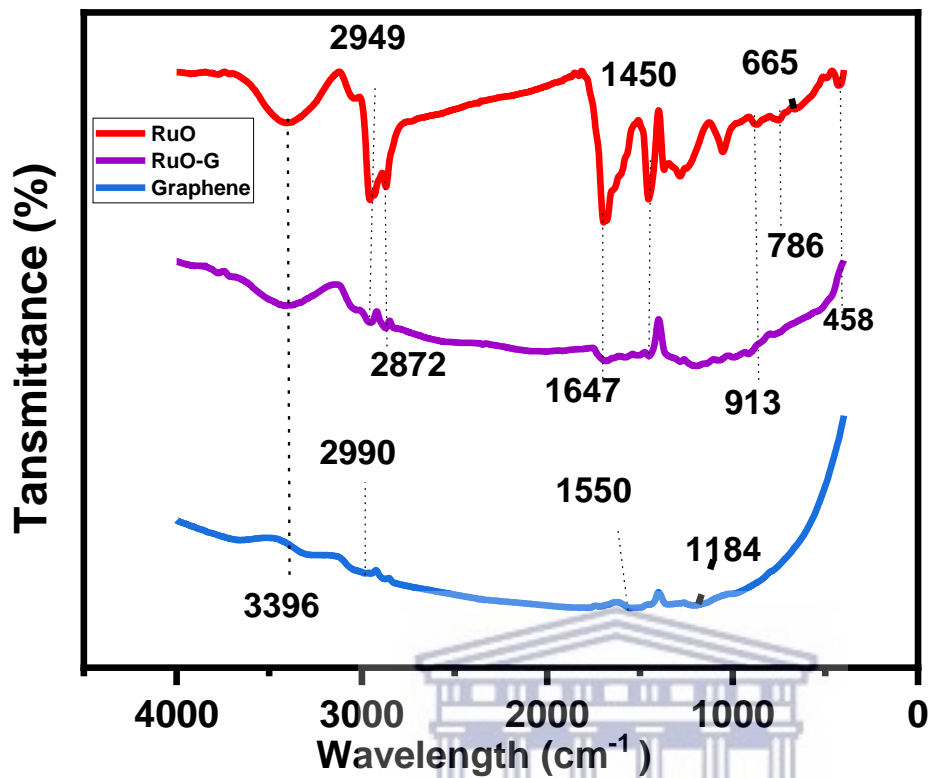
Figure 4.16: FTIR spectra of RuO and RuO-G overlayed on graphene
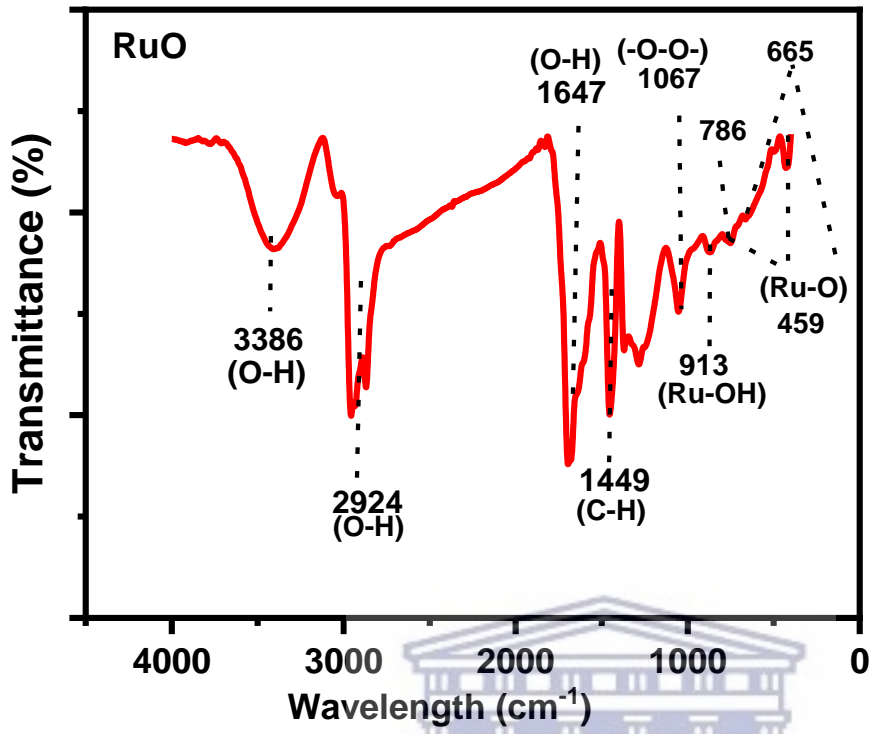
Figure 4.17: FTIR spectrum of RuO
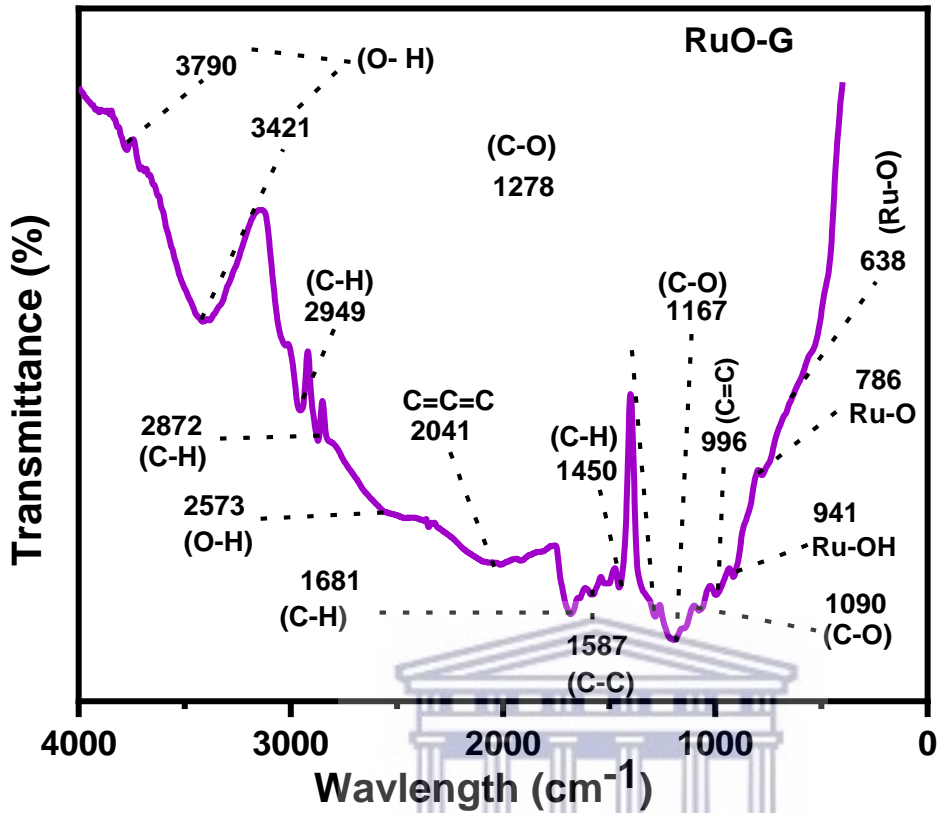
Figure 4.18: FTIR spectrum of RuO-G

Table 4-2: Functional groups and vibrational bands of RuO and RuO-G

Functional group	Material/ wavenumber (cm^{-1})[a1]	
	RuO	RuO-G
O-H	3386	3790
C-H		2949

C=C		2041
C-O		1278
-O-O-	1067	
Ru-O	913	941

4.3.2.5   Raman spectroscopy

The Raman spectra of RuO and RuO-G are displayed in Figure 4.19 to further define their phase

structure. The stretching of Ru-O bonds is assigned to a strong B_{1g} phonon mode at 97 cm^{-1}[24].

Other prominent Raman bands, such as the E_g and A_{1g} modes of RuO, are found at at 2 and 6 cm^{-1}, with weak intensities [25][26][27]. The D (2) and G (5) bands, which are present in all carbon

materials due to defect and sp^2 C-C bonds, are also present in the RuO-G composite, implying

that the in situ reduction of RuO and GO to RuO-G was accomplished using microwave radiation

[28]. The carbon adhesive used to place the samples on the SEM stubs causes the G band to

appear in the RuO. When comparing the Raman spectra of graphene to that of the RuO-G, the

peak locations of DG and 2D were found to be unchanged. However, due to a drop in the intensity

of the D-band, which relates to the flaw in the graphene layer, there was a significant change in

the ID/IG ratio. As a result, the RuO-G hybrid has fewer defects, probably due to the correction

of partial dangling bonds at the graphene's reactive edges [29][14].
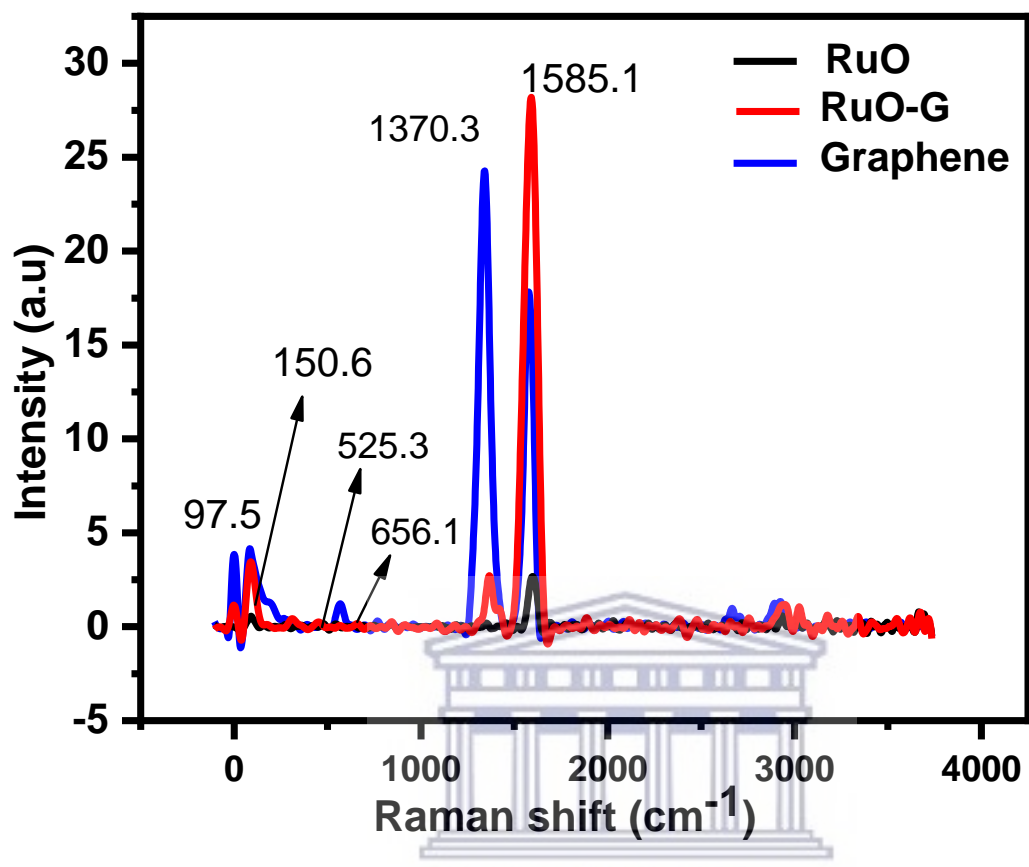
Figure 4.19: Raman spectra of RuO and RuO-G overlayed on graphene
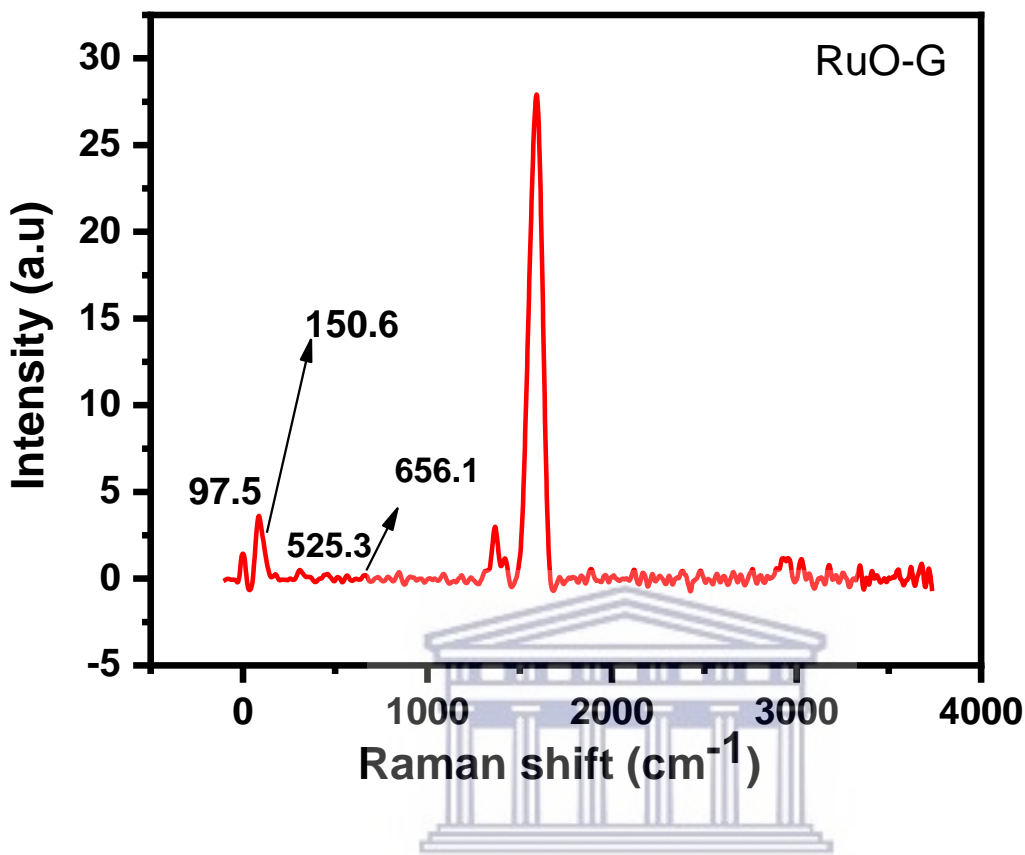
Figure 4.20: Raman spectrum of RuO-G

4.3.2.6   UV-Vis spectroscopy

The UV-Vis absorption test confirms the presence of RuO nanoparticles. The UV-Vis absorption spectra of RuO and RuO-G nanoparticles are depicted in Figure 4.21. All RuO nanoparticles have apparent exponential decay curves in the range of 200- 400 nm when compared to pristine graphene, which could be attributed to Mie scattering [30]. This indicates the stability of Ru nanoparticles as well as their good solvent dispersion [31]. The curve exhibits a more noticeable exponential decay with the inclusion of graphene, showing that the RuO-G nanoparticles have improved dispersion capabilities. Using the Taucs plot from origin software, the band gaps of RuO

and RuO-G were estimated to be 1.48 and 1.25 eV, respectively [32]. When compared to pure

RuO nanoparticles, the bandgap of the RuO-G composite is lowered due to the development of

Ru-O-C bonds. Because the carbon content of the G alters the molecular orbital of RuO, the RuO-

G composite has a smaller conduction band than RuO [33][34]. The link that exists between Ru

and C facilitates the transmission of charges [35].
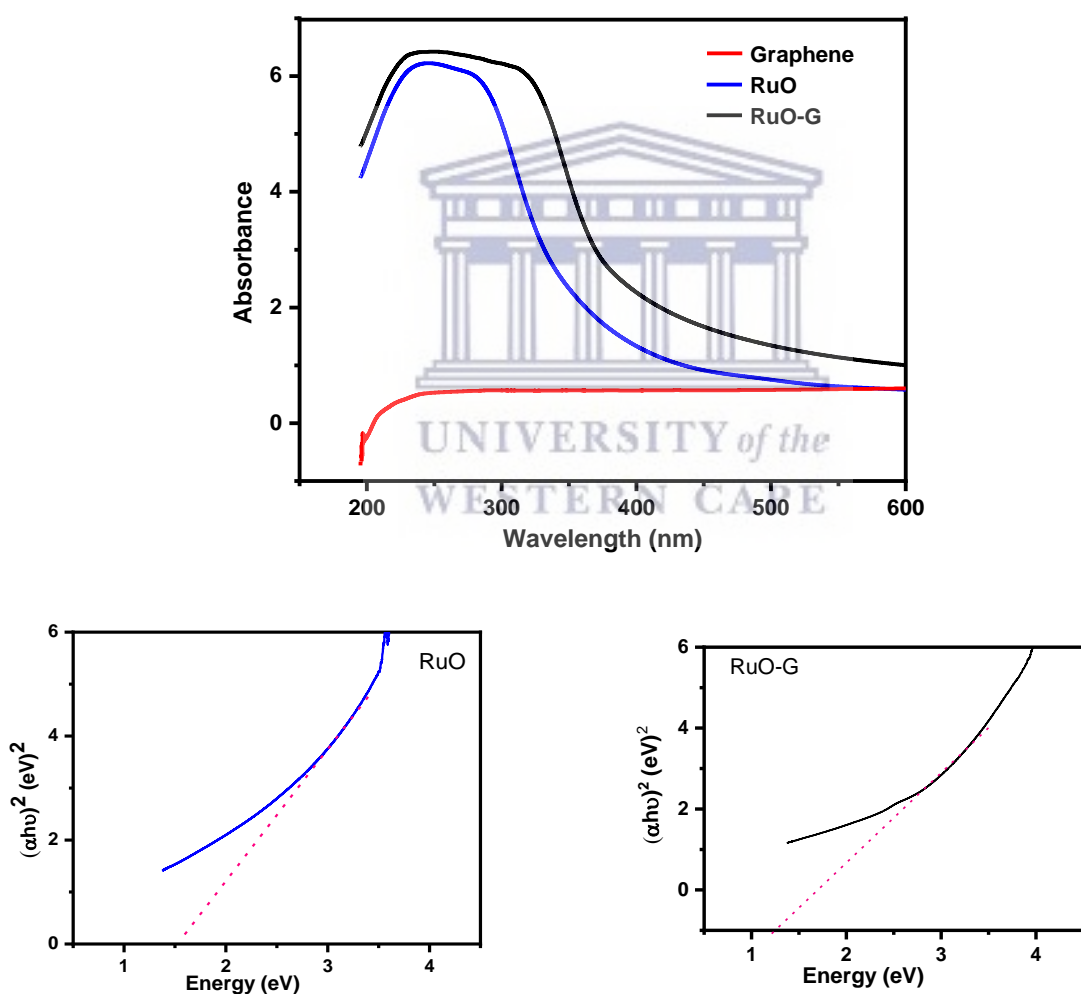
Figure 4.21: a) UV spectra of RuO and RuO-G overlayed with graphene (b,c) Taucs plot for RuO

and RuO-G respectively.

4.3.2.7 Photoluminescence spectroscopy (PL)

The photoluminescence spectra were obtained to explore photo-excited electron transport in RuO and RuO-G composites. The PL emission spectra of RuO and RuO-G hybrids dispersed in ethanol solution and excited at 230 nm at room temperature are shown in Figure 4.22. In the RuO, a near band edge emission peak at 383 nm and a broad shoulder at the low energy side (456) was observed which arise from the metal to ligand charge transfer (MLCT) excited-state emission [36]. The addition of graphene layers caused a noticeable alteration in the photoluminescence spectra of the RuO-G composite, with the intensities of the UV emission peaks decreasing significantly when compared to the RuO sample. In general, the intensity of emission is determined by radiative and non-radiative transitions [37]. Crystal flaws, such as point defects, dislocations, and grain boundaries, cause the nonradiative transition. These flaws generate a variety of non-radiative centres and lower the strength of the RuO's emission. [38]. The randomly distributed graphene layers around RuO in the RuO-G composite may act as a barrier to prevent RuO particle agglomeration. As a result, charge career recombination is encouraged. The bandgaps of the samples can be calculated from the PL wavelengths using

$$Eg = hc\lambda \qquad\qquad\qquad\qquad 4\text{-}1$$

where, h is the Planck constant; c is the velocity of light, and λ is the wavelength of the absorption peak [39]. The bandgap for RuO was 3.20 eV while that of RuO-G was 2.70 eV. the reduced

bandgap in the composite will facilitate the transfer of charge. Therefore RuO-G is expected to have a better electrochemical performance.
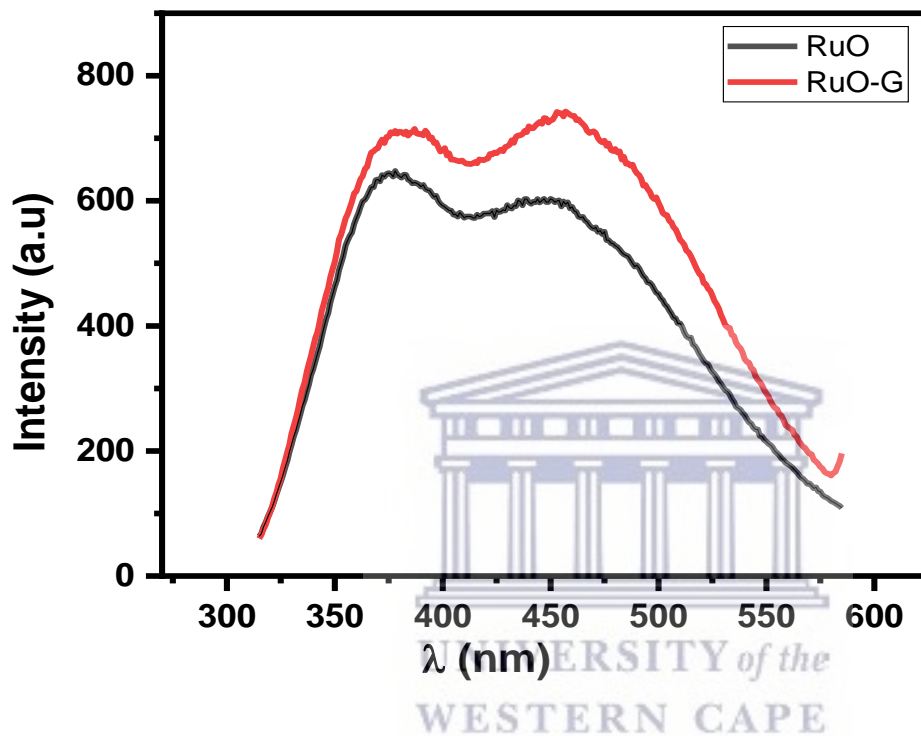
Figure 4.22: The PL emission spectra of RuO and RuO-G

4.3.3 Electrochemical studies

Cyclic voltammetry (CV), electrochemical impedance spectroscopy (EIS) and galvanostatic charge-discharge (GCD) techniques were used to assess the electrochemical capacitance behaviour of RuO and RuO-G.

174

4.3.3.1   Cyclic voltammetry

CV curves of RuO and RuO-G at different scan rates in 1M Li$_2$SO$_4$ electrolytes are shown in Figure 4.23 and Figure 4.24. Both samples' CV curves were nearly rectangular, at a low scan rate and no redox peak was found, showing that the materials had nearly perfect capacitive behaviour. The absence of the redox peak can be explained by the very quick reversible redox reaction that happened on the surface of the RuO and RuO-G nanoparticles, which can be attributed to their ultra-small size. According to Zhang *et al*. [40], redox reactions can occur to a depth of 2 nm from the particle's surface; given the ultra-small size of the RuO nanoparticles, the redox reaction took place on their surface. As the scan rate increases, the capacitive current also increases and the shape of CV plots also changed gradually from rectangular to oval due to the internal resistance of the electrode, which may be due to the limited charge accumulation and low conductivity of Li$_2$SO$_4$ aqueous solution, as well as the diffusion limits of Li$^+$ and SO$_4^{-2}$ ions in the electrode, s [41]. The CV plot of RuO-G and RuO is compared in Figure 4.25 and it indicates that the CV plot of RuO-G has a stronger current response than RuO, implying a larger area of charge accumulation and hence higher capacitance than the RuO. This is due to the integration of graphene into the material, which has resulted in a superior surface morphology for charge accumulation. The specific capacitance of the three materials was calculated from the equation below:

$$C_{sp} = \frac{1}{2mv \triangle V} \int_{-v}^{+v} Idv \qquad\qquad 4\text{-}2$$

where m is the active mass of the electrode (g), v is the scan rate (V s^{-1}), $\triangle$V is the potential window in (V) and $\int_{-v}^{+v} Idv$ is the charge obtained from the integrated area of the voltammogram.

RuO-G showed a better electrochemical performance with a higher specific capacitance of 39.77 F g^{-1} at 10 mV s^{-1} and up to 17.66 F g^{-1} at 100 mV s^{-1}. The values were 6 F g^{-1} at 10 mV s^{-1} to 1.76 F g^{-1} at 100 mV s^{-1} for RuO. Table 4-2 and Table 4-3 is the capacitance of RuO and RuO-G at different scan rates. The specific capacitance values are plotted against potential sweep rates as shown in Figure 4.25. When the voltage scan rate was raised, the specific capacitance values for both materials decreased gradually. This is due to insufficient time for electrolyte ion diffusion, and charge storage is limited to the outer surface area only [42].
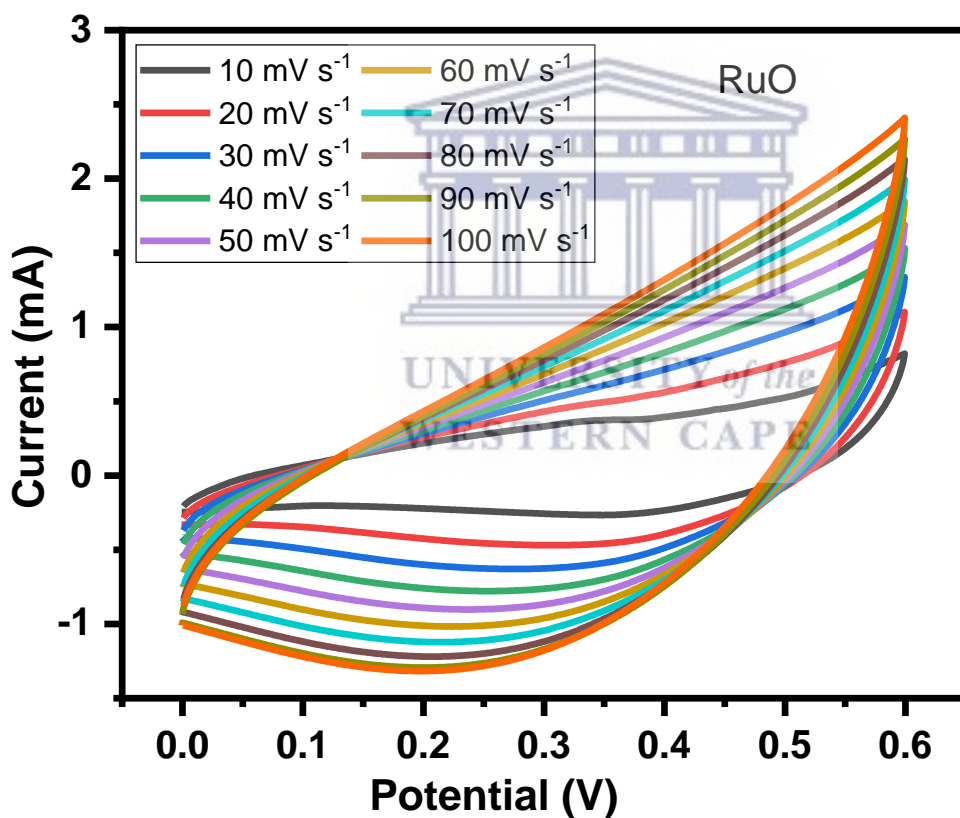
Figure 4.23: CV analysis of RuO at different scan rates from 10-100 mV s^{-1} in 1 M Li$_2$SO$_4$
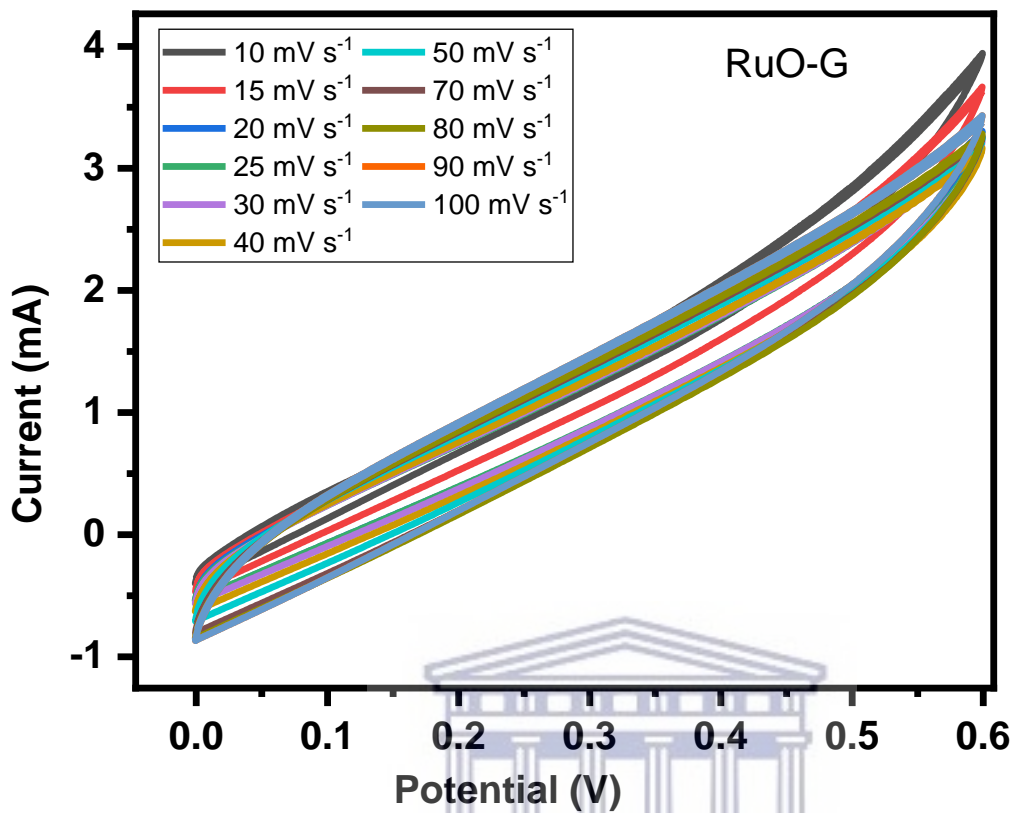
Figure 4.24: CV analysis of RuO-G at different scan rates from 10-100 mV s^{-1} in 1 M Li$_2$SO$_4$.
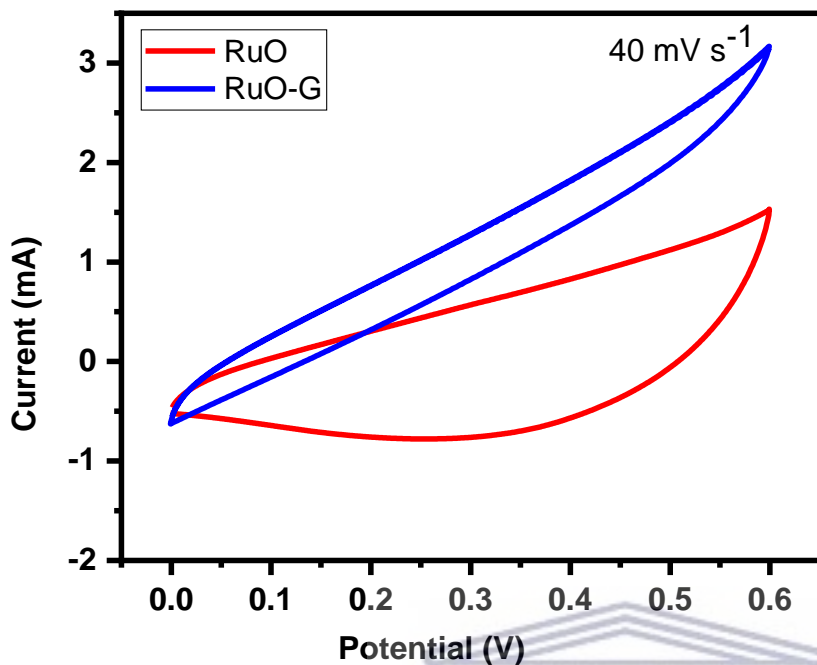
Figure 4.25: CV analysis of RuO and RuO-G at 40 mV s^{-1} in 1 M Li$_2$SO$_4$
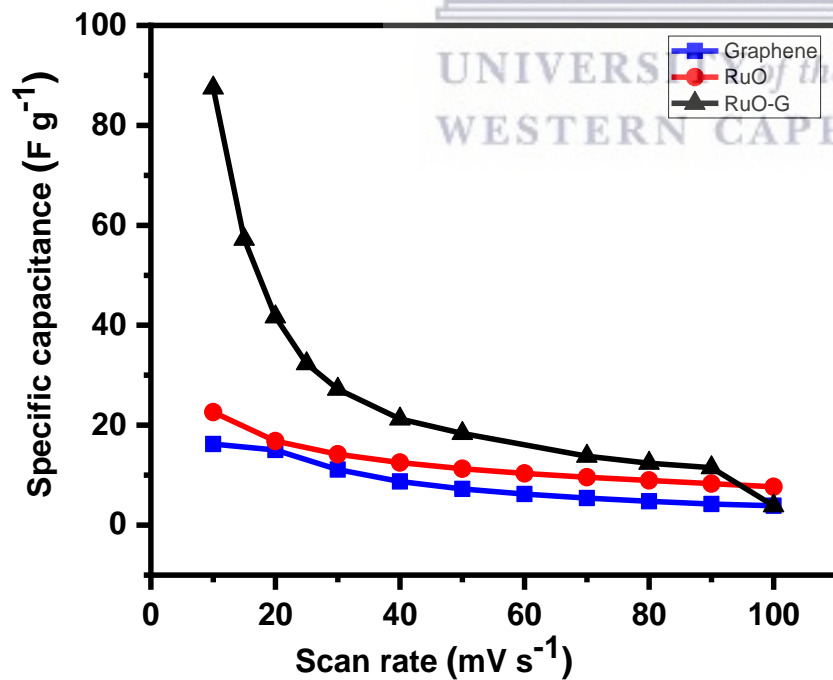
Figure 4.26: The relationship between Cs and scan rate for RuO and RuO-G

Table 4-3: The capacitance of RuO and RuO-G at different scan rates

Scan rates (mV s^{-1})	Capacitance (F g^{-1})	
	RuO	RuO-G
10	17.66	39.77
20	13.15	18.94
30	11.06	12.37
40	9.79	9.66
50	8.83	8.33
70	7.50	6.28
80	6.98	5.63
90	6.49	5.22
100	6.00	1.76

4.3.3.2   Galvanostatic charge discharge

The performance of RuO and RuO-G was investigated at different current densities. The presence of the near triangular curves confirms the electric double layer capacitive charge storage mechanism occurring at the electrode-electrolyte interface of RuO and RuO-G [43]. The GCD curves of RuO and RuO-G were symmetrically triangular, which is another indication of ideal

capacitive behaviour. A small IR drop was observed at the beginning of the discharge curve, especially for RuO in Li_2SO_4 implying the low internal resistance within the electrode. The timing for the charge and discharge process is near similar, indicating a high Coulombic efficiency and electrochemical reversibility [44]. These observations are consistent with the oxidation and reduction profiles reported in the CV curves. The specific capacitance (C) was determined using the equation

$$C_s = \frac{I \ x \ t}{m \ x \ V - IR_{drop}} \qquad\qquad 4\text{-}3$$

where I is the constant current, m is the active material mass, and t is the discharge time corresponding to the voltage change V [22]. The RuO-G electrode has the highest specific capacitance at the same current density when compared to RuO electrodes. The highest capacitance (C) of the RuO-G electrode, for example, reached up to 134.66 F g^{-1} at 0.1 A g^{-1}, while RuO was 84.91 F g^{-1} at 0.1 A g^{-1}. This is due to graphene's porous microstructure, which facilitates electrolyte infiltration and contributes to the development of electric double-layer capacitance. The specific capacitance decreases as the current increases. The drop in specific capacitance values was noticeable in the discharge time of GCD curves. This drop-in specific capacitance at increased current density could be attributed to the limited flow of electrolyte ions into the active material's inner side [45]. Figure 4.1 shows a comparison of RuO and RuO-G electrodes at a current density of 0.2 A g^{-1}. RuO-G has a specific capacitance of 102.16 F g^{-1}, which is substantially higher than that of RuO (40.83 F g^{-1}). As the current density increased to 2 A g^{-1}, the RuO -G electrode maintained a capacitance of 16.88 F g^{-1}, retaining 12% of its capacitance. RuO on the

other hand, exhibit poorer capacitance retention with less than 1% of its capacitance retained. This indicates that the structure of the graphene embedded in the RuO improved electrolyte ion diffusion.
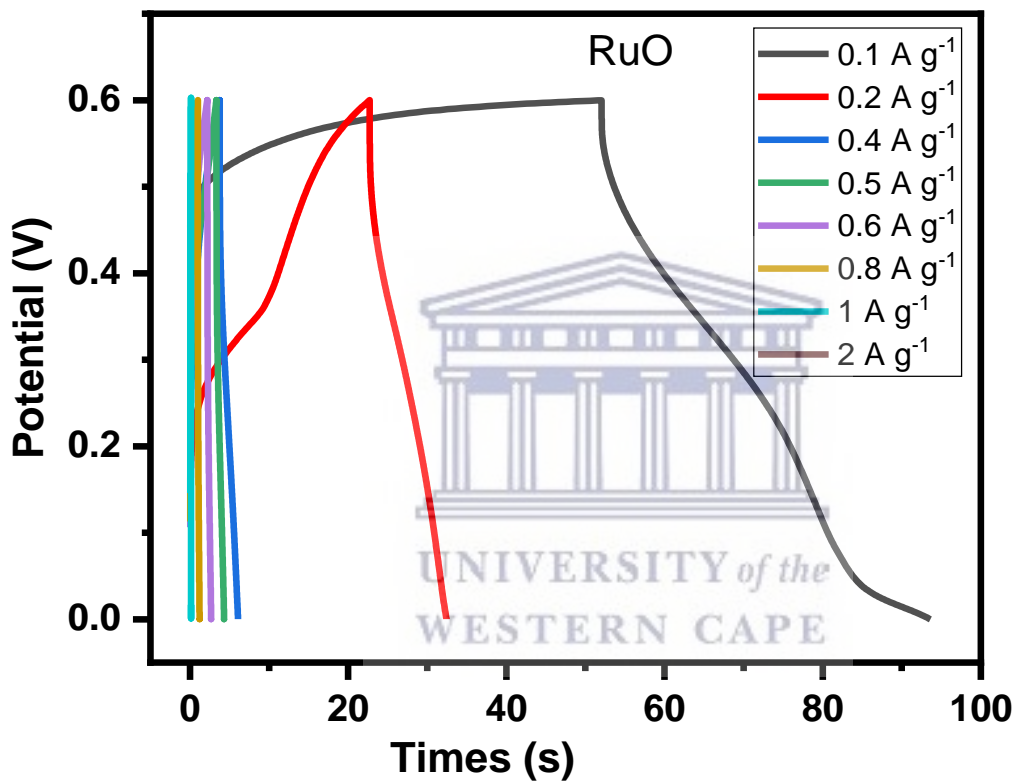
Figure 4.27: GCD of RuO at different current densities.
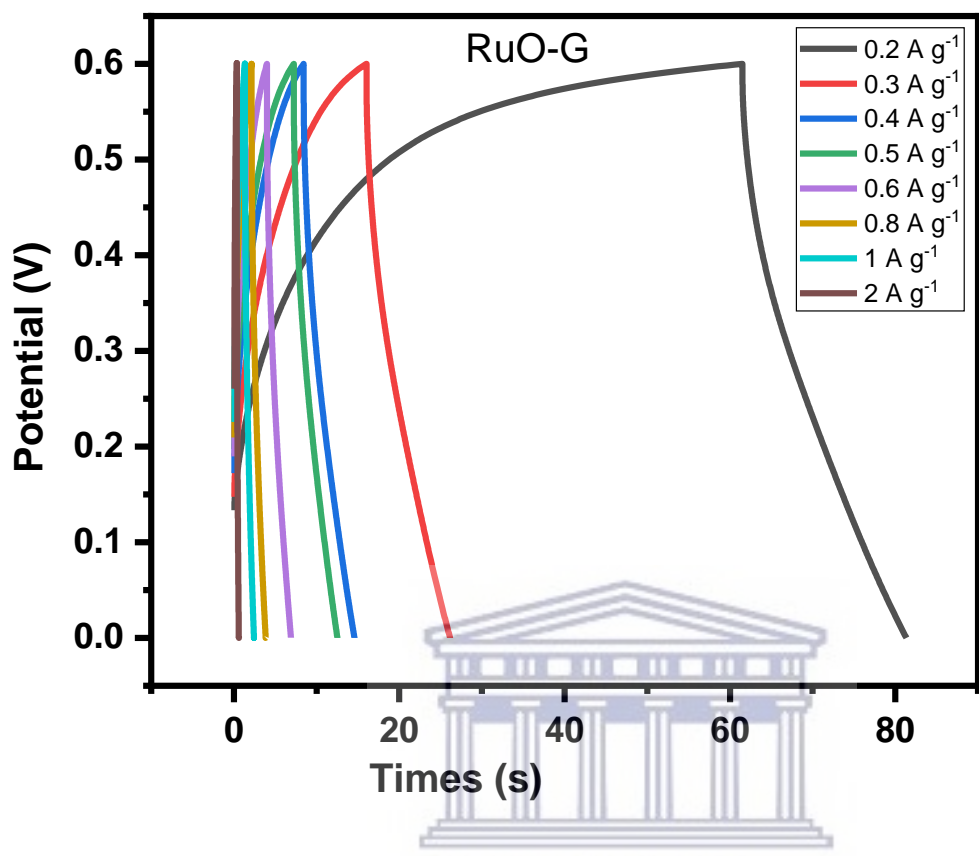
Figure 4.28: GCD of RuO-G at different current densities.
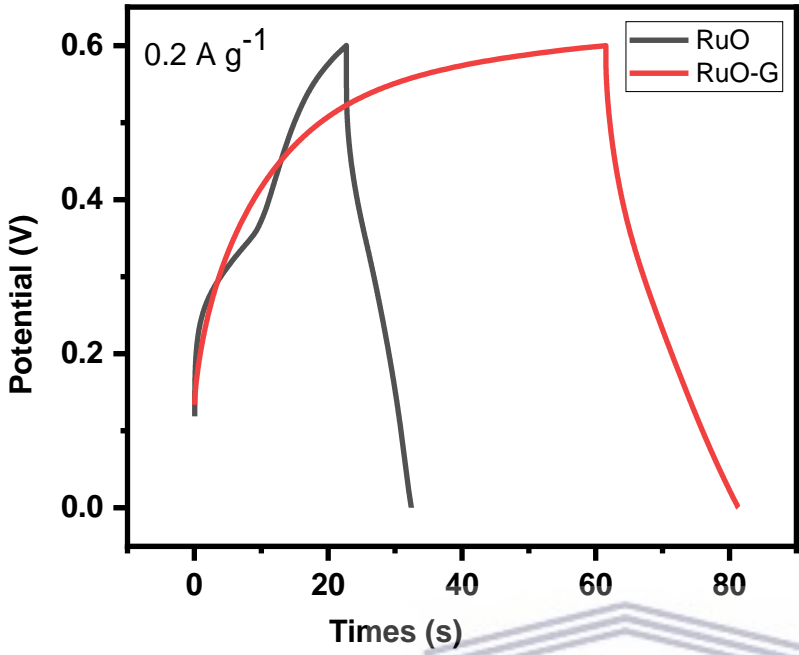
Figure 4.29: GCD curve of RuO and RuO-G at 0.2 A g^{-1}
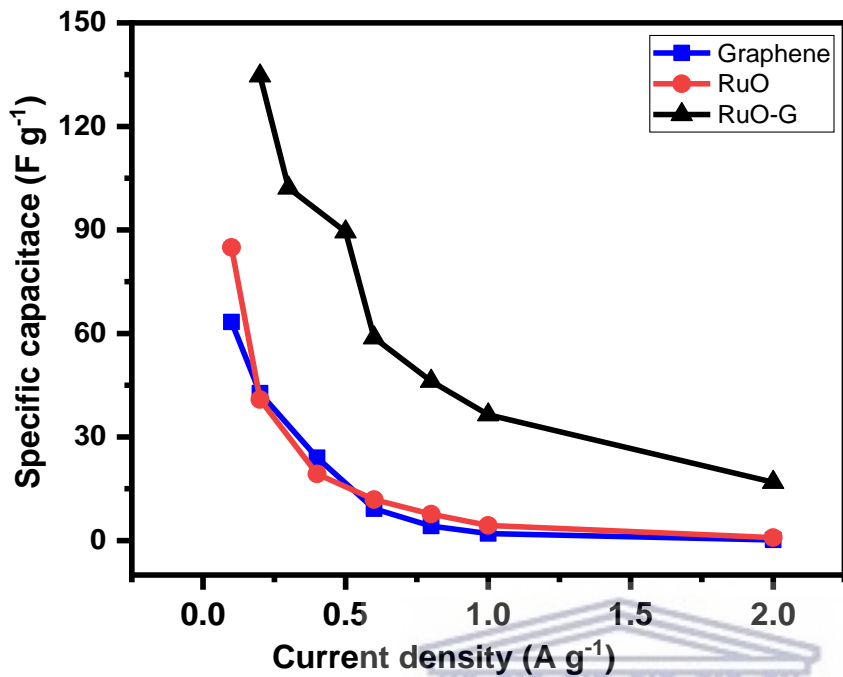
Figure 4.30: Plot showing the relationship between Cs and current density for RuO, RuO-G and graphene.

4.3.3.3   Electrochemical impedance spectroscopy

Figure 4.31 is the Nyquist plots used to analyze the electrochemical impedance spectroscopy (EIS) data and are displayed with an equivalent circuit inset. Both electrodes displayed typical alternating current impedance characteristics of supercapacitors [46]. In the high-frequency region, the intersection of the curve at the real component reveals the bulk resistance of the electrochemical system. This includes ionic resistance from the electrolytes, intrinsic grain to grain resistance of the electrode, and contact resistance at the interphase between the active material and the substrate [47]. The radius of the semicircle in the high-frequency region displays the charge-transfer process, at the interface of the electrode and the electrolyte and as we approach lower frequencies the semicircle breaks into a 45° nearly vertical line which is related

to the Warburg (W_2) diffusion of ions within the electrode inter-phase [48][49]. From the EIS the R_s is 10.72 Ω for RuO and 10.87 Ω for RuO-G. The RuO and RuO-G have fitting R_{ct} values of 15.98 Ω and 6.34 Ω respectively. The Lower R_{ct} of RuO-G shows that the incorporation of graphene increased ion mobility, which is reflected in the voltammogram. The slope of the 45° section of the curves in the intermediate frequency area was used to illustrate the Warburg resistance, which indicates ion diffusion/transport in the electrolyte and its relationship to frequencies. A well-defined and short Warburg area part in the RuO-G compared to RuO demonstrates that the ions in the electrolyte have a short and equal diffusion path length. Furthermore, the Warburg resistance value (Table 4-4) is much lower in the RuO-G (80.21 Ω) than in the RuO (690.2 Ω). Because of the low charge transfer resistance and lower diffusion effect, relatively reversible reactions can occur at the interface, which explains why the voltammogram has no redox peaks and the GCD has no plateau [50].
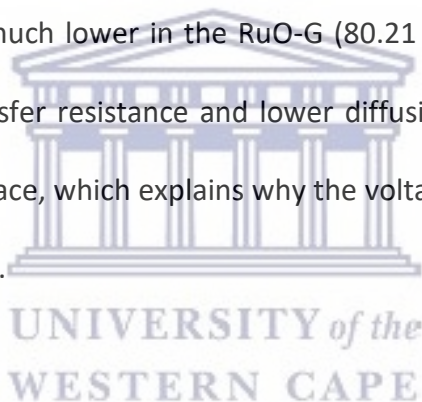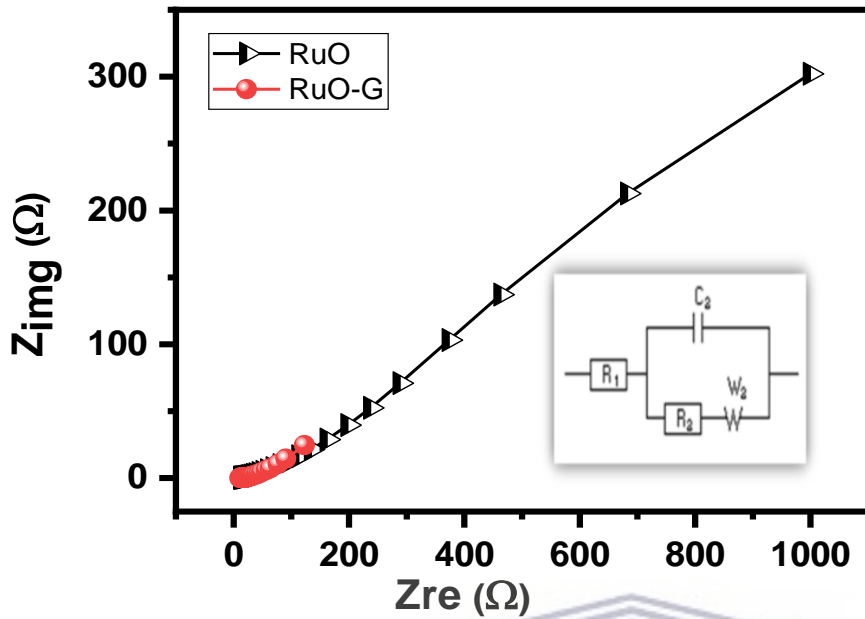
Figure 4.31: Nyquist plot of RuO and RuO-G the inset is the equivalent circuit, the inset is the equivalent circuit.
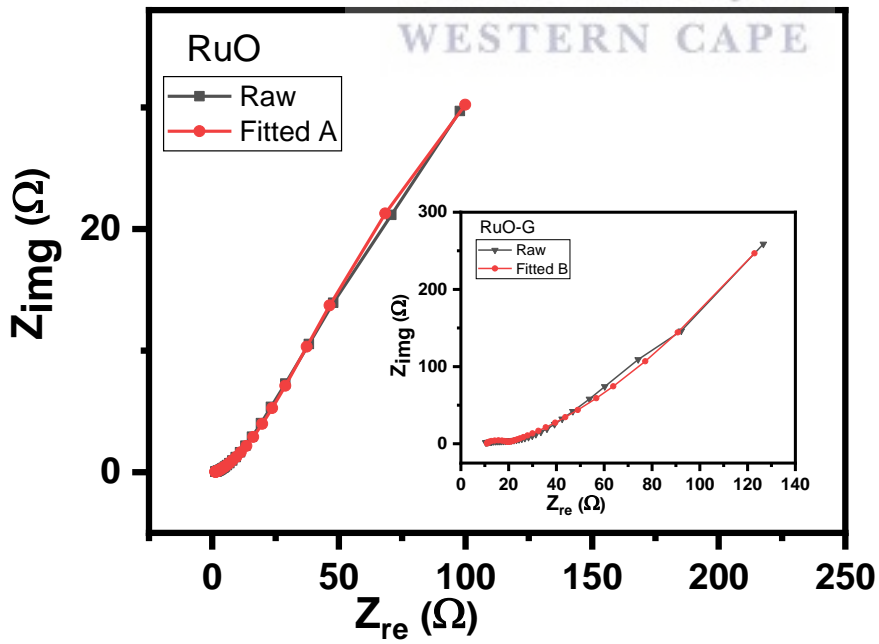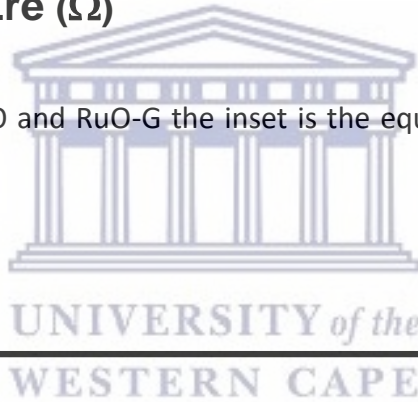
Figure 4.32: Nyquist plot of RuO-G showing the raw and fitted data, the inset is the plot of RuO showing the raw and fitted data.

Table 4-4: EIS curve fitting data of RuO and RuO-G electrode material.

Sample	R_s	CPE	R_{ct}	W^2	Phase angle
	(Ω)	(μF)	(Ω)	$(\Omega\ s\text{-}\frac{1}{2})$	$(^0)$
RuO	10.72	3.6	15.9	80.21	72.7
RuO-G	10.87	6.33	6.34	690.2	64.2

The Bode plot from the EIS data is shown as the phase angle and total impedance plot in Figure 4.33 and Figure 4.34. The phase angle for RuO was 72.7º while that of RuO-G was 64.2º. The face angle for both materials shows that the materials have the contribution of energy storage from both EDL and Pseudocapacitance. The phase angle of RuO is closer to 90º, therefore, showing more EDLC phase angles. This can also be confirmed by the voltammograms where the CV of the RuO-G shows more deviation from a rectangular to an oval shape due to an increase in pseudocapacitance because of the incorporation of graphene. It is clear from the face angle that the materials store charges utilizing both the EDL and the pseudocapacitive mechanisms. The magnitude of total impedance was lowest in RuO-G. The constant phase element (CPE) was also derived from the Bode total impedance plot the CPE impedance is given by

$$Z_{CPE} = a^{-1}(jw)^{-n} \qquad\qquad\qquad 4\text{-}4$$

where a is the frequency-independent constant related to the roughness of the surface features, and the exponent n is determined by the slope of log z vs. log f. The coefficient 'a' is resistive when n = 0, capacitive for n = 1 and a Warburg impedance (charge transfer impedance) for n = 0.5. The value of n for RuO and RuO-G was 0.69, 0.63 respectively. The change in n confirms a change in the morphology of the material, both values show that the materials are capacitive as their values approach 1[51]. The total CPE values obtained from the fitted Nyquist plot are shown in Table 4-4.
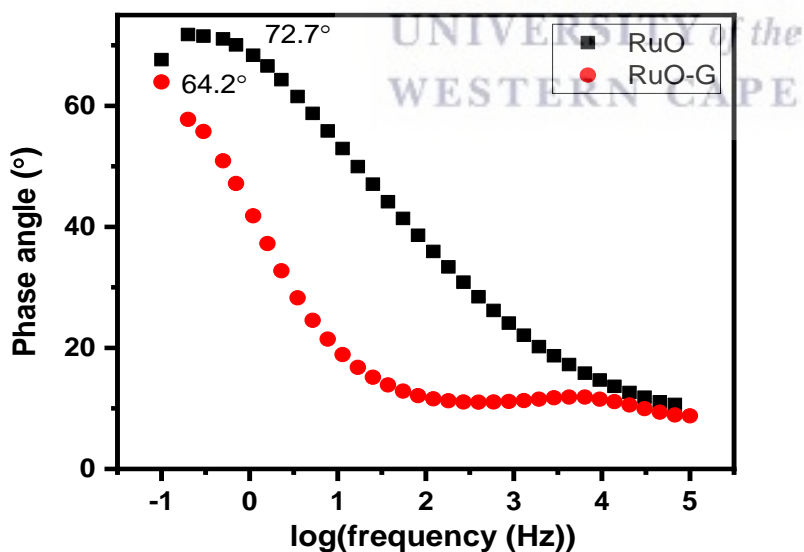
Figure 4.33: Bode plot of RuO and RuO-G
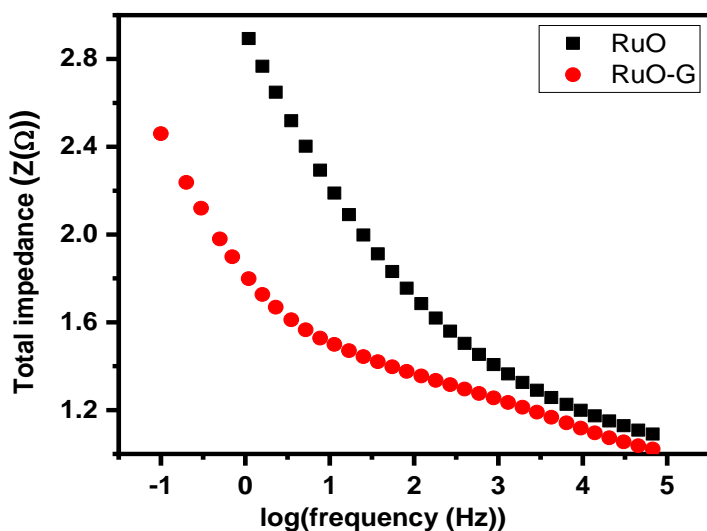
Figure 4.34: Total impedance plot of RuO and RuO-G

4.3.4 Device fabrication

To investigate the potential of as-synthesized RuO and RuO-G nanoparticles in a full-cell set-up, an ASC with RuO/ RuO-G as positive and activated carbon as negative electrode material were designed. It is well understood that charge storage in activated carbon occurs via the creation of an electrical double layer. As demonstrated in Figure 4.35, the performance of AC carbon is further validated in an aqueous solution of 1 M Li_2SO_4 in a half-cell arrangement. In ASC, the potential window of two electrodes fabricated with different characteristics is used. Thus, giving the full cell operation voltage window higher than the individual electrodes. This leads to a higher energy density of the device. The steady electrochemical performance of the activated carbon anode throughout a potential window of 0 to 1 V (vs Ag/AgCl) in this study allows for a full-cell

voltage of 1.8 V when connected with the RuO or RuO-G positive electrode, as shown in **Figure 4.36**.

To determine the stable operating voltage window for the AC/RuO-G ASC, CV and GCD data are collected at various voltage windows and plotted in Figure 4.36 and Figure 4.37 respectively. When the cell voltage is increased from 0.8 to 1.8 V, the ASC exhibits semi-rectangular CV loops with substantially triangular charge-discharge patterns, indicating steady electrode activity [13].
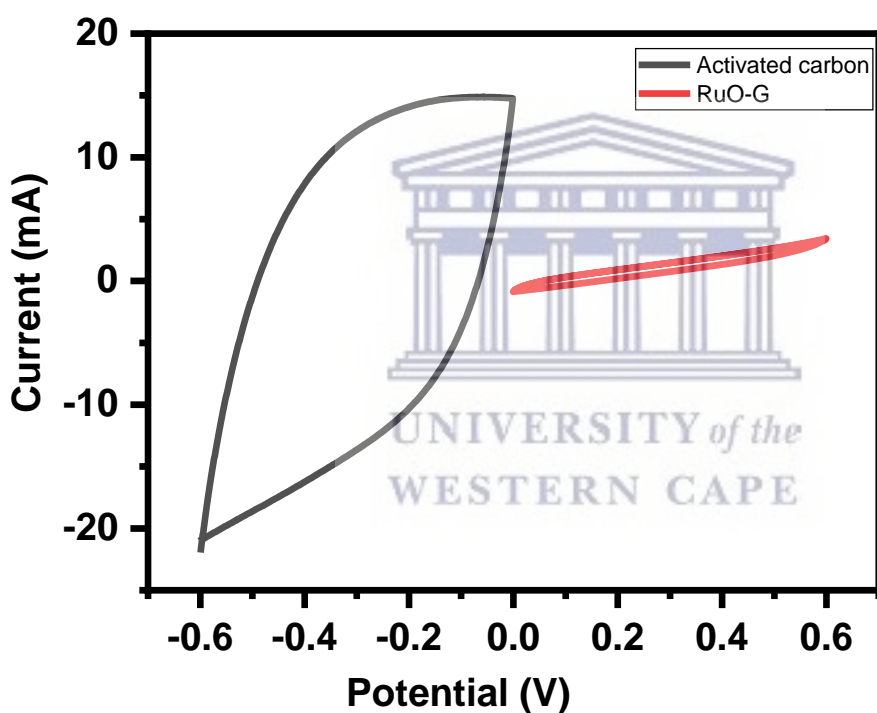
Figure 4.35: CV plot of RuO and activated carbon in a 3 electrode sell at 30 mV s^{-1}showing the suitability of AC as the negative electrode.
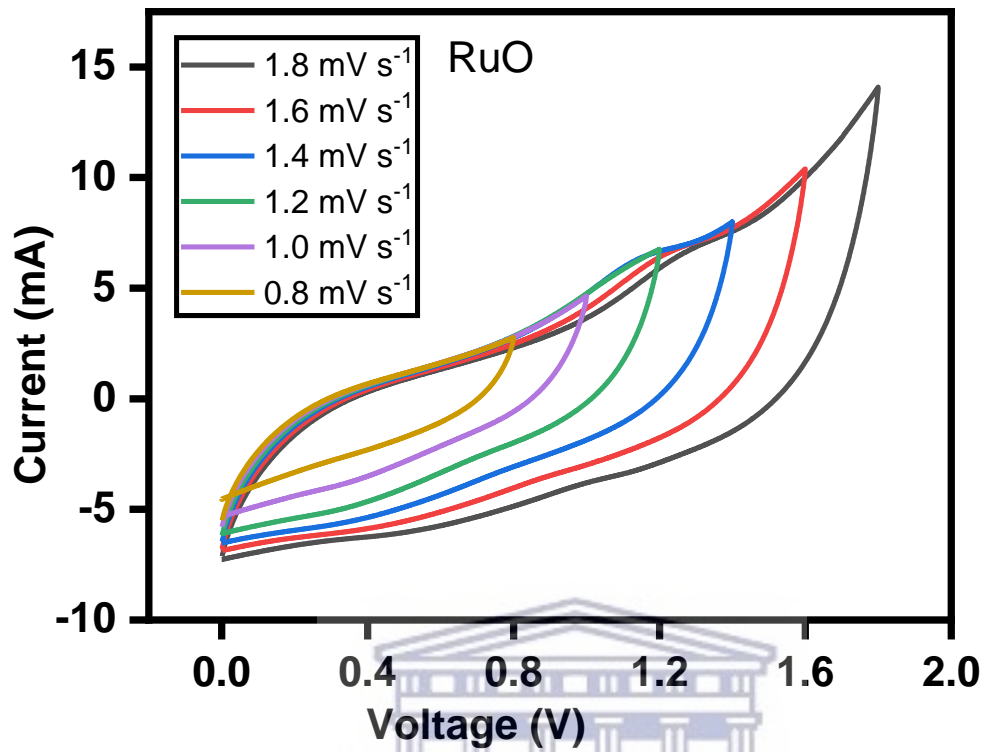
Figure 4.36: CV of AC// RuO at 50 mV s⁻ⁱ different voltages.
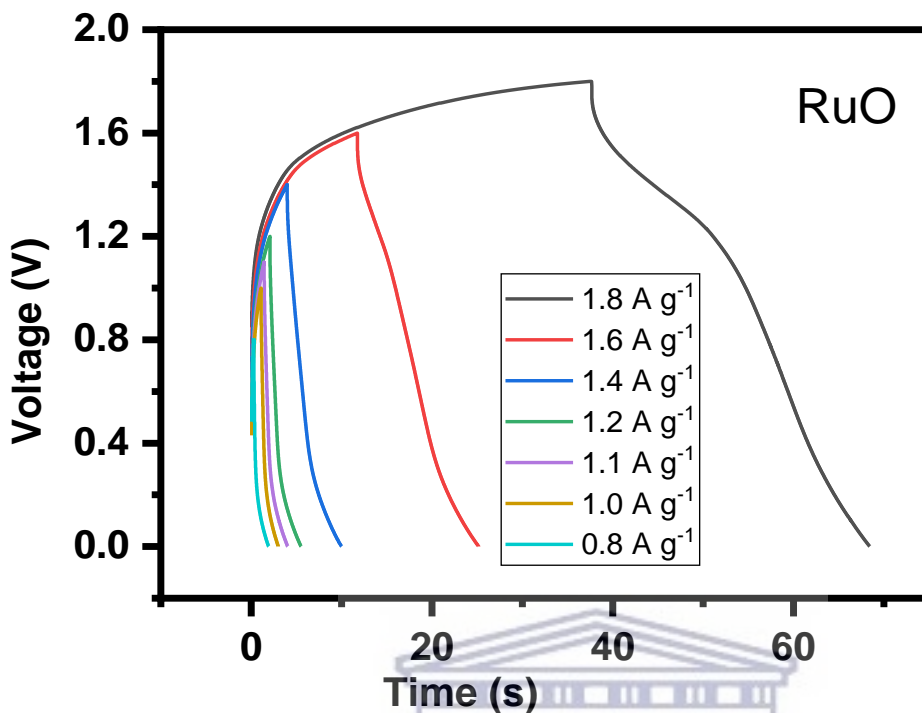
Figure 4.37: GCD of AC// RuO at 0.4 A g^{-1} collected at different voltages.

4.3.4.1 Galvanostatic charge discharge

The GCD plot of RuO and RuO-G as shown in Figure 4.38 and Figure 4.39 was carried out at different current densities (0.1 A g^{-1}, 0.2 A g^{-1},0.4 A g^{-1}, 0.5 A g^{-1}, 0.6 A g^{-1} ,0.8 A g^{-1} and 1 A g^{-1}) the capacitance at each current density was calculated and the result is as shown in Table 4-5 and Table 4-6. The result showed an improved performance in the RuO-G device than in the RuO electrode device. Figure 4.42 shows the relationship between the capacitance and the current density, the capacitance reduced with an increase in the current density. Both devices show poor rate capability as most of the capacitance is lost with an increase in current density. This is due to the poor accessibility of the electrolyte ions into the inner pores of the material at a higher

scan rate. Using a physical method of synthesis could be a good way to improve the materials surface area [52]. The specific energy and power were calculated according to the following equations:

$$E_{sp}\left(^{Wh}/_{Kg}\right) = \frac{CV^2}{2m} \times \frac{1}{3.6}$$

4-5

$$P_{max}\left(^{W}/_{Kg}\right) = \frac{E}{\triangle t} \times 3600$$

4-6

where C ($F\ g^{-1}$) is the specific capacitance determined from equation 3-2, V is the maximum working potential, m (kg) is the mass of the active material in the electrode, and $\triangle t$ is the capacitors discharge time. Figure 4.43 is a Ragone plot showing the relationship between energy density and power density of the asymmetric device at different current densities. An optimal supercapacitor device would have a high energy density at a high-power density. The asymmetric Cs cell delivered a maximum energy density of 1.41 W h kg^{-1} at a power density of 360 W kg^{-1} at 0.1 A g^{-1} current load for RuO, while RuO-G delivered an energy density of 3.98 W h kg^{-1} at a power density of 360 W kg^{-1} at 0.1 A g^{-1}. The maximum energy density of RuO-G was 5.29 W h kg^{-1} at a power density of 180 W kg^{-1} at 0.05 A g^{-1}. The energy density and power density were enhanced by the addition of graphene which led to increased surface area for charge-discharge.
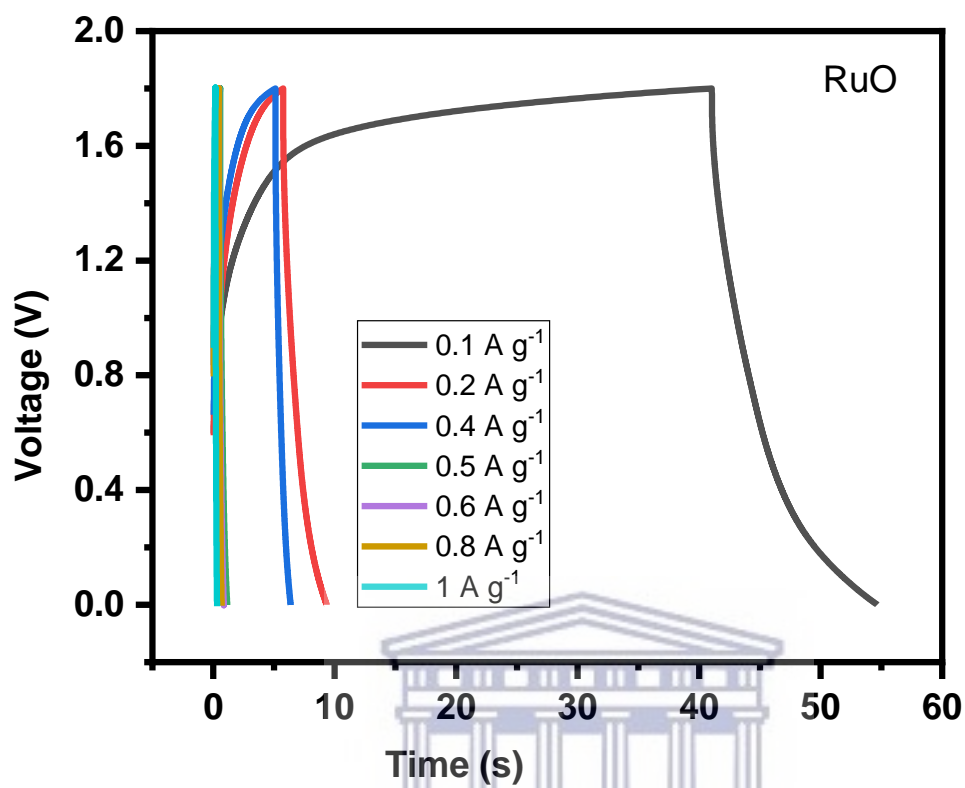
Figure 4.38: GCD profile for AC// RuO at different current densities
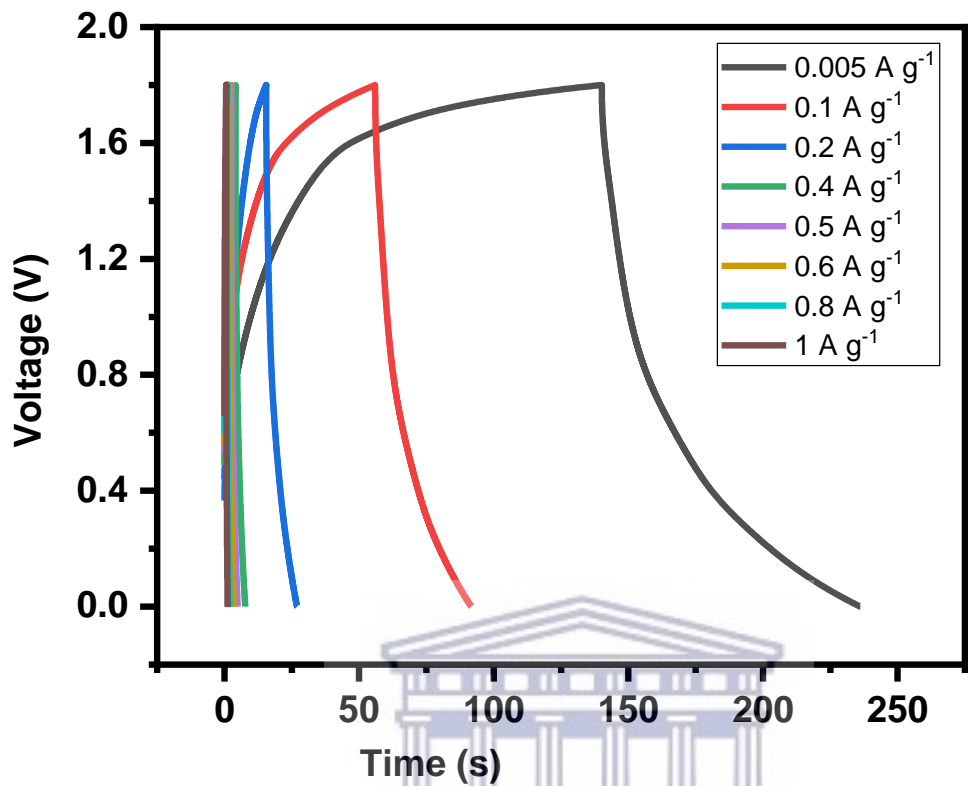
Figure 4.39: GCD profile of AC// RuO -G at different current density
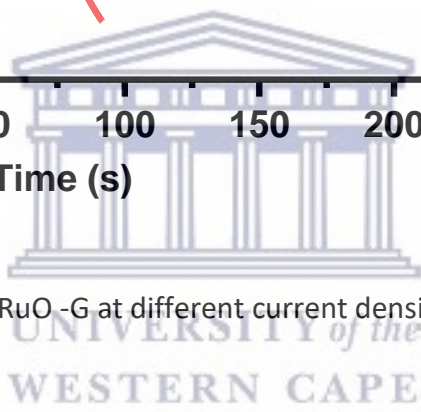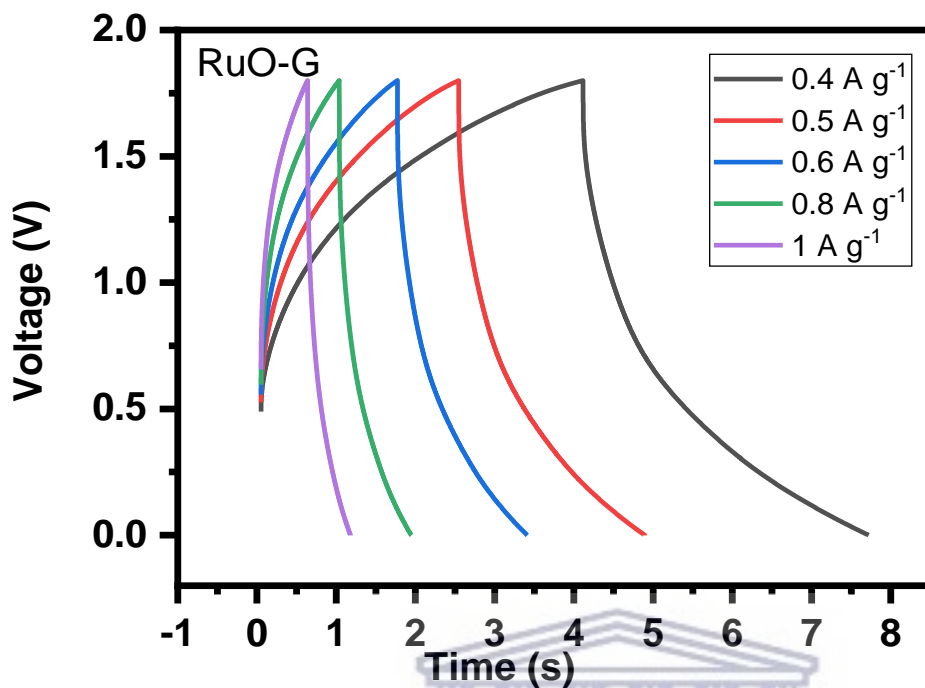
Figure 4.40: GCD plot of AC//RuO-G from 0.4 to 1 Ag $^{-1}$
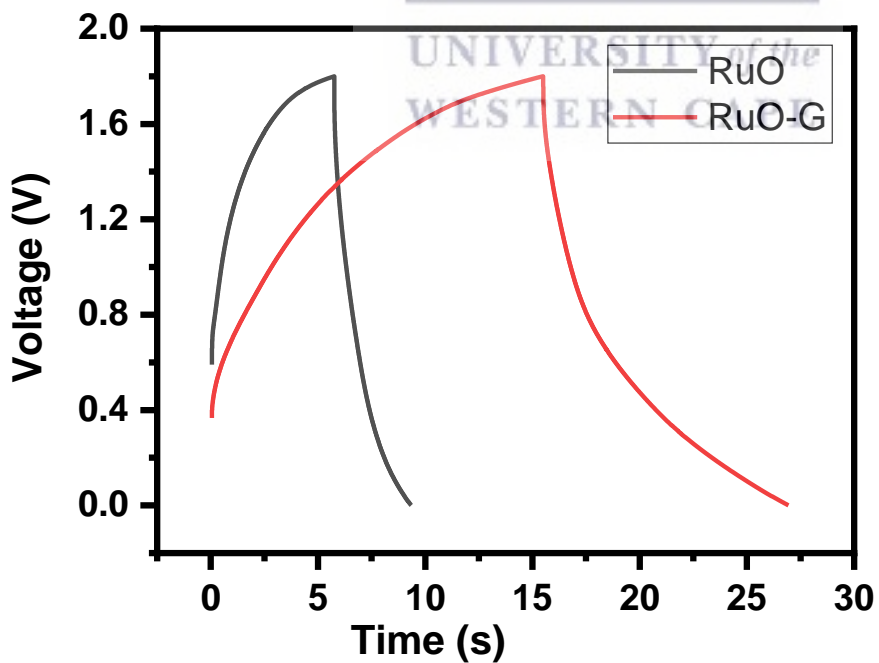
Figure 4.41: GCD plot comparing AC// RuO and AC// RuO -G at 0.2 A g^{-1}
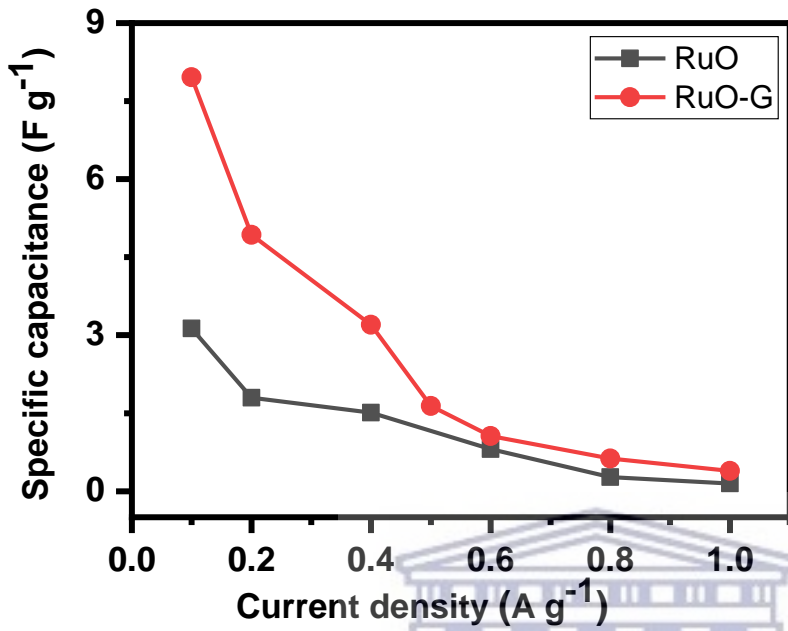
Figure 4.42: Plot comparing the current density vs capacitance of AC//RuO and AC//RuO-G
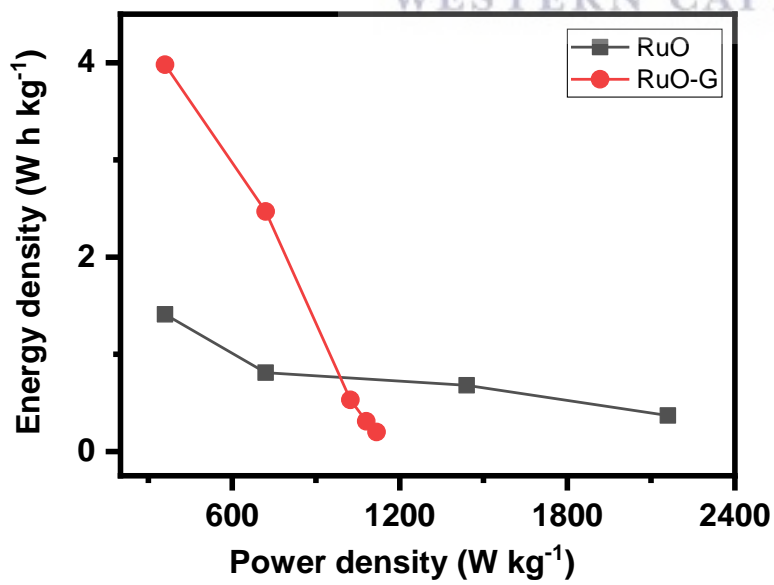
Figure 4.43: Ragone plot of AC// RuO and AC//RuO-G

Table 4-5: Capacitance, ED and PD of AC// RuO carbon device from the GCD data.

RuO

CD (A g^{-1})	Capacitance (F g^{-1})	PD (W kg^{-1})	ED (W h kg^{-1})
0.1	3.13	360	1.41
0.2	1.8	720	0.81
0.4	1.51	1440	0.68
0.6	0.81	2160	0.37
0.8	0.27	1851.43	0.12
1	0.15	1705.26	0.07

Table 4-6: Capacitance, ED and PD of AC// RuO-G device from the GCD data.

RuO-G

CD (A g^{-1})	Capacitance (F g^{-1})	PD (W kg^{-1})	ED (W h kg^{-1})
0.05A	10.59	180.00	5.29
0.1A	7.96	360.00	3.98
0.2A	4.93	720.00	2.47

0.4A	3.20	1440.00	1.60
0.5A	1.64	1157.14	0.82
0.6A	1.06	1023.16	0.53
0.8A	0.63	1080.00	0.31
1	0.39	1117.24	0.20

4.3.4.2   Electrochemical impedance spectroscopy

Figure 4.44 is the Nyquist plot of the RuO and RuO-G asymmetric device. The in-set is the fitted

equivalent circuit data and the parameters obtained are represented in Table 4-7 below. The EIS

which is primarily affected by the electrolyte is higher in the RuO-G than in the RuO material [53].

However, the charge-transfer resistance at the interface of the electrode and the electrolyte was

lower for RuO-G (2.48 Ω) as compared to RuO (3.2 Ω), showing that more facile charge transfer

occurred between the Li^+ and SO_4^{-2} ions in the RuO-G [53] [54]. A well-defined and short Warburg

area part in the RuO-G compared to the RuO device demonstrates that the ions in the electrolyte

have a short and equal diffusion path length. Thus, because of the low charge transfer resistance

and lower diffusion effect, relatively reversible reactions can occur at the interface [50]. The Bode

plot from the EIS data is shown as the phase angle and total impedance plot in Figure 4.46 and

Figure 4.47 respectively. The phase angle of RuO is 55.17° while that of the RuO-G device is at

65.04°, indicating a capacitive behaviour which is from the contribution of both EDLC and

pseudocapacitance. The magnitude of total impedance had a value of 0.07 Ω for RuO and 0.16 Ω

for RuO-G. Both plots confirm a capacitive electrode.
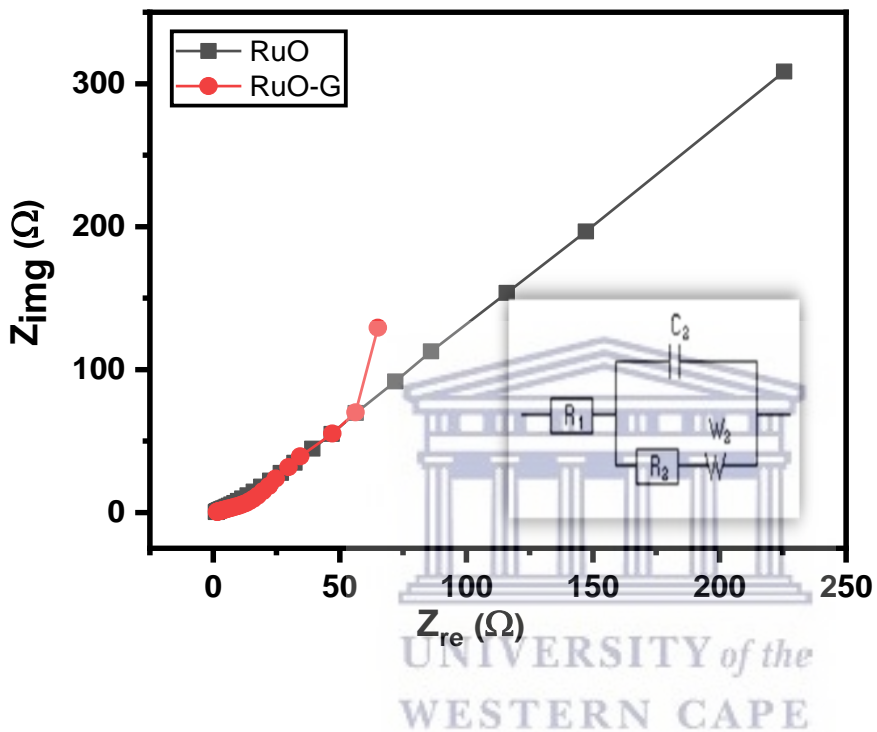
Figure 4.44: Nyquist plot of AC//RuO and AC//RuO-G electrode, the inset is the equivalent circuit.
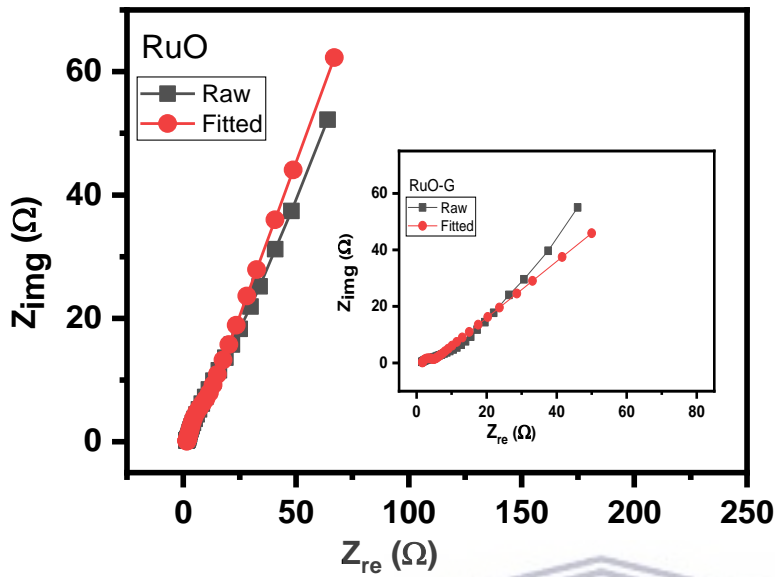
Figure 4.45: Nyquist plot of AC//RuO and AC//RuO-G electrode showing the raw and fitted data.
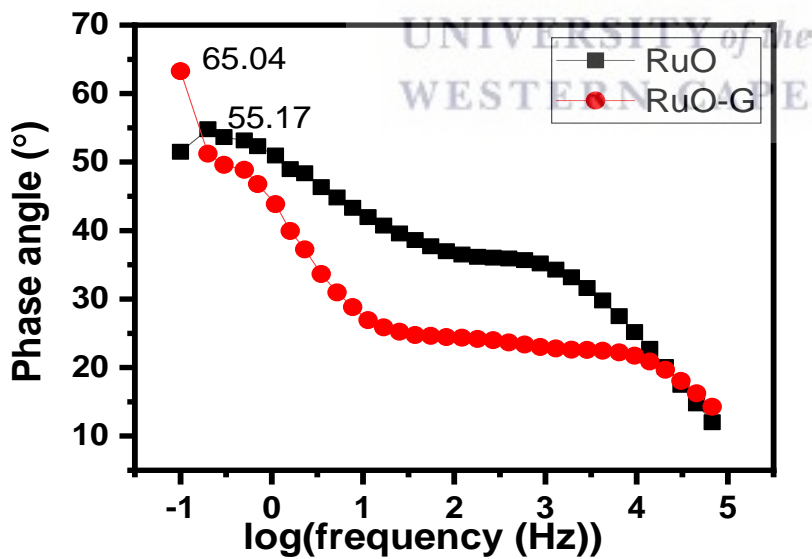
Figure 4.46: Bode plot of AC//RuO and AC//RuO-G electrode represented as a phase angle plot.
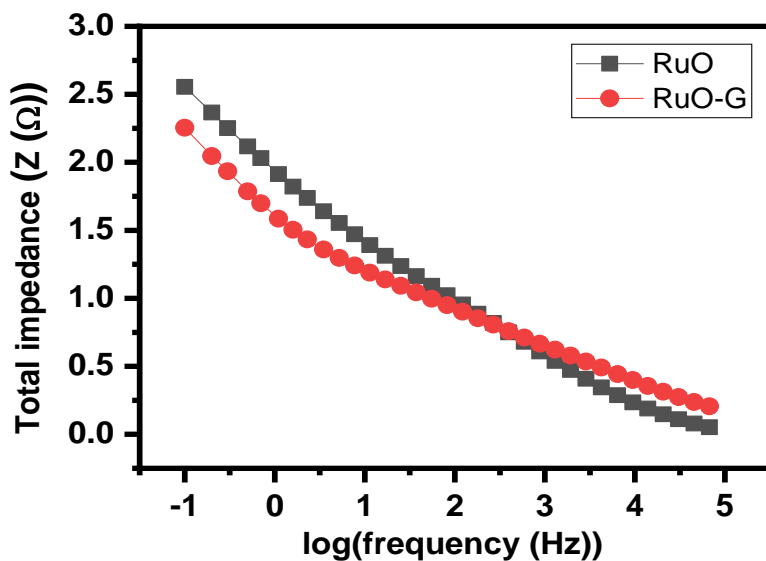
Figure 4.47: Bode plot of AC//RuO and AC//RuO-G electrode represented as a total impedance plot.

Table 4-7: EIS curve fitting data of RuO and RuO-G electrode material.

Electrolytes	R_s	CPE	R_{ct}	W^2	Phase angle
	(Ω)	(μF)	(Ω)	$(\Omega \, s^{-\frac{1}{2}})$	$(^{o})$
RuO	1.5	1.74	3.2	49.39	55.17
RuO-G	1.58	1.58	2.48	51.51	65.04

4.3.4.3 Cycle life

Long cycle life is an important criterion for supercapacitors, the cyclic stability was performed using the galvanostatic charge-discharge techniques at a current density of 0.5 A g^{-1} and a voltage

range of 0-1.8 V. Figure 4.48 shows that the RuO system remained stable for more than 3500 charging and discharging cycles and maintained ~ 65% of its initial capacitance. However, the system maintained a 100 % Coloumbic efficiency throughout the period. As seen in the in-set, the shape of the CV plot did not change after the cycling. However, the area of the curve reduced significantly showing a loss in capacitance as represented by the GCD data. The EIS of the device does not also change after the cycling. The RuO-G device showed better capacitance retention as seen in Figure 4.49. The device maintained 100% capacitance retention after the cycling test. This is evidence in the voltammogram which do not change after the charge and discharge test. The Columbic efficiency was also maintained at 100% throughout the cycling. This improved stability is because of the incorporation of a more stable carbon matrix, thus improving the cycle life of the device. The EIS plot changed in the Warburg area, the shorter Warburg line might be due to the opening of the pores of the material because of continuous ion penetration.
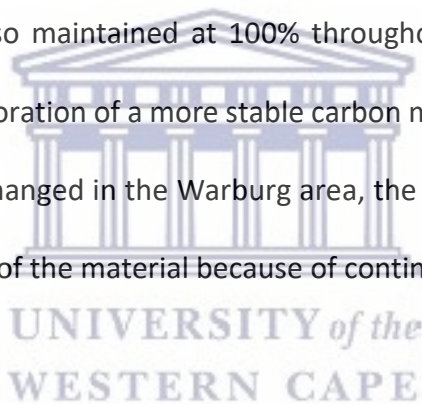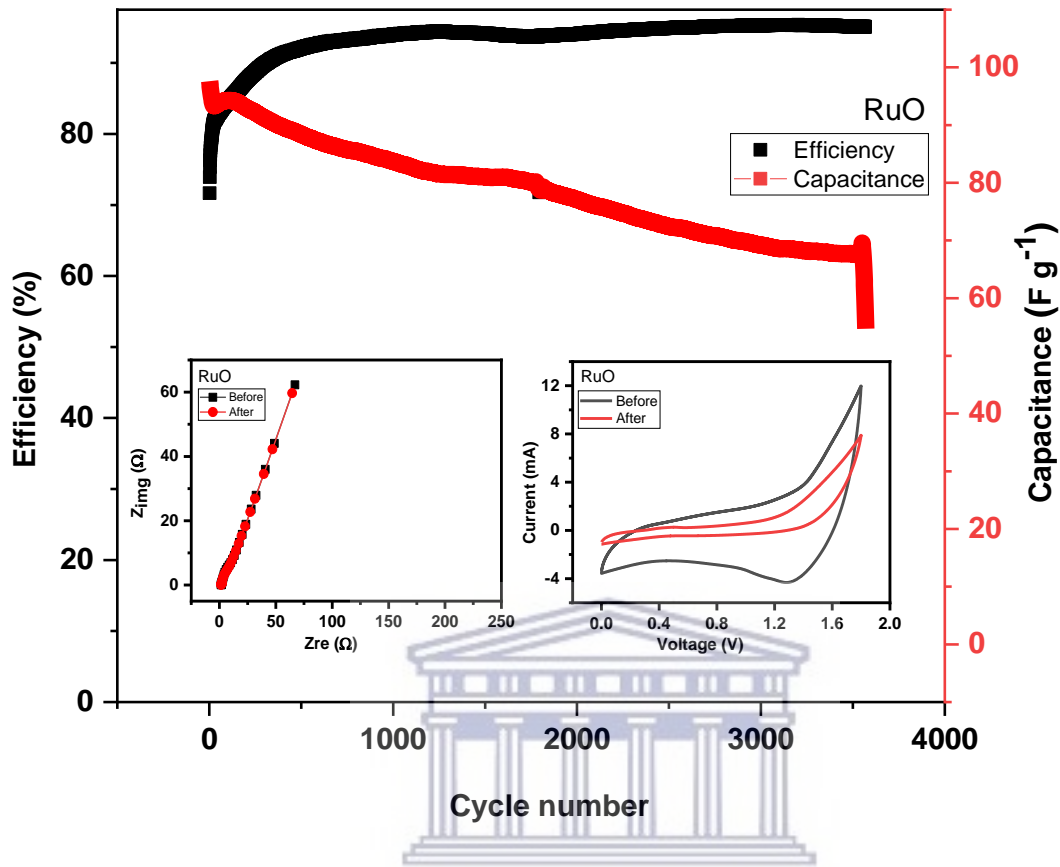
Figure 4.48: Cycling stability of AC// RuO supercapacitor over 3500 cycles in 1 M Li$_2$SO$_4$ the in-set

is the EIS and CV (50 mV s^{-1}) plot before and after cycling.
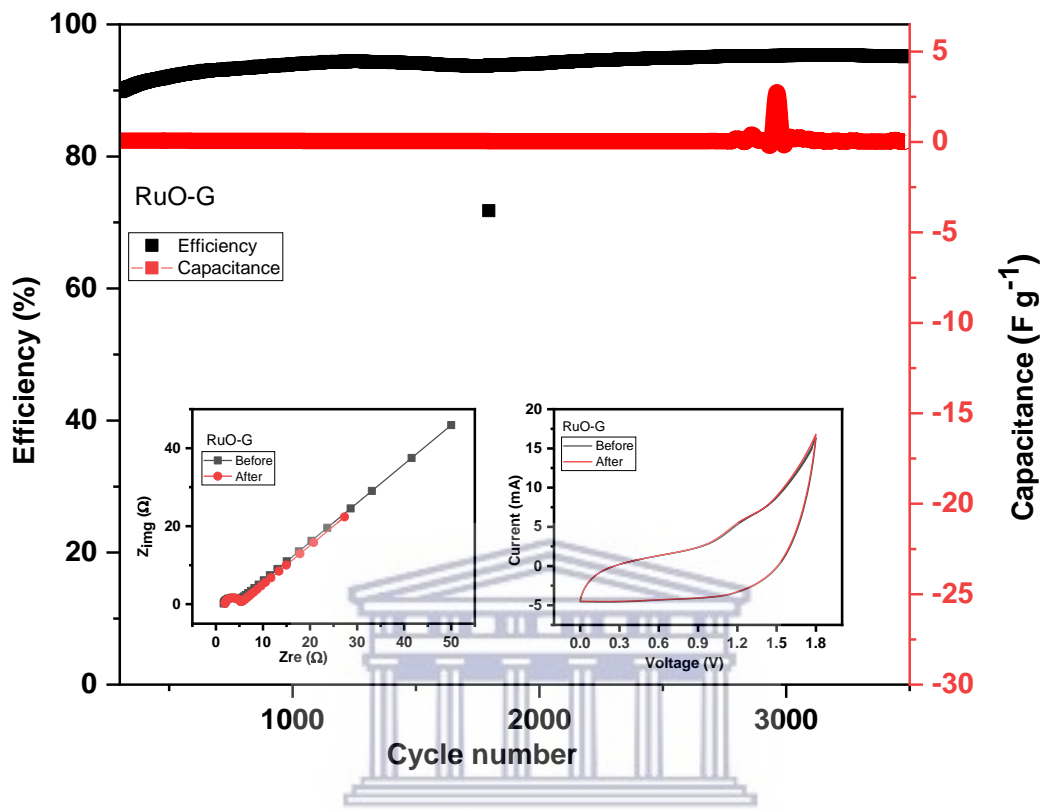
Figure 4.49: Cycling stability of AC// RuO-G supercapacitor over 3500 cycles in 1 M Li₂SO₄ the in-

set is the EIS and CV (50 mV s⁻¹) plot before and after cycling.

4.4 CONCLUSION

RuO and RuO-G were synthesized as supercapacitor electrodes via a microwave aided technique. In the RuO-G samples, ultra-small RuO nanoparticles with sizes ranging from 5 to 10 nm operate as spacers between the graphene sheets. The overall capacitance increased from 84.91 F g^{-1} for the RuO to 134.66 F g^{-1} for the RuO-G. The improved specific capacitance of RuO-G exhibits a good synergistic impact of graphene nanosheets and RuO due to the use of the combined benefits of separated graphene nanosheets to have a wide and more accessible surface area and a high conductive network of fine RuO nanoparticles. RuO and RuO-G were employed as positive electrodes in an asymmetric supercapacitor device, whilst activated carbon was used as the negative electrode. The asymmetric Cs cell delivered a maximum energy density of 1.41 W h kg^{-1} at a power density of 360 W kg^{-1} at 0.1 A g^{-1} current density for RuO, while RuO-G delivered an energy density of 3.98 W h kg^{-1} at a power density of 360 W kg^{-1} at the same current.
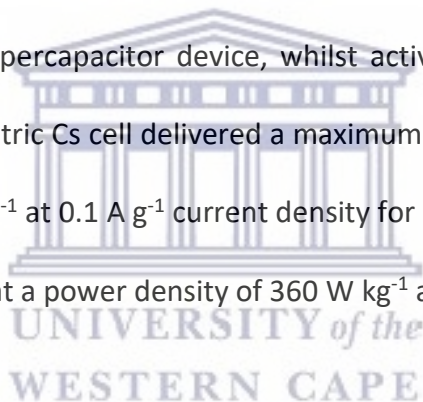
4.5 REFERENCE

[1]   Y. Yan, T. Wang, X. Li, H. Pang, H. Xue, Noble metal-based materials in high-performance supercapacitors, Inorg. Chem. Front. 4 (2017) 33–51. https://doi.org/10.1039/c6qi00199h.

[2]   J. Shen, J. Wu, L. Pei, M.T.F. Rodrigues, Z.Q. Zhang, F. Zhang, X. Zhang, P.M. Ajayan, M. Ye, $CoNi_2S_4$-Graphene-2D-$MoSe_2$ as an Advanced Electrode material for supercapacitors, Adv. Energy Mater. 6 (2016) 1–8. https://doi.org/10.1002/aenm.201600341.

[3]   R. Ramachandran and F. Wang, F., 2018. Electrochemical capacitor performance: influence of aqueous electrolytes. Supercapacitors-Theor Pract Solut InTech, pp.51-68.

[4]   F. Barzegar, D.Y. Momodu, O.O. Fashedemi, A. Bello, J.K. Dangbegnon, N. Manyala, Investigation of different aqueous electrolytes on the electrochemical performance of activated carbon-based supercapacitors, RSC Adv. 5 (2015) 107482–107487. https://doi.org/10.1039/c5ra21962k.

[5]   C. Xu, H. Du, B. Li, F. Kang, Y. Zeng, Asymmetric activated carbon-manganese dioxide capacitors in mild aqueous electrolytes containing alkaline-earth cations, J. Electrochem. Soc. 156 (2009) A435. https://doi.org/10.1149/1.3106112.

[6]   C. Mevada, M. Mukhopadhyay, Electrochemical performance of aqueous asymmetric supercapacitor based on synthesized tin oxide positive and commercial titanium dioxide negative electrodes, J. Energy Storage. 33 (2021) 102058. https://doi.org/10.1016/j.est.2020.102058.

[7]   A.M. Patil, X. An, S. Li, X. Yue, X. Du, A. Yoshida, X. Hao, A. Abudula, G. Guan, Fabrication of three-dimensionally heterostructured rGO/WO$_3$·0.5H$_2$O@Cu$_2$S electrodes for high-energy solid-state pouch-type asymmetric supercapacitor, Chem. Eng. J. 403 (2021) 126411. https://doi.org/10.1016/j.cej.2020.126411.

[8]   J.H. Chae, G.Z. Chen, 1.9 v aqueous carbon-carbon supercapacitors with unequal electrode capacitances, in: Electrochim. Acta, Pergamon, 2012: pp. 248–254. https://doi.org/10.1016/j.electacta.2012.07.033.

[9]   S. Asim, M.S. Javed, J. Khan, M. Khalid, S.S.A. Shah, M. Idrees, M. Imran, M. Usman, S. Hussain, I. Ahmad, T.S. AlGarni, Energy storage performance of binder-free ruthenium-oxide nano-needles based free-standing electrode in neutral pH electrolytes, Electrochim. Acta. 378 (2021) 138139. https://doi.org/10.1016/j.electacta.2021.138139.

[10]   J. Zhang, J. Jiang, H. Li, X.S. Zhao, A high-performance asymmetric supercapacitor fabricated with graphene-based electrodes, Energy Environ. Sci. 4 (2011) 4009–4015. https://doi.org/10.1039/c1ee01354h.

[11]   D. Xuan, W. Chengyang, C. Mingming, J. Yang, W. Jin, Electrochemical performances of nanoparticle Fe$_3$O$_4$/activated carbon supercapacitor using KOH electrolyte solution, J. Phys. Chem. C. 113 (2009) 2643–2646. https://doi.org/10.1021/jp8088269.

[12]   B. Asbani, K. Robert, P. Roussel, T. Brousse, C. Lethien, Asymmetric micro-supercapacitors based on electrodeposited RuO$_2$ and sputtered VN films, Energy Storage Mater. 37 (2021) 207–214. https://doi.org/10.1016/j.ensm.2021.02.006.

[13]   A. Kumar, D. Das, D. Sarkar, K.K. Nanda, S. Patil, A. Shukla, Asymmetric Supercapacitors

with Nanostructured RuS$_2$, Energy and Fuels. 35 (2021) 12671–12679. https://doi.org/10.1021/acs.energyfuels.1c01488.

[14] B.Z. Wu, D. Wang, W. Ren, J. Zhao, G. Zhou, Anchoring hydrous RuO$_2$ on graphene sheets for high-performance electrochemical capacitors, Advanced Functional Materials 20.20 (2010) 3595–3602. https://doi.org/10.1002/adfm.201001054.

[15] O.M. Lopez, M.C. Hegy, T.M. Missimer, Statistical comparisons of grain size characteristics, hydraulic conductivity, and porosity of barchan desert dunes to coastal dunes, Aeolian Res. 43 (2020) 100576. https://doi.org/10.1016/j.aeolia.2020.100576.

[16] M.H. Chakrabarti, E.P.L. Roberts, C. Bae, M. Saleem, Ruthenium based redox flow battery for solar energy storage, Energy Convers. Manag. 52 (2011) 2501–2508. https://doi.org/10.1016/j.enconman.2011.01.012.

[17] B. Francis Ntumba Muya, S. Africa Supervisor Priscilla Baker Co-supervisor Emmanuel Iwuoha, Hydrogel encapsulated biosensors for the detection of biologically significant vanadium and selenium, (2017). http://etd.uwc.ac.za/ (accessed October 27, 2021).

[18] T.K. Das, S. Banerjee, M. Pandey, B. Vishwanadh, R.J. Kshirsagar, V. Sudarsan, Effect of surface functional groups on hydrogen adsorption properties of Pd dispersed reduced graphene oxide, Int. J. Hydrogen Energy. 42 (2017) 8032–8041. https://doi.org/10.1016/j.ijhydene.2016.12.024.

[19] V.S.R. Channu, R. Holze, S.A.W. Sr., E.H.W. Jr., Q.L. Williams, R.R. Kalluru, Synthesis and Characterization of (Ru-Sn)O<sub>2</sub> Nanoparticles for Supercapacitors, Mater. Sci. Appl. 02 (2011) 1175–1179. https://doi.org/10.4236/msa.2011.29158.

[20]   X. Leng, J. Zou, X. Xiong, H. He, Hydrothermal synthesis and pseudo capacitance behavior of a highly homogeneous dispersed graphene sheets/ruthenium oxide nanocomposite, RSC Adv. 4 (2014) 61596–61603. https://doi.org/10.1039/c4ra10321a.

[21]   I.S. El-Hallag, M.N. El-Nahass, S.M. Youssry, R. Kumar, M.M. Abdel-Galeil, A. Matsuda, Facile in-situ simultaneous electrochemical reduction and deposition of reduced graphene oxide embedded palladium nanoparticles as high performance electrode materials for supercapacitor with excellent rate capability, Electrochim. Acta. 314 (2019) 124–134. https://doi.org/10.1016/j.electacta.2019.05.065.

[22]   N. B., V. Y., S. Abdul Razack, Enhanced formation of ruthenium oxide nanoparticles through green synthesis for highly efficient supercapacitor applications, Adv. Powder Technol. 31 (2020) 1001–1006. https://doi.org/10.1016/J.APT.2019.12.026.

[23]   P.R. Deshmukh, S.N. Pusawale, A.D. Jagadale, C.D. Lokhande, Supercapacitive performance of hydrous ruthenium oxide ($RuO_2 \cdot nH_2O$) thin films deposited by SILAR method, J. Mater. Sci. 2011 473. 47 (2011) 1546–1553. https://doi.org/10.1007/S10853-011-5946-1.

[24]   Y.S. Huang, F.H. Pollak, Raman investigation of rutile RuO_2, Solid State Commun. 43 (1982) 921–924. https://doi.org/10.1016/0038-1098(82)90930-9.

[25]   Y. Chen, X. Zhang, D. Zhang, Y. Ma, One-pot hydrothermal synthesis of ruthenium oxide nanodots on reduced graphene oxide sheets for supercapacitors, J. Alloys Compd. 511 (2012) 251–256. https://doi.org/10.1016/J.JALLCOM.2011.09.045.

[26]   Z. Jian, P. Liu, F. Li, P. He, X. Guo, M. Chen, H. Zhou, Core-shell-structured CNT@RuO$_2$

composite as a high-performance cathode catalyst for rechargeable Li-O$_2$ batteries, Angew. Chemie - Int. Ed. 53 (2014) 442–446. https://doi.org/10.1002/anie.201307976.

[27]   S. Bhaskar, P.S. Dobal, S.B. Majumder, R.S. Katiyar, X-ray photoelectron spectroscopy and micro-Raman analysis of conductive RuO$_2$ thin films, J. Appl. Phys. 89 (2001) 2987–2992. https://doi.org/10.1063/1.1337588.

[28]   Q. Zhang, Z. Hu, Y. Yang, Z. Zhang, X. Wang, X. Yang, Y. An, B. Guo, Metal organic frameworks-derived porous carbons/ruthenium oxide composite and its application in supercapacitor, J. Alloys Compd. 735 (2018) 1673–1681. https://doi.org/10.1016/j.jallcom.2017.11.268.

[29]   Z.J. Han, S. Pineda, A.T. Murdock, D.H. Seo, K.K. Ostrikov, A. Bendavid, RuO$_2$-coated vertical graphene hybrid electrodes for high-performance solid-state supercapacitors, J. Mater. Chem. A. 5 (2017) 17293–17301. https://doi.org/10.1039/c7ta03355a.

[30]   Y. Guo, W. Zhang, Y. Sun, M. Dai, Ruthenium nanoparticles stabilized by mercaptan and acetylene derivatives with supercapacitor application, Electrochim. Acta. 270 (2018) 284–293. https://doi.org/10.1016/j.electacta.2018.03.037.

[31]   Y. Guo, Z. Li, Y. Xia, Y. Wei, J. Zhang, Y. Wang, H. He, Facile synthesis of ruhtenium nanoparticles capped by graphene and thiols for high-performance supercapacitors, Electrochim. Acta. 391 (2021) 138990. https://doi.org/10.1016/j.electacta.2021.138990.

[32]   Y. Guo, Y. Wu, R. Cao, S. Zheng, Y. Yang, M. Chen, Platinum nanoparticles functionalized with acetylene derivatives and the influence of ligand length on their electrocatalytic activity, J. Electroanal. Chem. 785 (2017) 159–165.

https://doi.org/10.1016/j.jelechem.2016.12.035.

[33]   Z. Sun, H. Chang, Graphene and graphene-like two-dimensional materials in photodetection: Mechanisms and Methodology, ACS Nano. 8 (2014) 4133–4156. https://doi.org/10.1021/NN500508C.

[34]   S. Akshatha, S. Sreenivasa, K.Y. Kumar, S. Archana, M.K. Prashanth, B.P. Prasanna, P. Chakraborty, P. Krishnaiah, M.S. Raghu, H. Alrobei, Rutile, mesoporous ruthenium oxide decorated graphene oxide as an efficient visible light driven photocatalyst for hydrogen evolution reaction and organic pollutant degradation, Mater. Sci. Semicond. Process. 116 (2020) 105156 https://doi.org/10.1016/j.mssp.2020.105156.

[35]   F. El-Tantawy, A.A. Al-Ghamdi, A.A. Al-Ghamdi, Y.A. Al-Turki, A. Alshahrie, F. Al-Hazmi, O.A. Al-Hartomy, Optical properties of nanostructured ruthenium dioxide thin films via sol–gel approach, J. Mater. Sci. Mater. Electron. 28 (2017) 52–59. https://doi.org/10.1007/s10854-016-5491-4.

[36]   R. Vinoth, S.G. Babu, V. Bharti, V. Gupta, M. Navaneethan, S.V. Bhat, C. Muthamizhchelvan, P.C. Ramamurthy, C. Sharma, D.K. Aswal, Y. Hayakawa, B. Neppolian, Ruthenium based metallopolymer grafted reduced graphene oxide as a new hybrid solar light harvester in polymer solar cells, Sci. Rep. 7 (2017) 1–14. https://doi.org/10.1038/srep43133.

[37]   R. Hong, W. Tuo, D. Zhang, C. Tao, D.H. Zhang, Comparative characterisations of structural and optical properties of zinc oxide modified by carbon nanotubes and graphene, Int. J. Nanotechnol. 12 (2015) 793–801. https://doi.org/10.1504/IJNT.2015.071790.

[38]   Y. Chen, D.M. Bagnall, H.J. Koh, K.T. Park, K. Hiraga, Z. Zhu, T. Yao, Plasma assisted

molecular beam epitaxy of ZnO on c-plane sapphire: Growth and characterization, J. Appl. Phys. 84 (1998) 3912–3918. https://doi.org/10.1063/1.368595.

[39]   A.M. Teli, S.A. Beknalkar, S.A. Pawar, D.P. Dubal, E ff ect of Concentration on the Charge Storage Kinetics, Energies. 13 (2020) 6124.

[40]   G. Wang, L. Zhang, J. Zhang, A review of electrode materials for electrochemical supercapacitors, Chem. Soc. Rev. 41 (2012) 797–828. https://doi.org/10.1039/c1cs15060j.

[41]   Z. Li, Y. Mi, X. Liu, S. Liu, S. Yang, J. Wang, Flexible graphene/MnO_2 composite papers for supercapacitor electrodes, J. Mater. Chem. 21 (2011) 14706–14711. https://doi.org/10.1039/c1jm11941a.

[42]   J. Yan, T. Wei, W. Qiao, B. Shao, Q. Zhao, L. Zhang, Z. Fan, Rapid microwave-assisted synthesis of graphene nanosheet/Co_3O_4 composite for supercapacitors, Electrochim. Acta. 55 (2010) 6973–6978. https://doi.org/10.1016/j.electacta.2010.06.081.

[43]   C. Wang, J. Zhao, S. Luo, X. Yu, Improved Pseudocapacitive performance of graphene architectures modulating by nitrogen/phosphorus dual-doping and steam-activation, Macromol. Res. 29 (2021) 582–588. https://doi.org/10.1007/s13233-021-9075-7.

[44]   T. Pettong, P. Iamprasertkun, A. Krittayavathananon, P. Sukha, P. Sirisinudomkit, A. Seubsai, M. Chareonpanich, P. Kongkachuichay, J. Limtrakul, M. Sawangphruk, High-performance asymmetric supercapacitors of $MnCo_2O_4$ Nanofibers and n-doped reduced graphene oxide aerogel, ACS Appl. Mater. Interfaces. 8 (2016) 34045–34053. https://doi.org/10.1021/acsami.6b09440.

[45]   M. Dvoyashkin, D. Leistenschneider, J.D. Evans, M. Sander, L. Borchardt, Revealing the

impact of hierarchical pore organization in supercapacitor electrodes by coupling ionic dynamics at micro- and macroscales, Adv. Energy Mater. 11 (2021) 2100700. https://doi.org/10.1002/aenm.202100700.

[46]   D. Qu, Studies of the activated mesocarbon microbeads used in double-layer supercapacitors, J. Power Sources. 109 (2002) 403–411.

[47]   D. Mandal, P. Routh, A.K. Mahato, A.K. Nandi, Electrochemically modified graphite paper as an advanced electrode substrate for supercapacitor application, J. Mater. Chem. A. 7 (2019) 17547–17560. https://doi.org/10.1039/c9ta04496e.

[48]   Y. Gong, D. Li, Q. Fu, C. Pan, Influence of graphene microstructures on electrochemical performance for supercapacitors, Prog. Nat. Sci. Mater. Int. 25 (2015) 379–385. https://doi.org/10.1016/j.pnsc.2015.10.004.

[49]   M.M. Ndipingwi, C.O. Ikpo, N.W. Hlongwa, Z. Myalo, N. Ross, M. Masikini, S. V. John, P.G. Baker, W.D. Roos, E.I. Iwuoha, Orthorhombic nanostructured Li_2MnSiO_4/Al_2O_3 supercapattery electrode with efficient lithium-ion migratory pathway, Batter. Supercaps. 1 (2018) 223–235. https://doi.org/10.1002/batt.201800045.

[50]   N. Bundaleska, J. Henriques, M. Abrashev, A.M. Botelho do Rego, A.M. Ferraria, A. Almeida, F.M. Dias, E. Valcheva, B. Arnaudov, K.K. Upadhyay, M.F. Montemor, E. Tatarova, Large-scale synthesis of free-standing N-doped graphene using microwave plasma, Sci. Rep. 8 (2018) 1–11. https://doi.org/10.1038/s41598-018-30870-3.

[51]   H. Wei, C. He, J. Liu, H. Gu, Y. Wang, X. Yan, J. Guo, D. Ding, N.Z. Shen, X. Wang, S. Wei, Z. Guo, Electropolymerized polypyrrole nanocomposites with cobalt oxide coated on carbon

paper for electrochemical energy storage, Polymer (Guildf). 67 (2015) 192–199. https://doi.org/10.1016/J.POLYMER.2015.04.064.

[52]   M.F. El-Kady, V. Strong, S. Dubin, R.B. Kaner, Laser scribing of high-performance and flexible graphene-based electrochemical capacitors, Science. 335 (2012) 1326–1330. https://doi.org/10.1126/science.1216744.

[53]   D. Mandal, P. Routh, A.K. Mahato, A.K. Nandi, Electrochemically modified graphite paper as an advanced electrode substrate for supercapacitor application, J. Mater. Chem. A. 7 (2019) 17547–17560. https://doi.org/10.1039/c9ta04496e.

[54]   K. Yang, K. Cho, S. Kim, Effect of carbon black addition on thermal stability and capacitive performances of supercapacitors, Sci. Rep. 8 (2018) 1–7. https://doi.org/10.1038/s41598-018-30507-5.
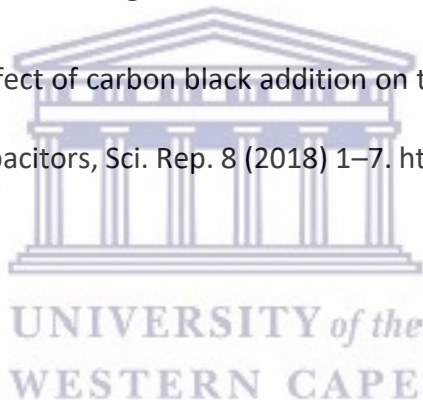
CHAPTER FIVE

MICROWAVE SYNTHESIS OF ANTIMONY OXIDE GRAPHENE NANOPARTICLES – A NEW ELECTRODE MATERIAL FOR SUPERCAPACITOR

Highlights

- Novel microwave synthesis route of antimony oxide (SbO) and graphene stabilized antimony oxide (SbO-G) nanoparticles for supercapacitors.

- XPS analysis confirms the presence of Sb_2 oxidational states of antimony.

- SbO-G showed better electrochemical behaviors in Li_2SO_4 electrolytes than SbO due to structural differences.

- SbO-G asymmetric supercapacitor device demonstrated an impressive level of stability and efficiency after ~3500 charge and discharge cycles.

ABSTRACT

For the first time, an antimony oxide nanoparticle was produced using a microwave technique and evaluated as a supercapacitor electrode. The specific capacitance derived from the material's galvanostatic charge-discharge curve was 98 F g^{-1} in 1M Li_2SO_4 electrolyte at 0.1 A g^{-1} current density. The charge storage mechanism visible in the CV curve is nearly rectangular and identical to the EDLC charge storage mechanism. Additionally, antimony species were chemically attached to graphene oxide using antimony (III) chloride precursor and subsequently microwave aided

procedures were used to convert the antimony species to SbO-G nanocomposites. The results of the energy-dispersive X-ray spectroscopy demonstrated the pure character of the produced material. In a three-electrode cell arrangement, the resulting composite was electrochemically characterized. The cyclic voltammogram results showed that among the pristine SbO, graphene, and SbO-G materials, SbO-G had a higher specific capacitance value of 37.58 F g^{-1} than the others, at a scan rate of 10 mV s^{-1}. The material has also demonstrated good conductivity characteristics based on electrochemical impedance spectroscopy research. After 3500 galvanostatic charge-discharge cycles, the material had excellent cycling stability of ~100%. All the remarkable capacitive properties demonstrated by this material indicate that it can be a viable choice in the field of energy storage devices.

KEYWORDS

Antimony oxide, asymmetric supercapacitors, energy density, graphene, pseudocapacitance.

5.1 INTRODUCTION

As a result of the rapid development in the chemical industry, finding a good balance between gaining more resources and maintaining a good sustainable environment is gaining more attention [1]. The need to have access to clean, reliable and renewable energy is an urgent need to create a sustainable society, therefore emerging. Emerging technologies associated with energy conversion and storage, have become very paramount. A Supercapacitor is one of the

energy storage devices capable of satisfying our energy requirement. Compared to batteries, supercapacitors have a higher power density and life cycle and are safer to use [2]. Due to their highunique power density, their electrochemical and morphological characteristics have gained a great deal of interest in the manufacturing of these devices. Their energy density, however, is low, and new materials are always being researched to improve it. Many antimony-based composites have recently demonstrated high capacity, which has spurred a lot of research into their use for energy storage. Because of its large theoretical capacity and adequate working voltage, antimony chalcogenide, for example, is now widely researched as a promising electrode material for batteries. Currently, antimony is widely used in semiconductors, antifriction alloys, small arms and tracer bullets, cable sheathing, flame retardant addition in large amounts [3] and has a large alloying/dealloying potential as well as a high capacity (660 mAhg^{-1})). [4]. It is well known that antimony corrodes easily and can flow through a negative electrode in lead batteries, through corrosion of current leads, leading to a reduction in battery service life [5]. However, further research has shown that the antimony-containing corrosion layer discharges slowly, allowing the active material to discharge faster than the corrosion layer and preventing the formation of a passivation layer at the electrolyte/active material interface [6]. As a result, it appears that adding antimony to the electrode's active material effectively reduces capacitance loss. Antimony has been widely investigated as an addition in newer energy storage sources, such as lithium-ion batteries (LIB), liquid metal batteries, and fuel cells. Antimony is hypothesized to perform two roles in LIB.lithium-ion batteries. It serves two purposes: first, it functions as a spacer to prevent major volume changes in the electrode during the charging/discharging cycles; second, it can hold up to three lithium atoms and provide additional capacitance. Metallic

antimonySb in a sodium-ion battery (SIB) or LIB,a lithium-ion battery (LIB), on the other hand, exhibits a considerable volume expansion during sodation/desodiation or lithiation/delithiation in each battery system, resulting in a decrease in the device's long-term cycle performance. Several methodstactics have been employed to decrease volume expansion, including (1) the production of metallic alloys, (2) the formation of a stable heterostructure oxide (e.g., Sb/S_2bO_3), and (3) nanoscale tailoring and anchoring in a carbon matrix. Antimony's Sb's excellent performance and long and steady cycle life can be created by anchoring it in or with carbon. Several studies on the synthesis of an antimony carbon composite for usage in energy storage have recently been published.
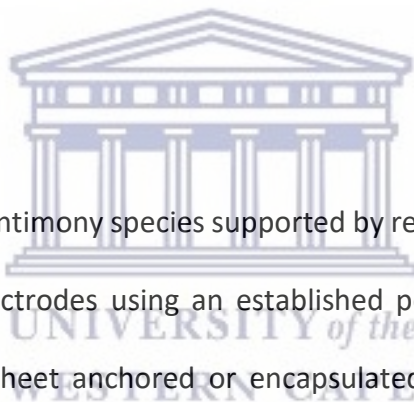
Ciszewski et al. [7] reported on antimony species supported by reduced graphene oxide for high-performance supercapacitor electrodes using an established polyol method. Sahoo et al. [8] designed sulfur-doped carbon sheet anchored or encapsulated Sb_2S_3 nanoparticles for high-performance supercapacitors using microwave-assisted synthesis. Xio et al. [9] presented a tin antimony oxide/ @graphene novel anode material for lithium-ion batteries, by a hydrothermal method. Hai et al. [10] also synthesized a paste electrode made of multiwall carbon nanotubes modified with antimony oxide (Sb_2O_3/MWCNTs) for simultaneous electrochemical detection of cadmium and lead ions. The key goals of combining carbon with Sb as the buffer layer are to (1) provide structural stability with improved conductivity and surface area, hence increasing capacitance, and (ii) decrease volume expansion and agglomeration of Sb particles during the cycle life. LIBs, as well as catalytic and supercapacitive applications, have shown that Sb particles anchored in carbon and Sb-based chalcogenides offer greater potential.

In this study we present the synthesis of two types of materials, SbO and SbO-G nanoparticles, using a simple microwave approach. Various techniques are used to analyze the structure, morphology, crystalline phase, and surface area of both samples. In a 1 M Li_2SO_4 electrolyte, the SC performance of each material is measured using a three-electrode electrochemical setup. In a positive potential window (0–0.6 V), the SbO and SbO-G electrodes exhibit an electrostatic double-layer capacitance characteristic. The specific capacitance, rate capability, energy density, power density, and durability of an asymmetric SC are also tested. The carbon in the SbO nanoparticles served as a buffer layer that prevented structural degradation while also increasing the effective contact area between the electrode and the electrolyte. These studies suggest that antimony chemistry could be important in the development of new energy storage devices. Although antimony has been used severally as dopant or additive in supercapacitor materials, as far as we know, we have not found any application of pure antimony oxide as a supercapacitor electrode reported. This research could lead to new ideas for using SbO-based electrodes with high reversible capacities in SC applications.

5.2 EXPERIMENTAL

5.2.1 Materials

Microcrystalline graphite (2-15 µm, 99.99%) was purchased from Alfar Aesar (Kandel, Germany) Nickel foam (1.6 mm thick, 0.25 µm pore diameter) was purchased from MTI Corporation, (Richmond, Califonia, USA). Hydrogen peroxide solution (30 wt. % in water, American chemical

society (ACS) reagent), concentrated hydrochloric acid (reagent grade and assay 36.5-38.0%), sodium borohydride (98.0%), potassium permanganate (≥ 99.0%, ACS reagent), concentrated sulphuric acid (99.999%), Antimony pentachloride (99.999% trace metal bases), polytetrafluoroethylene (mean particle size 20 μm), activated charcoal (Norit ® pallets), anhydrous N-methyl-2-pyrrolidone (99.5%) and carbon black (4 μm mesoporous carbon matrix, ≥ 99.95% metal bases), ethylene glycol (EG) (99.8%), ethanol (absolute, ≥ 99.8%) were purchased from Sigma-Aldrich (St Louis, Missouri, USA) and were all used without further purification.

5.2.2 Microwave-assisted synthesis of SbO and SbO-G nanocomposite.

The MW-assisted synthesis of SbO was carried out using an Anton Parr multi-wave Pro microwave system. It is equipped with an IR temperature sensor that controls the temperature during the process. $SbCl_5$ (1 mmol) was added to 30 mL of ethylene glycol with continuous stirring for 0.5 h. $NaBH_4$ (1.5 g) was slowly added to the above-mixed solution, sonicated for 10 min, and allowed to cool. The resultant mixture was MW-irradiated at 190 ℃ for 10 min. The resulting products were separated by centrifuging, washed with deionized water, and dried at 60 ℃ under vacuum for 12 h.

In another reaction vessel, one hundred milligrams of synthesized GO is added to 30 mL of ethylene glycol and sonicated for 2 h to form a homogenous dispersion. $SbCl_5$ (1 mmol) was added to the dispersed solution and sonicated for 0.5 h. $NaBH_4$ (2 g) was slowly added to the above mixture, which was sonicated for 10 min and transferred to a microwave vessel. The

resultant mixture was MW-irradiated at 190 ℃ for 10 min. The resulting products were separated

by centrifuging, washed with deionized water, and dried at 60 ℃ under vacuum for 12 h.

5.2.2.1   Material characterization

The elemental and morphological composition of the nanoparticles were obtained using a Carl

ZEISS ULTRA scanning electron microscope GmbH. Fitted with an energy dispersion

spectrometer. (Jena, Germany). All analysis was performed on a nickel-copper grid. The samples

for TEM characterization were drop-coated into the Cu TEM grids and scanned in high-resolution

transmission electron microscopy (HR-TEM) with an FEI Technai G20 F20X-Twin MAT 200 Kv Field

Emission Transmission Electron Microscope (Eindhoven, Netherlands) equipped with both EDS

and selected area electron diffraction (SAED). The X-ray powder diffraction (XRD) pattern was

obtained for all the nanoparticles with a D8 advance multipurpose X-ray diffractometer

(BRUCKER-AXS, Berlin, Germany) using copper kα1 radiation (λ ~ 0.154 nm) operating at 40 kV

and 40 mA. XRD patterns were collected from 15 to 70 (2q) with step size of 0.034° in 2q. The

functional group present in the sample was determined using a Perkin Elimer Spectrum 100 series

Attenuated Total Reflectance (ATR) Fourier Transform Infra-red spectrometer with 4 cm^{-1}

resolutions (Perkin-Elmer, Boston, MA, USA). The particle size distribution was determined by a

small-angle X-ray scattering (SAXS) measurement, performed on an Anton Paar GmbH SAXSpace

P/N 100100 (Graz, Austria). It was equipped with a 1 D mythen 2 position-sensitive detectors, a

beamstop alignment, and a Copper Kα (0,154 nm) instrument radiation was used. The

nanoparticles Raman spectra were obtained using an Xplora Olympus BX41 Raman Spectrometer

(Horiba, Tokyo, Japan) using a 532 nm laser as the excitation source. Optical absorption spectra were acquired from ethanolic dispersions of the nanocrystals at room temperature using a Varian Cary 300 UV-Vis-NIR spectrophotometer (Agilent, Santa Clara, CA, USA). At room temperature, infrared spectroscopic investigations between 4000 and 400 cm^{-1} were carried out. The powdered nanocrystals were deposited on a diamond disc, and infrared spectra were acquired using an Attenuated Total Reflectance/Perkin-Elmer Spectrum 100 Series Fourier Transform Infrared (FTIR) Spectrometer (Perkin-Elmer, Boston, MA, USA). The photoluminescence properties were obtained from NanoLog HORIBA using the software FluorEssence V3.9. (Johannesburg, South Africa). All electrochemical studies were performed on a VMP-300 potentiostat from the Bio-Logic instrument (France).
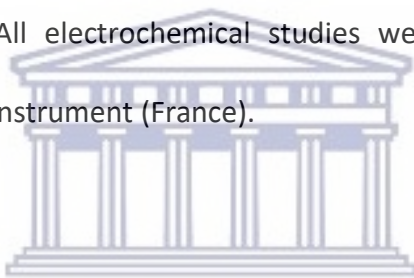
5.2.2.2 Electrode preparation and electrochemical measurements

To prepare the working electrode, the active material; SbO and SbO-G (70%), a conducting agent; carbon black (20%) and a binder; polytetrafluoroethylene (10%) were mixed in a mortar, and crushed to fine powder, then 3 drops of anhydrous N-methyl-2-pyrrolidone were added and mixed to form a uniform slurry. Nickel foam was cut into rectangular shapes of 0.5 x 1cm^2 and coined shapes of 20 mm in diameter. The foams were cleaned to remove all surface oxide layers in 1 M HCL solution, absolute ethanol and deionized water respectively, with ultra-sonication for 15 min in each solvent, and dried at 90 ^{o}C for 12 h. The homogenous paste was coated on 0.5 cm^2 diameter of the nickel foam and dried at 80 ^{o}C for 12 h. In a three-electrode cell setup, Ag/AgCl and Pt wire were used as the reference and counter electrode respectively. While for

the full cell, the paste was coated into the coin-shaped nickel foam and assembled in a Swagelok with activated carbon as the negative electrode. The cyclic voltammograms were recorded between -0 to 0.6V potential window at different scan rates, the electrochemical impedance measurements were obtained at a frequency range of 0.1 MHz to 100 MHz with 10 points per decade, and the galvanostatic charge-discharge profiles were measured at different current densities. All electrochemical characterization of material was done in the three-electrode cell using 1 M Li_2SO_4, electrolyte. The device testing was done at 1.8 V in the same electrolyte.

5.2.3 Morphological studies

5.2.3.1   Scanning electron microscopy (SEM)

The surface morphology, mean particle size, and shape of SbO and SbO-G nanoparticles were studied using SEM. Figure 5.1 depicts spherically shaped particles ranging in size from 1020 to 5080 nm that are uniformly dispersed. The SEM microgram of SbO-G shows a visible graphene sheet with SbO nanoparticles dispersed randomly on the surface. As a result, antimony nanoparticles must have acted as spacers, reducing graphene aggregation. This will result in increased surface area and, consequently, increased charge storage and capacitance.
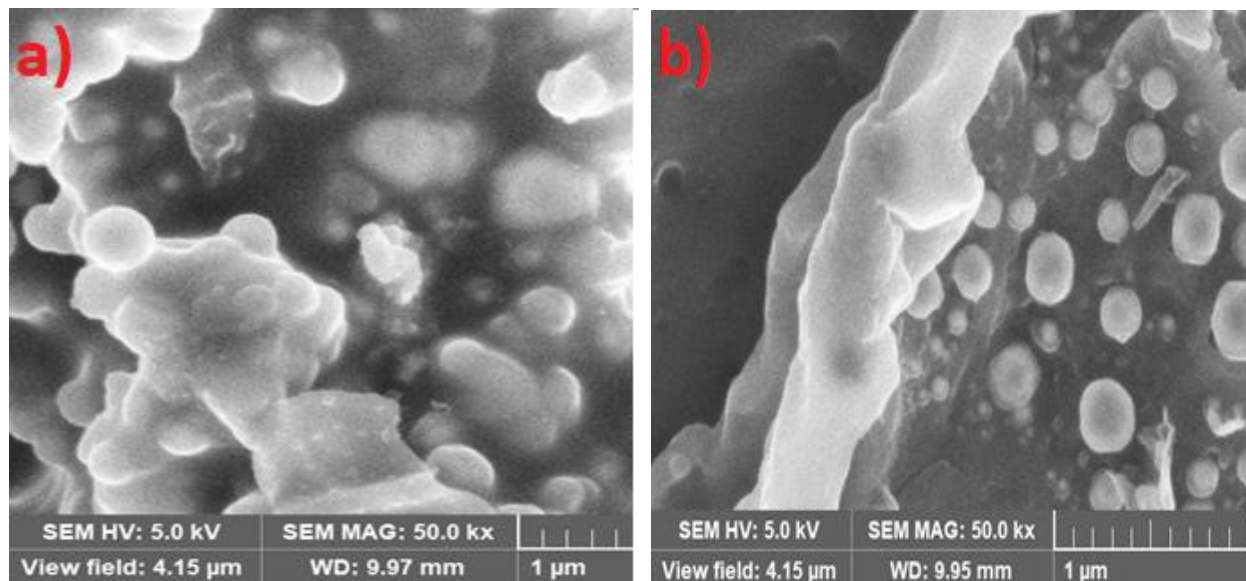
Figure 5.1: SEM images of SbO and SbO-G
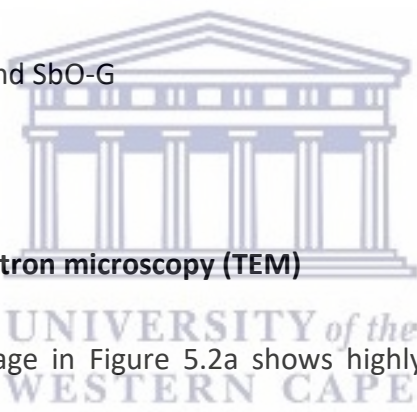
5.2.3.2   Transmission electron microscopy (TEM)

For the pure SbO, the TEM image in Figure 5.2a shows highly spherically shaped randomly distributed nanoparticles as seen in the SEM with particle sizes ranging from 10 to 45 nm. Figure 5.2b displays a large triangular shape of the grain, the lattice space of 0.3 nm obtained from the high-resolution TEM examination on the triangular SbO, corresponds to the (012) plane of SbO. This is consistent with the TEM results obtained when Yang *et al*. synthesized single crystals of ultrathin-antimony oxide [11]. The spherical nanoparticles may be seen randomly distributed on the surface of the graphinized material with an average particle size between 10-40 nm. This shows that SbO nanoparticles were successfully graphinised. Despite the high degree of aggregation, the material's small grain size indicates that it is highly permeable [12]. Porosity would improve the ion transfer process and, as a result, the energy storage efficiency [13]. In the

corresponding SAED pattern, all rings can be indexed to the diffraction peaks of orthorhombic Sb_2O_3. Due to the polycrystallinity of the material, the selected area electron diffraction (SAED) pattern exhibits concentric circles, indicating that the material is crystalline in the (212), (110), (104), (012) directions for SbO and (012), (104) and (110) direction for SbO-G. The higher the crystallinity of the material, the faster the ion transit within the grains and the higher the conductivity [24]. The interlayer spacing was also calculated from the SAED images. The d spacing for SbO was calculated to be 2.07 nm while that of SbO-G was calculated to be 2.32 nm. This shows that the incorporation of graphene into the SbO lattice increased the interlayer spacing of the material. The increased spacing will give rise to quicker ion movement thus higher power density. As a result of the inclusion of graphene, the HRTEM confirms a structural change.
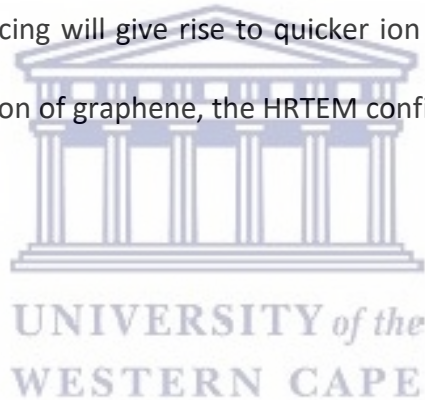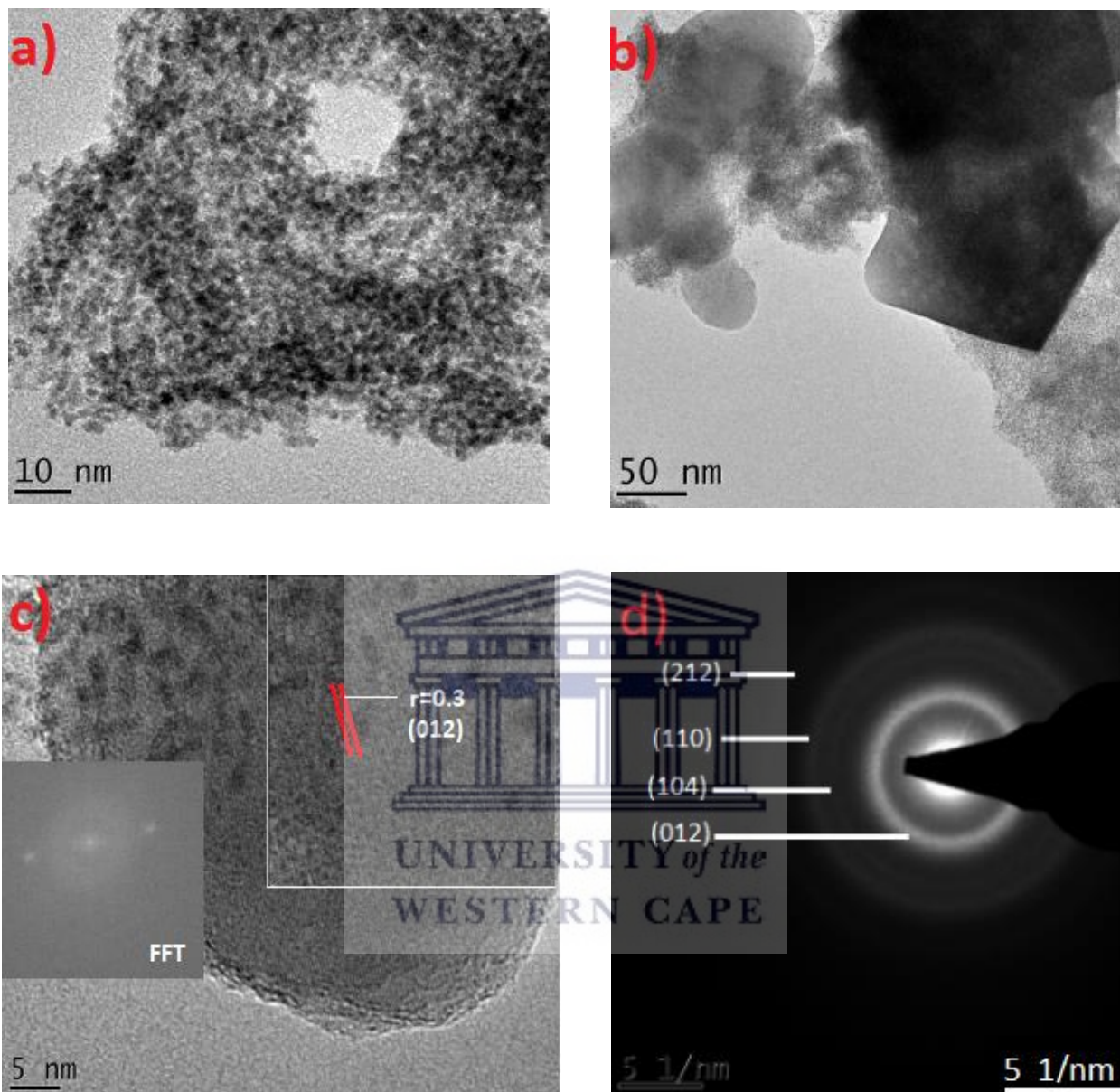
Figure 5.2: SbO: a,b) TEM images at different magnifications; c) HRTEM image showing the lattice fringes, the inset is the FFT; d) SAED pattern.
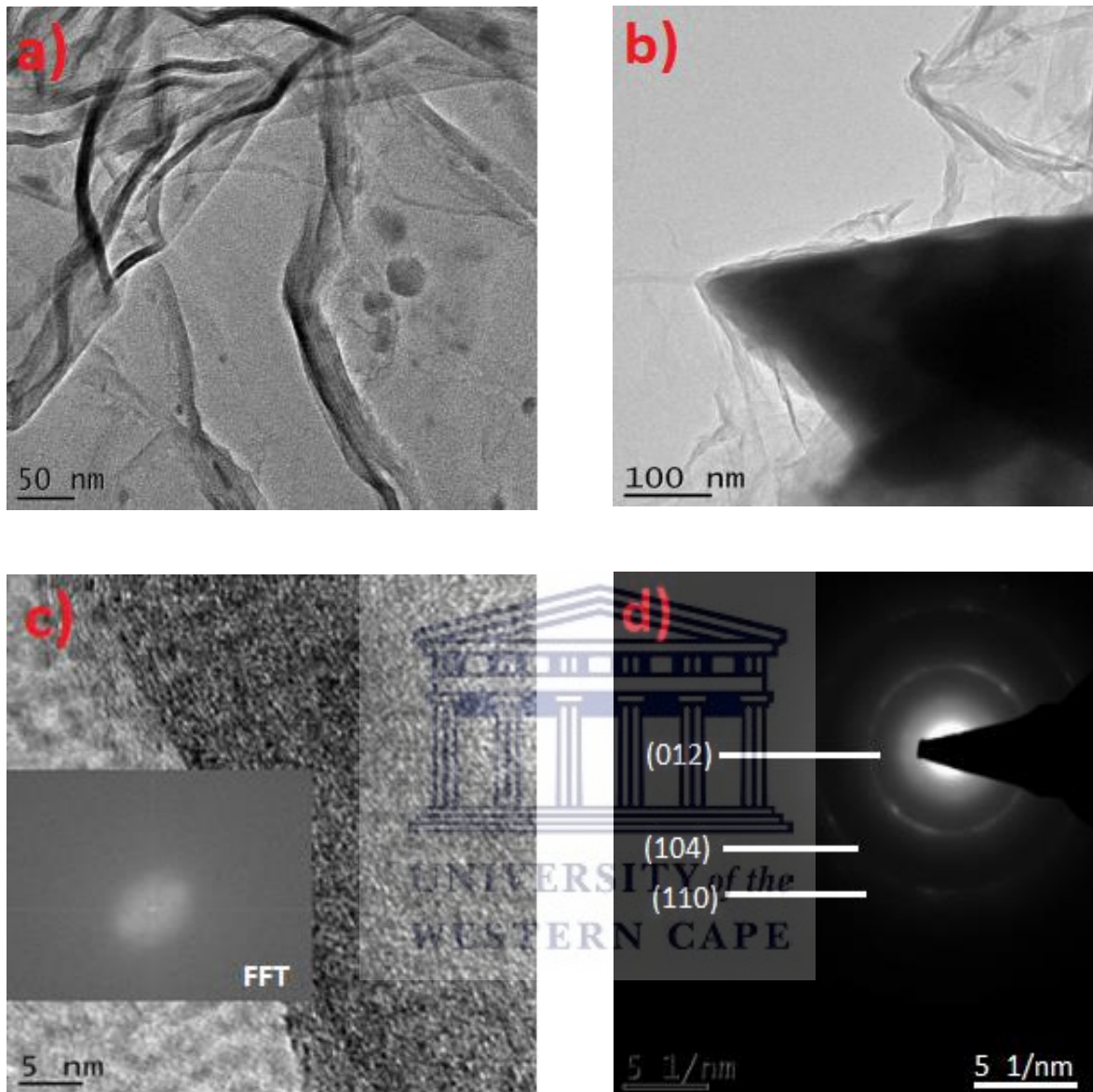
Figure 5.3: SbO-G: a,b) TEM images at different magnifications; c) HRTEM image showing the lattice fringes, the inset is the FFT; d) SAED pattern.

5.2.3.3 Atomic force microscopy

Atomic force microscopy (AFM) is an important tool for examining surface topography and roughness parameters of materials. The AFM micrographs of SbO films deposited on screen plated electrodes are shown in Figure 5.4, and Figure 5.5. The surface topography of the SbO and film shows that grains are uniformly distributed, without any fractures or voids in the film's surface. The thin film surface roughness was also derived from AFM investigations. The root mean square roughness (Rq) and the average roughness (Ra) were found to be 68.4 nm and 56.2 nm, respectively. Table 5-1 is the list of all parameters obtained from the AFM analysis [14].

Table 5-1: AFM parameters for SbO and SbO-G

Parameters	SbO	SbO-G
	(μm)	(mm)
Ra	1841.8	6.153
Rms/Rq	51657	6.848
Surface area	1448	6.05
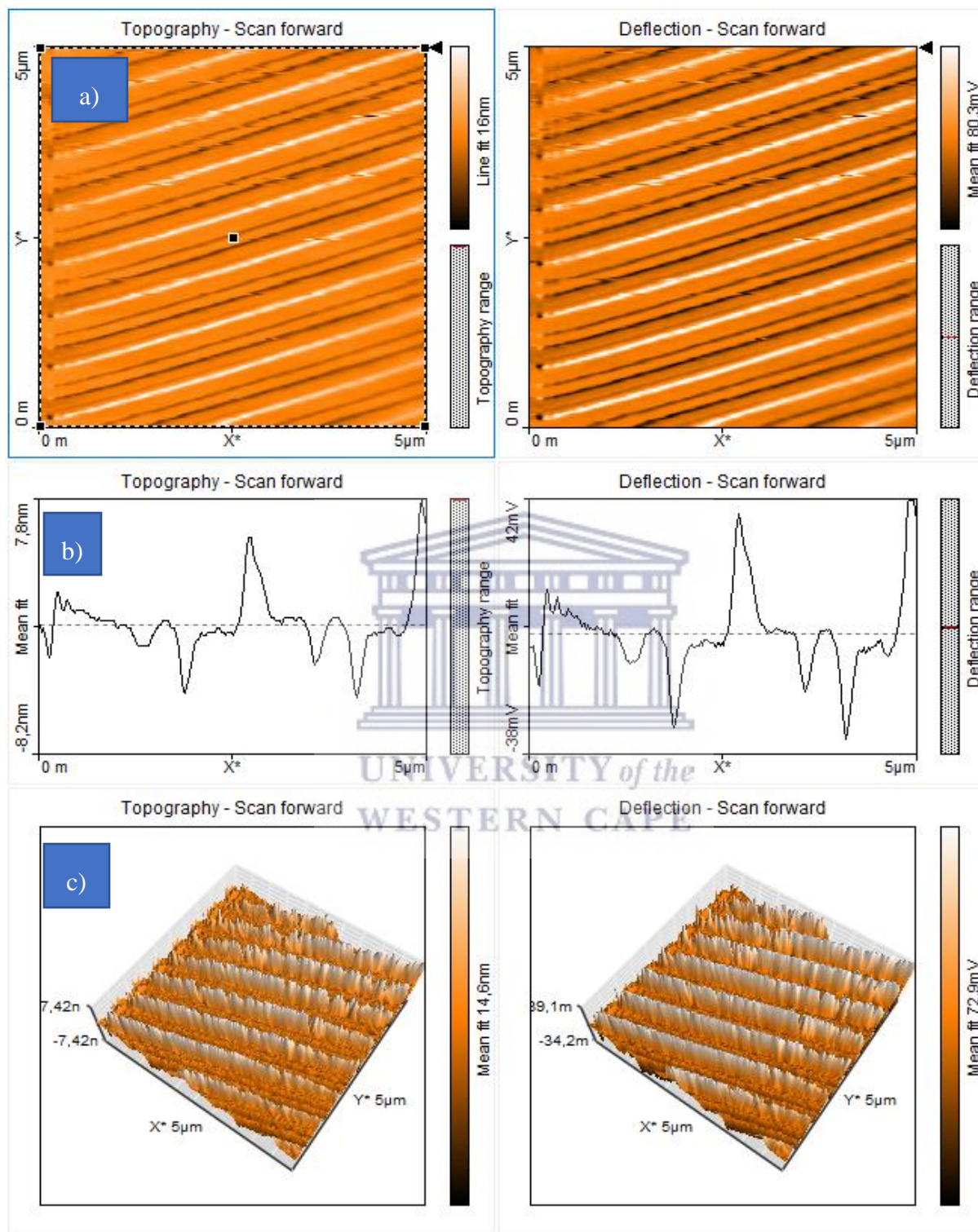
Figure 5.4: AFM a) 2D, b) line and c) 3-D topography and deflection images of SbO.
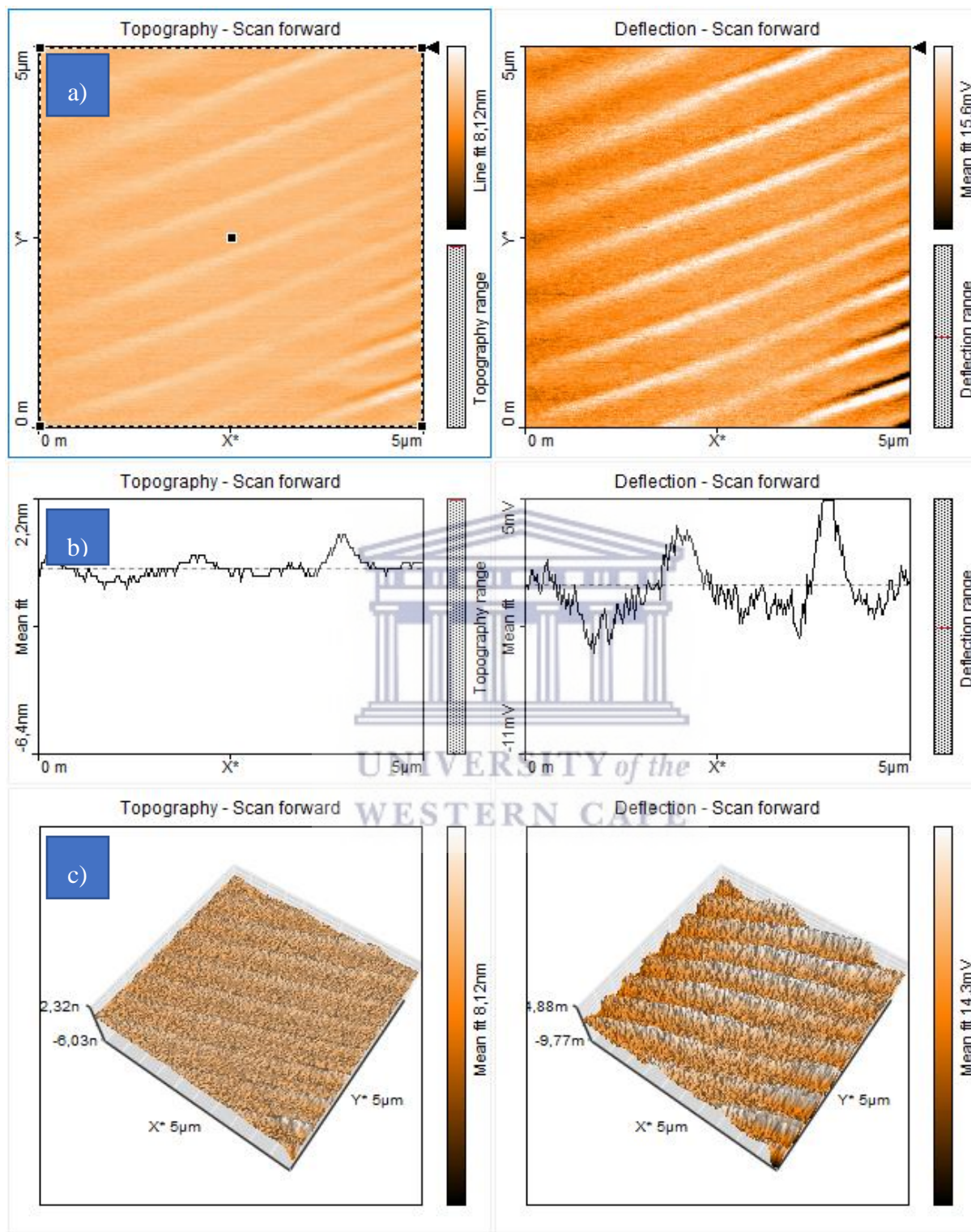
Figure 5.5: AFM a) 2D, b) line and c) 3-D topography and deflection images of SbO-G.

5.2.4 Spectroscopical studies

5.2.4.1 Energy-dispersive X-ray spectroscopy (EDS)

The creation of SbO and SbO-G nanoparticles has been verified using EDS. Figure 5.6 and Figure 5.7 shows EDS focused on several spectrum areas and accompanying peaks. The presence of Sb and O in SbO is confirmed by EDS analysis. In SbO-G, there's Sb, O, and C elements present. In the inset, the quantity of each element measured in atom per cent is displayed. The result shows that the composite has a considerable quantity of graphene, which will improve the composite's stability and limit any volume expansion caused by antimony.
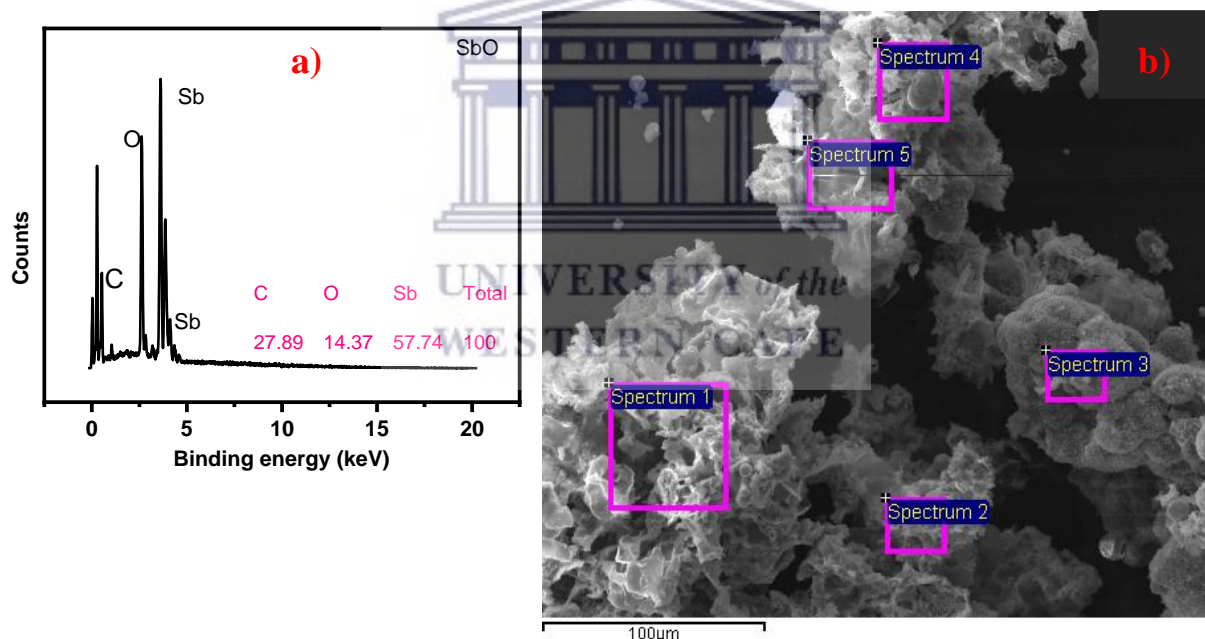
Figure 5.6: EDS spectrum a) and SEM image b) of SbO . Inset in (a) is the percentage elemental composition. The labels in the SEM image (b) represent sampling points for the EDS.
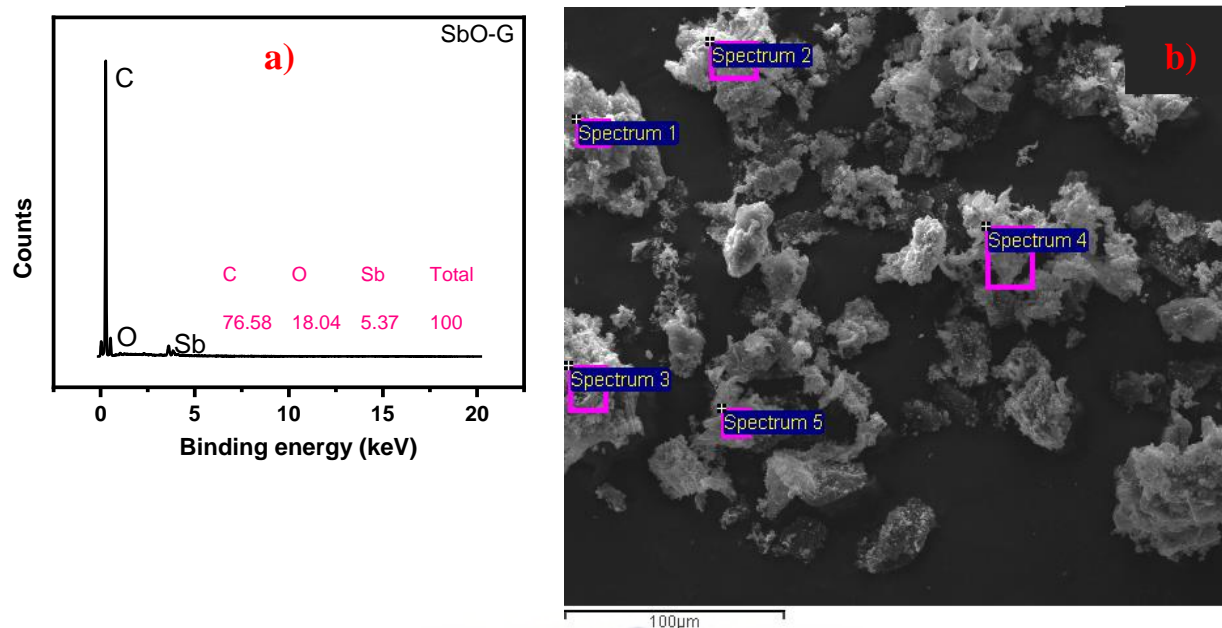
Figure 5.7: EDS spectrum a) and SEM image b) of SbO-G. Inset in (a) is the percentage elemental composition. The labels in the SEM image (b) represent sampling points for the EDS.

5.2.4.2 X-ray powder diffraction (XRD)

The crystal structure of SbO-G was investigated using XRD analysis. The XRD spectrum of SbO and SbO-G are shown in Figure 5.8 a. SbO and SbO-G were indexed into an orthorhombic structure. Space group (Pnnm (58)).; JCPD card No 2_34-0340), with lattice parameter a = 5.95140 Å and c = 6.67430 Å. The sample shows diffraction peaks at 2θ = 28.59º, 39.98º, 41.84º 51.5º2, 68.52º, 65.88º and 75.26º which belongs to the (012), (104), (110), (015), (212), (024), (116), (122) and (214) phase of SbO_2 for both SbO and SbO-G samples. Both samples seem to have the same phases, however, with the addition of graphene, the peak intensity increased and broadened in SbO-G. For example, when comparing the intensity of SbO and SbO-G XRD diffraction peaks, the

(012) plane in the XRD spectrum had the highest diffraction peak intensity. The (012) plane of SbO was situated at 28.59°, and the (002) plane of graphene was also located at 28.54°. The coincidence of the two crystal surface diffraction peaks may be the cause of the increase in the intensity of (012) diffraction peaks in the SbO-G XRD spectrum [9]. As shown in Figure 5.8, the crystal plane values of SbO-G (002) are 2θ = 28.59 and d_{012}= 3.12, respectively, compared to those of SbO-G, which are 2θ = 28.4 and d_{012} = 3.29. The interplanar spacing of SbO-G (3.29) is slightly higher than that of SbO (3.12) due to the retention of a few functional groups and curved surface structures following reduction. The most intense peak in SbO-G composite (2θ = 28.54º) is slightly shifted to a lower angle as compared to pristine SbO nanoparticle (2θ = 28.59º) indicating the enlargement in SbO interlayers due to defects/embedding of the graphene nanoparticles. A clear shift in the interlayer spacing between SbO and SbO-G indicates that the addition of graphene can effectively expand the interlayer spacing of the composite, which will facilitate the diffusion and transport of electrolyte ions during the charge/discharge process [15].

The XRD data also suggests that the possible crystal structure of the SbO is orthorhombic this was achieved through estimated refinement and simulation with VESTA software as shown in figures 5.11- figure 5.14 below. Crystal size was also estimated using the Debye-Scherer formula for the most intense peaks in the XRD patterns. The size was an average of ~46.63 nm and ~ 40.3 nm for SbO and SbO-G respectively confirming the smaller crystal size in RuO-G as estimated by the SEM and TEM analysis.
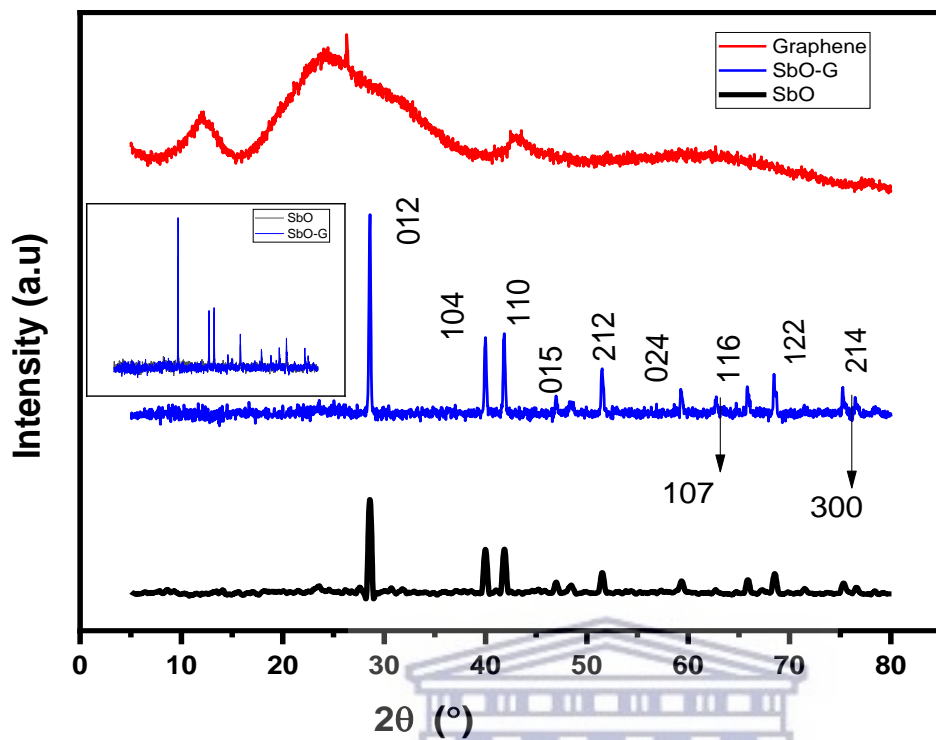
Figure 5.8: XRD analysis of SbO and SbO-G overlayed with graphene. The inset is the spectra

of SbO and SbO-G alone comparing their intensity.
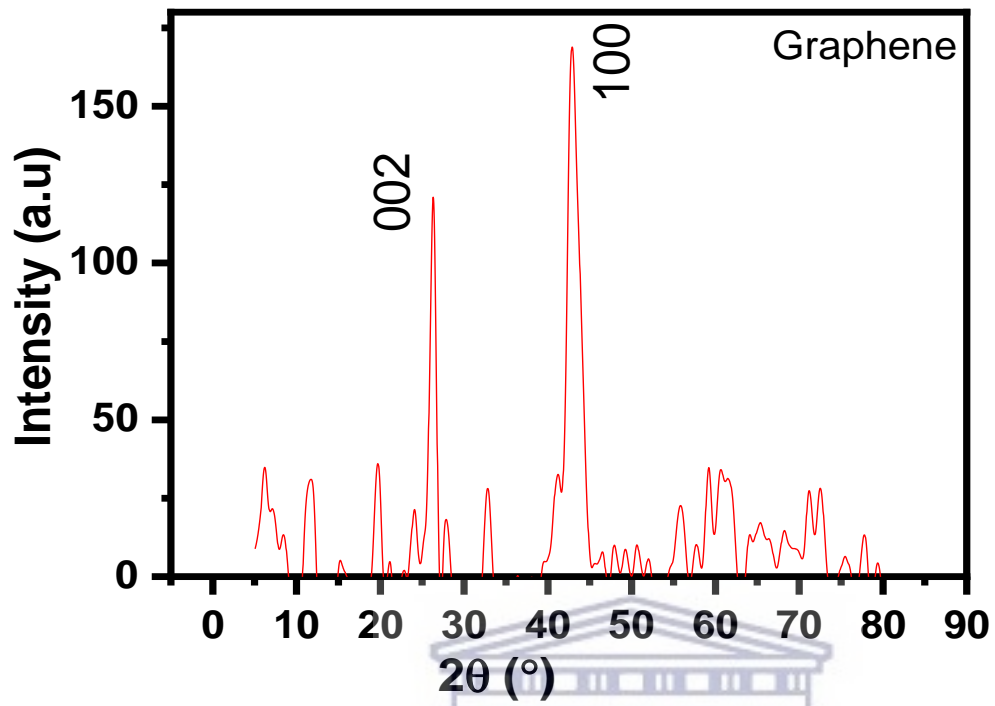
Figure 5.9: XRD analysis of graphene
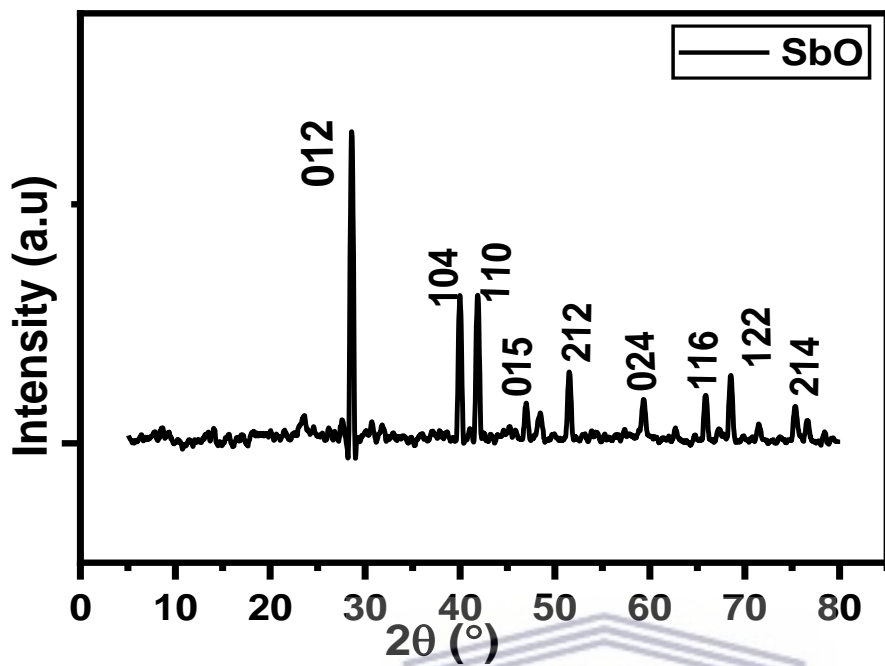
Figure 5.10: XRD analysis of SbO.

Blue - O

Red - Sb
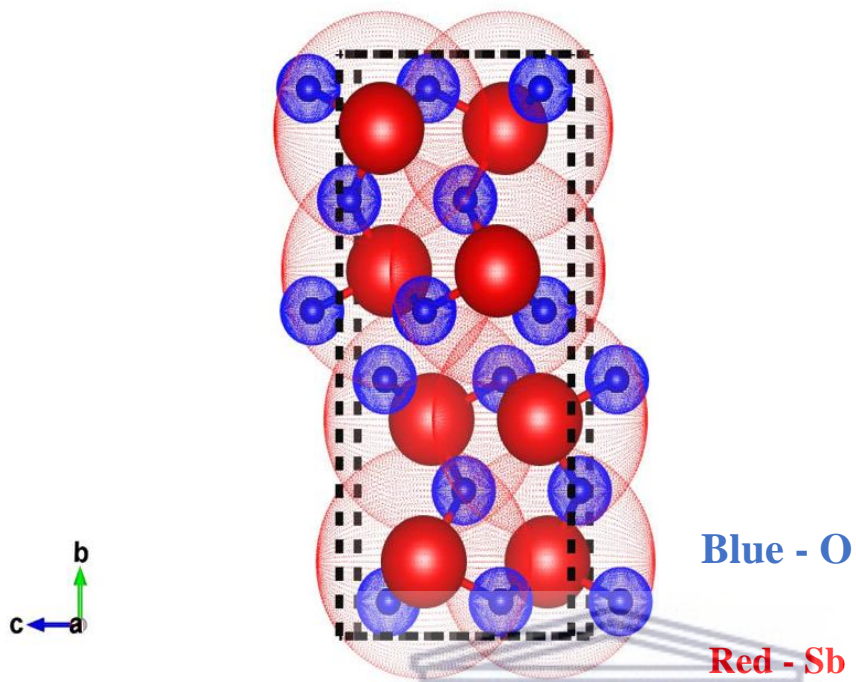
Figure 5.11: Crystal structure models of SbO simulated from VESTA from XRD data, an

Orthorohombic unit cell of SbO with reduced spheres.

Blue - O

Red - Sb
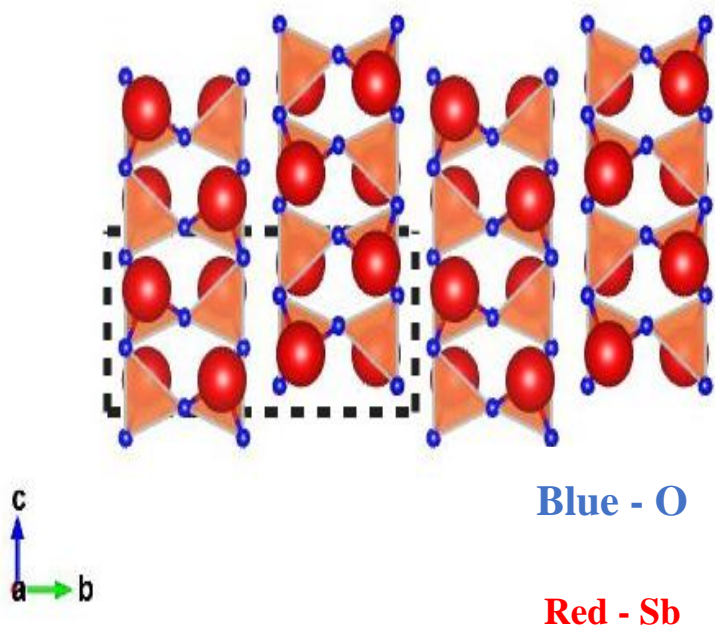
Figure 5.12: Closely packed orthorhombic structure in a polyhedron with the Sb atom located at the middle of the polyhedron. The stacking sequence of the closely packed layer is 'ABAB'

Blue - O
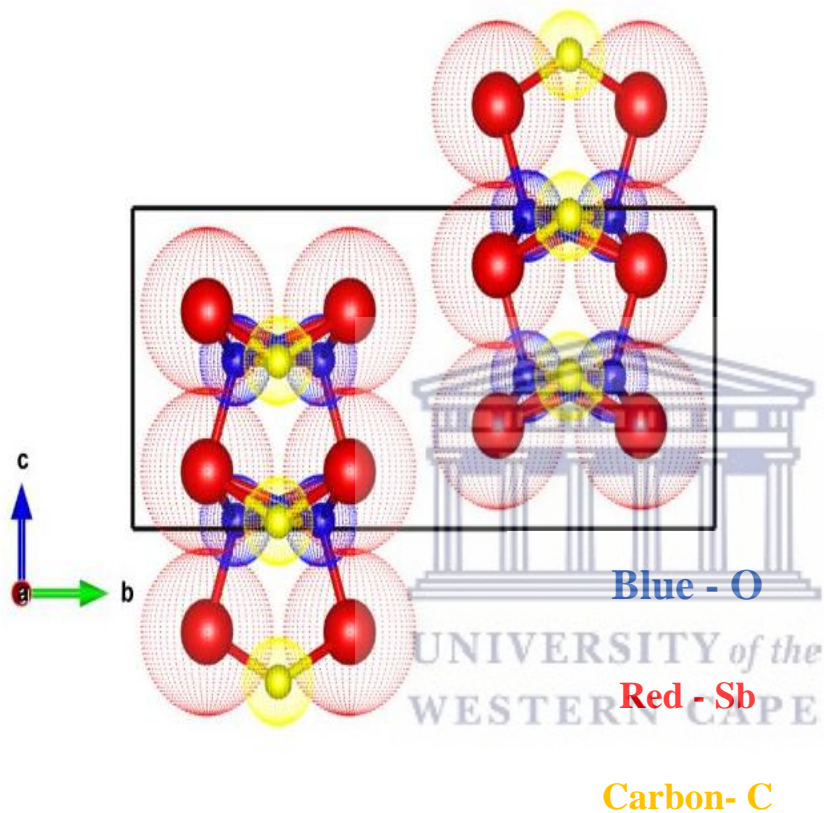
Red - Sb

Carbon- C

Figure 5.13: Crystal structure models of SbO-G simulated from VESTA from XRD data, an Orthorhombic unit cell with reduced spheres.

Blue - O

Red - Sb

Carbon- C
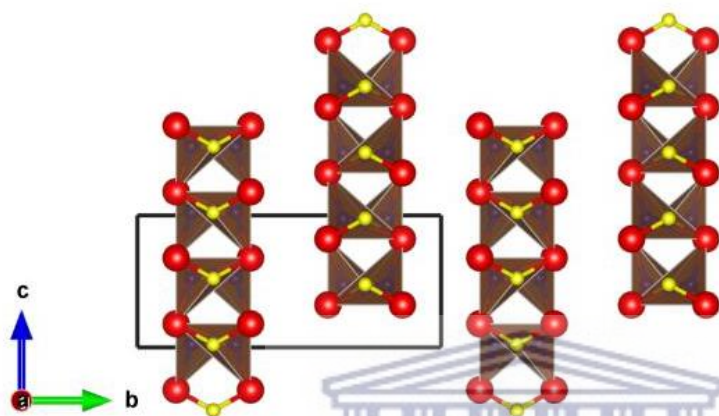
Figure 5.14: Closely packed orthorohmbic structure of SbO-G in a polyhedral with the Sb atom located at the middle of the polyhedron. The stacking sequence of the closely packed layer is 'ABAB'

5.2.4.3 Fourier transform infra-red spectroscopy (FTIR)

The FTIR absorption spectra of SbO, and SbO-G in the 4000-400 cm^{-1} region is shown in Figure 5.15. The investigation was carried out to determine the presence of bending or stretching vibrations in the synthesized SbO and SbO-G. The distinctive OH stretch is confirmed by the broadband at 3669 cm^{-1} in the SbO spectrum. The vibration of molecular water's hydroxyl groups and the stretching vibration of the peroxo group induce the absorption band around 1647, and

1067 cm^{-1}. The Sb-O stretching is visible in the SbO spectrum at 468, 550 and 790 cm^{-1}[16]. In the FTIR absorption spectrum of SbO-G, distinctive OH stretch is confirmed by the vibrational band at 3790 cm^{-1} and broadband at 3385 cm^{-1} in the spectrum. The bending and stretching of C-H, C=C=C, C-O, C-C group induce the absorption band around 3000 -1000 cm^{-1}. The vibrational band at 512 cm^{-1} is characterized by the presence of SbO, whereas the tiny band at 776 cm^{-1} is induced by the asymmetric stretch of SbO. The shift in the band position and intensity for SbO-G in comparison to the pristine materials plus the presence of the bending and stretching of the graphitic bonds in the SbO-G spectrum indicates the creation of a new structural material. All distinct functional groups present in the samples are shown in Table 5-2.
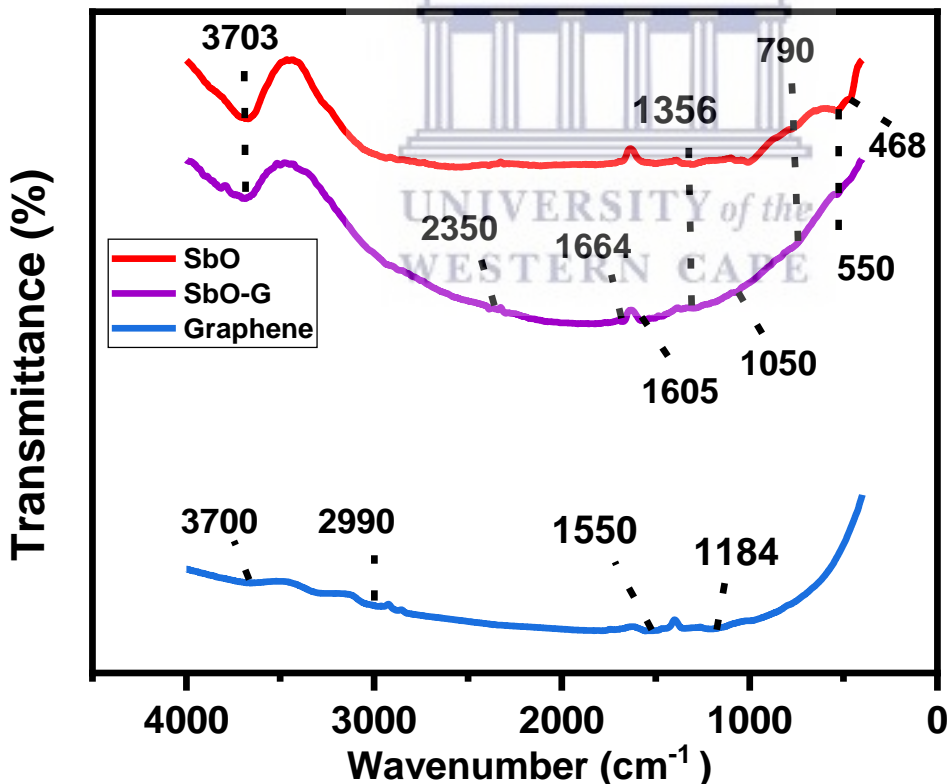
Figure 5.15: FTIR spectra of SbO and SbO-G overlayed on graphene.
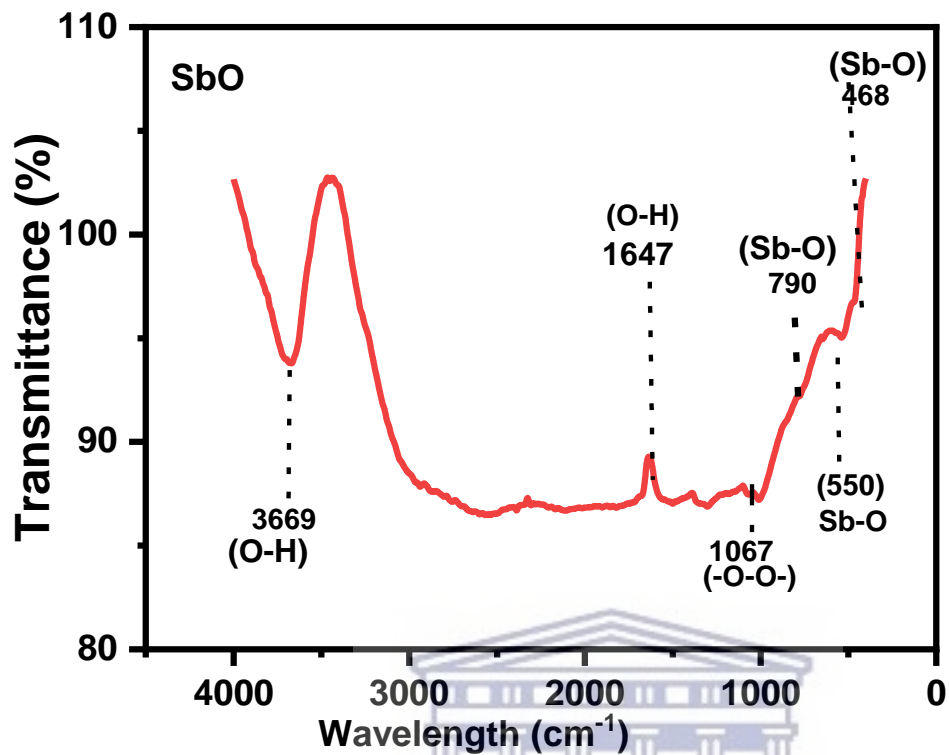
Figure 5.16: FTIR spectrum of SbO.
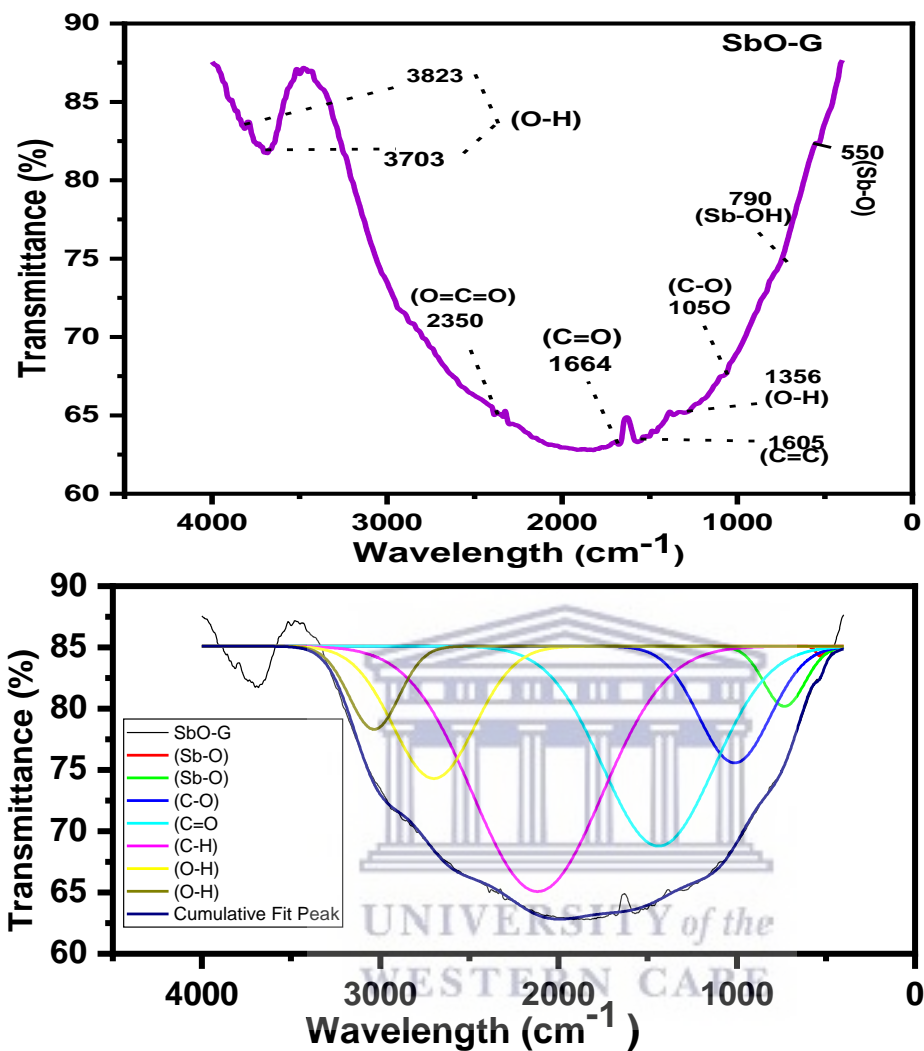
Figure 5.17: FTIR spectra of SbO-G alone, deconvoluted absorption bands SbO-G showing the

presence of both SbO related bands and carbon-based bands.

Table 5-2: Functional groups and vibrational bands of SbO and SbO-G.

Functional group	Material/
	wavenumber (cm^{-1})

	SbO	SbO-G
O-H	3669	3703
C-H		2350
C=O		1664
-O-O-	1067	
C-O		1050
Sb-O	550	512

5.2.4.4   X-ray photoelectron spectroscopy

XPS is a useful supplementary technique for determining the oxidation states and stoichiometry

of SbO. In Figure 5.18, the elements Sb and O were detected in the SbO nanomaterial. The high-

resolution O1s spectrum of SbO was split into three peaks at 540, 532 and 531 eV. The peaks at

540 and 531 eV can be attributed to Sb_2O_5/Sb_2O_3, implying that the SbO sample contains a

considerable quantity of Sb_2 [17]. The MW synthesis successfully introduced antimony atoms into

the graphene matrix, according to Figure 5.19. The high-resolution Sb 3d +O1s spectrum of SbO-

G (Figure 5.19a) was split into six peaks at 540, 533, 531, and 530 eV. The peaks at 540 and 530

eV can be attributed to Sb_2O_5/Sb_2O_3, implying that the SbO-G samples contain Sb_2 in a large

amount at its outer surface. C=O and C-O can be ascribed to the 533 and 531 eV peaks,

respectively. The presence of Sb_2O_5 is suggested by the high peaks at 540 and 530 eV. The

presence of carbon-oxygen components, such as C–O, C=O, and O–C=O, was demonstrated by

the presence of peaks at 287, 285, and 284 eV in the C1s spectrum (Figure 5.19). When Sb_3 d3 of SbO-G is compared to SbO (Figure 5.20), a change to lower binding energy is seen, implying a larger electron density at Sb_3 sites in the SbO-G sample [18][19].
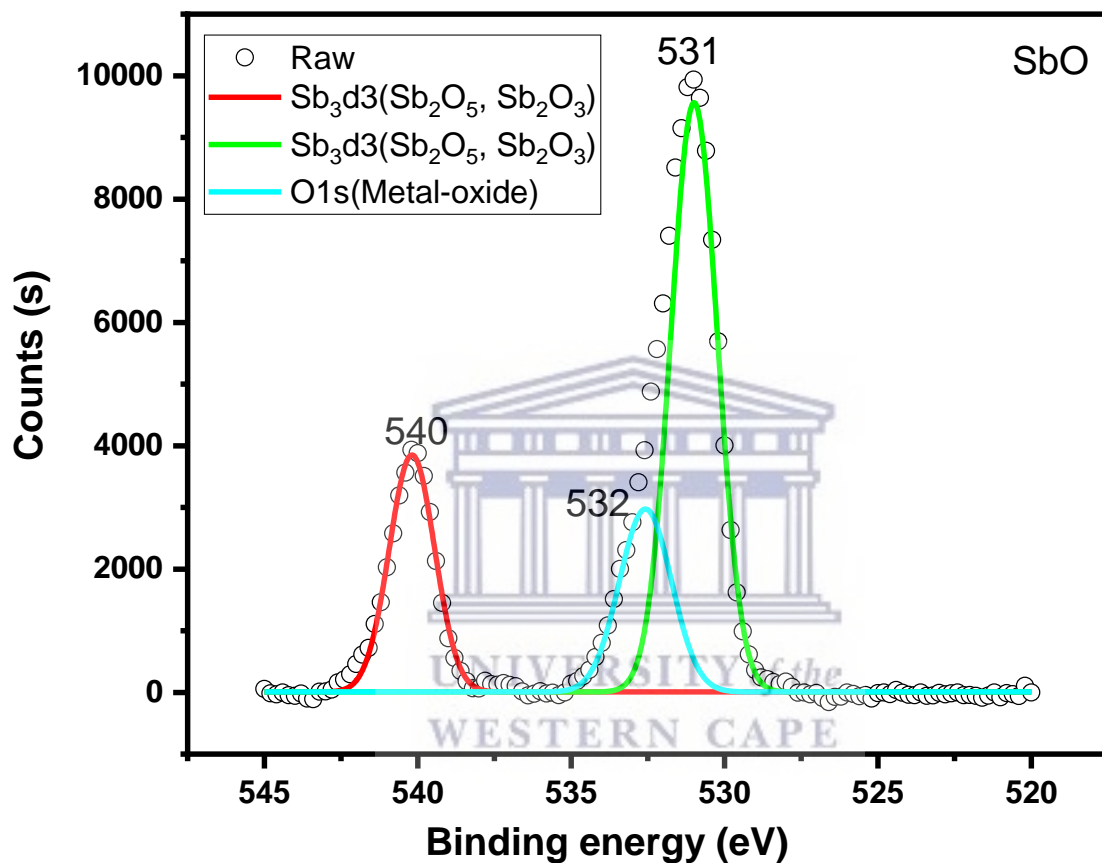
Figure 5.18: XPS spectrum of SbO; Sb 3d+O1s scan.
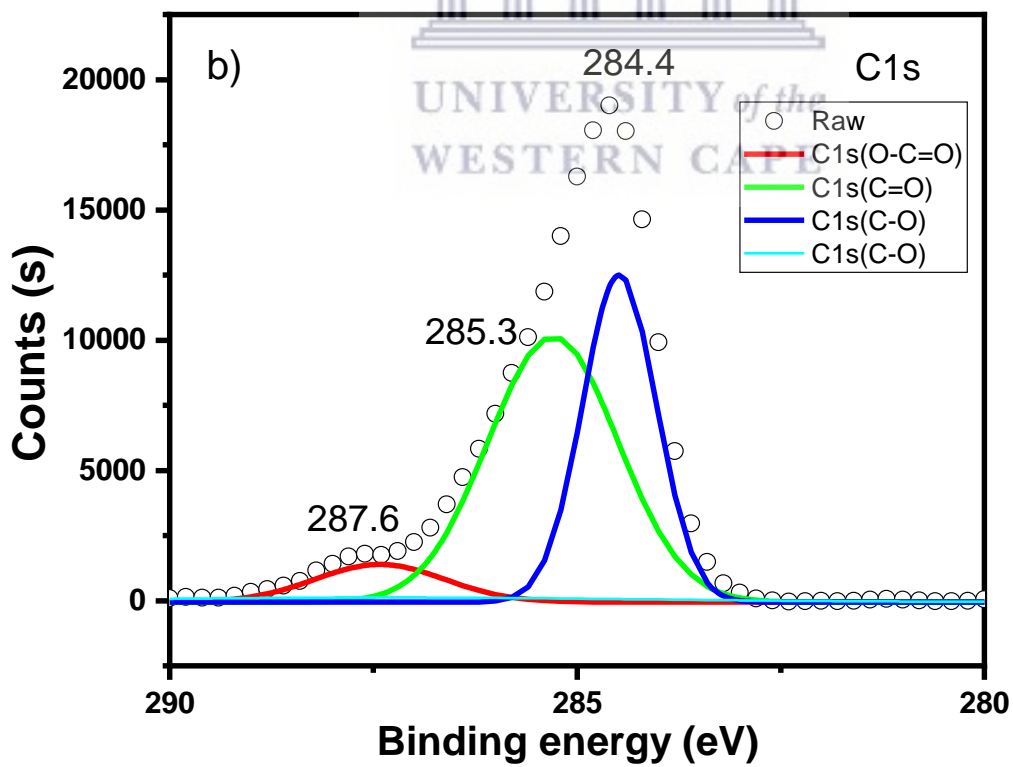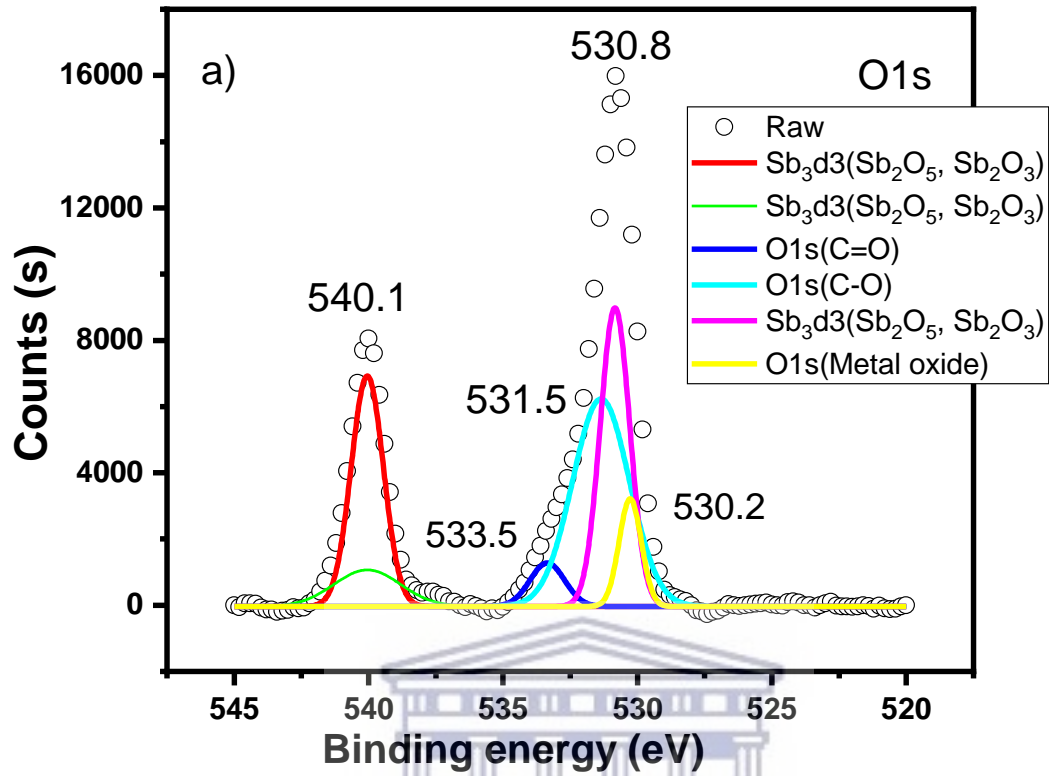
Figure 5.19: XPS spectrum of SbO-G; a) Sb 3d+O1s, b) C1s scan.
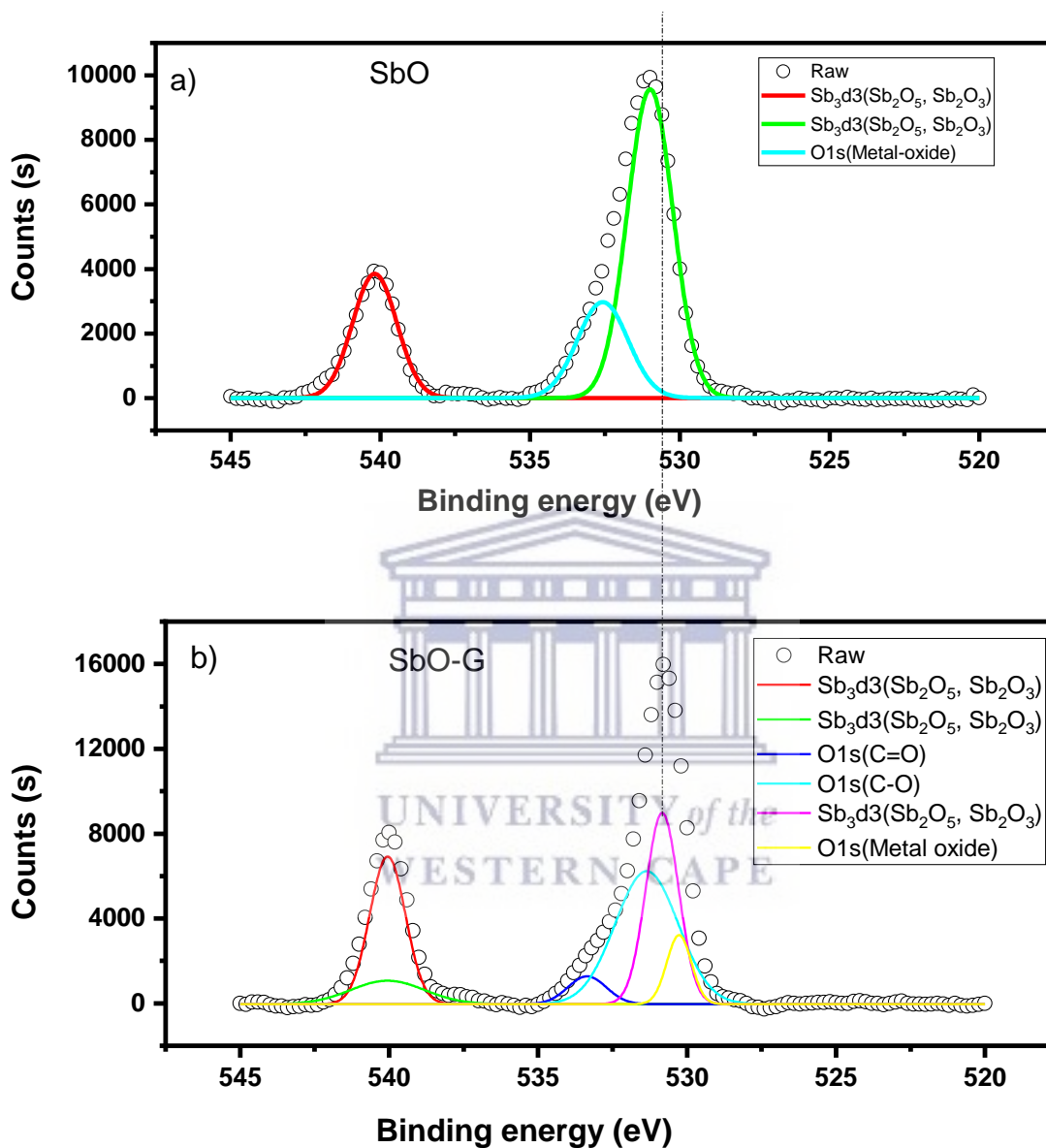
Figure 5.20: XPS spectrum of SbO and SbO-G showing the Sb$_3$ d3 position.

5.2.4.5   Raman spectroscopy

The SbO and SbO-G materials were further characterized using Raman spectroscopy, which provided the structural fingerprint by which antimony oxide is detected. SbO and SbO-G revealed a visible peak at 87.6 cm^{-1} that belonged to F_{2g} Sb_2O_3 in the Raman spectra Figure 5.21 [20]. The typical E_g(113.1 cm^{-1}) and A_{1g} (153.2 cm^{-1}) belonging to the in-plane and out-of-plane vibrational modes of Sb-O was also identified, [21][22] [11] confirming that SbO nanoparticles have been obtained after reduction. Additional peaks related to antimony oxides (Sb_2O_4) were detected at 412.96 and 549.47 cm^{-1}, confirming the production of microcrystalline Sb_2O_4 [23]. The Raman spectra of SbO-G were not different from those of pure SbO, but the typical peaks of carbon D (2) and G (5) bands were present, showing that the in-situ reductions of SbO and GO to SbO-G was successful using microwave radiation [24]. The G band appears in the SbO because of the carbon glue used to adhere the samples to the SEM stubs. The graphene in SbO-G was shown to be less with less defect than pristine graphene, based on the ID/IG ratio and the very low intensity of D. According to the ID/IG ratio and also the reduced D, band SbO-G resulted to be less defected than graphene [25]. This is obvious in the TEM results.
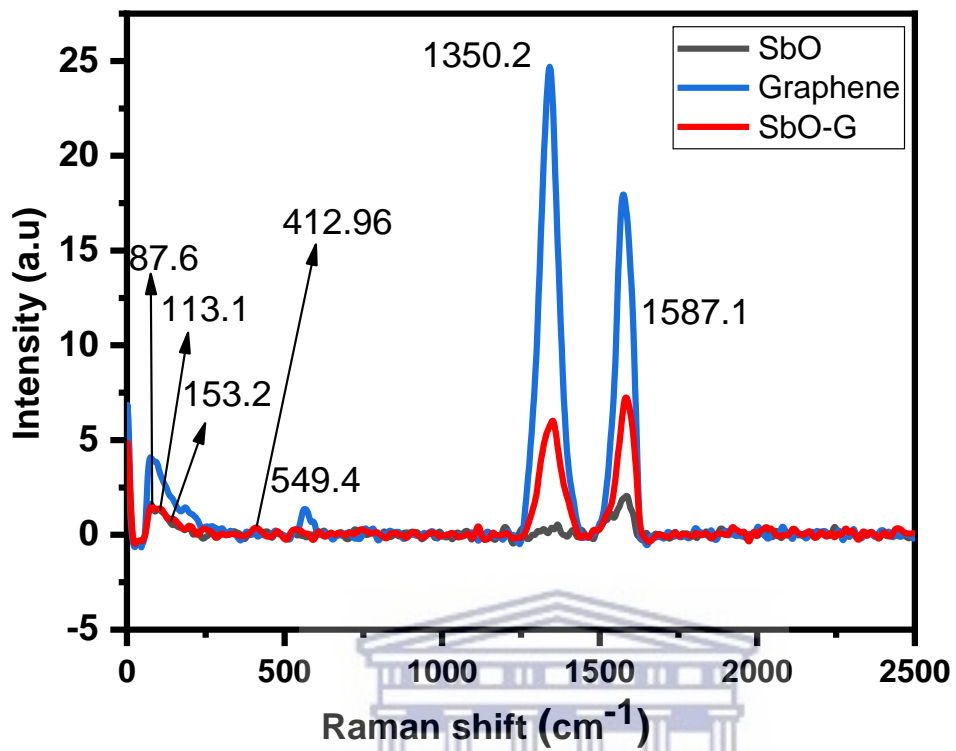
Figure 5.21: Raman spectrum of SbO and SbO-G overlayed on graphene.
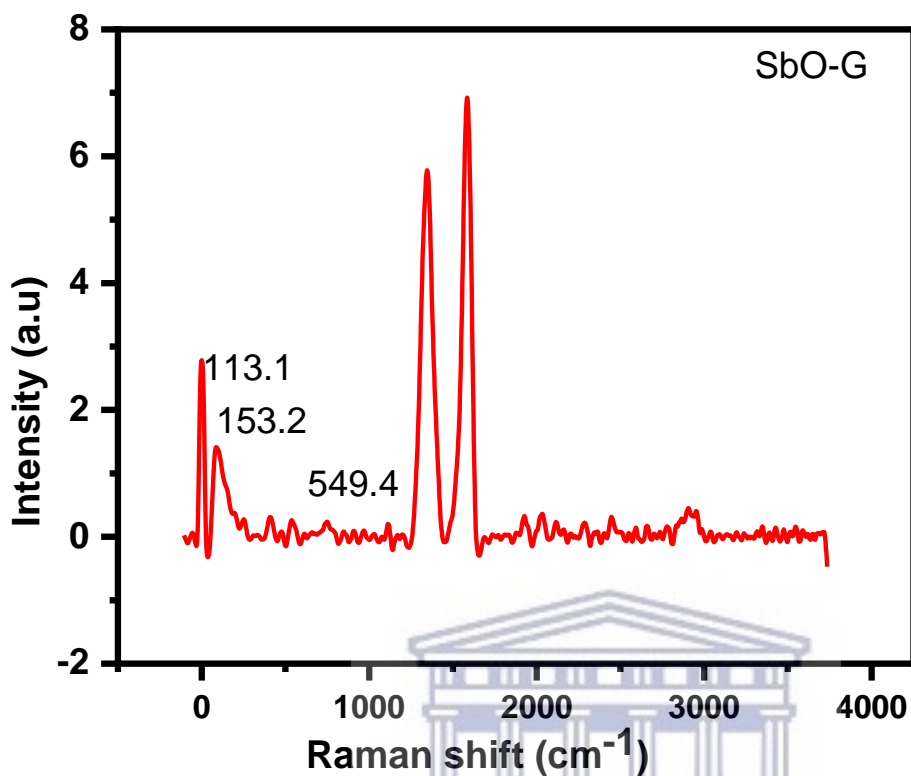
Figure 5.22: Raman spectrum of SbO-G alone defining the modes clearly.

5.2.4.6 Solid-state nuclear magnetic resonance spectroscopy (NMR)

Figure 5.23 shows the NMR spectra of SbO-G and graphene. The carbon environment of pure graphene was compared to that of graphene samples with SbO-G. The prominent peak at 117 ppm, which belongs to graphitic sp^2 carbon as seen in graphene, shifted to 143 ppm, while a shoulder peak can be seen at 169 ppm which when deconvoluted (the inset) reveals a broad peak with FWHM- 34 ppm, indicating that the chemical environment of carbon must have been influenced by the interaction of SbO nanoparticles with graphene [26].
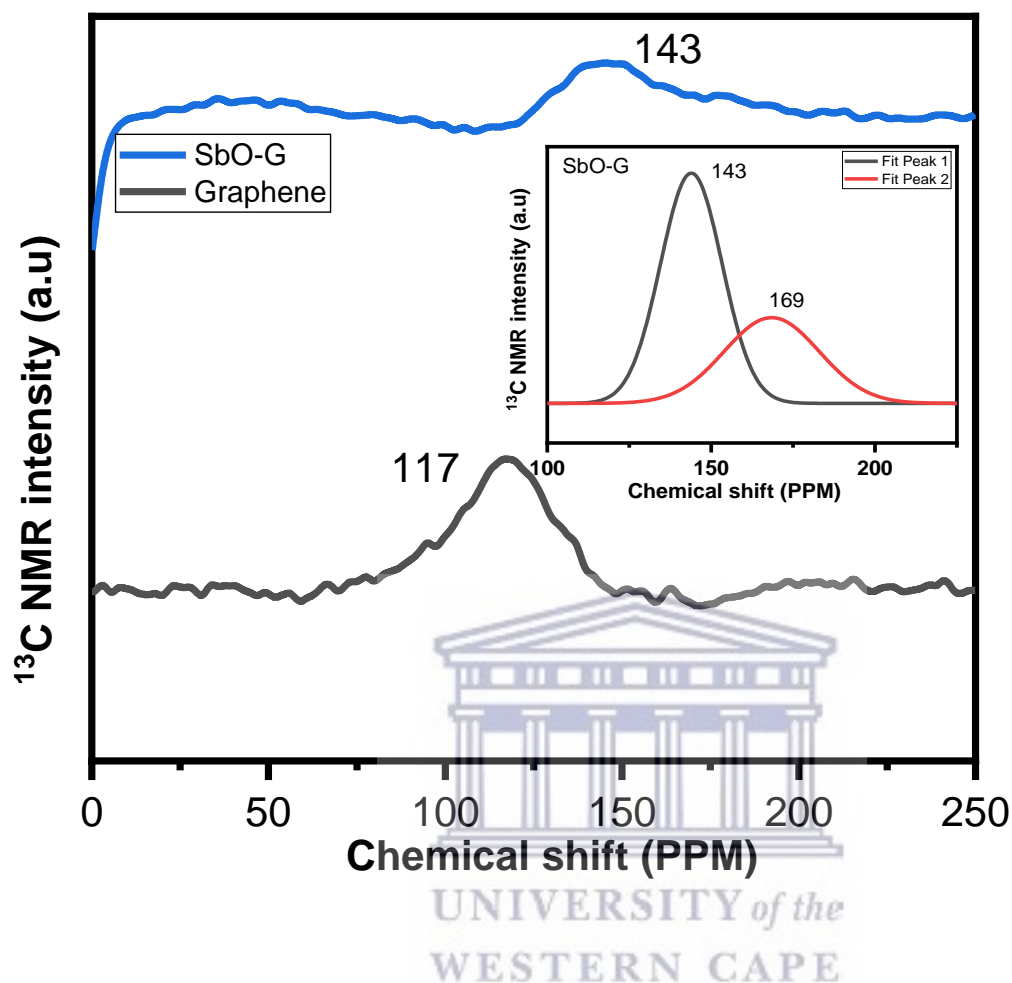
Figure 5.23: NMR results spectra of graphene and SbO-G the inset is the deconvoluted 126 ppm peak of SbO-G.

5.2.4.7   UV-vis spectroscopy

Figure 5.24 shows the UV-vis absorption spectra of SbO and SbO-G. The UV-vis absorption spectra revealed that SbO and SbO-G have a broad UV-vis absorption range, with the highest absorption at 206 nm. The absorption intensity of SbO-G is higher than that of pure SbO, which may be attributed to the sum of the absorption for graphene and SbO [27][28], indicating that the SbO-G nanoparticle was successfully synthesized. With the addition of graphene, the curve exhibits a

more evident exponential decay, indicating that the SbO-G nanoparticles have increased dispersion capacities. Using the Taucs plot from origin software (the inset a and b), the band gaps of SbO and SbO-G were estimated to be 0.46 and 0.34 eV, respectively [31]. When compared to pure SbO nanoparticles, the bandgap of the SbO-G composite is lowered due to the development of Sb-O-C bonds [32][33]. The charge transmission is facilitated by the link that exists between Sb and C. It is worth mentioning that the lower bandgap value found in this study could be attributed to the enhanced crystallinity of the nanoparticles [34].
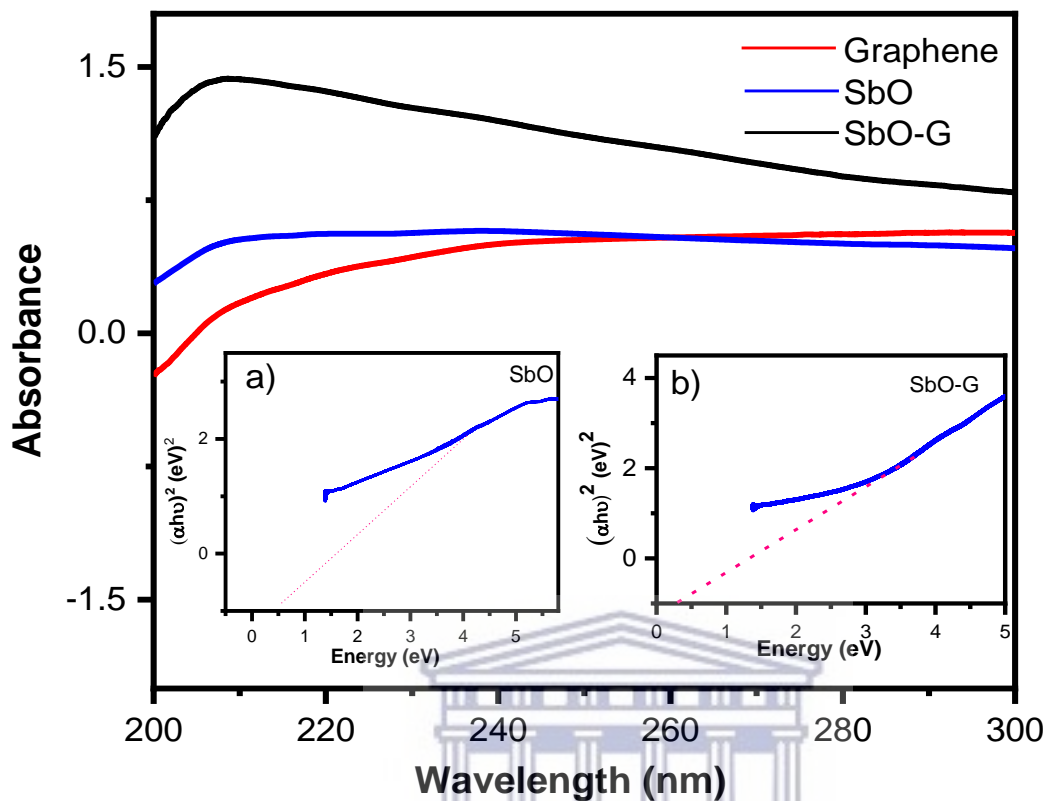
Figure 5.24: a) UV spectra of SbO and SbO-G overlayed with graphene (b,c) Taucs plot for SbO

and SbO-G respectively.

5.2.4.8 Photoluminescence spectroscopy

The photoluminescence spectra (PL) were obtained to evaluate the photo-excited electron

transport in SbO and SbO-G composites. The PL emission spectra of SbO and SbO-G hybrids are

shown in Figure 5.25. At room temperature, the dispersed sample in ethanol solution was excited

at 210 nm and measured. The PL spectra of SbO has a green-blue spectrum with the highest

intensity at 367 nm and SbO-G shows higher intensity than SbO [29]. The results show that the

recombination capability rate of electrons, as well as holes, is strengthened considerably in the

SbO-G composite [30]. The bandgaps of the samples can be calculated from the PL wavelengths using

$$Eg = hc\lambda \hspace{8cm} 5\text{-}1$$

where, h is the Planck constant; c is the velocity of light, and λ is the wavelength of the absorption peak [31]. The bandgap for SbO was 3.31 eV while that of SbO-G was 3.30 eV. The reduced bandgap in the composite will facilitate the transfer of charge. Therefore RuO-G is expected to have a better electrochemical performance.
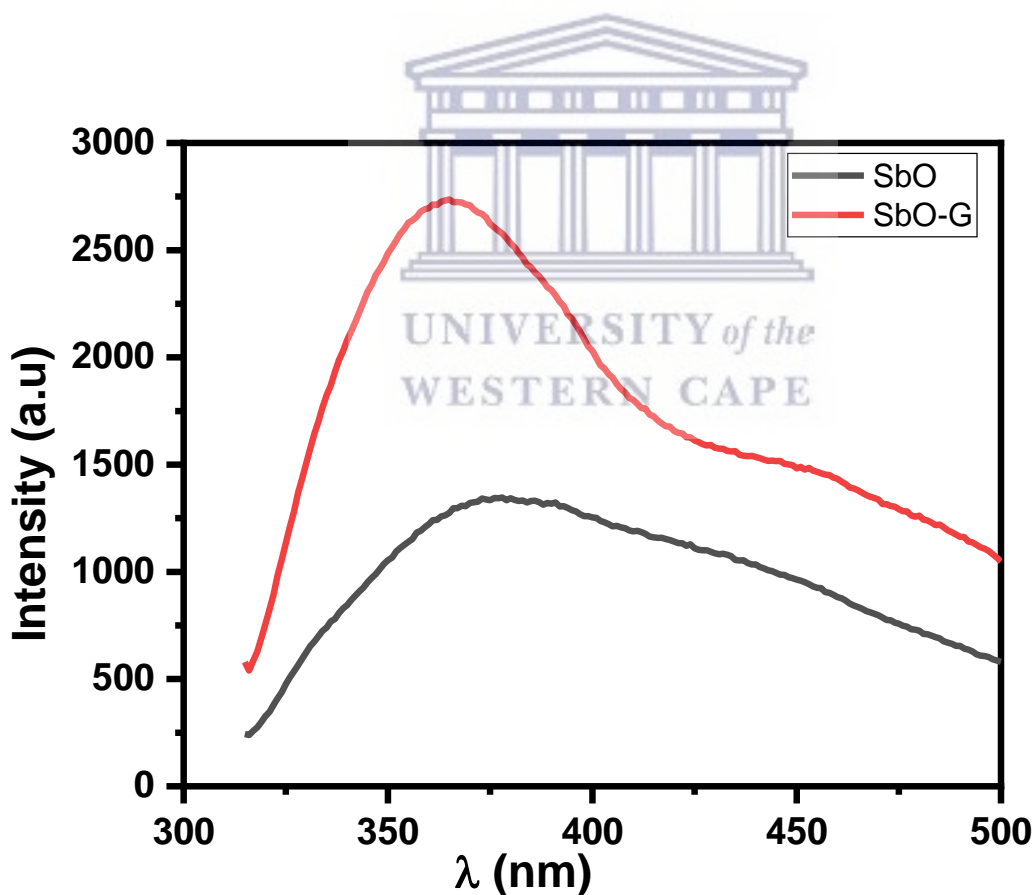
Figure 5.25: The PL emission spectra of SbO and SbO-G.

5.2.5 Electrochemical studies

5.2.5.1   Cyclic voltammetry

Cyclic voltammetry was used to investigate the SbO and SbO-G compounds in a 1 M Li_2SO_4 electrolyte. At scan rates ranging from 10 to 100 mV s^{-1}, capacitive currents were observed between 0.0 and 0.6 V vs. Ag/AgCl electrode. Both materials showed a steady increase in cathodic currents as potential rises with no pseudocapacitive/redox peak (Figure 5.26 and Figure 5.27). This demonstrates superior capacitive behaviour, resulting in increased power [32]. As the scan rate increases, the capacitive currents in the cyclic voltammograms indicate a substantial increase. This means the charge storage mechanism is capacitive and the process is reversible electrochemically [33]. Voltammograms of SbO have a nearly rectangular shape, resembling the behaviour of a perfect EDLC. According to Trasitti *et al.* [34], the charge storage mechanism of metal oxide is divided into outer and inner site charge contributions [35]. As a result, at a high scan rate, when the inner sites are all exonerated from the capacitance contribution, the charge/discharge occurs so quickly at the outer site, giving rise to the rectangular shape seen in the carbon voltamogram. Secondly, if the material is porous and the inner sites are easily accessible, charge and discharge will occur at a rapid rate, resulting in a rectangular shape [36]. Therefore, the voltammogram of SbO suggest high porosity of the material. SbO-G voltammogram shows a slight deviation from perfect EDLC behaviour. The quasi-rectangular voltammogram of the SbO -G materials demonstrates that EDLC and the pseudocapacitance charge storage mechanism both play a role. The deviation of the voltammogram from the ideal rectangular form increased as the voltage scan rate increased. This could be due to the

electrode's electrochemical polarization. The pseudocapacitance contribution and the electrochemical polarization of the electrode are caused by the numerous functional groups present in the SbO-G as shown in the FTIR [37]. The specific capacitance of the three materials was calculated from the equation below:

$$C_{sp} = \frac{1}{2mv \triangle V} \int_{-v}^{+v} Idv \; C_{sp} = \frac{1}{2m??V} \int_{-v}^{+v} Idv \qquad \text{5-2}$$

where m is the active mass of the electrode (g), v is the scan rate (V s^{-1}), $\triangle$V is the potential window in (V) and $\int_{-v}^{+v} Idv$ is the charge obtained from the integrated area of the voltammogram. The SbO-G showed a better electrochemical performance with a specific capacitance 37.58 F g^{-1} at 10 mV s^{-1} and up to 11.41 F g^{-1} at 100 mV s^{-1}. The values were 16.80 F g^{-1} at 10 mV s^{-1} and 6.32 F g^{-1} at 100 mV s^{-1} for SbO. The specific capacitance values are plotted against potential sweep rates as shown in Figure 5.27 (c). The specific capacitance values for both materials gradually reduced when the voltage scan rate was increased as shown in Table 5-3. This is owing to the short time interval, which precludes the contribution of the electrode's inner surfaces. [38]. The CV curves of SbO and SbO-G are shown in Figure 5.28 at a scan rate of 40 mV s^{-1}. The area under the CV curve of the SbO-G is greater than the area of the SbO. Because the average value of the area under the CV curves is directly related to the capacitance value, this finding demonstrated that SbO-G had enhanced capacitive behavior. The greater the area under the CV curves, the greater the amount of charge held by the electrode material. The high capacitance of the SbO-G is mostly owing to the composite's large specific surface area and the high conductivity of graphene [39].
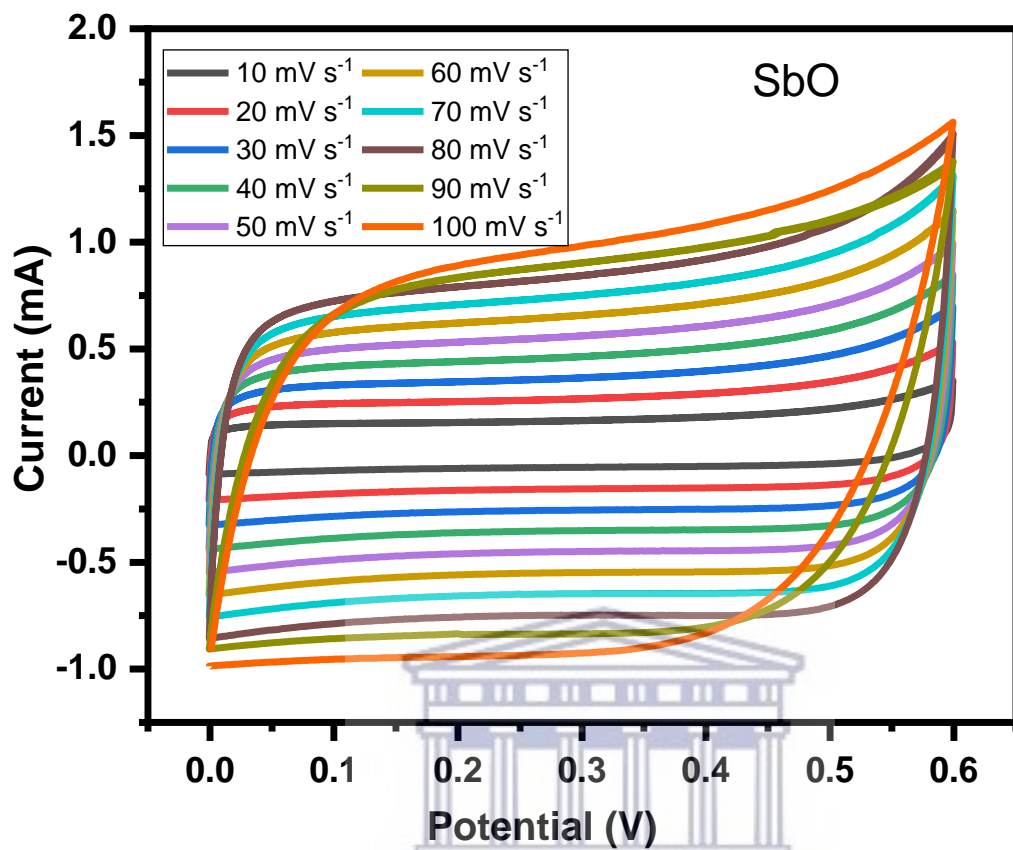
Figure 5.26: CV plot of SbO at different scan rates.
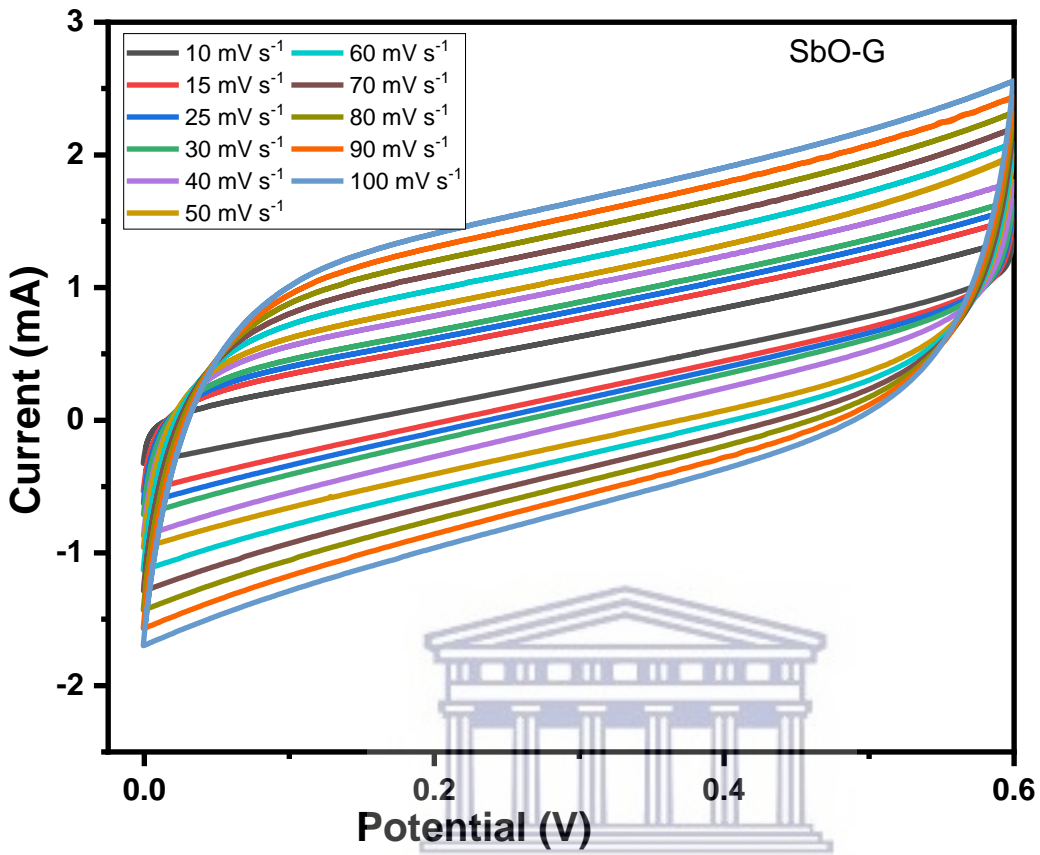
Figure 5.27: CV plots of SbO-G at different scan rates.
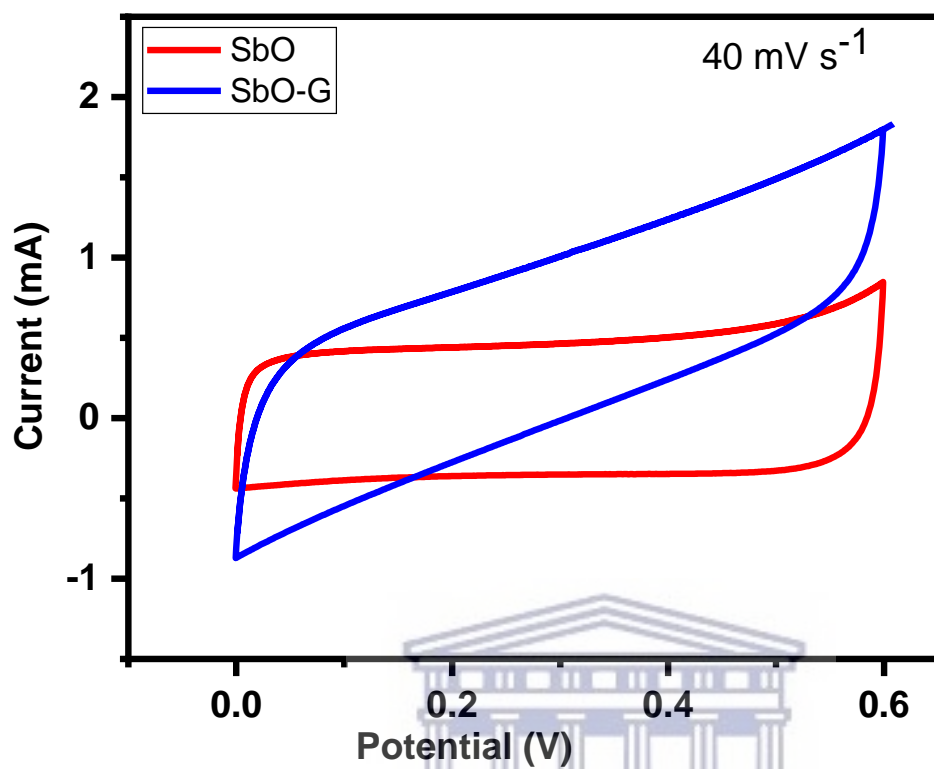
Figure 5.28: CV plots of SbO and SbO-G at 40 mV s^{-1}.
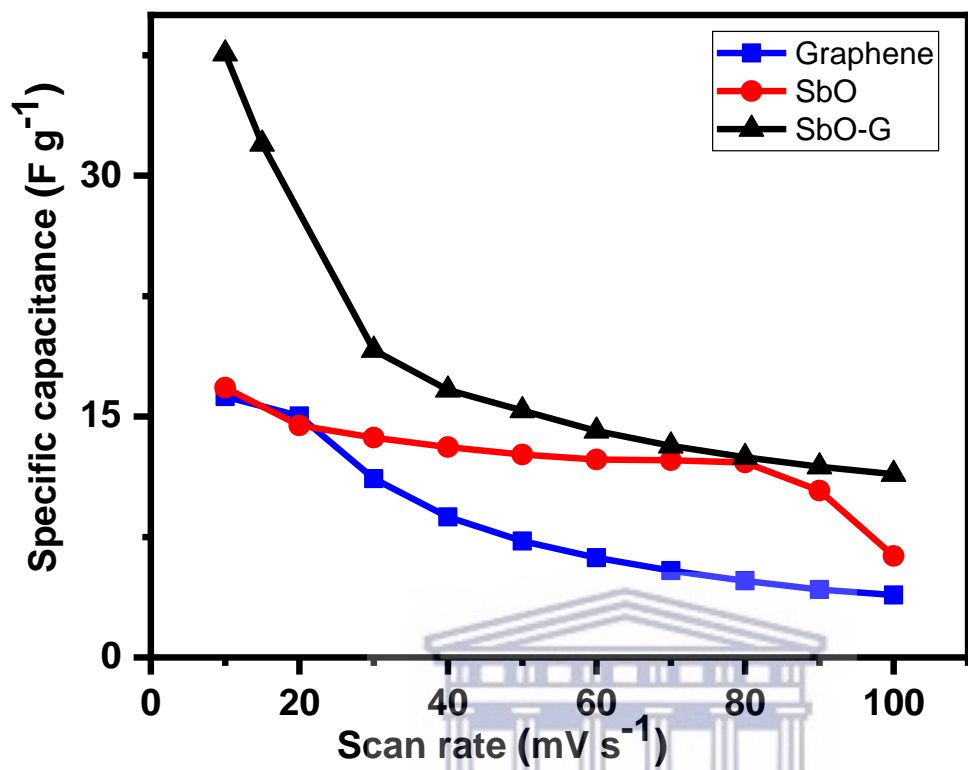
Figure 5.29: Plot showing the relationship between Cs and scan rate for SbO and SbO-G.

Table 5-3: The capacitance of RuO and RuO-G at different scan rates

Scan rates (mV s^{-1})	Capacitance (F g^{-1})	
	SbO	SbO-G
10	16.80	37.58
30	13.69	19.14
40	13.10	16.65
50	12.63	15.37
60	12.32	14.10
70	12.28	13.17
80	12.13	12.46
90	10.38	11.88
100	6.32	11.41

5.2.5.2 Galvanostatic charge discharge

The performance of SbO and SbO-G electrodes was investigated at current densities of 0.1, 0.2, 0.4, 0.5, 0.6, 0.8, 1, 2 and 5 A g^{-1} (Figure 5.30 and Figure 5.32). The SbO-G electrode's GCD curves show a high specific capacitance when compared to SbO. The presence of typical triangular curves confirms the electric double layer capacitive charge storage mechanism occurring at the electrode-electrolyte interface [40]. The GCD curves are nearly symmetrical, with only a minor voltage drop due to the equivalent series resistance (ESR). The timing for the charge and discharge process is similar especially at higher current, indicating a high Coulombic efficiency and electrochemical reversibility [39]. These observations are consistent with the oxidation and reduction profiles reported in the CV curves. The specific capacitance was determined using the equation
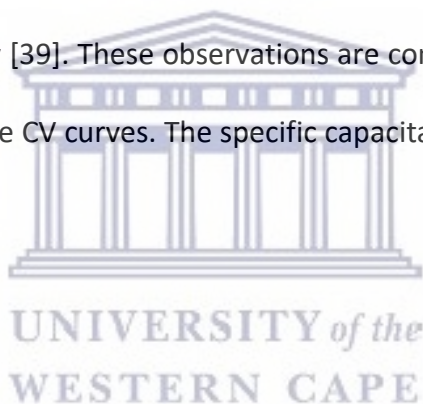
$$C_s = \frac{I \times t}{m \times V - IR_{drop}}$$ 5-3

where I is the constant current, m is the active material mass, and t is the discharge time corresponding to the voltage change, V [22]. Figure 5.34 shows a comparison of the rate capabilities of SbO and SbO-G electrodes at various current densities. At a current density of 5 A g^{-1}, SbO-G has a specific capacitance 3.27 F g^{-1}, which is substantially lower than that of SbO (11.3 F g^{-1}). From the rate capability analysis SbO electrodes, exhibit better capacitance retention retaining ~80% of its capacitance at 1 A g^{-1} and ~40% at 5 A g^{-1}. This is due to the fast redox reaction happening at the material's surface as confirmed by its near rectangular voltammogram. The SbO-G electrode has the highest specific capacitance at the same current density when

compared to SbO electrodes. The highest capacitance of SbO-G electrode, for example, reached up to 98 F g^{-1} at 0.1 A g^{-1}, while SbO was 25.11 F g^{-1}. This is due to the contribution from EDLC and pseudocapcitnace and the more porous microstructure, which facilitates electrolyte infiltration and contributes to the development of electric double-layer capacitance. The specific capacitance decreases as the current increases Figure 5.35 . The drop in specific capacitance values was noticeable in the discharge time of GCD curves. This drop-in specific capacitance at increased current density could be attributed to the limited flow of electrolyte ions into the active material's inner sites [41].
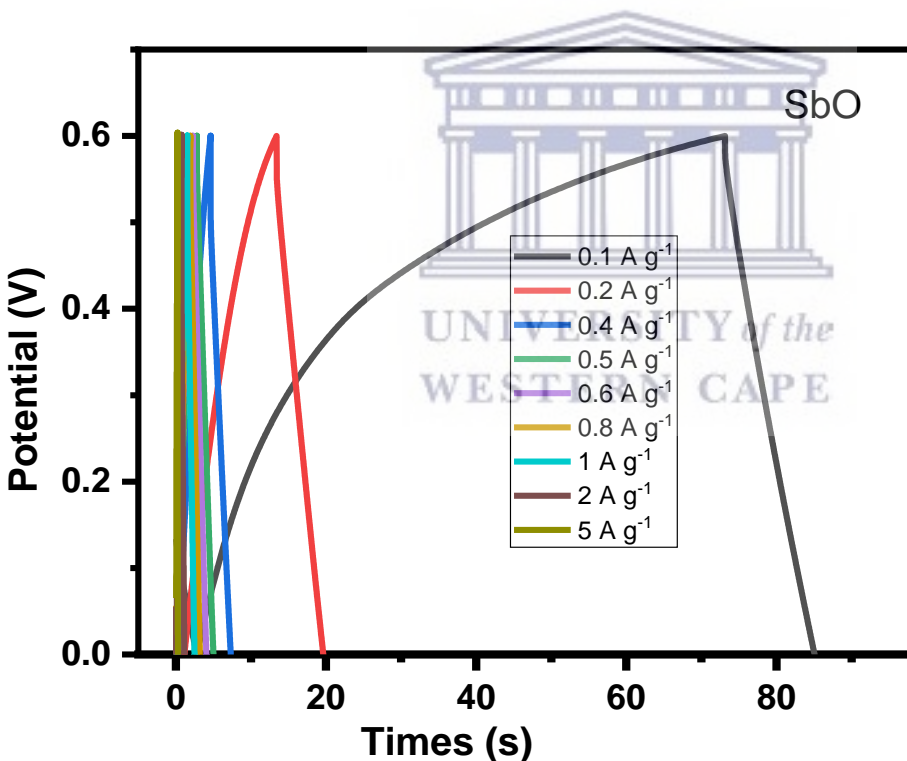
Figure 5.30: GCD of SbO at different current densities.
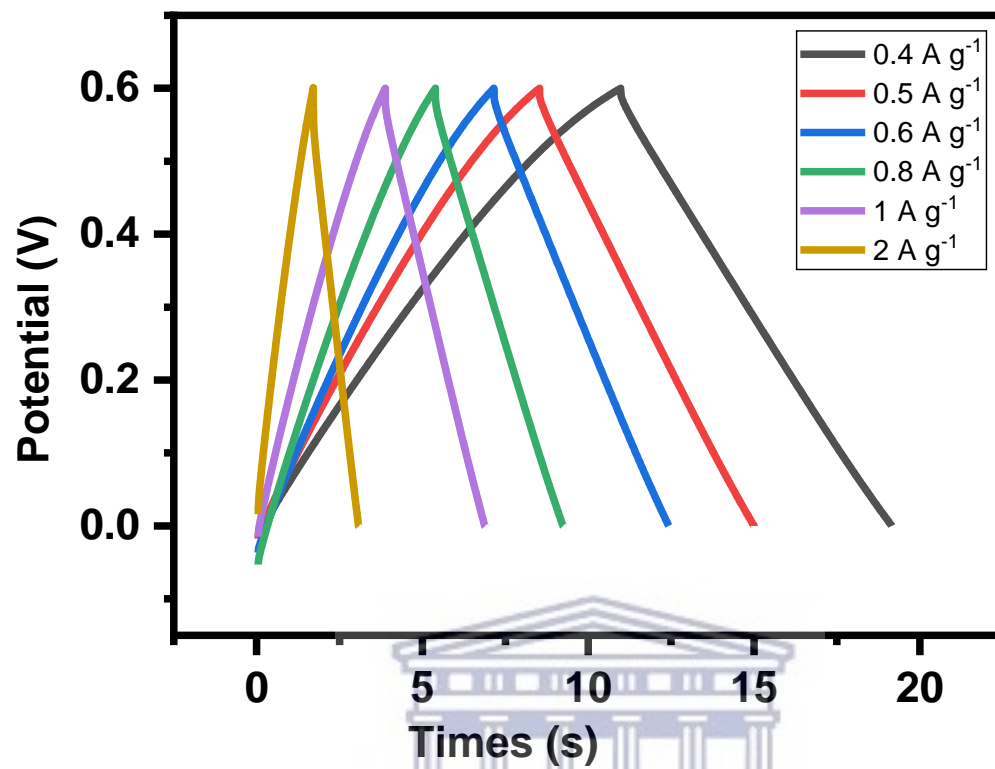
Figure 5.31: GCD of SbO at different current densities at higher scan rates only.
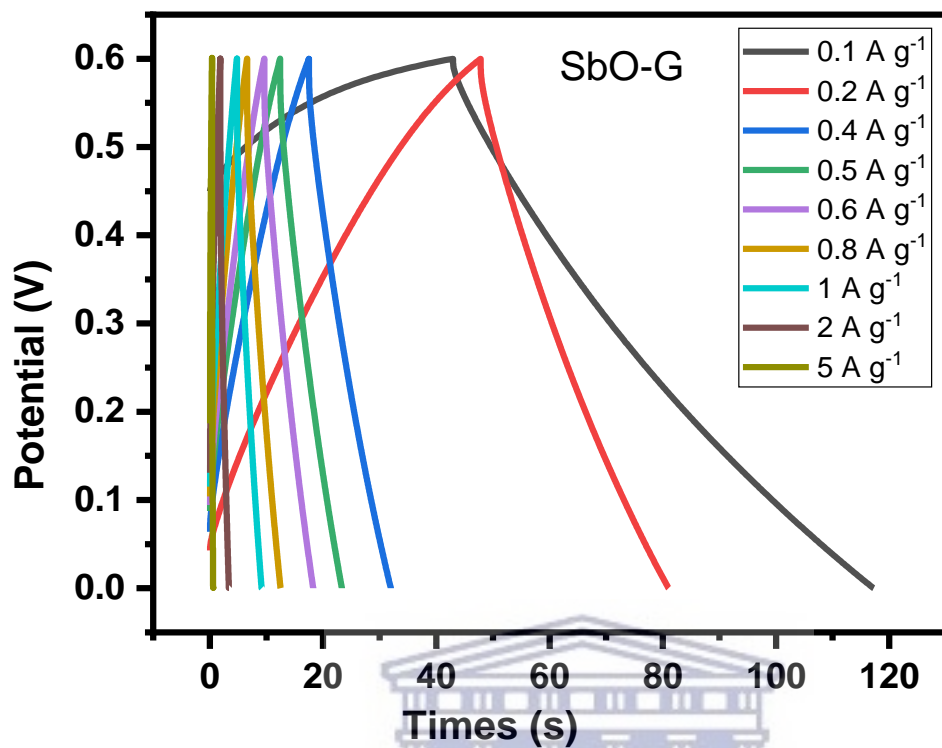
Figure 5.32: GCD of SbO-G at different current densities.
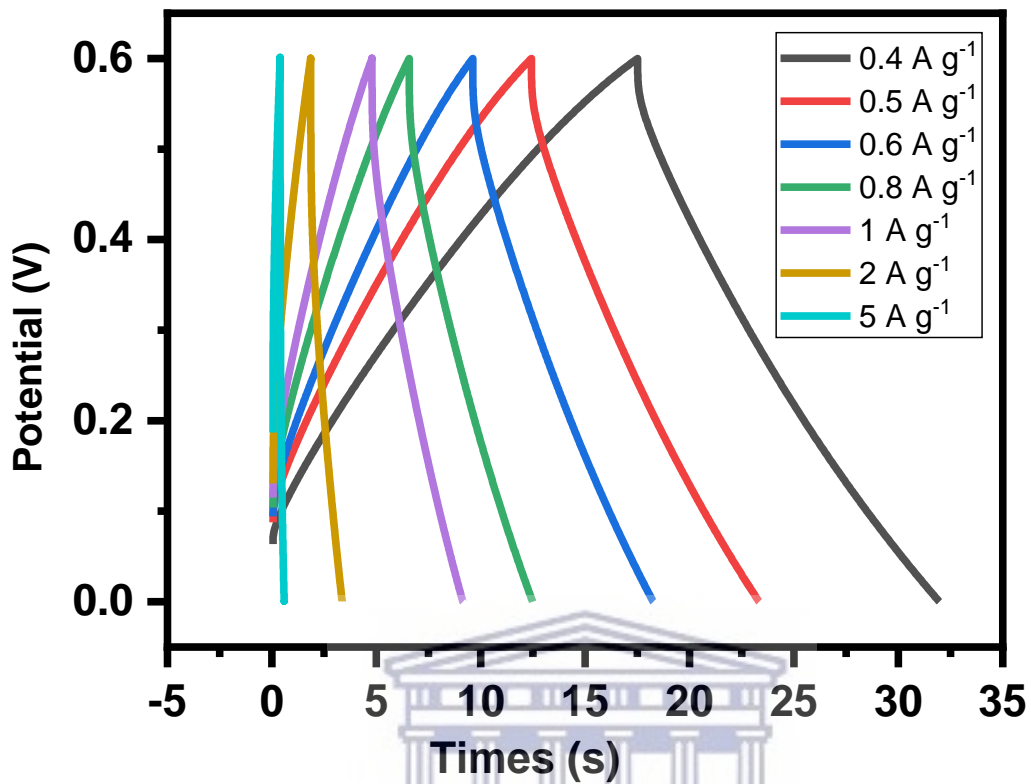
Figure 5.33: GCD of SbO-G at different current densities at higher scan rates only.
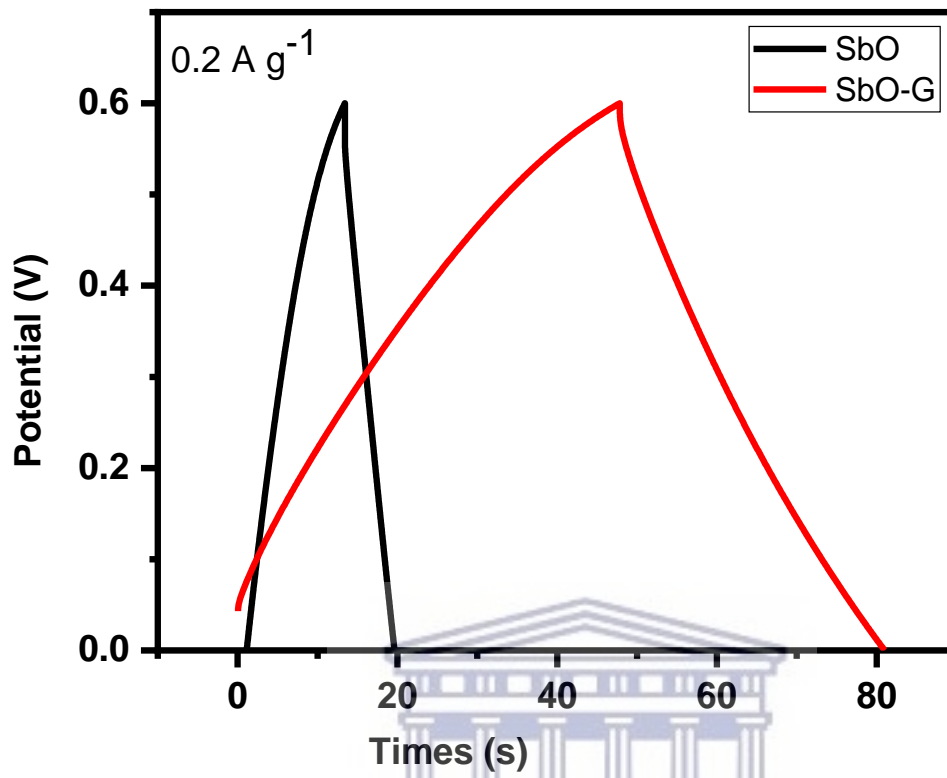
Figure 5.34: GCD curve of SbO and SbO-G at 0.2 A g^{-1}.
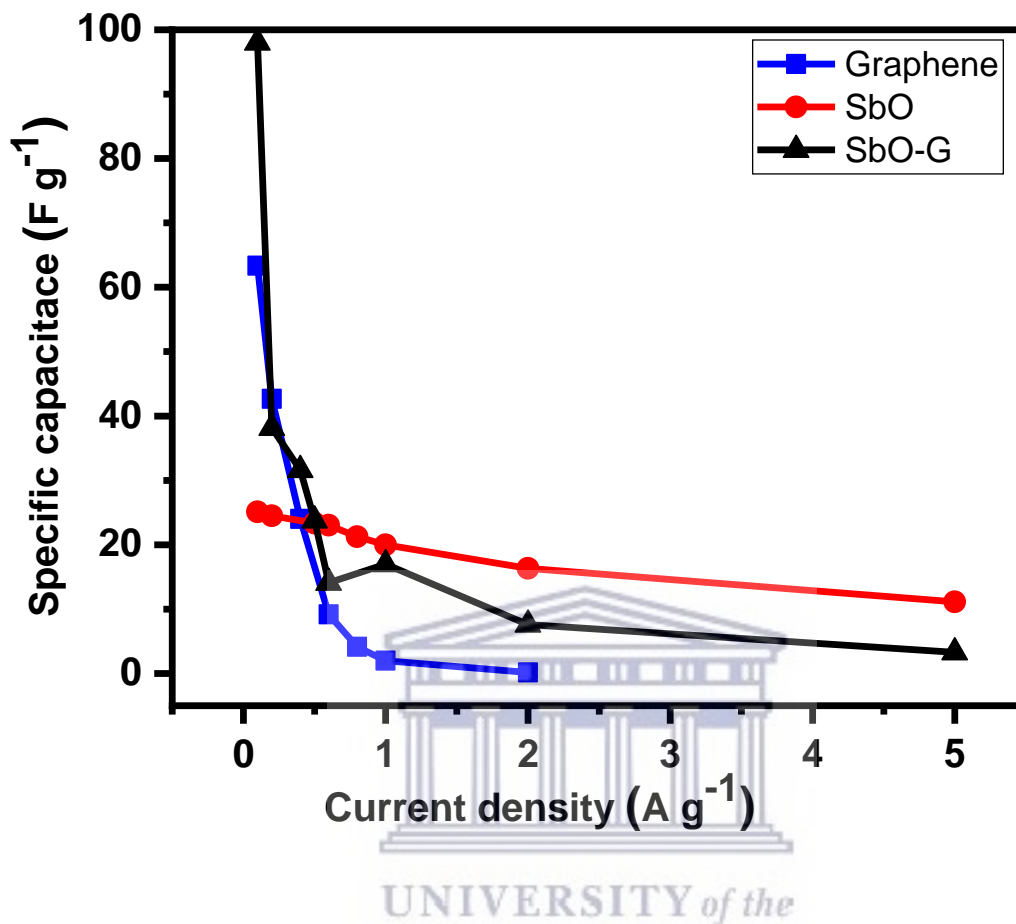
Figure 5.35: Plot showing the relationship between Cs and current density for SbO, SbO-G and graphene.

5.2.5.3 Electrochemical impedance spectroscopy

As illustrated in Figure 5.36, Nyquist plots were used to analyze the electrochemical impedance spectroscopy (EIS) data and were displayed with an equivalent circuit inset. [42].

In the high-frequency region, the intersection of the curve at the real component reveals the bulk resistance of the electrochemical system. This includes ionic resistance from the electrolytes, intrinsic grain to grain resistance of the electrode, and contact resistance at the interphase

between the active material and the substrate [43]. The radius of the semicircle in the high-frequency region displays the charge-transfer process, at the interface of the electrode and the electrolyte. As we approach lower frequencies the semicircle breaks into a 45° nearly vertical line which is related to the Warburg (W_2) diffusion of ions within the electrode inter-phase [32]. The EIS graphs demonstrated that SbO (4.8 Ω) had a greater Rs than SbO-G (3.2 Ω) SbO also shows a small semi-circle in the high-frequency region however with the addition of graphene the semi-circle disappears given a near-perfect capacitive response. SbO and SbO-G have fitting R_{ct} values of 7.35, and 3.75 Ω respectively. Also, as observed in the curve, the SbO-G electrodes exhibit better capacitive behaviour with an almost vertical line [44]. The slope of the 45° section of the curves in the intermediate frequency area was used to illustrate the Warburg resistance, which indicates ion diffusion/transport in the electrolyte and its relationship to frequencies. Furthermore, the Warburg resistance value (Table 5-4) is lower in the SbO-G. Because of the low charge transfer resistance and lower diffusion effect, relatively reversible reactions can occur at the interface, which explains the rectangular voltammogram of both materials and why the rectangular nature is retained even at high scan rates.
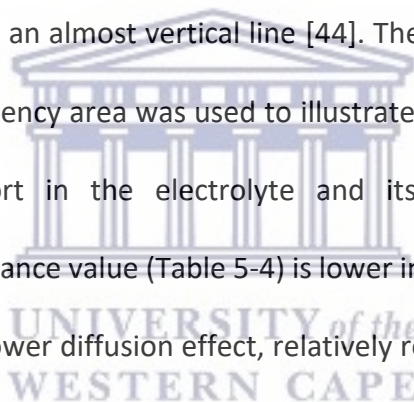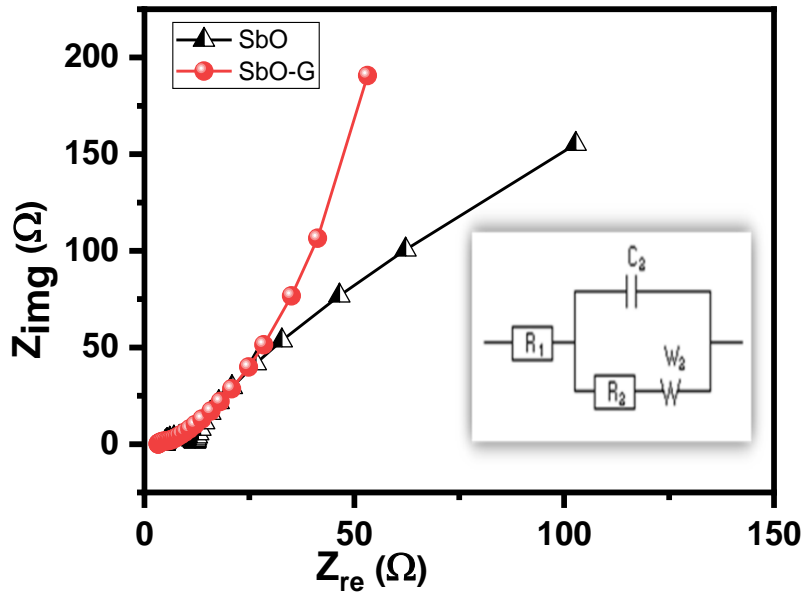
Figure 5.36: Nyquist plot of SbO and SbO-G the inset is the equivalent circuit, the inset is the equivalent circuit.
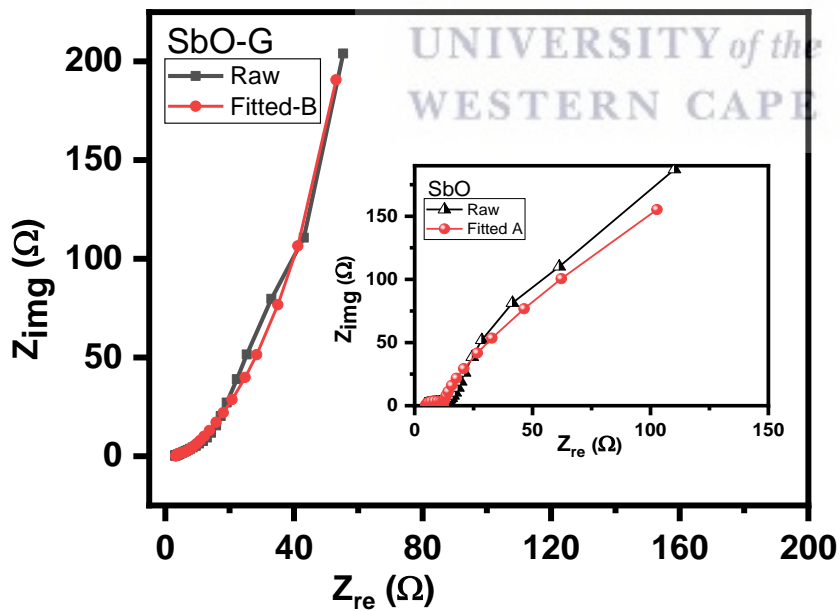
Figure 5.37: Nyquist plot of SbO-G showing the raw and fitted data, the inset is the plot of SbO showing the raw and fitted data.

Table 5-4: EIS curve fitting of SbO and SbO-G electrode material.

Sample	R_s (Ω)	CPE (µF)	R_{ct} (Ω)	W^2 (Ω s- ½)	Phase angle (º)
SbO	5.561	5.54	7.46	154.3	64.4
SbO-G	3.203	0.22	1.51	42.39	75.7

The Bode plot from the EIS data is shown as the phase angle and total impedance plot in Figure 5.38. The phase angle for SbO is 64.4º while that of SbO-G was 75.7º. The phase angle of SbO-G is closer to 90º, therefore, showing more capacitive phase angles as seen in the Warburg diffusion area. It is clear from the face angle that the materials store charges utilizing both the EDL and the pseudocapacitive mechanisms. The magnitude of total impedance was lowest in SbO-G as seen in Figure 5.39. The constant phase element (CPE) was also derived from the Bode total impedance plot. The CPE impedance is given by

$$Z_{CPE} = a^{-1}(jw)^{-n} \qquad\qquad 5\text{-}4$$

where a is the frequency-independent constant related to the roughness of the surface features, and the exponent n is determined by the slope of log z vs. log f. The coefficient 'a' is resistive when n = 0, capacitive for n = 1 and a Warbug impedance (charge transfer impedance) for n = 0.5

the value of n for SbO and SbO-G was 0.78, 0.69 respectively. The change in n confirms a change

in the morphology of the material, both values show that the materials are capacitive as their

values approach 1[45] the total CPE values obtained from the fitted Nyquist plot are shown in

Table 5-4.
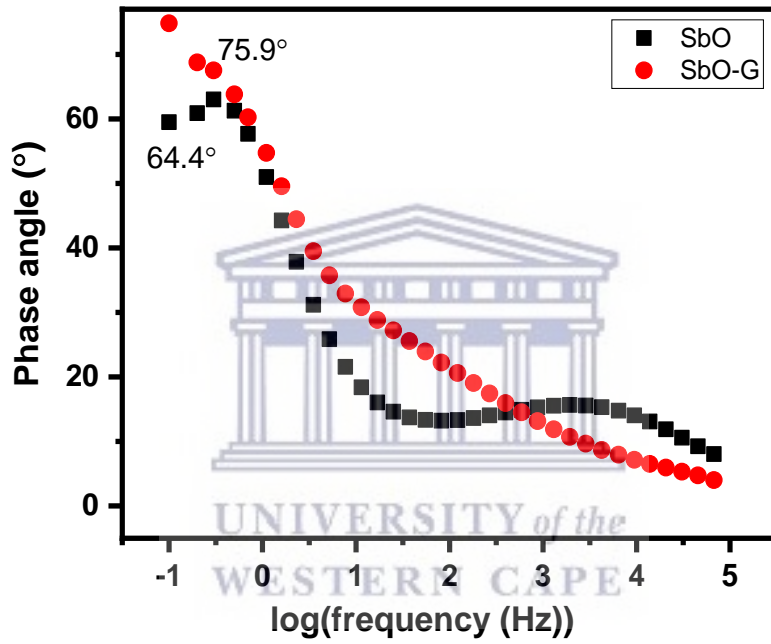
Figure 5.38: Bode plot of SbO and SbO-G.
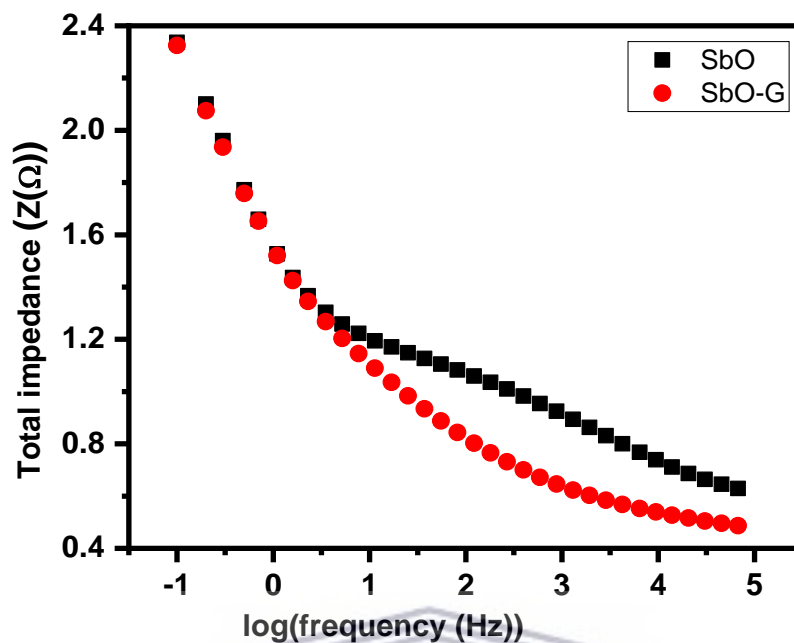
Figure 5.39: Total impedance plot of SbO and SbO-G.
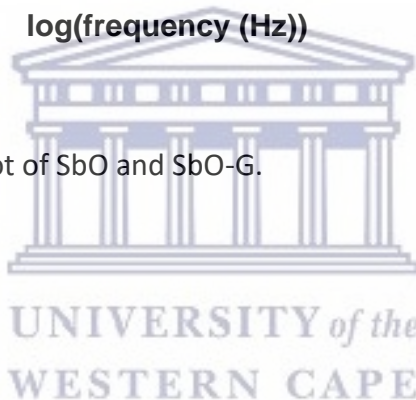
5.2.6 Device fabrication

To investigate the potential of as-synthesized SbO and SbO-G nanoparticles in a full-cell configuration, an ASC with SbO/ SbO-G as positive and activated carbon as negative electrode material was designed. The charge storage in activated carbon occurs via the creation of an electrical double layer. Figure 5.40, shows the performance of AC in an aqueous solution of 1 M Li_2SO_4 in a half-cell arrangement with SbO electrode to ascertain the suitability of activated carbon as a negative electrode.
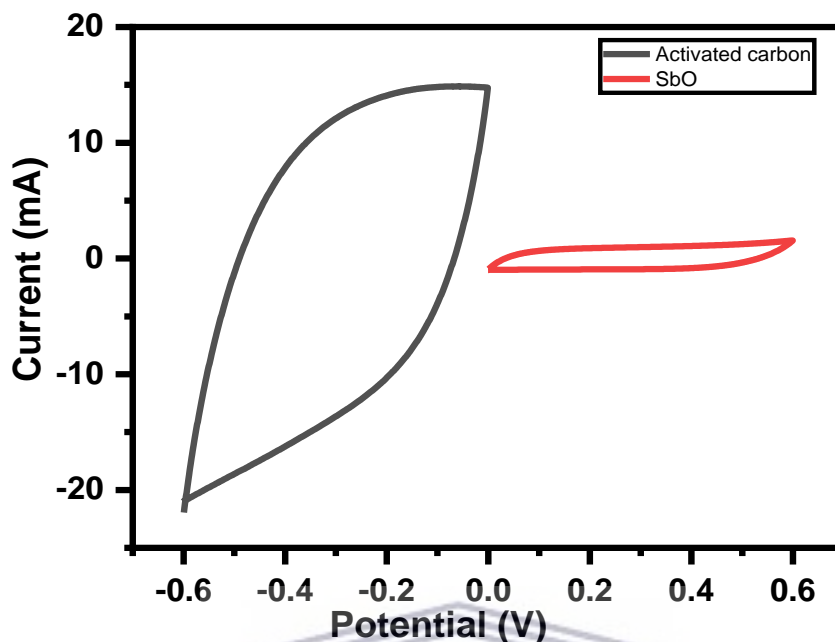
Figure 5.40: CV plot of SbO and activated carbon in 3 electrodes set up showing the suitability of activated carbon as the negative electrode.
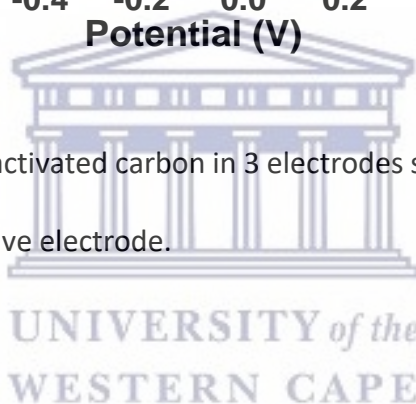
5.2.6.1 Galvanostatic charge discharge

The GCD plot as shown in Figure 5.41 and Figure 5.42 was carried out at different current densities (0.1 A g⁻¹, 0.2 A g⁻¹,0.4 A g⁻¹, 0.5 A g⁻¹, 0.6 A g⁻¹, 0.8 A g⁻¹, 1 A g⁻¹ and 2 A g⁻¹). The capacitance at each current density was calculated and the result is as shown in Table 5-5 and Table 5-6. The result showed an improved performance in the SbO-G device compared to the SbO electrode device. Figure 5.43 shows the relationship between the capacitance and the current density, the capacitance reduced with an increase in the current density. At a current density of 0.2 A g⁻¹, SbO-G has a specific capacitance 32.89 F g⁻¹, which is higher than that of SbO (5.5 F g⁻¹). Notably, as the current density increased to 1 A g⁻¹, the SbO-G maintained a high

capacitance of 9.33 F g⁻¹, retaining 64% of its capacitance. The SbO device, on the other hands, exhibit poorer capacitance retention of 12.6%, indicating that the structure of the graphene improved electrolyte ion diffusion. The specific energy and power were calculated according to the following equations:

$$E_{sp}\left(\frac{Wh}{Kg}\right) = \frac{CV^2}{2m} \times \frac{1}{3.6}$$

5-5

$$P_{max}\left(\frac{W}{Kg}\right) = \frac{E}{\triangle t} \times 3600$$

5-6

where C (F g⁻¹) is the specific capacitance determined from equation 5-4, V is the maximum working potential, m (kg) is the mass of the active material in the electrode, and $\triangle t$ is the capacitors discharge time. Figure 5.45 is a Ragone plot which depicts the relationship between the asymmetric device's energy density and power density at various current densities. An ideal supercapacitor device would have a high energy density while also having a high-power density. Interestingly, the asymmetric Cs cell had the highest energy density. 2.50 W h kg⁻¹ at a power density of 720 W kg⁻¹ at 0.2 A g⁻¹ current load for SbO, while SbO-G delivered an energy density of 14.8 W h kg⁻¹ at a power density of 360 W kg⁻¹ at 0.2 A g⁻¹. The energy density and power density were enhanced by the addition of graphene which led to increased surface area for charge-discharge.
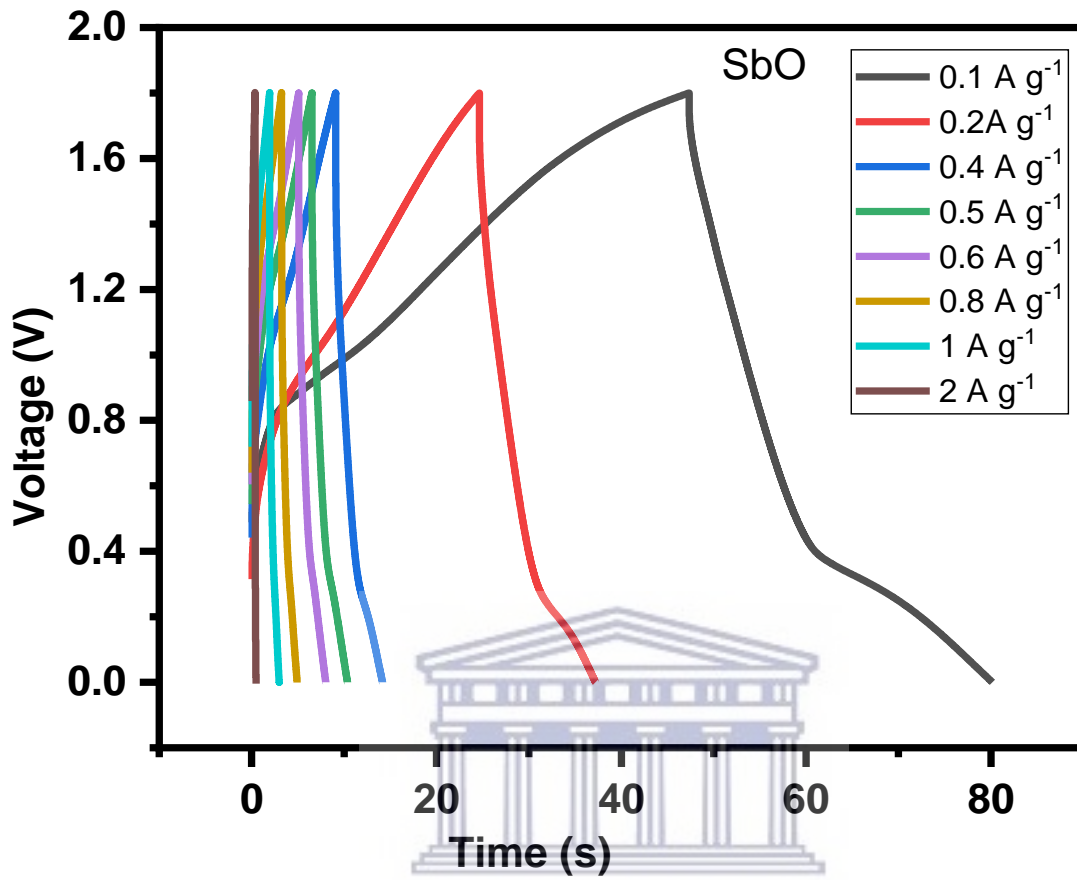
Figure 5.41: GCD profile for AC//SbO at different current densities.
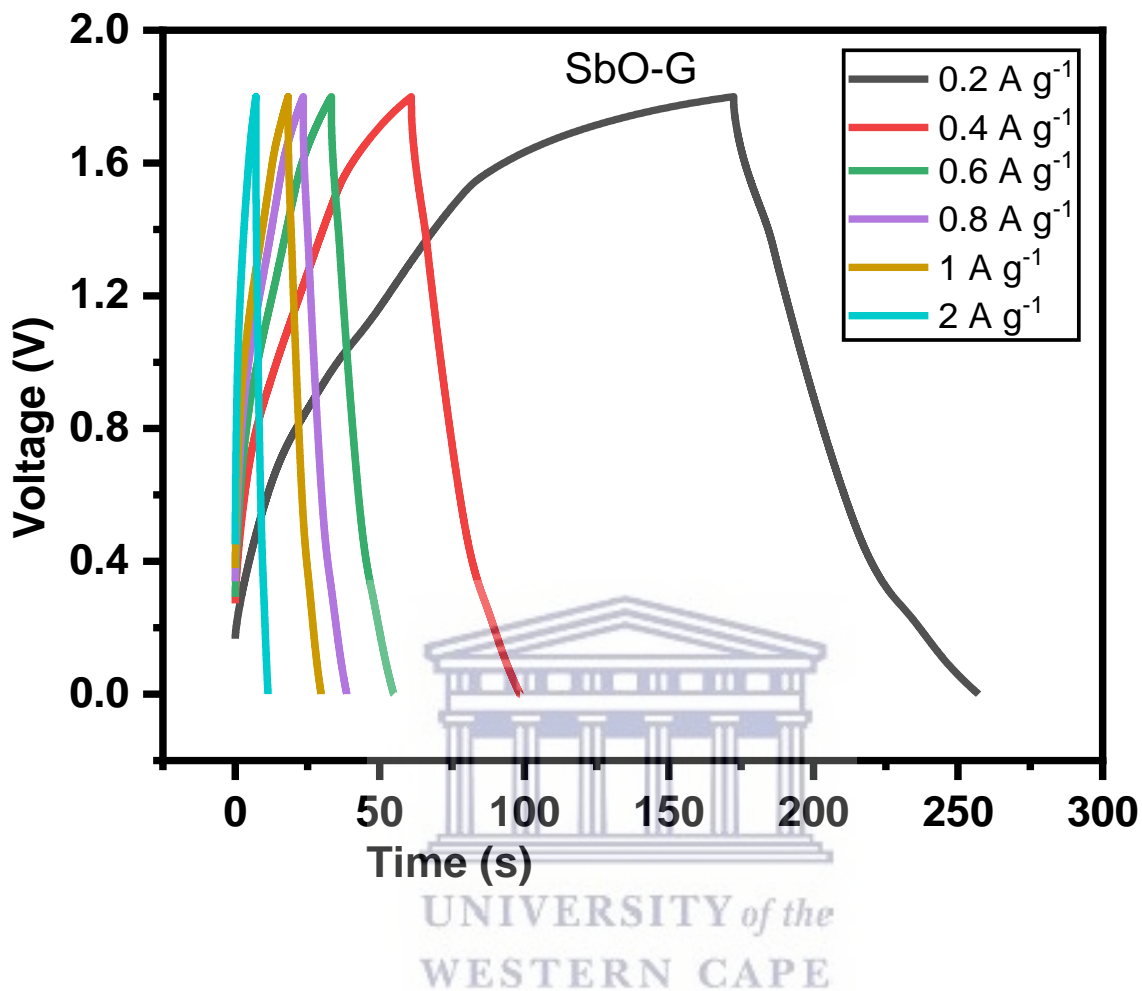
Figure 5.42: GCD profile for AC//SbO-G at different current densities.
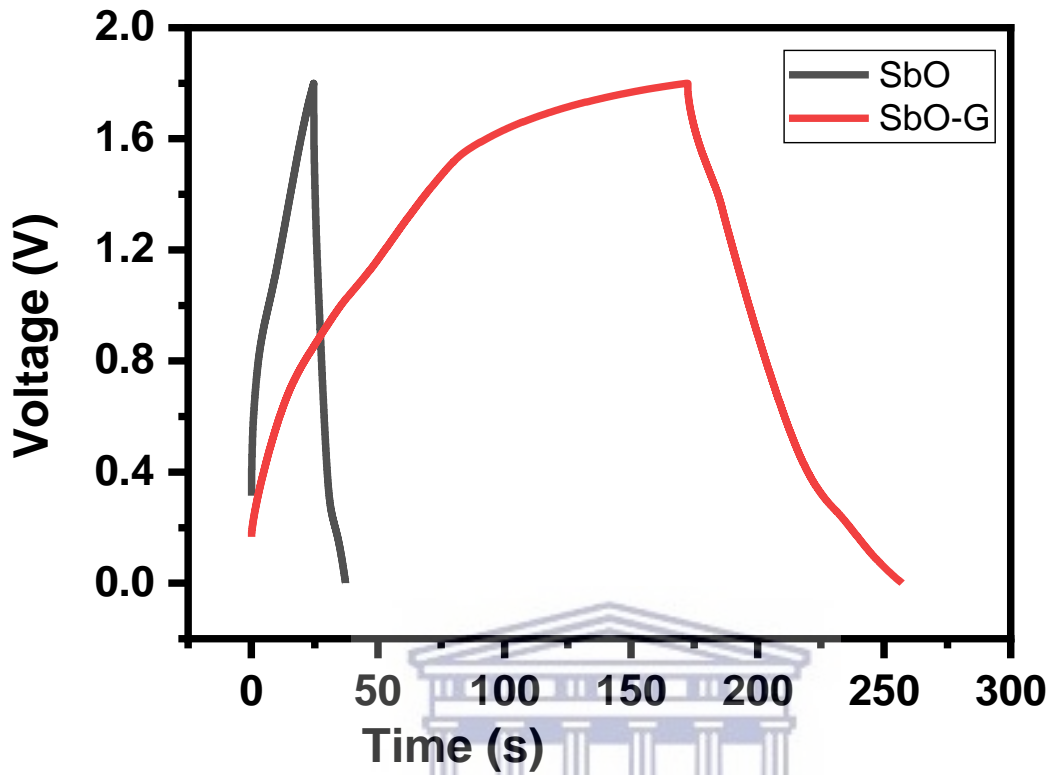
Figure 5.43: GCD plot comparing AC//SbO and AC//SbO-G at 0.2 A g^{-1}.
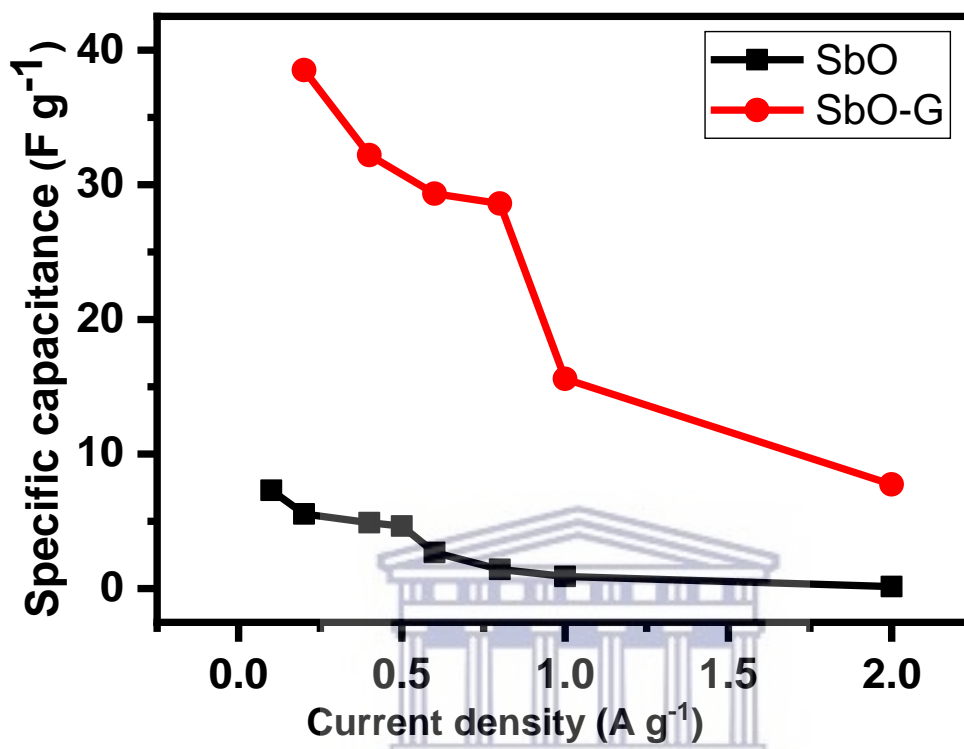
Figure 5.44: Plot comparing the current density vs capacitance of AC//SbO and AC//SbO-G.
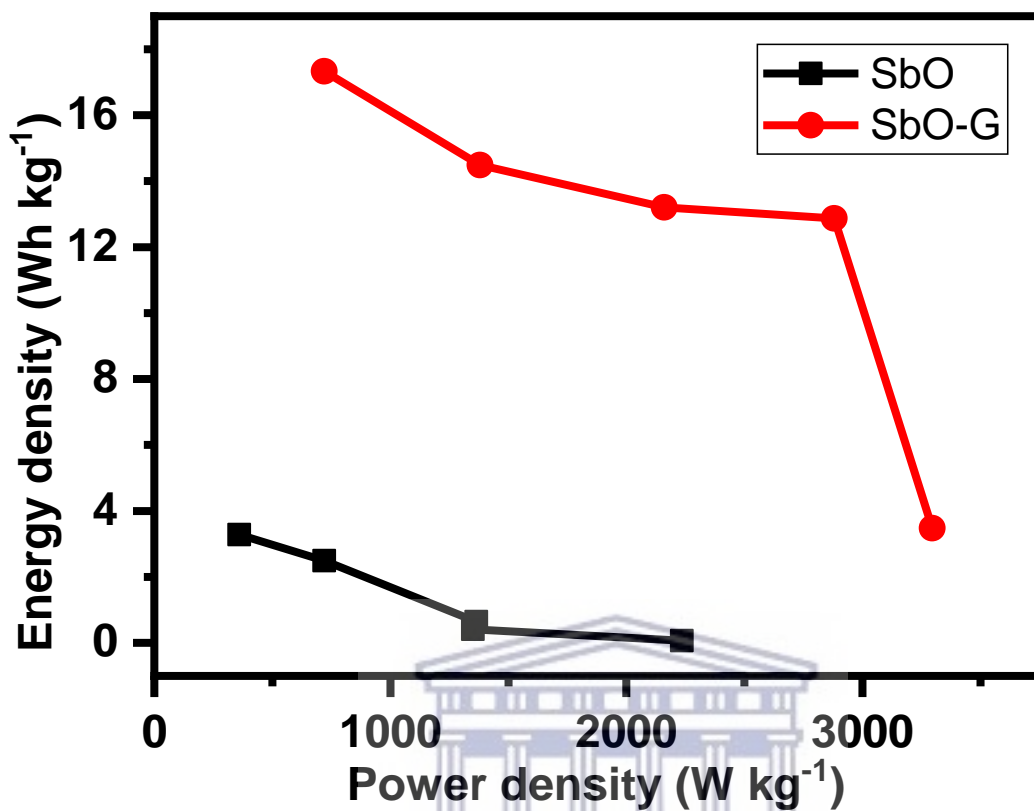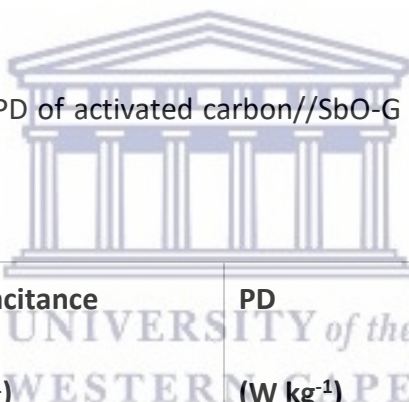
Figure 5.45: Ragone plot of AC//SbO and AC//SbO-G.

Table 5-5: Capacitance, ED and PD of activated carbon//SbO carbon device from the GCD data.

Current density (A g^{-1})	Capacitance (F g^{-1})	PD (W kg^{-1})	ED (W h kg^{-1})
0.1	7.30	360.00	3.29
0.2	5.55	720.00	2.50
0.4	4.89	1440.00	2.20

0.5	4.66	1800.00	2.10
0.6	2.68	1388.57	1.21
0.8	1.43	1364.21	0.64
1	0.92	1350.00	0.41
2	0.15	2234.48	0.07

Table 5-6: Capacitance, ED and PD of activated carbon//SbO-G carbon device from the GCD data.

Current density (A g^{-1})	Capacitance (F g^{-1})	PD (W kg^{-1})	ED (W h kg^{-1})
0.2	32.89	360.00	14.80
0.4	29.33	720.00	13.20
0.5	25.42	1440.00	11.44
0.6	24.82	1800.00	11.17
0.8	24.15	2160.00	10.87
1	21.16	2880.00	9.52

2	19.33	3600.00	8.70

5.2.6.2   Electrochemical impedance spectroscopy

Figure 5.46 is the Nyquist plot of the SbO and SbO-G asymmetric devices. The in-set is the fitted

equivalent circuit data and the parameters obtained are represented in Table 5-7 below. Figure

5.47 shows the fitted and raw plots of SbO-G and those of SbO in the in-set. The EIS is lower in

the SbO-G (1.33 Ω) than in the SbO material (1.5 Ω). Also, the impedance of charge-transfer

process at the interface of the electrode and the electrolyte was much lower for SbO-G (0.7 Ω)

as compared to SbO (13.7 Ω), as can be seen by the smaller semi-circle in the high-frequency

area. This shows that more facile charge transfer occurred between the Li^+ and SO_4^{-2} ions and

the SbO-G [46] [47]. A well-defined, near-vertical and shorter Warburg area part in the SbO-G

compared to SbO device demonstrates that the ions in the electrolyte have a short and equal

diffusion path length. Thus, because of the low charge transfer resistance and lower diffusion

effect, relatively reversible reactions can occur at the interface, which explains the shape of the

voltammogram and GCD profile [44]. The Bode plot from the EIS data is shown as the phase angle

and total impedance plot in Figure 5.48 and Figure 5.49. The phase angle of SbO is 68.06° while

that of SbO-G device is at 72.5°, indicating a capacitive behaviour which is from the contribution

of both EDLC and pseudocapacitance. The magnitude of total impedance had a value of 0.25 Ω

for SbO and 0.12 Ω for SbO-G. Both Bode plots confirm a capacitive electrode.
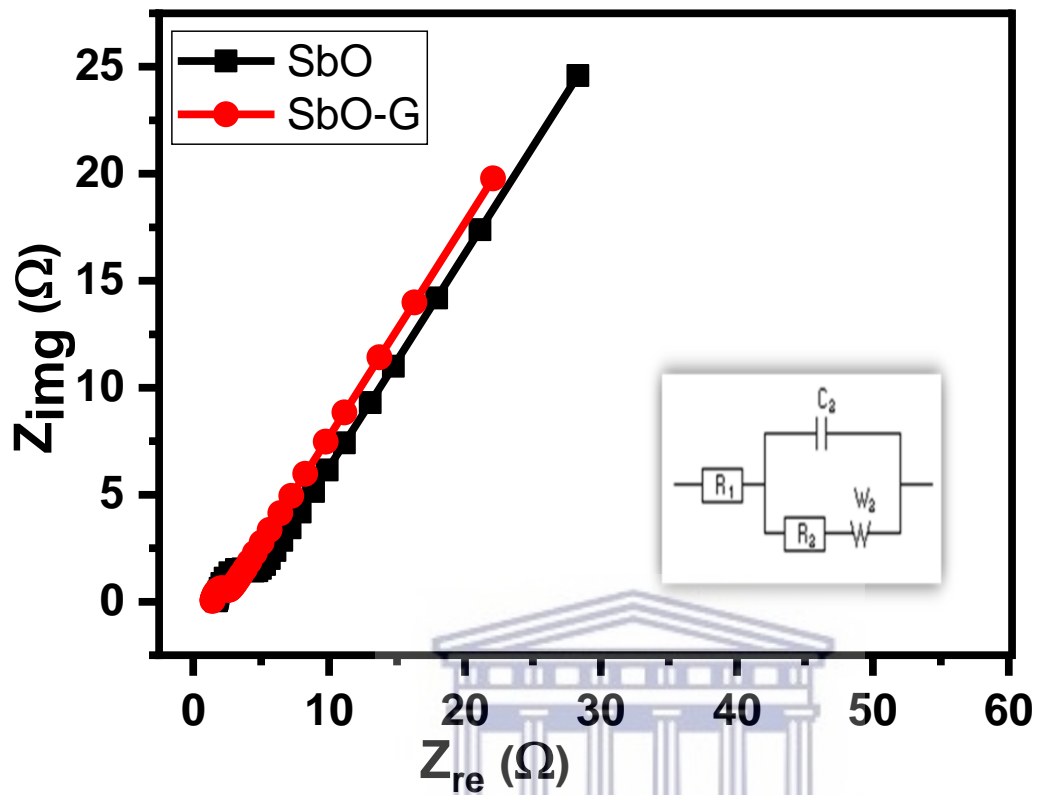
Figure 5.46: Nyquist plot of AC//SbO and AC//SbO-G electrode, the inset is the equivalent

circuit.
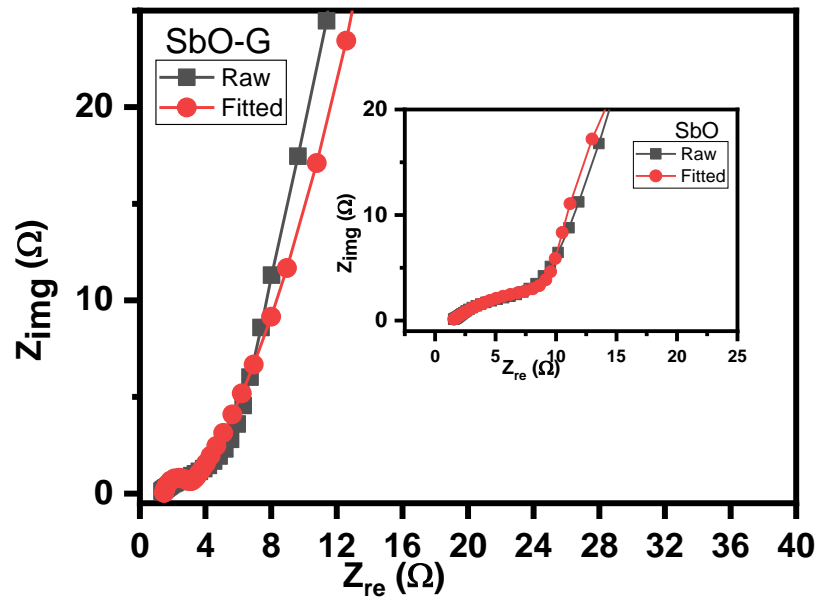
Figure 5.47: Nyquist plot of AC//SbO and AC//SbO-G electrode showing the raw and fitted data.
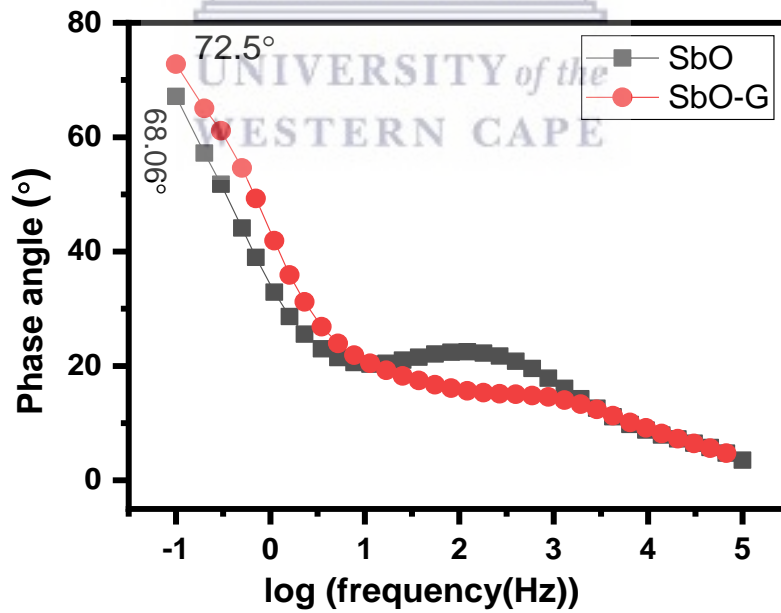
Figure 5.48: Bode plot of AC//SbO and AC//SbO-G electrode represented as a phase angle plot.
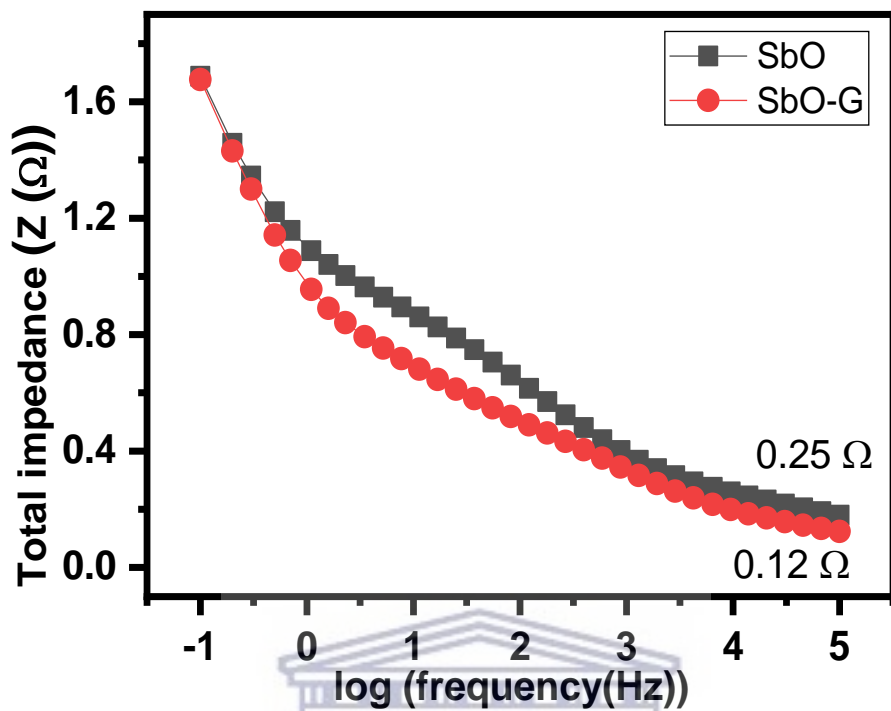
Figure 5.49: Bode plot of AC//SbO and AC//SbO-G electrode represented as total impedance plot.

Table 5-7: EIS curve fitting data of AC//SbO and AC//SbO-G electrode material.

Electrolytes	R_s (Ω)	CPE (μF)	R_{ct} (Ω)	W^2 (Ω s- $\frac{1}{2}$)	Phase angle (º)
SbO	1.5	1.74	13.7	17.79	68.06
SbO-G	1.33	14.72	0.7	15.42	72.5

5.2.6.3   Cycle life

Long cycle life is an important criterion for supercapacitors, the cyclic stability was performed using the galvanostatic charge-discharge techniques at a current density of 0.5 A g^{-1} and a voltage range of 0-1.8V. Figure 5.50 shows that the SbO device remained stable for more than 3500 charging and discharging cycles. And maintained ~ 58% of its initial capacitance. However, the system maintained a 100 % Coloumbic efficiency throughout the period. As seen in the in-set, the shape of the CV plot changed after the cycling. This is due to material distortion caused by the volume expansion of the Sb metal as a result of ion migration in and out of its pores. [48]. The EIS of the device also changes after the cycling. The SbO-G device showed better capacitance retention as seen in Figure 5.51. The device maintained 100% capacitance retention after the cycling test. This is evidence in the voltammogram which do not change after the charge and discharge test. The Columbic efficiency was also maintained at 100% throughout the cycling. This improved stability is because of the incorporation of a more stable carbon matrix, thus improving the cycle life of the device. The EIS plot changed in the Warburg area, showing a more diffusion-controlled reaction [2].
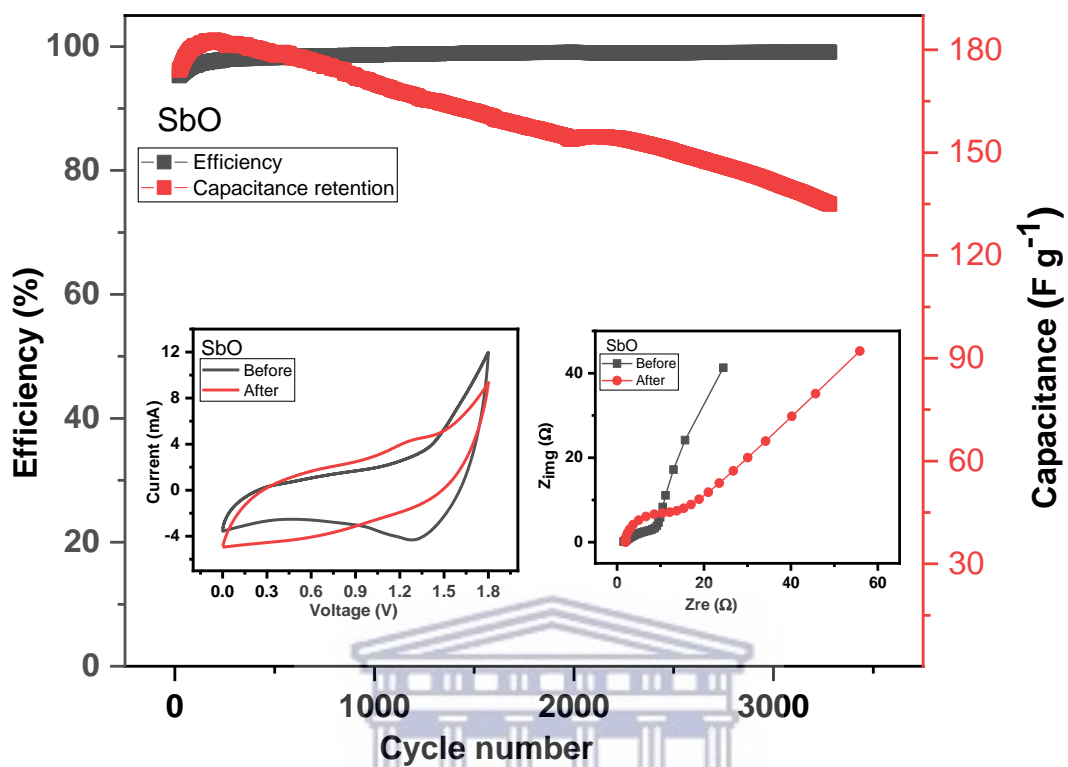
Figure 5.50: Cycling stability of AC//SbO supercapacitor over 3500 cycles in 1 M Li$_2$SO$_4$, the in-

set is the EIS and CV (50 mV s^{-1}) plot before and after cycling.
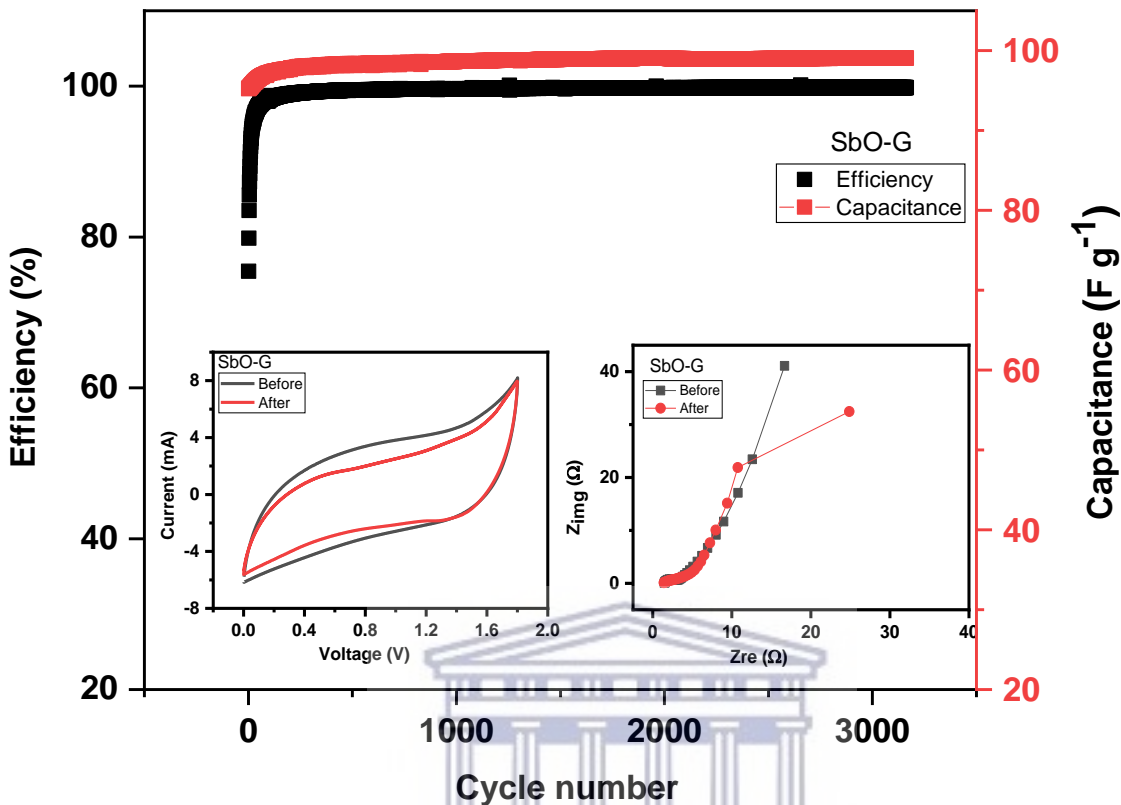
Figure 5.51: Cycling stability of AC//SbO-G supercapacitor over 3500 cycles in 1 M Li$_2$SO$_4$, the in-set is the EIS and CV (50 mV s^{-1}) plot before and after cycling.

5.3 CONCLUSION

SbO and SbO-G was synthesized as electrode for supercapacitors using microwave assisted method. For the SbO-G samples, SbO nanoparticles are well distributed on the graphene sheets with a size of 10–50 nm acting as spacers between the graphene sheets. The charge storage mechanism visible in the CV curve of SbO is nearly rectangular and identical to the EDLC charge storage mechanism. The total capacitance increased from 25.11 F g^{-1} for the SbO to 98.00 F g^{-1}

for the SbO-G. The increased specific capacitance of SbO-G demonstrates positive synergistic effect of graphene nanosheets and SbO due to the utilization of the combined advantages of separated graphene nanosheet to have a large and more accessible surface area and a high conductive network of fine SbO nanoparticle. SbO and SbO-G was used to fabricate an asymmetric supercapacitor device as a positive electrode while activated carbon was used as the negative electrode. The asymmetric Cs cell delivered a maximum energy density of 2.52 W h kg^{-1} at a power density of 720 W kg^{-1} at 0.2 A g^{-1} current density for SbO, while SbO-G delivered an energy density of 14.80 W h kg^{-1} at a power density of 360 W kg^{-1} at the same current density. The energy density and power density where enhanced by the addition of graphene which led to increase surface area for charge discharge. This result shows that, apart from the conventional ruthenium oxide and carbon material used for supercapacitors, antimony oxides upon optimization, will result in an excellent electrode material for energy storage. This study opens a new horizon for the exploration of new categories of nanomaterials, like 'antimony oxides based materials' for supercapacitor application.
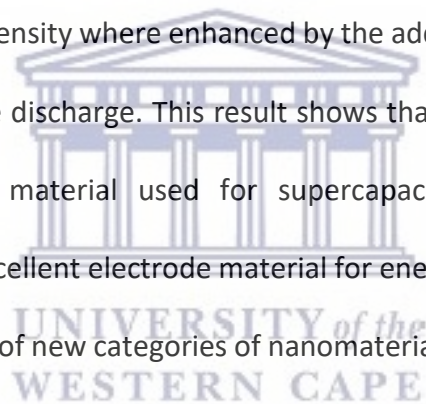
5.4 REFERENCE

[1] Y. Anil Kumar, K. Dasha Kumar, H.J. Kim, A novel electrode for supercapacitors: Efficient PVP-assisted synthesis of Ni_3S_2 nanostructures grown on Ni foam for energy storage, Dalt. Trans. 49 (2020) 4050–4059. https://doi.org/10.1039/d0dt00191k.

[2] A. Noori, M.F. El-kady, M.S. Rahmanifar, R.B. Kaner, M.F. Mousavi, Chem Soc Rev metrics for batteries , supercapacitors and beyond, Chem. Soc. Rev. (2019). https://doi.org/10.1039/c8cs00581h.

[3] M. Filella, N. Belzile, Y.W. Chen, Antimony in the environment: A review focused on natural waters I. Occurence, Earth-Science Rev. 57 (2002) 125–176. https://doi.org/10.1016/S0012-8252(01)00070-8.

[4] Y. Yuan, S. Jan, Z. Wang, X. Jin, A simple synthesis of nanoporous Sb/C with high Sb content and dispersity as an advanced anode for sodium ion batteries, J. Mater. Chem. A. 6 (2018) 5555–5559. https://doi.org/10.1039/c8ta00592c.

[5] Y.B. Kamenev, A. V Kiselevich, E.I. Ostapenko, Y. V Skachkov, Antimony-free alloys for unattended (sealed) lead batteries, Russ. J. Appl. Chem. 75 (2002) 548–551. https://doi.org/10.1023/A:1019548510196.

[6] M. Kosai, S. Yasukawa, S. Osumi, M. Tsubota, Effect of antimony on premature capacity loss of lead/acid batteries, J. Power Sources. 67 (1997) 43–48. https://doi.org/10.1016/S0378-7753(97)02496-8.

[7] M. Ciszewski, A. Mianowski, G. Nawrat, P. Szatkowski, Reduced graphene oxide supported antimony species for high-performance supercapacitor electrodes, ISRN Electrochem.

2014 (2014) 1–7. https://doi.org/10.1155/2014/826832.

[8]   R.K. Sahoo, S. Singh, J.M. Yun, S.H. Kwon, K.H. Kim, Sb2S3 Nanoparticles Anchored or Encapsulated by the Sulfur-Doped Carbon Sheet for High-Performance Supercapacitors, ACS Appl. Mater. Interfaces. 11 (2019) 33966–33977. https://doi.org/10.1021/acsami.9b11028.

[9]   B. Xiao, G. Wu, T. Wang, Z. Wei, Y. Sui, B. Shen, J. Qi, F. Wei, Q. Meng, Y. Ren, X. Xue, J. Zheng, J. Mao, K. Dai, Q. Yan, Tin antimony oxide @graphene as a novel anode material for lithium ion batteries, Ceram. Int. (2021). https://doi.org/10.1016/j.ceramint.2021.09.300.

[10]   T. Le Hai, L.C. Hung, T.T.B. Phuong, B.T.T. Ha, B.S. Nguyen, T.D. Hai, V.H. Nguyen, Multiwall carbon nanotube modified by antimony oxide (Sb_2O_3/MWCNTs) paste electrode for the simultaneous electrochemical detection of cadmium and lead ions, Microchem. J. 153 (2020) 104456. https://doi.org/10.1016/j.microc.2019.104456.

[11]   K. Yang, T. Zhang, B. Wei, Y. Bai, S. Jia, G. Cao, R. Jiang, C. Zhang, E. Gao, X. Chang, J. Li, S. Li, D. Zhu, R. Tai, H. Zhou, J. Wang, M. Zeng, Z. Wang, L. Fu, Ultrathin high-κ antimony oxide single crystals, Nat. Commun. 11 (2020) 7–12. https://doi.org/10.1038/s41467-020-16364-9.

[12]   O.M. Lopez, M.C. Hegy, T.M. Missimer, Statistical comparisons of grain size characteristics, hydraulic conductivity, and porosity of barchan desert dunes to coastal dunes, Aeolian Res. 43 (2020) 100576. https://doi.org/10.1016/j.aeolia.2020.100576.

[13]   M.H. Chakrabarti, E.P.L. Roberts, C. Bae, M. Saleem, Ruthenium based redox flow battery

for solar energy storage, Energy Convers. Manag. 52 (2011) 2501–2508. https://doi.org/10.1016/j.enconman.2011.01.012.

[14] B. Francis Ntumba Muya, S. Africa Supervisor Priscilla Baker Co-supervisor Emmanuel Iwuoha, Hydrogel encapsulated biosensors for the detection of biologically significant vanadium and selenium, (2017). http://etd.uwc.ac.za/ (accessed October 27, 2021).

[15] I.S. El-Hallag, M.N. El-Nahass, S.M. Youssry, R. Kumar, M.M. Abdel-Galeil, A. Matsuda, Facile in-situ simultaneous electrochemical reduction and deposition of reduced graphene oxide embedded palladium nanoparticles as high performance electrode materials for supercapacitor with excellent rate capability, Electrochim. Acta. 314 (2019) 124–134. https://doi.org/10.1016/j.electacta.2019.05.065.

[16] W. Xu, H. Wang, R. Liu, X. Zhao, J. Qu, The mechanism of antimony(III) removal and its reactions on the surfaces of Fe–Mn Binary Oxide, J. Colloid Interface Sci. 363 (2011) 320–326. https://doi.org/10.1016/J.JCIS.2011.07.026.

[17] S. Wolff, S. Roscher, F. Timmermann, M. V Daniel, F. Speck, M. Wanke, M. Albrecht, T. Seyller, Quasi-Freestanding Graphene on SiC(0001) by Ar-Mediated Intercalation of Antimony: A Route Toward Intercalation of High-Vapor-Pressure Elements, Ann. Phys. 531 (2019). https://doi.org/10.1002/andp.201900199.

[18] I. Martini, E. Chevallay, V. Fedosseev, C. Hessler, H. Neupert, V. Nistor, M. Taborelli, Surface characterization at CERN of photocathodes for photoinjector applications, in: 6th Int. Part. Accel. Conf. IPAC 2015, 2015: pp. 1703–1705. http://xpssimplified.com/periodictable.ph (accessed November 11, 2021).

[19] Y. Lin, Z. Tian, L. Zhang, J. Ma, Z. Jiang, B.J. Deibert, R. Ge, L. Chen, Chromium-ruthenium oxide solid solution electrocatalyst for highly efficient oxygen evolution reaction in acidic media, Nat. Commun. 10 (2019) 1–13. https://doi.org/10.1038/s41467-018-08144-3.

[20] A.L.J. Pereira, L. Gracia, D. Santamaría-Pérez, R. Vilaplana, F.J. Manjón, D. Errandonea, M. Nalin, A. Beltrán, Structural and vibrational study of cubic Sb_2O_3 under high pressure, Phys. Rev. B - Condens. Matter Mater. Phys. 85 (2012) 174108. https://doi.org/10.1103/PhysRevB.85.174108.

[21] M. Assebban, C. Gibaja, M. Fickert, I. Torres, E. Weinreich, S. Wolff, R. Gillen, J. Maultzsch, M. Varela, S. Tan Jun Rong, K.P. Loh, E.G. Michel, F. Zamora, G. Abellán, Unveiling the oxidation behavior of liquid-phase exfoliated antimony nanosheets, 2D Mater. 7 (2020). https://doi.org/10.1088/2053-1583/ab755e.

[22] N.E. Drewett, I.M. Aldous, J. Zou, L.J. Hardwick, In situ Raman spectroscopic analysis of the lithiation and sodiation of antimony microparticles, Electrochim. Acta. 247 (2017) 296–305. https://doi.org/10.1016/j.electacta.2017.07.030.

[23] H. Zhang, K. Sun, Z. Feng, P. Ying, C. Li, Studies on the SbOx species of SbOx/SiO2 catalysts for methane-selective oxidation to formaldehyde, Appl. Catal. A Gen. 305 (2006) 110–119. https://doi.org/10.1016/j.apcata.2006.02.038.

[24] Q. Zhang, Z. Hu, Y. Yang, Z. Zhang, X. Wang, X. Yang, Y. An, B. Guo, Metal organic frameworks-derived porous carbons/ruthenium oxide composite and its application in supercapacitor, J. Alloys Compd. 735 (2018) 1673–1681. https://doi.org/10.1016/j.jallcom.2017.11.268.

[25] A. Simion, N. Candu, B. Cojocaru, S. Coman, C. Bucur, A. Forneli, A. Primo, I.C. Man, V.I. Parvulescu, H. Garcia, Nanometer-thick films of antimony oxide nanoparticles grafted on defective graphenes as heterogeneous base catalysts for coupling reactions, J. Catal. 390 (2020) 135–149. https://doi.org/10.1016/j.jcat.2020.07.033.

[26] T.K. Das, S. Banerjee, M. Pandey, B. Vishwanadh, R.J. Kshirsagar, V. Sudarsan, Effect of surface functional groups on hydrogen adsorption properties of Pd dispersed reduced graphene oxide, Int. J. Hydrogen Energy. 42 (2017) 8032–8041. https://doi.org/10.1016/j.ijhydene.2016.12.024.

[27] H. Xue, K. Chen, Q. Zhou, D. Pan, Y. Zhang, Y. Shen, Antimony selenide/graphene oxide composite for sensitive photoelectrochemical detection of DNA methyltransferase activity, J. Mater. Chem. B. 7 (2019) 6789–6795. https://doi.org/10.1039/c9tb01541h.

[28] P. Molaei, I. Kazeminezhad, Extended photocurrent performance of antimony trisulfide/reduced graphene oxide composite prepared via a facile hot-injection route, Ceram. Int. 44 (2018) 13191–13196. https://doi.org/10.1016/j.ceramint.2018.04.144.

[29] Y. Tang, N. Rong, F. Liu, M. Chu, H. Dong, Y. Zhang, P. Xiao, Enhancement of the photoelectrochemical performance of CuWO 4 films for water splitting by hydrogen treatment, Appl. Surf. Sci. 361 (2016) 133–140. https://doi.org/10.1016/j.apsusc.2015.11.129.

[30] E. Dhandapani, S. Prabhu, N. Duraisamy, R. Ramesh, Bifunctional copper zinc bimetallic tungstate nanoparticles decorated reduced graphene oxide (CuZnWO$_4$/rGO) for high-performance photocatalytic and supercapacitor application, J. Mater. Sci. Mater. Electron.

(2021). https://doi.org/10.1007/s10854-021-06339-x.

[31] A.M. Teli, S.A. Beknalkar, S.A. Pawar, D.P. Dubal, E ff ect of Concentration on the Charge Storage Kinetics, Energies. 13 (2020) 6124.

[32] Y. Gong, D. Li, Q. Fu, C. Pan, Influence of graphene microstructures on electrochemical performance for supercapacitors, Prog. Nat. Sci. Mater. Int. 25 (2015) 379–385. https://doi.org/10.1016/j.pnsc.2015.10.004.

[33] Poonam, K. Sharma, A. Arora, S.K. Tripathi, Review of supercapacitors: Materials and devices, J. Energy Storage. 21 (2019) 801–825. https://doi.org/10.1016/j.est.2019.01.010.

[34] V. Venezlan, " INNER " AND " OUTER " ACTIVE SURFACE ELECTRODES OF RuO , (1989) 5–9.

[35] D. Galizzioli, F. Tantardini, S. Trasatti, Ruthenium dioxide: a new electrode material. I. Behaviour in acid solutions of inert electrolytes, J. Appl. Electrochem. 4 (1974) 57–67. https://doi.org/10.1007/BF00615906.

[36] Q. Xue, H. Gan, Y. Huang, M. Zhu, Z. Pei, H. Li, S. Deng, F. Liu, C. Zhi, Boron Element Nanowires Electrode for Supercapacitors, Adv. Energy Mater. 8 (2018) 1–8. https://doi.org/10.1002/aenm.201703117.

[37] B.J. Choudhury, K. Roy, V.S. Moholkar, Improvement of Supercapacitor Performance through Enhanced Interfacial Interactions Induced by Sonication, Ind. Eng. Chem. Res. 60 (2021) 7611–7623. https://doi.org/10.1021/acs.iecr.1c00279.

[38] J. Yan, T. Wei, W. Qiao, B. Shao, Q. Zhao, L. Zhang, Z. Fan, Rapid microwave-assisted

synthesis of graphene nanosheet/Co 3O4 composite for supercapacitors, Electrochim. Acta. 55 (2010) 6973–6978. https://doi.org/10.1016/j.electacta.2010.06.081.

[39] T. Pettong, P. Iamprasertkun, A. Krittayavathananon, P. Sukha, P. Sirisinudomkit, A. Seubsai, M. Chareonpanich, P. Kongkachuichay, J. Limtrakul, M. Sawangphruk, High-Performance Asymmetric Supercapacitors of $MnCo_2O_4$ Nanofibers and N-Doped Reduced Graphene Oxide Aerogel, ACS Appl. Mater. Interfaces. 8 (2016) 34045–34053. https://doi.org/10.1021/acsami.6b09440.

[40] C. Wang, J. Zhao, S. Luo, X. Yu, Improved Pseudocapacitive Performance of Graphene Architectures Modulating by Nitrogen/Phosphorus Dual-Doping and Steam-Activation, Macromol. Res. 29 (2021) 582–588. https://doi.org/10.1007/s13233-021-9075-7.

[41] M. Dvoyashkin, D. Leistenschneider, J.D. Evans, M. Sander, L. Borchardt, Revealing the Impact of Hierarchical Pore Organization in Supercapacitor Electrodes by Coupling Ionic Dynamics at Micro- and Macroscales, Adv. Energy Mater. 11 (2021) 2100700. https://doi.org/10.1002/aenm.202100700.

[42] D. Qu, Studies of the activated mesocarbon microbeads used in double-layer supercapacitors, J. Power Sources. 109 (2002) 403–411.

[43] D. Mandal, P. Routh, A.K. Mahato, A.K. Nandi, Electrochemically modified graphite paper as an advanced electrode substrate for supercapacitor application, J. Mater. Chem. A. 7 (2019) 17547–17560. https://doi.org/10.1039/c9ta04496e.

[44] N. Bundaleska, J. Henriques, M. Abrashev, A.M. Botelho do Rego, A.M. Ferraria, A. Almeida, F.M. Dias, E. Valcheva, B. Arnaudov, K.K. Upadhyay, M.F. Montemor, E. Tatarova,

Large-scale synthesis of free-standing N-doped graphene using microwave plasma, Sci. Rep. 8 (2018) 1–11. https://doi.org/10.1038/s41598-018-30870-3.

[45]   H. Wei, C. He, J. Liu, H. Gu, Y. Wang, X. Yan, J. Guo, D. Ding, N.Z. Shen, X. Wang, S. Wei, Z. Guo, Electropolymerized polypyrrole nanocomposites with cobalt oxide coated on carbon paper for electrochemical energy storage, Polymer (Guildf). 67 (2015) 192–199. https://doi.org/10.1016/J.POLYMER.2015.04.064.

[46]   D. Mandal, P. Routh, A.K. Mahato, A.K. Nandi, Electrochemically modified graphite paper as an advanced electrode substrate for supercapacitor application, J. Mater. Chem. A. 7 (2019) 17547–17560. https://doi.org/10.1039/c9ta04496e.

[47]   K. Yang, K. Cho, S. Kim, Effect of carbon black addition on thermal stability and capacitive performances of supercapacitors, Sci. Rep. 8 (2018) 1–7. https://doi.org/10.1038/s41598-018-30507-5.

[48]   S. Manoharan, D. Kesavan, P. Pazhamalai, K. Krishnamoorthy, S.J. Kim, Ultrasound irradiation mediated preparation of antimony sulfoiodide (SbSI) nanorods as a high-capacity electrode for electrochemical supercapacitors, Mater. Chem. Front. 5 (2021) 2303–2312. https://doi.org/10.1039/d0qm00863j.
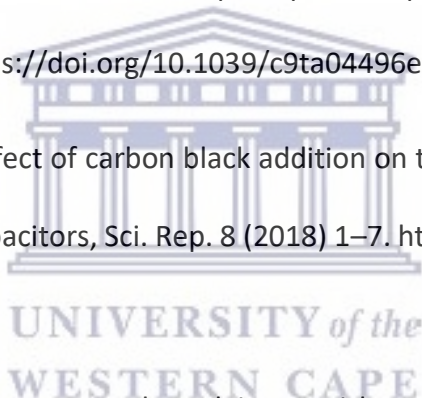
CHAPTER SIX

GRAPHENE STABILISED RUTHENIUM ANTIMONIDE NOVEL NANOMATERIAL FOR ULTRA-EFFICIENT SUPERCAPACITOR.

Highlights

- Microwave synthesis of novel ruthenium antimony oxide (RuSbO) and graphene stabilized ruthenium antimony oxide (RuSbO-G) nanoparticles.

- XPS, EDS, XRD amongst other analysis, confirmed the elemental composition and structure of the nanomaterials.

- RuSbO-G showed better electrochemical behaviors in Li_2SO_4 electrolytes than RuSbO due to structural differences.

- RuSbO-G asymmetric supercapacitor device demonstrated an impressive level of stability and efficiency after ~4900 charge and discharge cycles.

ABSTRACT

Ruthenium antimony oxide (RuSbO), and ruthenium antimony oxide graphene (RuSbO-G) nanomaterial was synthesized via the microwave-assisted method for the first time and tested as a possible electrode material for an asymmetric supercapacitor device. The formation of the nanocomposites was confirmed by scanning electron microscopy (SEM) and transmission electron microscopy (TEM) images where the RuSbO material show randomly distributed spherically shaped nanoparticles, and the RuSbO-G showed ruthenium and antimony
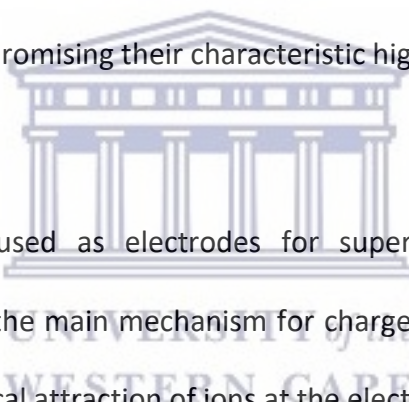
nanoparticles scattered randomly on the graphene sheets. The SEM-electron dispersion X-ray spectroscopy (SEM-EDS) showed significant proof for nanoparticle formation with the elemental composition, while the X-ray photoelectron spectroscopy confirmed the oxidation states of the elements present. Both materials were further characterized in a three-electrode cell setup using cyclic voltammetry (CV), galvanostatic charge-discharge (GCD) and electrochemical impedance spectroscopy (EIS) and their electrochemical properties were compared to establish their suitability for energy storage purposes. From the result, different double layer properties were shown by the RuSbO and RuSbO-G in the 1 M Li_2SO_4 electrolyte. When compared to the RuSbO electrode, the composite had greater energy storage capabilities with a maximum capacitance of 289.47 F g^{-1} at 0.1 A g^{-1} current load. An efficiency of ~100% was reached at a current density of 0.5 A g^{-1}. Subsequently, both materials were used to fabricate a portable asymmetric supercapacitor. The RuSbO-G device yielded a maximum specific capacitance of 167.96 F g^{-1}, resulting in an energy density of 75.58.0W h kg^{-1} at a power density of 360 W kg^{-1} at 0.1 A g^{-1} current load, with ~100% charge retention after 4900 cycles. This study turns a new research light on RuSbO based materials as an energy storage material for supercapacitors.

KEYWORDS

Energy density, microwave synthesis, ruthenium antimony oxide, pseudocapacitance, supercapacitors

6.1 INTRODUCTION

As the world's population continues to increase the consumption of energy also increases [1-2]. The current dependency on conventional energy sources is gradually shifting towards renewable sources. However for this shift to transcend smoothly, energy storage systems are required to work optimally to achieve a complete chain. Supercapacitors are one of those high-power devices that are being used for energy storage purposes. A supercapacitor has very high-power density and cycle life but relatively low energy density when compared to other storage devices. To achieve high energy density, new and advanced materials are needed to improve the capacitance of supercapacitors without compromising their characteristic high-power density and cycle life.

Carbon materials have been used as electrodes for supercapacitors for long, and the electrochemical double-layer is the main mechanism for charge storage. These materials store charges solely through the physical attraction of ions at the electrode/electrolyte interface, with no further chemical activities taking place. As a result, they have quite high charge and discharge rates, which leads to a high-power density; nevertheless, due to their low energy density, they have not sufficiently met the need for an excellent energy storage device [3][4]. Pseudocapacitors are principally made up of metal oxides and conducting polymers, they store charges using a different mechanism known as pseudocapacitance, these are fast Faradaic reactions happening at the electrode surface of metal oxides or conducting polymer [5]. Currently, pseudocapacitance materials are being researched as alternative electrode materials, however, they offer enhanced energy density at the cost of cyclic stability and power density which characterizes an ideal

supercapacitor [6]. So far, an intense effort has been made to improve traditional materials such as carbon materials, transition metal-based materials and conducting polymers. Ruthenium oxide has been one of the most widely researched transition metal-based materials [7-9]. In recent times, however, novel materials including sulphides, nitrides and selenides have been synthesized and proposed to be capacitive [10-12]. For instance, other compounds of ruthenium like its nitrides [13-[13]15], sulphides[16-18], and even tellurides [16] have been explored, however until date, its antimonide counterpart has never been investigated.

Antimony based compounds that are gradually gaining popularity in sodium/ lithium (Na/Li) ion batteries as efficient anode materials have a theoretical capacity of up to 660 mAh g^{-1}[20,21]. Its compounds have been tried for supercapacitor applications severally. Copper antimony sulphide (Cu_3SbS_4) was successfully synthesized by Mariapan *et al.* and yielded a capacitance of up to 60 F g^{-1} at 5 mV s^{-1} resulting in an energy density of 11.373 W h Kg^{-1} at a power density of 175 W Kg^{-1} and good capacitance retention after 2500 cycles [19]. The major drawback for antimony is the resultant effect of its volume expansion which results in reduced stability. However, the use of carbon material such as graphene has been found to provide stability, by acting like a mechanical buffer that will reduce the volume change while facilitating electron transport during the charge-discharge process [20].

In this report, a new energy storage material based on a binary metal oxide composite stabilised with graphene is presented. Ruthenium antimony oxide-graphene nanocomposite (RuSbO-G)

was synthesized via microwave-assisted (MW) method. First graphene oxide was synthesized from graphite powder using the Hummers method, then the pristine RuSbO compound and the RuSbO-G nanocomposites were synthesized via MW synthesis. The materials were thoroughly characterized morphologically, spectroscopically, and electrochemically. Interestingly, the as-prepared RuSbO-G electrode demonstrated a very capacitive energy storage mechanism, with CV curves that match the behaviour of typical pseudocapacitance materials. The materials were used as an electrode for an asymmetric supercapacitor device and a capacitance of 167.96 F g^{-1}, which translated into an energy density of 75.58W h kg^{-1} at a power density of 360 W kg^{-1} and at 0.2 A g^{-1} current load for the graphinised composite was obtained.

6.2 EXPERIMENTAL

6.2.1 Materials

Microcrystalline graphite (2-15 µm, 99.99%) was purchased from Alfar Aesar (Kandel, Germany) Nickel foam (1.6 mm thick, 0.25 µm pore diameter) was purchased from MTI Corporation, (Richmond, Califonia, USA). Hydrogen peroxide solution (30 wt. % in water, American chemical society (ACS) reagent), concentrated hydrochloric acid (reagent grade and assay 36.5-38.0%), sodium borohydride (98.0%), potassium permanganate (≥ 99.0%, ACS reagent), concentrated sulphuric acid (99.999%), Ruthenium (III) chloride hydrate (99.98% trace metal bases), antimony pentachloride (99.999% trace metal bases), polytetrafluoroethylene (mean particle size 20 µm), activated charcoal (Norit ® pallets), anhydrous N-methyl-2-pyrrolidone (99.5%) and carbon black (4 µm mesoporous carbon matrix, ≥ 99.95% metal bases), ethylene glycol (EG) (99.8%), ethanol

(absolute, ≥ 99.8%) were purchased from Sigma-Aldrich (St Louis, Missouri, USA) and were all used without further purification.

6.2.2 Microwave-assisted synthesis of SbO and SbO-G nanocomposite

The MW-assisted synthesis of RuSbO was carried out using an Anton Parr multi-wave Pro microwave system. It is equipped with an IR temperature sensor that controls the temperature during the process. $RuCl_3.xH_2O$ (1 mmol) and 2 mmol of $SbCl_5$ was added to 30 mL of ethylene glycol with continuous stirring for 0.5 h. $NaBH_4$ (1.5 g) was slowly added to the above-mixed solution, sonicated for 10 min and allowed to cool. The resultant mixture was MW-irradiated at 190 ℃ for 10 min. The resulting products were separated by centrifuging, washed with deionized water and dried at 60 ℃ under vacuum for 12 h.

One hundred milligrams of the as-synthesized GO (as described in chapter 3) is dissolved in 30 mL of ethylene glycol and sonicated for 2 h to form a homogenous dispersion. $RuCl_3.xH_2O$ (1 mmol) and 2 mmol of $SbCl_5$ were added to the dispersed solution and sonicated for 0.5 h. $NaBH_4$ (2 g) was slowly added to the above mixture, which was sonicated for 10 min and transferred to a microwave vessel. The resultant mixture was MW-irradiated at 190 ℃ for 10 min. The resulting products were separated by centrifuging, washed with deionized water, and dried at 60 ℃ under vacuum for 12 h.

6.2.3 Material characterization

The elemental and morphological composition of the nanoparticles were obtained using a Carl ZEISS ULTRA scanning electron microscope GmbH. Fitted with an energy dispersion spectrometer. (Jena, Germany). All analysis was performed on a nickel-copper grid. The samples for TEM characterization were drop-coated into the Cu TEM grids and scanned in high-resolution transmission electron microscopy (HR-TEM) with an FEI Technai G20 F20X-Twin MAT 200 Kv Field Emission Transmission Electron Microscope (Eindhoven, Netherlands) equipped with both EDS and selected area electron diffraction (SAED). The X-ray powder diffraction (XRD) pattern was obtained for all the nanoparticles with a D8 advance multipurpose X-ray diffractometer (BRUCKER-AXS, Berlin, Germany) using copper kα1 radiation (λ ~ 0.154 nm) operating at 40 kV and 40 mA. XRD patterns were collected from 15 to 70 (2q) with step size of 0.034^o in 2q. The functional group present in the sample was determined using a Perkin Elimer Spectrum 100 series Attenuated Total Reflectance (ATR) Fourier Transform Infra-red spectrometer with 4 cm^{-1} resolutions (Perkin-Elmer, Boston, MA, USA). The particle size distribution was determined by a small-angle X-ray scattering (SAXS) measurement, performed on an Anton Paar GmbH SAXSpace P/N 100100 (Graz, Austria). It was equipped with a 1 D mython 2 position-sensitive detector, a beamstop alignment, and a Copper Kα (0,154 nm) instrument radiation was used. The nanoparticles Raman spectra were obtained using an Xplora Olympus BX41 Raman Spectrometer (Horiba, Tokyo, Japan) using a 532 nm laser as the excitation source. Optical absorption spectra were acquired from ethanolic dispersions of the nanocrystals at room temperature using a Varian Cary 300 UV-Vis-NIR spectrophotometer (Agilent, Santa Clara, CA, USA). At room temperature, infrared spectroscopic investigations between 4000 and 400 cm^{-1} were carried out. The

powdered nanocrystals were deposited on a diamond disc, and infrared spectra were acquired using an Attenuated Total Reflectance/Perkin-Elmer Spectrum 100 Series Fourier Transform Infrared (FTIR) Spectrometer (Perkin-Elmer, Boston, MA, USA). The photoluminescence properties were obtained from NanoLog HORIBA using the software FluorEssence V3.9. (Johannesburg, South Africa). All electrochemical studies were performed on a VMP-300 potentiostat from the Bio-Logic SAS instrument (France).

6.2.4 Electrode preparation and electrochemical measurements

To prepare the working electrode, the active material; RuSbO and RuSbO-G (70%), a conducting agent; carbon black (20%) and a binder; polytetrafluoroethylene (10%) was mixed in a mortar, and crushed to fine powder, then 3 drops of anhydrous N-methyl-2-pyrrolidone was added and mixed to form a uniform slurry. Nickel foam was cut into rectangular shapes of 0.5 x 1cm^2 and coined shapes of 20 mm in diameter. The foams were cleaned to remove all surface oxide layers in 1 M HCL solution, absolute ethanol, and deionized water respectively, with ultra-sonication for 15 min in each solvent, and dried at 90 ℃ for 12 h. The homogenous paste was coated on 0.5 cm^2 diameter of the nickel foam and dried at 80 ℃ for 12 h. In a three-electrode cell setup, Ag/AgCl and Pt wire were used as the reference and counter electrode respectively. While for the full cell, the paste was coated into the coin-shaped nickel foam and assembled in a Swagelok with activated carbon as the negative electrode. The cyclic voltammograms were recorded between -0 to 0.6V potential window at different scan rates, the electrochemical impedance measurements were obtained at a frequency range of 0.1 MHz to 100 MHz with 10 points per

decades, and the galvanostatic charge-discharge profiles were measured at different current densities. All electrochemical characterisation of material was done in the three-electrode cell using 1 M Li_2SO_4, electrolyte, and the device was tested at 1.8 V in 1 M Li_2SO_4.

6.3 RESULT AND DISCUSSION

6.3.1 Morphological studies

6.3.1.1   SEM and TEM analysis

SEM was used to investigate the surface morphology, average particle size and shape of the nanoparticles. The SEM image for the pristine RuSbO (Figure 6.1) revealed clustered spherically shaped particles that ranges between 10 nm and 40 nm, while those of RuSbO-G was more dispersed on the graphene layer with sizes ranging from 8 nm to 35 nm. The TEM result as shown in Figure 6.2 confirms that while the RuSbO was severally agglomerated, the RuSbO-G was more dispersed (Figure 6.3), therefore the graphene must have acted as a dispersing agent and the metal oxides must have also acted as a spacer for the graphene sheets [21]. The more dispersed material is expected to provide more intercalation sites for electrolytes ions, resulting in higher electrochemical performance [22]. The more dispersed composite material will also have an improved surface area and several accessible pores for the electrolyte thus increasing ion mobility. Therefore, the addition of graphene showed a better structural property [23]. The RuSbO-G particles have a diameter between 9 nm-25 nm from the TEM data. The particles are better distributed in the composite as seen in the TEM image than in the RuSbO. This will give

rise to better packing porosity and geometrical tortuosity thereby having better pathways for the

electrolyte ions [24],[25].
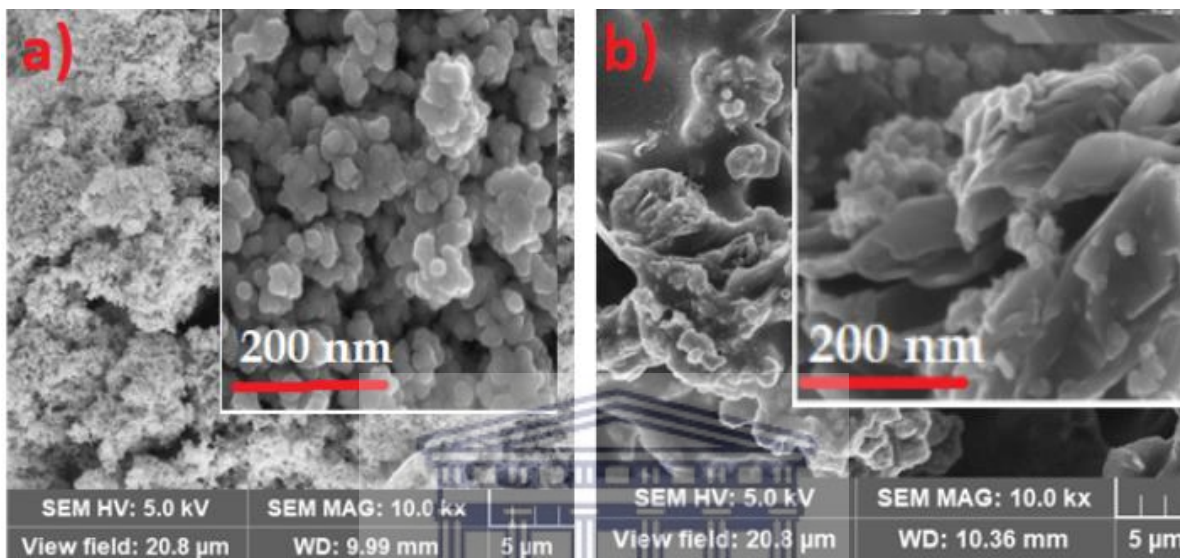
Figure 6.1: SEM images of RuSbO and RuSbO-G.
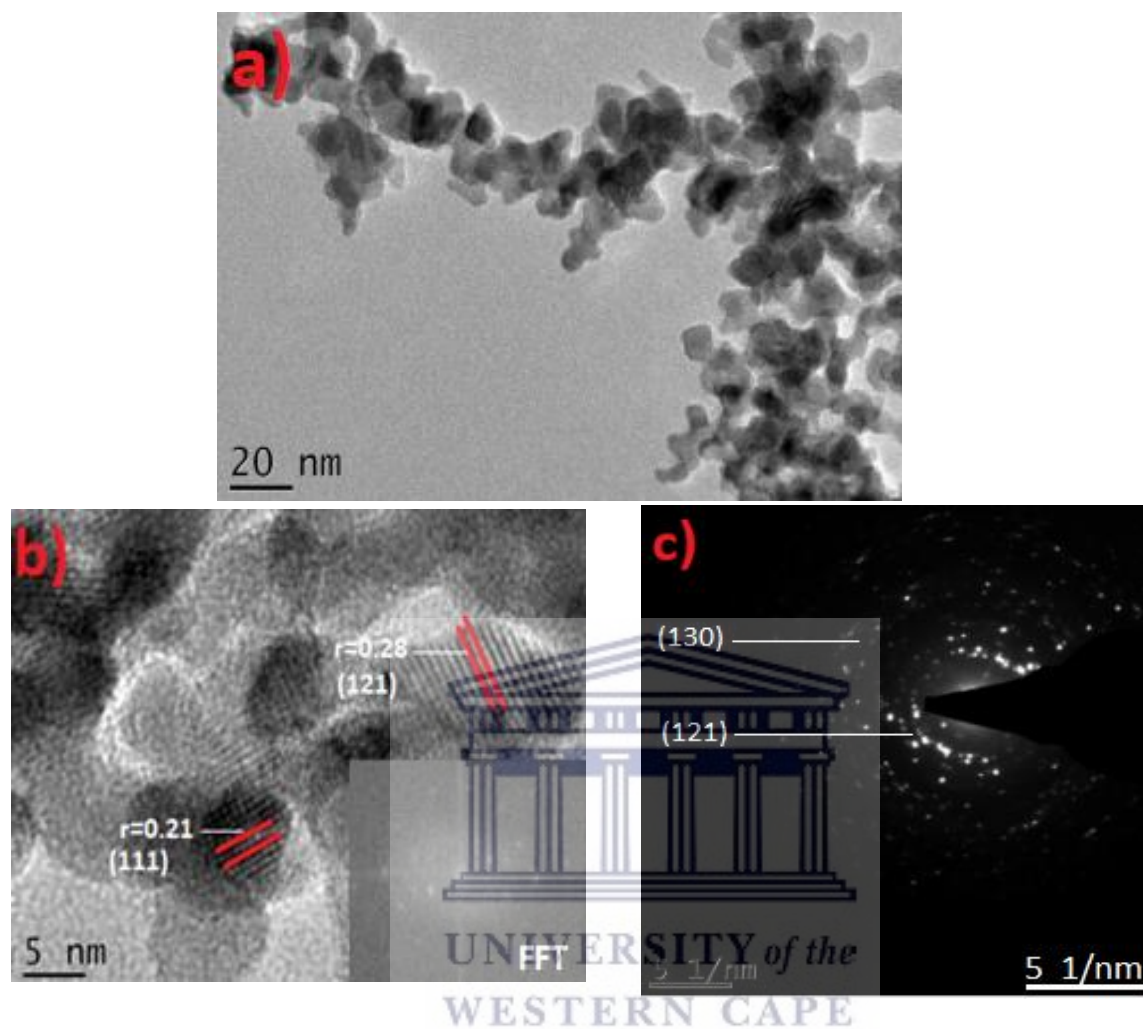
Figure 6.2: RuSbO: a) TEM image; b) HRTEM image showing the lattice fringes, the inset is the

FFT; c) SAED pattern.
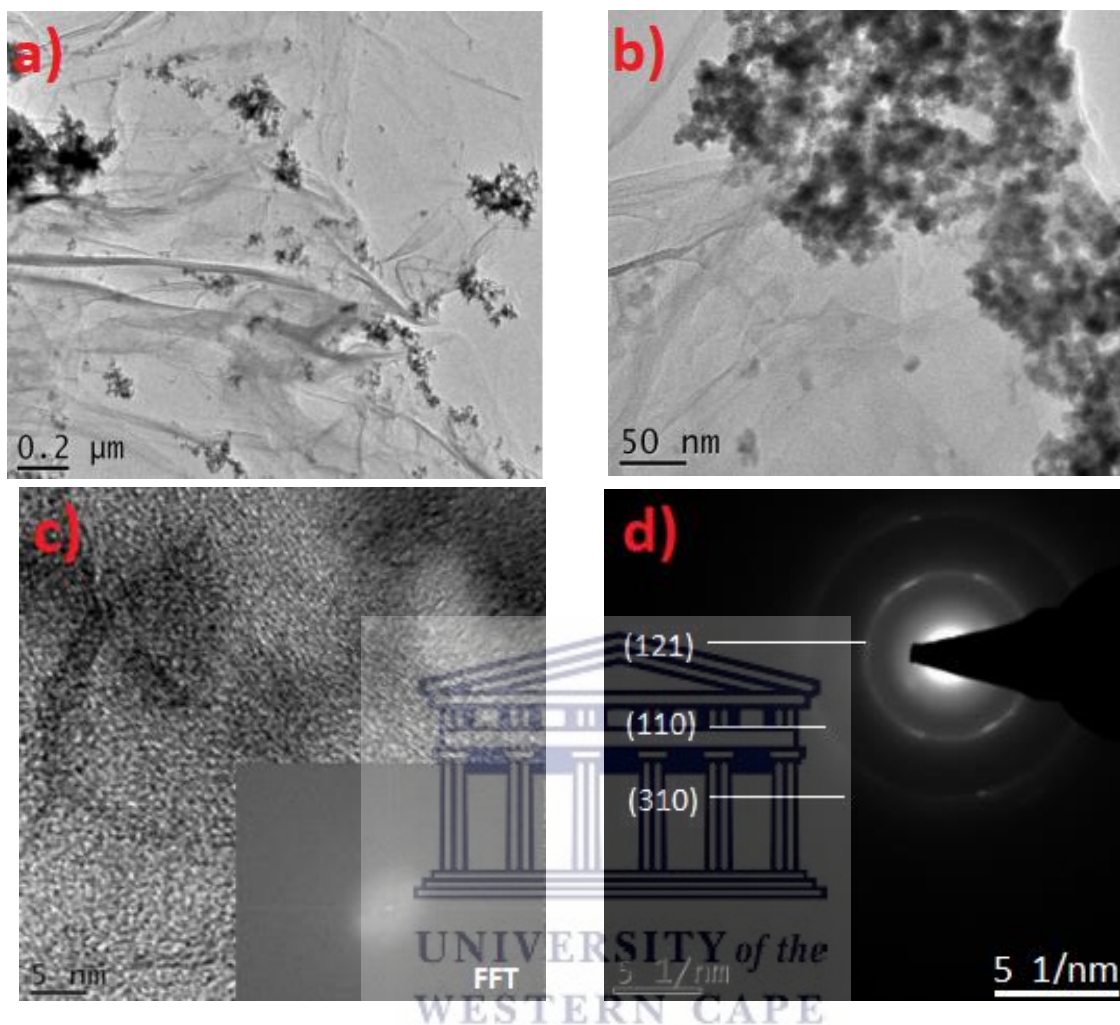
Figure 6.3: RuSbO-G: a,b) TEM images at different magnifications; c) HRTEM image showing

the lattice fringes, the inset is the FFT; d) SAED pattern.

The fast Fourier transform (FFT) image in Figure 6.2b was obtained from the lattice fringes of the

RuSbO TEM monogram and was used to confirm the d-spacing and possible phases of the

particles obtained from XRD data. By analysing the TEM image, the lattice fringes are shown to

be 0.28 nm, 0.21 nm, in the RuSbO, they are along the (121) and (111) plane which is following

the XRD data. For the RuSbO-G the lattice fringes were not obvious (Figure 6.3b). This is due to

the incorporation of amorphous graphene into its structure. The selected area electron diffraction (SAED) pattern shows that the composite is crystalline in the (130), (121) direction for the RuSbO compound and in the (121), (110), (310) direction of the RuSbO-G nanocomposite. This is also confirmed by the data from the XRD analysis.

6.3.1.2   Atomic force microscopy

AFM was used to characterize the topography of RuSbO and RuSbO-G nanoparticles. The results were analyzed using Gwyddion software and reported in terms of topographic and diffraction images, with 2D, Line, and 3D chart types. The surface roughness and height distribution were the parameters extracted from the analysis. The surface topography of the RuSbO and film shows that grains are uniformly distributed, without any fractures or voids in the film's surface. (Figure 6.4). The 3D diffraction image of RuSbO-G Figure 6.5c shows a brighter surface which might mean higher conductivity [26]. The average surface roughness (Ra) and the root mean square roughness (Rq) were used to study the changes in electrode modifications (Table 6-1). The surface area of the pristine RuO electrode (6.18 nm^2) increased drastically after modification with the graphene (3.96 μm^2) due to the prominent surface features of the graphene [27].

Table 6-1: AFM parameters for RuSbO and RuSbO-G

Parameters	RuSbO (mm)	RuSbO-G (mm)
Ra	2.72	5.55
Rms/Rq	4.125	9.53
Surface area	3.8	5.3
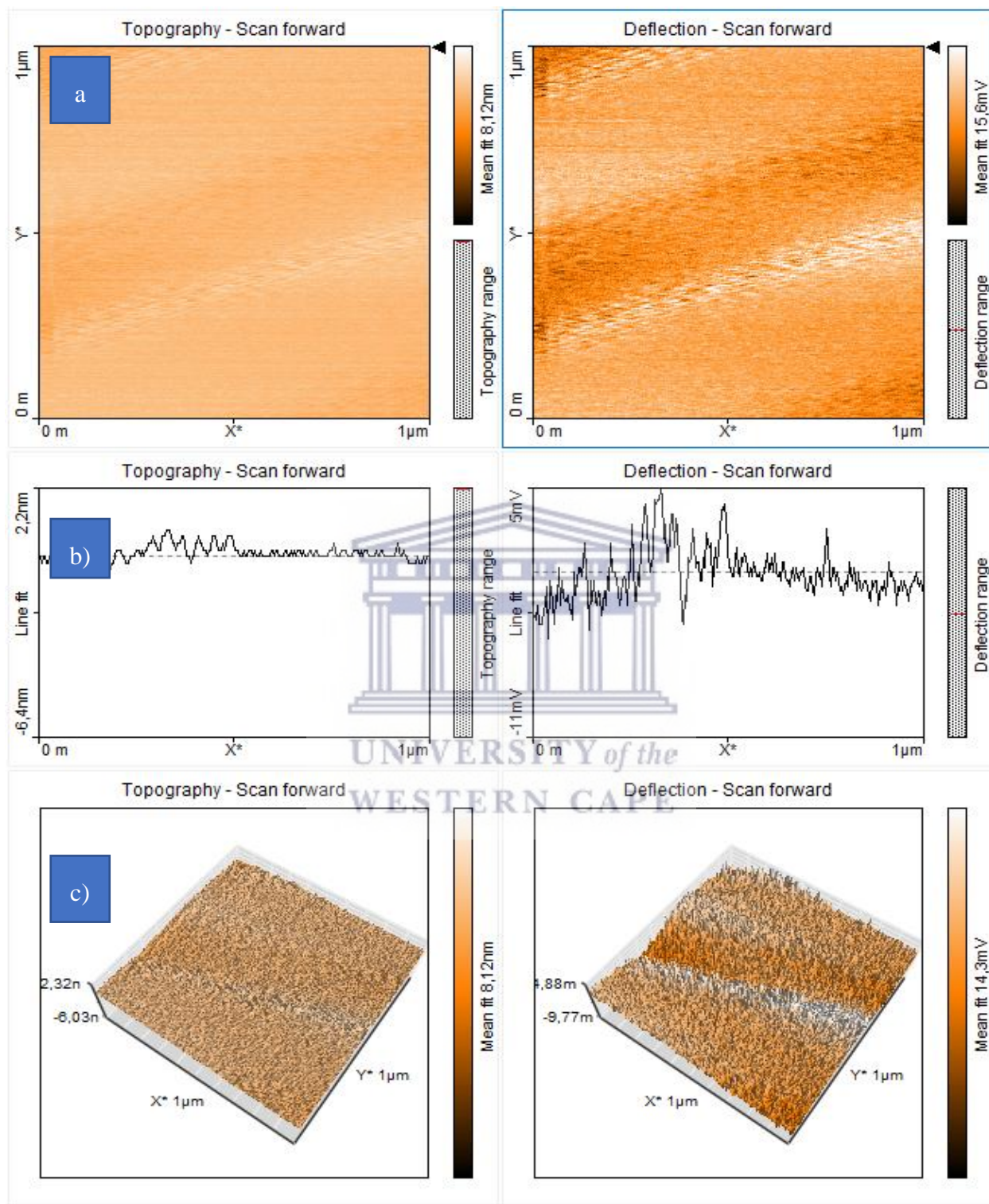
Figure 6.4: AFM a) 2D, b) line and c) 3-D topography and deflection images of RuSbO.
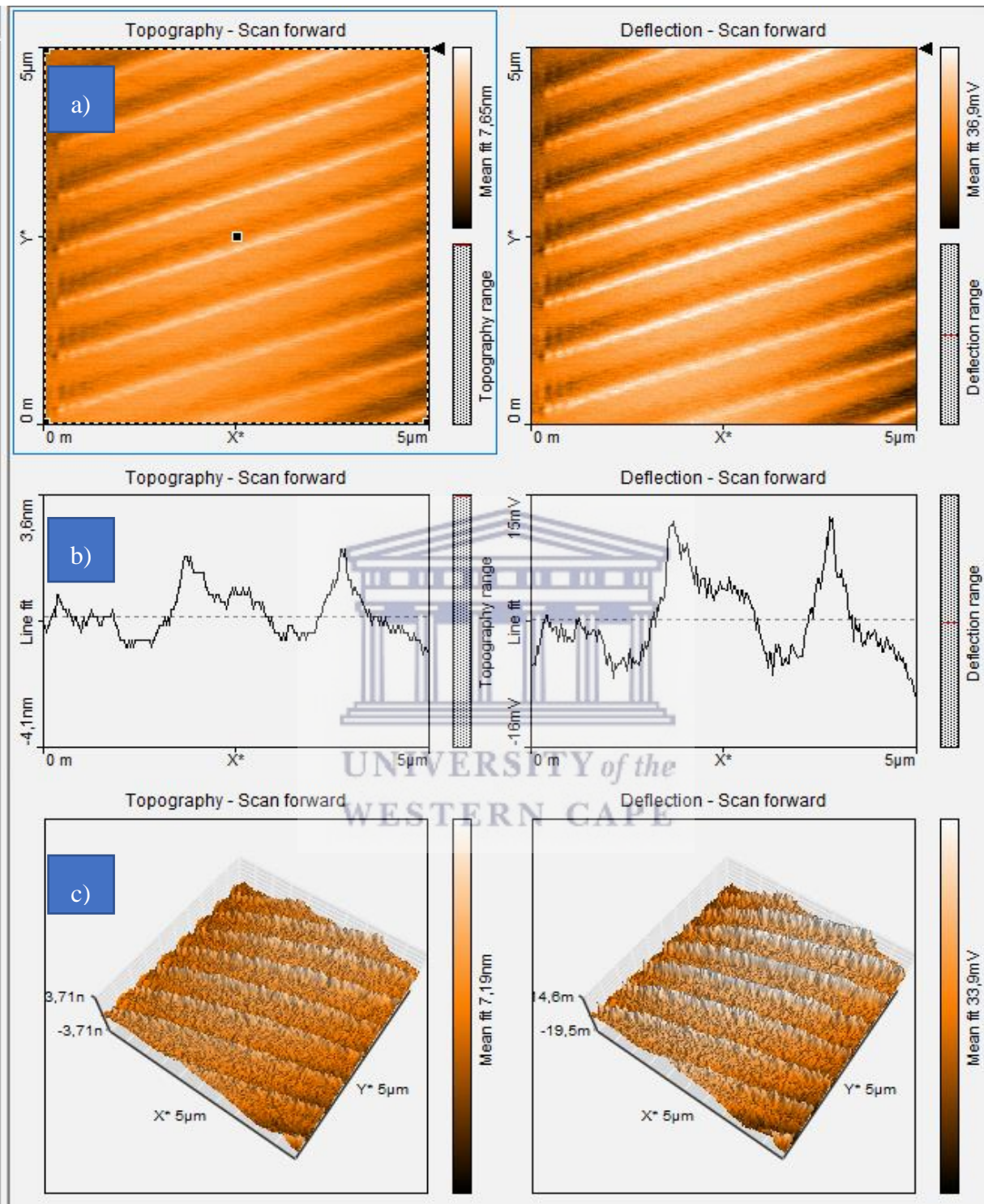
Figure 6.5: AFM a) 2D, b) line and c) 3-D topography and deflection images of RuSbO-G.

6.3.2 Spectroscopical studies

6.3.2.1   Energy-dispersive X-ray spectroscopy (EDS)

EDS from the SEM analysis was used to ascertain the elemental composition of RuSbO and RuSbO-G. Figure 6.6 and Figure 6.7 shows the SEM from where EDS was taken, the EDS analysis confirms the presence of Ru, Sb and O in RuSbO and Ru, Sb, O and C in RuSbO-G was also confirmed. The EDS data reveals that Sb was in a high quantity in the pristine material than in the composite. This could mean that the presence of graphene inhibited the nucleation/ growth of Sb nanoparticles. The data in the inset reflect the weight percent of each element. The data reveals that a substantial amount of graphene was in the composite. This will increase the composite's stability and limit the volume expansion of Sb and Ru.
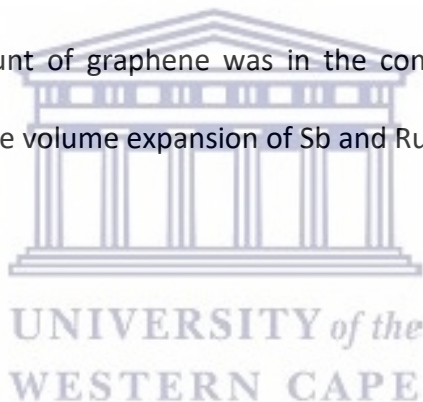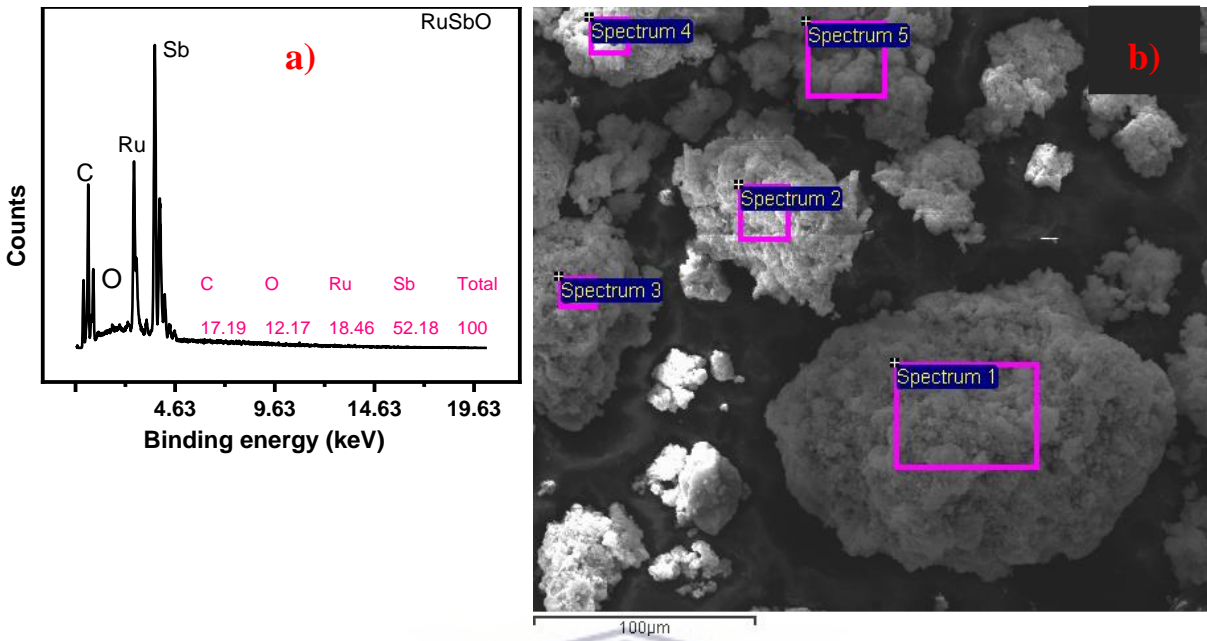
Figure 6.6: EDS spectrum a) and SEM image b) of RuSbO-G. Inset in (a) is the percentage elemental composition. The labels in the SEM image (b) represent sampling points for the EDS.
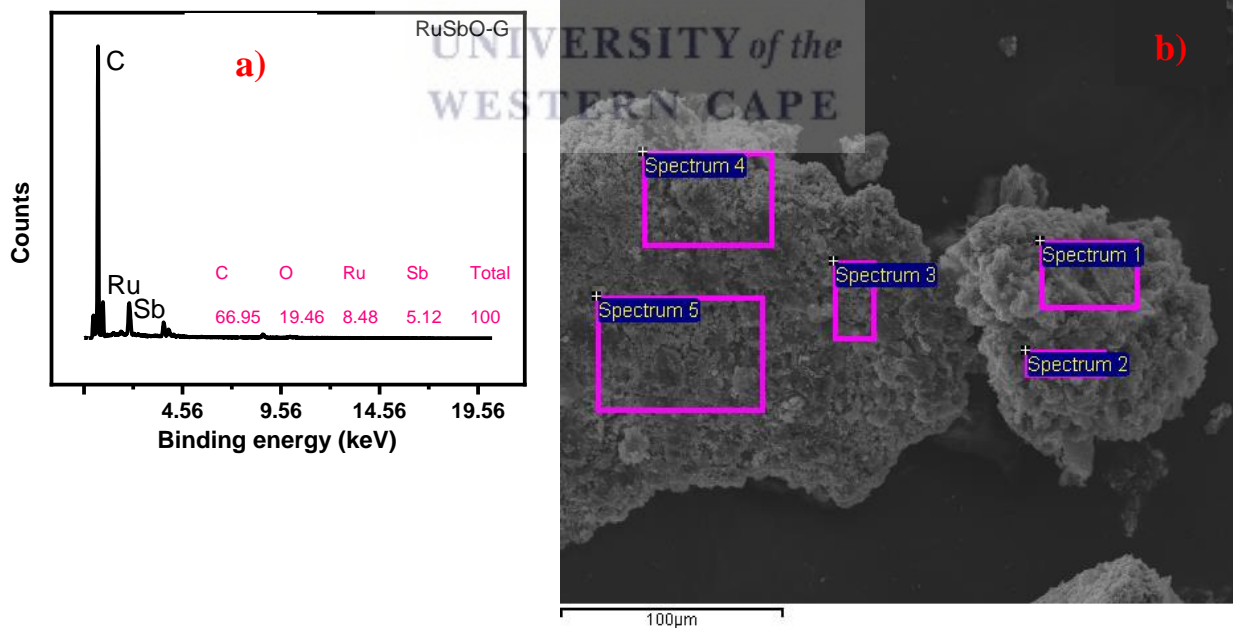
Figure 6.7: EDS spectrum a) and SEM image b) of RuSbO-G. Inset (a) is the percentage elemental composition. The labels in the SEM image (b) represent sampling points for the EDS.

6.3.2.2 X-ray powder diffraction (XRD)

Figure 6.8 shows the XRD pattern of the RuSbO and RuSbO-G materials. Samples were observed as Ru, RuO_2, and Sb_2O_4. All the diffraction peaks are indexed to base-centered orthorhombic Sb_2O_4 according to the Joint committee on powder diffraction standards. (JCPDs card No _2 37 08 54) with lattice parameter a =6.50900 Å, b=6.51200 Å, c=3.08300 Å and tetragonal RuO_2 (JCPD card No 2_43-1027) with lattice parameter a = 4.4994 Å and c= 3.10710 Å. The sample shows a diffraction peak at 2θ = 27.83°, 34.8°, 44.02°, 53.1°, 69.17° which belongs to the (200), (101), (100), (131), (211) phase of RuO_2, and Sb_2O_4. The most intensive peak at 44.0° shifted to 43.83° for the RuSbO-G XRD graph, this increase in the volume of the unit cell could be related to the presence of Sb in the structure of Ru. Since the atomic size of Ru is smaller than Sb, substitutional occupancy of the Sb atoms on the Ru lattice would expand the lattice and shift to lower angles [28][29]. The same reasons can be attributed to the peak at 54.3° belonging to (131) phase of antimony in RuSbO which shifted from a lower angle (2θ = 53. 5°) as seen in the RuSbO-G (311). This is suspected to be due to the incorporation of ruthenium in the antimony lattice. The XRD analysis was also used to quantify the difference in interlayer spacing arising from the attachment of graphene to the RuSbO nanocomposite. A clear shift in the peak to an increase of 0.4 nm in the spacing between the layers indicates that the addition of graphene can effectively expand the interlayer spacing of the composite, which will facilitate the diffusion and transport of electrolyte ions during the charge/discharge process [30]. The composite, RuSbO-G showed

diffraction peaks at 2θ = 37.55º, 40.99º, 43.09º, 55.3º, 68.4º, 83.08º belonging to (100), (131), (211) phases. With the addition of graphene two characteristics peaks at 2θ = 27.83º and 34.88 belonging to the (200) and (101) phase of RuO_2 and Sb_2O_4 significantly reduced, indicating that the structure of the material changed with the addition of graphene. The increase in intensity and shift in the position of the peaks in RuSbO-G compared to those of RuSbO as shown in Figure 6.8b is an indication of a structural change owing to the addition of graphene. The XRD data also suggests that the possible crystal structure of the RuSbO and RuSbO-G is tetragonal this was achieved through estimated refinement and simulation with VESTA software as shown in Figure 6.9 to Figure 6.12 for the pristine material. Crystal size was also estimated using the Debye-Scherer formula for the most intense peaks in the XRD patterns. The size was an average of 37.30 nm in the pristine material and 36.33 nm in the composite material. the difference in diameter is due to the incorporation of graphene and it is confirmed in the SEM and TEM analysis.
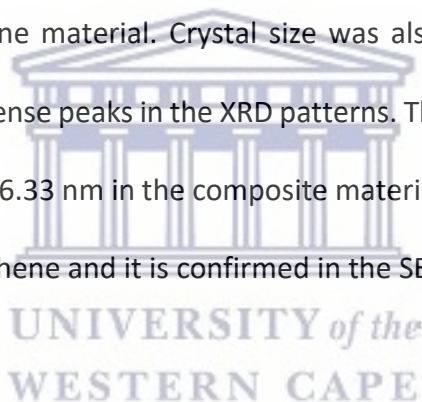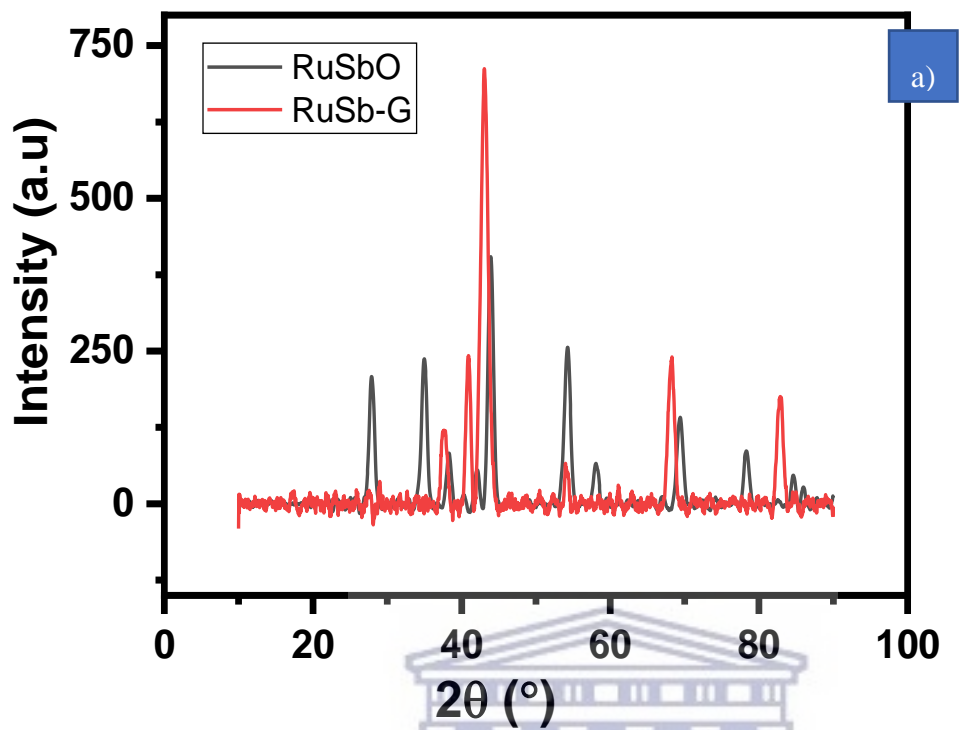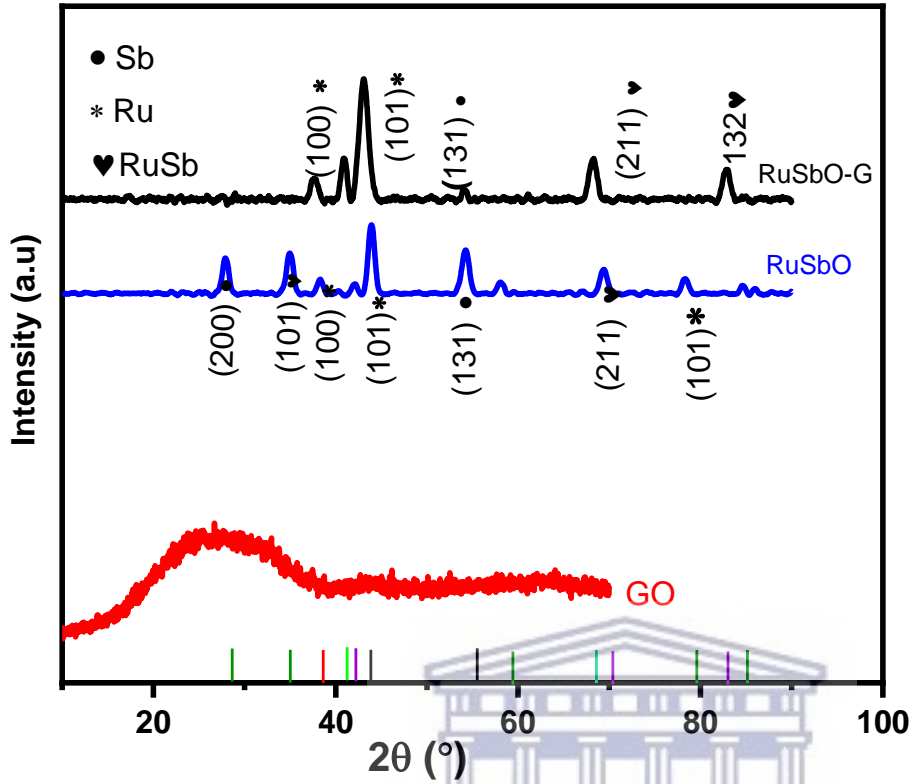
Figure 6.8: XRD analysis of a) RuSbO and RuSbO-G showing the change of intensity and peak position of the phases b) RuSbO and RuSbO-G overlayed with graphene.

Blue - O

Red - Ru
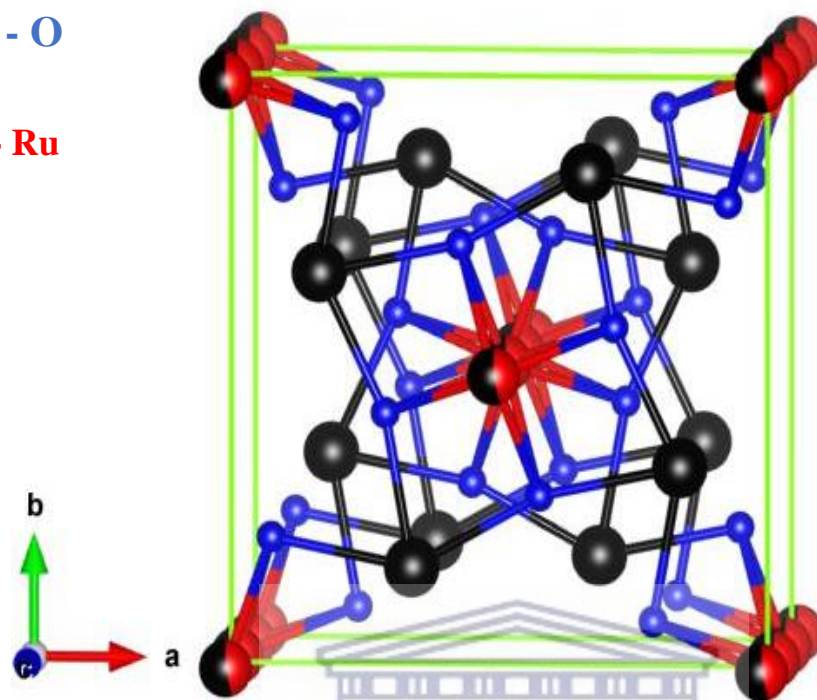
Figure 6.9: Crystal structure models of RuSbO simulated from VESTA from XRD data, BC tetragonal unit cell with Ru and Sb atom located at the BC position

Blue - O

Red - Ru

b

a
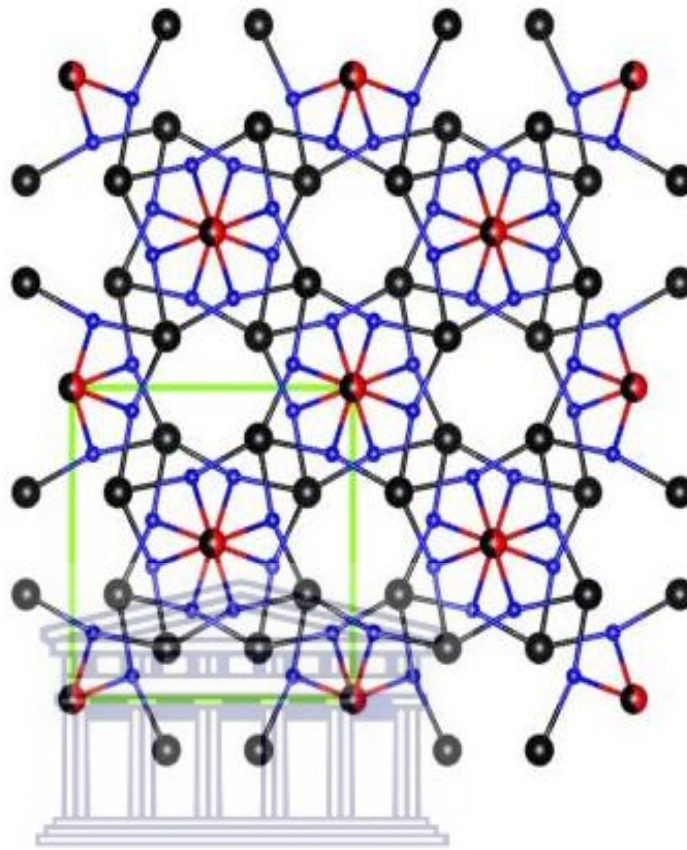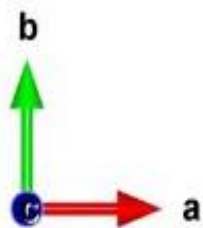
Figure 6.10: Closely packed tetragonal structure, repeated unit cells along with the a' b and c

coordinate showing consistency in the crystal arrangement.

Blue - O

Red - Ru

Black - Sb

Carbon- C
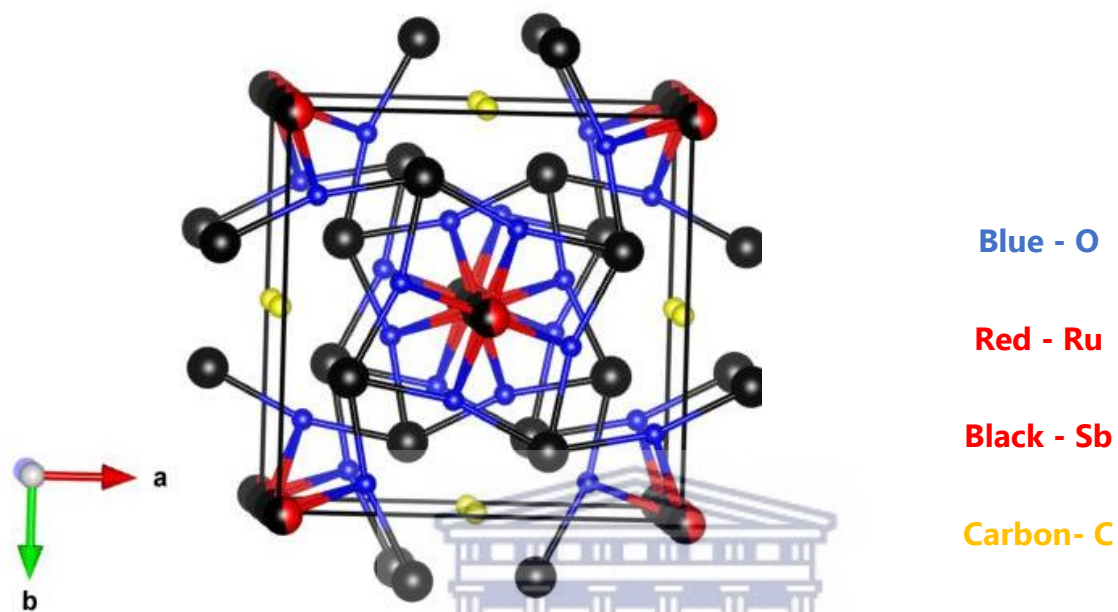
Figure 6.11: Crystal structure models of RuSbO-G simulated from VESTA from XRD data, a

Tetragonal unit cell of RuSbO-G showing a body centered packing.

Blue - O

Red - Ru

Black - Sb

Carbon- C
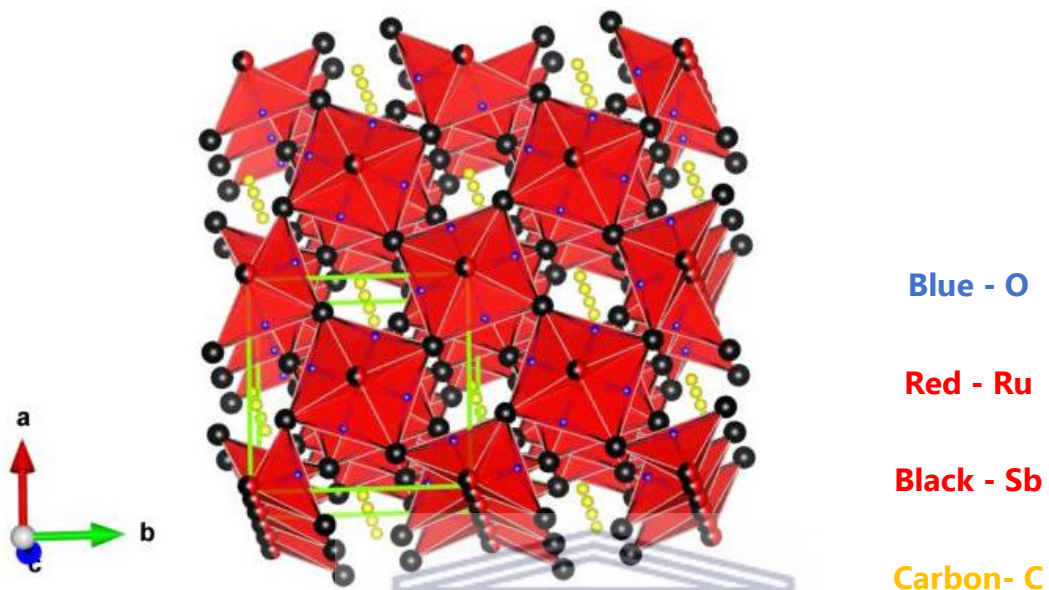
Figure 6.12: Repeated unit cells along the a, b and c coordinate in a polyhedral showing consistency in the crystal arraignment of RuSbO-G, the Sb atom is located at the middle of the polyhedral

6.3.2.3 Fourier transform infra-red spectroscopy (FTIR)

The FTIR absorption spectra of RuO, SbO, and RuSbO in the 4000-400 cm^{-1} region is shown in Figure 6.13. The investigation was carried out to determine the presence of bending or stretching vibrations in the synthesized RuO, SbO, and RuSbO. The distinctive OH stretch is confirmed by the broadband at 3385 cm^{-1} in the RuO_2 spectrum. The vibration of molecular water's hydroxyl groups and the stretching vibration of the peroxo group induce the absorption band around 2928, 1647, and 1067 cm^{-1}. The vibrational band at 981 is characterized by the presence of Ru-OH,

whereas the tiny band at 459 cm^{-1} is induced by the asymmetric stretch of Ru-O [31]. The Sb-O stretching is visible in the SbO spectrum at 550 cm^{-1}[32]. The metal-oxygen stretching absorption recorded in 550 cm^{-1} and 459 cm^{-1} for SbO and RuO is stronger in RuSbO. The shift in vibrational band position and intensity for RuSbO in comparison to the pristine materials indicates the creation of new structural material. Figure 6.14 shows the FTIR absorption spectra of RuO-G, SbO-G, and RuSbO-G in the 4000-400 cm^{-1} region. The distinctive OH stretch is confirmed by the band at 3790 and broadband at 3385 cm^{-1} in the RuO-G spectrum. The bending and stretching of the C-H, C=C, C-O, C-C group induce the absorption band around 3000 -1000 cm^{-1}. The band at 941, 786 and 638 cm^{-1} is induced by the asymmetric stretch of RuO$_2$ [33][31]. On the SbO-G spectrum, the O-H stretch is visible at 3703 cm^{-1}. The absorption band around 1664, 1605, 1356, 1050 cm^{-1} is caused by the stretching and bending of C-OH, C-H, C=O, C=C, C-O groups. The Sb-O stretching is visible at 550 cm^{-1} [32]. The functional groups present in RuO-G and SbO-G are also visible in the RuSbO-G spectrum. The metal-oxygen group induced vibrations at 880, 790, 640, 488, and 455 cm^{-1} for Ru-O, and Sb-O are visible with increased intensity [34][35]. The shift in band position and intensity in the RuSbO and RuSbO-G samples in comparison to their pristine material indicates the creation of new structural material. Table 6-2 shows all the distinct functional groups present in RuSbO and RuSbO-G.
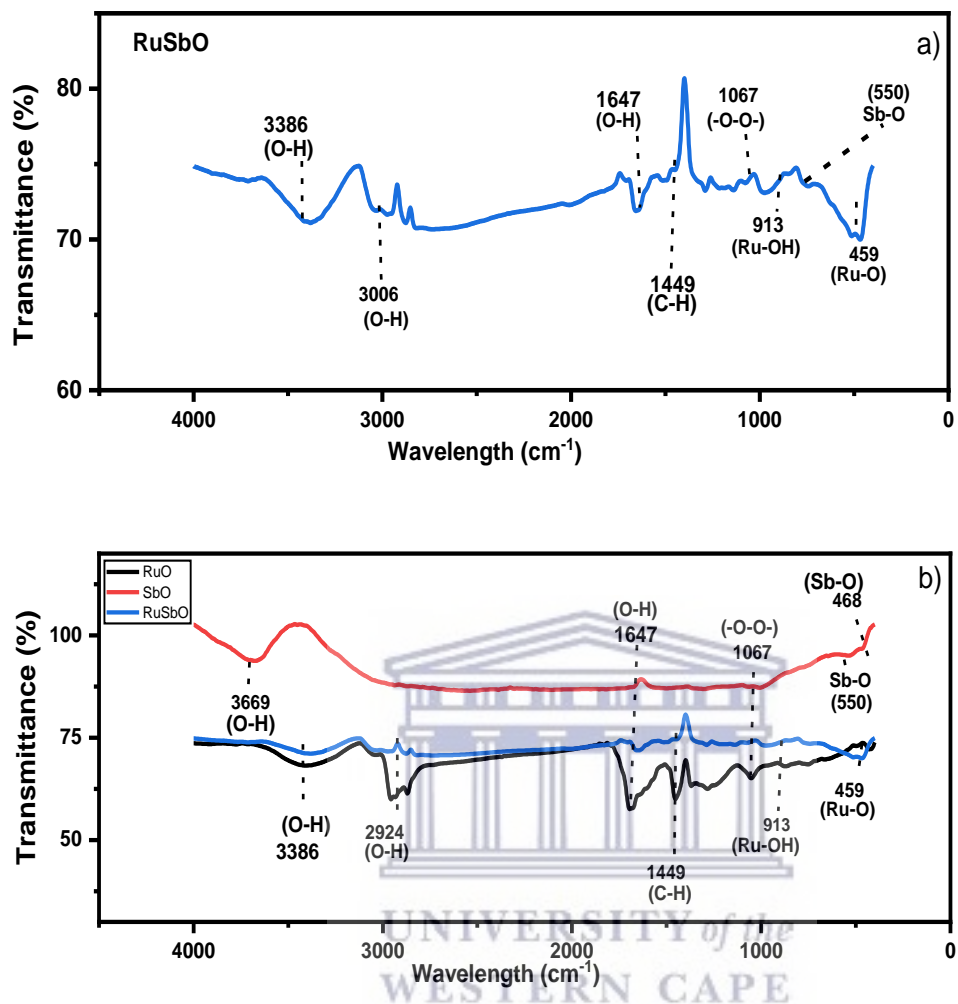
Figure 6.13: FTIR spectra of a) RuSbO, b) RuO, SbO and RuSbO.

,
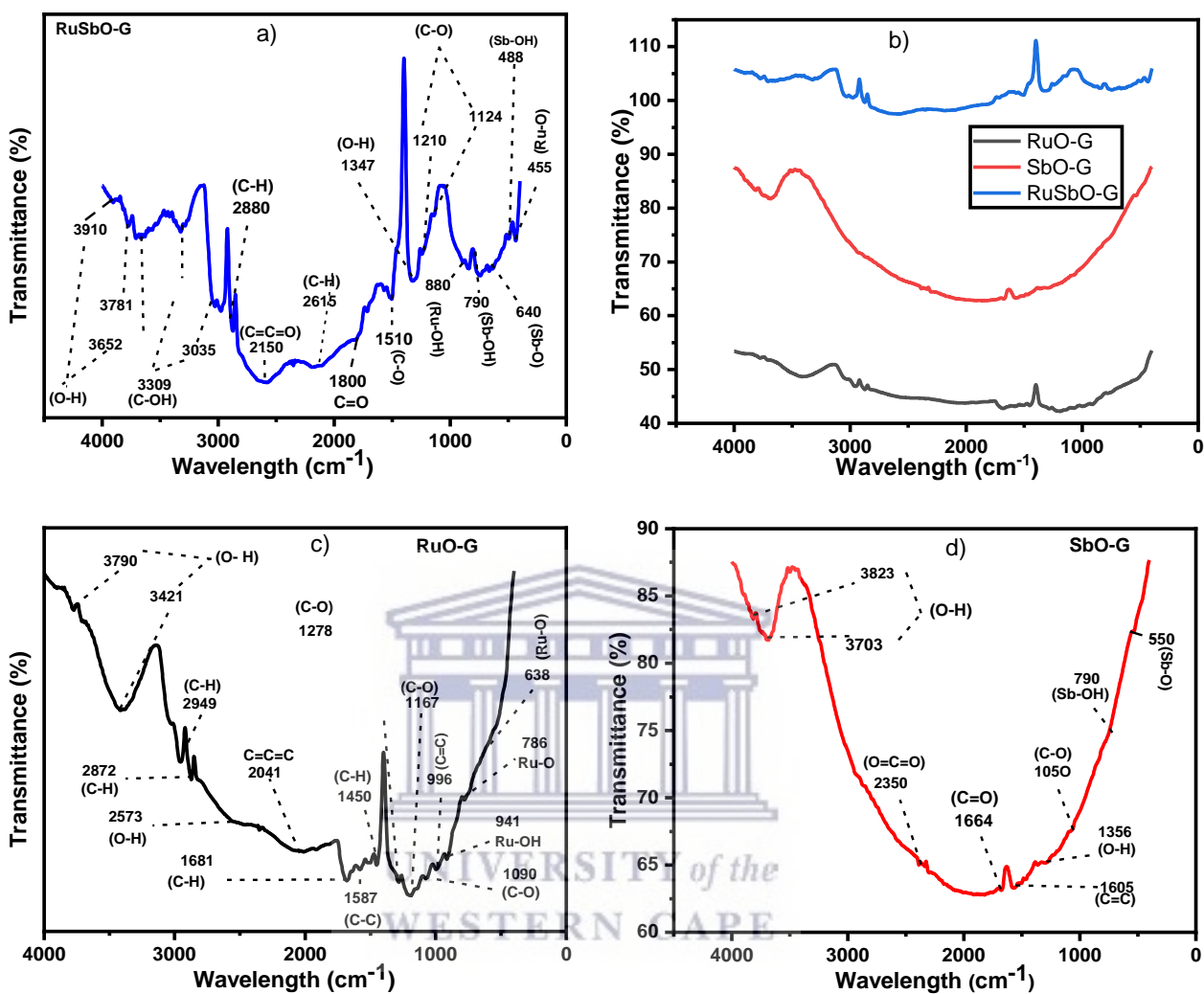
Figure 6.14: FTIR spectra of a) RuSbO-G, b) RuO-G, SbO-G and RuSbO-G, c) RuO-G, d) SbO-G.

Table 6-2: Functional groups and vibrational bands of RuSbO and RuSbO-G

Functional group	Material/ wavenumber
	(cm^{-1})[a2]

326

	RuSbO	RuSbO-G
O-H	3386	3781
C-H		288
C=C		2041
C=O		1800
C-O		1510
Sb-O	650	550
Ru-O	455	459

6.3.2.4   X-ray photoelectron spectroscopy

XPS technique was used to determine the oxidation states and stoichiometry of RuSbO-G. Using

full-spectrum XPS analysis. In Figure 6.15, the elements Ru, Sb C and O were detected in the

RuSbO-G nanomaterial. The high-resolution Ru 3d +C1s scan of RuSbO-G (Figure 6.15b) was split

into six peaks at 289.3, 287.3, 285.8, 285.3, 284.5 and 280.1 eV. This indicates the presence of

carbon-oxygen components (O-C=O, C=O, C-O,) sp2 hybridized carbon (C-C) and Ru/RuO$_2$ as seen

in the FTIR analysis [36][37]. The high-resolution Sp$_3$ d3 + O1s spectrum of the composite (Figure

6.15c) was split into four main peaks at 539.9, 537.6, 530.7 and 528.6 eV. Which belonged to

Sb$_3$O$_5$/Sb$_2$O$_3$, Sb$_3$d$_3$, C=O, C-O and Sb [38]. The MW synthesis successfully introduced antimony

and ruthenium atoms into the graphene matrix. When Sb$_3$ d3 of RuSbO-G is compared to pristine

SbO in, a change to lower binding energy is seen, implying a larger electron density at Sb_3 sites in

the RuSbO-G sample [39][40].
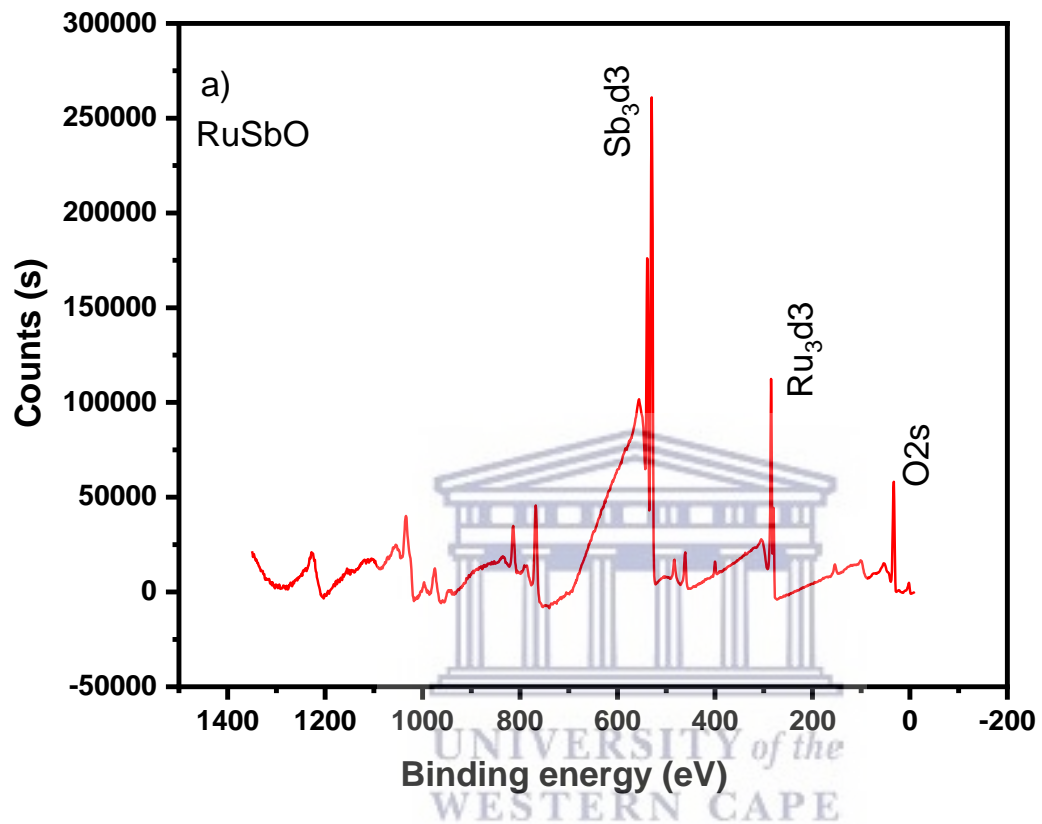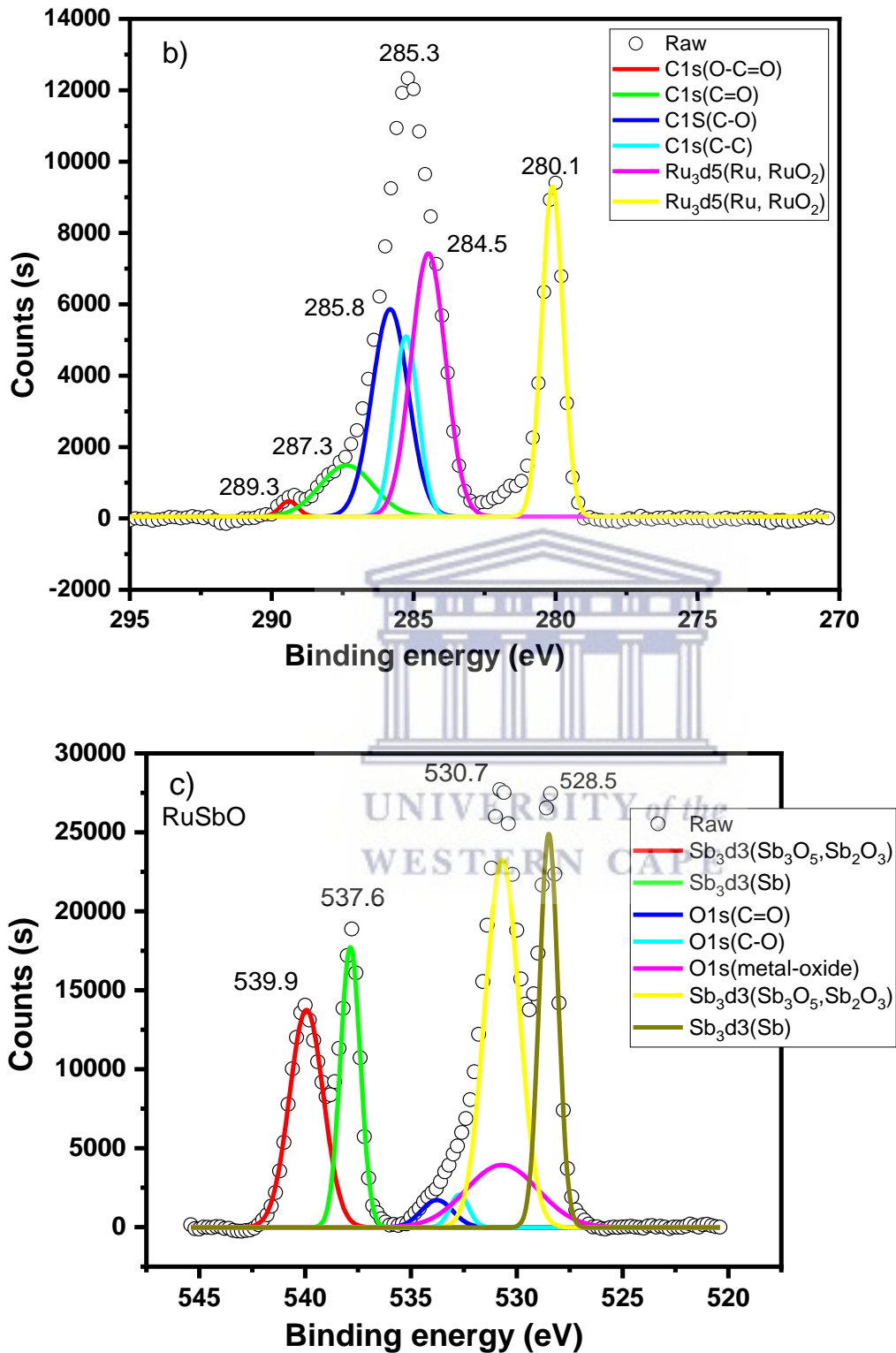
Figure 6.15: XPS Spectrum of; a) RuSbO-G, b) Ru 3d+C1s, c) Sb 3d +O1s b).
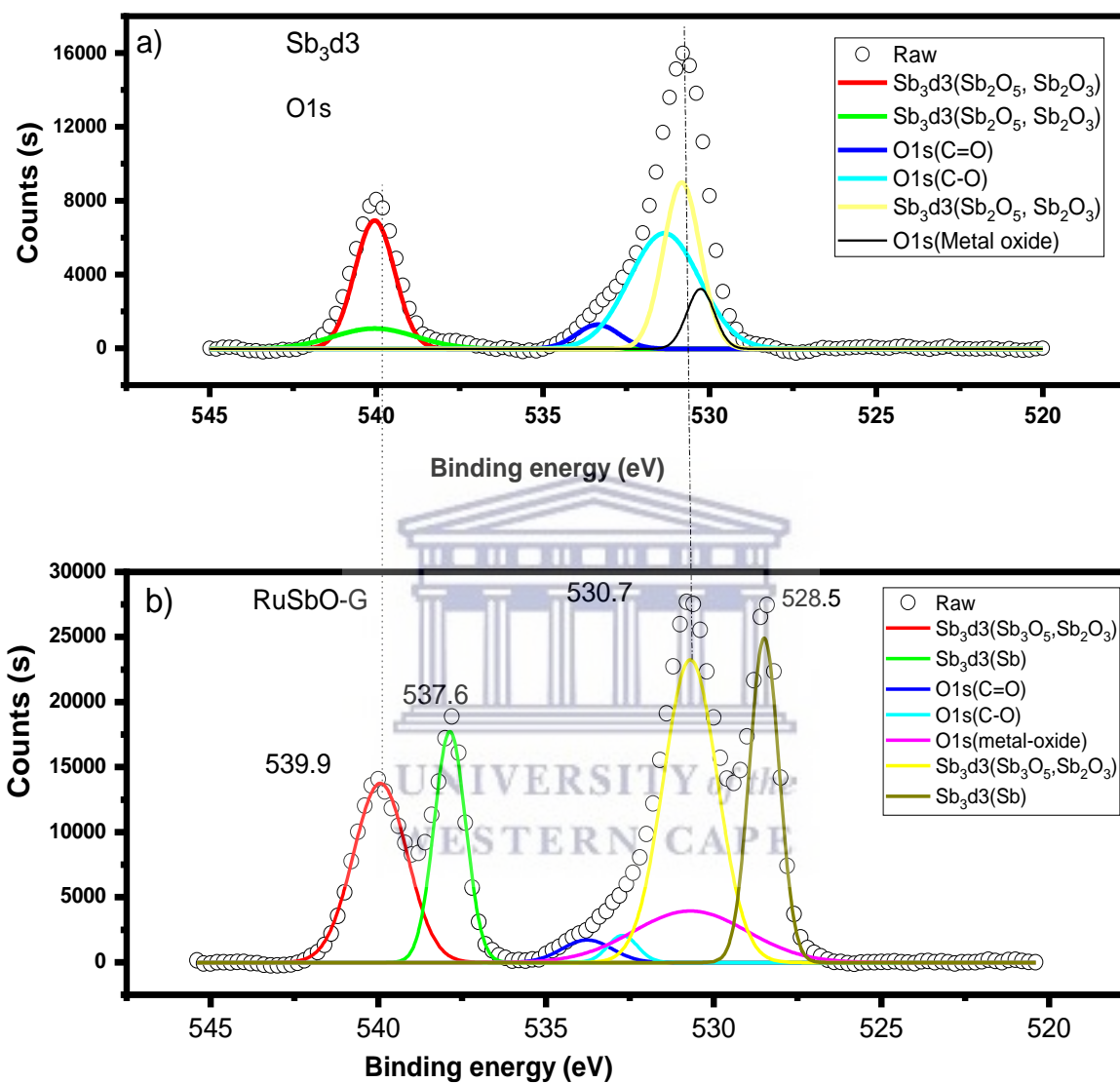
Figure 6.16: XPS spectrum of a) SbO and b) RuSbO-G showing the Sb₃ d3 position.

6.3.2.5   Raman spectroscopy

The Raman spectroscopy of RuSbO and RuSbO-G was carried out to further establish the structural properties of RuSbO material. From the spectrum, as represented in Figure 6.17 the

characteristics of Ru-O peaks can be identified at the 153 and 526 cm^{-1} positions. The bands at

(113.1 cm^{-1}) and (153.2 cm^{-1}) belong to the E_g and A_{1g} vibrational modes of Sb-O [41][42], while

the band around 560 cm^{-1} is related to Sb_2O_4. The slight change in peak position and the increase

in the peak intensity in RuSbO as compared to the pristine RuO and SbO is an indication of the

formation of a new structure. In the composite's material, the peaks belonging to RuO and SbO

are present alongside the peaks belonging to carbon. Figure 6.18 shows the spectrum RuSbO-G

alone and the inset is the deconvoluted spectrum emphasizing the peak positions. The carbon

bands intensity reduced drastically compared to when each material was combined with

graphene separately. However, the material maintained a higher ID/IG ratio than pristine

graphene as seen in the pristine materials.
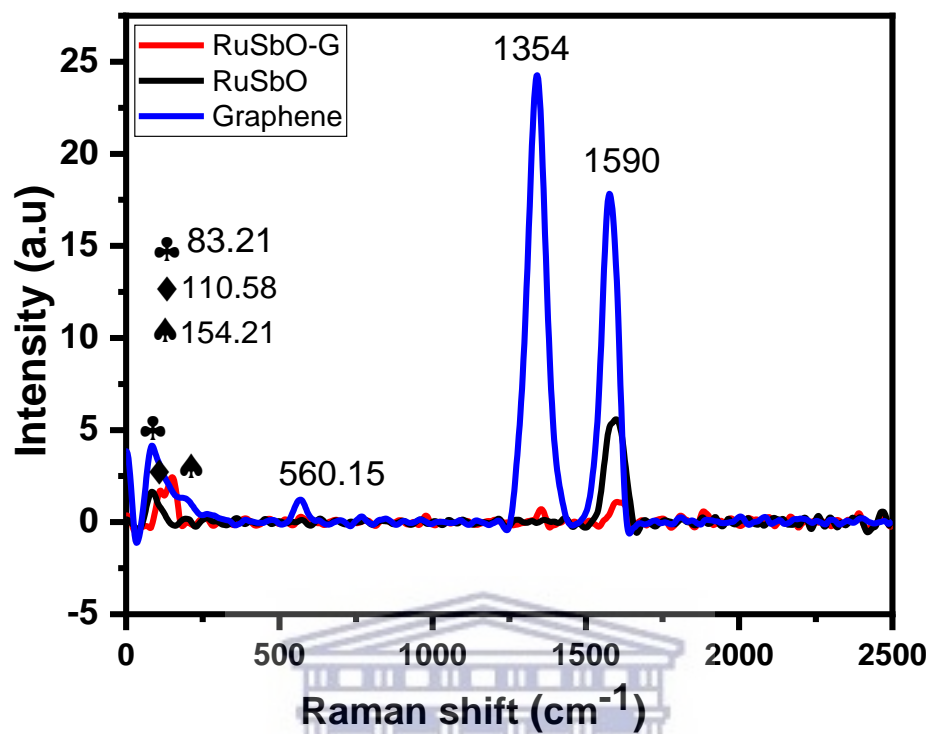
Figure 6.17: Raman spectra of RuSbO and RuSbO-G overlayed on graphene.
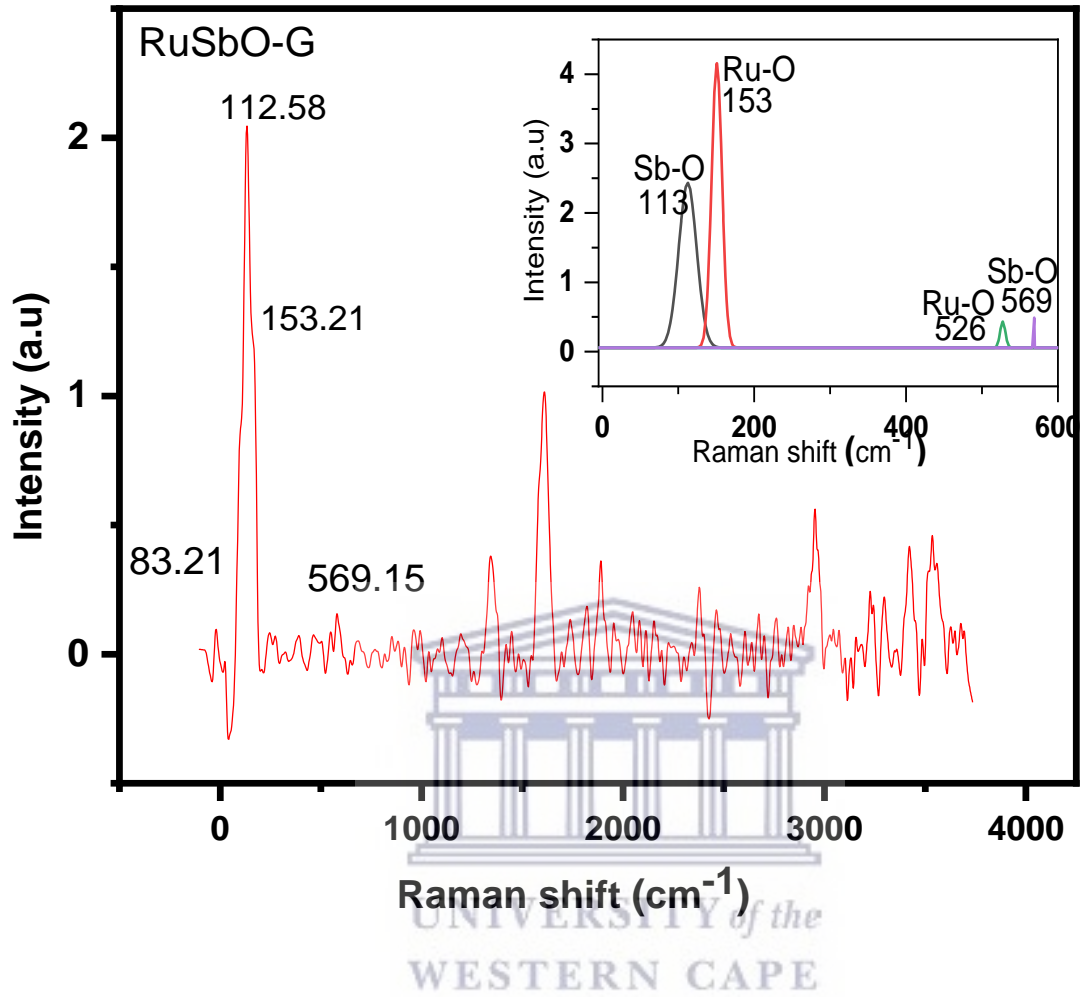
Figure 6.18: Raman spectroscopy of RuSbO-G, the inset is the deconvoluted bands, at a reduced scale.
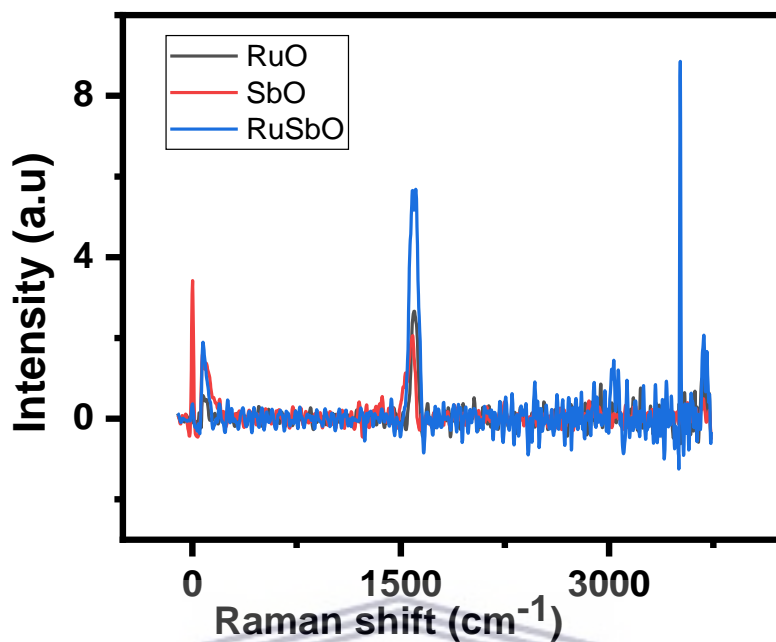
Figure 6.19: Raman spectroscopy of RuO, SbO and RuSbO.
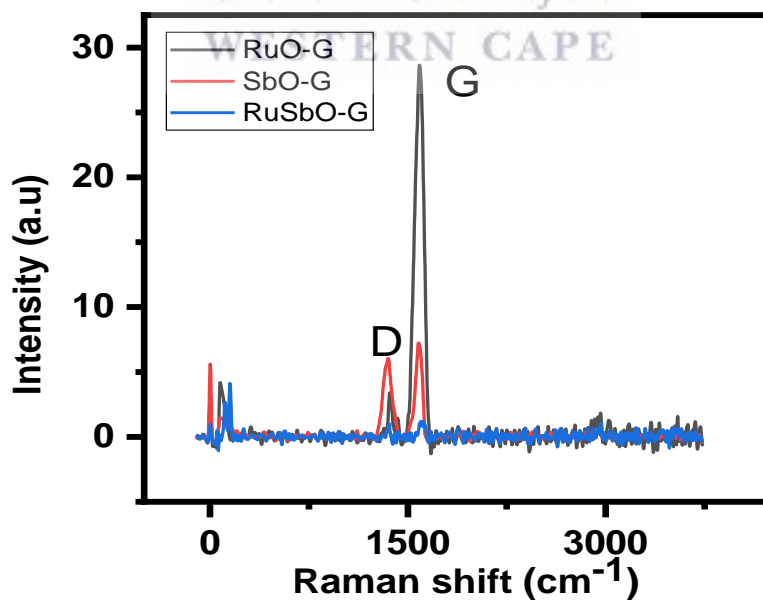
Figure 6.20: Raman spectroscopy of RuO-G, SbO-G and RuSbO-G.

6.3.2.6   Solid-state nuclear magnetic resonance spectroscopy (NMR)

The NMR spectra of RuSbO-G and graphene are shown in Figure 6.21. Pure graphene's carbon environment was compared to that of RuSbO-G samples. The prominent peak at 117 ppm, which belongs to graphitic sp^2 carbon as seen in graphene, shifted to 125 ppm, while a shoulder peak can be seen at 104 ppm, like that seen in RuO-G, and at 166 ppm, like that seen in SbO-G. Other shoulder peaks can be seen at 92 and 138 ppm. The inset shows the graph of the deconvoluted peaks showing that the chemical environment of carbon is different from those of graphene, RuO-G and SbO-G. The FWHM of the most intense peak of graphene, RuO-G, SbO-G and RuSbO-G samples are 31, 23, 22 and 25 ppm [43][44].
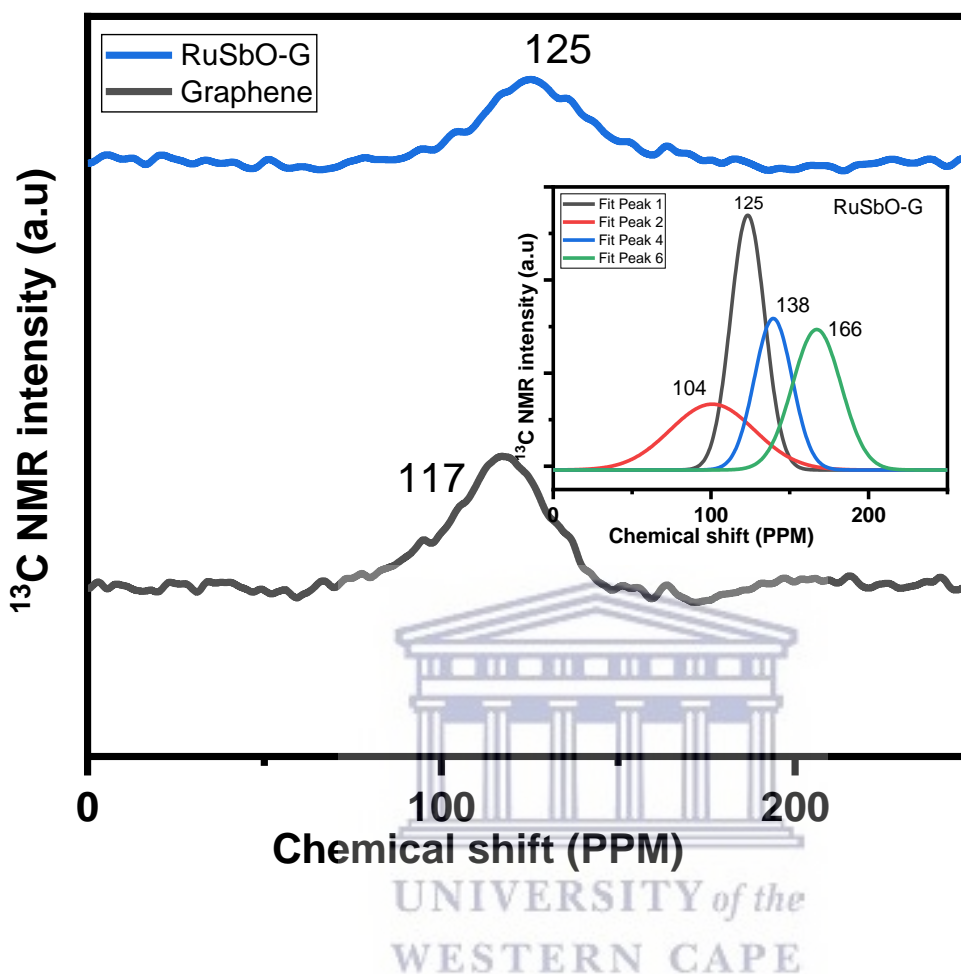
Figure 6.21: NMR results spectrum of graphene and RuSbO-G the inset is the deconvoluted 126 ppm peak of RuSbO-G.

6.3.2.7 UV-vis spectroscopy

The presence of Ru and Sb nanoparticles is confirmed by the UV-Vis absorption test. When compared to pristine graphene, all RuSbO nanoparticles have apparent exponential decay curves in the 200-400 nm region, which could be attributable to Mie scattering (Figure 6.22) [45][46]. This indicates the stability of RuSbO nanoparticles as well as their good solvent dispersion [47].

With the addition of graphene, the curve exhibits a more evident exponential decay, indicating that the RuSbO-G nanoparticles have increased dispersion capacities. The bandgaps of RuSbO and RuSbO-G were estimated to be 0.50 and 0.24 eV, respectively, using the Taucs plot from the origin program (Figure 6.22, inset) [48]. When compared to RuSbO nanoparticles, the bandgap of RuSbO-G composite is smaller due to the effect of carbon [49][50]. The smaller conduction band indicates that the synergy between Ru, Sb and C can facilitate the transmission of charges, which will induce high power density, The small band gap value of this material might be owing to their high crystallinity [51][52].
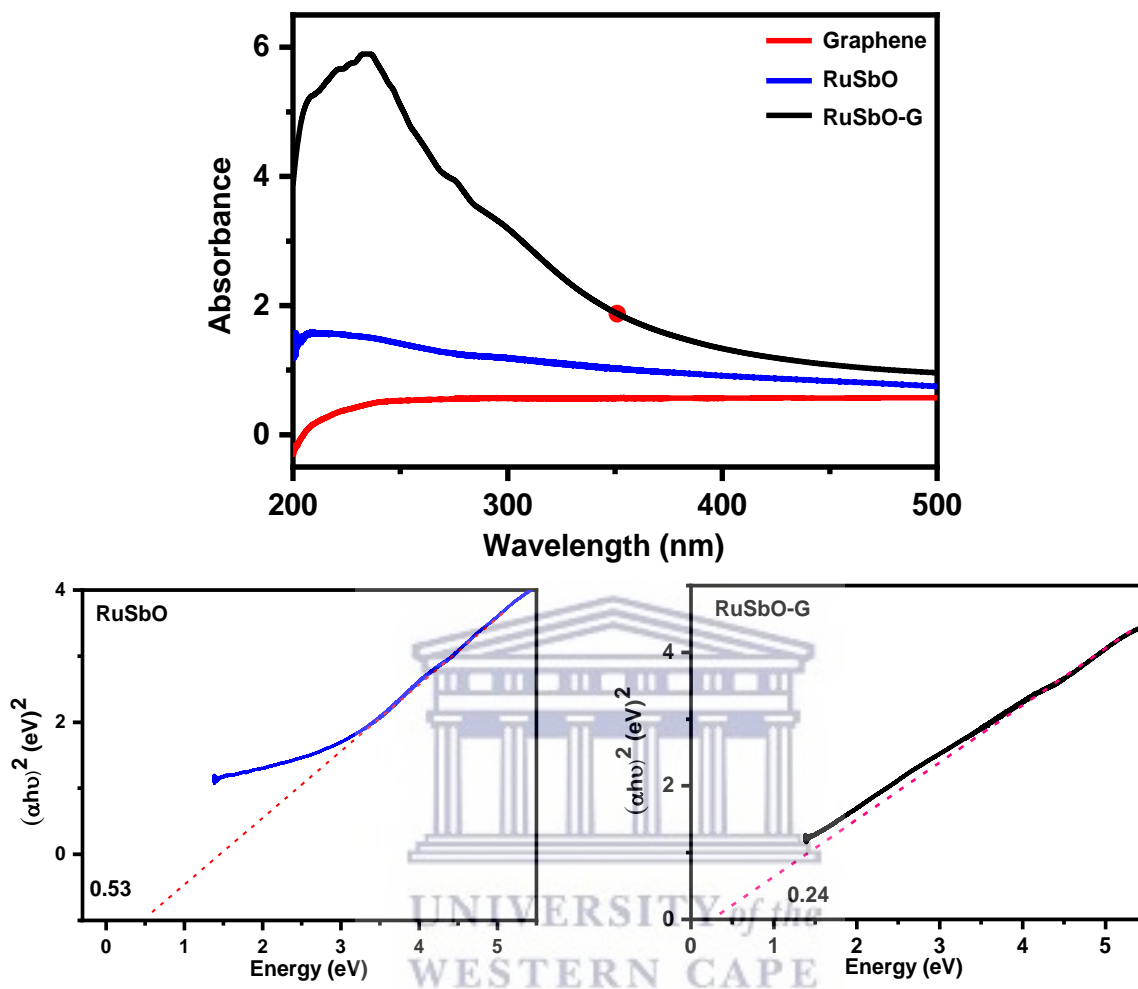
Figure 6.22: UV spectra of SbO and SbO-G overlayed with graphene (b,c) Taucs plot for SbO

and SbO-G respectively.

6.3.2.8 Photoluminescence spectroscopy

To investigate the photo-excited electron transfer in RuSbO and RuSbO-G composites, the

photoluminescence spectra (PL) were obtained. Figure 6.23 depicts the PL emission spectra of

RuSbO and RuSbO-G hybrids. The dispersed sample in ethanol solution was measured at room

temperature and was excited at 235 nm. In the RuSbO, a near band edge emission peak at 383 nm and a broad shoulder at the low energy side (456) was observed which arise from the MLCT excited-state emission [53]. The intensity of the PL peak of RuSbO is lower than that of RuSbO-G. It may be noted that the introduction of graphene reduced the agglomeration of the RuSbO samples as seen in the TEM and SEM images. These may also have generally reduced surface defects and decreased the number of trap sites in the system [54]. On the other hand, the agglomeration in RuSbO must have introduced lattice strain, caused contraction of lattice parameter, and given rise to defects and vacancies in the system. All these together can initiate indirect transitions in the system, thus reducing the PL intensity [55]. A sample's particle size and morphological characteristics have a substantial influence on its bandgap energy, which is also essential in defining its electrochemical activity. The bandgaps of the samples can be calculated from the PL wavelengths using.
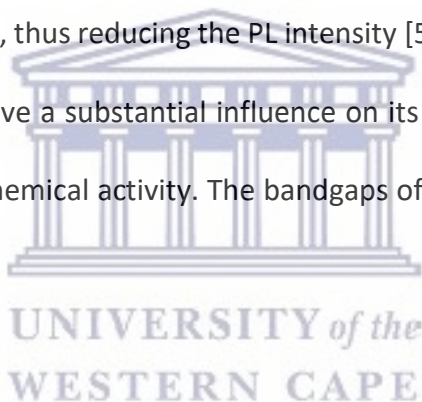
$$E = hC\lambda \hspace{6cm} 6\text{-}1$$

where h is the Planck constant; c is the velocity of light, and λ is the wavelength of the absorption peak [56]. The bandgap for RuSbO was 3.48 eV while that of RuO-G was 3.18 eV. The reduced bandgap in the composite will facilitate the transfer of charge. Therefore RuSbO-G is expected to have a better electrochemical performance.
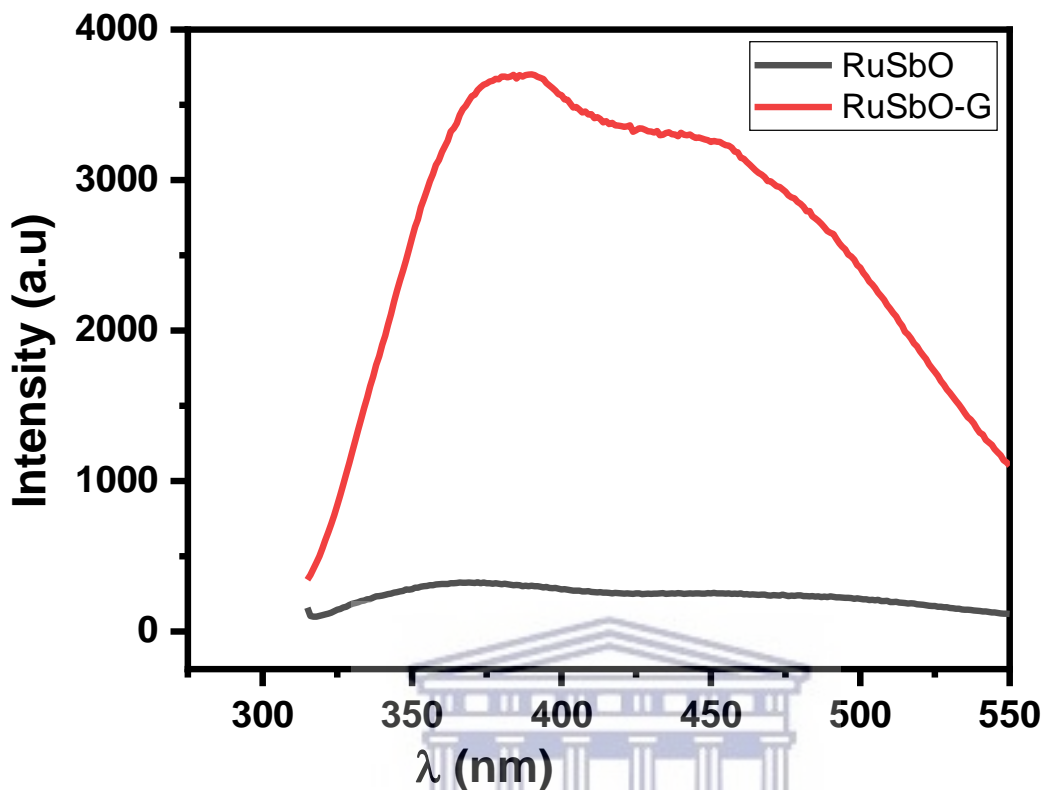
Figure 6.23: The PL emission spectra of RuSbO and RuSbO-G.

6.3.2.9 Small angle X-ray scattering

The SAXs spectra of RuSbO and RuSbO-G are shown in Figure 6.24 with respect to its intensity vs scattering vector and 2θ. In Figure 6.24a the RuSbO displays distinct scattering peaks at 0.72, 1.76, 2.8, 4.5 and 5.8 nm^{-1} while RuSbO-G display scattering peaks at 0.74, 1.90, 2.8, 4.5, 5.8 nm^{-1} indicating the existence of aggregated nano particle clusters as seen in the TEM and SEM images. According to the Braggs equation $\left(d = {2\pi}/{q}\right)$ [57], the corresponding Bragg spacing *d* of the nanoparticle is shown in Table 6-1. The graphene in the composite reduced the aggregation in the composite. Consequently, the composite nanoparticle exhibits decreased *d* values as

observed. This is in good agreement with the TEM, SEM and AFM data. The scattering patterns and pair distance distribution functions [P(r)] according to the physical volume of scattered particles and the number of scattered particles is shown in Figure 6.24 and b. The shape of the particles can be deduced by looking at the pair distance distribution functions. In Figure 6.25 the particle size distribution by volume for both materials is a polydisperse spherical nano-particle, with the radius of gyration for RuSbO-G at 14.9 and 90 nm and for RuSbO at 29.0 and 59.9 nm, respectively. The RuSbO-G distribution profile shows that the small particle sizes have higher intensity than the larger particles at 90 nm. The shoulder peak at 25.1 nm indicates an agglomeration in the sample. In the RuSbO the probability of pair distance distribution function encounter two maxima located at 29.0 nm and 59.86 nm with similar intensity. Therefore, the average particle sizes of RuSbO are larger than that of RuSbO-G as confirmed by the XRD data. The particle size distribution by number indicated in Figure 6.26. shows slightly skewed nature of the particle size distribution of RuSbO and RuSbO-G nanoparticles, the profile shows that the particle has a globular nature and a variation in particle sizes the profile confirms a polydisperse spherical nano-particle distribution by number of scattered particles with maximum primary particles at 60.8 nm for RuSbO while that of RuSbO-G is at 13.7 nm. The shoulder peaks at 31.2 nm and 25.6 nm in RuSbO and RuSbO-G respectively is because of agglomeration in the sample.
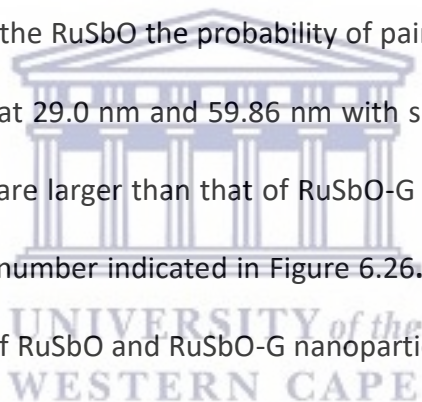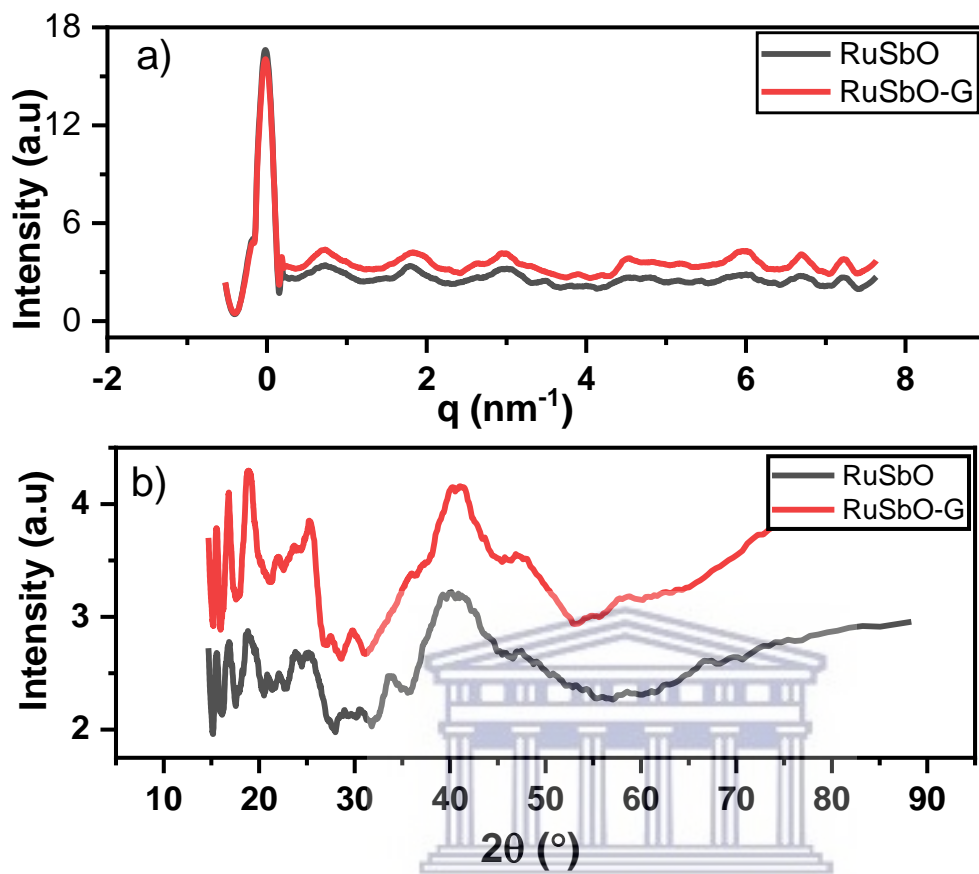
Figure 6.24: SAXS spectra of RuSbO and RuSbO-G.
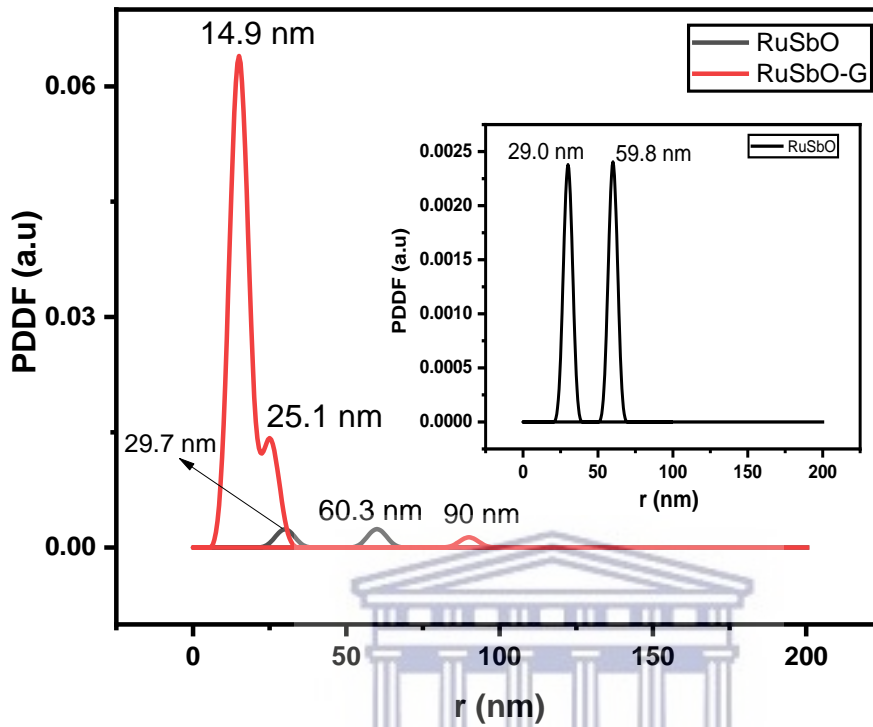
Figure 6.25: SAXS pair-distance distribution function (PDDF) by volume of RuSbO and RuSbO-

G scattered (inset is enlarged RuSbO).
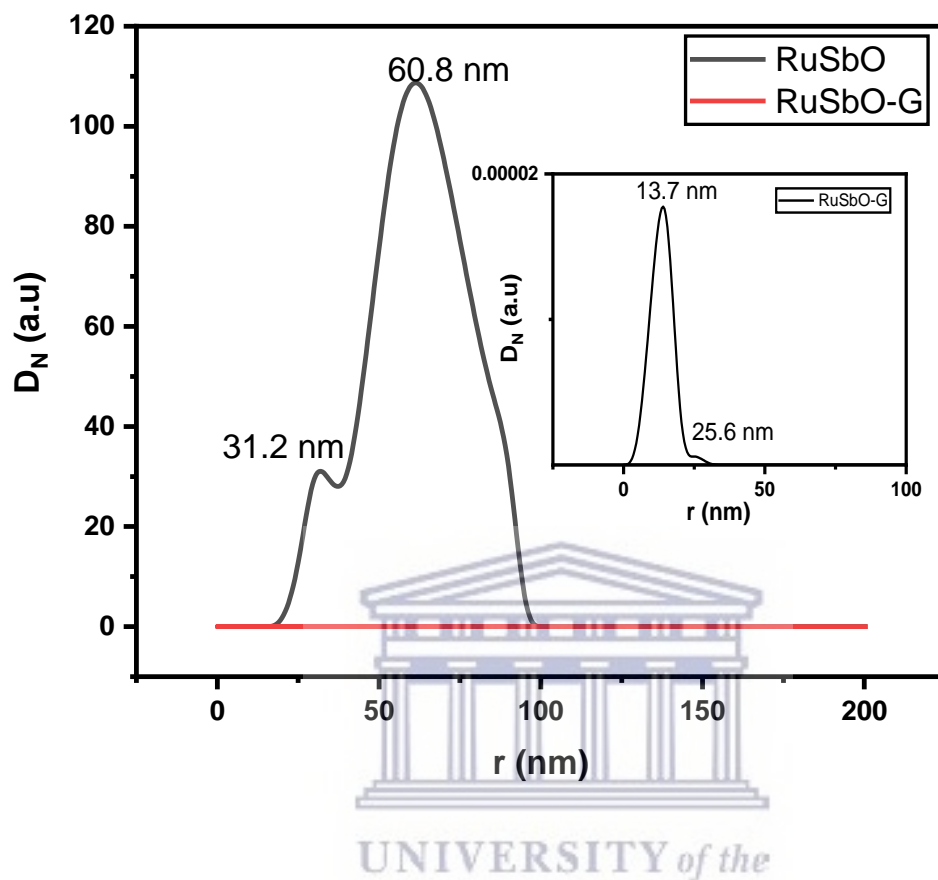
Figure 6.26: SAXS pair-distance distribution function (PDDF) by number of RuSbO and RuSbO-G scattered (inset is enlarged RuSbO-G).

Table 6-3: d-spacing of RuSbO and RuSbO-G from SAXS spectra

RuSbO-G		RuSbO	
r (nm)	d-spacing (nm)	r (nm)	d-spacing (nm)
0.72	8.69	0.74	8,46
1.79	3.49	1.86	3.36
2.96	2.19	3	2.08
4.51	1.29	4.55	1.38

5.92	1.06	5.99	1.05
6.66	0.93	6.75	0.92

6.3.3 Electrochemical studies

6.3.3.1 Cyclic voltammetry

The electrochemical performance of the pristine and composite material was investigated by cyclic voltammetry (CV), galvanostatic charge-discharge (GCD) and electrochemical impedance spectroscopy (EIS) measurement with 1 M Li_2SO_4 as the electrolyte. In the half cell, otherwise called the three-electrode system, CVs were run at scan rates ranging from 10 mV s^{-1} to 100 mV s^{-1} at a potential window of 0.0 V to 0.6 V (Figure 6.27 and Figure 6.28). At a low scan rate, the CV curves of both samples were virtually rectangular, and no redox peak was seen, indicating that the materials had nearly perfect capacitive behaviour. The lack of a redox peak can be explained by the extremely fast reversible redox reaction that occurred on the surface of the RuSbO and RuSbO-G nanoparticles. The capacitive current increases as the scan rate increases and the shape of the CV plots gradually changes from rectangular to oval due to the internal resistance of the electrode, which may be due to the limited charge accumulation and low conductivity of Li_2SO_4 aqueous solution, as well as the diffusion limits of Li^+ and SO_4^{-2} ions in the electrodes [58] [59]. As the voltage scan rate increased, the deviation of the voltammogram from the ideal rectangular structure also increased. This can be attributed to the electrochemical polarization of the electrode with the graphenized material showing a higher degree of polarization. The oxygen groups at the edges of the graphene nanosheet as seen in the FTIR are

responsible for the pseudocapacitance contribution and the electrochemical polarization of the electrode [60] [61]. Increasing the scan rate limited the redox reaction site thus exonerating the contribution of the inner sites [62]. In Figure 6.29 the CV plots of RuSbO-G and RuSbO are compared at 40 mV s^{-1}, and the CV plot of RuSbO-G has a higher current response than the CV plot of RuSbO, it also reflected a bigger area of charge buildup and hence higher capacitance than the CV plot of RuSbO. This is because graphene has been integrated into the material, resulting in a superior surface for charge buildup. Figure 6.29b shows the CV plots of graphene, RuO, SbO, RuO-G, SbO-G RuSbO and RuSbO-G, from the plots the RuSbO-G composite performed better than all the other materials. This is because; 1) combining two metal structures creates an open micro/nano-architecture with more contact sites, and optimizes electrochemical activity in the contact site, which results in a synergistic impact in the electrochemical performance [63][64]. 2) addition of graphene must have increased the conductivity of the material, by providing better surface area and a quicker diffusion pathway [65]. The specific capacitance of the three materials was calculated from the equation below:

$$C_{sp} = \frac{1}{2mv \triangle V} \int_{-v}^{+v} Idv$$ 6-2

Where m is the active mass of the electrode (g), v is the scan rate (V s^{-1}), $\triangle$V is the potential window in (V) and $\int_{-v}^{+v} Idv$ is the charge obtained from the integrated area of the voltammogram. RuSbO-G showed a better electrochemical performance with a high specific capacitance of 109.53 F g^{-1} at 10 mV s^{-1} and up to 21.19 F g^{-1} at 100 mV s^{-1}. While for RuSbO the values were 43.9 F g^{-1} at 10 mV s^{-1} to 14.63 F g^{-1} at 100 mV s^{-1}. The specific capacitance values are plotted against

potential sweep rates as shown in Figure 6.30 When the voltage scan rate was raised, the specific

capacitance values for both materials decreased gradually. The drop in capacitance value as the

scan rate increases is a frequent phenomenon caused by insufficient time for electrolyte ion

diffusion, and charge storage is limited to the outer surface area only [66]. The specific

capacitance values were also plotted against the scan rate for graphene RuO, SbO, RuO-G, SbO-

G, RuSbO and RuSbO-G Figure 6.30b from the plot, the RuSbO-G can be seen to have the highest

specific capacitance with a slow decrease at higher scans, thus showing its high-rate capability.

Figure 6.30c shows the same plot excluded RuSbO-G, RuSbO had a higher performance than the

older materials, however as the scan rate increased the steepness of the curve indicates higher

capacitance loss. The better performance of RuSbO-G across all scan rates is mostly owing to the

integration of graphene into the RuSbO matrix, thus improving the morphology for better charge

storage and stability [67]. The specific capacitance of RuSbO and RuSbO-G across all scan rates

are represented in Table 6-4
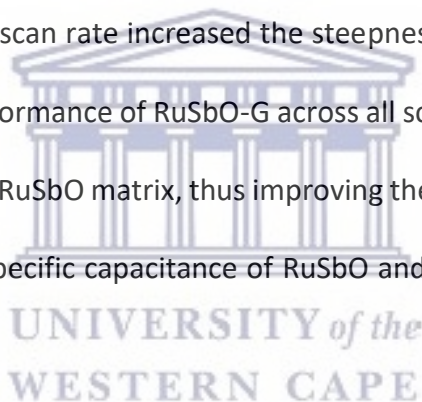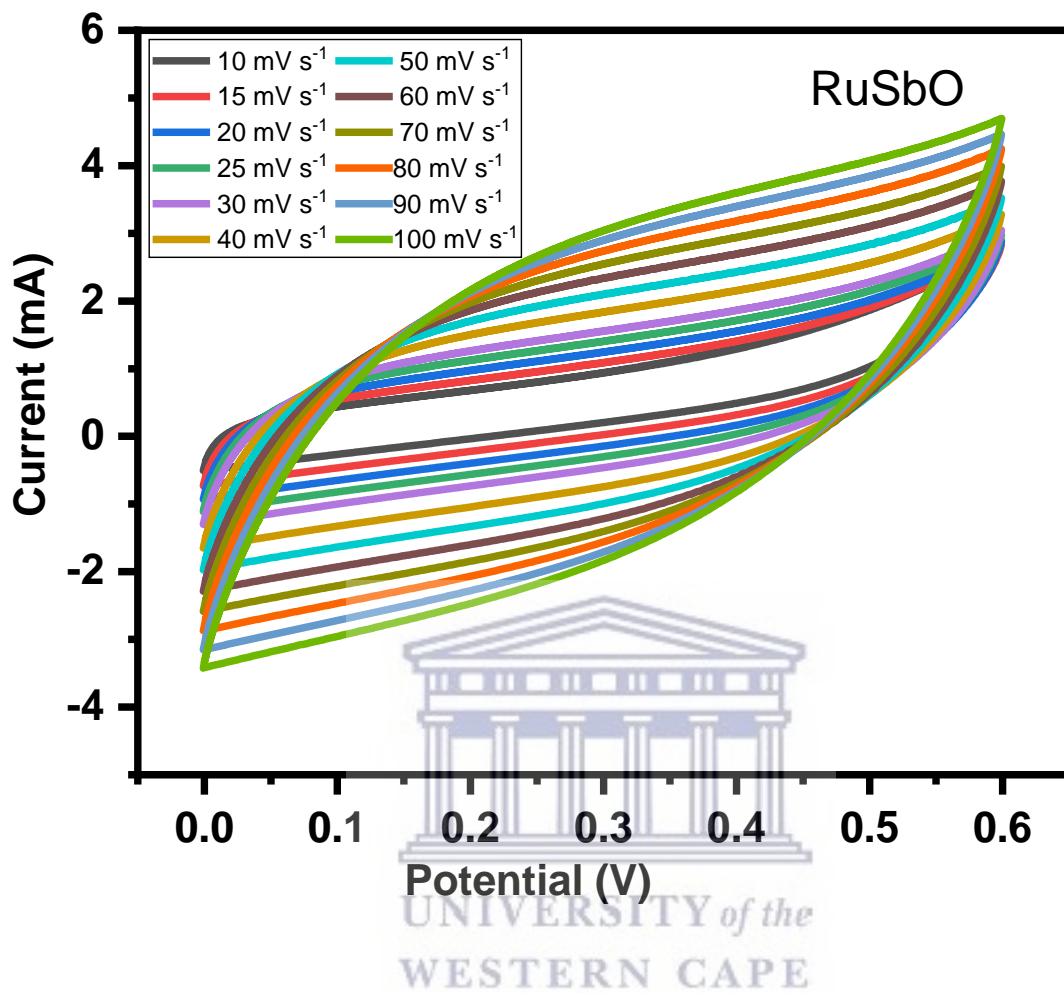
Figure 6.27: CV plot of RuSbO
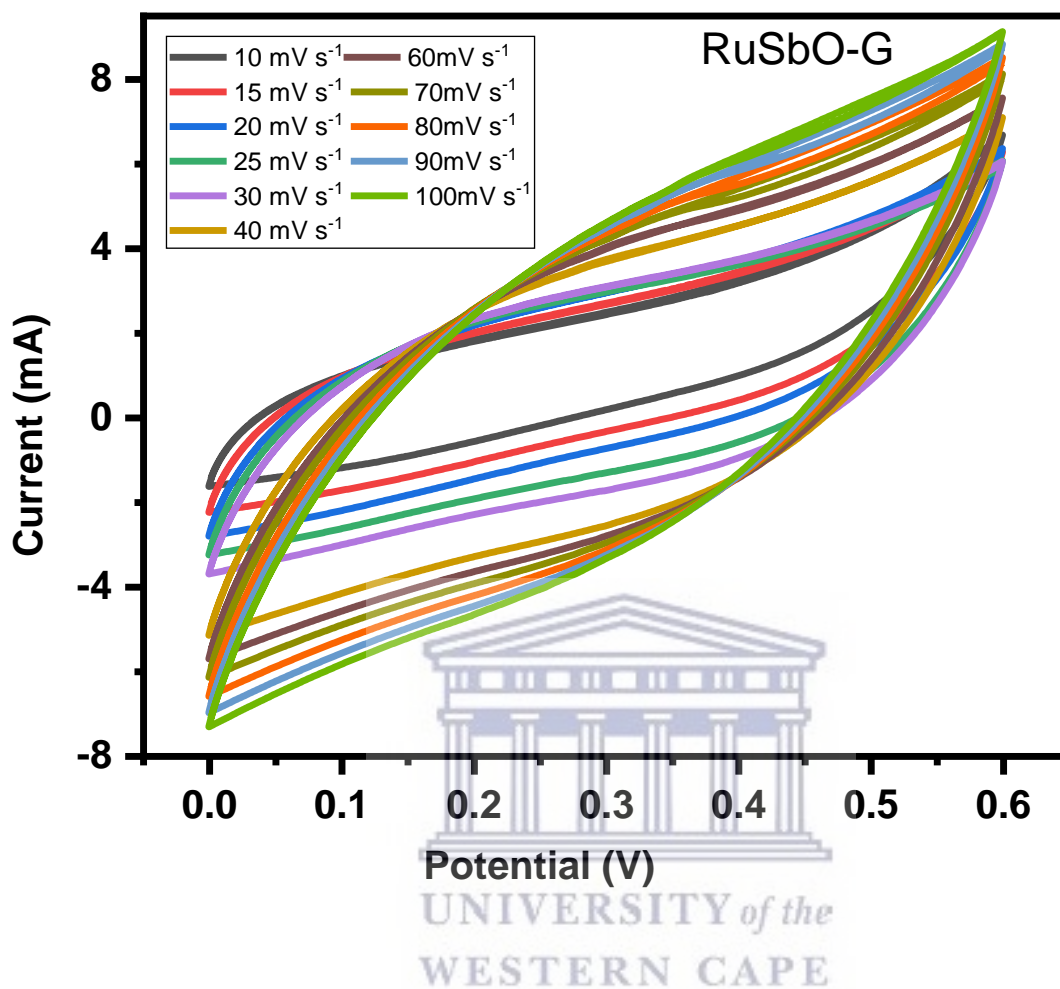
Figure 6.28: CV plot of RuSbO-G

Table 6-4: The capacitance of RuSbO and RuSbO-G at different scan rates.

Scan rates	Capacitance (F g^{-1})	
	RuSbO	**RuSbO-G**
10	43.9	109.53
15	34.69	83.07
20	30.49	69.64
25	27.64	58.9
30	25.75	51.89

40	23.07	45.95
60	19.31	30.63
70	17.89	27.73
80	16.67	25.44
90	15.58	23.29
100	14.63	21.49
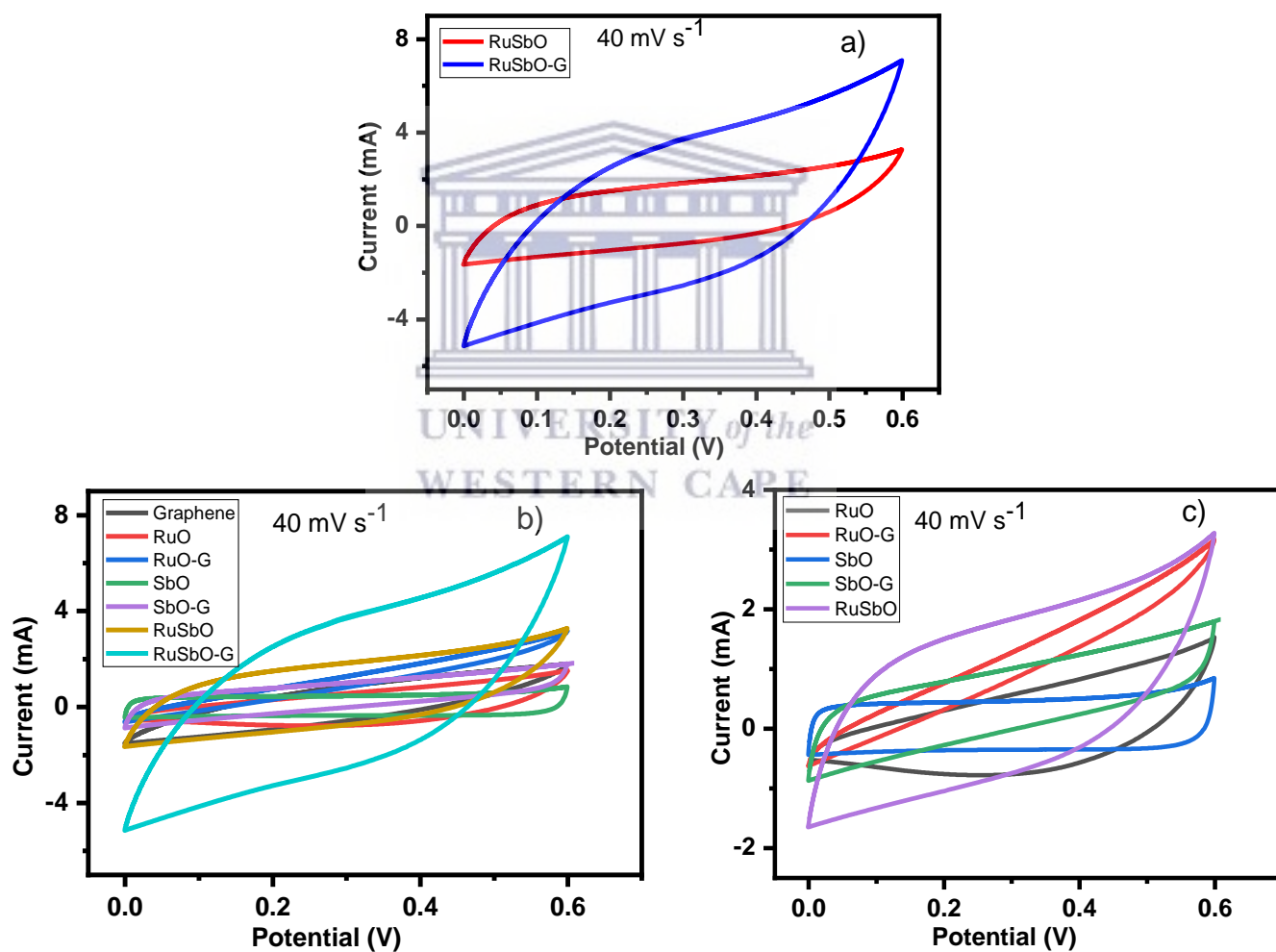
Figure 6.29: CV plots of a) RuSbO and RuSbO-G, b,c) RuSbO and RuSbO-G compared with their stating materials at 40 mV s^{-1}.
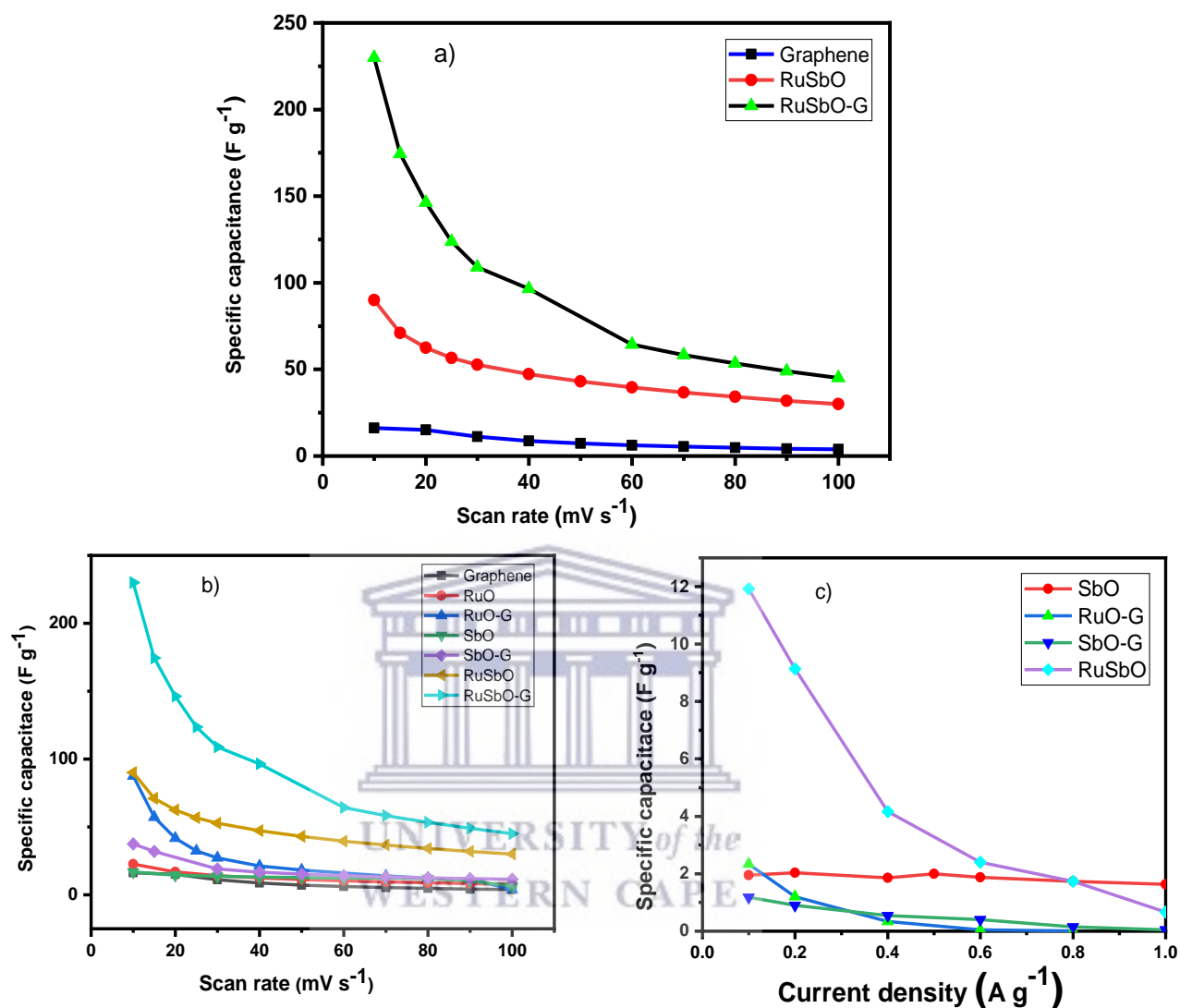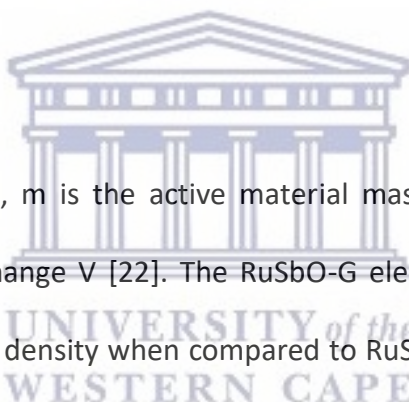
Figure 6.30: Plot showing the relationship between Cs and scan rate for a) RuSbO and RuSbO-

G, b, c) RuSbO and RuSbO-G compared with their stating materials.

6.3.3.2   Galvanostatic charge discharge

The performance of RuSbO and RuSbO-G electrodes was investigated at current densities of 0.1

0.2, 0.4, 0.6, 0.8, 1, and 2 A g^{-1} (Figure 6.31 and Figure 6.32). The RuSbO-G electrode's GCD curves

show a high specific capacitance when compared to RuSbO. The presence of near triangular

curves confirms the electric double layer capacitive charge storage mechanism occurring at the

electrode-electrolyte interface [68]. The GCD curves are almost symmetrical, with only a minimal

voltage drop caused by the equivalent series resistance (ESR). The charge and discharge

processes have matching duration, indicating a high Coulombic efficiency and electrochemical

reversibility [67]. These observations are consistent with the oxidation and reduction profiles

reported in the CV curves. The specific capacitance (C) was determined using the equation.

$$C_s = \frac{I \times t}{m \times V - IR_{drop}}$$
19

where I is the constant current, m is the active material mass, and t is the discharge time

corresponding to the voltage change V [22]. The RuSbO-G electrode has the highest specific

capacitance at the same current density when compared to RuSbO. The highest capacitance of

the RuSbO-G electrode, for example, reached up to 289.47 F g^{-1} at 0.1 A g^{-1}, while RuSbO was

95.33 F g^{-1}. This is due to graphene's porous microstructure, which facilitates electrolyte

infiltration and contributes to the development of electric double-layer capacitance. Figure 6.34

shows a comparison of the rate capabilities of RuSbO-G and RuSbO electrodes at various current

densities. At a current density of 0.2 A g^{-1}, RuSbO-G has a specific capacitance of 236.07 F g^{-1},

which is substantially higher than that of RuSbO (73.07 F g^{-1}). Notably, as the current density

increased to 1 A g^{-1}, the RuSbO-G maintained a high capacitance of 74.05 F g^{-1}, retaining 30 % of

its capacitance. RuSbO electrodes, on the other hand, exhibit poorer capacitance retention of

10%, indicating that the structure of the RuSbO-G improved electrolyte ion diffusion. The specific

capacitance decreases as the current increases. The drop in specific capacitance values was noticeable in the discharge time of GCD curves and the capacitance vs current density plot (Figure 6.2). This drop-in specific capacitance at increased current density could be attributed to the limited flow of electrolyte ions into the active material's inner side [69].
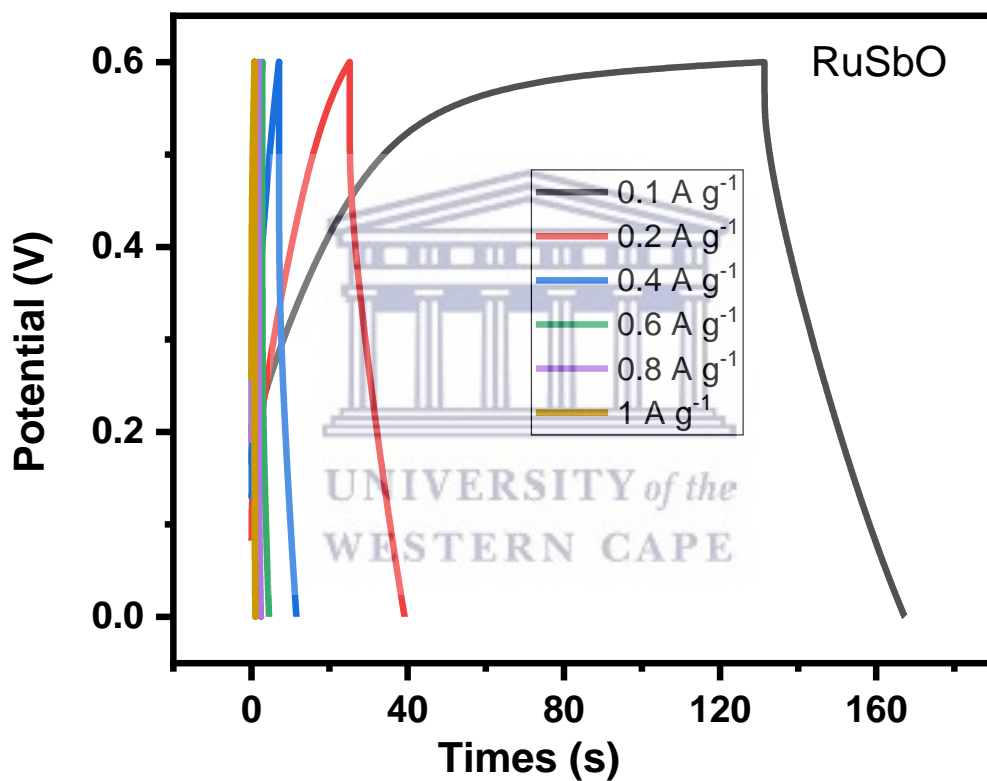
Figure 6.31: GCD of RubO at different current densities.

354
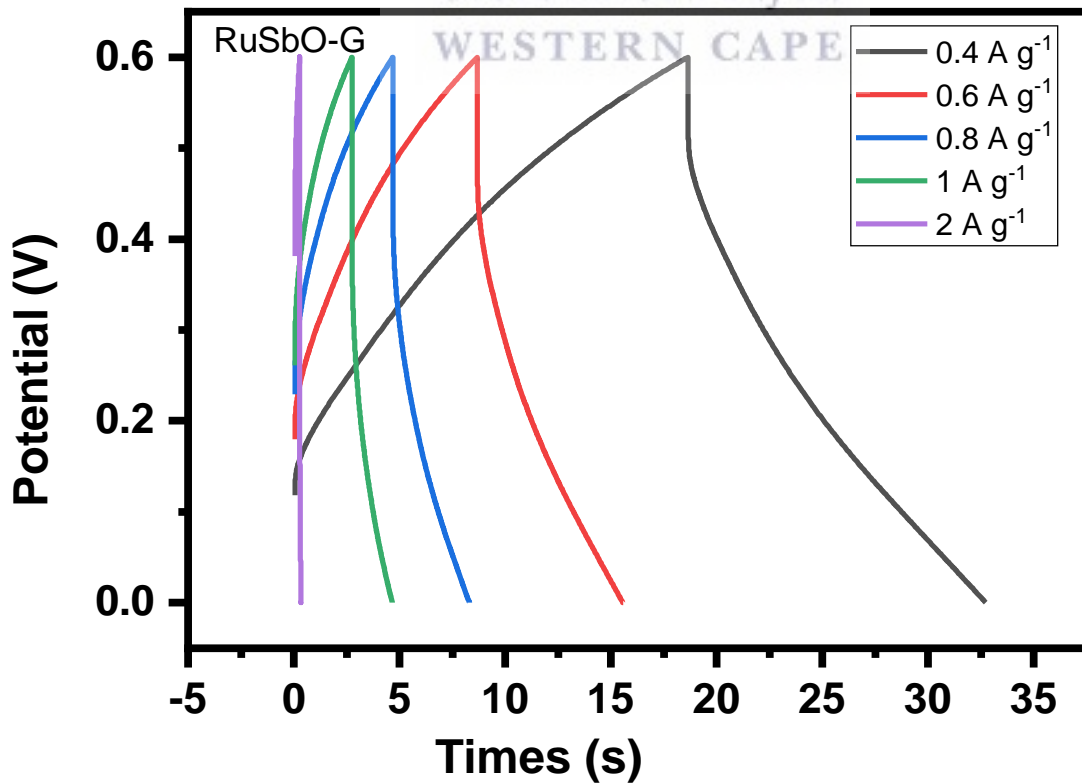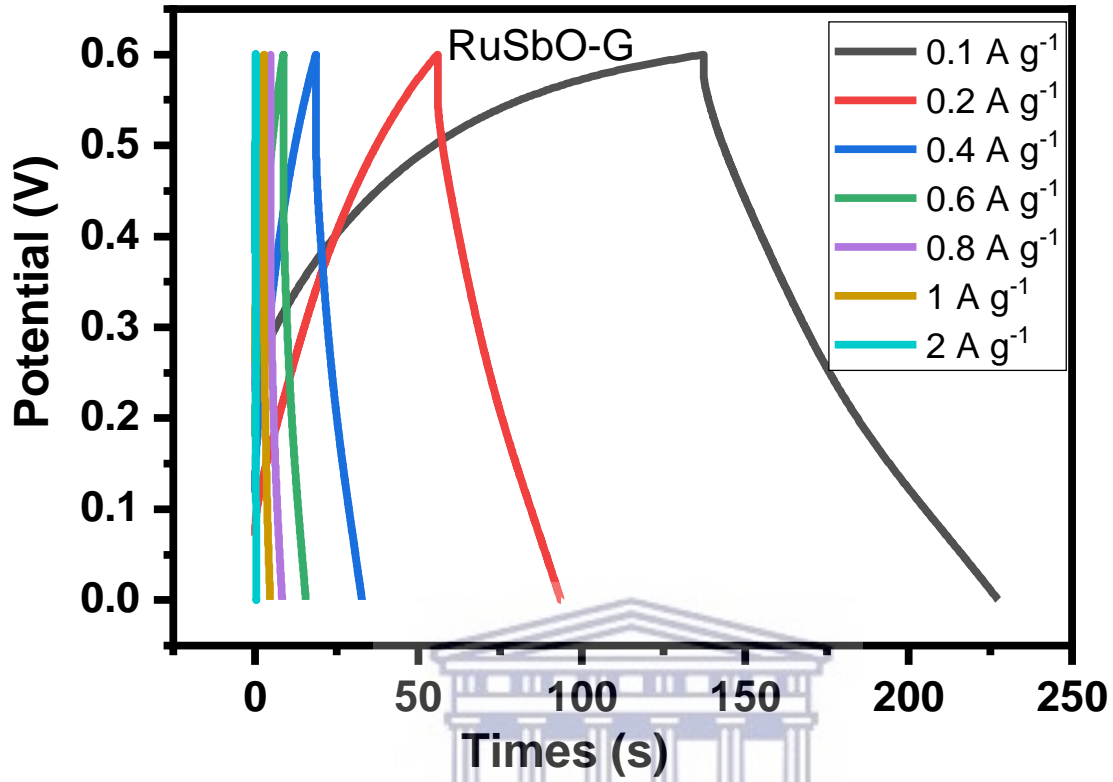
Figure 6.32: GCD of RuSbO-G at different current densities.
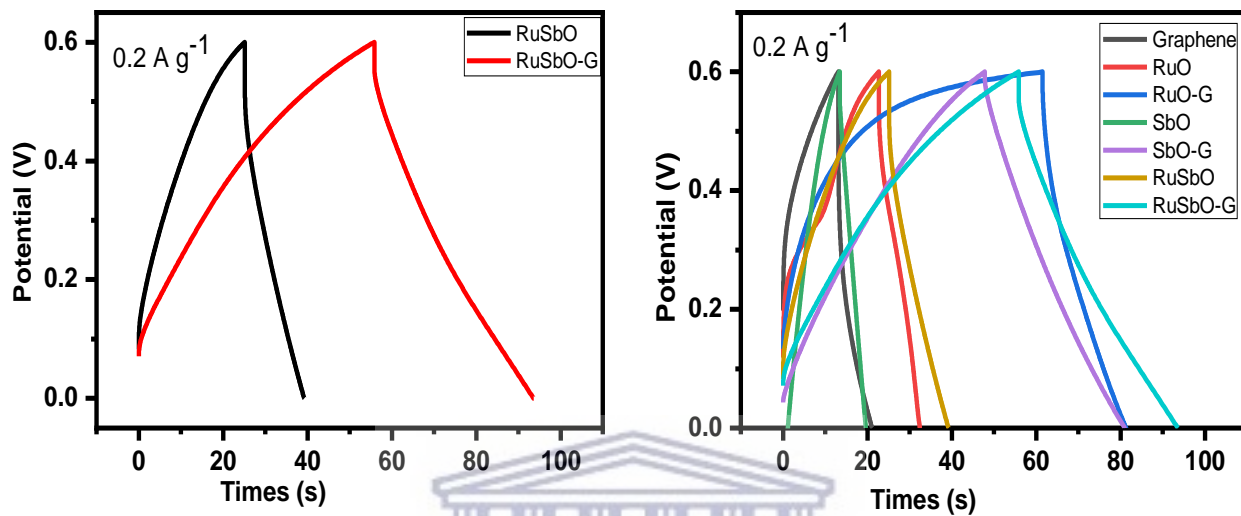
Figure 6.33: GCD profile comparing a) RuSbO and RuSbO-G at 0.2 A g^{-1} b) the GCD profile for RuSbO and RuSbO-G compared with their stating materials.

Figure 6.34: Plot showing the relationship between Cs and current density for a) SbO, SbO-G and graphene, b) for RuSbO and RuSbO-G compared with their starting materials.
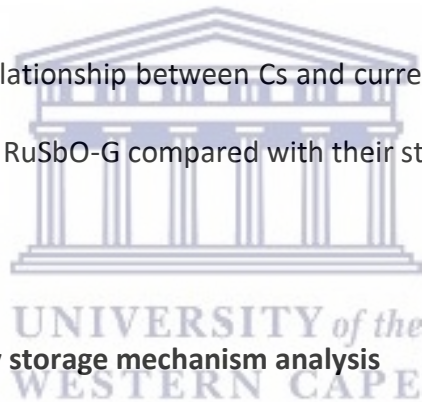
6.3.3.3 Dominant energy storage mechanism analysis

The capacitance of supercapacitors mainly arises from two mechanisms; the contribution from the surface capacitive process and the diffusion-controlled energy storage process [70]. The diffusion rate of the species into the bulk of the electroactive material could be controlled by the scan rate (v) during a CV test, utilizing the equation as proposed by *Trasitti et al.* [62][71]:

$$Q_{Total} = Q_{out} + Q_{In} \qquad\qquad 6\text{-}3$$

where Q_{total} is the total charge stored by the material, Q_{out} is the surface charge purely from a capacitive process which is from physical adsorption, Q_{in} is the pseudocapacitive contribution.

Figure 6.35a shows the inverse relationship between charge and scan rate. As scan rate increases, charge decreases. As *v* approaches 0, the diffusion-controlled process could access all the available pores inside the bulk of the electroactive material, thus both the Faradaic process and the capacitive process are occurring concurrently. On the other hand, as the scan rate tends to infinity, more of the diffusion-controlled redox sites are less accessible by the species since the Faradaic charge process is too slow to happen at higher scan rates. The extrapolation of the linear fit (Figure 6.35 b,d) of $Q(V)$ vs $v^{-1/2}$ Plot to the y-intercept (i.e., $v^{-1/2} = 0$) gives the capacitive storage charge Q_{out}. On the other hand, as v approaches 0, the diffusion-controlled process could access all the available pores inside the bulk of the electroactive material, thus both the Faradaic process and the capacitive process are occurring concurrently. Exploration of the linear fit (Figure 6.35 c,e) to the y-intercept gives the total charge. The difference between the capacitive charge storage and the total charge is assumed to equal the pseudocapacitance contribution [62]. The pseudocapacitance for the RuSbO-G was calculated to be 94.4% while it's about 99.65% pseudocapacitance contribution for RuSbO. This difference shows the EDL contribution from the graphene added.
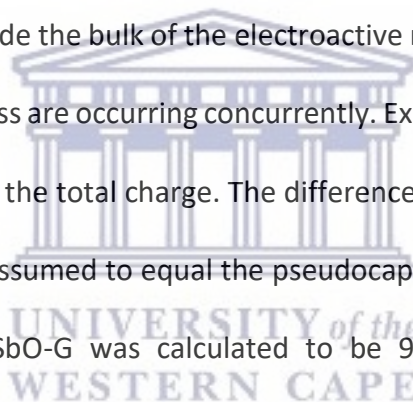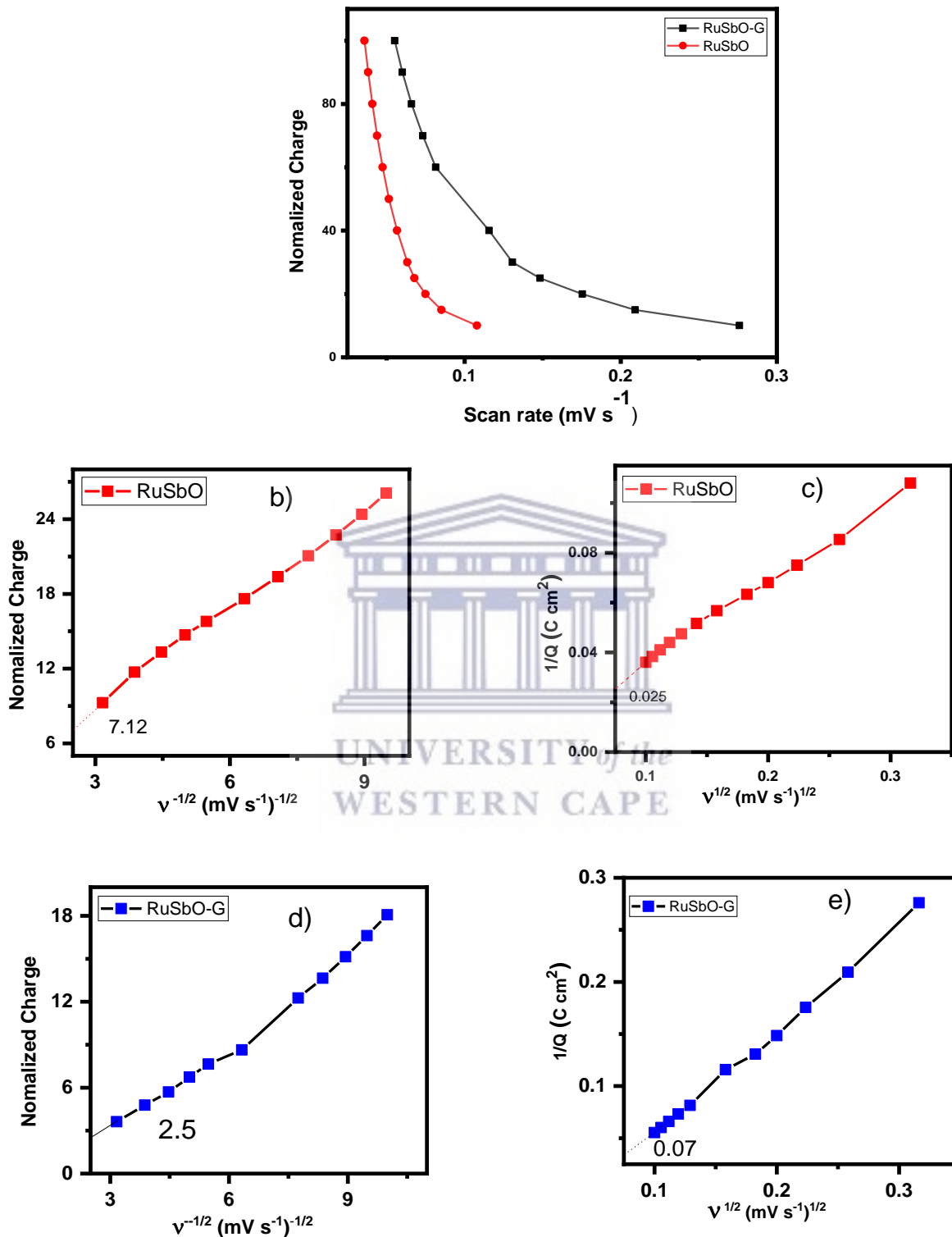
Figure 6.35: plot of charge vs scan rate showing their linear relationship, b,d) plot of charge vs

$v^{-1/2}$ for RuSbO and RuSbO-G, and c,e) plot of the inverse of charge vs $v^{1/2}$.

6.3.3.4 Electrochemical impedance spectroscopy

As illustrated in Figure 6.36, Nyquist plots were used to analyze the electrochemical impedance spectroscopy data and were displayed with an equivalent circuit inset. Three electrodes all displayed typical AC impedance characteristics of supercapacitors [72]. In the high-frequency region, the intersection of the curve at the real component reveals the bulk resistance of the electrochemical system. This includes ionic resistance from the electrolytes, intrinsic grain to grain resistance of the electrode, and contact resistance at the interphase between the active material and the substrate [73]. The radius of the semicircle in the high-frequency region displays the charge-transfer process, at the interface of the electrode and the electrolyte and as we approach lower frequencies the semicircle breaks into a 45° nearly vertical line which is related to the Warburg (W_2) diffusion of ions within the electrode inter-phase [74]. The EIS graphs demonstrated that RuSbO (7.62 Ω) had a greater Rs than RuSbO-G (6.5 Ω). The point where the semi-circle intersects with the real access is at a higher frequency. RuSbO and RuSbO-G have fitting R_{ct} values of 4.30 Ω, and 3.05 Ω respectively. The lower R_{ct} in RuSbO-G will contribute to improved electrochemical properties. The slope of the 45° section of the curves in the intermediate frequency area was used to illustrate the Warburg resistance, which indicates ion diffusion/transport in the electrolyte and its relationship to frequencies. The slanted vertical further confirms the pseudocapacitive contribution in the CV measurement. Furthermore, the Warburg resistance value is lower in the RuSbO-G (13.51 Ω) (Table 6-5). Because of the low charge transfer resistance and lower diffusion effect, very reversible processes can occur at the interface, which is why both materials exhibit a rectangular voltammogram and maintain the

rectangular feature even at high scan rates. The Bode plot from the EIS data is shown as the phase angle and total impedance plot in Figure 6.36 and Figure 6.37 respectively. The phase angle for RuSbO is 56.79° while that of RuSbO-G was 60.77°. The phase angle of RuSbO-G is closer to 90°, therefore, showing more capacitive behaviour. It is clear from the phase angle that the materials store charges utilizing both the EDL and the pseudocapacitive mechanisms. The magnitude of total impedance was similar in both materials with a magnitude of 0.8 Ω. The constant phase element (CPE) was also derived from the Bode total impedance plot, the CPE impedance is given by

$$Z_{CPE} = a^{-1}(jw)^{-n} \qquad\qquad\qquad 6\text{-}4$$

where a is the frequency-independent constant related to the roughness of the surface features, and the exponent n is determined by the slope of log Z vs. log f. the coefficient 'a' is resistive when n = 0, capacitive for n = 1 and a Warburg impedance (charge transfer impedance) for n = 0.5. The value of n for RuSbO and RuSbO-G was 0.37, 0.3 respectively. The change in n confirms a change in the morphology of the material. The value demonstrates a slow transition from resistive to capacitive behaviour [75]. The total CPE values obtained from the fitted Nyquist plot are shown in Table 6-5
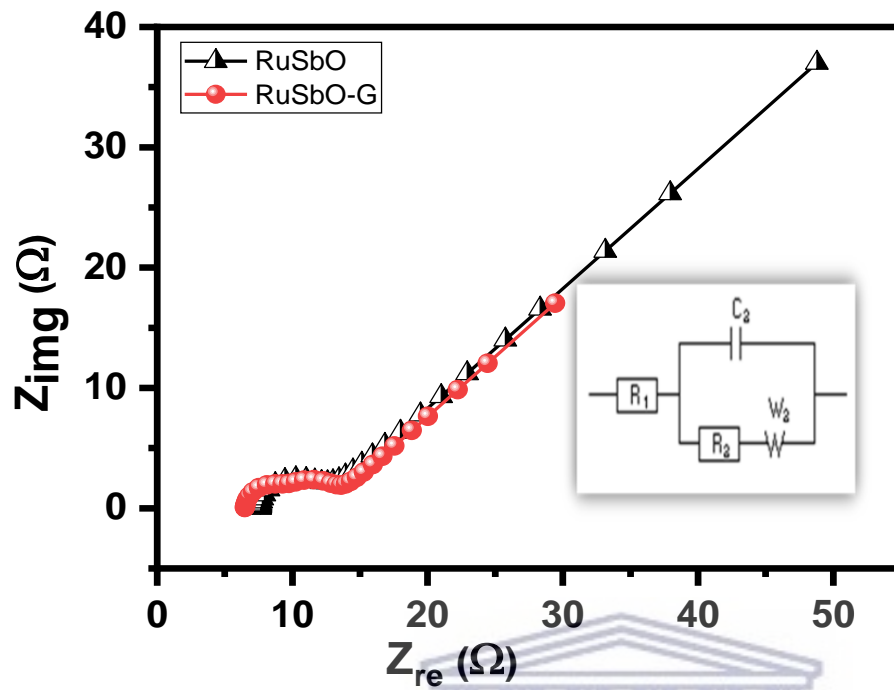
Figure 6.36: Nyquist plot of RuSbO and RuSbO-G the inset is the equivalent circuit, the inset is

the equivalent circuit.
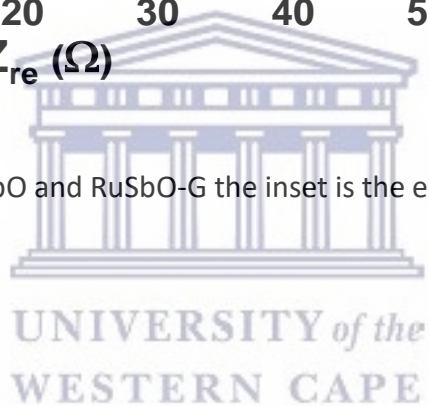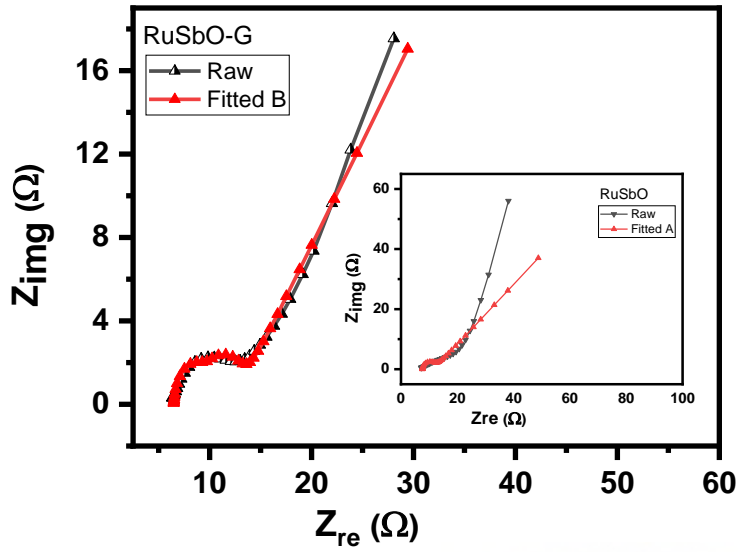
Figure 6.37: Nyquist plot of RuSbO-G showing the raw and fitted data, the inset is the plot of RuSbO showing the raw and fitted data.
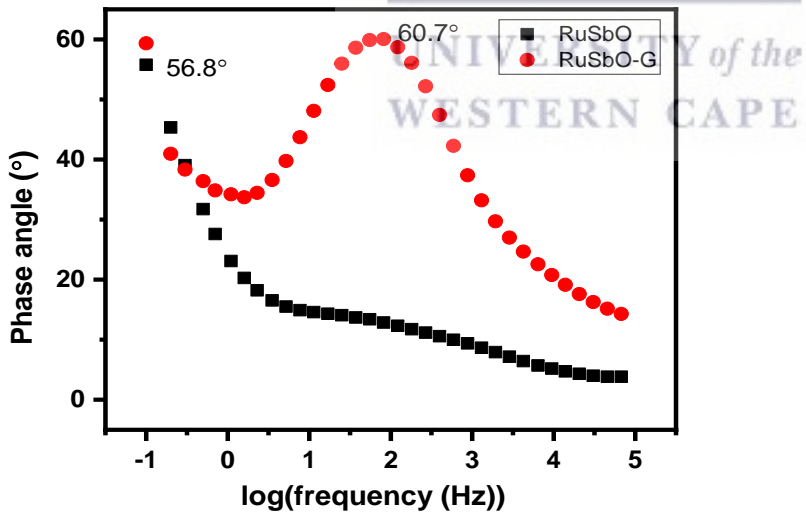
Figure 6.38: Bode plot of RuSbO and RuSbO-G
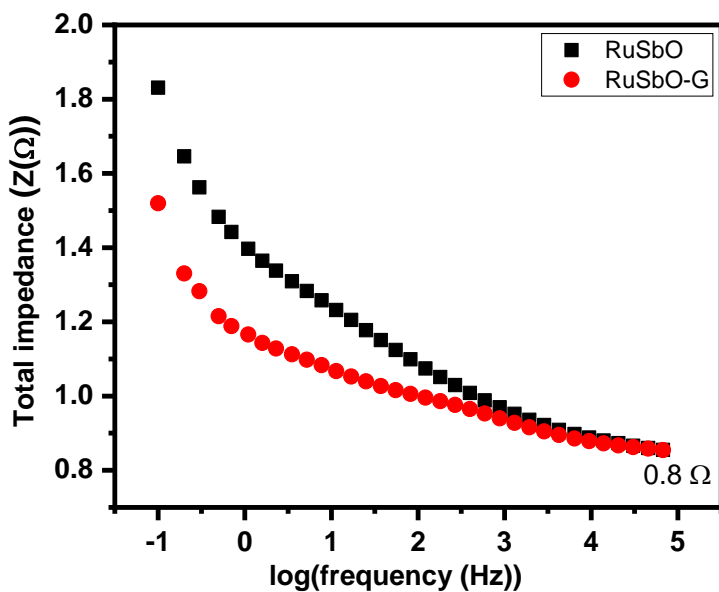
Figure 6.39: Total impedance plot of RuSbO and RuSbO-G.

Table 6-5: EIS curve fitting data of RuSbO and RuSbO-G electrode material.

Sample	R_s	CPE	R_{ct}	W^2	Phase angle
	(Ω)	(μF)	(Ω)	$(\Omega\ s\text{-}\ \frac{1}{2})$	(º)
RuSbO	7.627	66.2	4.3	29.34	56.8
RuSbO-G	6.471	580	3.05	13.51	60.7

6.3.4 Device fabrication

In a two-electrode cell configuration with filter paper as the separator and 1 M Li_2SO_4 as the electrolyte, the RuSbO-G was coated on a Ni foam substrate and used in an asymmetric cell configuration, with activated carbon as the negative electrode. As demonstrated in Figure 6.40, the performance of AC carbon is first validated in an aqueous solution of 1 M Li_2SO_4 in a half-cell arrangement.
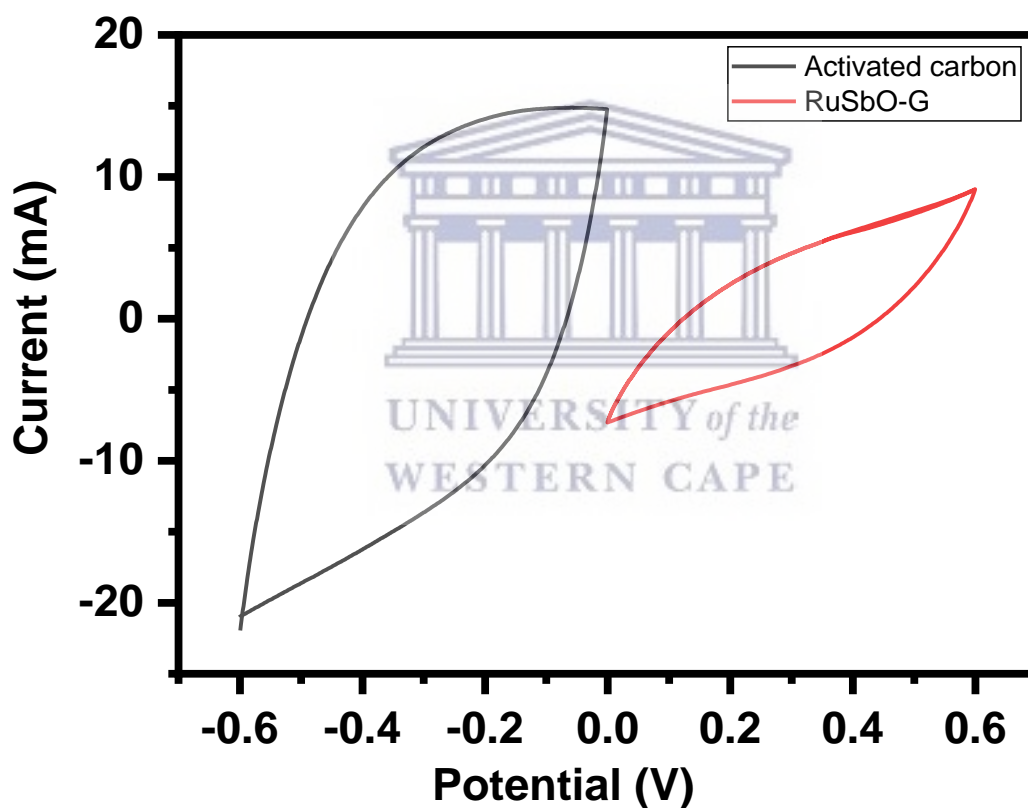
Figure 6.40: CV plot of RuSbO-G and activated carbon. In a 3-electrode cell set up showing the suitability of activated carbon as the negative electrode.

6.3.4.1   Galvanostatic charge discharge

The capacitance of the RuSbO and RuSbO-G was calculated from the GCD profile (Figure 6.41 and

Figure 6.42). The GCD profile is near triangular confirming the electric double layer capacitive

charge storage mechanism [68], and that the redox activity is a pseudocapacitive electrochemical

absorption-desorption process, happening at the surface of the RuSbO and RuSbO-electrode

[71]. The timing for the charge and discharge process is near similar, indicating a high Coulombic

efficiency and electrochemical reversibility [67]. These observations are consistent with the

oxidation and reduction profiles reported in the CV curves. The specific capacitance was

determined using the equation

$$C_s = \frac{I \times t}{m \times V - IR_{drop}}$$

6-5

where I is the constant current, m is the active material mass, and t is the discharge time

corresponding to the voltage change V [22]. The RuSbO-G electrode has the highest specific

capacitance at the same current density when compared to RuSbO electrodes. The capacitance

of the RuSbO-G electrode, for example, reached up to 129.71 F g^{-1} at 0.2 A g^{-1}, while RuSbO was

26.09 F g^{-1} at 0.2 A g^{-1}. This is due to graphene's porous microstructure, which facilitates

electrolyte infiltration and contributes to the development of electric double-layer capacitance.

A small IR drop was observed at the beginning of the discharge curve, especially for RuSbO in 1

MLi$_2$SO$_4$ implying the low internal resistance within the electrode. It was observed that the

specific capacitance decreased with an increase in the current load as seen in Figure 6.44 showing

the capacitance vs current density plot. At the highest current density of 2 A g^{-1} the specific

capacitance of the RuSbO-G reached 40.71 F g^{-1} retaining 31% of its capacitance, while that of

RuSbO was at 2.27 F g^{-1}, retaining only about 8% of its capacitance. Optimizing this materials

surface area by using other synthesis routes that will reduce agglomeration might be a good way

of improving the rate capability of this material. The two most important metrics for determining

the performance of an energy storage device are energy density and power density. The

following equations were used to compute specific energy and power:

$$E_{sp}\left(Wh/Kg\right) = \frac{CV^2}{2m} \times \frac{1}{3.6} \qquad \text{6-6}$$

$$P_{max}\left(W/Kg\right) = \frac{E}{\triangle t} \times 3600 \qquad \text{6-7}$$

where C (F g^{-1}) is the specific capacitance determined from equation 6-3, V is the maximum

working potential, m (kg) is the mass of the active material in the electrode, and $\triangle t$ is the

capacitors discharge time. Figure 6.45 is a Ragone plot which depicts the relationship between

the asymmetric device's energy density and power density at various current densities. An ideal

supercapacitor device would have a high energy density while also having a high-power density.

The asymmetric Cs cell delivered a maximum energy density of 75.58 W h kg^{-1}, at a power density

of 360 W kg^{-1}, at 0.1 A g^{-1} current load for RuSbO-G. At 0.2 A g^{-1} the capacitance of the composite

decreased to 58.32 W h kg^{-1}, at a power density of 720 W kg^{-1}, while at the same current density,

RuSbO delivered an energy density of 11.74 W h kg^{-1}, at a power density of 800 W kg^{-1} . At a high

power of 7200 W kg^{-1}, the RuSbO-G composite maintained an energy density of 18.2 W h kg^{-1}.

The energy density and power density were enhanced by the addition of graphene which lead to increased surface area for charge discharge [76]. Details of the GCD result is recorded in Table 6-6 and Table 6-7.
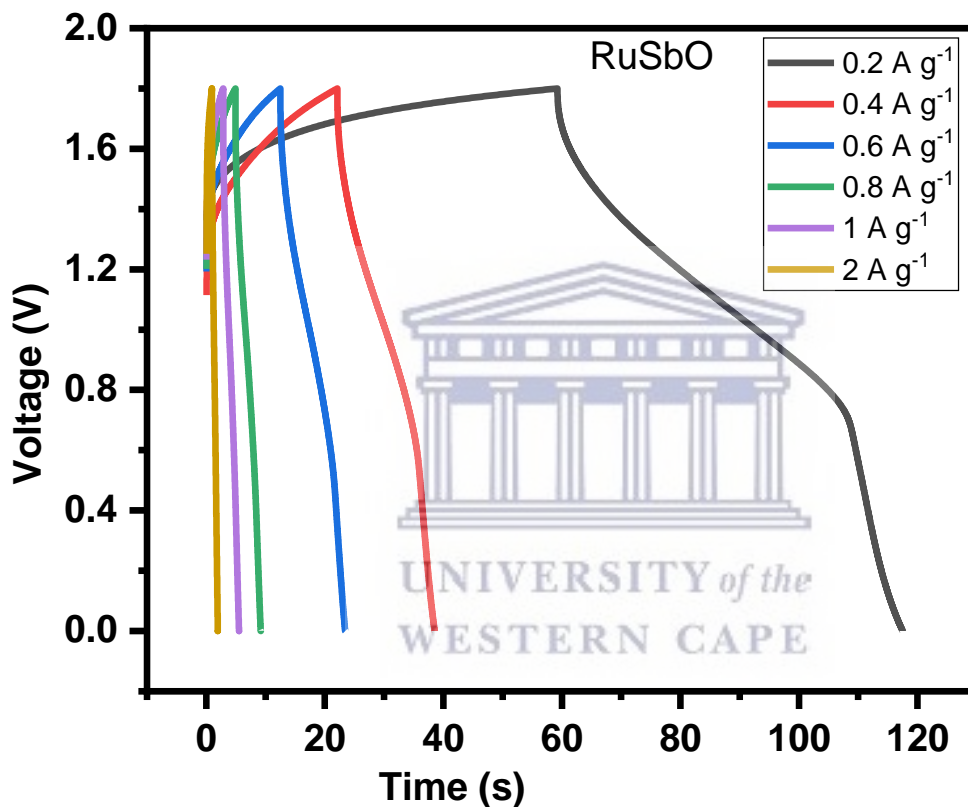
Figure 6.41: GCD profile for AC//RuSbO at different current densities.
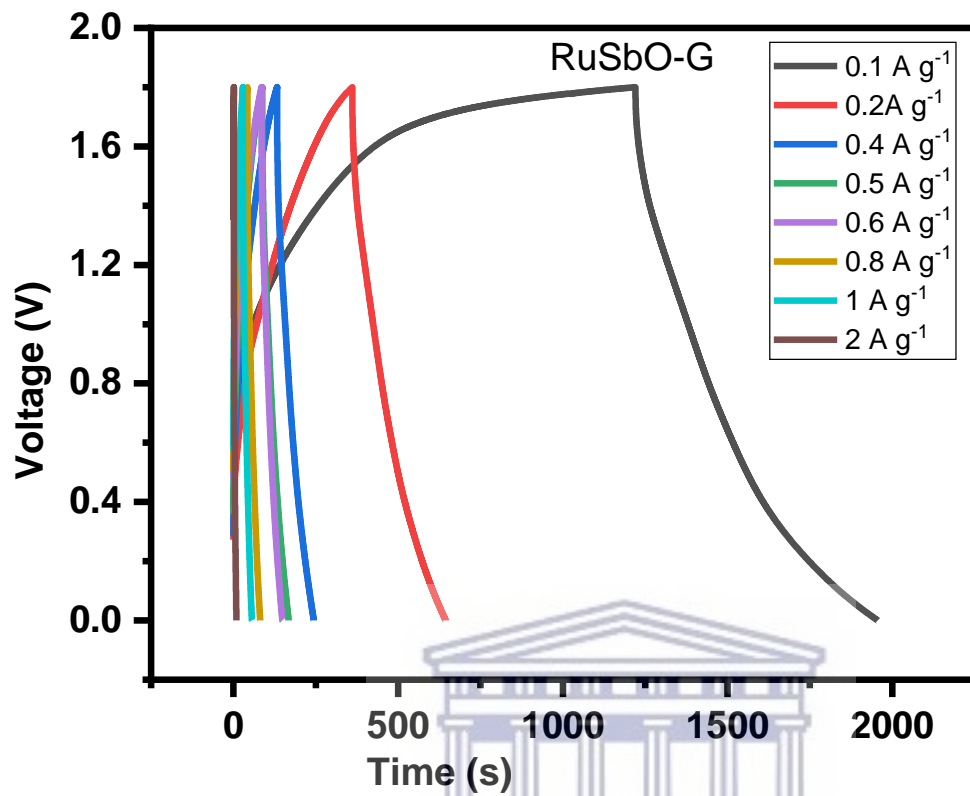
Figure 6.42: GCD profile for AC//RuSbO-G at different current densities.
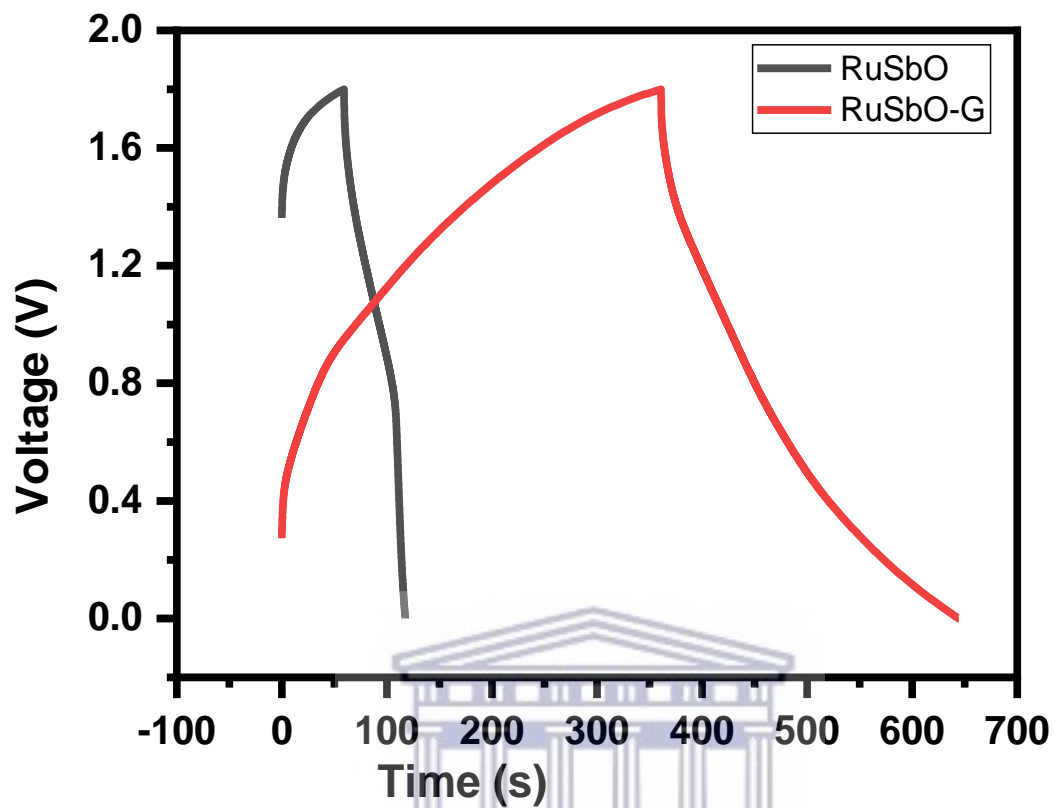
Figure 6.43: GCD plot comparing AC//RuSbO and AC//RuSbO-G at 0.2 A g^{-1}.
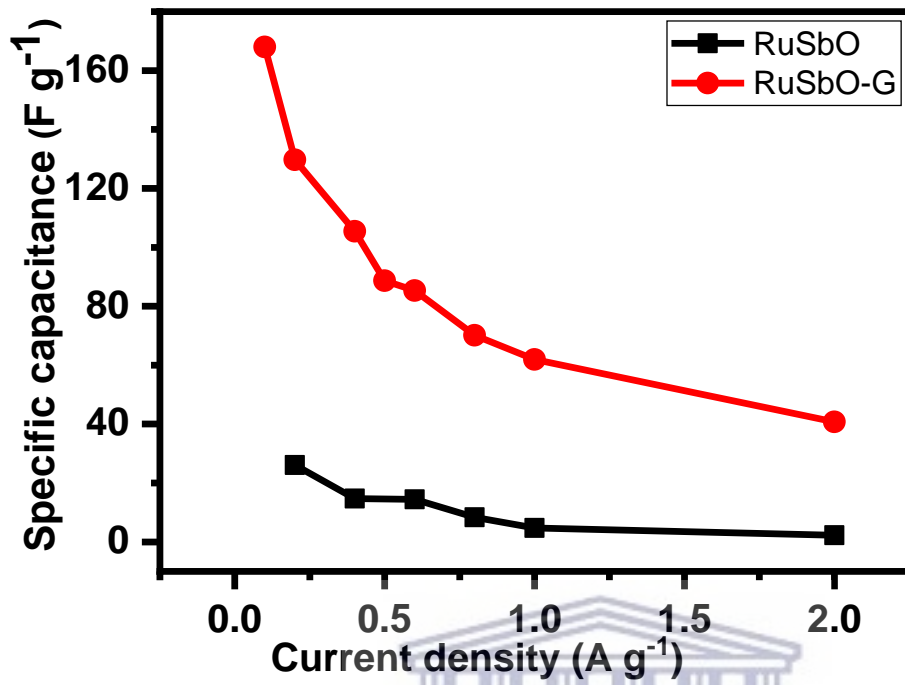
Figure 6.44: Plot comparing the current density vs capacitance of RuSbO and RuSbO-G.
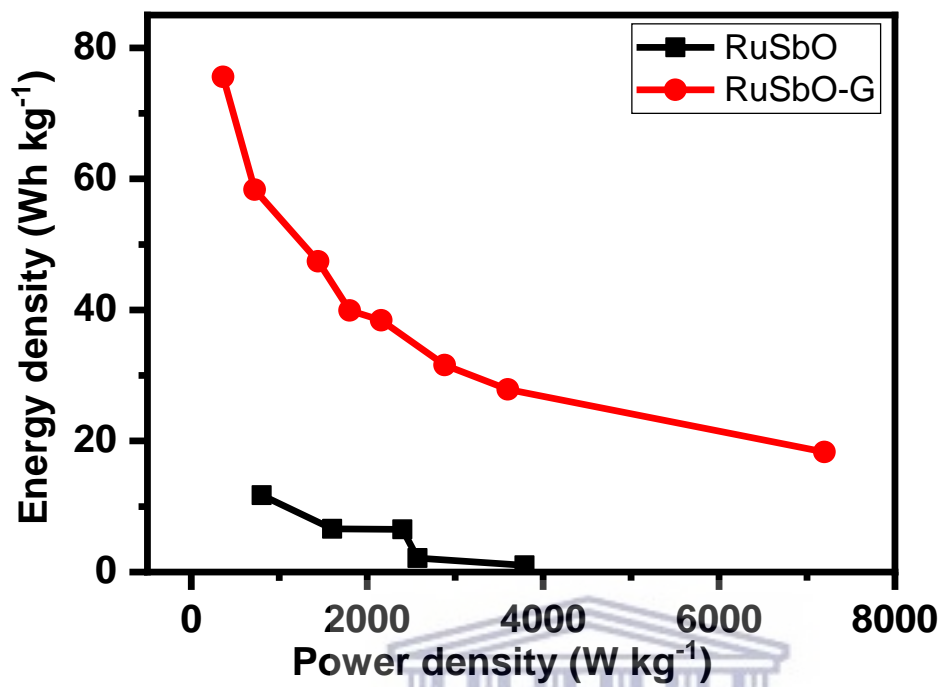
Figure 6.45: Ragone plot of RuSbO and RuSbO-G.

Table 6-6: Capacitance, ED and PD of activated carbon//RuSbO carbon device from the GCD data.

RuSbO			
Current density (A g^{-1})	Capacitance (F g^{-1})	Power density (W kg^{-1})	Energy density (W h kg^{-1})
0.2	26.09	800.00	11.74
0.4	14.67	1600.00	6.60
0.6	14.45	2400.00	6.50
0.8	8.36	3200.00	3.76
1	4.71	2571.43	2.12
2	2.27	3789.47	1.02

Table 6-7: Capacitance, ED and PD of activated carbon//RuSbO-G carbon device from the GCD data.

RuSbO-G			
Current density (A g^{-1})	Capacitance (F g^{-1})	Power density (W kg^{-1})	Energy density (W h kg^{-1})
0.1	167.96	360.00	75.58

0.2	129.71	720.00	58.37
0.4	105.39	1440.00	47.42
0.5	88.67	1800.00	39.90
0.6	85.33	2160.00	38.40
0.8	70.17	2880.00	31.58
1	61.93	3600.00	27.87
2	40.71	7200.00	18.32

6.3.4.2 Electrochemical impedance spectroscopy

Figure 6.46 is the Nyquist plot of the RuSbO and RuSbO-G asymmetric device. The in-set is the fitted equivalent circuit data, and the parameters obtained are represented in Table 6-8 below, while Figure 6.47 shows the profile for the raw and fitted data of RuSbO and RuSbO-G. It can be seen that the EIS which is primarily affected by the electrolyte is higher in the RuSbO-G (2.13 Ω) than in the RuSbO (1.3 Ω) material [77]. However, the charge-transfer resistance at the interface of the electrode and the electrolyte was very much lower for RuSbO-G (2.82 Ω) as compared to RuSbO (19.67 Ω), as can be seen in the semi-circle at the high-frequency region of the Nyquist plot. This shows that more facile charge transfer occurred between the Li^+ and SO_4^{-2} ions and the RuSbO-G [77] [78]. The presence of a defined and short Warburg area section in the RuSbO-G device when compared to the RuSbO device reveals that the ions in the electrolyte have a short and equal diffusion path length. As a result of the low charge transfer resistance and decreased

diffusion activity, relatively reversible processes can occur at the interface, which is why there are no redox peaks on the voltammogram [79]. The Bode plot from the EIS data is shown as the phase angle and total impedance plot in Figure 6.48 and Figure 6.49. The phase angle of RuSbO is 37.7° while that of the RuSbO-G device is at 61.05°. The composite indicates a more capacitive behaviour than the RuSbO device as its value is closer to 90° degrees which is the ideal phase angle for an EDLC. This further confirms the contribution of both EDLC and pseudocapacitance charge storage mechanisms in the composite material. The RuSbO material shows a greater resistance in transiting from resistive to capacitive behaviour, hence its low phase angle. The magnitude of total impedance as shown in Figure 6.49, had a value of 0.13 Ω for RuSbO, and 0.06 Ω for RuSbO-G, confirming the low resistance in the RuSbO-G as seen in the Nyquist plot and the phase angle plot.
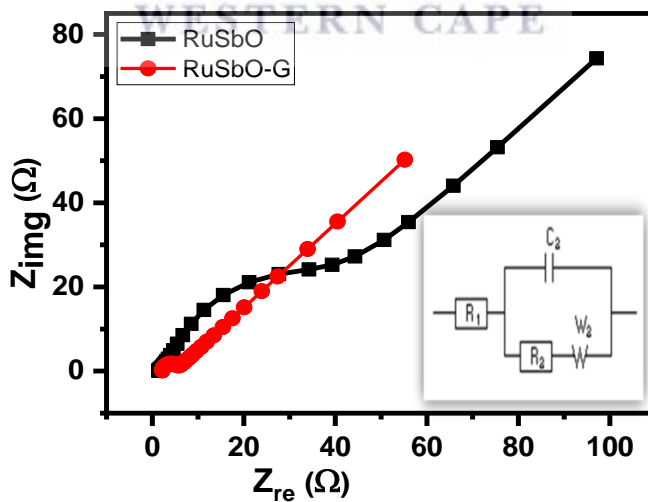
Figure 6.46: Nyquist plot of AC//RuSbO and AC//RuSbO-G electrode, the inset is the equivalent circuit.
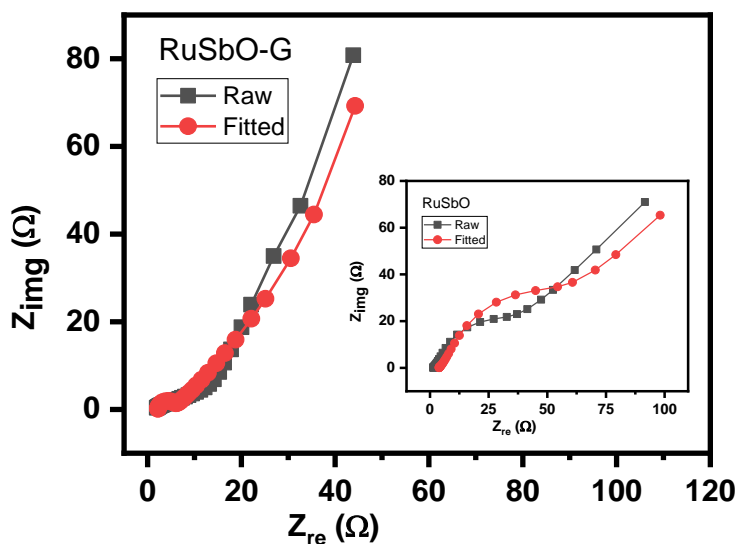
Figure 6.47: Nyquist plot of AC//RuSbO and AC//RuSbO-G electrode showing the raw and fitted data.
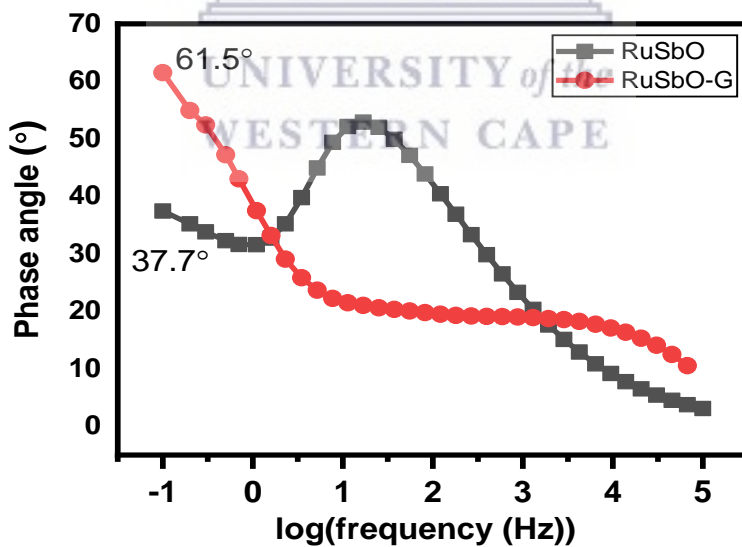
Figure 6.48: Bode plot of AC//RuSbO and AC//RuSbO-G electrode represented as a phase angle plot.
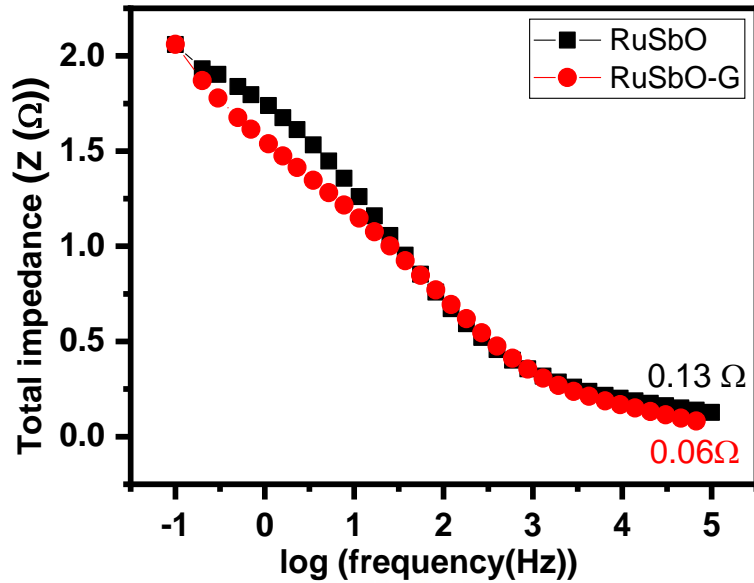
Figure 6.49: Bode plot of AC//RuSbO and RuSbO-G electrode represented as total impedance plot.

Table 6-8: EIS curve fitting data of AC//RuSbO and AC//RuSbO-G electrode material.

Electrolytes	R_s (Ω)	CPE (µF)	R_{ct} (Ω)	W^2 (Ω s- ½)	Phase angle (º)
RuSbO	1.3	149	19.67	55.99	61.5
RuSbO-G	2.13	28	2.82	39.83	37.7

6.3.4.3   Cycle life

The cycling performance of both ASC is evaluated through ~4800 CV cycles at a current density of 0.5 A g^{-1} (Figure 6.50). The ASC of RuSbO retains about 82% of its first cycle capacitance during

the test, within a voltage window of 0 to 1.8 V. A comparison of Nyquist plots before and after the cycle test (in-set) demonstrates an increase in the semi-circle area, therefore the charge transfer resistance increased during circling (Table 6-9). A similar variation of the CV plot before and after circling (in-set) implies a variation in the morphology of the material after cycling. The ASC of RuSbO-G on the other showed a better cycling performance preserving about 96% of its first cycle capacitance during the test, demonstrating a better electrode performance and electrolyte stability within the same voltage window (Figure 6.51). The curve shows an initial loss in capacitance from 0 to about 280 cycles, then an increase in capacitance until about 1800 cycles, and finally a steady capacitance for the remaining 4900 cycles. The initial rise in capacitance could be attributed to electrode material activation caused by enhanced wetting of the electrode, making it easier for hydrated ions to diffuse during cycling [80]. A comparison of Nyquist plots before and after the cycle test (in-set) demonstrates a minor change in the device's Ohmic resistance during cycling, confirming the outstanding stability of electrode materials (Table 6-9). No significant change in the shape of the voltammogram was observed, however, the area under the CV curve decreased a little, showing that the device is more stable than the RuSbO. Therefore, the addition of graphene to the RuSbO increased the stability of the material [81].
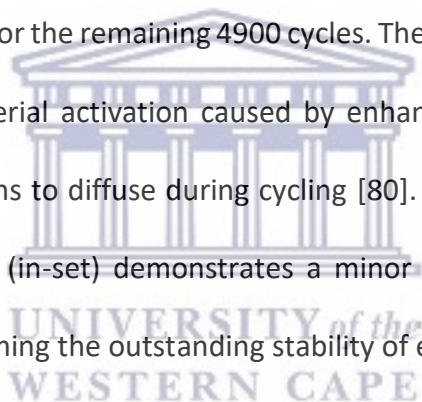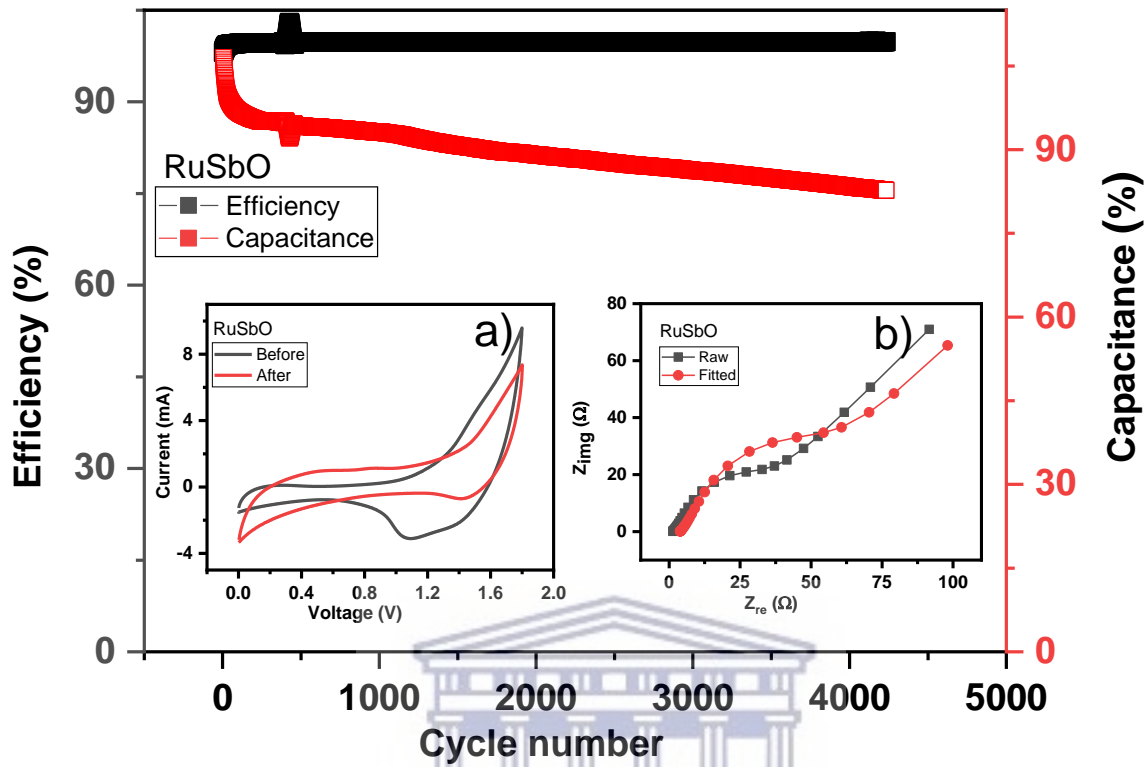
Figure 6.50 Cycling stability of AC//RuSbO supercapacitor over 4500 cycles in 1 M Li$_2$SO$_4$ the in-

set is the CV (50 mV s^{-1}) and EIS plot before and after cycling.
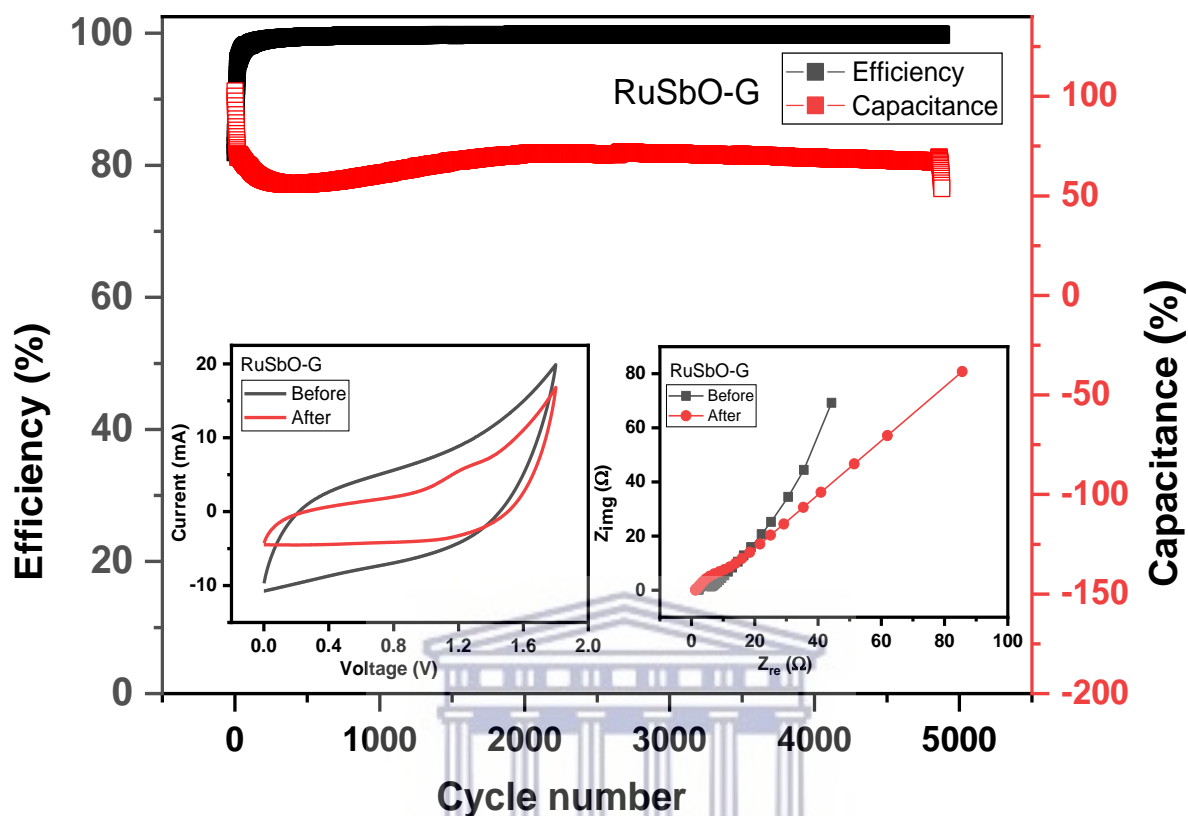
Figure 6.51: Cycling stability of AC//RuSbO supercapacitor over 4500 cycles in 1 M Li$_2$SO$_4$ the inset is the CV (50 mV s^{-1}) and EIS plot before and after cycling.

Table 6-9: EIS curve fitting data of AC//RuSbO and AC//RuSbO-G electrode material after cycling.

	RuSbO		RuSbO-G	
	R$_s$ (Ω)	R$_{ct}$ (Ω)	R$_s$ (Ω)	R$_{ct}$ (Ω)
Before	1.33	19.67	2.13	2.6

After	3.81	30.83	1.16	3.65

6.4 CONCLUSION

For the first time, RuSbO and RuSbO-G were synthesized and used as an electrode material for a supercapacitor device. The pristine material RuSbO and the composite RuSbO-G were prepared via microwave-assisted methods and were morphologically and structurally characterized to ascertain the successful synthesis of the material. The particle size of the pristine RuSbO was 37.30 nm from the XRD data, while those of RuSbO-G was 36.33 nm with an increased interlayer spacing of 0.8nm, showing successful attachment of the graphene material to the composite. Further electrochemical characterization revealed the capacitive nature of the novel material and its charge storage mechanism. In all the experiments, RuSbO-G showed better electrochemical performance than the pristine material. This is because, graphene must have acted as a dispersing agent for the RuSbO species and prevented the nanoparticles from agglomerating, thus providing better ionic pathways for the electrolyte ions, while the RuSbO nanoparticles must have acted as spacers for the graphene sheet to prevent severe agglomeration, thus harnessing the unique 2D characteristics of graphene. RuSbO-G electrode was used to fabricate an asymmetric capacitor, with a capacitance of 167.96 F g^{-1} at a current density of 0.1 A g^{-1}. 94.4% of the total capacitance was contributed by very fast surface Faradaic activities as determined by the Trassiti dominant charge storage mechanism analysis, and as revealed in the shape of its voltammogram at high and low scan rates. The composite material showed impressive cyclic stability and maintained high Columbic efficiency throughout its cycle life, owing to the mechanical stability provided by the graphene network. These studies open a new dimension for the exploration of new categories of nanomaterials particularly the antimonide based nanomaterials for supercapacitor application.

6.5 REFERENCE

[1] P.D. Wall, Scientists and the CIA, Science, 136 (1962) 173–173. https://doi.org/10.1126/science.136.3511.173.

[2] C. CLARK, World Population, Nature. 181 (1958) 1235–1236. https://doi.org/10.1038/1811235a0.

[3] I. Yang, D. Kwon, M.S. Kim, J.C. Jung, A comparative study of activated carbon aerogel and commercial activated carbons as electrode materials for organic electric double-layer capacitors, Carbon N. Y. 132 (2018) 503–511. https://doi.org/10.1016/j.carbon.2018.02.076.

[4] S. Han, F. Hou, X. Yuan, J. Liu, X. Yan, S. Chen, Continuous hierarchical carbon nanotube/reduced graphene oxide hybrid films for supercapacitors, Electrochim. Acta. 225 (2017) 566–573. https://doi.org/10.1016/j.electacta.2016.12.159.

[5] G. Wang, L. Zhang, J. Zhang, A review of electrode materials for electrochemical supercapacitors, Chem. Soc. Rev. 41 (2012) 797–828. https://doi.org/10.1039/c1cs15060j.

[6] S. Chen, R. Ramachandran, V. Mani, R. Saraswathi, Recent Advancements in Electrode Materials for the High- performance Electrochemical Supercapacitors : A Review, 9 (2014) 4072–4085.

[7] D. Galizzioli, F. Tantardini, S. Trasatti, Ruthenium dioxide: a new electrode material. I. Behaviour in acid solutions of inert electrolytes, J. Appl. Electrochem. 4 (1974) 57–67. https://doi.org/10.1007/BF00615906.

[8]   M. Ates, C. Fernandez, Ruthenium oxide–carbon-based nanofiller-reinforced conducting polymer nanocomposites and their supercapacitor applications, Polym. Bull. (2018) 1–19. https://doi.org/10.1007/s00289-018-2492-x.

[9]   Y. Guo, W. Zhang, Y. Sun, M. Dai, Ruthenium nanoparticles stabilized by mercaptan and acetylene derivatives with supercapacitor application, MethodsX. 5 (2018) 795–796. https://doi.org/10.1016/j.mex.2018.07.004.

[10]   H. Li, R. Wang, R. Cao, Physical and electrochemical characterization of hydrous ruthenium oxide/ordered mesoporous carbon composites as supercapacitor, Microporous Mesoporous Mater, 111 (2008) 32–38. https://doi.org/10.1016/j.micromeso.2007.07.002.

[11]   K.Y. Kumar, S. Archana, R. Namitha, B.P. Prasanna, S.C. Sharma, M.S. Raghu, Ruthenium oxide nanostring clusters anchored Graphene oxide nanocomposites for high-performance supercapacitors application, Mater. Res. Bull. 107 (2018) 347–354. https://doi.org/10.1016/j.materresbull.2018.08.011.

[12]   D. Rosestolato, G. Battaglin, S. Ferro, Charge-storage process of stoichiometric and nanostructured ruthenium nitride thin films, Batteries, 1 (2015) 11–21. https://doi.org/10.3390/batteries1010011.

[13]   D. Rosestolato, G. Battaglin, S. Ferro, Electrochemical properties of stoichiometric RuN film prepared by rf-magnetron sputtering: A preliminary study, Electrochem. Commun. 49 (2014) 9–13. https://doi.org/10.1016/j.elecom.2014.09.019.

[14]   S. Bouhtiyya, R. Lucio Porto, B. Laïk, P. Boulet, F. Capon, J.P. Pereira-Ramos, T. Brousse, J.F.

Pierson, Application of sputtered ruthenium nitride thin films as electrode material for energy-storage devices, Scr. Mater. 68 (2013) 659–662. https://doi.org/10.1016/j.scriptamat.2013.01.030.

[15]   R. Bolagam, S. Um, L-cysteine-assisted synthesis of ruthenium sulfide/thermally reduced graphene oxide nanocomposites: Promising electrode materials for high-performance energy storage applications, Electrochim. Acta, 281 (2018) 571–581. https://doi.org/10.1016/j.electacta.2018.06.004.

[16]   F.J. Berry, C.D. Gibbs, C. Greaves, Structural properties of the molybdenum-ruthenium telluride of composition Mo4.5Ru1.5Te8, J. Solid State Chem. 92 (1991) 148–153. https://doi.org/10.1016/0022-4596(91)90251-C.

[17]   T. Cao, Y. Shi, Y. Jiang, N. Cai, Q. Gong, Performance enhancement of liquid antimony anode fuel cell by in-situ electrochemical assisted oxidation process, Energy, 125 (2017) 526–532. https://doi.org/10.1016/j.energy.2017.02.106.

[18]   E. Martínez-Periñán, M.P. Down, C. Gibaja, E. Lorenzo, F. Zamora, C.E. Banks, Antimonene: A Novel 2D Nanomaterial for Supercapacitor Applications, Adv. Energy Mater, 8 (2018) 1–8. https://doi.org/10.1002/aenm.201702606.

[19]   V.K. Mariappan, K. Krishnamoorthy, P. Pazhamalai, S. Sahoo, S.J. Kim, Layered famatinite nanoplates as an advanced pseudocapacitive electrode material for supercapacitor applications, Electrochim. Acta, 275 (2018) 110–118. https://doi.org/10.1016/j.electacta.2018.04.126.

[20]   J. Sun, H.W. Lee, M. Pasta, H. Yuan, G. Zheng, Y. Sun, Y. Li, Y. Cui, A phosphorene-graphene

hybrid material as a high-capacity anode for sodium-ion batteries, Nat. Nanotechnol,10 (2015) 980–985. https://doi.org/10.1038/nnano.2015.194.

[21]   N.A. Luechinger, N. Booth, G. Heness, S. Bandyopadhyay, R.N. Grass, W.J. Stark, Surfactant-Free, Melt-Processable Metal-Polymer Hybrid Materials: Use of Graphene as a Dispersing   Agent,   Adv.   Mater,   20   (2008)   3044–3049. https://doi.org/10.1002/adma.200800026.

[22]   X. Wang, J. Wang, H. Cheng, P. Yu, J. Ye, L. Mao, Graphene as a spacer to layer-by-layer assemble electrochemically functionalized nanostructures for molecular bioelectronic devices, Langmuir, 27 (2011) 11180–11186. https://doi.org/10.1021/la202018r.

[23]   I.S. El-Hallag, M.N. El-Nahass, S.M. Youssry, R. Kumar, M.M. Abdel-Galeil, A. Matsuda, Facile in-situ simultaneous electrochemical reduction and deposition of reduced graphene oxide embedded palladium nanoparticles as high performance electrode materials for supercapacitor with excellent rate capability, Electrochim. Acta, 314 (2019) 124–134. https://doi.org/10.1016/j.electacta.2019.05.065.

[24]   W. Sobieski, S. Lipiński, The influence of particle size distribution on parameters characterizing the spatial structure of porous beds, Granul. Matter, 21 (2019) 1–15. https://doi.org/10.1007/s10035-019-0866-x.

[25]   N. Ouchlyama, T. Tanaka, Porosity estimation from particle size distribution, Ind. Eng. Chem. Fundam. 25 (1986) 125–129. https://doi.org/10.1021/i100021a019.

[26]   S. Prasad, G. Durai, D. Devaraj, M.S. AlSalhi, J. Theerthagiri, P. Arunachalam, M. Gurulakshmi, M. Raghavender, P. Kuppusami, 3D nanorhombus nickel nitride as stable and

cost-effective counter electrodes for dye-sensitized solar cells and supercapacitor applications, RSC Adv. 8 (2018) 8828–8835. https://doi.org/10.1039/c8ra00347e.

[27] B. Francis Ntumba Muya, S. Africa Supervisor Priscilla Baker Co-supervisor Emmanuel Iwuoha, Hydrogel encapsulated biosensors for the detection of biologically significant vanadium and selenium, (2017). http://etd.uwc.ac.za/ (accessed October 27, 2021).

[28] E. Antolini, F. Cardellini, Formation of carbon supported PtRu alloys: An XRD analysis, J. Alloys Compd. 315 (2001) 118–122. https://doi.org/10.1016/S0925-8388(00)01260-3.

[29] A.S. Patil, J.L. Gunjakar, C.D. Lokhande, U.M. Patil, S. V. Sadavar, N.S. Padalkar, R.B. Shinde, M.M. Wagh, J.S. Bagi, Nanocrystalline copper-chromium-layered double hydroxide with tunable interlayer anions for electrochemical capacitor application, Synth. Met. 264 (2020) 116371. https://doi.org/10.1016/J.SYNTHMET.2020.116371.

[30] R.S. Rajaura, S. Srivastava, V. Sharma, P.K. Sharma, C. Lal, M. Singh, H.S. Palsania, Y.K. Vijay, Role of interlayer spacing and functional group on the hydrogen storage properties of graphene oxide and reduced graphene oxide, Int. J. Hydrogen Energy, 41 (2016) 9454–9461. https://doi.org/10.1016/J.IJHYDENE.2016.04.115.

[31] P.R. Deshmukh, S.N. Pusawale, A.D. Jagadale, C.D. Lokhande, Supercapacitive performance of hydrous ruthenium oxide ($RuO_2 \cdot nH_2O$) thin films deposited by SILAR method, J. Mater. Sci. 2011 473. 47 (2011) 1546–1553. https://doi.org/10.1007/S10853-011-5946-1.

[32] W. Xu, H. Wang, R. Liu, X. Zhao, J. Qu, The mechanism of antimony(III) removal and its reactions on the surfaces of Fe–Mn Binary Oxide, J. Colloid Interface Sci. 363 (2011) 320–

326. https://doi.org/10.1016/J.JCIS.2011.07.026.

[33] N. B., V. Y., S. Abdul Razack, Enhanced formation of ruthenium oxide nanoparticles through green synthesis for highly efficient supercapacitor applications, Adv. Powder Technol. 31 (2020) 1001–1006. https://doi.org/10.1016/J.APT.2019.12.026.

[34] B. Liu, M. Jian, H. Wang, G. Zhang, R. Liu, X. Zhang, J. Qu, Comparing adsorption of arsenic and antimony from single-solute and bi-solute aqueous systems onto ZIF-8, Colloids Surfaces A Physicochem. Eng. Asp. 538 (2018) 164–172. https://doi.org/10.1016/J.COLSURFA.2017.10.068.

[35] H. Li, M. Sztukowska, H. Liu, H. Dong, D. Małaszkiewicz, H. Zhang, X. Wang, Infrared barriering behavior of reduced graphene oxide aerogel/ antimony tin oxide-polyaniline hybrids, Ceram. Int. 46 (2020) 10971–10978. https://doi.org/10.1016/J.CERAMINT.2020.01.112.

[36] X. Zhang, X. Chen, C. Chen, T. Liu, M. Liu, C. Zhang, T. Huang, A. Yu, Ruthenium oxide modified hierarchically porous boron-doped graphene aerogels as oxygen electrodes for lithium-oxygen batteries, RSC Adv. 8 (2018) 39829–39836. https://doi.org/10.1039/C8RA08763F.

[37] H.K. Hassan, N.F. Atta, M.M. Hamed, A. Galal, T. Jacob, Ruthenium nanoparticles-modified reduced graphene prepared by a green method for high-performance supercapacitor application in neutral electrolyte, RSC Adv. 7 (2017) 11286–11296. https://doi.org/10.1039/c6ra27415c.

[38] S. Wolff, S. Roscher, F. Timmermann, M. V Daniel, F. Speck, M. Wanke, M. Albrecht, T.

Seyller, Quasi-Freestanding Graphene on SiC(0001) by Ar-Mediated Intercalation of Antimony: A Route Toward Intercalation of High-Vapor-Pressure Elements, Ann. Phys. 531 (2019). https://doi.org/10.1002/andp.201900199.

[39] I. Martini, E. Chevallay, V. Fedosseev, C. Hessler, H. Neupert, V. Nistor, M. Taborelli, Surface characterization at CERN of photocathodes for photoinjector applications, in: 6th Int. Part. Accel. Conf. IPAC 2015, 2015: pp. 1703–1705. http://xpssimplified.com/periodictable.ph (accessed November 11, 2021).

[40] Y. Lin, Z. Tian, L. Zhang, J. Ma, Z. Jiang, B.J. Deibert, R. Ge, L. Chen, Chromium-ruthenium oxide solid solution electrocatalyst for highly efficient oxygen evolution reaction in acidic media, Nat. Commun. 10 (2019) 1–13. https://doi.org/10.1038/s41467-018-08144-3.

[41] M. Assebban, C. Gibaja, M. Fickert, I. Torres, E. Weinreich, S. Wolff, R. Gillen, J. Maultzsch, M. Varela, S. Tan Jun Rong, K.P. Loh, E.G. Michel, F. Zamora, G. Abellán, Unveiling the oxidation behavior of liquid-phase exfoliated antimony nanosheets, 2D Mater. 7 (2020). https://doi.org/10.1088/2053-1583/ab755e.

[42] N.E. Drewett, I.M. Aldous, J. Zou, L.J. Hardwick, In situ Raman spectroscopic analysis of the lithiation and sodiation of antimony microparticles, Electrochim. Acta, 247 (2017) 296–305. https://doi.org/10.1016/j.electacta.2017.07.030.

[43] T.K. Das, S. Banerjee, M. Pandey, B. Vishwanadh, R.J. Kshirsagar, V. Sudarsan, Effect of surface functional groups on hydrogen adsorption properties of Pd dispersed reduced graphene oxide, Int. J. Hydrogen Energy. 42 (2017) 8032–8041. https://doi.org/10.1016/j.ijhydene.2016.12.024.

[44] F.T. Johra, J.W. Lee, W.G. Jung, Facile and safe graphene preparation on solution based platform, J. Ind. Eng. Chem. 20 (2014) 2883–2887. https://doi.org/10.1016/j.jiec.2013.11.022.

[45] Y. Guo, W. Zhang, Y. Sun, M. Dai, Ruthenium nanoparticles stabilized by mercaptan and acetylene derivatives with supercapacitor application, Electrochim. Acta. 270 (2018) 284–293. https://doi.org/10.1016/j.electacta.2018.03.037.

[46] H. Xue, K. Chen, Q. Zhou, D. Pan, Y. Zhang, Y. Shen, Antimony selenide/graphene oxide composite for sensitive photoelectrochemical detection of DNA methyltransferase activity, J. Mater. Chem. B. 7 (2019) 6789–6795. https://doi.org/10.1039/c9tb01541h.

[47] Y. Guo, Z. Li, Y. Xia, Y. Wei, J. Zhang, Y. Wang, H. He, Facile synthesis of ruhtenium nanoparticles capped by graphene and thiols for high-performance supercapacitors, Electrochim. Acta, 391 (2021) 138990. https://doi.org/10.1016/j.electacta.2021.138990.

[48] Y. Guo, Y. Wu, R. Cao, S. Zheng, Y. Yang, M. Chen, Platinum nanoparticles functionalized with acetylene derivatives and the influence of ligand length on their electrocatalytic activity, J. Electroanal. Chem. 785 (2017) 159–165. https://doi.org/10.1016/j.jelechem.2016.12.035.

[49] Z. Sun, H. Chang, Graphene and Graphene-like Two-Dimensional Materials in Photodetection: Mechanisms and Methodology, ACS Nano, 8 (2014) 4133–4156. https://doi.org/10.1021/NN500508C.

[50] S. Akshatha, S. Sreenivasa, K.Y. Kumar, S. Archana, M.K. Prashanth, B.P. Prasanna, P. Chakraborty, P. Krishnaiah, M.S. Raghu, H. Alrobei, Rutile, mesoporous ruthenium oxide

decorated graphene oxide as an efficient visible light driven photocatalyst for hydrogen evolution reaction and organic pollutant degradation, Mater. Sci. Semicond. Process, 116 (2020) 105156. https://doi.org/10.1016/j.mssp.2020.105156.

[51]   F. El-Tantawy, A.A. Al-Ghamdi, A.A. Al-Ghamdi, Y.A. Al-Turki, A. Alshahrie, F. Al-Hazmi, O.A. Al-Hartomy, Optical properties of nanostructured ruthenium dioxide thin films via sol–gel approach, J. Mater. Sci. Mater. Electron. 28 (2017) 52–59. https://doi.org/10.1007/s10854-016-5491-4.

[52]   P. Molaei, I. Kazeminezhad, Extended photocurrent performance of antimony trisulfide/reduced graphene oxide composite prepared via a facile hot-injection route, Ceram. Int. 44 (2018) 13191–13196. https://doi.org/10.1016/j.ceramint.2018.04.144.

[53]   R. Vinoth, S.G. Babu, V. Bharti, V. Gupta, M. Navaneethan, S.V. Bhat, C. Muthamizhchelvan, P.C. Ramamurthy, C. Sharma, D.K. Aswal, Y. Hayakawa, B. Neppolian, Ruthenium based metallopolymer grafted reduced graphene oxide as a new hybrid solar light harvester in polymer solar cells, Sci. Rep. 7 (2017) 1–14. https://doi.org/10.1038/srep43133.

[54]   R. Mondal, K. Sarkar, S. Dey, D. Majumdar, S.K. Bhattacharya, P. Sen, S. Kumar, Magnetic, pseudocapacitive, and H_2O_2-electrosensing properties of self-assembled superparamagnetic Co0.3Zn0.7Fe$_2$O$_4$ with enhanced saturation magnetization, ACS Omega. 4 (2019) 12632–12646. https://doi.org/10.1021/acsomega.9b01362.

[55]   G. Chen, S. Wu, L. Hui, Y. Zhao, J. Ye, Z. Tan, W. Zeng, Z. Tao, L. Yang, Y. Zhu, Assembling carbon quantum dots to a layered carbon for high-density supercapacitor electrodes, Sci. Rep. 6 (2016) 1–9. https://doi.org/10.1038/srep19028.

[56] A.M. Teli, S.A. Beknalkar, S.A. Pawar, D.P. Dubal, E ff ect of Concentration on the Charge Storage Kinetics, Energies, 13 (2020) 6124.

[57] D. Zhang, S. Xu, R. Wan, Y. Yang, R. He, Functionalized graphene oxide cross-linked poly(2,6-dimethyl-1,4-phenylene oxide)-based anion exchange membranes with superior ionic conductivity, J. Power Sources, 517 (2022) 230720. https://doi.org/10.1016/J.JPOWSOUR.2021.230720.

[58] Z. Li, Y. Mi, X. Liu, S. Liu, S. Yang, J. Wang, Flexible graphene/MnO_2 composite papers for supercapacitor electrodes, J. Mater. Chem. 21 (2011) 14706–14711. https://doi.org/10.1039/c1jm11941a.

[59] H.L. Girard, H. Wang, A.L. D'Entremont, L. Pilon, Enhancing Faradaic Charge Storage Contribution in Hybrid Pseudocapacitors, Electrochim. Acta, 182 (2015) 639–651. https://doi.org/10.1016/j.electacta.2015.09.070.

[60] B.J. Choudhury, K. Roy, V.S. Moholkar, Improvement of Supercapacitor Performance through Enhanced Interfacial Interactions Induced by Sonication, Ind. Eng. Chem. Res. 60 (2021) 7611–7623. https://doi.org/10.1021/acs.iecr.1c00279.

[61] J. Shen, J. Wu, L. Pei, M.T.F. Rodrigues, Z.Q. Zhang, F. Zhang, X. Zhang, P.M. Ajayan, M. Ye, $CoNi_2S_4$-Graphene-2D-$MoSe_2$ as an Advanced Electrode Material for Supercapacitors, Adv. Energy Mater, 6 (2016) 1–8. https://doi.org/10.1002/aenm.201600341.

[62] V. Venezlan, " INNER " AND " OUTER " ACTIVE SURFACE ELECTRODES OF RuO , (1989) 5–9.

[63] T. Wang, H.C. Chen, F. Yu, X.S. Zhao, H. Wang, Boosting the cycling stability of transition

metal compounds-based supercapacitors, Energy Storage Mater, 16 (2019) 545–573. https://doi.org/10.1016/j.ensm.2018.09.007.

[64] M. Guo, L. Ye, L. Zhao, Solid-state-grinding method to synthesize NiCoFe alloy/NiCoFe–OH nanosheets for asymmetric supercapacitor, J. Alloys Compd. 850 (2021) 156787. https://doi.org/10.1016/j.jallcom.2020.156787.

[65] E.E. Mathew, M. Balachandran, Crumpled and porous graphene for supercapacitor applications: a short review, Carbon Lett. 31 (2021) 537–555. https://doi.org/10.1007/s42823-021-00229-2.

[66] J. Yan, T. Wei, W. Qiao, B. Shao, Q. Zhao, L. Zhang, Z. Fan, Rapid microwave-assisted synthesis of graphene nanosheet/Co_3O_4 composite for supercapacitors, Electrochim. Acta. 55 (2010) 6973–6978. https://doi.org/10.1016/j.electacta.2010.06.081.

[67] T. Pettong, P. Iamprasertkun, A. Krittayavathananon, P. Sukha, P. Sirisinudomkit, A. Seubsai, M. Chareonpanich, P. Kongkachuichay, J. Limtrakul, M. Sawangphruk, High-Performance Asymmetric Supercapacitors of $MnCo_2O_4$ Nanofibers and N-Doped Reduced Graphene Oxide Aerogel, ACS Appl. Mater. Interfaces, 8 (2016) 34045–34053. https://doi.org/10.1021/acsami.6b09440.

[68] C. Wang, J. Zhao, S. Luo, X. Yu, Improved Pseudocapacitive Performance of Graphene Architectures Modulating by Nitrogen/Phosphorus Dual-Doping and Steam-Activation, Macromol. Res. 29 (2021) 582–588. https://doi.org/10.1007/s13233-021-9075-7.

[69] M. Dvoyashkin, D. Leistenschneider, J.D. Evans, M. Sander, L. Borchardt, Revealing the Impact of Hierarchical Pore Organization in Supercapacitor Electrodes by Coupling Ionic

Dynamics at Micro- and Macroscales, Adv. Energy Mater. 11 (2021) 2100700. https://doi.org/10.1002/aenm.202100700.

[70]   Q. Xue, H. Gan, Y. Huang, M. Zhu, Z. Pei, H. Li, S. Deng, F. Liu, C. Zhi, Boron Element Nanowires Electrode for Supercapacitors, Adv. Energy Mater, 8 (2018) 1–8. https://doi.org/10.1002/aenm.201703117.

[71]   A. Noori, M.F. El-kady, M.S. Rahmanifar, R.B. Kaner, M.F. Mousavi, Chem Soc Rev metrics for batteries , supercapacitors and beyond, Chem. Soc. Rev. (2019). https://doi.org/10.1039/c8cs00581h.

[72]   D. Qu, Studies of the activated mesocarbon microbeads used in double-layer supercapacitors, J. Power Sources. 109 (2002) 403–411.

[73]   D. Mandal, P. Routh, A.K. Mahato, A.K. Nandi, Electrochemically modified graphite paper as an advanced electrode substrate for supercapacitor application, J. Mater. Chem. A. 7 (2019) 17547–17560. https://doi.org/10.1039/c9ta04496e.

[74]   Y. Gong, D. Li, Q. Fu, C. Pan, Influence of graphene microstructures on electrochemical performance for supercapacitors, Prog. Nat. Sci. Mater. Int. 25 (2015) 379–385. https://doi.org/10.1016/j.pnsc.2015.10.004.

[75]   H. Wei, C. He, J. Liu, H. Gu, Y. Wang, X. Yan, J. Guo, D. Ding, N.Z. Shen, X. Wang, S. Wei, Z. Guo, Electropolymerized polypyrrole nanocomposites with cobalt oxide coated on carbon paper for electrochemical energy storage, Polymer (Guildf), 67 (2015) 192–199. https://doi.org/10.1016/J.POLYMER.2015.04.064.

[76]   A.G. Pandolfo, A.F. Hollenkamp, Carbon properties and their role in supercapacitors, J.

Power Sources. 157 (2006) 11–27. https://doi.org/10.1016/j.jpowsour.2006.02.065.

[77]   D. Mandal, P. Routh, A.K. Mahato, A.K. Nandi, Electrochemically modified graphite paper as an advanced electrode substrate for supercapacitor application, J. Mater. Chem. A. 7 (2019) 17547–17560. https://doi.org/10.1039/c9ta04496e.

[78]   K. Yang, K. Cho, S. Kim, Effect of carbon black addition on thermal stability and capacitive performances of supercapacitors, Sci. Rep. 8 (2018) 1–7. https://doi.org/10.1038/s41598-018-30507-5.

[79]   N. Bundaleska, J. Henriques, M. Abrashev, A.M. Botelho do Rego, A.M. Ferraria, A. Almeida, F.M. Dias, E. Valcheva, B. Arnaudov, K.K. Upadhyay, M.F. Montemor, E. Tatarova, Large-scale synthesis of free-standing N-doped graphene using microwave plasma, Sci. Rep. 8 (2018) 1–11. https://doi.org/10.1038/s41598-018-30870-3.

[80]   P. Tamilarasan, S. Ramaprabhu, Ionic liquid-functionalized partially exfoliated multiwalled carbon nanotubes for high-performance supercapacitors, J. Mater. Chem. A. 2 (2014) 14054–14063. https://doi.org/10.1039/c4ta02718c.

[81]   M. Ciszewski, A. Mianowski, G. Nawrat, P. Szatkowski, Reduced Graphene Oxide Supported Antimony Species for High-Performance Supercapacitor Electrodes, ISRN Electrochem. 2014 (2014) 1–7. https://doi.org/10.1155/2014/826832.

CHAPTER SEVEN

## 7.1 CONCLUSION AND RECOMMENDATION

7.1.1 SUMMARY OF MAIN THESIS FINDINGS

Materials with nanostructures, often show exceptional electronic, magnetic, optical, thermal, mechanical, and physical properties, holding great potential for a wide spectrum of applications. This project entails the development of various nanoparticles as well as their use in supercapacitors via microwave-assisted methods. The nanomaterials investigated in this research include ruthenium oxide (RuO), antimony oxide (SbO) ruthenium oxide-graphene (RuO-G), antimony oxide graphene (SbO-G), ruthenium antimony oxide (RuSbO) and ruthenium antimony oxide graphene (RuSbO-G). Scanning and transmission electron microscopy, X-ray diffraction, and Fourier transform infrared were used to investigate the morphological, structural, and spectroscopic properties of the various nanostructures. Cyclic voltammetry, electrochemical impedance spectroscopy, and galvanostatic charge-discharge experiments were used to determine electrochemical properties. The energy storage capacitance of the various nanostructured electrodes was investigated as an individual and as a composite electrode for a supercapacitor device. The study's most important results are described below.

RuO and RuO-G nanoparticle with particle sizes of ~5-10 nm was tested as electrode material in an asymmetric supercapacitor device with activated carbon (RuO//AC and RuO-G//AC). The asymmetric Cs cell delivered a maximum energy density of 1.41 W h kg^{-1} at a power density of 360 W kg^{-1} at 0.1 A g^{-1} current density for RuO, while RuO-G delivered an energy density of 3.98

W h kg^{-1} at a power density of 360 W kg^{-1} at the same current density. The maximum energy density of RuO-G was 5.29 W h kg^{-1} at a power density of 180 W kg^{-1} at 0.05 A g^{-1}. The energy density and power density were enhanced by the addition of graphene which led to increased surface area for charge-discharge.

SbO and SbO-G nanoparticle with particle sizes of 10-50 nm was tested as electrode material in an asymmetric supercapacitor device with activated carbon (SbO//AC and SbO-G//AC). The asymmetric Cs cell delivered a maximum energy density of 2.52 W h kg^{-1} at a power density of 720 W kg^{-1} at 0.2 A g^{-1} current density for SbO, while SbO-G delivered an energy density of 14.80 W h kg^{-1} at a power density of 360 W kg^{-1} at the same current density. The energy density and power density were enhanced by the addition of graphene which led to increased surface area for charge-discharge.
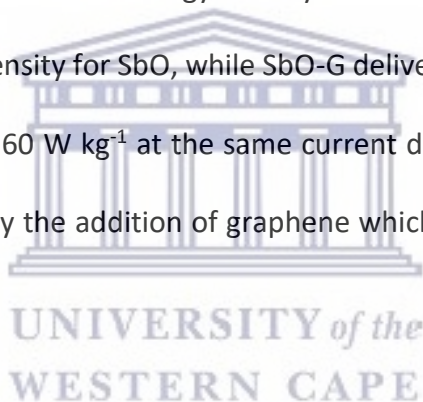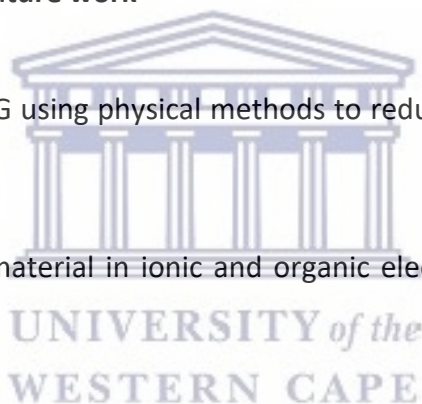
Finally, RuSbO and RuSbO-G nanoparticles with particle sizes of 10-50 nm. Both materials were first characterized in a three-electrode cell setup and their electrochemical properties were compared to establish their suitability for energy storage purposes. Their dominating energy storage mechanism was also analyzed by looking into the kinetics of the electrochemical processes. Subsequently, the RuSbO and RuSbO-G electrode was tested as electrode material in an asymmetric supercapacitor device with activated carbon (SbO//AC and SbO-G//AC). The device-specific capacitance reached a maximum energy density of 2.52 W h kg^{-1}, at a power density of 720 W kg^{-1} at 0.2 A g^{-1} current density for RuSbO, while RuSbO-G delivered an energy

density of 14.80 W h kg^{-1} at a power density of 360 W kg^{-1} at the same current density. The efficiency and capacitance of the supercapacitor with RuSbO-G//AC electrode were maintained at 100% throughout 4900 cycles. The various nanostructured electrode materials developed and studied, revealed good electrochemical efficiency, and cycling stability, as supercapacitors electrodes. This study, therefore, provides new research information on antimony-based materials as an energy storage material for supercapacitors.

7.1.2 Recommendations for Future work

- Synthesis of RuSbO and RuSbO-G using physical methods to reduce agglomeration and provide better ionic pathway.

- Electrochemical testing of the material in ionic and organic electrolytes for maximum energy density.

- The use of spectroelectrochemical experiments to better understand the charge storage mechanism of the material.

- Computational analysis of materials using density functional theory to determine the structural formation and electron movement plus material bonding and quantum capacitance.

400